

Suspensions de particules cisaillées à bas nombre de Reynolds : micro-hydrodynamique, dispersion et mélange

Bloen Metzger

▶ **To cite this version:**

Bloen Metzger. Suspensions de particules cisaillées à bas nombre de Reynolds : micro-hydrodynamique, dispersion et mélange. Mécanique des fluides [physics.class-ph]. aix marseille université, 2018. ⟨tel-01768661⟩

HAL Id: tel-01768661

https://hal.science/tel-01768661v1

Submitted on 17 Apr 2018

HAL is a multi-disciplinary open access archive for the deposit and dissemination of scientific research documents, whether they are published or not. The documents may come from teaching and research institutions in France or abroad, or from public or private research centers.

L'archive ouverte pluridisciplinaire **HAL**, est destinée au dépôt et à la diffusion de documents scientifiques de niveau recherche, publiés ou non, émanant des établissements d'enseignement et de recherche français ou étrangers, des laboratoires publics ou privés.



HAL Authorization

UNIVERSITÉ d'AIX-MARSEILLE
Laboratoire IUSTI CNRS UMR 7343

Mémoire présenté pour l'obtention de

$\star\star\star$

L'HABILITATION À DIRIGER DES RECHERCHES

$\star\star\star$

Par

Bloen Metzger

Suspensions de particules cisaillées à bas nombre de Reynolds : micro-hydrodynamique, dispersion et mélange

---

Soutenue le 4 avril 2018 devant le jury composé de :

Elisabeth Lemaire	Rapporteur
Emmanuelle Gouillart	Rapporteur
Eric Clément	Rapporteur
Cathy Castelain	Examinatrice
Marc Médale	Examinateur
Emmanuel Villermaux	Examinateur

Table des matières

1 Introduction générale **1**

2 Microhydrodynamique des suspensions cisaillées **3**
2.1 Introduction et problématique . . . 3
2.2 Un modèle minimal pour décrire les suspensions cisaillées . . . 7
2.2.1 Rôle des interactions hydrodynamiques longues portées . . . 7
2.2.2 Rôle des forces de lubrification . . . 9
2.3 Les contacts à l'origine de la diffusion induite par cisaillement . . . 11
2.3.1 Nuage de particules dans un cisaillement oscillant . . . 11
2.3.2 Evidence directe du contact solide . . . 12
2.3.3 Origine de l'amplitude critique de déformation . . . 13
2.3.4 Effet de la rugosité sur la diffusion induite par cisaillement . . . 15
2.4 Conclusion . . . 16

3 Dispersion et mélange au sein des suspensions cisaillées **21**
3.1 Introduction et problématique . . . 21
3.2 Intensification du transfert de chaleur . . . 22
3.3 Dispersion du fluide interstitiel . . . 22
3.3.1 L'expérience de Taylor revisitée . . . 22
3.3.2 "Rolling-coating" en proche paroi . . . 24
3.4 Lois d'étirement : conséquences pour le mélange . . . 26
3.5 conclusion . . . 28

4 Perspectives **29**
4.1 Micro-hydodynamique des suspensions cisaillées : . . . 29
4.1.1 Migration . . . 29
4.1.2 Diffusion induite par cisaillement : cas des suspensions polydisperses . . . 30
4.1.3 Le rheo-épaississement : une transition frictionnelle ? . . . 30
4.2 Mélange . . . 33
4.2.1 Evolution des distributions de concentration dans les suspensions cisaillées . . . 33
4.2.2 Mélange dans les milieux poreux . . . 34

5 Curriculum vitæ **37**

6 Articles **45**
6.1 Micro-hydrodynamique des suspensions cisaillées . . . 45
6.2 Dispersion et mélange . . . 98
6.3 Autres articles . . . 174

Bibliographie **241**

CHAPITRE 1

Introduction générale

Ce mémoire d'habilitation présente un résumé des travaux de recherche que j'ai menés depuis mon recrutement au CNRS en 2007 comme chargé de recherche au sein du laboratoire IUSTI à Marseille. Ces travaux sont centrés sur le comportement des suspensions non-Browniennes et non-inertielles soumises à un cisaillement. Ces systèmes, du fait de la présence de particules immergées au sein du fluide, se singularisent des fluides homogènes par l'apparition spontanée de fluctuations de vitesse. Comprendre l'origine de ces fluctuations et leurs conséquences sur la dispersion et le mélange d'un scalaire (chaleur et masse) sont les deux thématiques principales que je développerai dans ce manuscript.

Le premier chapitre porte sur la microhydrodynamique des suspensions non-Browniennes et non-inertielles soumises à un cisaillement. Une question majeure est de comprendre l'origine des fluctuations qui s'y développent et en particulier, d'élucider le rôle joué par les contacts solides entre particules dans ce phénomène. Nous présenterons notre contribution aux avancées récentes dans ce domaine qui a fortement évolué au cours de ces dix dernières années. En particulier, je décrirai le modèle numérique minimal que nous avons développé au cours de la thèse de P. Phong en collaboration avec J. Butler de l'université de Floride, ainsi que les expériences qui nous ont permis de mettre en évidence le rôle prépondérant des interactions de contact.

Le chapitre 2 est dédié à l'étude d'un nouveau mode d'intensification des transferts. Comme la tortuosité des parois dans les milieux poreux ou la présence d'inertie dans les écoulements turbulents, la présence des particules au sein des suspension cisaillées, en dispersant la phase fluide, induit une accélération du processus de mélange. Bien que très peu étudié, ce mécanisme d'intensification des transferts semble d'autant plus important qu'il apparaît spontanément à bas nombre de Reynolds, conditions d'écoulement particulièrement désavantageuse vis à vis du mélange. Notre objectif est d'étudier cette intensification dans le cas du transfert de chaleur, projet qui a bénéficié du soutien d'une ANR jeune Chercheur. J'ai ensuite élargi cette activité au transfert de masse (thèse de M. Souzy) afin de visualiser et de caractériser, à l'échelle de la taille des particules, les processus à l'origine de cette intensification.

Ce manuscript se termine par des perspectives (chapitre 3), où je présente les orientations que je souhaite donner à mes activités de recherche. Il est complété par un curriculum vitæ (chapitre 4) où figure ma liste de publications et le détail de mes activités de recherche. Enfin, le chapitre 5 reproduit l'ensemble de mes publications post-thèse.

Par souci de cohérence, ce manuscript ne présente que le résumé des travaux directement en lien avec la microhydrodynamique des suspensions cisailléees et avec la problématique de mélange dans ces systèmes. Les autres travaux que j'ai pu mener, notamment sur la rhéologie des milieux granulaires, ne seront pas détaillés ; ces travaux sont néanmoins consultables dans leur version intégrale au chapitre 6.

Les travaux présentés dans ce mémoire ont bénéficié de nombreuses collaborations, d'étudiants en stage de master et d'école d'ingénieur, du travail de thèse de Pham Phong et de Mathieu Souzy. Pour chaque étude, le lecteur trouvera la liste des personnes impliquées en tête de chapitre.

CHAPITRE 2

Microhydrodynamique des suspensions cisaillées

2.1 Introduction et problématique

Dans l'ensemble de ce manuscript, l'objet d'étude sont les suspensions constituées de particules sphériques, monodisperses et rigides, immergées dans un fluide Newtonien et suffisamment visqueux afin que tout effet inertiel puisse être négligé. Ce type de suspension, qui constitue une idéalisation des suspensions que l'on rencontre partout aussi bien dans l'industrie (bétons, pâte à papier, peintures) que dans la nature (torrent de boue, écoulement sanguin, colonie de bactéries), résiste toujours, malgré sa simplicité, à la compréhension des chercheurs. Phénomènes de migration, diffusion athermique des particules, rhéologie complexe, contraintes normales... tels sont les comportements fascinants que l'on rencontre dans ce type de système. Bien que des progrès majeurs ont été réalisé dans leur compréhension, des questions fondamentales persistent et divisent la communauté, en particulier celui du rôle des contacts entre particules. Peut-on décrire les suspensions par une approche 'purement hydrodynamique', où les particules n'interagiraient qu'au travers du fluide ou, doit on considérer l'effet des interactions de contact solide entre particules ? Cette question, aussi élémentaire qu'elle puisse paraître, fait l'objet de débat et conduit, en fonction de la réponse qu'on lui donne, à des interprétations très différentes de certains phénomènes. C'est dans ce contexte, que j'ai commencé à m'intéresser au comportement fluctuant des particules au sein des suspensions de particules cisaillées. Dans ce chapitre, afin de clarifier quelles sont les interactions élémentaires dominantes pour décrire ces systèmes, je mets en perspective le comportement des suspensions cisaillées avec celui des suspensions en sédimentation.

Mouvement d'une particule dans un fluide visqueux

Une particule en sédimentation : Le problème d'une particule sphérique de rayon a tombant à $Re = 0$ dans un fluide Newtonien a complètement été résolu par Stokes en 1851 [51]. La mouvement de la particule sous l'action de la gravité induit dans le fluide une perturbation d'écoulement qui, au premier ordre, est donnée par le Stokeslet,

$$\mathbf{u}(\mathbf{r}) = \frac{\mathbf{F}}{8\pi\mu}(\frac{\mathbf{I}}{r} + \frac{\mathbf{rr}}{r^3}), \tag{2.1}$$

où r est la distance au centre de la particule, $\mathbf{F} = 4\pi a^3/3(\rho_p - \rho)\mathbf{g}$ est la force de gravité avec ρ_p et ρ qui représentent respectivement la densité de la particule et celle du fluide. La perturbation d'écoulement induite est représenté sur la figure 2.1a : le fluide est poussé à l'avant de la sphère le long de lignes de courant divergentes et il est ramené à l'arrière de façon symétrique. Comme on le verra par la suite, le point important est que l'amplitude de cette perturbation d'écoulement décroît lentement comme r^{-1} .

Une Particle dans un cisaillement simple : Dans un écoulement de cisaillement simple, lorsque la densité du fluide est la même que celle de la particule, une sphère isolée ne génère pas de Stokeslet car aucune force extérieure n'est appliquée à la sphère. Cependant, la non-déformabilité de la sphère induit une perturbation d'écoulement qui est

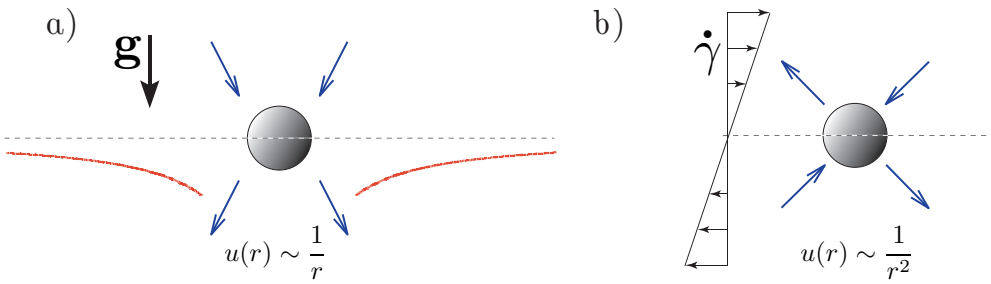


FIGURE 2.1 – Premier ordre de la perturbation d'écoulement généré a) par la chute d'une sphère dans un fluide visqueux : Stokeslet, b) par une particule sphérique dans un cisaillement linéaire : Stresslet.

donné au premier ordre par le Stresslet. Le champ d'écoulement correspondant, qui est représenté schématiquement sur la figure 2.1b, s'écrit

$$\mathbf{u}(\mathbf{r}) = -\frac{3\mathbf{S}}{8\pi\mu}\left(\frac{\mathbf{rrr}}{r^5}\right), \tag{2.2}$$

où $\mathbf{S} = 20\pi\mu a^3\mathbf{E}/3$ avec $\mathbf{E}$ le tenseur de déformation. Cette fois l'amplitude de déformation décroît comme r^{-2}.

Dynamique collective et fluctuations

Cas de la sédimentation : La lente décroissance du Stokeslet a des conséquences importantes lorsque l'on considère la dynamique collective d'un grand nombre de particules en sédimentation dans un fluide visqueux. En effet, la trajectoire de chute verticale de chaque particule est déviée par l'ensemble des perturbations d'écoulement générées par les autres particules même lorsqu'elles sont relativement éloignées les unes des autres. La sédimentation de particules fait ainsi partie des problèmes à N-corps, comme les planètes en interaction gravitaire, ou les gaz d'électrons. Ici, la lente décroissance des interactions hydrodynamiques couple la dynamique de l'ensemble des particules du système et génère des comportements complexes. Nicolai *et al.* [39] ont par exemple observé, en suivant les trajectoires individuelles de quelques particules en sédimentation au sein d'une suspension homogène, que ces trajectoires sont fortement tortueuses et présentent des fluctuations de vitesse importantes de l'ordre de la vitesse moyenne de sédimentation, cf. figure 2.2a. Ce type de comportement complexe apparait en fait dès lors que le nombre de particules est supérieur à 2. A l'instar du problème à 3-corps, 3 particules en sédimentation constituent un système chaotique [21]. Comme illustré par la figure 2.2b, les trajectoires de 3 particules en sédimentation obtenues pour deux simulations dont les conditions initiales sont légèrement perturbées l'une par rapport à l'autre, montrent qu'au delà d'un certain temps, les deux simulations évoluent vers des trajectoires différentes. Cette sensibilité aux conditions initiales est la signature d'un comportement chaotique.

Les interactions hydrodynamiques longues portées génèrent aussi des comportement collectifs fascinants tel que la recirculation toroïdale observée lors de la sédimentation d'un nuage de particules. Metzger *et al.* [33] ont montré que ce comportement collectif ainsi que l'évolution complexe du nuage : formation d'un tore puis cascades successives de déstabilisation en goutellettes (figure 2.2c.) peut être modélisé en ne décrivant que le premier ordre des perturbations d'écoulement induites par les particules.

Cas des suspensions cisaillées : Considérons maintenant une suspension cisaillée pour laquelle la densité des particules est la même que celle du fluide. Dans un tel système, des fluctuations similaires à celles évoquées plus haut ont été observées. Comme illustré sur la figure 2.3a, les particules au sein d'une suspension cisaillée sont déviées des lignes de courant moyennes. Si l'on suit une particule donnée et que l'on soustrait la partie affine de son déplacement (celle due à l'écoulement de cisaillement), cette trajectoire non-affine possède alors toutes les caractéristiques d'un mouvement diffusif. Il est important de remarquer que pour des particules de cette taille, ce mouvement diffusif n'est pas d'origine thermique, mais résulte des interactions avec les autres particules qui sont induites par la mise en écoulement de la suspension : ce phénomène est ainsi appelé la *diffusion induite par cisaillement*. Une manière astucieuse de directement observer ces fluctuations consiste à appliquer un cisaillement périodique –au lieu d'un cisaillement continu– et d'observer le système de façon stroboscopique à la fin de chaque cycle de cisaillement. Dans cette configuration, la partie affine (réversible) de l'écoulement s'annule à la fin de chaque cycle et seules les fluctuations induites par les interactions entres les particules sont conservées. Il a été montré que, soumises à un cisaillement oscillant, les suspensions de particules non-Browniennes subissent une transition de phase [42]. Pour une

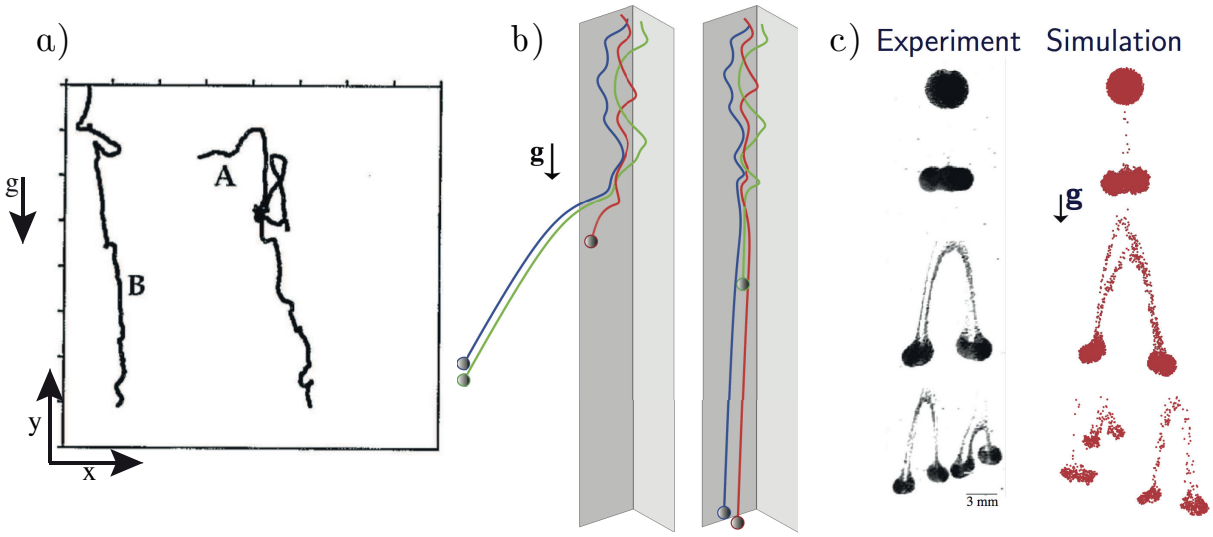


FIGURE 2.2 – a) Exemple de trajectoires de particules lors de la sédimentation d'une suspension homogène de fraction volumique $\phi = 30\%$ (Nicolai *et al.* [39]). b) Simulations numériques de la sédimentation de 3 particules ponctuelles partant de configurations initiales légèrement perturbées l'une par rapport à l'autre. c) Evolution d'un nuage de particules en sédimentation à bas nombre de Reynolds : expérience et simulations de particules ponctuelles (Stokeslet) (Metzger *et al.* [33]).

fraction volumique en particule donnée, lorsque l'amplitude de déformation est faible, la suspension relaxe vers un état réversible où chacune des particules revient à sa position initiale à la fin de chaque cycle de cisaillement. Lorsque l'amplitude de déformation dépasse une valeur critique, la suspension transite vers un état fluctuant : les particules ne retournent plus à leur position initiale mais, lorsqu'elles sont suivies de façon stroboscopique, les particules font l'objet d'importante fluctuations, cf. figure 2.3b. Dans la suite, je présente les différents mécanismes qui ont été proposés pour expliquer cette transition.

Considérons d'abord l'interaction entre deux particules dans un cisaillement simple. Dans la limite dite 'purement hydrodynamique' (pour des sphères infiniment lisses qui n'interagiraient que via le fluide), la réversibilité des équations de Stokes implique que les trajectoires relatives de ces deux particules sont symétriques comme illustré sur la figure 2.4. Cela étant, ces trajectoires hydrodynamiques font approcher les surfaces des particules à des distances si faible ($< 10^{-5}a$ où a est le rayon des particules), que pour des particules réelles ayant une rugosité finie, le contact solide entre celles-ci est inévitable. Arp et Mason [23] on montré, en 1976, que la présence de rugosité à la surface des particules brise la symétrie des trajectoires purement hydrodynamiques. Le contact solide entre les deux particules induit une déviation transverse des trajectoires d'autant plus grande que la rugosité des particules augmente, cf. figure 2.4. En décrivant cet effet des contacts solides entre particules, Da Cunha and Hinch [11] ont pu grâce à des calculs numériques, déterminer de façon convenable le comportement diffusif des particules pour des suspensions diluées cisaillées de façon continue.

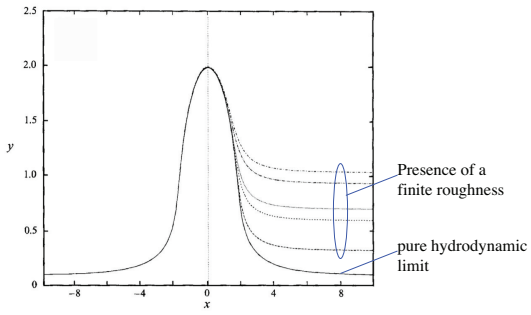


FIGURE 2.4 – Trajectoire relative entre deux particules dans un écoulement de cisaillement obtenu dans la limite purement hydrodynamique et en présence de rugosité (Da Cunha and Hinch [11]). L'offset final augmente avec la rugosité des particules.

Au début des années 2000, le phénomène de diffusion induite par cisaillement fut cependant abordé sous un tout autre angle. Plusieurs auteurs ont proposé que les suspensions cisaillées, comme les suspensions en sédimentation, constituent un système chaotique du fait de la présence d'interactions hydrodynamiques longues portées [12, 36]. Dans un tel système, comme nous l'avons évoqué plus haut dans le cadre de particules en sédimentation, toute source de bruit est amplifié par la nature chaotique des interactions hydrodynamiques. Cette amplification conduit à une perte de

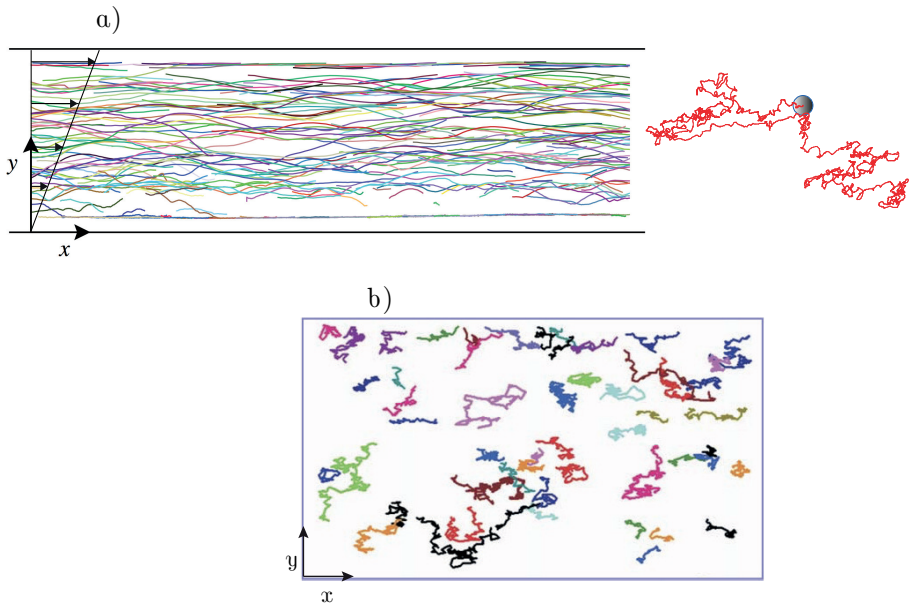


FIGURE 2.3 – a) *gauche :* Trajectoires de particules dans une suspension cisaillées de façon continue $\phi = 35\%$. *droite :* trajectoire non affine d'une particule (Metzger *et al.* [34]). b) Trajectoires stroboscopiques construites à partir des positions des particules mesurées à la fin de chaque cycle de cisaillement dans un cisaillement périodique (Pine *et al.* [42]). Chaque couleur indique une particule différente.

réversibilité permettant d'expliquer le mouvement diffusif des particules [12,15,29,36,42]. Par des études de sensibilité aux conditions initiales, certains auteurs ont montré que les suspensions cisaillées sont caractérisées par un coefficient de Lyapunov positif, montrant ainsi que les suspensions cisaillées constituent un système chaotiques [12, 42]. Ces dernières études proposent donc une interprétation bien différente de celles mentionnées plus haut : le comportement diffusif des particules est ici attribué à la nature chaotiques des interactions hydrodynamiques et non pas à la présence de contacts solides.

Avant de d'exposer la problématique de ce chapitre, il est important de rappeler qu'historiquement les suspensions de particules ont été étudiée à partir de la limite diluée pour laquelle une description hydrodynamique prévaut. En 1906, Einstein [17] prédit le premier la viscosité d'une suspension $\mu_r = 1+2.5\phi+\mathcal{O}(\phi^2)$ pour des fraction volumique ϕ inférieure à 10%. Puis Batchelor [2] étend cette relation au second ordre : $\mu_r = 1 + 2.5\phi + 7.6\phi^2 + \mathcal{O}(\phi^3)$. Plusieurs lois empiriques, qui couvrent une gamme plus importante de fraction volumique, ont ensuite été proposées (Krieger and Dougherty [24], Ferrini *et al.* [18]). Les années 80 voient le développement de simulations numériques qui adoptent cette même approche hydrodynamique. Plusieurs méthodes ont été proposées : Stokesian Dynamics (SD) [5], multipole expansions [8, 25], boundary integral methods [43], Lattice-Boltzmann Method (LBM) [38], et plus récemment la Force-Coupling Method (FCM) [54]. La plus influente est probablement la dynamique Stokésienne. Cette méthode fut développée pour simuler le comportement des suspensions de particules aussi bien en sédimentation que soumises à un cisaillement, avec l'idée que le comportement de ces systèmes est dominé par l'effet des interactions hydrodynamiques. La Dynamique Stokésienne propose donc une description détaillée de ces interactions qui incluent les interactions hydrodynamiques longues portées et les forces de lubrifications. Les interactions hydrodynamiques qui sont calculées au second ordre, tiennent compte des interactions de paires et sont formulées de manière à décrire les interactions multi-corps [5, 15]. La Dynamique Stokésienne comprend aussi une force répulsive courte portée, non pas pour décrire directement le rôle des contacts entre particules mais plutôt pour éviter la divergence et régulariser les forces de lubrification lorsque la distance de séparation entre les surfaces des particules tend vers zéro.

On remarquera finalement qu'au cours de ces dix dernière années, les suspensions ont été abordée depuis l'autre limite : celle des suspensions très denses proche du 'Jamming'. En transposant aux suspensions les méthodes et les modèles développés pour les milieux granulaires secs, des progrès majeurs ont été réalisés dans la compréhension des écoulements de suspensions en particulier proche du 'Jamming'. Par exemple, Boyer *et al.* [4] ont montré que la rhéologie des suspensions denses partage de fortes similarités avec celle des milieux granulaires. En régime quasi-statique par exemple, une suspension dense et le milieu granulaire sec correspondant ont le même coefficient de friction. Ce résultat suggère que même en suspension, la dynamique des particules est largement influencé par la

présence de contacts frictionnels entre les particules.

Problématique

La courte introduction présenté ci-dessus montre que dans la description des suspensions cisaillées, la question du rôle joué par les contacts solides entre particules reste à clarifier. Certaines études proposent une approche purement hydrodynamique alors que d'autres attribuent aux contacts solides un rôle prépondérant. La question de l'origine physique de la diffusion induite par cisaillement est au coeur de cette problématique : naît elle de la nature chaotique des interactions hydrodynamiques longues portées ou bien de la nature irreversible des contacts solides entre particules ?

C'est dans ce contexte qu'a démarré le master puis la thèse en co-tutelle de Pham Phong que j'ai co-encadré avec Ouamar Rahli à l'IUSTI et Jason E. Butler de l'Université de Floride entre 2011 et 2016. L'objectif de sa thèse était d'étudier systématiquement l'origine de la diffusion induite par cisaillement, et de déterminer quels sont les ingrédients essentiels nécessaires pour décrire les suspensions cisaillées. Les questions que l'on a abordées sont les suivantes : les interactions hydrodynamiques longues portées génèrent elles un comportement chaotique pouvant expliquer la perte de réversibilité observées dans les suspensions cisaillées de façon périodique ? Quel est le rôle des forces de lubrification ? Les particules viennent elles au contact solide ? Si contact solide il y a, comment affectent ils la dynamique du système et quel modèle doit on utiliser pour les décrire ? Comme évoqué plus haut, le mouvement des particules au sein d'une suspension cisaillée est potentiellement influencé par trois types de forces : les interactions hydrodynamiques longues portées données au premier ordre par le Stresslet, les forces de lubrification lorsque la distance de séparation inter-particule devient très petite et, les contacts solides lorsque la rugosité des particules brise les films de lubrifications. La méthodologie que l'on a employée fut de séparer ces différentes contributions afin d'estimer l'importance relative de chacune de ces forces. Cette approche systématique, qui n'avait jamais été mise à l'oeuvre auparavant, nous a permis d'élaborer un modèle numérique minimal pour décrire les suspensions de particules cisaillées. Des expériences modèles nous ont aussi permis de mettre en évidence le rôle prépondérant des contacts et de tester l'influence de la rugosité des particules.

Bien que historiquement la sédimentation de particules et les suspensions cisaillées ont été décrit à l'aide des mêmes approches et surtout des mêmes outils numériques, dans ce chapitre nous montrerons que la physique de ces deux systèmes est très différente. Si le premier est largement dominé par l'hydrodynamique longue portée et l'aspect multi-corps qui en résulte, les suspensions cisaillées y sont beaucoup moins sensibles et doivent donc être décrites à l'aide de modèles différents.

2.2 Un modèle minimal pour décrire les suspensions cisaillées

Par une approche numérique, l'idée ici est d'estimer l'importance relative des forces susceptibles d'influencer le comportement des suspensions cisaillées et d'élaborer un modèle minimal capable de reproduire leur dynamique.

2.2.1 Rôle des interactions hydrodynamiques longues portées

Article dans Phys. Rev. E [31] en collaboration avec J. E. Butler (Univ. Florida USA)

Un modèle de simulation numérique directe nous permet ici d'isoler l'effet des interactions hydrodynamiques longues portées (Stresslets) afin d'étudier si ces interactions génèrent un comportement chaotique pouvant expliquer la perte de réversibilité observée dans les suspensions cisaillées de façon périodique. Le système consiste en N particules de rayon a initialement distribuées aléatoirement dans un écoulement de cisaillement simple. La vitesse, $\mathbf{u}_n$, de la particule n, est donnée par la somme de sa vitesse d'advection due à l'écoulement de cisaillement périodique imposé, de l'ensemble des perturbations d'écoulement induites par la présence des autres particules (interaction hydrodynamiques longues portées) et du mouvement induit par les forces répulsives de contact (RF),

$$\mathbf{u}_n = \dot{\gamma} y_n sin(\omega t)\mathbf{e}_x + \sum_{m \neq n}^{N} \bar{\mathbf{U}}_m(\mathbf{x}) + \frac{1}{\xi} \sum_{m \neq n}^{N} \mathbf{F}_{nm}. \tag{2.3}$$

où $\dot{\gamma}$ est le taux de cisaillement, y_n est la position de la particule n dans la direction transverse à l'écoulement et ω la période du cisaillement périodique imposé. Le premier ordre de la perturbation hydrodynamique (Stresslet) due à la particule m à l'endroit ou se trouve la particule n est donné par $\bar{\mathbf{U}}_m$ et enfin, $\mathbf{F}_{nm}$ représente la force de contact entre

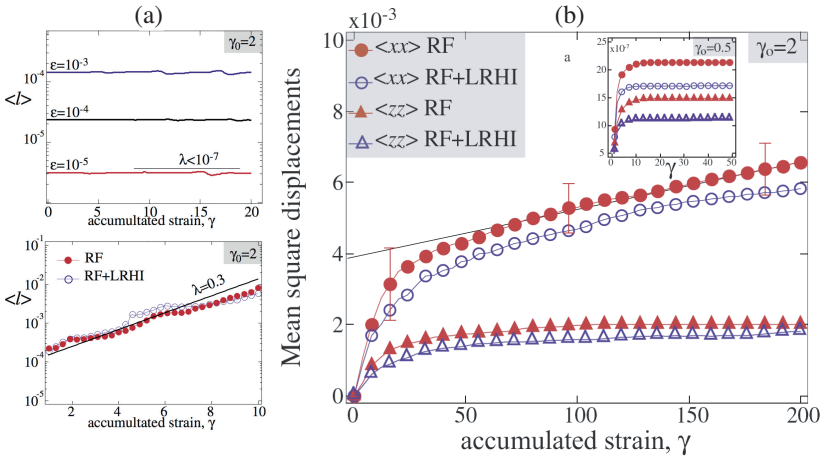


FIGURE 2.5 – Rôle des interactions hydrodynamiques longues portées : a) Distance de séparation $< \ell >$ entre deux simulations initialement légèrement perturbées l'une par rapport à l'autre en fonction de la déformation accumulée, γ. (haut) Limite purement hydrodynamique : les interactions hydrodynamiques longues portées ne conduisent pas à une amplification de la perturbation initiale ϵ. (Bas) En présence de contacts -RF-, la distance de séparation augmente exponentiellement indiquant un comportement chaotique. Le taux de croissance de l'exponentielle (coefficient de Lyapunov) reste inchangé en présence ou non des interactions hydrodynamiques longues portées -LRHI-. b) Déplacement carré moyen des particules versus amplitude de déformation accumulée. La présence des LRHI diminue légèrement la dispersion des particules.

la particule m et la particule n. Ce modèle décrit les interactions multi-corps dû aux interactions hydrodynamiques longues portées et les interactions stériques de contact solide. Il n'inclut pas les forces de lubrification et cela à dessein car le but ici est d'isoler l'effet des interactions hydrodynamiques. Nous avons comparé la dynamique du système dans les trois cas limites suivant : les particules interagissent i) uniquement via les forces hydrodynamiques longue portées (LRHI), ii) uniquement via les forces de contacts (RF), iii) via les deux types interactions (RF+ LRHI).

Les résultats obtenus sont les suivant :

- ✓ En testant la sensibilité du système aux conditions initiales, nous avons montré que les interactions hydrodynamiques longues portées (Stresslets) seules ne génèrent pas de comportement chaotique observable, cf. figure 2.5b. Le comportement chaotique est largement dominé par l'effet des interactions de contact solide.
- ✓ Les interactions hydrodynamiques longues portées en présence des forces de contact ne sont pas source d'irréversibilité, ni amplificateur d'irréversibilité.
- ✓ L'effet d'encombrement stérique décrit par les forces de contacts domine le comportement irréversible des particules et permet de reproduire la transition d'irréversibilité observée expérimentalement.

Contrairement à ce qui était attendu, cette étude montre que dans les suspensions cisaillées de façon périodique, les interactions hydrodynamiques longues portées jouent en rôle négligeable dans le processus de dispersion des particules. Ces interactions tendent en fait plutôt à légèrement diminuer l'agitation des particules, cf. figure 2.5a, en raison de leur nature attractive quand les particules sont en récessions [36].

Les résultats obtenus ici précisent en partie le cadre adéquat pour décrire les suspensions cisaillées. Ces dernières diffèrent fondamentalement des suspensions en sédimentation : lors d'un processus de sédimentation, le seul écoulement existant au sein du fluide est induit par à la chute des particules elles mêmes ; cet écoulement résulte de la somme des perturbations générées par la chute de l'ensemble des particules du système. Dans ce cas, on peut montrer que l'amplitude des perturbations d'écoulement (Stokeslet) est typiquement de l'ordre de la vitesse moyenne de sédimentation des particules ; ces perturbations affectent donc profondément la dynamique des particules et sont à l'origine des fluctuations observées. Dans le cas des suspensions cisaillées, la situation est bien différente ; cette fois un écoulement de cisaillement est imposé par les parois ; les interactions hydrodynamiques induites (Stresslet) sont négligeables devant le mouvement des particules produit par cet écoulement et par les collisions solides qui en résultent.

On pourra remarquer que décrire l'effet des interactions hydrodynamiques longues portées est numériquement très couteux (temps de calcul $\sim N^2$). Ne pas prendre en compte ces interactions offre aux modèles numériques

des perspectives intéressantes comme par exemple simuler un plus grand nombre de particules, des configurations d'écoulement plus complexes etc...

2.2.2 Rôle des forces de lubrification

Article dans Phys. Rev. E [34] en collaboration avec P. Phong (doctorant) & J. E. Butler (Univ. Florida USA)

Nous avons montré dans l'étude précédente que les interactions hydrodynamiques longues portées jouent un rôle négligeable dans le processus de dispersion des particules. Comme expliqué dans l'introduction, les autres forces hydrodynamiques pouvant affecter la dynamique des suspensions cisaillées sont les forces de lubrification. Ces interactions sont réversibles au sens où inverser la direction du cisaillement revient à inverser la direction du temps. Cela étant, si plusieurs particules interagissent simultanément via des forces de lubrification, la dynamique résultante peut être chaotique et donc induire un comportement irréversible des particules. Le but de cette étude est d'évaluer numériquement le rôle joué par les forces de lubrification sur le processus de dispersion des particules. Pour aborder ce problème, nous avons développé un code simple qui décrit l'effet de l'écoulement de cisaillement périodique, la composante normale des forces de lubrification entre particules, et les forces de contacts. En l'absence d'inertie, la somme des forces hydrodynamiques $\mathbf{F}_i^h$, et des forces de contacts $\mathbf{F}_{ij}^c$ s'annulent pour chaque particule i,

$$\mathbf{F}_i^h + \sum_{j\neq i}^{N} \mathbf{F}_{ij}^c = 0. \tag{2.4}$$

Les force hydrodynamiques exercées sur la particule i sont respectivement la trainée causée par l'écoulement de cisaillement imposé $\mathbf{u}_{i\infty}$ et les forces de lubrifications générées par les particules voisines $j(i)$. Ces dernières sont proportionnelles aux différences de vitesse $\mathbf{u}_i - \mathbf{u}_j$ entre les particules voisines i et j et inversement proportionnelles à leurs distances de séparation h_{ij}. Les forces hydrodynamiques s'écrivent donc

$$\mathbf{F}_i^h = 3\pi\mu d(\mathbf{u}_i - \mathbf{u}_{i\infty}) + \sum_{j(i)} \frac{3\pi\mu d^2}{8h_{ij}} \mathbf{n}_{ij}(\mathbf{u}_i - \mathbf{u}_j)\cdot\mathbf{n}_{ij}, \tag{2.5}$$

avec μ la viscosité du fluide et d le diamètre des particules. Les forces de contact sont modélisés de la manière la plus simple par

$$\mathbf{F}_{ij}^c = \begin{cases} F_0\mathbf{n}_{ij} & \text{if } |\mathbf{h}_{ij}| \leqslant 2\epsilon_r \\ 0 & \text{if } |\mathbf{h}_{ij}| > 2\epsilon_r, \end{cases} \tag{2.6}$$

avec F_0 l'amplitude de la force répulsive et ϵ_r la rugosité apparente des particules que l'on a fait varier entre 0 (particules infiniment lisses n'interagissant que via les forces de lubrification) et $10^{-2}d$. D'autres modèles de force (contact de Hertz, force à décroissance exponentielle utilisée en dynamique Stokésienne) ont été testé. Comme tous ces modèles donnent des résultats similaires, nous avons donc opté pour la forme la plus simple, Equ. 2.6.

Les résultats de ces simulations montrent que les forces de lubrification génère un comportement chaotique (exposant de Lyapunov positif), mais comme l'illustre la figure 2.6a, celui-ci n'est pas suffisant pour induire un comportement irréversible significatif des particules lorsque la suspension est cisaillée de façon périodique. L'irréversibilité est dominée cette fois encore par les interactions de contacts. La lubrification joue néanmoins un rôle très important car elle empêche les particules de s'organiser en couches régulières. Le caractère attractif/répulsif des forces de lubrification maintient un certain désordre dans la suspension qui permet aux collisions par contact de perdurer. La suspension peut ainsi s'établir aux grandes déformations dans un état stationnaire fluctuant tel que celui observé expérimentalement, cf. figure 2.6b.

Une description minimale des suspensions cisaillées peut donc se résumer aux effets de l'advection induit par l'écoulement de cisaillement imposé et à ceux de forces courtes portées qui sont les forces répulsives de contact et les forces de lubrification. Ce modèle implique seulement deux paramètres : F_0 l'amplitude de la force répulsive et ϵ_r qui décrit une rugosité effective des particules et fixe la distance de séparation entre les surfaces des particules pour laquelle les particules passent d'une interaction de lubrification à une interaction de contact. Ce modèle peut sembler rudimentaire en comparaison des modèles existants évoqués dans l'introduction. On montrera cependant, par des comparaisons à des expériences réelles, que ce modèle décrit convenablement le comportement des suspensions cisaillées.

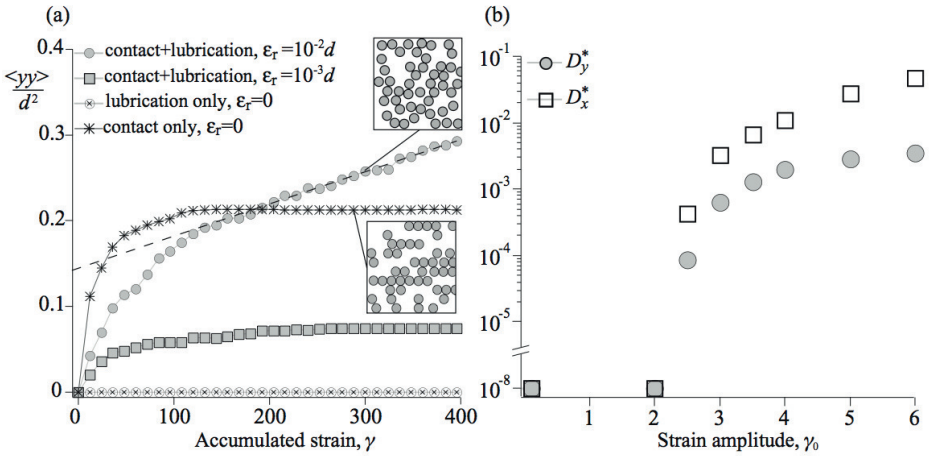


FIGURE 2.6 – *Rôle des forces de lubrification : a) Déplacement carré moyen des particules après chaque cycle de cisaillement. En interaction de lubrification seule, les trajectoires sont réversibles à l'échelle de la taille des particules. En interaction de contact seul, les particules s'organisent en couche puis cessent de diffuser. En interaction de contact + lubrification, la suspension atteint un état stationnaire fluctuant. b) Coefficient de diffusion des particules versus amplitude déformation. Comme observé dans les expériences [42], le modèle incluant les interactions de contact et de lubrification prédit une transition vers un état fluctuant au delà d'une amplitude de déformation critique.*

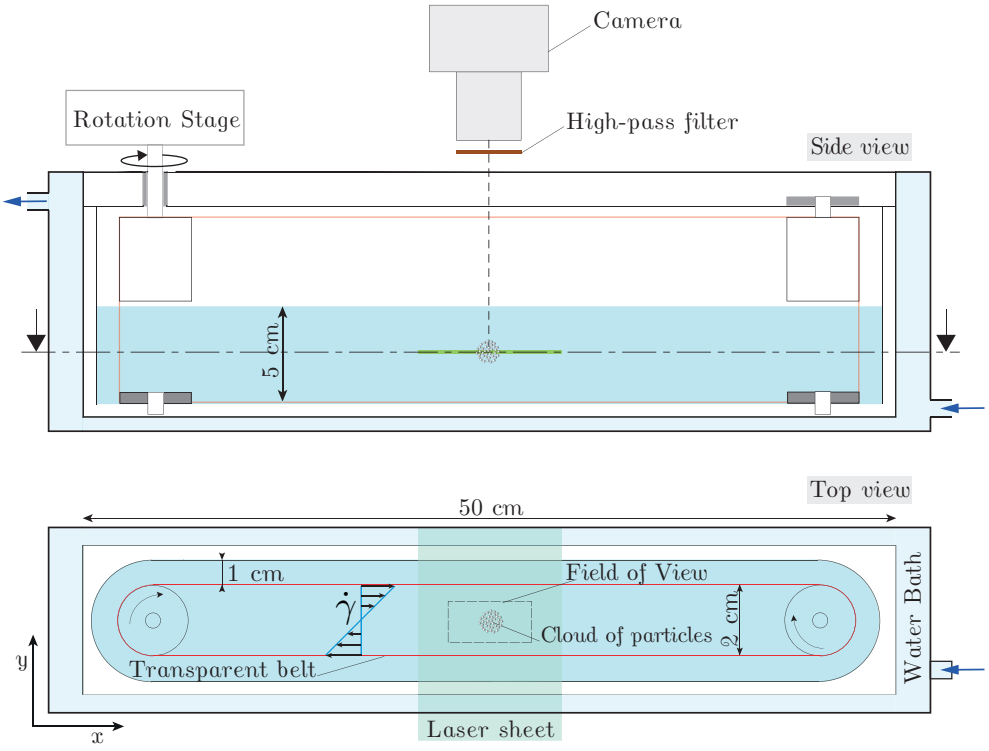


FIGURE 2.7 – *Schéma du dispositif expérimental de type Couette-Plan.*

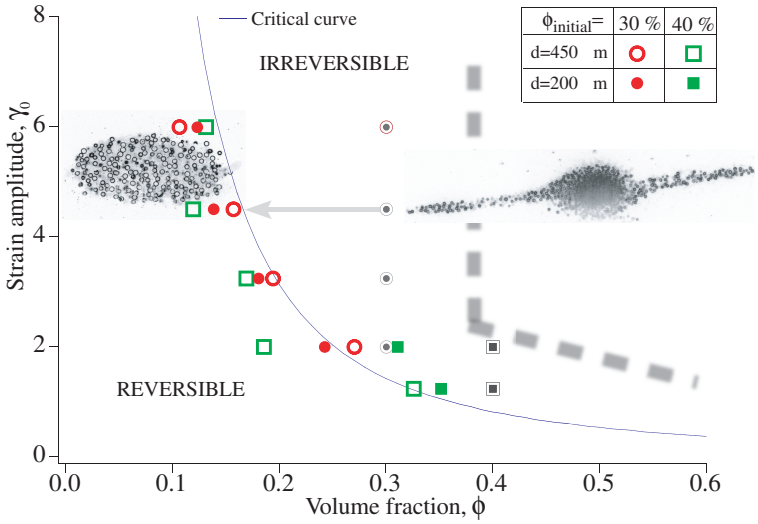


FIGURE 2.8 – *Les nuages initialement dilués ($\phi < 40\%$) diffusent progressivement vers un état réversible par diminution de leur fraction volumique (flèche grise). Les points gris et colorés indiquent respectivement la fraction volumique initiale et finale des nuages. Les nuages se comportent de façon réversible dès lors qu'ils traversent la courbe critique qui séparent la zone irréversible de la zone réversible. Les nuages initialement concentrés évoluent vers un pattern en forme de "galaxie" du fait de la rotation solide du coeur du nuage pendant son cisaillement.*

2.3 Les contacts à l'origine de la diffusion induite par cisaillement

En parallèle de l'approche numérique présentée plus haut, des expériences ont été réalisée afin de mettre en évidence le rôle prépondérant des contacts solides dans le processus de dispersion des particules. Nous avons pour cela développé un dispositif original de type Couette-Plan. Le schéma du dispositif est représenté sur la figure 2.7. Il consiste en une cuve rectangulaire dans laquelle une courroie tendue entre deux cylindres verticaux est mise en rotation. Le déplacement de la courroie induit un écoulement de cisaillement linéaire en son sein. La transparence de la courroie permet d'illuminer la suspension avec une nappe laser horizontale et d'effectuer les visualisations par le dessus. L'optique pour réaliser la nappe laser, constituée d'un miroir tournant et de lentilles semi-cylindriques, permet d'obtenir une nappe très fine d'épaisseur $\lesssim 60\mu$m, générant ainsi des images bien piquées. L'indice de réfraction et la densité du fluide suspendant sont ajustés avec l'indice et la densité des particules de PMMA. Un bain thermo-staté contrôlant la température de l'ensemble du dispositif permet d'ajuster les indices de réfraction des particules à celui du fluide (à la quatrième décimale) assurant ainsi une bonne transparence de la suspension. Les particules, dans le plan de la nappe laser, sont visualisées par fluorescence soit en colorant le fluide avec un traceur fluorescent soit en dopant préalablement les particules avec ce même traceur.

2.3.1 Nuage de particules dans un cisaillement oscillant

Article dans Physics of Fluids [32] en collaboration avec J. E. Butler (Univ. Florida, USA)

Pour étudier le comportement irréversible des particules, on s'est inspiré de l'expérience de G. I. Taylor qui illustre la réversibilité des équations de Stokes. Utilisant le fait qu'une goutte d'encre injectée dans une cellule de couette remplie de fluide visqueux se reforme à l'identique après chaque cycle de cisaillement, on a ici simplement remplacé la goutte d'encre par un nuage de particules (iso-denses et iso-indices). La position des particules est enregistrée à la fin de chaque cycle de cisaillement. Cet enregistrement stroboscopique annule la partie affine (réversible) du déplacement des particules et met en évidence toute apparition d'irréversibilité, phénomène auquel on s'intéresse.

Les résultats obtenus sont les suivants :

✓ les nuages initialement dilués ($\phi < 40\%$) se dispersent progressivement dans le fluide environnant au cours des cycles de cisaillement pour finalement s'auto-organiser dans un état réversible. Leur état devient réversible

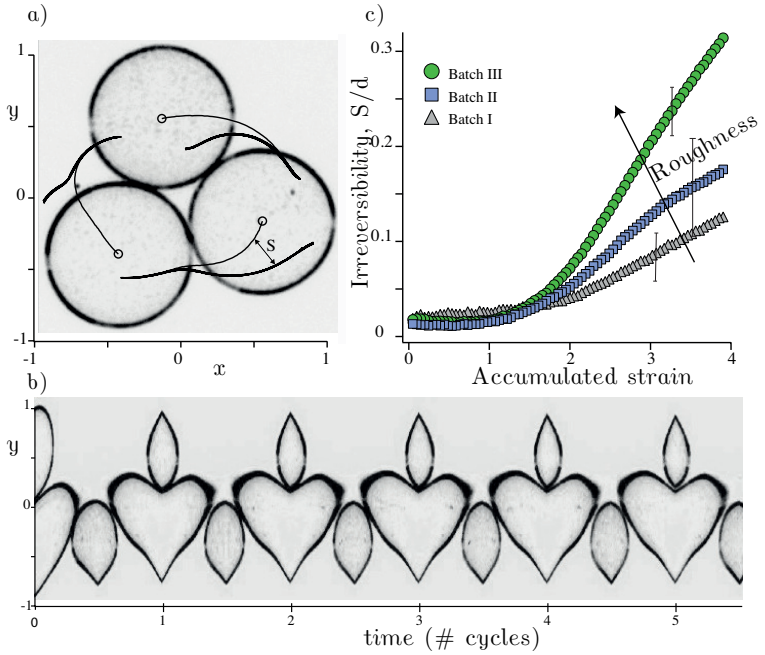


FIGURE 2.9 – *a) Expériences : disposition initiale des particules dans le plan de cisaillement et trajectoires de chacune des particules au cours des 10 premiers cycles de cisaillement : le premier cycle est irréversible, les suivants sont réversibles. b) Spatio-temporel montrant que toute l'irréversibilité a lieu lors du premier cycle de cisaillement. c) Magnitude de l'irréversibilité, S/d, versus déformation lors du premier cycle de cisaillement pour des particules ayant des rugosités différentes.*

lorsqu'ils atteignent la courbe critique [1] séparant la zone réversible de la zone irréversible obtenue par Pine *et al.* [42] pour une suspension homogène, cf. figure 2.8. Cette évolution du nuage vers un état réversible suggère que les contacts sont responsables du processus de dispersion. En effet, au début de l'expérience, les particules sont proches les unes des autres et la déformation imposée induit des collisions irréversibles entre les particules qui font se disperser l'ensemble du nuage. Au cours de ce processus de dispersion irréversible, la fraction volumique du nuage diminue. Au moment où les distantes inter-particules deviennent suffisamment grandes, il n'y a alors plus de collisions solides entre particules et le comportement observé est réversible.

✓ Les nuages initialement concentrés (au maximum packing) évoluent vers un pattern en forme de petite "galaxie", cf. Figure 2.8. Nous avons montré que ce pattern naît de la rotation solide du coeur du nuage pendant son cisaillement. La rotation solide du nuage de particules n'est pas un phénomène trivial car il n'y a pas d'échelle de contrainte externe (force de gravité ou tension capillaire) qui permet de maintenir les grains bloqués les uns contre les autres. Le mécanisme que nous avons proposé est basé sur l'effet de la pression de pore : pour être cisaillé, le nuage initialement très compact doit se dilater entrainant ainsi un écoulement du fluide de l'extérieure vers l'intérieur du nuage. Cet écoulement, de type Darcy, s'oppose au mouvement des grains et plaque les grains les uns contre les autres, les maintenant transitoirement dans un état bloqué [40]. Une analyse dimensionnelle simple, que je ne développerai pas ici, permet de montrer que la pression de pore est suffisamment forte pour maintenir les grains en structure rigide si $D/d \geqslant 1/(\mu_s \tan(\psi))$, où D est le diamètre du nuage, d celui des particules, μ_s le coefficient de friction solide des grains et ψ l'angle de dilatance. Pour observer la rotation solide du nuage et une évolution en forme de galaxie, Il faut donc des nuages tels que $D/d \geqslant 15$. Ces prédictions sont en bon accord avec les observations expérimentales.

2.3.2 Evidence directe du contact solide

Article dans Physics of Fluids [41] en collaboration avec P. Phong (doctorant) & J. E. Butler (Univ. Florida)

1. Cette courbe sépare la zone "état réversible" de la zone "état fluctuant" dans le diagramme amplitude de déformation/fraction volumique [42].

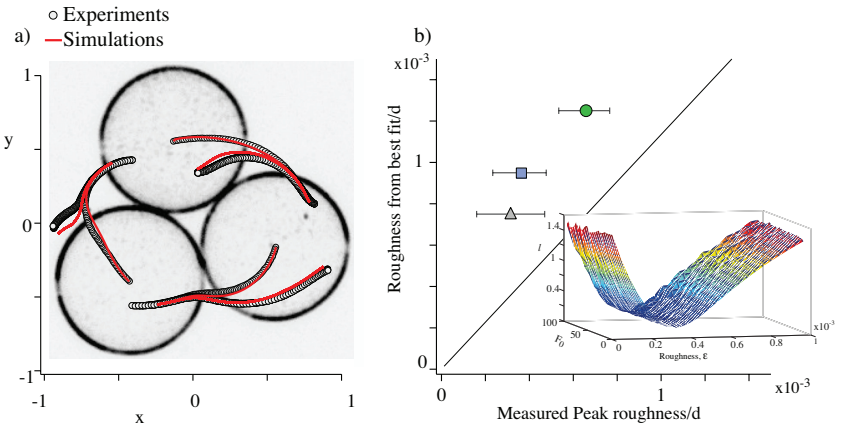


FIGURE 2.10 – *a) Comparaison entre les trajectoires expérimentales et celles obtenues numériquement avec le modèle présenté au § 2.2.2. b) Rugosité optimum obtenue pour la simulation numérique versus rugosité maximales mesurée à l'AFM. Inset : distance l entre les trajectoires obtenues numériquement et celles mesurées expérimentalement en fonction de l'amplitude de la force répulsive F_0 et de la rugosité des particules.*

Prouver expérimentalement que les particules viennent au contact solide n'est pas simple. Pour cela, nous nous sommes intéressé à une configuration à trois particules disposées initialement dans le plan de cisaillement $(x-y)$, cf. Figure 2.9.a. Cisaillées périodiquement, les particules se repoussent de façon irréversible au cours du premier cycle puis évoluent ensuite sur des trajectoires réversibles comme l'illustre le spatio-temporel de la figure 2.9.b. Pour mettre en évidence le rôle des contacts dans ce comportement irréversible, nous avons utilisé les mêmes particules de PMMA que nous avons préalablement polies à l'aide de solutions diamantées de différents grades afin de modifier leur rugosité. Le résultat marquant est que l'amplitude de l'irréversibilité S/d augmente systématiquement avec la rugosité des particules, cf. figure 2.9.c. Ces expériences montrent que les contacts sont bien à l'origine du comportement irréversible des particules.

Le modèle numérique présenté au § 2.2.2 permet de reproduire de façon satisfaisante les trajectoires expérimentales suivies par les particules, cf. figure 2.10. Comme illustré dans l'inset de la figure 2.10b, la distance l entre les trajectoires obtenues numériquement et celles mesurées expérimentalement ne dépend pas de l'amplitude de la force répulsive F_0. En revanche, varier la rugosité présente un optimum. L'optimum de rugosité trouvé numériquement est en bon accord avec la rugosité maximale mesurée expérimentalement, cf. figure 2.10b.

2.3.3 Origine de l'amplitude critique de déformation

Article dans Physics Review Fluids en collaboration avec P. Phong (doctorant IUSTI/Univ. Florida) & J. E. Butler

On a vu plus haut qu'une suspension homogène de particules non-Browniennes suspendues dans un fluide visqueux et soumise à un cisaillement périodique transite d'un état réversible, à faible amplitude de déformation, vers un état fluctuant au delà d'une amplitude de déformation critique [42]. Cette transition a attiré l'attention d'un grand nombre de chercheurs [14,22,28,30,42] intéressés par ce système a priori gouverné par des équations réversibles (les équations de Stokes) et dans lequel inverser la direction du cisaillement est équivalent à inverser la direction du temps. Les suspensions furent alors considérées comme une opportunité unique d'étudier, dans un système gouverné par des lois réversibles en temps, l'émergence d'irréversibilité macroscopique après inversion de sa dynamique [22].

Cette interprétation longue-portée et multi-corps du problème diffère fondamentalement de celle mise en avant par Corté *et al.* [9] qui assume la présence de collisions solides entre particules. Corté *et al.* ont modélisé la dynamique de la suspension en advectant des particules le long de leur lignes de courant non-perturbées. A chaque fois qu'une collision a lieu, les particules sont déplacées d'un diamètre de particule dans une direction aléatoire. Ce 'Toy-model', bien qu'excessivement simple, permet d'expliquer l'existence d'un seuil de déformation et produit spontanément un état réversible à faible amplitude de déformation. Le succès de ce modèle de collision-induite [9] n'est pas surprenant en regard des résultats que nous avons obtenus et qui soutiennent l'idée que les déplacement irréversibles résultent de l'effet des contacts solides entre particules.

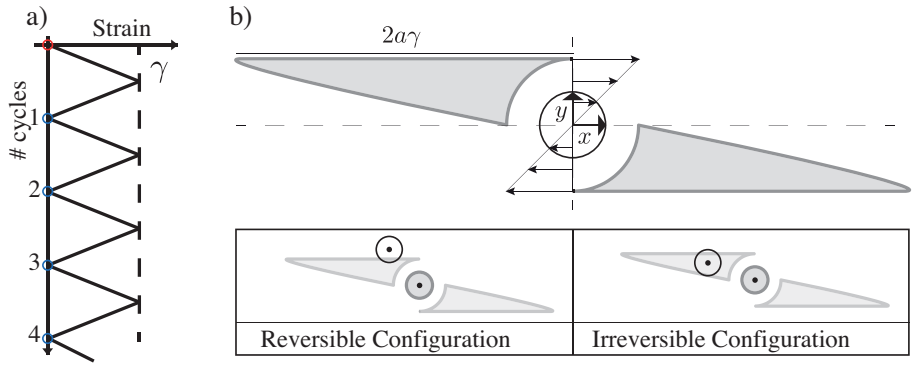


FIGURE 2.11 – *a) Schéma illustrant la déformation périodique imposée au système. (b) Pour une amplitude de déformation donnée γ, toute particule localisée dans la zone grise (volume exclu) doit entrer en collision solide avec la particule de référence localisée à l'origine du repère. Le tableau illustre une configuration réversible (pas de collision) et une configuration irréversible (collision).*

Pour confirmer ce scénario et mieux comprendre cette transition de phase, nous avons étudié expérimentalement l'influence de la rugosité des particules sur la valeur de l'amplitude critique de déformation dans une suspension cisaillée de façon périodique. Les résultats expérimentaux montrent que pour une fraction volumique donnée, des particules plus lisses nécessitent une amplitude de déformation plus grande pour transiter de l'état réversible vers l'état fluctuant. Dans la suite nous présentons un modèle simple, basé sur l'hypothèse que tout contact entre particules conduit à un comportement irréversible, qui explique cette tendance.

L'idée est de considérer des particules effectives telles que celle représentée sur la figure 2.11b. Faisons d'abord le raisonnement en 2D en négligeant toute interaction hydrodynamique. Sous l'effet d'une déformation γ, toute particule localisée initialement dans la zone grisée, qu'on appellera volume exclu, doit entrer en collision avec la particule de référence et donc produire un déplacement irréversible. On peut ainsi considérer que chaque particule à une aire effective $A_{eff} = \pi a^2 + 4\gamma a^2$ qui est donnée par son aire réelle, à laquelle s'ajoute l'aire de la zone grisée. Si l'on est capable d'organiser N particules effectives dans le système d'aire totale A_t sans qu'elles ne se recouvrent, *i.e* si $NA_{eff} < \beta A_t$ avec β une constante inférieure à 1, alors le système peut s'auto-organiser dans un état réversible. En revanche, si $NA_{eff} > \beta A_t$ alors les collisions sont inévitables et le système doit fluctuer de façon permanente. Ce raisonnement conduit à l'expression de la déformation critique suivante

$$\gamma_c = \frac{\pi}{4}(\frac{\beta}{\phi} - 1), \tag{2.7}$$

où $\phi = N\pi a^2/A_t$. Ce modèle géométrique prédit le scaling $\gamma_c \propto \phi^{-1}$ qui est en accord avec les résultats de Corté *et al.* [10]. On peut à présent suivre le même raisonnement en 3D et en incluant les effets de la lubrification qui vont distordre la forme du volume exclu, et de la rugosité dont le volume exclu doit dépendre ; la rugosité fixe en effet la distance de séparation à laquelle les particules viennent au contact. La forme du volume exclu est calculé numériquement, cf. figure 2.12a. Ce volume augmente avec l'amplitude de déformation mais aussi lorsque la rugosité des particules augmente. Ce comportement vient de la non linéarité des forces de lubrifications qui divergent quand la distance de séparation entre les particules tend vers zéro. Ainsi, plus les particules sont proches, plus une déformation macroscopique importante est nécessaire pour approcher les particules d'une quantité donnée. En 3D, le volume effectif des particules peut s'écrire $V_{eff} = 4\pi a^3/3 + f(\epsilon)\gamma a^3$ avec $f(\epsilon) = 19.4\epsilon^{0.5}$ obtenue numériquement. L'amplitude de déformation critique résultante est donnée par

$$\gamma_c = \frac{0.22}{\epsilon^{1/2}}(\frac{\beta}{\phi} - 1). \tag{2.8}$$

Cette amplitude de déformation critique doit tendre vers zéro au maximum packing ; cela fixe $\beta = 0.58$ [4]. Cette relation prédit aussi que pour une suspension de particules infiniment lisses, l'amplitude de déformation critique tend vers l'infini.

Pour tester ce modèle, nous avons mesuré expérimentalement l'amplitude de déformation critique en fonction de la fraction volumique pour deux lots de particules ayant des rugosité différentes. Les résultats sont présentés sur la figure 2.12b. Le modèle (Eq. 2.8) prédit quantitativement les résultats expérimentaux pour des valeurs de rugosité ϵ

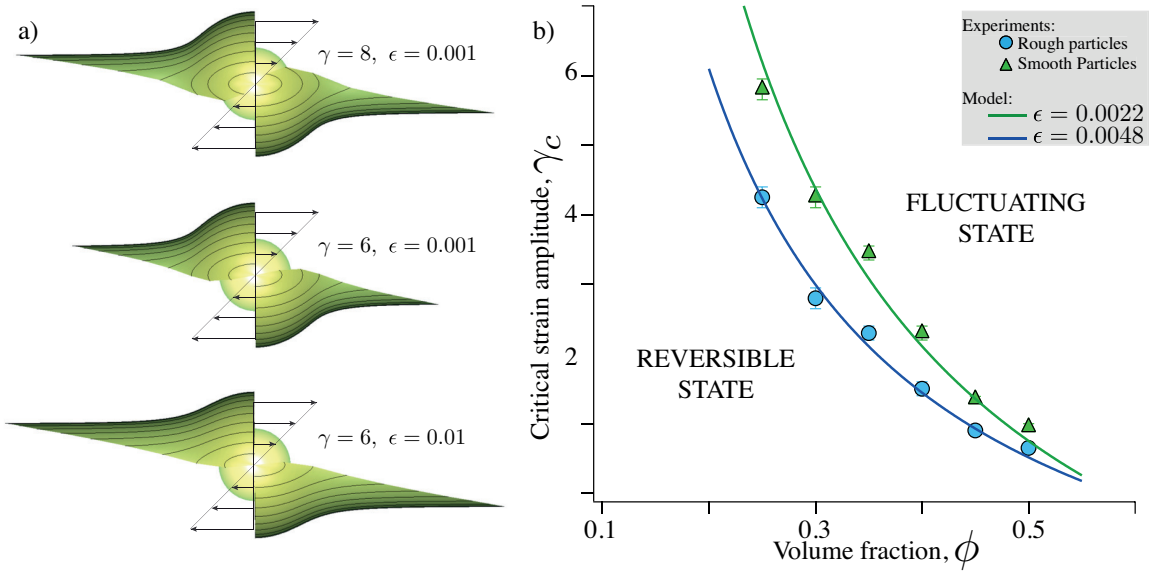


FIGURE 2.12 – *a) Forme tri-dimensionnelle des particules effectives. Le volume exclu dépend de l'amplitude de déformation γ et de la rugosité des particules, ϵ. b) Amplitude critique de déformation versus fraction volumique mesurée expérimentalement pour deux lots de particules lisses ($\epsilon = 0.0019$) et rugueuse ($\epsilon = 0.0055$). Les courbes correspondent au modèle : $\gamma_c = 0.22(0.58/\phi - 1)/\epsilon^{0.5}$, cf. Eq. 2.8, avec ϵ comme seul paramètre de fit.*

très proches de celles mesurées expérimentalement. Le fit du modèle aux données expérimentales, utilisant ϵ comme seul paramètre ajustable, donne $\epsilon = 0.0022$ pour les particules lisses et $\epsilon = 0.0048$ pour les particules rugueuse. Les rugosités expérimentales, mesurées au MEB, sont respectivement $\epsilon = 0.0019 \pm 0.0014$ et $\epsilon = 0.0055 \pm 0.003$. Le succès de ce modèle indique que la transition d'irréversibilité observée dans les suspensions cisaillées de façon périodique, peut être expliquée entièrement par des arguments géométriques.

2.3.4 Effet de la rugosité sur la diffusion induite par cisaillement

Article en préparation pour Journal of Fluid Mechanics en collaboration avec P. Phong (doctorant IUSTI/Univ. Florida) & J. E. Butler (Univ. Florida)

Si on considère l'interaction entre deux particules dans un cisaillement simple, alors l'offset final Δ_y^∞, qui correspond à la déviation transverse par rapport à la ligne de courant sur laquelle se trouve la particule de référence (inset de la figure 2.13), dépend uniquement de la rugosité des particules. Cela vient du fait que la rugosité impose la distance de séparation des particules lorsqu'elle sont à l'apex de leur interaction. En réalisant des simulations numériques à deux particules et en faisant varier la rugosité ϵ, on trouve que, pour deux particules dans le plan de cisaillement, $\Delta_y^\infty = 1.53\epsilon^{0.245}$, cf. figure 2.13a. Pour des suspensions diluées, dans lesquelles les collisions binaires dominent, le temps entre deux collisions successives est $\tau = 1/\phi\dot{\gamma}$ et, pour chaque collision, chaque particule subit un déplacement $l = \Delta_y^\infty d/2$. On s'attend donc à ce que le coefficient de diffusion caractérisant l'agitation des particules dans la direction transverse y, s'écrivent $D_{yy} = l^2/\tau \sim \phi\epsilon^{1/2}\dot{\gamma}d^2$. Ainsi, plus la rugosité des particules est élevée, plus la diffusion induite par cisaillement doit être importante. Ces prédictions, valables dans la limite diluée, sont effectivement en bon accord avec les résultats obtenus par simulations directes utilisant le modèle présenté au § 2.2.2 et pour une suspension de fraction volumique $\phi = 5\%$, voir figure 2.13b.

A plus forte fraction volumique, le comportement du coefficient de diffusion avec la rugosité est très différent : celui-ci diminue quand la rugosité des particules augmente ! Ce comportement, à priori contre intuitif, est observé à la fois dans les expériences où nous avons fait des mesures de coefficient de diffusion pour des particules de rugosité différente (Figure 2.14a), mais aussi dans les simulations directes utilisant le modèle présenté au § 2.2.2 que nous avons étendu à trois dimensions (Figure 2.14b). A fraction volumique modérée, $\phi = 25\%$, l'effet de la rugosité des particules est négligeable, cf. figure 2.14c. En revanche, a forte fraction volumique $\phi = 45\%$, augmenter la rugosité diminue significativement l'agitation des particules. Ce comportement s'explique par un changement de microstructure : comme l'illustre la figure 2.14d où l'on a représenté la fraction volumique locale $\langle\phi_y\rangle$ en fonction

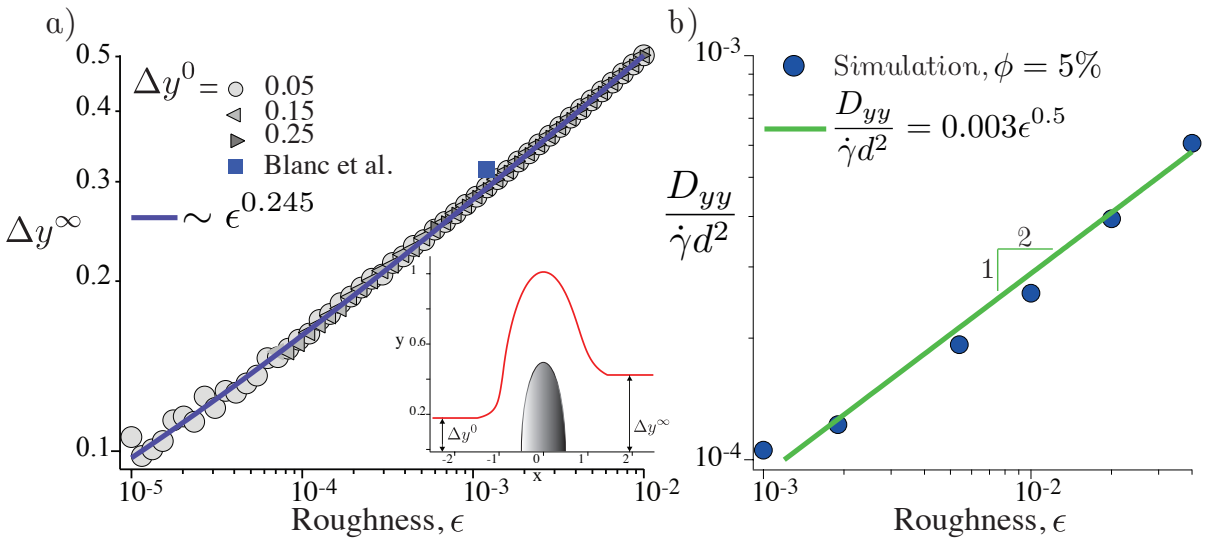


FIGURE 2.13 – *a) Simulation à 2 particules : offset final Δ_y^∞ versus rugosité des particules ϵ pour trois offset initiaux Δ_y^0 différents. L'offset final Δ_y^∞ est entièrement prescrit par la rugosité des particules tel que $\Delta_y^\infty = 1.53\epsilon^{0.245}$. Inset : definition de l'offset initial et final lors de l'interaction entre deux particules. b) Coefficient de diffusion normalisé versus rugosité obtenu pour des simulations à N=100 particules avec $\phi = 5\%$ et comparaison au modèle $D_{yy}/\dot\gamma d^2 = l^2/\tau \sim \phi\epsilon^{1/2}$.*

de la position transverse à l'écoulement y/d, les particules lisses ($\epsilon = 10^{-4}$) sont réparties de façon relativement homogène. En revanche, les particules rugueuses s'organisent spontanément en couches successives. Cette organisation spatiale des particules diminue l'occurrence de collisions solides et donc diminue leur agitation. Ce changement de microstructure s'explique par la diminution relative des forces de lubrification lorsque l'on augmente la rugosité des particules. On se retrouve ainsi en présence du même phénomène que l'on avait déjà observé sur la figure 2.6a : lorsque les forces de lubrification sont faibles, les particules s'organisent spontanément en couches successives et voient leur coefficient de diffusion diminuer. Ce comportement, non trivial, est aussi bien observé dans les expériences que dans nos simulations numériques directes.

Dans cet article, nous avons aussi étudié de façon systématique l'influence du confinement, des conditions aux limites (périodiques ou parois rigides) et de la polydispersité des particules sur la diffusion induite par cisaillement. Ce travail nous a permis d'explorer les potentialités et la robustesse du modèle présenté au § 2.2.2. Il est intéressant de constater que ce modèle, malgré sa simplicité, reproduit par exemple les microstructures obtenues avec d'autres codes numériques beaucoup plus sophistiqués tels que la dynamique Stokésienne [6], cf. figure 2.15a, ou bien la Force Coupling Method (FCM) [54], cf. figure 2.15b.

2.4 Conclusion

Dans ce chapitre consacré à la micro-hydrodynamique des suspensions cisaillées, nous avons d'abord par une approche numérique réexaminé le rôle respectif des forces hydrodynamiques longues portées, des forces de lubrification et des forces de contact afin de résoudre la controverse portant sur l'origine des fluctuations dans ce type de système. Certaines études attribuaient la diffusion induite par cisaillement à la présence de contacts solides [1, 11] alors que d'autres l'expliquaient dans un cadre purement hydrodynamique [12, 42]. Après avoir montré que la contribution des interactions hydrodynamiques longues portées est négligeable dans ce processus, nous avons développé un modèle minimal ne décrivant que l'effet de l'advection dû à l'écoulement de cisaillement, l'effet des forces normales de lubrification et ceux des contacts solides entre particules. Ce modèle simple permet de reproduire un grand nombre de comportements observés expérimentalement comme par exemple le comportement irréversible d'un triplet de particules soumis à un cisaillement périodique, la transition d'irréversibilité observée dans les suspensions homogènes soumises à un cisaillement périodique, l'augmentation de l'agitation des particules avec la rugosité à faible fraction volumique, ou encore, la transition micro-structurelle en couches successives observée à forte fraction volumique et la diminution des fluctuations qui en résulte lorsque la rugosité des particules augmente.

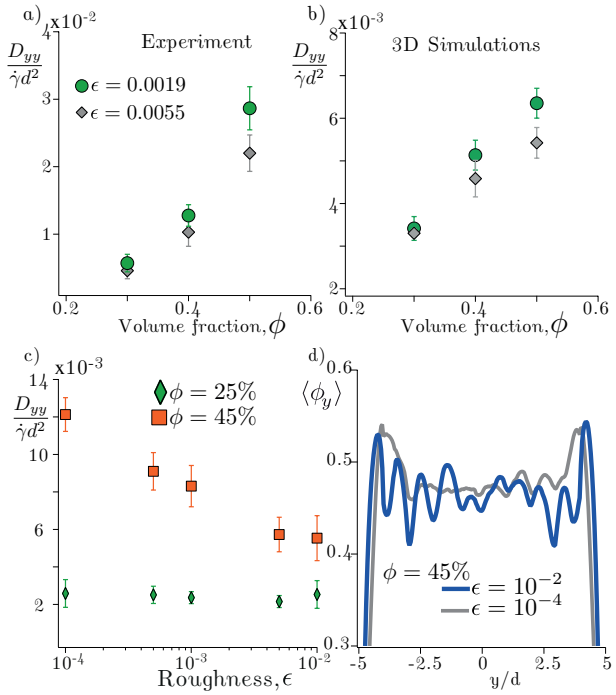


FIGURE 2.14 – *Coefficients de diffusion transverse normalisé $D_{yy}/\dot{\gamma}d^2$ versus fraction volumique obtenus a) expérimentalement pour des particules de rugosité $\epsilon = 0.0019$ et 0.0055 et b) pour des simulations numériques 3D à partir du modèle présenté au § 2.2.2 et en utilisant les mêmes rugosités. Le coefficient de diffusion obtenu est plus faible pour des billes plus rugueuses. c) Coefficients de diffusion transverse normalisé versus rugosité des particules pour deux fractions volumiques. d) Fraction volumique locale, $\langle \phi_y \rangle$, en fonction de la position transverse, y/d, pour des billes lisses ($\epsilon = 10^{-4}$) ou rugueuses ($\epsilon = 10^{-2}$).*

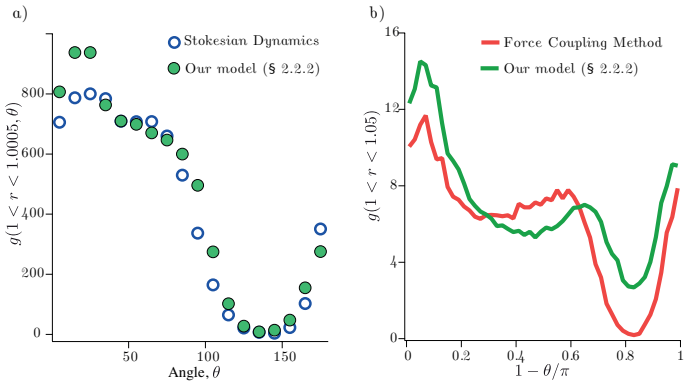


FIGURE 2.15 – *a) Comparaison des fonctions de distribution angulaire, $g(r, \theta)$, au contact calculées à partir des particules situées au centre du gap ($-1 < y/d < 1$) pour une fraction surfacique de 65%, obtenues par Dynamique Stokésienne (Bricker & Butler [6]) et grâce au modèle présenté § 2.2.2. b) Comparaison des Fonctions de distribution angulaire, $g(r, \theta)$ au contact ($2 < r < 2.1$), calculées à partir des particules situées proche du centre du gap ($-2.5 < y/d < 2.5$), obtenues par Force Coupling Method (Yeo and Maxey [54]) et grâce au modèle présenté § 2.2.2.*

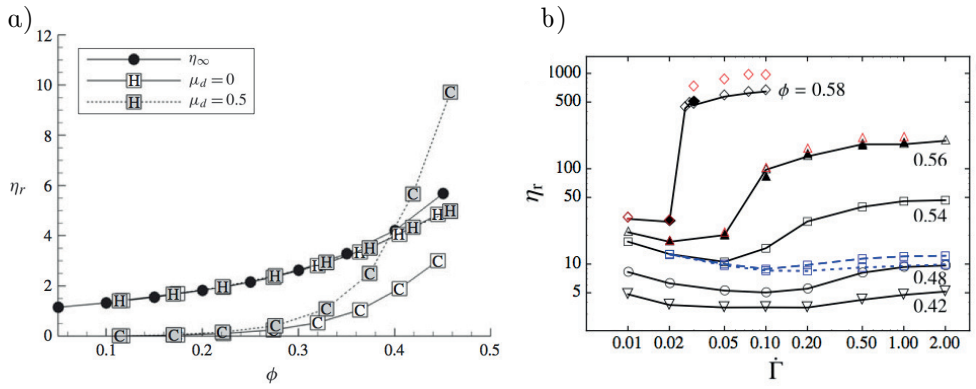


FIGURE 2.17 – a) Contribution respective de l'hydrodynamique (H) et des contacts (C) à la viscosité d'une suspension pour différent coefficients de friction μ_d (Gallier *et al.* [19]). b) Viscosité versus taux de cisaillement adimensionné pour différente fraction volumique et pour une suspension de grains frictionnels interagissant via une force répulsive courte porté (Seto *et al.* [45]).

Par ailleurs, une série d'expériences dédiées nous aura aussi permis, en particulier en modifiant la rugosité des particules, de montrer que les contacts solides entre particules ont lieu et jouent un rôle majeur dans la dynamique de ces systèmes. L'utilisation conjointe de l'approche numérique et expérimentale fut particulièrement fertile pour révéler le couplage entre la divergence des forces de lubrification et l'effet de la rugosité des particules qui conduit, par exemple en cisaillement périodique, à une dépendance non-triviale de l'amplitude de déformation critique avec la rugosité des particules, ou encore en cisaillement continu, à une transition structurelle à forte fraction volumique qui affecte le comportement diffusif des particules.

Enfin, les études présentées dans ce chapitre mettent en évidence les différences fondamentales entre suspensions en sédimentation et suspensions cisaillées. Ces dernières, qui peuvent être décrites à l'aide d'une approche beaucoup plus simple ne faisant intervenir que des forces de type courte portée (lubrification et contact solide), sont largement dominées par l'influence des contacts solides entre particules.

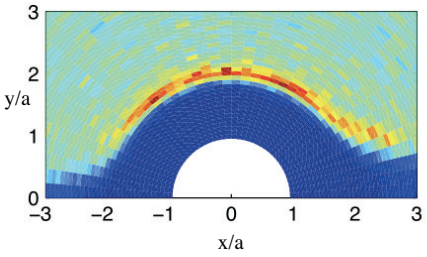


FIGURE 2.16 – L'asymétrie de la fonction de distribution de paire mesurée expérimentalement dans le plan de cisaillement pour une fraction volumique $\phi = 5\%$ (Blanc *et al.* [3]) indique la présence de contacts solides entre particules.

Il est important de mentionner que d'autres travaux très récents soutiennent ce même paradigme. Par exemple, les fonctions de distribution de paire obtenues par Blanc *et al.* [3] dans une suspension homogène montrent une forte asymétrie de microstructure indiquant la présence de contacts solides même à faible fraction volumique (5%), cf. figure 2.16. Par ailleurs, les simulations numériques de Gallier *et al.* [19] mettent en évidence le rôle des contacts et en particulier de la friction entre particules. La viscosité de la suspension dépend significativement du coefficient de friction et, comme illustré sur la figure 2.17, la contribution des contacts à la viscosité augmente fortement avec le coefficient de friction. Attribuer aux effets d'encombrement stérique un rôle dominant et négliger les interactions longues portées autorise la simulation de systèmes plus complexes. Cette approche, qui a récemment été adoptée pour simuler la dynamique d'une suspension de fibres, reproduit convenablement la microstructure [47] et le comportement des contraintes normales [46]. Cette approche a aussi permis des avancées importantes dans la compréhension du comportement rhéologique des suspensions proche de la transition de blocage [26].

Le travail présenté dans ce chapitre participe ainsi à l'emergence d'un consensus fort sur le rôle prépondérant des contacts solides entre particules dans les suspensions cisaillées. Cette description, très différente de celle qui prévalait il y a une dizaine d'années, offre de nouvelles perspectives. Les industriels sont intéressés par cette approche qui autorise la simulation de systèmes plus grands, plus complexes et donc plus proche de configurations réelles. Nous avons en l'occurrence été sollicité par le CPaSS (Center for Particulate & Surfactant Systems, http ://iucrc.perc.ufl.edu/goals.asp), consortium d'industriels américains pour développer d'avantage le modèle présenté au

§ 2.2.2. Les objectifs, qui seront présentés en détail dans les perspectives de ce manuscript, sont de simuler des configurations d'écoulement inhomogène dans lesquelles des effets de migration importants sont attendus et aussi, de décrire la diffusion induite par cisaillement pour des systèmes polydisperses.

La perspective la plus prometteuse et qui illustre probablement le mieux l'importance des contacts dans les suspensions cisaillées est celle ouverte par les modèles récemment (2014) proposés par Seto *et al.* et Wyart & Cates [45,53] pour expliquer la transition de rhéo-épaississement, cf. figure 2.17b. Ces travaux théoriques et numériques proposent une vision novatrice pour expliquer ce phénomène. Ils montrent que l'introduction d'une force répulsive courte portée entre les particules induit un comportement rhéo-épaississant dans une suspension de particules frictionnelles cisaillée. Ce scénario simple, s'il s'applique aux suspensions réelles, ouvre des possibilités très intéressantes telles que le contrôle des propriétés rhéologiques des suspensions. On présentera dans les perspectives quelques pistes envisagées qui nous permettrons de tester expérimentalement ce modèle.

CHAPITRE 3

Dispersion et mélange au sein des suspensions cisaillées

3.1 Introduction et problématique

Dans le chapitre précédent, nous avons étudié le processus de dispersion que subissent les particules au sein d'une suspension cisaillée. La question abordée dans ce nouveau chapitre est de comprendre l'effet de cette agitation des particules sur les propriétés de transfert de masse et de chaleur des suspensions soumises à un cisaillement. Les particules immergées dans le fluide peuvent être vues comme autant de petits agitateurs qui confèrent à l'écoulement une composante stochastique génératrice de mélange. Ce désordre qui apparait spontanément même pour des écoulement à bas nombre de Reynolds, constitue un mode d'intensification des transferts spécifique aux suspensions de particules. Typiquement une collision a lieu tous les $1/\dot{\gamma}$, induisant un déplacement des particules dont l'échelle est fixé par d le diamètre des particules. Dimensionnellement, le coefficient de diffusion qui décrit cette agitation s'écrit $D_p \sim f(\phi)\dot{\gamma}d^2$, où ϕ est la fraction volumique en particules. Pour une suspension de particules de 1 mm de diamètre, cisaillée par un taux de déformation $\dot{\gamma} = 10$ s^{-1} (typique des écoulements de boues ou de ciments) et en prenant $f(\phi) = 10^{-2}$ (cf. figure 2.14a), le coefficient de diffusion des particules vaut alors $D_p \approx 10^{-7}$ m^{2}s^{-1}, soit environ 1000 fois la valeur typique du coefficient de diffusion moléculaire d'une espèce chimique dans l'eau ($\sim 10^{-10}$ m^{2}s^{-1}). Si l'agitation au sein du fluide est du même ordre que l'agitation des particules, on peut s'attendre à ce que le processus de diffusion induite par cisaillement accélère significativement les processus de transfert.

En 1977, Eckstein est le premier à s'intéresser à ce problème afin de mieux comprendre le transport de l'oxygène dans le sang [16]. Il anticipe que l'intensification des transferts qui résulte de l'agitation des globules rouges dans le sang devraient permettre de réduire significativement la taille des dispositifs assurant l'oxygénation du sang, cf. figure 3.1a. Pour démontrer cet effet, Eckstein commence par étudier le phénomène de diffusion induite par cisaillement dans une suspension modèle. Cette étude à suscité un intérêt majeur dans la communauté des rhéologues. Le comportement

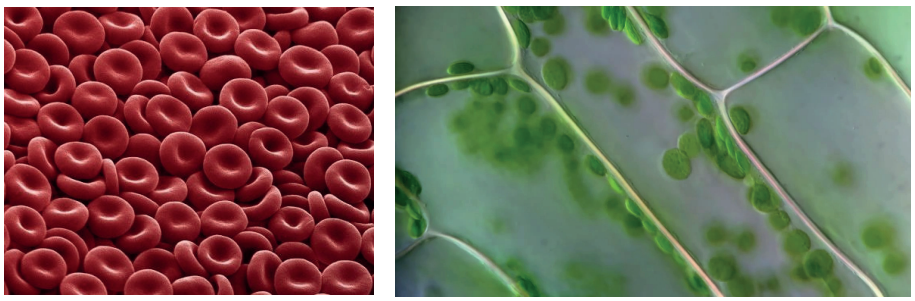


FIGURE 3.1 – *a) Intensification du transport d'oxygène par la présence de globules rouges dans les écoulements sanguins [16]. b) Intensification du transport de nutriments au sein des cellules biologiques par la présence de chloroplastes advectés par le cytoplasmique streaming [20].*

diffusif des particules induit en effet dans les écoulements inhomogènes des effets de migration des particules qui affectent profondément la rhéologie de ces systèmes [37]. Un grand nombre de travaux vont alors être dédiés à la caractérisation de la diffusion induite par cisaillement. En revanche, il est notable que très peu d'étude vont suivre la motivation initiale de Eckstein, à savoir comprendre l'intensification des transferts résultant de cette diffusion induite par cisaillement.

Ce problème semble pourtant important de par le grand nombre d'applications potentielles : fluide caloporteur de conductivité ajustable, contrôle de cinétique chimique, mélange microfluidique. Il a aussi des implications dans la nature. Par exemple, dans certaines cellules biologiques de grande taille, la diffusion moléculaire est trop lente pour assurer le transport de nutriments. Pour palier à ce problème, ces organismes ont développé une stratégie : des moteurs moléculaires parcourent collectivement les parois de la cellule afin d'induire un écoulement du fluide intra-cellulaire pouvant atteindre 100μm s^{-1}. Cet écoulement, appelé le 'cytoplasmic streaming', a longtemps été conjecturé comme aidant à remédier à la lenteur du processus de diffusion moléculaire [20]. Cependant, le fait que des particules telles que des chloroplastes (cf. figure 3.1b), des macro-molécules ou des micro-tubules sont présents dans ces cellules n'a jamais été considéré. Savoir si la diffusion induite par cisaillement décrite plus haut participe au transport des nutriments dans les cellules, autorisant ainsi l'émergence d'espèces constituées de cellules de grande taille, constitue une question totalement ouverte.

Dans ce chapitre, l'objectif est d'étudier, d'abord d'un point de vue macroscopique, quel est l'effet de la diffusion induite par cisaillement sur le transfert de chaleur (ou de masse), en se posant la question de l'influence de la taille des particules, de leur fraction volumique et du cisaillement imposé. Des experiences seront ensuite présentées afin de bien illustrer et comprendre quels sont les mécanismes, à l'échelle de la taille des particules, à l'origine de cette intensification.

3.2 Intensification du transfert de chaleur

Article publié dans Journal of Fluid Mechanics *[34], collaboration avec Ouamar Rahli (IR, IUSTI), Xiaolong Yin (Colorado USA)*

Les suspensions de particules s'avèrent constituer un système quasi-unique où un processus de dispersion efficace se développe spontanément à bas nombre de Reynolds. Un dispositif expérimental original de type Taylor-Couette, cf. Figure 3.2a, nous a permis d'isoler l'effet de la diffusion induite par cisaillement sur le transfert de chaleur au travers d'une suspension cisaillée. Grâce à ce dispositif, nous montrons que l'intensification des transferts de chaleur peut atteindre 200% lorsque la suspension est mise en écoulement. Pour les fractions volumiques inférieures à 40%, le coefficient de diffusion thermique effectif de la suspension α suit une loi simple : $\alpha/\alpha_0 = 1 + 0.046\phi Pe$ où α_0 est le coefficient de diffusion thermique de la suspension au repos et Pe est le nombre de Péclet thermique $Pe = \dot{\gamma}d^2/\alpha_0$, cf. Figure 3.2c. Par ailleurs, une technique numérique (Passive Brownian Tracer Method) a aussi été utilisé afin de simuler simplement le transfert de chaleur dans la suspension cisaillée. L'idée est d'injecter un grand nombre de traceurs passifs Browniens dans la suspension dont l'écoulement est calculé par ailleurs à l'aide d'un code de type Lattice-Boltzman. Le couplage advection-diffusion est directement résolu en laissant les traceurs diffuser dans l'écoulement. Les trajectoires de ces traceurs sont ensuite utilisées afin d'extraire leur coefficient effectif de diffusion. L'accord entre expériences et simulations est excellent, cf. Figure 3.2d.

Le coefficient de diffusion thermique effectif atteint un maximum pour $\phi \approx 40\%$. Le système d'imagerie permettant la visualisation directe des particules et leur tracking nous a permis de montrer que le coefficient de diffusion thermique est directement corrélé au coefficient de diffusion translationel des particules. Au delà de $\phi = 40\%$, les particules s'organisent en couches (frustration stérique des parois) ; le coefficient de diffusion des particules diminue et par conséquent la diffusion thermique effective de la suspension, elle aussi, diminue.

3.3 Dispersion du fluide interstitiel

3.3.1 L'expérience de Taylor revisitée

Article publié dans Physical Review Fluids *[49] collaboration avec Mathieu Souzy (doctorant IUSTI), Pham Phong (doctorant IUSTI/Univ. Florida)*

Dans l'étude précédente sur le transfert de chaleur, nous avons mesuré le coefficient de diffusion thermique effectif de la suspension. Bien que l'on ait pu montrer une corrélation entre l'agitation des particules et le coefficient de

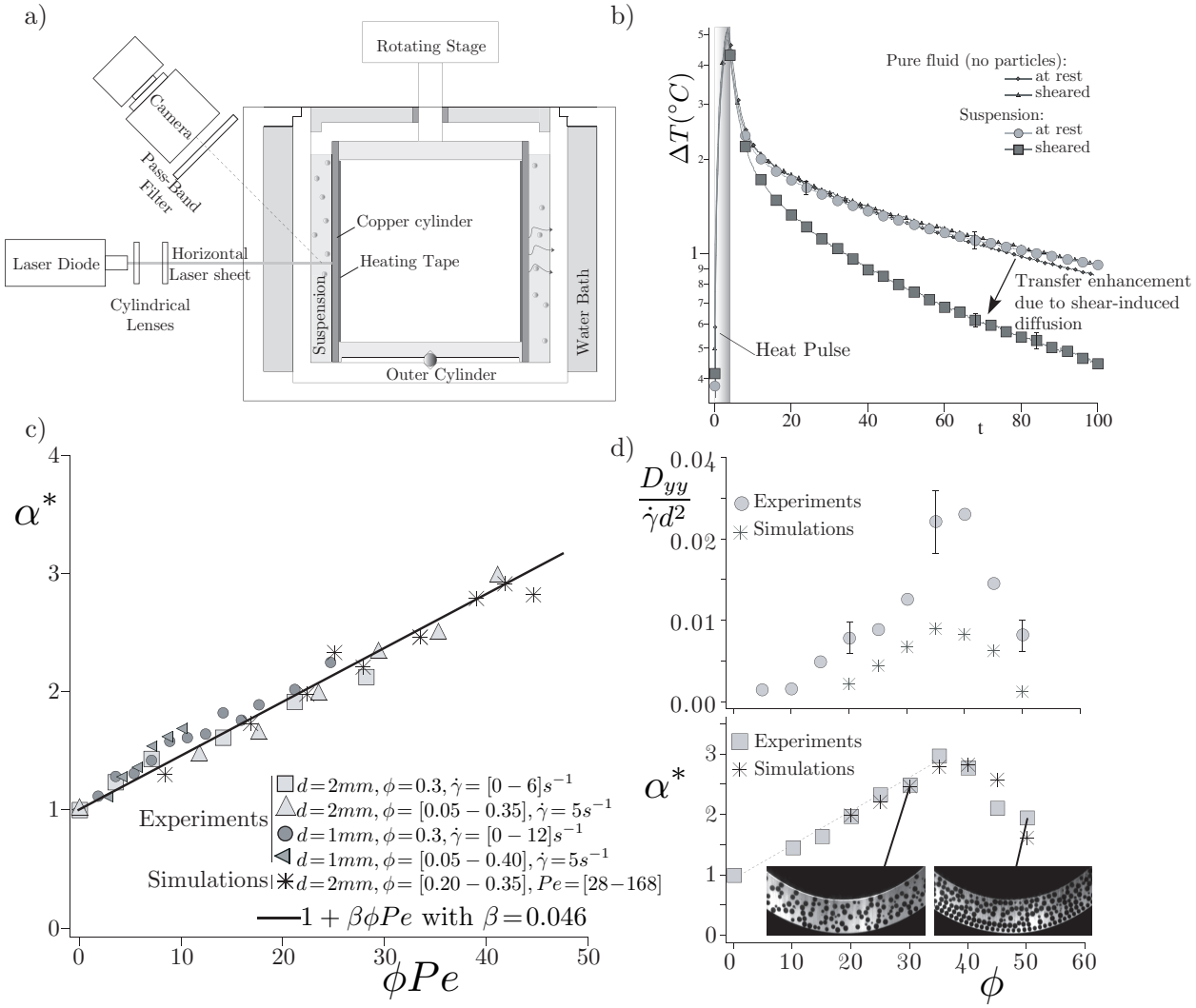


FIGURE 3.2 – *a) Dispositif expérimental de Taylor-Couette thermostaté pour la mesure du coefficient de diffusivité thermique α de la suspension. Le cylindre interne de la cellule est en cuivre ; chauffé de manière pulsé, sa décroissance en température est utilisé pour déterminer le coefficient de diffusion thermique de la suspension lorsqu'elle est soumise à un cisaillement. b) Evolution de la température du cylindre interne soumise à un 'pulse' de chaleur dans un fluide pur, au repos et cisaillé, et dans une suspension, au repos et cisaillée. La rapide décroissance de la température du cylindre, dans le cas de la suspension cisaillée, illustre l'intensification du transfert induit par la présence des particules. c) Coefficient de diffusivité thermique effectif α^* versus ϕPe pour l'ensemble des données expérimentales et numériques obtenues pour des tailles de particules, des taux de cisaillement et des fractions volumiques différentes. d) Comparaison entre l'évolution du coefficient de dispersion transverse des particules $D_{yy}/\dot\gamma d^2$ et du coefficient de diffusivité thermique effectif α^* de la suspension. A forte fraction volumique, l'organisation en couche des particules diminue leur agitation et par conséquent l'intensification du transfert.*

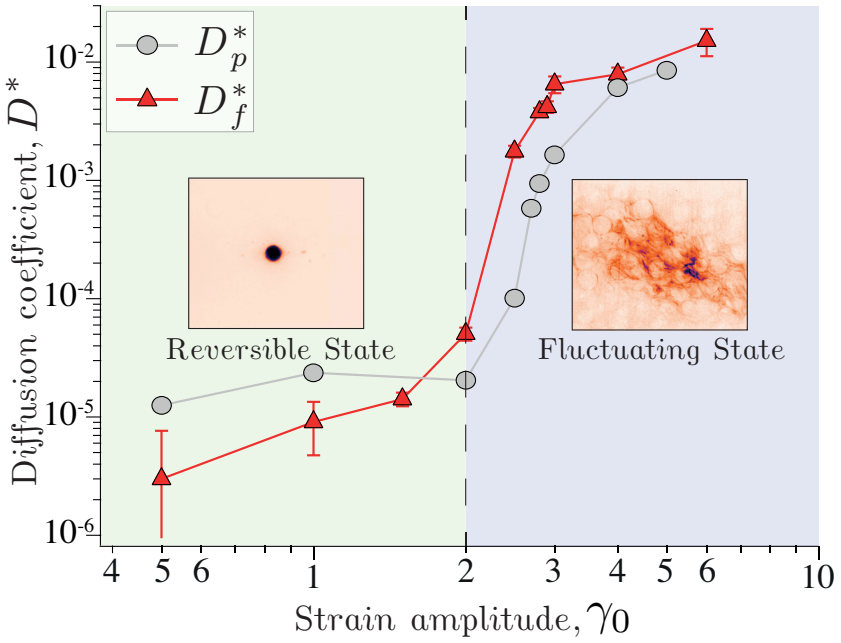


FIGURE 3.3 – *Coefficients de dispersion des particules D_p^* et du fluide D_f^* en fonction de l'amplitude de déformation γ_0 des cycles de cisaillement. Inserts : images du blob de colorant après 40 cycles de cisaillement.*

diffusion thermique, l'approche reste macroscopique et les mécanismes à l'origine de l'intensification ne sont pas bien identifiés. L'idée ici est de directement visualiser le processus de dispersion afin de mieux comprendre ces mécanismes. Pour cela, nous déclinons à nouveau l'expérience de Taylor, cette fois afin d'étudier l'évolution d'un blob de colorant injecté au sein d'une suspension de particules non-Browniennes soumise à un cisaillement périodique. Comme évoqué dans le premier chapitre, la suspension transite vers un état fluctuant au delà d'une certaine amplitude de déformation critique. Nous montrons que cette transition induit une forte accélération de la dispersion du blob de colorant, cf. figure 3.4. En mesurant l'évolution des profils de concentration du colorant, on trouve que le coefficient de diffusion effectif décrivant la dispersion de la phase fluide est bien décrit par le coefficient de dispersion des particules. Ce coefficient peut excéder de quatre ordres de grandeur le coefficient de diffusion moléculaire du colorant.

3.3.2 "Rolling-coating" en proche paroi

Article publié dans Physics of Fluids *[50] en collaboration avec Mathieu Souzy (doctorant IUSTI), Xiaolong Yin (Colorado USA), Emmanuel Villermaux (IRPHE) & Nora Abid (IUSTI)*

Afin de mieux comprendre l'influence des parois, nous étudions ici la dispersion d'une couche de colorant (Rhodamine 6G) initialement déposée sur le cylindre externe de la cellule de Couette, cf. figure 3.4a. Lorsque la suspension est soumise à un cisaillement, la couche de colorant envahit progressivement l'intégralité du gap entre les deux cylindres, cf. figure 3.4a. Ces visualisations directes du processus de dispersion montre que la présence des particules induit des patterns d'écoulement complexes qui contribuent a intensifier la dispersion du colorant. Ces patterns, bien que l'on soit dans des conditions d'écoulement à bas nombre de Reynolds, rappellent ceux observés dans les écoulement turbulents, cf figure 3.4c. Le résultat marquant de ces expériences est le rôle important, en proche paroi, de la rotation des particules : les particules qui tournent sur elles-même du fait du cisaillement imposé, advectent la rhodamine de la paroi vers le bulk de la suspension. Ce mécanisme appelé "Roalling-coating" a pour effet de générer un flux constant de colorant de la paroi vers le bulk, courcircuitant ainsi la couche limite diffusive postulée par Wang *et al.* [27]. Nous avons par ailleurs établit, à partir de la mesure des fluctuations de vitesse du fluide interstitiel, que le profil de dispersion de la phase fluide augmente linéairement avec la distance à la paroi. On peut ainsi décrire le processus de dispersion de la couche de colorant par une équation de diffusion ayant un coefficient de diffusion effectif qui augmente linéairement avec la distance à la paroi et en considérant un flux de masse constant comme condition à la paroi. L'évolution des profils de concentration mesurés expérimentalement est bien prédite par ce modèle dont la solution est de type gamma incomplète.

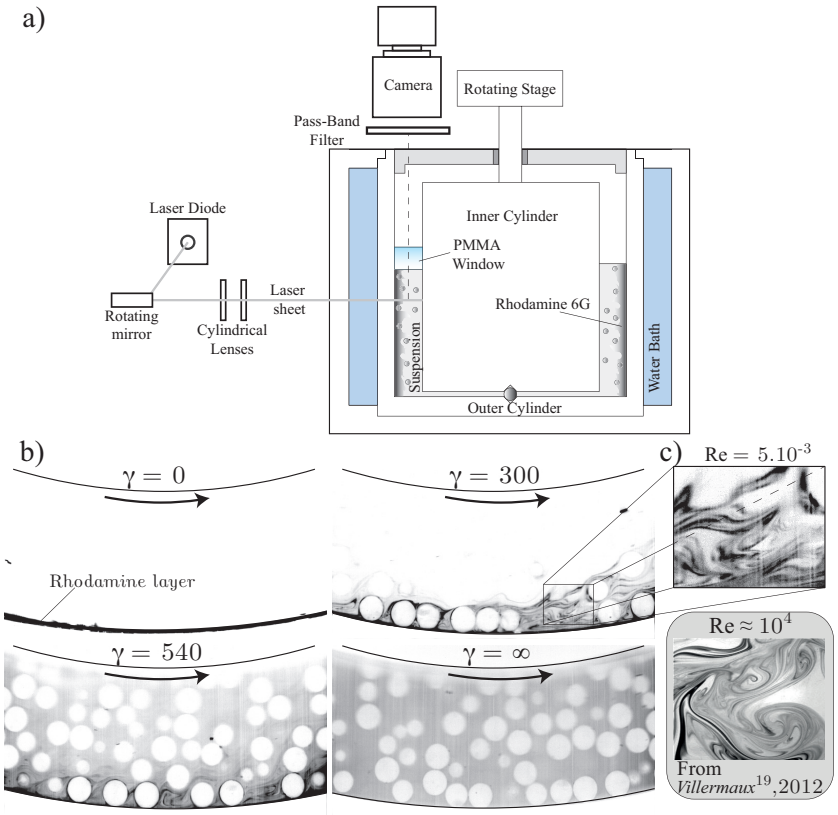


FIGURE 3.4 – *a) Dispositif expérimental pour la visualisation du mélange d'une couche de colorant initialement déposé sur la surface du cylindre externe. b) Images successives de la suspension. La couche de Rhodamine, initialement sur le cylindre externe, envahit progressivement l'intégralité du gap entre les deux cylindres. c) Pattern de mélange comparé à un pattern typiquement observé en écoulement turbulent.*

3.4 Lois d'étirement : conséquences pour le mélange

Article publié dans Journal of Fluid Mechanics *[48] en collaboration avec Mathieu Souzy (doctorant IUSTI), Emmanuel Villermaux (IRPHE) & Henri Lhuissier (IUSTI)*

Dans les deux études présentées ci-dessus, la question du transfert a été traitée en caractérisant le processus par un coefficient de dispersion effectif. Cette approche décrit le processus de dispersion du colorant dans son ensemble et permet de rendre compte de l'intensification des transferts qui a lieu dans les suspensions de particules soumises à un cisaillement. A présent, l'objectif est de s'intéresser au processus de mélange, *i.e.* à l'homogénéisation des niveaux de concentration qui résulte de couplage advection diffusion. Nous nous placerons cette fois dans le bulk (loin des parois) et la suspension sera soumise à un cisaillement continu. Les objectifs sont de comprendre comment un système initialement ségrégé (un blob de colorant) s'homogénéise dans le système, et de répondre à une question particulièrement importante qui est de prédire la durée de ce processus. Pour cela, la stratégie employée sera de désimbriquer l'effet de l'advection et de la diffusion moléculaire. En s'appuyant sur l'approche dite 'lamellaire' [44], on déterminera dans un premier temps les loi d'étirements qui quantifient la cinématique de déformation du système. On pourra ensuite y coupler l'effet de la diffusion moléculaire afin de prédire la durée caractéristique du processus de mélange.

Comprendre le processus de mélange, *i.e.* l'homogénéisation des niveaux de concentration, nécessite dans un premier temps de connaitre la cinématique de déformation induite par le champ d'écoulement. Pour cela nous avons effectué des mesures fines du champ d'écoulement au sein du fluide interstitiel, cf figure 3.5a. Ces mesures ont nécessité un ajustement précis (à la quatrième décimale) des indices de refraction entre les deux phases. Ces champs de vitesse ont ensuite été utilisés afin de reconstruire l'historique d'étirement de lignes matérielles au sein du fluide en s'appuyant sur la *Diffusive Strip Method* développée par Meunier & Villermaux [35]. En pratique, les champs de vitesses expérimentaux sont utilisés afin d'advecter numériquement des traceurs passifs discrétisant des lignes matérielles du fluide interstitiels, cf. figure 3.5b. Ces lignes s'étirent, parfois se replient sur elles mêmes, au grè des fluctuations de vitesses induites par la présence des particules et du cisaillement moyen. En moyennant les étirements subits par un grand nombre de lignes matérielles, on obtient les lois d'étirements (figure 3.5c) qui décrivent l'étirement moyen et la distribution des étirements.

Un résultat majeur est que la présence des particules dans le fluide change la nature des lois d'étirement. Celles-ci passent de linéaires dans un fluide pur, à exponentielles en présence de particules. Nos résultats montrent que la moyenne $\langle\rho\rangle$ et l'écart type σ_ρ des étirements croissent exponentiellement avec le temps, et que la distribution des étirements converge vers une distribution log-normale. Nous avons par ailleurs pu extraire deux grandeurs importantes : la distribution des taux de cisaillements locaux ainsi que leur temps de persistance. A partir de ces deux quantités, on peut décrire l'historique d'étirement des lignes matérielles comme un processus multiplicatif qui consiste en une succession de cycles d'étirements décorrélés les uns des autres. L'idée est que chaque portion de ligne matérielle subit localement, à une échelle petite devant la taille des particules, une succession d'étirements linéaires (fixés par les taux de cisaillement locaux) et qui durent chacun un certain temps (donné par le temps de persistance du champ de vitesse). L'étirement de cette portion de ligne, au bout d'un certain temps, correspond au produit des étirements successifs qu'il a subit durant chaque cycle. Ces étirements étant décorrélés les uns des autres, l'étirement résultant en vertu du théorème central limite, est distribué de façon log-normal et sa moyenne augmente de façon exponentielle. Ce modèle simple prédit quantitativement l'évolution de la moyenne, de la variance, et la forme log-normale des distributions d'étirements mesurées expérimentalement.

La connaissance de ces lois d'étirement en y couplant l'effet de la diffusion moléculaire, permet de prédire le processus de mélange (si on néglige l'effet de coalescence entre filaments voisins). En particulier, nous comprenons maintenant quantitativement la distribution très large des temps de mélange qui traduit le fait que les zones du fluide fortement étirées se mélangent plus rapidement que celles subissant une contraction. La comparaison de l'évolution d'une goutte de colorant cisaillée à bas nombre de Reynolds dans un fluide pur ou, dans une suspension de particules, cf figure 3.6, illustre bien cette phénoménologie. La présence des particules augmente fortement la dispersion du colorant mais les étirements sont très inhomogènes par rapport au cas du fluide pur. La description du processus de mélange, offerte ici par l'approche 'lamellaire', permet d'appréhender cette complexité. Le processus de mélange n'est pas caractérisé par un seul temps de mélange comme dans le cas du cisaillement simple, mais par une distribution de temps de mélanges bien représentée, comme la distribution des taux d'étirements, par une distribution Gaussienne. Certaines régions du fluide, fortement étirées, atteignent leur temps de mélange très rapidement. En revanche, nous avons montré que tant que le nombre de Péclet est inférieur à $\sim 10^5$, les régions qui sont sujettes à une compression peuvent atteindre leur temps de mélange plus tardivement que dans un fluide pur cisaillé. Cet aspect, que nous avons mis en évidence et quantifié, est important pour la compréhension du processus de mélange dans les suspensions

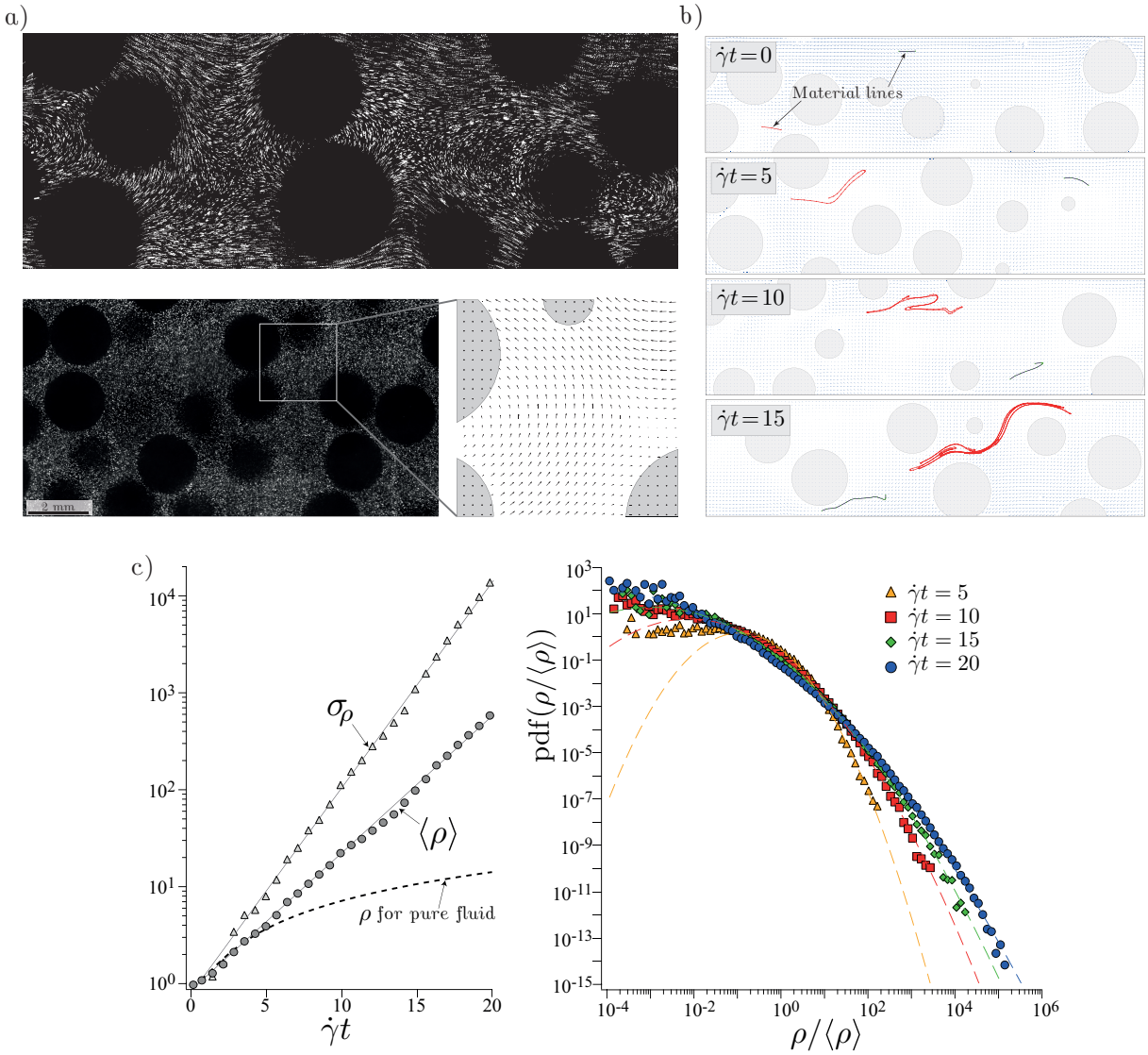


FIGURE 3.5 – *a) Ligne de courant au sein d'une suspension de particules cisaillée, image typique de la suspension et zoom sur le champ de vitesse obtenu par PIV. b) Advection numérique de deux lignes matérielles à partir des champs de vitesses expérimentaux. c) Lois d'étirement : (à gauche) étirement moyen $\langle\rho\rangle$ et déviation standard des étirements $\langle\sigma_\rho\rangle$ en fonction du temps. (à droite) Evolution des distribution d'étirements normalisés par l'étirement moyen.*

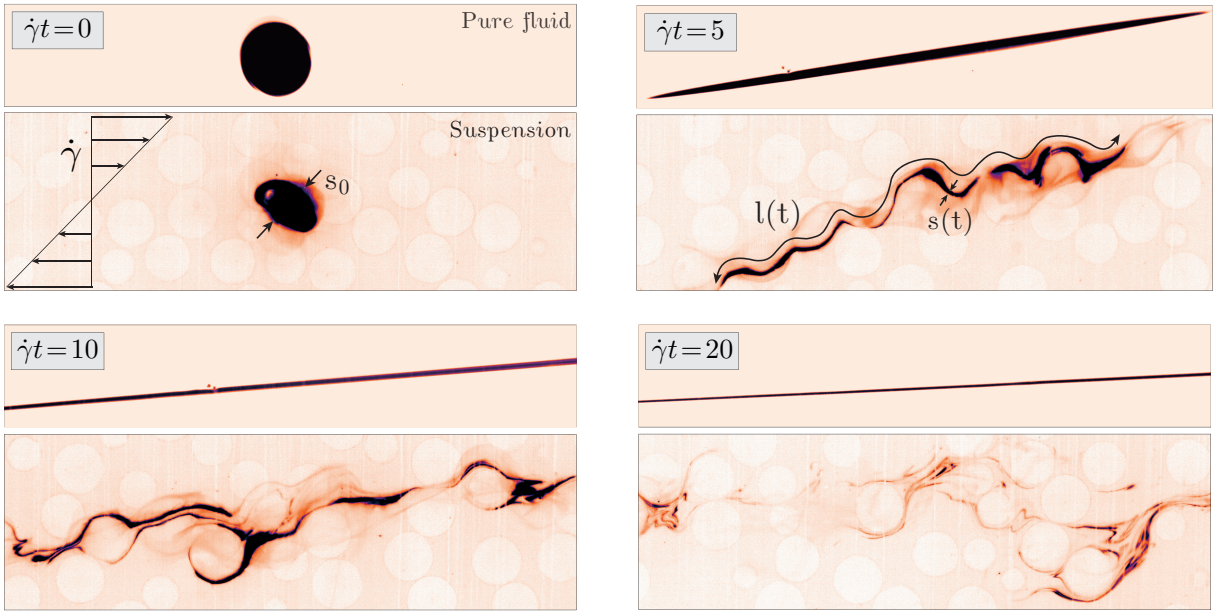


FIGURE 3.6 – *Comparaison du processus d'étirement d'un blob de colorant cisaillé à grand Péclet et petit nombre de Reynolds dans un fluide pur (en haut) et dans une suspension de particules (en bas).*

cisaillées.

3.5 conclusion

Les études présentées ci-dessus montrent que dans les suspensions non-Browniennes et non-inertielles, la présence des particules accélère les processus de transferts. Le désordre instationnaire induit par les collisions successives entre les particules génère une dispersion importante que nous avons quantifiée en étudiant le transfert de chaleur au travers d'une suspension cisaillée et la dispersion d'un colorant soit injecté dans le bulk, soit en proche paroi. Inspiré par ces études, le groupe de Dijksman a élaboré en 2015 un prototype de mélangeur micro-fluidique astucieux basé sur la diffusion induite par cisaillement, cf. figure 3.7. Les fluides à mélanger sont injectés dans une large chambre remplie de particules mises en mouvement par un barreau magnétique. Cette configuration est particulièrement adapté aux systèmes microfluidiques car elle conduit à une homogénéisation rapide des deux fluides tout en assurant une faible perte de charge [52].

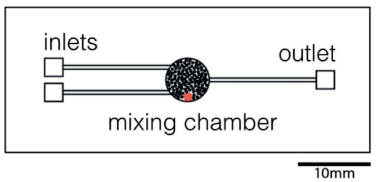


FIGURE 3.7 – Schéma d'un mélangeur microfluidique utilisant la diffusion induite par cisaillement [52].

Nous avons aussi abordé le processus de mélange par l'approche dite 'lamellaire'. L'utilisation que nous avons faite de la Diffusive Strip Method [35] est novatrice car elle a pour la première fois été appliquée à un champ de vitesse mesuré expérimentalement. Comme nous le verrons dans le chapitre consacré aux perspectives, la procédure employée ouvre un champ d'application à cette méthode qui peut à présent être étendue aux configurations pour lesquelles la forme analytique du champ de vitesse n'est pas connue. L'approche 'lamellaire', qui consiste à caractériser la cinématique de déformation induite par l'écoulement pour ensuite y coupler l'effet de la diffusion moléculaire, est particulièrement efficace car elle permet de prédire l'ensemble du processus d'homogénéisation. L'évolution des distributions de temps de mélange, que nous pouvons maintenant décrire analytiquement, caractérise en partie ce processus. Pour aller plus loin, ils nous faut à présent mesurer et décrire l'évolution des distributions de concentration. Ce travail dont je décrirai les jalons dans le chapitre consacré aux perspectives, devrait offrir une description globale des processus de mélange dans les suspensions de particules soumises à un cisaillement.

CHAPITRE 4

Perspectives

La dernière partie de ce mémoire d'habilitation s'ouvre sur les projets de recherche que je souhaite développer dans le futur.

Micro-hydodynamique des suspensions cisaillées : La mise en évidence du rôle prépondérant des contacts et surtout la description minimale des suspensions cisaillées présentée en première partie offre de nouvelles possibilités. On abordera en particulier le phénomène de migration qui a un impact majeur sur le comportement des suspensions et reste néanmoins encore mal compris. On s'intéressera aussi à la diffusion induite par cisaillement dans le cas de suspensions polydisperses qui sont rencontrées dans la plupart des procédés industriels ou des phénomènes naturels. L'étude du rôle des interactions de contact m'amène aussi vers un sujet nouveau : le rhéo-épaississant des suspensions denses, pour lequel des propositions théoriques récentes indiquent que les interactions de champ proche (contacts frictionnels et forces répulsives courtes portées) pourraient jouer un rôle important.

Mélange : Nous avons montré que la présence de particules au sein d'un fluide cisaillé change la nature de la cinématique de l'écoulement : les étirements sont linéaires dans un fluide pur cisaillé ; ils sont exponentiels dans une suspension. Ce changement, qui a un impact considérable sur le processus d'étirement, devrait permettre d'expliquer quantitativement l'intensification des transferts observés dans les suspensions de particules cisaillées. L'objectif sera de clarifier et quantifier ces effets d'abord en mesurant l'évolution de la distribution de concentration d'un scalaire initialement ségrégé, puis en comparant ces mesures aux prédictions théoriques découlant de la connaissance de la cinématique de l'écoulement. Par ailleurs, un sujet entièrement nouveau sera abordé, celui de la dispersion et du mélange dans les milieux poreux.

Dans ce qui suit, je développe ces différentes pistes de recherche.

4.1 Micro-hydodynamique des suspensions cisaillées :

4.1.1 Migration

Collaboration avec J. E. Butler (Univ. Florida)

La migration est une conséquence directe de la nature irréversible des interactions entre particules dans les suspensions cisaillées. En présence d'un gradient de cisaillement, comme par exemple dans un écoulement de type Poiseuille, l'agitation des particules est plus intense au niveau des zones de fort cisaillement. Les particules migrent alors spontanément vers la zone centrale du canal [46]. Cette migration des particules a suscité un grand intérêt étant donné son impact majeur sur le comportement rhéologique macroscopique des suspensions. Les industriels du consortium américain CPaSS nous ont sollicité afin que l'on développe notre modèle numérique pour décrire ces phénomènes dans des configurations d'écoulement complexe. Nous étudierons d'abord une configuration de type

Poiseuille pour lesquelles des données expérimentales sont disponibles [46]. Il sera intéressant par la même occasion d'extraire les contraintes normales et d'étudier les relations qui lient les gradients de cisaillement et de fraction volumique, aux contraintes normales et au flux instantané de particules. Des modèles de migrations existent [36] mais la description des transitoires reste encore largement débattue [46]. La simplicité de notre code numérique et sa rapidité devraient ensuite nous permettre d'aborder des configurations d'écoulement complexes plus proches de celles rencontrées dans l'industrie.

4.1.2 Diffusion induite par cisaillement : cas des suspensions polydisperses

Article en préparation pour Journal of fluid Mechanics, *collaboration avec J. E. Butler (Univ. Florida) et H. Lhuissier (CR IUSTI)*

Les suspensions que nous avons considérées jusqu'à présent sont monodisperses. Or dans la plupart des procédés industriels ou phénomènes naturels, les grains ne sont pas tous identiques et diffèrent souvent par leur taille. Les suspensions monodisperses sont bien caractérisées par un coefficient de diffusion transverse $D_{yy} \sim \phi\dot{\gamma}d^2$. Des résultats préliminaires obtenus grâce à nos simulations directes pour des suspensions polydisperses, montrent que le coefficient de dispersion transverse des particules, $D_{yy}/\dot{\gamma}\langle d\rangle^2$, dépend fortement de la polydipersité des particules, cf. figure 4.1. Comme à chaque collision, le déplacement typique des particules est une fraction de leur diamètre et que pour décrire la diffusion, c'est le carré des déplacements qui importe, on pourrait penser que la bonne normalisation serait d'utiliser la moyenne des carrés $\langle d^2\rangle$ au lieu du carré de la moyenne $\langle d\rangle^2$. Les données de la figure 4.1 montrent cependant que cette normalisation (par la moyenne des carrés) n'est pas satisfaisante. Cette dépendance non-triviale du coefficient de dispersion des particules constitue un problème statistique intéressant. En effet, si deux billes de tailles différentes se rencontrent dans un cisaillement simple, le déplacement transverse typique d'une bille est donné par le diamètre de l'autre. Les grosses billes ont cependant une section efficace plus importante ; elles devraient ainsi subir un plus grand nombre de collisions et par conséquent diffuser plus. Ce comportement est atypique car à l'opposé de la diffusion moléculaire pour laquelle les éléments de plus petite taille diffusent le plus. On s'attèlera à comprendre ce processus de diffusion en étudiant le comportement statistique d'un ensemble de particules polydisperses soumises à un cisaillement simple. Ce problème est important par exemple pour prédire la migration, l'amplitude des contraintes normales ou encore déterminer l'intensité du mélange dans de tels systèmes !

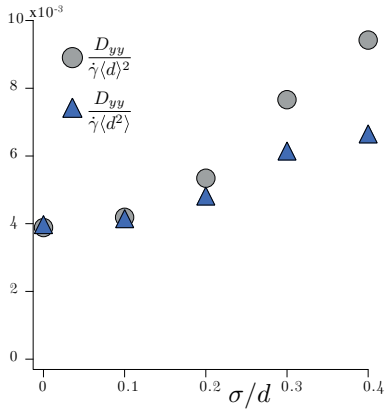


FIGURE 4.1 – Coefficients de dispersion transverse en fonction de la deviation standard σ de la distribution de taille (ici Gaussienne) des particules obtenus par simulations directes pour une suspension de fraction volumique $\phi = 30\%$.

4.1.3 Le rheo-épaississement : une transition frictionnelle ?

Article soumis à PNAS [7], collaboration avec C. Clavaud (doctorante), Y. Forterre (IUSTI) et M. Wyart (EPFL Suisse)

Le rhéo-épaississement est l'un des phénomènes les plus spectaculaire observé dans les fluides complexes. Il a lieu dans les suspensions dont la viscosité augmente brutalement, parfois de plusieurs ordres de grandeur, lorsque le taux de cisaillement imposé dépasse une valeur critique. L'origine de ce phénomène est longtemps restée obscure, cependant, des prédictions théoriques très récentes fournissent enfin un scénario cohérent pour expliquer cette transition [45, 53]. L'idée est que le rhéo-épaississement peut être induit dans les suspensions en introduisant une force répulsive courte portée entre les particules, par exemple en couvrant leurs surfaces avec un polymère choisi. A faible taux de cisaillement, cette force répulsive empêche les grains d'entrer en contact ; la suspension coule alors facilement comme si les particules avait un coefficient de friction nul. En revanche, à fort taux de cisaillement, la force répulsive est vaincue et les particules, poussées au contact solide, produisent un milieu fortement dissipatif : la suspension se transforme soudainement en solide. Ce scénario, de type transition frictionnelle, a reçu le soutient prometteur de simulations numériques et d'expériences très récentes. Cependant, les preuves expérimentales restent indirectes car les expériences, réalisées dans des configurations rhéologiques standards (à fraction volumique imposées), ne

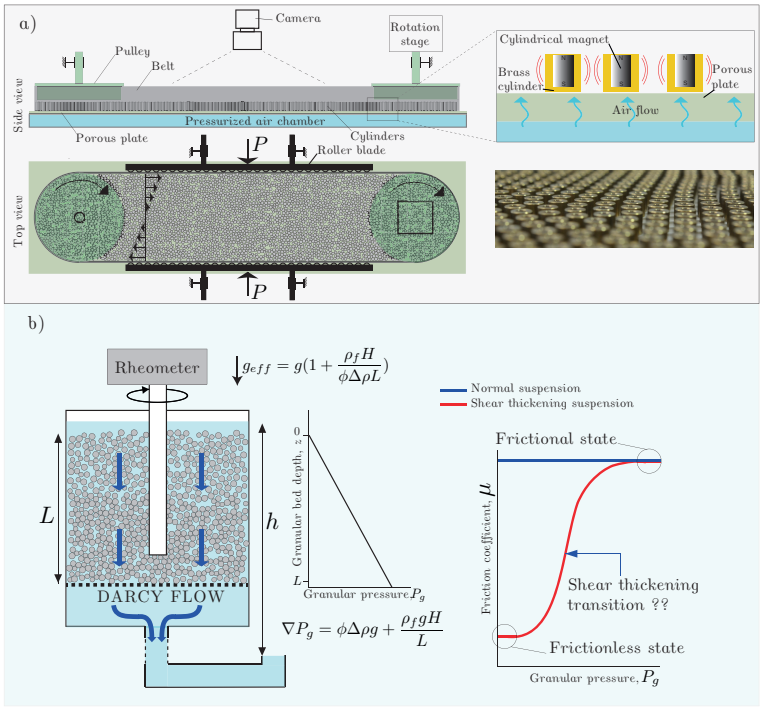


FIGURE 4.2 – a) Schéma du 'Stadium shear on air' : 5000 grains cylindriques sont mis en mouvement par une courroie soumise à une pression de confinement P. Cette configuration permet un cisaillement continu et une analyse à l'échelle des grains. Zoom : des aimants cylindriques sont placés à l'intérieur de chaque grain afin de générer une force répulsive isotrope entre les grains dans le plan de cisaillement. Les grains sont en lévitation sur une table à coussin d'air afin de s'affranchir des effets de la friction basale. b) Schéma du Darcytron : en variant la hauteur h de l'écoulement de liquide, on peut simplement ajuster la gravité effective, g_{eff} et donc la pression de confinement, P_g, ressentie par les grains. Le graphique de droite représente le comportement attendu du coefficient de friction en fonction de la pression de confinement pour une suspension frottante standard et pour une suspension rhéo-épaississante.

donnent pas accès au coefficient de friction effectif de la suspension, quantité clef pour comprendre cette transition. Nous envisageons de construire deux rhéomètres originaux : le 'Stadium-Shear on Air' et le 'Darcy-Rheometer', qui permettront précisément de mesurer cette quantité ainsi que d'étudier la rhéologie à pression imposée d'un matériaux granulaire modèle 2D, et de suspensions réelles rhéo-épaississantes, cf figure 4.2.

Le 'Stadium-Shear on Air' permettra de tester expérimentalement le modèle théorique présenté ci-dessus et en particulier de répondre à la question suivante : est-ce-que l'introduction d'une force répulsive entre les particules induit une rhéologie de type rhéo-épaississante ? Le 'Stadium-shear' permet d'étudier un écoulement granulaire 2D, composé de grains cylindriques frottants, dans chacun desquels est placé un aimant magnétique cylindrique générant une force répulsive isotrope entre les grains, cf figure 4.2a. Ce dispositif permettra de cisailler le système de façon continu, de contrôler la pression de confinement et fournira à la fois des informations à l'échelles des particules mais aussi la rhéologie macroscopique du système. On étudiera dans un premier temps le système sans force répulsive (système granulaire 2D classique). Dans ce cas le coefficient de friction macroscopique doit être indépendant de la pression de confinement. On insèrera ensuite les aimants dans chacun des grains. Cette force magnétique additionnelle devrait induire une rhéologie qui dépend de la pression de confinement et donner lieu à fraction volumique imposé à un comportement rhéo-épaississant. Ce dispositif donnera aussi la possibilité d'étudier la transition grains-mous-sans-frottement/grains-durs-frottants, sujet actuellement très débattu au sein de la communauté s'intéressant à la plasticité des systèmes amorphes [26].

Pour étendre la rhéologie à pression imposée aux suspensions rhéo-épaissaissantes, la taille micro-métrique des particules constitue une difficulté expérimentale majeure. L'idée principale ici est d'imposer la pression de confinement, non pas en utilisant une grille rigide mobile comme Boyer *et al.* [4], mais en imposant un écoulement vertical de type Darcy au travers du milieu granulaire, cf figure 4.2b. Ce 'Darcy-Rheometer' devrait permettre de directement mesurer le coefficient de friction (rapport entre la contrainte de cisaillement et la pression granulaire) de suspensions rhéo-épaississantes réelles. Nous calibrerons d'abord le 'Darcy-Rheometer' avec une suspension standard de grosses

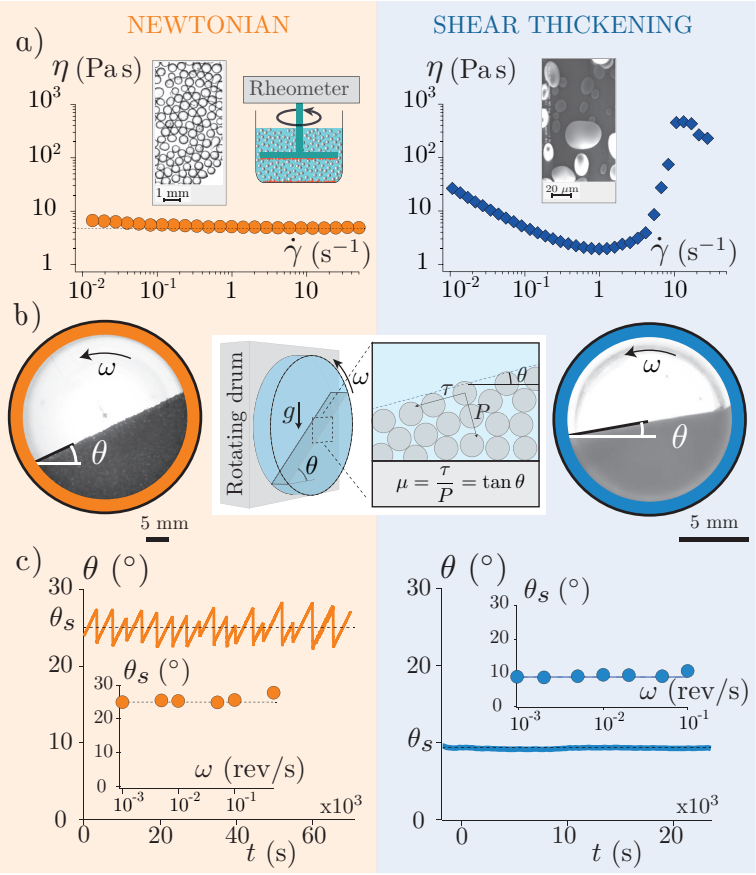


FIGURE 4.3 – a) Image et rhéogrammes (viscosité η versus taux de cisaillement $\dot{\gamma}$) d'une suspension Newtonienne de grosses billes de verre (à gauche) et d'une suspension rhéo-épaississante de grains d'amidon (à droite). b) Schéma du tambour tournant et images typiques d'avalanches stationnaires pour les billes de verres (à gauche) et pour les grains d'amidon (à droite). c) Angles d'avalanche en fonction du temps.

billes de verre immergées dans de l'eau. Dans ce cas, le coefficient de friction doit être indépendant de la pression granulaire. Nous étudierons ensuite des suspensions rhéo-épaississantes (billes de silices de petite taille ou particules d'amidon immergées dans de l'eau) en mesurant le coefficient de friction en fonction de la pression de confinement. Ce dispositif devrait nous permettre de savoir si le rhéo-épaississement correspond à une transition frictionnelle. Il nous permettra aussi d'étendre l'approche rhéologie à pression imposée aux système colloïdaux.

Ce projet a fait l'objet d'une demande d'ANR en 2017. Il constitue aussi le sujet de thèse de Cécile Clavaud qui a démarrée en octobre 2015 et que je co-encadre avec Yoel Forterre (IUSTI). En adoptant une approche de type pression-imposée inspirée des milieux granulaires, nous avons pu montrer que les suspensions rhéo-épaississantes sont effectivement caractérisées par un état sans frottement à faible pression de confinement. Cette phénoménologie est bien illustrée sur la figure 4.3. Dans une configuration de tambour tournant, une suspension de particules macroscopiques standard (ici des billes de verre de diamètre 500 μm) coule de façon stationnaire avec un angle de $25°$ caractéristique pour une suspension de particules frottantes. Dans les mêmes conditions, une suspension de grain d'amidon (modèle de suspension rhéo-épaississante) coule avec un angle de $8°$. Cet angle, très faible, indique que le coefficient de friction inter-grains est quasi nul.

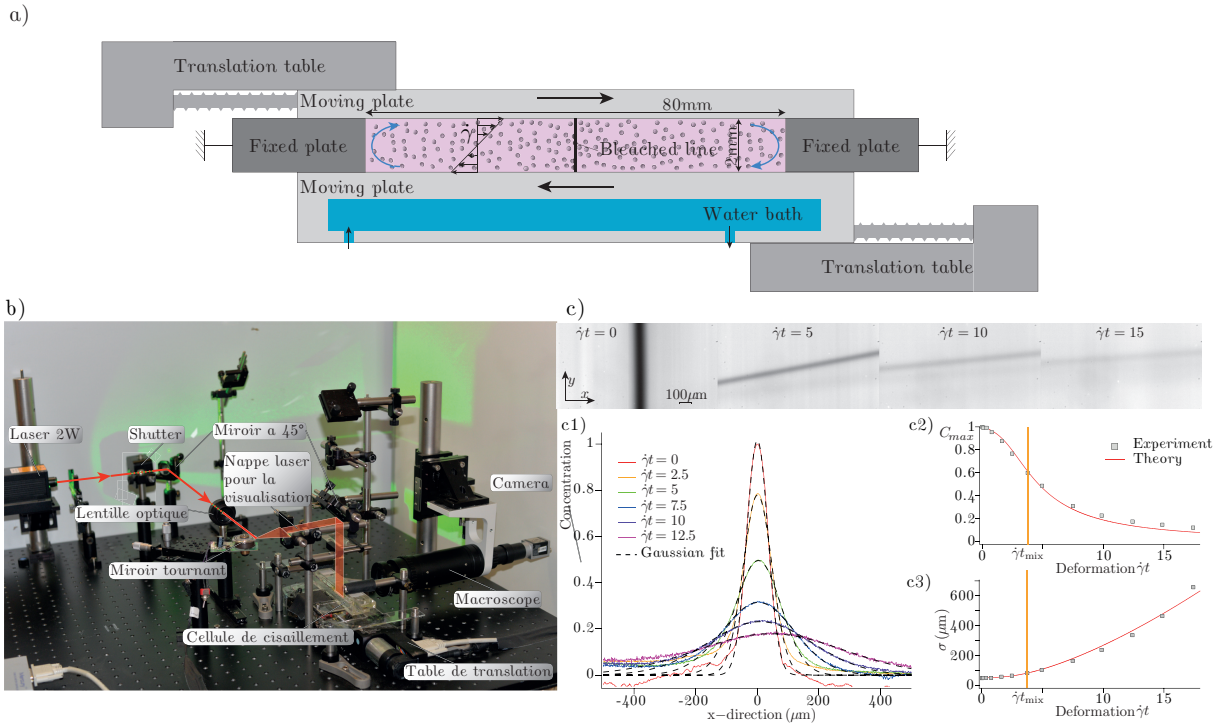


FIGURE 4.4 – a) Schéma de la cellule plan-plan pour la mesure de l'évolution de la distribution de concentration d'un blob de colorant. b) Photographie du dispositif expérimental. c) Evolution d'une ligne de colorant cisaillée dans un fluide pur (sans particule). Evolution des profils de concentration, de la concentration maximale $C_{\max}$ et de la largeur des profils σ en fonction de la déformation imposée $\dot{\gamma}t$.

4.2 Mélange

4.2.1 Evolution des distributions de concentration dans les suspensions cisaillées

Collaboration avec I. Zaier (Master 2), H. Lhuissier (CR IUSTI) et E. Villermaux (IRPHE)

La perspective la plus immédiate, en ce qui concerne le mélange dans les suspensions de particules cisaillées, est de comprendre l'évolution de la distribution de concentration d'un scalaire initialement ségrégé. Comme on l'a vue plus haut, la connaissance de la cinématique de l'écoulement (les lois d'étirements) nous indique comment un blob de taille initiale s_0 est étiré. Par conservation de la masse, cette information prescrit la vitesse à laquelle les filaments de colorant s'affinent au cours du temps. Si le champ d'advection affine les filaments de colorant, la diffusion moléculaire a l'effet opposé : elle élargit les dimensions transverses des filaments. Lorsque ces deux effets deviennent du même ordre, pour un temps appelé *temps de mélange*, les niveaux de concentration au sein des filaments de colorant commencent à baisser significativement. Ce *temps de mélange* est important car il indique i) à quel moment la distribution de concentration commence à évoluer de façon significative, et ii) quelle est la dimension transverse typique des filaments au moment où le mélange a lieu. Pour des étirements exponentiels tels que ceux rencontrés dans les suspensions de particules cisaillées, cette dimension transverse, aussi appelée *échelle de Batchelor*, vaut $s(t_{\rm mix}) \approx s_0/\sqrt{Pe}$ et décroît avec le nombre de Péclet Pe. Ainsi, pour caractériser l'évolution de la distribution de concentration $P(C,t)$, il faut (en l'abscence de coalescence) pouvoir résoudre cette échelle qui a grand Péclet peut être très petite. Ce point constitue un véritable challenge expérimental.

Afin de mesurer l'évolution de $P(C,t)$, il s'agit de mettre au point un dispositif de cisaillement dans lequel on est capable de résoudre l'échelle de Batchelor. Cela est possible en diminuant la taille du sytème et en appliquant des taux de cisaillement faible afin de favoriser l'effet de la diffusion moléculaire. Un schéma du dispositif est représenté sur la figure 4.4a. Il est constitué de deux plaques parallèles mises en mouvement par deux platines de translation. Le gap dans lequel la suspension est cisaillée est de petite taille (2 mm d'épaisseur) et nous utiliserons des particules de diamètre 100 μm. Dans ces conditions, le nombre de Péclet sera de l'ordre de 100 et l'échelle de Batchelor moyenne

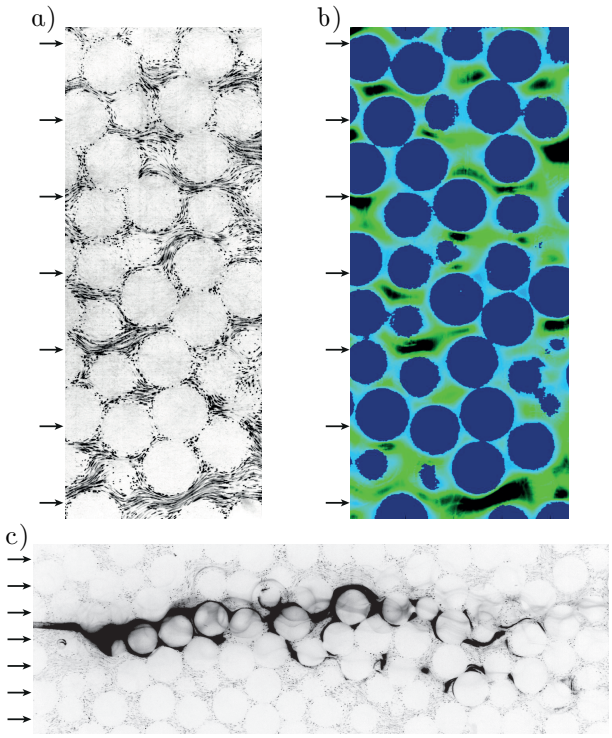


FIGURE 4.5 – a) Lignes de courant dans un milieux poreux 3D. b) Champ de vitesse correspondant. c) Injection de colorant au sein du milieu poreux

$s(t_{\mathrm{mix}}) \approx 16$ μm. Pour résoudre cette échelle et donc résoudre l'effet de la diffusion moléculaire, on utilisera un objectif de macroscope haute résolution. La figure 4.4b montre une image du dispositif de visualisation. Nous avons réalisé des expériences préliminaires où une ligne de colorant est cisaillée dans un fluide pur (sans particule). La figure 4.4c montre l'évolution de cette ligne à des déformations $\dot{\gamma}t$ successives et la comparaison avec la solution analytique pour c1) les profils de concentration successifs, c2) le maximum de concentration C_{max} et c3) la largeur σ de ces profils. Le bon accord entre les résultats expérimentaux et le modèle (sans paramètre ajustable) indique que ce dispositif permet de résoudre l'effet de la diffusion moléculaire et donc de fournir des mesures quantitatives de l'évolution des distribution de concentration.

Les objectifs sont les suivants :

— Des expériences seront réalisées afin de mesurer l'évolution des distributions de concentration d'un blob de colorant cisaillé dans une suspension de particules. Ces expériences seront réalisées dans une configuration de cisaillement continu mais aussi en cisaillement oscillant. La première configuration induit une élongation permanente du blob de colorant alors que dans la seconde, le blob se replie sur lui-même après chaque cycle de cisaillement, favorisant ainsi le phénomène de coalescence.

— Des développements théoriques sont nécessaires afin de prédire l'évolution de la distribution de concentration à partir des lois d'étirements. Ces développements seront d'abord faits dans le cadre du 'solitary strip' pour lequel on ne considère pas la coalescence entre filaments voisins. Ensuite ces prédictions devront inclure ces effets. Pour cela, on s'inspirera de travaux similaires réalisés par Duplat *et al.* 2010 [13].

— La comparaison entre les résultats expérimentaux et les prédictions théoriques nous dira si les mécanismes élémentaires à l'origine de l'accélération du mélange observé dans les suspensions de particules cisaillées sont bien compris.

4.2.2 Mélange dans les milieux poreux

Collaboration avec M. Souzy (Post-Doc), H. Lhuissier (IUSTI) et T. le Borgne (Univ. Rennes)

La technique consistant à reconstruire l'historique d'étirement inspirée de la Diffusive Strip method [35] fut pour la première fois appliquée à un champ de vitesse expérimental pendant la thèse de Mathieu Souzy. Cette approche nouvelle ouvre potentiellement cette technique à toute configuration où le champ de vitesse peut être mesuré expérimentalement. De là a démarré une nouvelle collaboration avec Tanguy le Borgne de l'institut de géosciences à Rennes afin d'étudier le mélange dans les milieux poreux. Mathieu Souzy a été recruté en post-Doc sur l'ERC de Tanguy Leborgne en octobre 2016. Les expériences sont réalisées à l'IUSTI.

Le milieu poreux envisagé est constitué d'un empilement aléatoire compact de billes ajustées en indice de réfraction avec le fluide. La figure 4.5 montre a) les lignes de courants obtenues en ensemençant le fluide à l'aide d'un grand nombre de traceurs fluorescents et b) le champ de vitesse correspondant. Par rapport aux suspensions cisaillées, l'écoulement est cette fois stationnaire. On peut dont effectuer des moyennes temporelles des champs de vitesse mais surtout effectuer un scan 3D de d'écoulement. L'approche sera la même que celle adoptée pour les suspensions cisaillées. Dans un premier temps, on s'attèlera à déterminer les lois d'étirements. On étudiera ensuite l'évolution de la distribution de concentration d'un colorant advecté au sein du milieu poreux, cf. figure 4.5c.

D'un point de vue plus fondamental, la comparaison entre milieux poreux et suspensions cisaillées devrait nous éclairer quand aux implications de la stationarité ou de l'instationarité de l'écoulement sur la nature du processus de mélange. Par ailleurs, l'accès au scan 3D du champ de vitesse du milieu poreux devrait aussi nous permettre de mieux comprendre dans quelle mesure la prise en compte de la troisième dimension du système a des conséquences sur les lois d'étirements et *in fine* sur le processus de mélange.

CHAPITRE 5

Curriculum vitæ

Bloen Metzger

Born september 15th 1979
37 years old

webpage: https://bloenmetzger.wordpress.com/

Diplomas

2003-06 **PhD University Aix-Marseille** at l'IUSTI-CNRS UMR 7343 Marseille

2002-03 **Master of Musical Acoustics**, University Aix-Marseille, Marseille, France, Mention Bien, 2nd/25.

Description **Magistère des Sciences de la Matière**, École Normale Supérieure de Lyon (E.N.S Lyon)

Research Experience

2007-Now **Chargé de recherche CNRS** (CR1) IUSTI-CNRS UMR 7343 Marseille.

january-june 2007 **Post-Doc** at Benjamin Levich Institut, New-York with J. Morris: "Heat transfer in sheared suspensions"

2003-06 **PhD** at IUSTI CNRS UMR 7343 Marseille, France with É. Guazzelli, "Sedimentation and Instabilities at low Reynolds number"

Research Interest

* Particles in fluids under low Reynolds number flows
* Micro-hydrodynamic of sheared suspensions
* Dispersion and mixing in sheared suspensions and porous media
* Shear thickening, jamming transition in amorphous media

National & International Collaborations

2016-present Tanguy Le Borgne, Professeur, UniversitÃĺ de Rennes, France.

2015-present Henri Lhuissier, CR2, IUSTI, Marseille France.

2014-present Yoel Forterre, Directeur de Recherche, IUSTI, Marseille France.

2014-present Sarah Hormozy, Assistant Professor, Ohio University, USA.

2012-present Matthieu Wyart, Professor, EPFL, Suisse.

2012-present Pierre Rognon, Associate Professor, Sydney University, Sydney, Australia.

2013-present Emmanuel Villermaux, Professor, IRPHE, Marseille, France.

2011-present Xiaolong Yin, Associate Professor, Engineering School of Mines, Colorado, USA.

2005-present Jason E. Butler, Professor, University of Florida, Gainsville, USA.

2007-10 Jeffrey Morris, Professor, Benjamin Levich Institute, CCNY, New York, USA.

2007-10 David Pine, Professor, New York University, USA.

2006-07 Eric S. G. Shaqfeh, Eric Darve et David Saintillan, Stanford University

2006-07 Maria Ekiel Jeżewska, Department of Mechanics and Physics of Fluids of the IPPT-PAN, Warsawa, Poland.

Awards

IUSTI CNRS UMR 7343 – Marseille, 13453
+334 91 10 68 89 • *bloen.metzger@univ-amu.fr*
http://bloenmetzger.wordpress.com

2008 Young Scientist Prizes Euromech.

List of Publications

1 Metzger B., Butler J. E. , & Guazzelli É. 2005 Large-Scale Streamers in the Sedimentation of a Dilute Fiber Suspension, **Phys. Rev. Lett.**, **95** 164506.

2 Ekiel-JezewskaM. L., Metzger B., & Guazzelli É. 2006 Spherical cloud of point particles falling in a viscous fluid, **Phys. Fluids**, **18** 038104.

3 Brancheriau L., Bailleres H., Detienne P., Kronland R. & Metzger B.,2006 Classifying xylophone bar materials by perceptual, signal processing and wood anatomy analysis, **Annals of Forest Science**, **63** 73-81.

4 Metzger B., Guazzelli É. & Butler J. E. 2007 Experimental investigation of the instability of a sedimenting suspension of fibres, **575** 307-332, **J. Fluid Mech.**.

5 Metzger B., Nicolas M. L., & Guazzelli É. 2007 Falling clouds of particles in viscous fluids, **580** 283-301, **J. Fluid Mech.**.

7 Metzger B., Butler J. E. , & Guazzelli É. 2007 On wavelength selection in the instability of settling fibers, **Phys. Fluids**, **19** 098105.

8 Metzger B., Nicolas M. , & Guazzelli É. 2008 On the settling of clouds of particles in viscous fluids, **European Journal of Mechanics/B**.

9 Metzger B., & Guazzelli É 2009 Des particules qui se la coulent douce..., **12**, **Reflets de la Physique**.

10 J. Park, Metzger B., Guazzelli É., & Butler J. E. 2010 A cloud of rigid fibres sedimenting in a viscous fluid, **648** 351-362, **J. Fluid Mech.**.

11 Metzger B. & Buler J. E. 2010 Irreversibility and chaos: Role of long-range hydrodynamic interactions in sheared suspensions, **Phys. Rev. E**, **82** 051406.

12 Kulkarni S. D., Metzger B. & Morris J. F. 2010 Particle-pressure-induced self-filtration in concentrated suspensions, **Phys. Rev. E**, **82** 010402.

13 Franceschini E. , Metzger B. , and Cloutier G. 2011 Forward problem study of an effective medium model for ultrasound blood characterization, **IEEE**, **58** 2668-2679.

14 Metzger B. and Butler J. E. 2012 Clouds of particles in a periodic shear flow, **Phys. Fluids**, **24** 021703.

15 Metzger B., Rahli O., & Yin X. 2013 Heat transfer across sheared suspensions: role of the shear-induced diffusion, **724** 527-552, **J. Fluid Mech.**.

16 Metzger B., Pham P. & Buler J. E. 2013 Irreversibility and chaos: Role of lubrication interactions in sheared suspensions, **Phys. Rev. E**, **00** 002300.

17 T. Miller, P. Rognon, B. Metzger, and I. Einav 2013 Eddy Viscosity in Dense Granular Flows, **Phys. Rev. Letters**, **111** 058002.

18 D. Griffani P. Rognon, B. Metzger, and I. Einav 2013 How rotational vortices enhance transfers, **Phys. Fluids**, **25** 093301.

19 P. G. Rognon, T. Miller, B. Metzger and I. Einav 2015 Long range wall perturbations in dense granular flows, **Journal of Fluid Mech.**, **764**, p. 171-192.

20 M. Souzy, X. Yin, E. Villermaux, C. Abid & Bloen Metzger 2015 Super-diffusion in sheared suspensions, **Phys. Fluids**, **27**, 041705.

21 P. Pham, B. Metzger & J. E. Butler 2015 Particle dispersion in sheared suspensions: Crucial role of solid-solid contacts, **Phys. Fluids 27**, 051701.

22 P. Pham, J. E. Butler & B. Metzger 2016 Origin of critical strain amplitude in periodically sheared suspensions, **Phys. Rev. Fluids 1**, 022201.

23 M. Souzy, P. Pham, & B. Metzger 2016 Taylors experiment in a periodically sheared particulate suspension, **Phys. Rev. Fluids**, **1**, 042001.

24 M. Souzy, H. Lhuissier, E. Villermaux, & B. Metzger (2017). Stretching and mixing in sheared particulate suspensions. **Journal of Fluid Mechanics**, 812, 611-635.

25 Clavaud, C., Berut, A., Metzger, B., & Forterre, Y. Revealing the frictional transition in shear thickening suspensions, **Proceedings of the National Academy of Sciences**, 201703926.

26 Clavaud, C., Berut, A., Metzger, B., & Forterre, Y. Suspensions rhéoépaissisantes: du principe aux applications, **Techniques de l'Ingénieur**, 2017.

Manuscripts submitted or in preparation:

27 P. Pham, J. E. Butler & B. Metzger 2017 Effet of particle roughness on shear induced diffusion, in preparation for **Journal of Fluid Mechanics**.

28 E. Degiuli, M. Wyart & B. Metzger 2017 Experimental evidence of lever effect at the jamming transition, in preparation for **Phys. Rev. Letters**.

29 M. Souzy, I. Zaier, H. Lhuissier & B. Metzger 2017 Mixing of lamellae in a laminar shear flow, submitted **JFM Rapids**.

Procceedings

B1 Metzger B, Guazzelli É., & Butler J. E. 2005 Sédimentation d'une suspension diluée de fibres à bas nombre de Reynolds, ***Proceedings du 17ième Congrès Francais de Méchanique (CFM)***, *Troyes, France*.

B2 Kulkarni S. D., Metzger B. & Morris J. F., 2008 Extreme velocity fluctuations: transient jamming in concentrated suspension flow, ***AIP Conf. Proc.***,*1027, 683 (2008)*.

B3 Metzger B. & Sierra C.,2010 Intensification des transferts dans les suspensions cisaillées, ***Proceedings Société Francaise de Thermique (SFT)***,*Touquet, France*.

B4 O. Rahli, X. Yin, P. Rognon & B. Metzger Turbulence at low Reynolds number: heat transfer enhancement in sheared suspensions., ***Proceedings THMTC 2012***, *Palerme, Italie*.

B5 M. Souzy, E. Villermaux, C. Abid & Bloen Metzger 2015 Expérience de Taylor dans une suspension de particules, ***Proceedings du 22ième Congrès Francais de Méchanique (CFM)***, Lyon, France.

Conferences

C1 Septembre 2005, ***17ième Congrès Francais de Mécanique (CFM)***, *Troyes, France* : "Etude expérimentale de la sédimentation d'une suspension diluée de fibres".

C2 Novembre 2005, au ***58th Meeting of the APS Division of Fluid Dynamics (APS)***, 19-22 novembre 2005, Chicago, USA : "Sedimentation of a cloud of particles at zero Reynolds number".

C3 Juin 2008, au ***AIP Conf.***, 25-30 juin 2008, Cappadocia, Turquie: "Extreme velocity fluctuations: transient jamming in concentrated suspension flow".

C4 Aout 2008, au ***XVth International Congress of Rheology***, 3-8 Aout 2008, Monterey, California, USA: "Extreme velocity fluctuations : Transient jamming in concentrated suspension flow".

C5 Novembre 2009, au ***AIChE***, Jackson, USA: "A cloud of rigid rods sedimenting in viscous fluid".

C6 Novembre 2010, au ***63rd Annual Meeting of the APS Division of Fluid Dynamics***, 21-23 Novembre 2010, Long Beach, California, USA: "Irreversibility and chaos: Role of long-range hydrodynamic interactions in sheared suspensions".

C7 Novembre 2011, au ***64rd Annual Meeting of the APS Division of Fluid Dynamics***, 21-23 Novembre 2011, Baltimore, USA: "Cloud of particles in a periodic shear flow".

C8 Novembre 2012, O. Rahli, X. Yin & B. Metzger, "Effect of sheared induced diffusion on the transfer of heat across a sheared suspension", ***65rd Annual Meeting of the APS Division of Fluid Dynamics***, Baltimore, USA.

C9 Juillet 2013, Miller T, Rognon P., Metzger B, Einav I., "Stadium shear experiments: eddy viscosity in dense granular flows" ***IMA conference***, Cambridge, UK.

C10 Novembre 2014, Phong Pham, Bloen Metzger and Jason E. Butler, "Effect of roughness in periodically sheared clouds of particles", ***67rd Annual Meeting of the APS Division of Fluid Dynamics***, San Francisco, USA.

C11 Novembre 2014, M. Souzy, E. Villermaux, C. Abid & Bloen Metzger, "Super diffusion in sheared suspensions", ***67rd Annual Meeting of the APS Division of Fluid Dynamics***, San Francisco, USA.

C12 April 2015, M. Souzy, N. C. Abid, E. Villermaux, X. Yin & Bloen Metzger "Mixing at low Reynolds number by shearing suspensions", ***10th Annual European Rheology Conference***, Nantes, France

C13 Aout 2015, M. Souzy, E. Villermaux, C. Abid & Bloen Metzger "Expérience de Taylor dans une suspension de particules", ***Congres Francais de Mecanique***, Lyon, France.

C14 Novembre 2015, M. Souzy, H, Lhuissier, E. Villermaux, & Bloen Metzger "Mixing in sheared suspensions", ***68rd Annual Meeting of the APS Division of Fluid Dynamics***, Boston, USA.

C15 April 2016, M. Souzy, H, Lhuissier, E. Villermaux, & Bloen Metzger "Mixing in sheared suspensions", ***Mixing Days***, Marseille, France.

C16 Novembre 2016, M. Souzy, H, Lhuissier, E. Villermaux, & Bloen Metzger "Mixing in sheared suspensions", ***Journées Suspensions Denses***, Marseille, France.

Invited seminars

S1 Juin 2006, ***IMFT Toulouse*** : "Sedimentation de particules et instabilités à bas nombre de Reynolds".

S2 Septembre 2006, ***Ladhyx Paris*** : "Sedimentation de particules et instabilités à bas nombre de Reynolds".

S3 Septembre 2008, ***Journees de Dynamique Non-lineaire*** : "Falling Clouds of Particles".

S4 Avril 2009, ***LPS, ENS-Paris*** : "Origine microscopique de la diffusion hydrodynamique?".

S5 Novembre 2009, ***Laboratoire de Physique de la Matière Condensée LPMC-Nice*** : "Origine microscopique de la diffusion hydrodynamique ?".

S6 Novembre 2010, au ***Chemical Engineering Department, Ithaca-Cornell, USA*** : "Microscopic origin of hydrodynamic diffusion".

S7 Novembre 2011, au ***Chemical Engineering Department, University of Florida, USA*** : "Heat/mass transfer in sheared suspensions".

S8 Avril 2012, au ***Chemical Engineering Department, University of Florida, USA*** : "Clouds of particles in a periodic shear flow".

S9 Novembre 2013, au ***Laboratoire Navier, Paris*** : "Origin of Hydrodynamic Diffusion & effect on the transfer of heat across a sheared suspension".

S10 Avril 2013, au ***Laboratoire LPMCN, Nice*** : "Microscopic origin of Hydrodynamic Diffusion".

S11 Novembre 2014, au ***Laboratoire LPMCN, Nice*** : "Mixing in shear particle suspensions".

S12 Octobre 2015, au ***Labex Tech21 Grenoble*** : "Physical origin of shear thickening".

S13 Novembre 2015, au ***Ohio University USA*** : "Microscopic origin of hydrodynamic diffusion".

S14 Decembre 2015, au ***Laboratoire Liphy grenoble*** : "Microscopic origin of hydrodynamic diffusion".

S15 Mai 2016, au ***Laboratoire IRPHE Marseille "Mixing days"*** : "Dispersion and mixing in sheared particulate suspensions".

S16 Juin 2016, au ***Laboratoire ENS Lyon*** : "Mixing in sheared particulate suspensions".

S17 Juin 2017, au ***ESPCI*** : "Mixing in sheared particulate suspensions".

Students

Post-Doc students

2017-present Regis Turuban co-directed with H. Lhuissier, IUSTI "Mixing in particulate suspensions".

2017-present Hugo Perrin co-directed with Y. forterre, IUSTI and M. Wyart, EPFL "Origin of hysteresis in granular and suspension flows ".

2016-present Mathieu Souzy co-directed with T. le Borgne, University of Rennes "Mixing in Porous media".

2014 Sarah Hormozi co-directed with Y. Forterre. "Shear thickening: from a 2D model experiment to cornstarch in water", now Assistant Professor Ohio University.

2011-12 Pierre Rognon, "Stadium shear: heat transfer in granular flow", now Associate Proffessor at Sydney University.

PhD students

2015-present Mohammadhossein Firouznia co-directed with Sarah Hormozi at Ohio University, "Micro-hydrodynamic of sheared suspension in yield stress fluids".

2015-present Sarabian Mohammad co-directed with Sarah Hormozi at Ohio University, "Particle migration in sheared suspensions of yield stress fluids".

2015-present Cécile Clavaud co-directed with Yoel Forterre, ERC PlantMove. "Physical origin of shear-thickening".

2013-2016 Mathieu Souzy co-directed with Nora-Cherifa Abid, MRE and defended on septembre 26th 2016: "Mixing in sheared particulate suspensions", now Post-Doc at University of Rennes.

2013-2016 Pham-Phong co-directed with Ouamar Rahli and Jason Bultler funded by PIRE-NSF and defended on April 19th 2016:"Particle dispersion in sheared suspensions", dual-degree between University of Florida and Aix-Marseille University, now Engineer at INTEL, USA.

2013-2016 Jie Lin co-directed with Matthieu Wyart, NSF grant. "Jamming and Yielding in granular flows", now Post-Doc at the Courant Institute.

2007-10 Sandeep Kulkarni co-directed with Jeffrey Morris at the Benjamin Levich Institut. PhD defended in july 2010, now Engineer at Halliburton, India.

Internships

2017 M1 Imen Zaier, "Mesure des distributions de concentration dans les suspensions cisaillées".

2017 M1 Alaa Fahs, "Le capilarytron : pour la rhéologie à pression imposée dans les suspensions de poudres".

2017 M2 Eduardo Fernandez, "Hystérèse dans les suspensions ?".

2016 M1 Loic Grasser, "Lever amplification near jamming".

2016 L2 Pauline Dame co-directed with Yoel Forterre, "Shear thickening a frictional transition ?"

2015 M1 Cécile Clavaud co-directed with Yoel Forterre, "Physical origin of shear-thickening".

2013 M2 Amandine Lechantre: "Shear thickening: from a 2D model experiment to cornstarch in water", co-advised with Y. Forterre, IUSTI.

2012 M2 Mathieu Souzy : “Mixing at low Reynolds number by shearing suspensions" co-advised with E. Villermaux, IRPHE.

2011 M1 Cyril Elouard , ENS Lyon : Irreversibilité et Chaos lors de la sédimentation de particules" en collaboration avec Denis Bartolo PMMH, Paris.

2011 M1 Pierre francois Carnet , IUSTI Marseille : “Threshold for irreversibility in sheared suspensions".

2010 M2 Gregory Charrier "Déstabilisation d'un nuage de particules soumis à un cisaillement périodique".

2010 M1 Gauthier Marais, Ecole de l'air de Salon de Provence : "Intensification des transferts dans les suspensions cisaillées".

2010 M1 Thimothé Menais, ENS Lyon : "Irreversibilité et Chaos lors de la sédimentation de particules".

2010 M1 Clément Thorey , ENS Lyon : "Periodic jamming and unjamming of dense suspensions: Experimental study", internship at Benjamin Levich Institute.

2009 L2 Mathieu Added, ENS Lyon : "Profil d'écoulement de suspensions dense à bas nombre de Reynolds: étude expérimentale".

2006 L2 Mr. Bouvard, Ecole de l'air de Salon de Provence : "Instabilité et cascade d'un nuage de particules".

2006 L1 Clément Brouder, Ecole de l'air de Salon de Provence : "Intensification des transferts dans les suspensions cisaillées".

2005 L1 Mr. Buscaglia, Ecole de l'air de Salon de Provence : "Sédimentation d'une goutte de particules à bas nombre de Reynolds".

Reviewer for

Physic Review Letters, Journal of Fluid Mechanics, Nature Communication, Physical Review Fluids, Physics of Fluids, Physic Review E, Journal of Statistical Physics, EPL, Journal of rheology, Journal of Geophysical Research.

Funding

2016 Proposal under examination for ANR JCJ "Custom designed rheology: towards a control of the flowing properties of particulate suspensions", collaboration with Y. Forterre (IUSTI) and M. Wyart (EPFL). 250 k€.

2016 Labex Mec, 20 k€, collaboration with H. Lhuissier (IUSTI) and E. Villermaux (IRPHE) on mixing in sheared particulate suspensions.

2015 Labex Mec, 15 k€, collaboration with M. Wyart (EPFL) on the Jamming transition in amorphous media.

2014 Labex Mec, 15 k€, on mixing in sheared particulate suspensions.

2010-13 ANR JCJ "Transfer Intensification in Sheared particulate suspensions", 155 k€.

2008-09 Institut Carnot Star, 50 k€.

Research & Education

2005 Art Exhibition “Mécanique Relative" for the world year of Physics.

2008-12 Seminars organizer of IUSTI Laboratory.

2009 Article de vulgarisation : Metzger B., & Guazzelli E. “Des particules qui se la coulent douce...", **12**, **Reflets de la Physique**.

2015 Constitution of the experimental equipment list of the Fédération Fabri de Peyresc

2015 Chairman at CFM de Lyon in the cession "Suspensions de sphères, de fibres et de cellules".

2015 Jury member of the PhD of D. Dherbecourt at CEA " Influence d'une phase dispersée sur le mélange dans l'écoulement de Taylor-Couette".

2016 Organization of the "journées suspensions denses à Marseille" funded by GRD MePhy & Phoenix, Labex Mec and Fédération Fabri de Peiresc.

CHAPITRE 6

Articles

6.1 Micro-hydrodynamique des suspensions cisaillées

Irreversibility and chaos: Role of long-range hydrodynamic interactions in sheared suspensions

Bloen Metzger[1] and Jason E. Butler[2]
[1]*IUSTI-CNRS UMR 6595, Polytech'Marseille, 13453 Marseille Cedex 13, France*
[2]*Department of Chemical Engineering, University of Florida, Gainesville, Florida 32611, USA*
(Received 6 July 2010; revised manuscript received 16 August 2010; published 30 November 2010)

Non-Brownian particles suspended in an oscillatory shear flow are studied numerically. In these systems it is often assumed that chaos (due to the long-range nature of the hydrodynamic interaction between particles) plus noise (contact or roughness) lead to irreversible behavior. However, we demonstrate that the long-range hydrodynamic interactions are not a source, nor even a magnifier, of irreversibility when coupled with non-hydrodynamic interactions. Additionally, analysis reveals that the apparent anisotropy of the particle diffusion is due to coupling of the shear flow and transverse diffusion.

DOI: 10.1103/PhysRevE.82.051406 PACS number(s): 83.80.Hj, 47.15.G−, 47.57.E−

I. INTRODUCTION

Particle dispersion in sheared suspensions has been a subject of intensive research since 1977 [1]. Even though many theories have been put forth to explain this phenomenon, some confusion remains about its physical origin. When the interactions are solely determined by Stokes flow, which is termed the "pure-hydrodynamic limit" (i.e., only hydrodynamic forces are present and the Reynolds number is zero), the motion of the particles is deterministic and expected to be reversible [2]. The observed dispersion was attributed to excluded volume effects [3]. In a shear flow, when two spheres approach, the minimum separation can be less than 10^{-4} of their radius. Surface asperities can therefore induce particle displacement, forcing particles from their reversible path; particles separate on streamlines further apart than on their approach. Within this frame, diffusivity coefficients were obtained using a path integration method [4]. Brady and Morris [5] extrapolated a scaling theory valid for dilute systems to describe shear-induced self-diffusion in the concentrated regime.

Drazer *et al.* [6] showed that the complex dynamics of sheared suspensions can be characterized as a chaotic motion in phase space. Chaos when coupled to any source of noise ensures that reversal of the velocities of all the particles does not, in practice, lead to a time-reversed motion; any small perturbation in the state of the system grows exponentially in time. Thus, small perturbations (weak Brownian motion, particle roughness, or any finite-ranged force), which are inevitably present in a real system [7], will grow. It is thus impossible for the system to retrace its dynamical path upon reversal.

For sedimenting particles, Jánosi *et al.* [8] demonstrated that chaos arises from long-range hydrodynamic interactions (LRHIs). The chaotic nature of hydrodynamic interactions was also invoked [9] to account for the observed irreversible behavior in sheared suspension. Sierou and Brady [10] mentioned that it is not clear whether the presence of an interparticle force is necessary for diffusive motion to appear. Marchioro and Acrivos [11] also suggested that in the absence of an interparticle force, diffusive like characteristics could be present owing to the chaotic nature of the many-body hydrodynamic interactions.

However, recent experimental studies [12] have shown that the extent of the irreversibility is strongly correlated with the particle roughness, as also found for the interaction between only two particles [3,13]; in the latter case, since only two particles are involved, one cannot invoke chaos to account for the irreversible motion of the particles. The microscopic origin of particle dispersion thus remains obscure. Several fundamental questions persist regarding the role of the long-range hydrodynamic interactions in generating chaos and whether contacts should be considered just a source of noise or as a primary source of irreversible displacements.

This paper reports on a simple numerical model developed to inquire specifically about the role of the long-range hydrodynamic interactions on particle dispersion and chaos in sheared suspension. In contrast to the case of sedimentation, we find that the long-range hydrodynamic interactions tend to damp the particle dispersion and do not contribute to the chaoticity of the system.

II. NUMERICAL MODEL

A minimal model is used to describe suspensions of non-Brownian particles within a periodic shear flow. A total of N particles is initially distributed in a monolayer with nonoverlapping positions to give the desired areal fraction; simulating a monolayer of particles provides substantial savings in computational time while maintaining an accurate description of the relevant physics. The particle positions are periodic in the flow (x) direction and are constrained in the z direction by solid walls. The velocity of particle n, $\mathbf{u}_n$, is the sum of the advection velocity due to the shear flow, the velocity disturbances generated by the straining flow, and the motion created by interparticle forces,

$$\mathbf{u}_n = \dot{\gamma} z_n \sin(\omega t)\mathbf{e}_x + \sum_{m\neq n}^{N} \bar{\mathbf{U}}_m(\mathbf{x}) + \frac{1}{\xi}\sum_{m\neq n}^{N} \mathbf{F}_{nm}, \qquad (1)$$

where $\bar{\mathbf{U}}_m$ is the disturbance velocity due to a sphere located at $\mathbf{x}_m$ at a distance $\mathbf{x}=\mathbf{x}_m-\mathbf{x}_n$ from the sphere n. The leading-order description is used to account for the LRHIs between particles [14],

 ©2010 The American Physical Society

$$\bar{\mathbf{U}}_i(\mathbf{x}) = \left[\mathbf{xx}\left(-\frac{5a^3}{2x^5} + \frac{5a^5}{2x^7} \right) - \mathbf{I}\frac{a^5}{x^5} \right] \cdot \mathbf{E} \cdot \mathbf{x}, \tag{2}$$

where $\mathbf{E}$ is the rate of strain and a is the particle radius. To account for steric effects, a pairwise-repulsive force (RF) is included. The repulsive force exerted by particle m on particle n is

$$\mathbf{F}_{nm} = \begin{cases} -F_0 \dfrac{\mathbf{x}}{|\mathbf{x}|} & \text{if } |\mathbf{x}| \le 2a \\ 0 & \text{if } |\mathbf{x}| > 2a, \end{cases} \tag{3}$$

where F_0 denotes the amplitude of the repulsive force and ξ in Eq. (1) is the Stokes resistance. We set $F_0/\xi=1$. Other values were tested for F_0 as well as other repulsive potentials [15], but all returned similar results.

This numerical model represents a rudimentary description relative to the substantially more accurate three-dimensional models existing in the literature [4,10]. However, this version includes long-range hydrodynamic interactions and captures the many-body hydrodynamic interactions at the level of multiple summed pairs. The model does not include lubrication forces purposely as we aim to investigate whether long-range hydrodynamic interactions engender chaos; as a result, effects such as closed trajectories of a pair of particles in close proximity are not observed from simulations at the level of Eqs. (1)–(3). However, comparisons of this model with a code containing multiple reflections and the velocity disturbance created by the repulsive force (i.e., Stokesian dynamics without lubrication interactions) demonstrated qualitative agreement in all respects, so the present model is used for the sake of simplicity.

Equations (1)–(3) are solved numerically. Knowing the positions of the particles at time $t=0$, the subsequent positions of each particle are calculated using a variable order Adams-Bashforth-Moulton solver. Simulations were performed with up to $N=50$ particles that were tracked over 25 cycles at strain amplitudes γ_0 between 0.25 and 3. One strain unit corresponds to a relative displacement of the cell walls equal to their separation distance. The total accumulated strain after n cycles is $\gamma=4n\gamma_0$, as γ_0 is the strain for a quarter cycle.

III. RESULTS

We first present results from simulations of 50 particles that neglect the LRHIs. We thus consider a suspension of hard spheres driven by an external shear flow where interaction between particles only occurs through the repulsive potential given by Eq. (3). At very short times, the mean-square particle displacements, $\langle xx \rangle$ and $\langle zz \rangle$, increase rapidly and then transition to a linear regime for $\gamma \ge 20$ as seen in Fig. 1(a). The transient regime, as previously observed [10,16], corresponds to the rearrangement of the initially random configuration into a self-organized one. The slopes of the mean-square particle displacements for $t>20$ define the dimensionless diffusivities $D_x^*=\langle xx \rangle/2a^2\gamma$ and $D_z^*=\langle zz \rangle/2a^2\gamma$ plotted in Fig. 1(b). The diffusion coefficients along, D_x^*, and

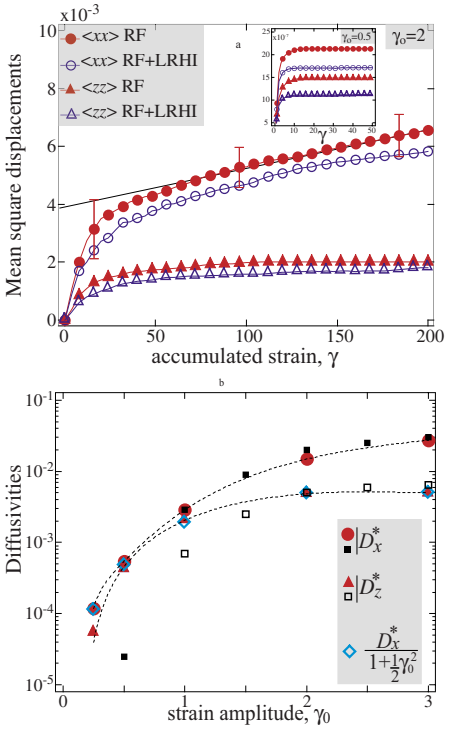


FIG. 1. (Color online) (a) Mean square displacements along and perpendicular to the flow direction, $\langle xx \rangle$ and $\langle zz \rangle$, versus accumulated strain, γ, for $\gamma_0=2$ and in the inset for $\gamma_0=0.5$. (b) Diffusivity coefficients, D_x^* and D_z^*, and normalized diffusivity coefficient $D_x^*/a^2(1+\frac{1}{2}\gamma_0^2)$ (which accounts for the advection-diffusion coupling) versus strain amplitude, γ_0. Squares are from experiments [9].

perpendicular, D_z^*, to the flow direction rapidly increase with strain amplitude.

These numerical results closely agree with the experimental data of Pine *et al.* [9] and successfully predict the transition of the particle dispersion at $\gamma_0 \approx 1$. For strain amplitudes smaller than 1, the system self-organizes into a nonfluctuating quiescent state [see inset of Fig. 1(a)] as suggested by the experiments of Corté *et al.* [16]. The structure of the self-organized state varies according to the concentration and the strain amplitude as demonstrated by Stokesian dynamics simulations [15].

An advection-diffusion coupling occurs when diffusion takes place in a shearing flow. In a channel, the sheared velocity profile interacts with cross channel diffusion to augment the dispersion along the channel. This effect, first studied by Taylor [17], was solved analytically in the specific case of a periodic shear flow and for a Brownian diffusion process [18]. The resulting effective diffusivity which arises from this coupling is $D(1+0.5\gamma_0^2)$, where D is the bulk isotropic diffusion coefficient. Normalizing D_x^* by $(1+0.5\gamma_0^2)$ collapses the points onto those of D_z^* as shown in Fig. 1(b). Hence, the larger diffusion coefficient measured along the flow direction does not arise from an intrinsic anisotropy of the particle diffusivity but more simply results from advection-diffusion coupling.

To test the effect of LRHIs, Eqs. (1)–(3) are solved fully including all terms. A striking result is that the mean-square

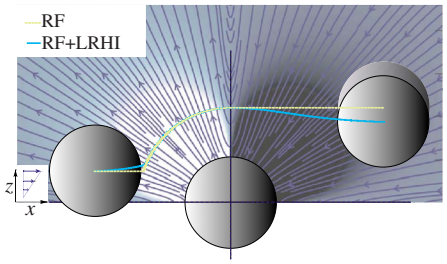


FIG. 2. (Color online) Effect of the LRHI on the relative trajectory of a pair of particles embedded in a simple shear flow. When in recession, the tensile normal stress brings the particles closer. The streamlines and the color scale represent, respectively, the flow disturbance [Eq. (2)] and the pressure field generated by the particle located at the origin.

displacements [see Fig. 1(a)] remain unchanged when the LRHIs are included. In fact, the simulations involving both repulsive forces and long-range hydrodynamic interactions generate slightly smaller particle mean-square displacements. This slight damping of the particle dispersion process may be understood considering the fore-aft symmetry of the hydrodynamic interaction between particle pairs, specifically the tensile normal stress of pairs when in recession [4,5]. Figure 2 illustrates this phenomenon. When particles are in recession, the LRHI is attractive. Not including the LRHI suppresses this effect and the resulting overall particle dispersion is larger.

However, this two-particle scenario omits the role of multiple particles colliding while also interacting hydrodynamically, which has been cited in the literature as a source of chaoticity [6,9,10,20]. To explore the role of LRHI on the chaoticity of multiple particles, simulations are undertaken with six particles; formally, the N-body problem only requires more than two particles to exhibit chaotic trends. Five hundred initial configurations are used and only those simulations that resulted in no particle contacts are retained within the analysis. Following Refs. [6,8,19], each initial condition is simulated twice, with two slightly different initial configurations, A and B. Configuration B is prepared from configuration A by displacing each particle in a random direction by a small distance ϵ. The Euclidian distance between these two simulations is computed in phase space as $l=\sqrt{\frac{1}{N}\sum_{i=1}^{N}(x_i^A-x_i^B)^2+(z_i^A-z_i^B)^2}$. In chaotic systems, l grows exponentially as $\epsilon e^{\lambda\gamma}$, where λ is the largest Lyapunov exponent. For three particles settling in a viscous fluid, Jànosi *et al.* found $\lambda\approx 0.04$, where γ corresponds to time, not strain, in their results. The positive value of the Lyapunov exponent clearly indicates chaos. Conversely when the particles solely interact through LRHI in periodic shear, the separation distance between two initially perturbed simulations remains unchanged as shown in Fig. 3(a). The corresponding Lyapunov exponent is too small ($\lambda<10^{-7}$) to observe chaotic behavior in the time frame of the simulations. This result is independent of the magnitude of the initial perturbation.

The separation distance is also evaluated for simulations of $N=50$ particles. This time, contact between the particles is allowed and simulations with and without LRHIs are compared. Figure 3(b) shows the exponential increase of the separation distance, l, with accumulated strain amplitude, γ. The positive growth rate, $\lambda\approx 0.3$, indicates a chaotic behavior. Note that the slope or chaoticity remains the same when neglecting the LRHIs.

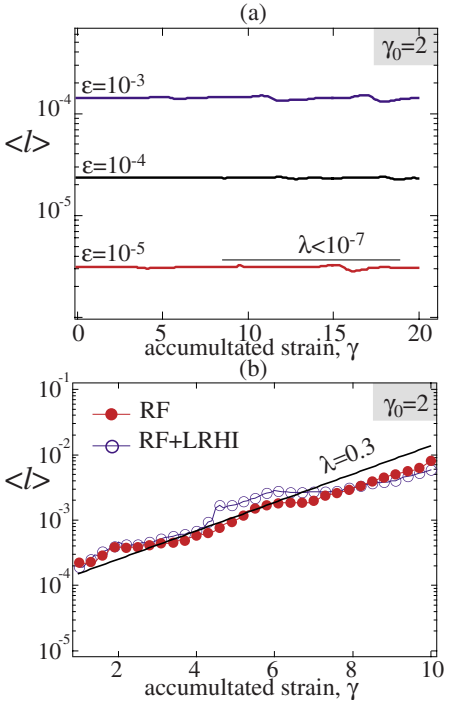


FIG. 3. (Color online) Separation distance, l, versus accumulated strain, γ, for a strain amplitude of $\gamma_0=2$. (a) Simulations are performed with $N=6$ particles interacting solely through LRHI. Different magnitudes of the initial perturbation, ϵ, are tested. (b) Simulations are performed with $N=50$ particles. Both sets of simulations (RF or RF+LRHI) started with the same initial positions.

IV. CONCLUSION

We have examined the nature of particle dispersion in sheared suspension of non-Brownian particles submitted to a periodic flow using a simple numerical model including a repulsive potential (to avoid particle overlap) and long-range hydrodynamic interactions (to capture the many-body and long-range nature of the hydrodynamic interactions between particles). In the studied range of parameters, three major conclusions can be made:

(i) Long-range hydrodynamic interactions are not a source of irreversibility nor even a magnifier of irreversibility when coupled with nonhydrodynamic interactions. In fact, as a result of the tensile normal stress between pairs when in recession, LRHIs damp the particle dispersion.

(ii) Long-range hydrodynamic interactions do not generate chaos in sheared suspension. If the particles solely interact through LRHI, the particle motion is reversible since the Stokes equations are linear and, as we have shown, insensitive to perturbations.

(iii) A minimal model, involving the particle steric effect only, can successfully predict the experimentally observed transition of the particle dispersion at $\gamma_0\approx 1$.

These results provide a perspective on sheared suspensions that differs fundamentally from that of sedimenting suspensions. In the latter case, the fluid flow is generated by the fall of the particles themselves and the ratio of the fluid flow disturbances (Stokeslets $\approx F/r$, where F is the body force acting on the particles) to the average velocity of the particles (mean settling velocity $\approx F/a$) is $\mathcal{O}(1)$ at one-particle diameter, $r=2a$, from any particle of the suspension. In sedimenting suspensions, these hydrodynamic interactions, which decay inversely with separation distance between the particles, indeed prevail [8,19,21]. Consequently, sedimenting particles (which solely interact through these long-range multibody hydrodynamic interactions) constitute a chaotic system. This was clearly demonstrated by Jánosi *et al.* [8].

Sheared suspensions are fundamentally different. This time, an external flow is imposed and the ratio of the disturbances (stresslets $\propto a^3E/r^2$), to the mean particle velocity ($\propto \dot{\gamma}L$), where L is the cell wall distance, is $\mathcal{O}(a/L)$ for $r=2a$. These weaker interactions, which decay as the square of the inverse separation distance, do not generate chaos.

The main constraint driving the system may thus more likely be stated as *particles cannot overlap*. This would explain why exceedingly simple descriptions such as the recent collision-induced model [16,22], which does not include any hydrodynamics, or the one presented here largely capture the dynamics observed in experiments. This also corroborates recent observations that the extent of the irreversibility strongly correlates with particle roughness [12,13]. To avoid particle overlap, one can use, as we did, a repulsive potential. Dispersion of the particles then naturally occurs as this interaction is by essence irreversible. Another candidate to prevent particles from overlapping is lubrication. Lubrication is a reversible interaction on account of the Stokes equations; it may nonetheless be a source of chaos. We plan to address this question in future work.

ACKNOWLEDGMENTS

We thank D. Bartolo for having thoughtful discussions. Visits were supported by the Partner University Fund on particulate flows, Aix-Marseille Universite (U1), and ANR JCJC SIMI 9.

[1] E. C. Eckstein, D. G. Bailey, and A. H. Shapiro, J. Fluid Mech. **79**, 191 (1977).
[2] I. E. Zarraga and D. T. Leighton, Phys. Fluids **13**, 565 (2001).
[3] P. A. Arp and S. G. Mason, J. Colloid Interface Sci. **61**, 44 (1977).
[4] F. R. Da Cunha and E. J. Hinch, J. Fluid Mech. **309**, 211 (1996).
[5] J. F. Brady and J. F. Morris, J. Fluid Mech. **348**, 103 (1997).
[6] G. Drazer, J. Koplik, B. Khusid, and A. Acrivos, J. Fluid Mech. **460**, 307 (2002).
[7] J. F. Morris, Rheol. Acta **48**, 909 (2009).
[8] I. M. Jánosi, T. Tél, D. E. Wolf, and J. A. C. Gallas, Phys. Rev. E **56**, 2858 (1997).
[9] D. J. Pine, J. P. Gollub, J. F. Brady, and A. M. Leshansky, Nature (London) **438**, 997 (2005).
[10] A. Sierou and J. F. Brady, J. Fluid Mech. **506**, 285 (2004).
[11] M. Marchioro and A. Acrivos, J. Fluid Mech. **443**, 101 (2001).
[12] M. S. Ingber, A. A. Mammoli, and P. Vorobieff, J. Rheol. **50**, 99 (2006).
[13] M. Popova, P. Vorobieff, M. S. Ingber, and A. L. Graham, Phys. Rev. E **75**, 066309 (2007).
[14] G. K. Batchelor and J. T. Green, J. Fluid Mech. **56**, 375 (1972).
[15] J. M. Bricker and J. E. Butler, J. Rheol. **51**, 735 (2007).
[16] L. Corté, P. M. Chaikin, J. P. Gollub, and D. J. Pine, Nat. Phys. **4**, 420 (2008).
[17] G. Taylor, Proc. R. Soc. London, Ser. A **219**, 186 (1953).
[18] W. R. Young, P. B. Rhines, and C. J. R. Garret, J. Phys. Oceanogr. **12**, 515 (1982).
[19] B. Metzger, M. Nicolas, and É. Guazzelli, J. Fluid Mech. **580**, 283 (2007).
[20] A. Deboeuf, G. Gauthier, J. Martin, Y. Yurkovetsky, and J. F. Morris, Phys. Rev. Lett. **102**, 108301 (2009).
[21] J. Park, B. Metzger, É. Guazzelli, and J. E. Butler, J. Fluid Mech. **648**, 351 (2010).
[22] L. Corté, S. J. Gerbode, W. Man, and D. J. Pine, Phys. Rev. Lett. **103**, 248301 (2009).

Irreversibility and chaos: Role of lubrication interactions in sheared suspensions

Bloen Metzger,[1] Phong Pham,[2] and Jason E. Butler[2]
[1]*IUSTI-CNRS UMR 7343, Aix-Marseille University, France*
[2]*Department of Chemical Engineering, University of Florida, Gainesville, Florida 32611, USA*
(Received 11 March 2013; published 16 May 2013)

We investigate non-Brownian particles suspended in a periodic shear-flow using simulations. Following Metzger and Butler [Phys. Rev. E **82**, 051406 (2010)], we show that the chaotic dynamics arising from lubrication interactions are too weak to generate an observable particle dispersion. The irreversibility observed in periodic flow is dominated by contact interactions. Nonetheless, we show that lubrication interactions must be included in the calculation to obtain results that agree with experiments.

DOI: 10.1103/PhysRevE.87.052304 PACS number(s): 83.80.Hj, 47.15.G−, 47.57.E−

I. INTRODUCTION

Viscous suspensions of non-Brownian and neutrally buoyant spheres in a periodic shear flow exhibit a remarkable transition. At a given volume fraction, if the strain amplitude surpasses a critical value, the suspension transitions to a fluctuating state: the particles do not return to their original positions and when tracked stroboscopically at the end of each cycle of shear, the particles exhibit large fluctuations analogous to a random walk [1–4].

This dispersion of particles has attracted a large interest since sheared suspensions often are assumed to be governed by reversible equations (Stokes equations). Within this "pure-hydrodynamic limit" (i.e., only hydrodynamic forces are present and the Reynolds number is zero), the irreversible motion of the particles was attributed to the chaoticity of the hydrodynamic interactions [2,5,6]. Chaos, when coupled to any source of noise, ensures that reversing the direction of flow does not in practice lead to a time-reversed motion for all of the particles; any small perturbation in the state of the system grows exponentially in time. Thus, according to this explanation, small perturbations (weak Brownian motion, particle roughness, or any finite-ranged force), which are inevitably present in real suspensions, are amplified and give rise to the observed particle dispersion.

However, other studies have shown that the extent of irreversibility in concentrated suspensions strongly correlates with the particles' roughness [7–9]. Similar observations were reported for very dilute suspensions [10] and for the interaction between two particles [7,11], where chaos cannot explain the lack of reversibility.

Thus, fundamental questions persist regarding the role of the hydrodynamic interactions and whether contacts should be considered just a source of noise or as a primary source of irreversible displacements. The suspension dynamics arise from three different contributions: (i) the long-range hydrodynamic interactions, (ii) lubrication, which results from the thin layer of viscous fluid that separates nearly touching particles, and (iii) contacts, which prevent particles from overlapping. It is difficult from experimental results or from existing numerical simulations (Stokesian dynamics) to discern which mechanism causes the irreversibility, as all three contributions are present at the same time.

Resolving the questions requires separating the different contributions to the particle dynamics and estimating their relative importance. This systematic approach already demonstrated that the long-range hydrodynamic interactions are not a source of chaos and are not responsible for the observed irreversibility [1]. The present work continues this investigation by probing the role of hydrodynamic interactions between particles at short range: the lubrication interaction.

II. MODEL

A minimal model was developed to inquire specifically about the role of lubrication in generating chaotic and irreversible behavior in sheared suspensions. A total of N particles is initially distributed in a square box with nonoverlapping positions to give an areal-fraction ϕ; simulating a monolayer of particles provides substantial savings in computational time while maintaining an accurate description of the relevant physics. The particle positions are periodic in the flow, or x, direction and are constrained in the gradient, or y, direction by solid walls. In the absence of inertia, the sum of the hydrodynamic forces, $\mathbf{F}_i^h$, and the contact forces, $\mathbf{F}_i^c$, on each particle i balance,

$$\mathbf{F}_i^h + \sum_{j\neq i}^{N} \mathbf{F}_{ij}^c = 0. \tag{1}$$

The hydrodynamic forces are given by

$$\mathbf{F}_i^h = 3\pi\mu d(\mathbf{u}_i - \mathbf{u}_{i\infty}) + \sum_{j(i)} \frac{3\pi\mu d^2}{8h_{ij}} \mathbf{n}_{ij}(\mathbf{u}_i - \mathbf{u}_j)\cdot\mathbf{n}_{ij}, \tag{2}$$

where μ denotes the fluid viscosity, d the particle diameter, and $\mathbf{u}_i$ the velocity of particle i. The fluid velocity at $\mathbf{x}_i = (x_i, y_i)$, the position of particle i, is $\mathbf{u}_{i\infty} = \dot{\gamma} y_i$ and $\dot{\gamma}$ is the shear rate. Lubrication forces between particle i and the particles $j(i)$ located within the lubrication range of particle i depend upon the relative velocities and separation distance $h_{ij} = |\mathbf{x}_{ij}| - d$, where $|\mathbf{x}_{ij}| = |\mathbf{x}_i - \mathbf{x}_j|$, of each pair. The particles $j(i)$ located within the lubrication range of particle i satisfy $2\epsilon_r \leqslant h_{ij} \leqslant d/2$, where ϵ_r is the particle roughness. The algorithm only accounts for the normal component of lubrication [12], which acts along the particles' common normal, $\mathbf{n}_{ij} = \mathbf{x}_{ij}/|\mathbf{x}_{ij}|$. The contact forces are given by

$$\mathbf{F}_{ij}^c = \begin{cases} F_0\mathbf{n}_{ij} & \text{if} \quad |\mathbf{h}_{ij}| \leqslant 2\epsilon_r \\ 0 & \text{if} \quad |\mathbf{h}_{ij}| > 2\epsilon_r, \end{cases} \tag{3}$$

 ©2013 American Physical Society

where F_0 denotes the amplitude of the repulsive force. We set $F_0 = 3\pi\mu\dot{\gamma}d^2H$, where H is the separation distance between the shearing walls, and ϵ_r was varied between 0 and $10^{-2}d$.

The equations presented above are solved for the velocities of the particles given their spatial positions. The positions are updated in time using a fourth-order Runge-Kutta method with a time step that ensures a displacement of less than $d/200$ for every particle. Simulations were performed with up to $N = 50$ particles that were tracked over a strain $\gamma = 10$ for continuous shear simulations. One strain unit corresponds to a relative displacement of the cell walls equal to their separation distance. We also performed simulations applying a periodic shear with strain amplitudes γ_0 between 0.5 and 6 and a total accumulated strain of 400. The total accumulated strain after n cycles is $\gamma = 4n\gamma_0$, as γ_0 is the strain for a quarter-cycle.

Equations (1)–(3) describe a sheared suspension of particles interacting through lubrication and contact forces. The model does not include long-range hydrodynamic interactions purposely, as we aim to investigate whether lubrication forces engender chaotic and irreversible behavior. The investigation is facilitated by simulating three different conditions: (i) the "pure lubrication limit," in which case the contact force and roughness are set to zero, $F_0 = 0$ and $\epsilon_r = 0$; (ii) the "pure contact limit," where the lubrication forces are not included; and (iii) simulations containing both lubrication and contact forces.

III. RESULTS

We first investigate the relative trajectory between two particles as calculated for the three different cases. The results, shown in Fig. 1, are compared to the full-solution obtained by integrating the equation of da Cunha and Hinch [13], which includes the long-range hydrodynamic interaction. The trajectory obtained with lubrication differs from the full-solution: deviation of the trajectory occurs only when the particles are very close (within the lubrication range). However the symmetry, and thus reversibility, of the trajectory is preserved. The minimum separation distance between the two particles is $h_{12} = 3 \times 10^{-6}d$. Similar to the observation of da Cunha and Hinch [13], the trajectory becomes asymmetric when the contact force is included and the minimum separation distance falls below $2\epsilon_r$. Including the contact force and ignoring lubrication results in an even larger asymmetry of the trajectory, as the motion of the particles follows the streamlines of the background shear flow after contacting.

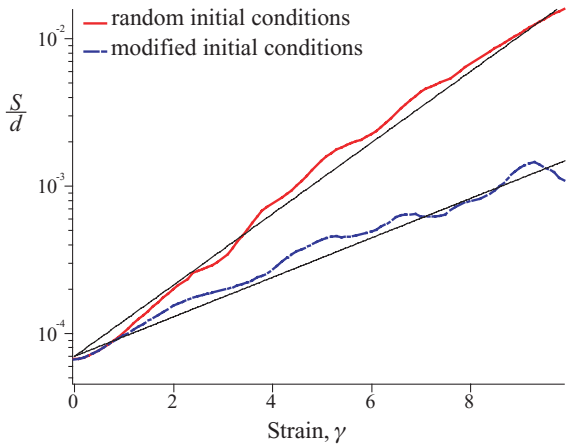


FIG. 2. (Color online) Separation distance, S, versus strain obtained in the "pure lubrication limit" ($F_0 = 0$) for $N = 50$, $\phi = 0.25$, and a steady shear flow.

Note that the equations can also be integrated for small total strains for multiple particles in the "pure lubrication limit" without violating the excluded volume restrictions. This allows us to investigate whether lubrication interactions alone lead to chaotic dynamics. Following Refs. [1,14–16], two random distributions of 50 particles each are simulated. The second distribution, labeled B, is prepared from the original configuration, labeled A, by displacing each particle in a random direction by a small distance $\epsilon = 10^{-4}d$. The Euclidian distance between these two simulations is computed in phase space as $S = \sqrt{\frac{1}{N}\sum_{i=1}^{N}(y_i^A - y_i^B)^2}$ [18]. For chaotic systems, S grows exponentially as $\epsilon e^{\lambda\gamma}$, where λ is the Lyapunov exponent. Figure 2 shows the exponential increase of the separation distance, S, with accumulated strain amplitude, γ. The positive value of the Lyapunov exponent, $\lambda = 0.56$, is a clear indicator of chaos. The separation distance was obtained by averaging data from nine sets of simulations.

We can identify two distinct mechanisms that potentially contribute to the amplification, seen in Fig. 2, of the initial perturbation. One contribution is from the N-body dynamics occurring through the lubrication interactions. The second is a two-body mechanism arising from the strong focusing and defocusing of streamlines, which is illustrated in Fig. 3(a). Two particles placed on top of each other separate on very different streamlines if a small perturbation is imposed on their initial position; see Fig. 3(b). We systematically quantify this effect by measuring the amplification factor, α/ϵ, where α and ϵ are the final and initial distance between these two streamlines,

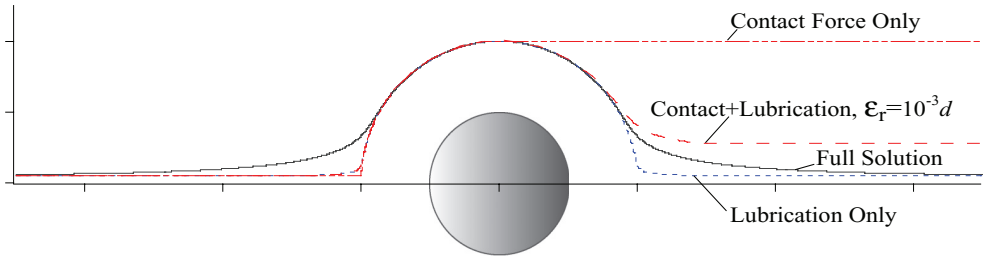


FIG. 1. (Color online) Relative trajectory between two particles initially located at $(x_1, y_1) = (0,0)$ and $(x_2, y_2) = (-10, 0.1)$.

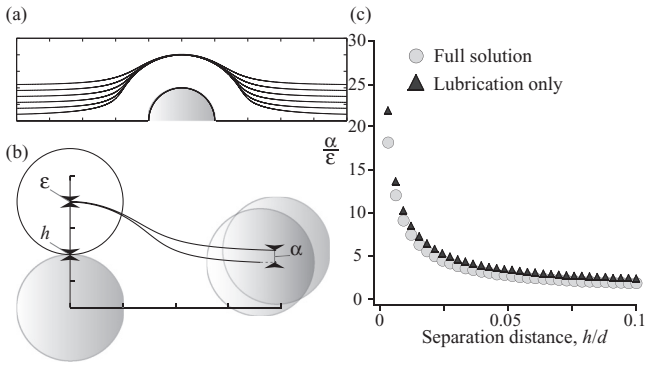


FIG. 3. (a) Illustration of the streamline focusing and defocusing before and after the apex of the interaction. (b) Relative trajectories for two particles initially displaced at $[(x_1,y_1)=(0,0),(x_2,y_2)=(0,d+h)]$, and at $[(x_1,y_1)=(0,0),(x_2,y_2)=(0,d+h+\epsilon)]$, with $h=5\times10^{-4}d$ and $\epsilon=5\times10^{-4}d$. The distance in the y direction between these two trajectories after a strain $\gamma=10$ is α. (c) Amplification caused by the streamline defocusing, α/ϵ, versus initial separation distance, h.

respectively, as the function of the initial particle separation distance h. Figure 3(c) shows that the amplification of an initial perturbation can be $O(20)$ for two particles initially separated by a small distance h. However, this effect decreases when the initial separation distance increases; two particles initially separated by a distance $h>0.1d$ are weakly sensitive to this mechanism as $\alpha/\epsilon\to1$. Note that this amplification is the same using the full solution of da Cunha and Hinch [13] or lubrication only.

To remove this effect in the estimation of the Lyapunov exponent, simulations were performed with altered initial conditions where the minimum separation distance between particles was set at $0.1d$ instead of zero. The results calculated from these initial conditions, labeled as "modified initial conditions" in Fig. 2, show that S still grows exponentially, albeit with a lower rate of $\lambda=0.31$. The lubrication interactions thus lead to a chaotic behavior.

In the following, we investigate whether this chaotic dynamics can be responsible for the irreversibility observed in periodically sheared suspensions. We performed simulations applying a periodic shear with strain amplitudes γ_0 between 0.5 and 6 and a total accumulated strain of 400. The particle mean square displacements are evaluated from the particle positions at the end of each cycle of shear. Changes in the mean-square displacements indicate the presence of irreversible dynamics, whereas the lack of a change in the mean-square displacements from cycle-to-cycle indicate that the system is in a reversible state.

The mean-square displacements obtained in the "pure lubrication limit" do not show, at the particle scale, any significant growth: the system behaves in a reversible way (cf. Fig. 4). This seems at first inconsistent with the chaotic nature of lubrication interactions shown above. However, considering a strain amplitude of $\gamma_0=3$, the amplification of perturbations caused by chaos is $e^{\lambda\gamma_0}\approx5$. The amplification of the noise present in our system [typically round-off error $O(10^{-8})$] is, thus, too small to produce an irreversible displacement observable at the particle scale $O(1)$. Therefore, the chaos arising from lubrication is not responsible for the irreversibility observed in periodically sheared suspensions.

In the "pure contact limit," the mean-square displacements increase rapidly and then plateau after an accumulated strain $\gamma\approx150$. The system freezes into a reversible state even at large strain amplitudes. This evolution occurs since the particles driven solely by contact forces organize into layers [see inset of Fig. 4(a)], a configuration in which collisions between particles cease.

A steady fluctuating state is attained at large strain amplitudes when both contact and lubrication interactions are included in the calculations. The lubrication interactions disrupt the formation of layers [see inset of Fig. 4(a)] and consequently particles remain on streamlines where collisions occur. We found that the slope of the mean-square displacement strongly depends on the particle roughness ϵ_r [shown on Fig. 4(a)] but weakly depends on the upper bound of the lubrication range. Note that the above dynamics (self-organization into layers when particles are solely interacting through contacts and the

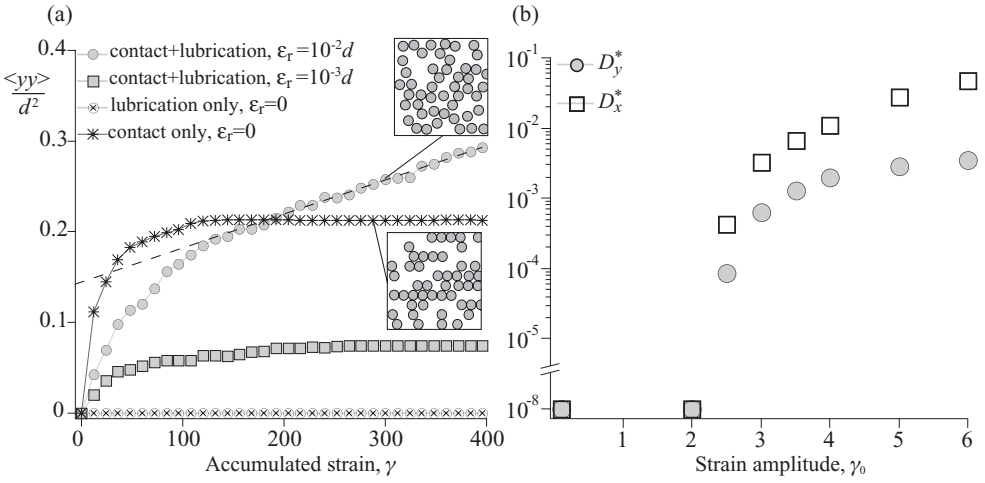


FIG. 4. (a) Mean square displacements versus accumulated strain for $\phi=0.4$ and $\gamma_0=3$. (b) Diffusion coefficients versus strain amplitude for simulations with contact and lubrication interactions for $\phi=0.5$ and $\epsilon_r=0.002d$.

disruption of particle layering when lubrication is included) are also observed when simulations are performed with $N = 200$ particles. This suggests that the results are not due to finite-size effects.

The slopes of the particle mean-square displacements for strains of $\gamma > 100$ are used in calculating the dimensionless diffusivities, $D_x^* = \langle xx \rangle / 2\gamma d^2$ and $D_y^* = \langle yy \rangle / 2\gamma d^2$, plotted in Fig. 4(b). The diffusion coefficients parallel, D_x^*, and perpendicular, D_y^*, to the flow direction rapidly increase with strain amplitude. These numerical results agree qualitatively with the experimental data of Pine *et al*. [2] and successfully predict the transition of the particle dispersion at $\gamma_0 \approx 2$. For strain amplitudes smaller than 2, the system self-organizes into a nonfluctuating quiescent state as suggested by the experiments of Corté *et al*. [17].

IV. CONCLUSIONS

We have examined the role of lubrication interactions in suspensions of non-Brownian particles submitted to a periodic shear-flow. We used a simple model that includes repulsive forces (to prevent overlap) and lubrication (to describe the interaction between particles). We found that chaos arises from the N-body dynamics occurring through the lubrication interactions. However, for the strain amplitudes considered here, $\gamma_0 = [0.25–6]$, this chaos is too weak to produce a significant irreversibility under oscillatory shear. Therefore, in periodically sheared suspensions, lubrication is not responsible for the irreversibility, which is dominated by contact interactions. Nonetheless, lubrication plays an important role by disrupting the particle layering that occurs if particles solely interact through contact forces. Lubrication thus ensures that the collision process perpetuates and allows the system to reach the steady fluctuating state observed in experiments at large strain amplitudes.

ACKNOWLEDGMENTS

This work was supported by the National Science Foundation (Grant No. 0968313), ANR JCJC SIMI 9, and Carnot Star.

[1] B. Metzger and J. E. Butler, Phys. Rev. E **82**, 051406 (2010).
[2] D. J. Pine, J. P. Gollub, J. F. Brady, and A. M. Leshansky, Nature **438**, 997 (2005).
[3] J. M. Bricker and J. E. Butler, J. Rheol. **51**, 735 (2007).
[4] B. Metzger and J. E. Butler, Phys. Fluids **24**, 021703 (2012).
[5] M. Marchioro and A. Acrivos, J. Fluid Mech. **443**, 101 (2001).
[6] J. F. Morris, Rheol. Acta **48**, 909 (2009).
[7] P. A. Arp and S. G. Mason, J. Colloid Interface Sci. **61**, 44 (1976).
[8] M. S. Ingber, A. A. Mammoli, and P. Vorobieff, J. Rheol. **50**, 99 (2006).
[9] F. Blanc, E. Lemaire, A. Meunier, and F. Peters, J. Rheol. **57**, 273 (2013).
[10] F. Blanc, F. Peters, and E. Lemaire, Phys. Rev. Lett. **107**, 208302 (2011).
[11] M. Popova, P. Vorobieff, M. S. Ingber, and A. L. Graham, Phys. Rev. E **75**, 066309 (2007).
[12] G. K. Batchelor and J. T. Green, J. Fluid Mech. **56**, 401 (1972).
[13] F. R. da Cunha and E. J. Hinch, J. Fluid Mech. **309**, 211 (1996).
[14] G. Drazer, J. Koplik, B. Khusid, and A. Acrivos, J. Fluid Mech. **460**, 307 (2002).
[15] I. M. Janosi, T. Tel, D. E. Wolf, and J. A. C. Gallas, Phys. Rev. E **56**, 2858 (1997).
[16] B. Metzger, M. Nicolas, and É. Guazzelli, J. Fluid Mech. **580**, 283 (2007).
[17] L. Corté, P. M. Chaikin, J. P. Gollub, and D. J. Pine, Nature Physics **4**, 420 (2008).
[18] The separation distance is computed in the y direction only, avoiding the necessity of correcting the calculation for the convective contribution to the separation, which arises from the shearing motion.

PHYSICS OF FLUIDS **24**, 021703 (2012)

Clouds of particles in a periodic shear flow

Bloen Metzger[1] and Jason E. Butler[2]
[1]*IUSTI-CNRS UMR 6595, Polytech Marseille, 13453 Marseille Cedex 13, France*
[2]*Department of Chemical Engineering, University of Florida, Gainesville, Florida 32611, USA*

(Received 25 October 2011; accepted 3 January 2012; published online 14 February 2012)

We have investigated the time evolution of a cloud of non-Brownian particles subjected to a periodic shear flow in an otherwise pure liquid at low Reynolds number. This experiment illustrates the irreversible nature of particulate systems submitted to a shear. When repeating the cycles of shear, we have found that clouds of particles progressively disperse in the flow direction until reaching a threshold critical volume fraction that depends upon the strain amplitude; this critical volume fraction coincides with measurements of the threshold for reversibility found from experiments on homogeneous suspensions in periodic shear. Two distinct patterns, including a "galaxy-like" shape, are observed for the evolution of the clouds and the transition between the patterns is identified using a simple scaling analysis. Movies are available with the online version of the paper. © *2012 American Institute of Physics*. [http://dx.doi.org/10.1063/1.3685537]

Half a century ago, Taylor proposed an experiment[1] which elegantly illustrates the reversibility of viscous fluid flows. A small blob of dye is inserted into a very viscous fluid contained in the gap between two concentric cylinders. The blob is first stretched into a long thin filament by rotating the inner cylinder several turns. Then upon reversing the rotation for the same number of turns, the drop astoundingly recovers its initial shape, except for some minor effects of molecular diffusion.

Inspired by Taylor's work, we perform a similar experiment on finite-sized clouds of non-Brownian particles. The key idea is to perform successive cycles of shear and measure the evolution of the shape of the clouds at the end of each cycle. This experiment is particularly advantageous for investigating the transition between reversible and irreversible dynamics in suspensions. In this stroboscopic measurement, the affine part of the particle motion, i.e., the advection motion, is eliminated. Hence, all departures from the initial cloud shape can be attributed to irreversible events caused by the interaction between particles.

The experiment also provides important clues regarding the nature of the interactions between particles that are very near to each other. The minimum separation distance between two approaching particles can be less than 10^{-4} of their radius,[2,3] though the question of whether particles make contact is still a matter of debate. Clarifying this issue would substantially enhance our understanding of suspension behavior.

For instance, homogeneous suspensions in a periodic shear undergo a remarkable transition[4] as the concentration and strain amplitude are varied. At each concentration, the suspension either transitions to a state where the particle positions are reversible or remain irreversible, if the strain amplitudes are below or above a critical value, respectively. Although, the phenomenology of this transition was captured by a numerical simulation within which particles that pass close to each other are given a small random displacement[5] and the microstructures of the reversible states can be predicted from more detailed simulations,[6] the physical origin of the irreversibility remains unclear.

Understanding the nature of any non-hydrodynamic particle interactions is also critical for modeling the rheology of suspensions and phenomena such as particle migration. For the latter case, a "revisited suspension balance model"[7] was applied to capture the migration process of a suspension submitted to a rotating rod; the work suggests that contact stress governs the

 © 2012 American Institute of Physics

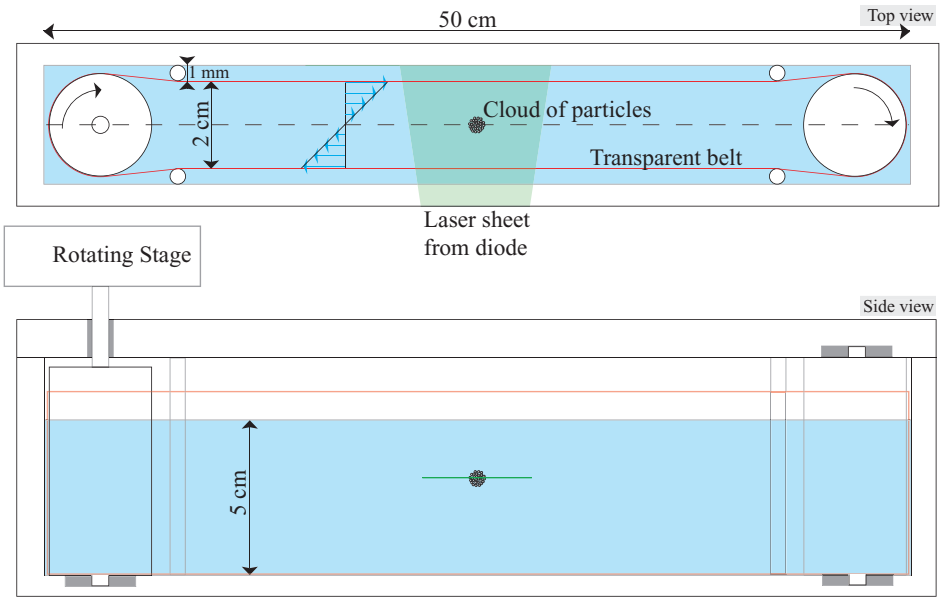


FIG. 1. (Color online) Sketch of the experimental shear-cell. The acrylic transparent walled vessel has inner dimensions $2 \times 7 \times 50$ cm^3 and was filled with fluid to a height of 5 cm to perform the experiments.

migration behavior.[8] However, other models assert that the stresslet contribution arising from the non-symmetric microstructure[9] is responsible, at least in part, for the migration.

The present work thus aims toward the challenging goal of getting a better grasp on how close particles interact in sheared suspensions. We have found that clouds of particles having an initially moderate volume fraction ($\phi = 20\%$–40%) progressively disperse in the flow direction until they reach a threshold critical volume fraction. For larger volume fractions, clouds can exhibit a different pattern of dispersion. We found that clouds initially at the maximum packing fraction can evolve into a "galaxy-like" shape.

The experimental set-up, inspired by Rampall *et al.*,[10] is sketched in Figure 1. A precision rotating stage (M-061.PD from PI piezo-nano positioning) with high angular resolution (3×10^{-5} rad) drove a transparent belt to create the shearing flow. The fluid was a Newtonian mixture of Triton X-100 (76.241 wt. %), zinc chloride (14.697 wt. %), and water (9.062 wt. %) having a viscosity of 3 Pa and a density of 1.18 g/cm^3 at room temperature. The composition was chosen to match both the refractive index and density of the acrylic particles. Carefully matching the fluid and particle densities was critical since the sedimentation rate of a cloud of particles greatly exceeds that of a single particle.[11,12] We achieved a density match that ensured that the cloud's settling velocity was lower than 10^{-7} m/s. A small amount of hydrochloric acid ($\approx$0.05 wt. %) was added to the solution to prevent the formation of zinc hypochlorite precipitate, thereby significantly improving the optical transparency of the solution.

We used two different batches of spherical acrylic particles of density 1.18 g/cm^3 having diameters of 200 ± 50 μm and 450 ± 50 μm. Suspensions of volume fractions $\phi = 30\%$ and 40% were first prepared in a small container and then were transferred into the shear cell using a pipette of inner diameter 3 mm. Clouds were injected into the cell two centimeters below the free surface of the fluid as shown in Figure 1. Clouds at maximum packing were prepared by partially filling the pipette with pure fluid so that about 3 mm of its tip remained free of liquid. Then, dry particles were directly poured into that remaining space and the fluid in the pipette was slowly pushed through the tightly packed bed of particles.

Before preparing the suspensions, the particles were dyed with rhodamine 6G by letting them soak for 40 min at 60°C in a mixture of 50 wt. % water, 50 wt. % ethanol, and a trace amount of rhodamine. This dye fluoresces under illumination provided by a green laser diode. Such a laser

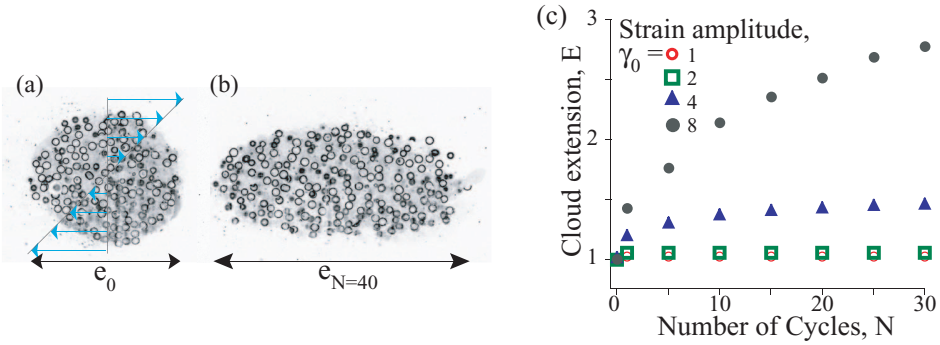


FIG. 2. (Color online) Evolution of clouds composed of particles with $d = 450\ \mu$m at an initial volume fraction 30%. Images were taken (a) initially and (b) after 40 cycles at a strain amplitude of $\gamma_0 = 6$. (c) Evolution of the cloud extension, $E(N) = e_N/e_0$, in the flow direction (enhanced online) [URL: http://dx.doi.org/10.1063/1.3685537.1] .

(100 mW power and wavelength of 532 nm) with a combination of plano-cylindrical lenses were used to generate a horizontal laser sheet of thickness ≈30 μm. The fluorescing particles within the plane of the laser sheet were imaged from the top using a high resolution digital camera (Nikon 300s) and a high quality magnification lens (Sigma APO-Macro-180 mm-F3.5-DG). A 550 nm longpass colored glass filter was positioned in front of the lens to remove any light scattered by the particle surfaces.

The cloud was sheared forwards then backwards in a repeating cycle. An image of the cloud was recorded at the end of each cycle. The total accumulated strain experienced by the cloud over a run is thus $\gamma = 2\gamma_0 N$, where γ_0 is the strain amplitude and N is the number of cycles. One strain unit corresponds to a relative displacement of the cell walls equal to their separation distance.

When sheared, clouds composed of the larger particles ($d = 450\mu$m) stretch along the flow as expected (cf. Video 1). Upon reversing the shear flow, the clouds do not reconstitute identically at the end of each cycle of shear, but instead progressively expand in the flow direction as seen in Figures 2(a) and 2(b). The dynamics of the cloud extension is shown in Figure 2(c) in terms of $E = e_N/e_0$, the cloud extension in the flow direction normalized by the initial size. The cloud initially extends rapidly and eventually reaches a steady state after a number of cycles that increases as the strain amplitude increases. After reaching steady state, the clouds become reversible and reform identically (within measurement capability) after each cycle.

The evolution of the cloud extension is similar to the self-organization into a reversible state observed from the periodic shear of homogeneous suspensions when the strain amplitude is small.[4,13] Here the volume fraction of the clouds is free to vary. Consequently, as the cloud disperses into the surrounding fluid, the volume fraction decreases until diluting to the threshold critical value for reversibility at that strain amplitude. Figure 3 shows that this principle holds over volume fractions of 30% and 40% and strain amplitudes of $\gamma_0 = 2$ to 6. The initial volume fraction of the clouds is represented by thin symbols on the phase diagram. The volume fraction of the cloud in its reversible state was calculated using $\phi_r = e_0\phi_i/e_r$, where e_0 and e_r denote the cloud dimension in the flow direction in its initial state and in its reversible state, respectively. This estimate of the concentration is reasonable since the dispersion occurs mainly in the plane of shear, as verified experimentally. Similarly, as one can observe from Figure 2, dispersion in the gradient direction is small relative to the large dispersion in the flow direction.

We found that dispersion stops once the volume fraction decreases below a critical value that matches the threshold for reversibility as measured from studies on homogeneous suspensions[4] as seen in Figure 3. The grey arrow in this figure indicates the evolution of a cloud initially prepared at $\phi = 30\%$ and periodically sheared with a strain amplitude of $\gamma_o = 4.5$. This cloud progressively disperses until reaching the reversible region of the diagram. Clouds follow that evolution independently of their initial volume fraction, particle size, and applied strain.

Clouds composed of the smaller diameter spheres are not represented in the diagram when $\phi = 40\%$ and for strains larger than 3. Clouds above this limit, represented in Figure 3 by the

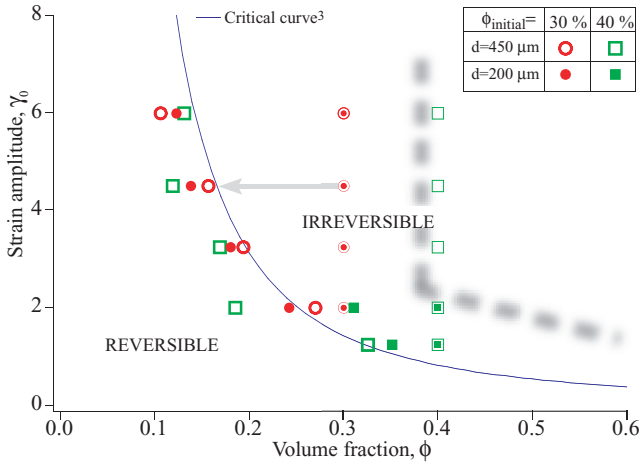


FIG. 3. (Color online) Phase diagram (γ_0-ϕ) for clouds initially prepared with volume fractions of 30% and 40%. Initial positions on the phase diagram are indicated by thin symbols and the corresponding positions of the reversible state are indicated with thick symbols. The grey arrow indicates the evolution of a cloud initially prepared at $\phi = 30\%$ and periodically sheared with a strain amplitude of $\gamma_o = 4.5$. This cloud progressively disperses until reaching the reversible region of the diagram. The critical curve, $\gamma_0 = C\phi^{-\alpha}$ (C = 0.14, $\alpha = -1.93$), is from experiments on homogeneous suspensions.[4]

thick dashed line, demonstrate a different mode of dispersion as pictured in Figure 4. These clouds produce a "galaxy-like" shape during large amplitude oscillations, wherein two thin tails of particles emanate from both sides of the cloud forming a slight angle with the direction of flow (cf. Video 2). During shear, the core of the cloud at maximum packing fraction rotates as a solid body (cf. Video in the supplementary material (Ref. 14)) and particles located at the cloud periphery shed into the surrounding fluid to form this pattern.

A simple model qualitatively reproduces the galaxy shape and provides insight into why particles do not return to their initial positions when shear is reversed. The core of the cloud is modeled as one large solid particle of radius a in a straining flow $\mathbf{E}$ generating a flow disturbance $\mathbf{u}$ at the position $\boldsymbol{r}$,[15]

$$\mathbf{u}(\mathbf{r}) = \mathbf{r}\cdot\mathbf{E}\cdot\left(\mathbf{rr}\left(-\frac{5a^3}{2r^5}+\frac{5a^5}{r^7}\right)-\mathbf{I}\frac{a^5}{r^5}\right). \tag{1}$$

This expression corresponds to the leading order term (stresslet) of the flow disturbance generated by a rigid spherical particle embedded in a shear flow. Particles located at the cloud periphery are represented by passive tracers that are initially distributed randomly in a thin layer around the

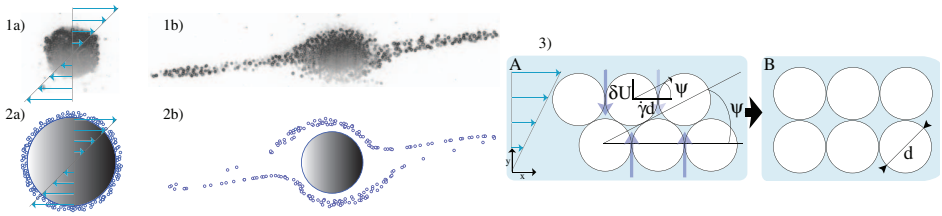


FIG. 4. (Color online) Comparison between an experiment and model for the evolution of a cloud composed of the small particles, initially prepared at the maximum packing fraction, and oscillated at a strain amplitude of $\gamma_0 = 6$. Images (a_1) and (b_1) show the initial conditions for the experiment and simulation, respectively. For the simulation, passive tracers are initially distributed in a thin layer around the core, which is progressively reduced in size. The distribution predicted by the simulation after 20 cycles appears in (b_2) and is compared to the distribution from the experiment after 20 cycles as shown in (a_2). (c) Schematic for the pore pressure feedback mechanism (enhanced online) [URL: http://dx.doi.org/10.1063/1.3685537.2] ; [URL: http://dx.doi.org/10.1063/1.3685537.3] .

core and that follow the fluid motion, which includes the imposed shearing flow and disturbance flow.

If one keeps the core size constant (a fixed) throughout each cycle of the periodic shear, the tracers return to their initial positions owing to the reversibility of Stokes equations. However, the core size reduces during shear owing to the loss of particles at the edge of the cloud as represented in part by the tracers. Hence, the size a is reduced during the forward motion of each cycle, when the shear rate is positive. As a result, the flow disturbance produced by the core is not the same during the backward as forward portions of each cycle and the tracer particles do not return to their original positions. The progressive shrinking of the core size over multiple cycles of shear opens more and more streamlines that allow particles to escape from the cloud. Such clouds are thus intrinsically unstable. A pattern similar to the one seen in the experiment develops from the simulation as seen in Figure 4(b) (cf. Video 3). In this simulation, the core size was reduced at every half cycle such that the total loss after 20 cycles was 30%.

The experimental observations indicate that the transition between the stretching and the rotating modes depends both on the cloud volume fraction and the particle size. The onset of the rotating mode relies on the appearance of a "pore-pressure feedback" effect.[16] The schematic in Figure 4(c) illustrates this mechanism. Densely packed granular material is known to dilate under an imposed shear.[17] Thus, when shearing a tight bed of particles from configuration A to B (see Figure 4(c)), the pores in between the particles become larger. This induces a motion of fluid (represented by the arrows) from outside of the densely packed region toward the center of the cloud. This fluid motion creates a pore-pressure gradient that tends to press the grains together, enhancing friction.

This so-called pore pressure can be estimated and balancing the shear stress with this pore pressure effect provides a simple and accurate prediction of the transition point for the behavior of the cloud. If the viscous stress generated by the surrounding shear flow on the cloud ($\eta\dot{\gamma}$, where η is the fluid viscosity and $\dot{\gamma}$ is the shear rate) is larger than the stress created by the pore-pressure ($\mu_s P^p$, with μ_s the friction coefficient and P^p the pore pressure), then the cloud should stretch; if it is smaller, the cloud should rotate. This latter pore-pressure stress is estimated using Darcy's law, $\nabla P^p \propto \eta \delta U/d^2$, where δU denotes the relative velocity between the fluid and the particle phase and d is the particle diameter.

To capture the dilation of the cloud network, we use the dilatancy angle ψ:[16] $\delta U = \dot{\gamma} d \tan(\psi)$ (see Figure 4(c)) which relates the normal and the transverse motion of the particles. The pore pressure at the center of the cloud is thus $P^p = \eta\dot{\gamma}\tan(\psi)D/d$, where D is the cloud diameter. This provides a criterion for the onset of rotation: if $D/d \geq 1/(\mu_s \tan(\psi))$, the cloud should rotate. This transition depends on the volume fraction through the dilatancy angle as $\tan(\psi) = K(\phi - \phi_{eq})$ which assumes that the dilatancy angle is proportional to the difference between the actual volume fraction, ϕ, and the steady state volume fraction ϕ_{eq}. Using the parameters from the experiment of $\phi \approx 0.63$ (maximum packing) and values provided in the literature of $K = 4.09$, $\phi_{eq} = 0.58$,[16] and $\mu_s = 0.32$,[8] we find that the onset for the rotating mode for $D/d \approx 15$; this prediction of the transition point for the two observed patterns is consistent with the experimental data. Indeed we found that at the maximum packing fraction, clouds composed of the smaller particles, where $D/d \approx 20$, do rotate, whereas clouds composed of the larger particles, where $D/d \approx 11$, stretch in the shear flow without rotating.

We have investigated the time evolution of a cloud of non-Brownian particles submitted to a periodic shear flow in an otherwise clarified, Newtonian fluid at low Reynolds number. Clouds at initially moderate concentrations ($\phi = 20\%$–40%) progressively disperse until diluting to a threshold critical volume fraction. These dynamics and the existence of a threshold concentration, below which particles cease to fluctuate between cycles, suggest that the irreversible behavior arises from particle-particle collisions. Above the threshold, collisions between the particles create the irreversible motion; below the threshold, particles solely interact through hydrodynamic interactions and their motion is reversible. This result corroborates previous observations from numerical simulations that the long range hydrodynamic interactions are not a source of irreversibility.[18] Stronger evidence of the importance of solid contacts would be to show that the irreversibility is dramatically reduced when the particle roughness is reduced. To tackle this issue, the same experiment will be performed with a stable emulsion at small capillary number.

Clouds initially prepared at the maximum packing fraction and composed of sufficiently small particles disperse into the surrounding fluid by producing a symmetric pattern that is reminiscent of the shape of a galaxy; this pattern differs from that observed for clouds made of larger particles. A simple model indicates that the formation of the galaxy pattern is directly related to the solid rotation of the core of the cloud. We also provided a dimensional analysis which suggests that the onset of the rotation of the cloud is caused by a "pore-pressure feedback effect" when $D/d > 15$. We plan to more fully test this hypothesis and resulting scaling for the transition by systematically varying D/d in future experiments.

We are thankful to Pierre-Francois Carnet for helping with the experiments. Visits were supported by the Partner University Fund on particulate flows, Aix-Marseille Université (U1) visiting professorships, and ANR JCJC SIMI 9.

[1] G. I. Taylor and J. Friedman, *Low Reynolds Number Flows*, National Committee on Fluid Mechanics Films (Encyclopedia Britannica Educational Corp., United States, 1966).
[2] P. A. Arp and S. G. Mason, "The kinetics of flowing dispersions IX. Doublets of rigid spheres (experimental)," J. Colloid Interface Sci. **61**(4095), 44 (1976).
[3] F. R. da Cunha and E. J. Hinch, "Shear-induced dispersion in a dilute suspension of rough spheres," J. Fluid Mech. **309**, 211 (1996).
[4] D. J. Pine, J. P. Gollub, J. F. Brady, and A. M. Leshansky, "Chaos and threshold for irreversibility in sheared suspensions," Nature (London) **438**, 997 (2005).
[5] L. Corté, P. M. Chaikin, J. P. Gollub, and D. J. Pine, "Random organization in periodically driven systems," Nat. Phys. **4**, 420 (2008).
[6] J. M. Bricker and J. E. Butler, "Correlation between stresses and microstructure in concentrated suspensions of non-Brownian spheres subject to unsteady shear flows," J. Rheol. **51**, 735 (2007).
[7] P. R. Nott, É. Guazzelli, and O. Pouliquen, "The suspension balance model revisited," Phys. Fluids **23**, 043304 (2011).
[8] F. Boyer, O. Pouliquen, and É. Guazzelli, "Dense suspensions in rotating-rod flows: normal stresses and particle migration," J. Fluid Mech. **686**, 5 (2011).
[9] I. E. Zarraga and D. T. Leighton, "Normal stress and diffusion in a dilute suspension of hard spheres undergoing simple shear," Phys. Fluids **13**, 565 (2001).
[10] I. Rampall, J. R. Smart, and D. T. Leighton, "The influence of surface roughness on the particle-pair distribution function of dilute suspensions of non-colloidal spheres in simple shear flow," J. Fluid Mech. **339**, 1 (1997).
[11] M. L. Ekiel-Jezewska, B. Metzger, and É. Guazzelli, "Spherical cloud of point particles falling in a viscous fluid," Phys. Fluids **18**, 038104 (2006).
[12] B. Metzger, M. Nicolas, and É. Guazzelli, "Falling clouds of particles in viscous fluids," J. Fluid Mech. **580**, 283 (2007).
[13] L. Corté, S. J. Gerbode, W. Man, and D. J. Pine, "Self-organized criticality in sheared suspensions," Phys. Rev. Lett. **103**, 248301 (2009).
[14] See supplementary material at http://dx.doi.org/10.1063/1.3685537 for continuous evolution of a cloud initially prepared at the maximum packing fraction.
[15] G. K. Batchelor and J. T. Green, "The hydrodynamic interaction of two small freely-moving spheres in a linear flow field," J. Fluid Mech. **56**, 375 (1972).
[16] M. Pailha and O. Pouliquen, "A two-phase flow description of the initiation of underwater granular avalanches," J. Fluid Mech. **633**, 115 (2009).
[17] O. Reynolds, "Dilatancy," Nature (London) **33**, 429 (1886).
[18] B. Metzger and J. E. Butler, "Irreversibility and chaos: Role of long-range hydrodynamic interactions in sheared suspensions," Phys. Rev. E **82**, 051406 (2010).

CrossMark
click for updates

PHYSICS OF FLUIDS **27**, 051701 (2015)

Particle dispersion in sheared suspensions: Crucial role of solid-solid contacts

Phong Pham,[1,2] Bloen Metzger,[1] and Jason E. Butler[2]
[1]*IUSTI-CNRS UMR 7343, Aix-Marseille University, 13453 Marseille Cedex 13, France*
[2]*Department of Chemical Engineering, University of Florida, Gainesville, Florida 32611, USA*

(Received 22 January 2015; accepted 20 April 2015; published online 1 May 2015)

We performed high resolution measurements of the dynamics of non-Brownian and neutrally buoyant particles subjected to a periodic shear flow under low Reynolds number conditions. By changing the particle roughness and showing that it significantly affects the particle motion, we provide direct evidence that particle solid-solid contacts occur in viscous suspensions and strongly influence the particle dynamics. An accurate prediction of the particle trajectories is obtained with a minimal model that solely includes normal lubrication interactions and a frictionless contact force. © *2015 AIP Publishing LLC.* [http://dx.doi.org/10.1063/1.4919728]

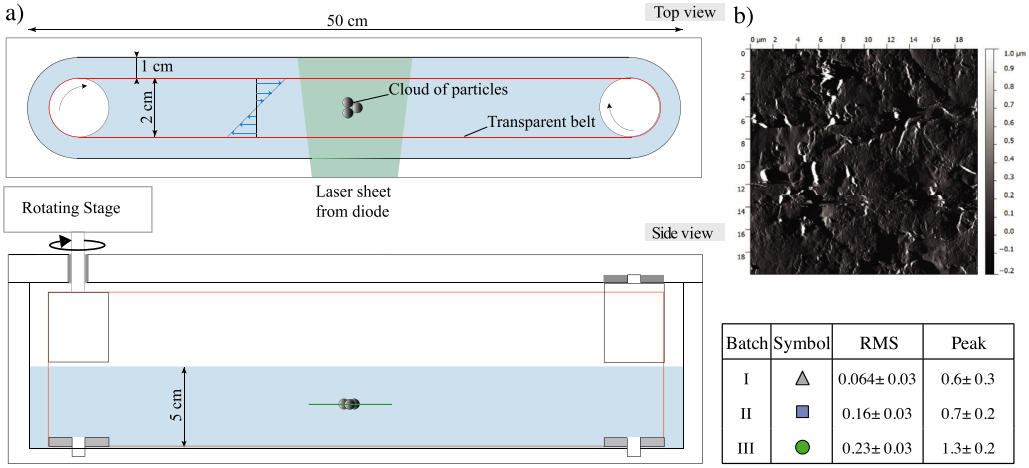
A different perspective, increasingly supported by experiments and numerical simulations, on how to describe sheared suspensions is emerging. Several experimental studies[1–4] have suggested that solid-solid contact causes irreversible displacement of particles when colliding in viscous shear flows. Recent numerical studies demonstrated that in sheared suspensions, neither the long range hydrodynamic[5] nor the lubrication interactions[6] generate sufficient chaos to produce the irreversible behaviors observed experimentally; rather, contacts between particles were found to largely dominate the particle dispersion phenomenon. Clouds of particles, submitted to a periodic flow, progressively disperse until the volume fraction drops below a critical threshold where particles cease to fluctuate between cycles.[7] This evolution also suggests that particle dispersion arises from contact interactions. More generally, simulations of shearing flows based on the simple rule that particles should not overlap[8,9] generate results that compare well with experimental observations, yet these methods are exceedingly simple relative to simulation methods that incorporate the effects of multi-body hydrodynamics.[10–12] Moreover, accurate measurements of pair distribution functions[4] revealed a strong fore-aft asymmetry in which a "high concentration tail" forms in the recession quadrant. This distribution function was identified by Blanc *et al.*[4] as consistent with that predicted for rough particles[13] having a similar roughness, hence providing the most direct evidence yet that solid-solid contacts influence suspension dynamics.

All of these numerical and experimental observations support the idea that irreversible dynamics in sheared suspensions are dominated by particle contacts and their associated steric effects. This hypothesis is a promising one, since not having to account for the long range hydrodynamic interactions could greatly simplify calculations and would focus attention on what may be the essential ingredient to accurately model sheared suspensions. In this letter, we perform high resolution measurements of the dynamics of small numbers of particles submitted to a periodic flow. By altering the particle roughness and showing that this directly affects the particle motion, we provide evidence that particle solid-solid contacts occur in viscous suspensions and strongly influence the particle dynamics.

The experimental setup, shown in Figure 1(a), is an improved version of the one used by Metzger and Butler.[7] A linear shear flow is generated by a transparent mylar belt that is mounted tightly on two rotating cylinders. The motion of the belt is controlled by a rotating stage (M-061.PD from PI Piezo-Nano Positioning) with high angular resolution (3×10^{-5} rad). The cell was carefully designed to ensure reversibility upon flow reversal. To avoid unwanted secondary fluid re-circulations, this new configuration enables the fluid to flow under the cylinders and a constant spacing between the belt and the inner wall of the cell is maintained all around the cell.

 ©2015 AIP Publishing LLC

This article is copyrighted as indicated in the article. Reuse of AIP content is subject to the terms at: http://scitation.aip.org/termsconditions. Downloaded to IP: 195.83.220.70 On: Tue, 12 May 2015 16:19:09



Batch	Symbol	RMS	Peak
I	△	0.064± 0.03	0.6± 0.3
II	□	0.16± 0.03	0.7± 0.2
III	○	0.23± 0.03	1.3± 0.2

FIG. 1. (a) Sketch of the experimental shear-cell. A linear shear flow is generated by moving the transparent mylar belt (in red). Fluorescent particles, which are initially placed carefully in the shear plane, are illuminated with a thin laser sheet. (b) AFM image of a particle and table of the RMS and peak roughness in μm, measured using AFM for the three different batches of particles.

The fluid is a mixture of Triton X-100 (76.241 wt. %), zinc chloride (14.697 wt. %), and water (9.062 wt. %). It is a Newtonian fluid with a viscosity of 3 Pa · s and a density of 1.18 g/cm^3 at room temperature. The composition was chosen to match both the refractive index and density of the particles, which are mono-disperse spheres of diameter $d = 2$ mm that are made of poly-methylmethacrylate (PMMA). The roughness of the particles was modified by stirring the particles at 60 rpm for one hour while immersed within a diamond paste solution (Presi Reflex LDP). Experiments were performed with three different batches of particles: the original ones and two other batches produced by polishing the original particles with solutions having different grades (0.25 μm and 15 μm). For each batch, the surface roughness of the particles was characterized by examining a total area of 400 μm^2 on four different particles. The data were processed using a standard method;[14] an example result over a 20×20 μm area is shown in Figure 1(b) and the root mean square and peak values of the surface roughness are reported for each batch. The error values of roughness are reported in Figure 1(b) also.

Initially, the particles were carefully placed approximately 2.5 cm below the free surface of the fluid (see Fig. 1(a)) and were confirmed to be in the flow-gradient plane prior to starting an experiment. Visualization of the particles was enhanced by coating them with Rhodamine 6G. The coating was applied by soaking the particles in an equal parts solution of water and ethanol doped with Rhodamine 6G for 30 min at 60 °C. The particles were sheared forward and backward for 10 cycles at a strain amplitude of $\gamma_0 = 4$, where each cycle required 20 s to complete; the Reynolds number, based upon the particle diameter, is consequently 3×10^{-4}. A laser sheet, generated by a green laser diode (100 mW power and wavelength of 532 nm), was used to illuminate the particles. The fluorescing particles were imaged from the top with a digital camera (Basler Ace) and a magnification lens (Sigma APO-Macro-180mm-F3.5-DG). A 550 nm high-pass filter was positioned before the lens to remove any light directly scattered by the particles. Images were then analyzed using a circular Hough transform to obtain the particle positions.

The experimental results were compared to a numerical model. This model represents a rudimentary description relative to the substantially more accurate models existing in the literature.[10,13] However, it was built[6] with the aim of determining the minimum physical ingredients needed to capture the dynamics of particles in sheared viscous suspensions. It includes the hydrodynamic drag on the particles from the background shear flow, a constant repulsive force, and the normal component of the lubrication force; long-range hydrodynamic interactions were not included in the model. In the absence of inertia, the sum of the hydrodynamic forces, $\mathbf{F}_i^h$, and the contact forces, $\mathbf{F}_i^c$, on each particle i balances

$$\mathbf{F}_i^h + \sum_{j \neq i}^{N} \mathbf{F}_{ij}^c = 0. \tag{1}$$

This article is copyrighted as indicated in the article. Reuse of AIP content is subject to the terms at: http://scitation.aip.org/termsconditions. Downloaded to IP: 195.83.220.70 On: Tue, 12 May 2015 16:19:09

In this minimal approach, we write the hydrodynamic forces as the sum of the drag due to the background shear flow and the normal components of the lubrication forces between neighboring particles,

$$\mathbf{F}_i^h = 3\pi\mu d(\mathbf{u}_i - \mathbf{u}_{i\infty}) + \sum_{j(i)} \frac{3\pi\mu d^2}{8h_{ij}} \mathbf{n}_{ij}(\mathbf{u}_i - \mathbf{u}_j) \cdot \mathbf{n}_{ij}, \tag{2}$$

where μ denotes the fluid viscosity, d the particle diameter, and $\mathbf{u}_i$ the velocity of particle i. The fluid velocity at $\mathbf{x}_i = (x_i, y_i)$, the position of particle i, is $\mathbf{u}_{i\infty} = \dot{\gamma} y_i \mathbf{e}_x$, where $\dot{\gamma}$ is the shear rate and $\mathbf{e}_x$ is the unit vector in the x-direction. Lubrication forces between particle i and the particles $j(i)$ located within the lubrication range of particle i depend upon the relative velocities and separation distance $h_{ij} = |\mathbf{x}_{ij}| - d$, where $|\mathbf{x}_{ij}| = |\mathbf{x}_i - \mathbf{x}_j|$, of each pair. The particles $j(i)$ located within the lubrication range of particle i satisfy $2\epsilon \leqslant h_{ij} \leqslant d/2$, where ϵ denotes the dimensionless roughness of the particles. The algorithm only accounts for the normal component of lubrication,[15] which acts along the vector $\mathbf{n}_{ij} = \mathbf{x}_{ij}/|\mathbf{x}_{ij}|$. The contact forces are given by

$$\mathbf{F}_{ij}^c = \begin{cases} F_0 \mathbf{n}_{ij} & \text{if } |\mathbf{h}_{ij}| \leqslant 2\epsilon \\ 0 & \text{if } |\mathbf{h}_{ij}| > 2\epsilon, \end{cases} \tag{3}$$

where F_0 denotes the amplitude of the repulsive force. This repulsive force was chosen for its simplicity. It is large enough so that particles do not overlap. If $|\mathbf{h}_{ij}| \leqslant 2\epsilon$, the particles are instantaneously pushed away from each other by the repulsive force which is much larger than any hydrodynamic force. During contact, the typical variation of the distance between particles is $O(10^{-6}d)$. Other, more sophisticated definitions of the repulsive force (such as Hertzian contacts or the exponentially decaying potential used in Stokesian dynamics[10]) were also tested and provide very similar particle trajectories. The equations presented above are solved for the velocities of the particles given their spatial positions. The positions are updated in time using a fourth-order Runge-Kutta method with a time step that ensures a displacement of less than $10^{-5}d$ at each time step.

Figure 2(a) shows the initial position of the particles and the corresponding relative trajectories recorded over 10 cycles of shear. Arrows indicate the direction of motion of the particles. The interesting feature is that during the backward part of the first cycle, particles are forced away from their reversible path: particles follow different trajectories, ending further apart than they were initially. This irreversible behavior occurs only during the first cycle. Over the next nine cycles, particles exhibit a reversible behavior, always retracing the same trajectory on the forward and backward portions of the cycles. This behavior is illustrated by the spatio-temporal plot shown in Figure 2(b). This spatio-temporal plot was constructed from the pixels highlighted by the dashed line on Figure 2(a), which was taken from each successive image and plotted side by side. During the first cycle, the spatio-temporal pattern changes indicating irreversibility. After that, reversibility is observed clearly as the patterns repeat.

The irreversible motion of the particles observed here is reminiscent of the behavior observed in homogeneous suspensions[5,6,16] or for clouds of particles subjected to a periodic flow.[7] To probe whether solid-solid contacts between particles are responsible for this behavior, the experiment

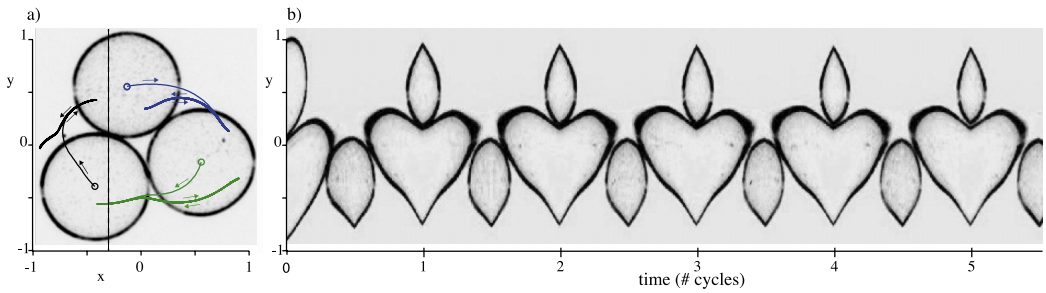


FIG. 2. Experiments: (a) Initial configuration of the cloud of particles and relative trajectories over 10 cycles for particles of Batch III. Arrows indicate the direction of motion of the particles. (b) Spatio-temporal plot of the dashed line shown in (a). A movie is available with the online version of the paper. (Multimedia view) [URL: http://dx.doi.org/10.1063/1.4919728.1]

This article is copyrighted as indicated in the article. Reuse of AIP content is subject to the terms at: http://scitation.aip.org/termsconditions. Downloaded to IP: 195.83.220.70 On: Tue, 12 May 2015 16:19:09

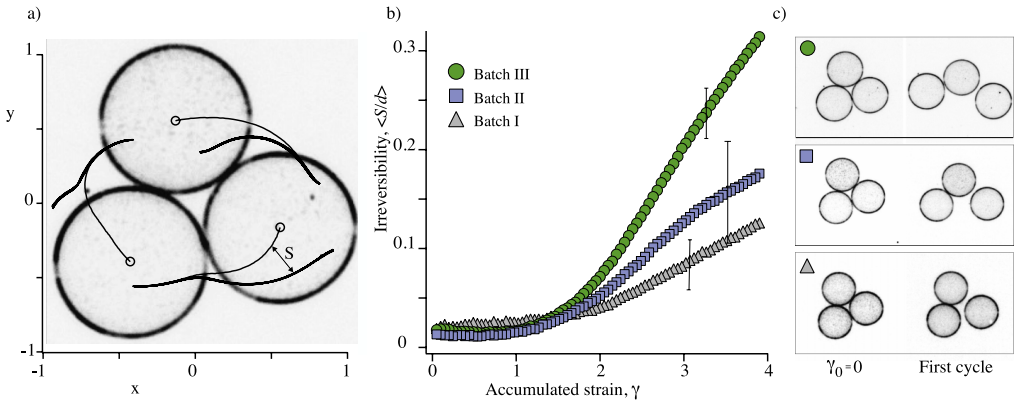


FIG. 3. Experiments: (a) Example of trajectories for particles of Batch III. (b) Magnitude of the irreversibility, $\langle S/d \rangle$, during the first cycle of shear versus accumulated strain for the three batches of particles. Errors bars correspond to the standard deviation calculated over the five experimental runs performed for each roughness. (c) Image of the particles at $\gamma_0 = 0$ and at the end of the first cycle.

was repeated with the three batches of particles having different roughnesses. For each run, the amount of irreversibility, $\langle S/d \rangle$, was quantified as the average separation distance between the forward and backward motions of the first cycle as shown in Figure 3(a). The striking result, shown in Figure 3(b), is that the amplitude of the irreversibility increases as the particle roughness is increased. For larger roughness, the particles end up further apart at the end of first cycle as shown in Figure 3(c). This measurement provides direct evidence that particle solid-solid contacts are at the origin of the irreversible behavior observed in sheared suspensions.

In the following, we investigate if the minimal model presented above can capture the particle dynamics. We assume the particles are initially at contact, forming an equilateral triangle. This defines the particle diameter, d, taken as the average initial separation distance between the particles. The model then only contains two adjustable parameters: the magnitude of force, F_0, and the surface roughness, ϵ. The optimum values for these parameters are determined by minimizing the distance, $\ell = \frac{1}{N}\sqrt{\sum_{i=1}^{t}\sum_{i=1}^{N}((x_i^A - x_i^B)^2 + (y_i^A - y_i^B)^2)}$, where A and B indicate the experimental and simulation data, respectively.

The inset of Figure 4(b) shows ℓ, as obtained for incremental values of the magnitude of the force, F_0, and of the particle roughness, ϵ. The distance between simulations and experiments

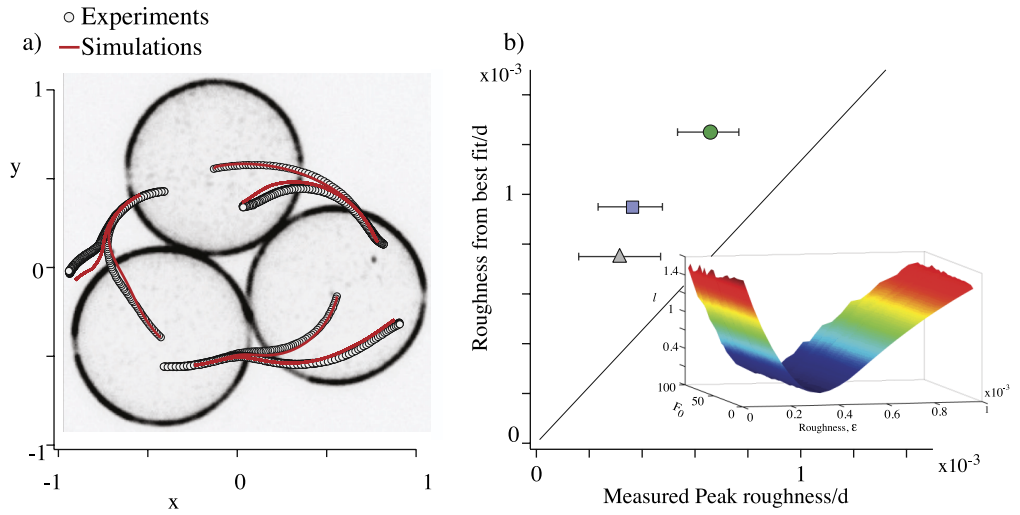


FIG. 4. Experiments and simulations: (a) Comparison of the trajectories obtained from simulations to experimental trajectories for particles of Batch III. (b) Dimensionless roughness obtained from the simulations trajectories providing the best fit with the experimental trajectories versus the dimensionless peak roughness obtained from AFM. Inset: Separation distance, ℓ, vs. magnitude of the repulsive force, F_0, and roughness, ϵ.

This article is copyrighted as indicated in the article. Reuse of AIP content is subject to the terms at: http://scitation.aip.org/termsconditions. Downloaded to IP: 195.83.220.70 On: Tue, 12 May 2015 16:19:09

behaves as a flat valley suggesting that the magnitude of the force, if chosen in a reasonable range, does not affect significantly the particle trajectories. Conversely, changing the roughness provides a well-defined minimum separation distance, which defines a roughness that optimizes the agreement between experimental and simulation trajectories. Trajectories obtained with the optimum roughness are shown in Figure 4(a): as observed in the experiment, the first cycle is irreversible, while the following cycles are reversible. This minimal model, which only includes a solid-solid contact force and the normal component of the lubrication force, quantitatively reproduces the trajectories that were measured experimentally.

In Figure 4(b), the roughness AFM measurements are compared to the optimum roughness obtained from the best fit of the numerical model to the experimentally measured trajectories. The results are close (within a factor 2) to the AFM peak values; the measured RMS values are one order of magnitude smaller than those obtained from the minimization, see Figure 1(b). This suggests that the relevant roughness is given by the peak value. This is consistent since when particles approach, the minimal separation distance at which the particles can touch is given by the peak value of the roughness, not by the RMS.

We have reported on highly resolved experimental measurements of the individual trajectories of small number of particles subjected to a periodic shear under creeping-flow conditions. These experiments provide evidence that particles experience solid-solid contacts, as increasing the roughness was found to increase the irreversibility of the particle trajectories. A minimal model that includes only hydrodynamic drag, the normal component of the lubrication interaction, and contact forces provides a quantitatively accurate description of the particle dynamics and consequently supports the idea that particle contacts are responsible for the experimental observations.

The authors thank P. Cervetti, S. Noël, and F. Ratouchniack for machining and helping with the design of the setup and A. Rangis (Aix-Marseille University) for the AFM measurements. This work was supported by the National Science Foundation (Grant No. 0968313), ANR JCJC SIMI 9 and has been carried out in the framework of the Labex MEC (ANR-10-LABX-0092) and of the A*MIDEX project (ANR-11-IDEX-0001-02), funded by the "Investissements d'Avenir" French Government program managed by the French National Research Agency (ANR).

[1] P. A. Arp and S. G. Mason, "The kinetics of flowing dispersions IX. Doublets of rigid spheres (Experimental)," J. Colloid Interface Sci. **61**, 44 (1977).
[2] I. Rampall, J. R. Smart, and D. T. Leighton, "The influence of surface roughness on the particle-pair distribution function of dilute suspensions of non-colloidal spheres in simple shear flow," J. Fluid Mech. **339**, 1 (1997).
[3] M. S. Ingber, A. A. Mammoli, P. Vorobieff, T. McCollam, and A. L. Graham, "Experimental and numerical analysis of irreversibilities among particles suspended in a Couette device," J. Rheol. **50**, 99 (2006).
[4] F. Blanc, F. Peters, and E. Lemaire, "Experimental signature of the pair-trajectories of rough spheres in the shear-induced microstructure in non-colloidal suspensions," Phys. Rev. Lett. **107**, 208302 (2011).
[5] B. Metzger and J. E. Butler, "Irreversibility and chaos: Role of long range hydrodynamic interactions in sheared suspensions," Phys. Rev. E **82**, 051406 (2010).
[6] B. Metzger, P. Pham, and J. E. Butler, "Irreversibility and chaos: Role of lubrication interactions in sheared suspensions," Phys. Rev. E **87**, 052304 (2013).
[7] B. Metzger and J. E. Butler, "Clouds of particles in a periodic shear flow," Phys. Fluids **24**, 021703 (2012).
[8] E. Lerner, G. Düring, and M. Wyart, "Simulations of driven overdamped frictionless hard spheres," Comput. Phys. Commun. **184**(3), 628-637 (2013).
[9] R. Seto, R. Mari, J. F. Morris, and M. M. Denn, "Discontinuous shear thickening of frictional hard-sphere suspensions," Phys. Rev. Lett. **111**, 218301 (2013).
[10] G. Bossis and J. F. Brady, "Dynamic simulation of sheared suspensions. I. General method," J. Chem. Phys. **80**, 5141 (1984).
[11] M. Abbas, E. Climent, and O. Simonin, "Fully coupled simulations of non-colloidal monodisperse sheared suspensions," Chem. Eng. Res. Des. **85**, 778 (2007).
[12] K. Yeo and M. R. Maxey, "Simulation of concentrated suspensions using the force-coupling method," J. Comput. Phys. **229**, 2401 (2010).
[13] F. R. da Cunha and E. J. Hinch, "Shear-induced dispersion in a dilute suspension of rough spheres," J. Fluid Mech. **309**, 211 (1996).
[14] D. Nečas and P. Klapetek, "Gwyddion: An open-source software for SPM data analysis," Cent. Eur. J. Phys. **10**(1), 181 (2012).
[15] G. K. Batchelor and J. T. Green, "The hydrodynamic interaction of two small freely-moving spheres in a linear flow field," J. Fluid Mech. **56**, 401 (1972).
[16] D. J. Pine, J. P. Gollub, J. F. Brady, and A. M. Leshansky, "Chaos and threshold for irreversibility in sheared suspensions," Nature **438**, 997 (2005).

This article is copyrighted as indicated in the article. Reuse of AIP content is subject to the terms at: http://scitation.aip.org/termsconditions. Downloaded to IP: 195.83.220.70 On: Tue, 12 May 2015 16:19:09

PHYSICAL REVIEW FLUIDS **1**, 022201(R) (2016)

Origin of critical strain amplitude in periodically sheared suspensions

Phong Pham,[1,2] Jason E. Butler,[2] and Bloen Metzger[1]
[1]*IUSTI, CNRS, UMR No. 7343, Aix-Marseille University, 13453 Marseille Cedex 13, France*
[2]*Department of Chemical Engineering, University of Florida, Gainesville, Florida 32611, USA*
(Received 1 February 2016; published 1 June 2016)

The role of solid-solid contacts on the transition between reversible and irreversible dynamics occurring in periodically sheared suspensions is investigated experimentally by modifying the particle roughness. Smoother particles lead to a larger critical strain amplitude. A geometrical model based on the assumption that colliding particles produce irreversibility is derived. The model, which considers a quasiparticle having a strain- and roughness-dependent effective volume, successfully reproduces the measured values of the critical strain amplitude as functions of the volume fraction and particle roughness.

DOI: 10.1103/PhysRevFluids.1.022201

When sheared periodically, non-Brownian particles suspended in a viscous fluid undergo a dynamical phase transition. For a given particulate volume fraction and a small enough strain amplitude, the suspension relaxes to an absorbing reversible state in which particles return to their original position after every cycle of shear. When the strain amplitude exceeds a critical value, the suspension transitions to a fluctuating state: The particles do not return to their original positions and when tracked stroboscopically at the end of each cycle of shear, the particles exhibit large fluctuations analogous to a random walk [1].

This transition caught the attention of a vast audience [1–5], owing to the assumption that the sheared suspensions are governed by reversible equations (the Stokes equations); in such a system, reversing the direction of shear would be equivalent to reversing time. Hence, suspensions were viewed as an opportunity to investigate experimentally the echo protocol, which consists of studying the evolution of a system after reversal of its dynamics [5] and addressing the emergence of macroscopic irreversibility in a system governed at the microscopic level by time-reversible laws. Within this framework, it was proposed that the irreversible motion of the particulates arises from the chaotic nature of the hydrodynamic interactions [1,6].

This long-range N-body interpretation of the problem differs from the short-range explanation put forward more recently by Corté *et al.* [7]. Without providing a clear mechanism for the physical origin of the irreversibility, Corté *et al.* modeled the suspension dynamics by convecting particles along their undisturbed streamlines until they collided, at which point the particles were displaced by a small random distance before continuing. This model, although exceedingly simple, was sufficient to explain the existence of a threshold strain amplitude and to spontaneously produce a self-organized reversible state at small strain amplitudes.

The success of the latter collision-induced model [7] is not so surprising when put in perspective with the following results: (i) Recent numerical results concluded that, in sheared suspensions, chaos arising from the long-range hydrodynamic interactions [8] or from lubrication forces [9] between particles is too weak to produce a significant irreversibility and (ii) experiments [10–14] have provided strong evidence that particle solid-solid contacts occur and significantly affect their dynamics. These studies support a growing consensus that the irreversible displacements of force-free particles in sheared suspensions are mainly driven by excluded-volume constraints.

To further assess the above paradigm and determine the physical origin of this transition, we experimentally investigated the influence of the particle roughness on the critical strain amplitude. For a given volume fraction, we find that smoother particles require a larger strain amplitude before transitioning from reversible to irreversible dynamics. A simple geometric model, based on the assumption that particle solid-solid encounters lead to irreversible displacements and which

 ©2016 American Physical Society

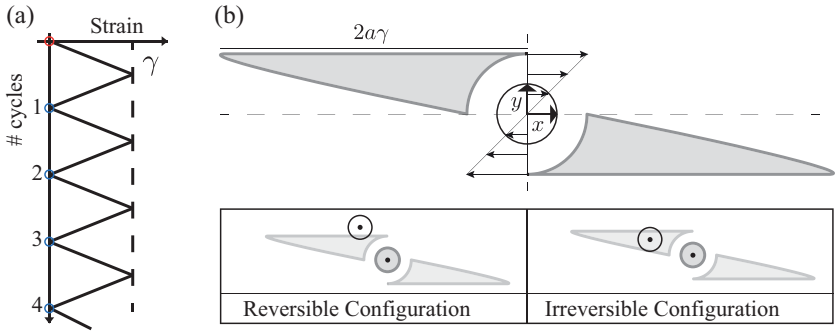


FIG. 1. (a) Schematic providing the definition of the applied strain. (b) Wing shape in two dimensions. For a given strain amplitude γ, any particle located within the gray area will eventually collide with the reference particle located at the origin.

accounts for hydrodynamic effects on the particle trajectories, is proposed and shown to predict the dependence of the critical strain amplitude on volume fraction and particle roughness.

For the sake of simplicity, we first derive the critical strain amplitude γ_c while accounting solely for the effect of the background advection flow and in a two-dimensional geometry. For a given applied strain amplitude γ [see Fig. 1(a)], any particle located within the shaded area, from now on referred to as the wings shown in Fig. 1(b), will eventually collide with the reference particle of radius a located at the origin. The area of the wings $W_{2D} = 4\gamma a^2$ is found to increase proportionally with the strain amplitude. Within the model, particles can be thought of as quasiparticles having an effective strain-dependent area $A_{\text{eff}} = \pi a^2 + 4\gamma a^2$, which is the sum of the "real" particle area plus the area of its wings.

Now consider that if N of these quasiparticles can be placed in a box of total area A without any overlap, the motion of each particle will be reversible; this condition corresponds to $NA_{\text{eff}} < \beta A$, where β denotes an order one constant. More generally, when this condition is met, we assume that the system under periodic strain can self-organize into a reversible state where no collision between the particles occurs, regardless of the initial arrangement of the particles. Conversely, if $NA_{\text{eff}} > \beta A$, the quasiparticles unavoidably overlap and produce collisions that result in irreversibility. Criticality is thus reached when $NA_{\text{eff}} = \beta A$. Using $\phi = N\pi a^2/A$, where ϕ is the real particle area fraction, the critical strain amplitude is

$$\gamma_c = \frac{\pi}{4}\left(\frac{\beta}{\phi} - 1\right). \tag{1}$$

The above simple geometrical argument predicts $\gamma_c \propto \phi^{-1}$. Despite having utilized a two-dimensional approximation, this scaling is consistent with the experimental results of Corté *et al.* [15] as well as with the scaling predicted from a three-dimensional model, which is developed next.

Using ideas similar to those above, the critical strain amplitude is now determined for fully three-dimensional suspensions while accounting for the effects of hydrodynamic interactions and short-range irreversibilities (i.e., particle roughness). The particle roughness ϵ is a dimensionless quantity that sets the distance $h = 2\epsilon a$ at which particles collide. The wing now has a more complex shape [see Fig. 2(a)]. The shape, as well as the associated volume W_{3D}, was computed numerically from predictions of the relative trajectory between two particles [16], which includes the effects of hydrodynamics and particle roughness. This Monte Carlo integration used randomly assigned positions of the particles within a box of large but fixed size together with an integration of the trajectories to identify the initial positions that result in an irreversible collision. The ratio of the number of trials that result in an irreversible collision to the total number of trials is the volume W_{3D}.

Figure 2(a) illustrates different wing shapes obtained for ($\gamma = 8, \epsilon = 10^{-3}$), ($\gamma = 6, \epsilon = 10^{-3}$), and ($\gamma = 6, \epsilon = 10^{-2}$). The wing volume is found to depend both on the strain amplitude and on particle roughness. As opposed to the former, one can anticipate the latter dependence to be nonlinear

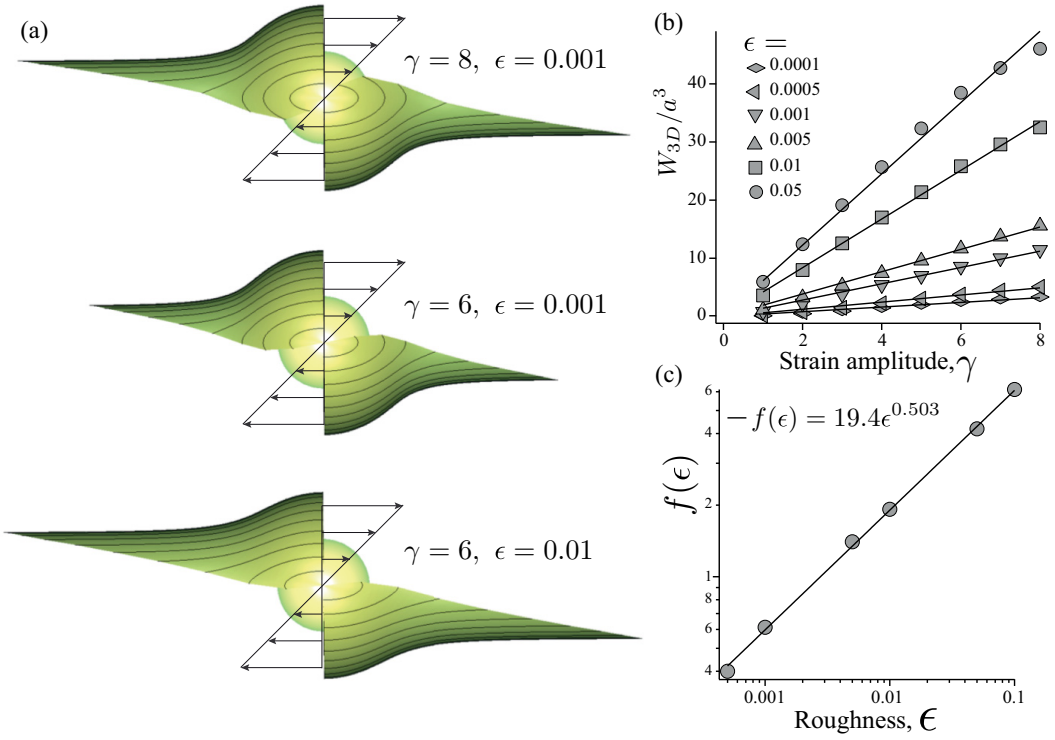


FIG. 2. (a) Wing shape in three dimensions and including the effect of hydrodynamics obtained for different strain amplitudes and particle roughness. (b) Wing volume W_{3D} versus applied strain amplitude γ for different particle roughness. The wing volume is fitted by $W_{3D}/a^3 = f(\epsilon)\gamma$. (c) The function $f(\epsilon)$ follows a power law $f(\epsilon) \propto \epsilon^{1/2}$.

as (i) the divergence of the lubrication force implies that decreasing h by a fixed amount requires an increasingly larger strain as h gets smaller and (ii) ϵ sets the distance at which particles make solid contact (when $h = 2\epsilon a$). These trends are shown in Figs. 2(b) and 2(c). Fitting the wing volume gives $W_{3D}/a^3 = f(\epsilon)\gamma$, where the function $f(\epsilon)$, as shown on Fig. 2(c), follows the power law $f(\epsilon) = 19.4\epsilon^{0.503}$, suggesting that $f(\epsilon) \propto \epsilon^{1/2}$.

For an imposed strain γ and a particle roughness ϵ, the particle effective volume in three dimensions is thus $V_{\text{eff}} = 4\pi a^3/3 + f(\epsilon)\gamma a^3$. The resulting prediction for the critical strain amplitude is

$$\gamma_c = \frac{0.22}{\epsilon^{1/2}}\left(\frac{\beta}{\phi} - 1\right). \tag{2}$$

Note that the critical strain amplitude γ_c must tend to zero at maximum packing: This sets $\beta = 0.58$ [17]. This relation also predicts that for a suspension composed of perfectly smooth spheres, i.e., $\epsilon \to 0$, the critical strain amplitude $\gamma_c \to \infty$.

To test the validity of the above relation, we performed experiments using the experimental setup in Fig. 3(a). A linear shear flow is generated by a transparent belt mounted on two vertical cylinders whose rotation is driven by a high-precision rotating stage. The fluid is a mixture of Triton X-100 (73.9 wt. %), zinc chloride (14.2 wt. %), and water (11.9 wt. %). Its composition was chosen to match both the refractive index and density of the particles, which are monodisperse spheres of poly(methyl methacrylate) with radius $a = 1$ mm. A water bath surrounding the shear cell controls the temperature at 22 °C, which is used to fine-tune the refractive index match between the particles and fluid; any adverse effects on the matching of the particle and fluid densities were small. A small amount of rhodamine 6G is added to the fluid so that, when illuminating a horizontal plane of the suspension with a (60-μm-thick) laser sheet, the particles within that plane appear as black disks as shown in Fig. 3(a) and [18].

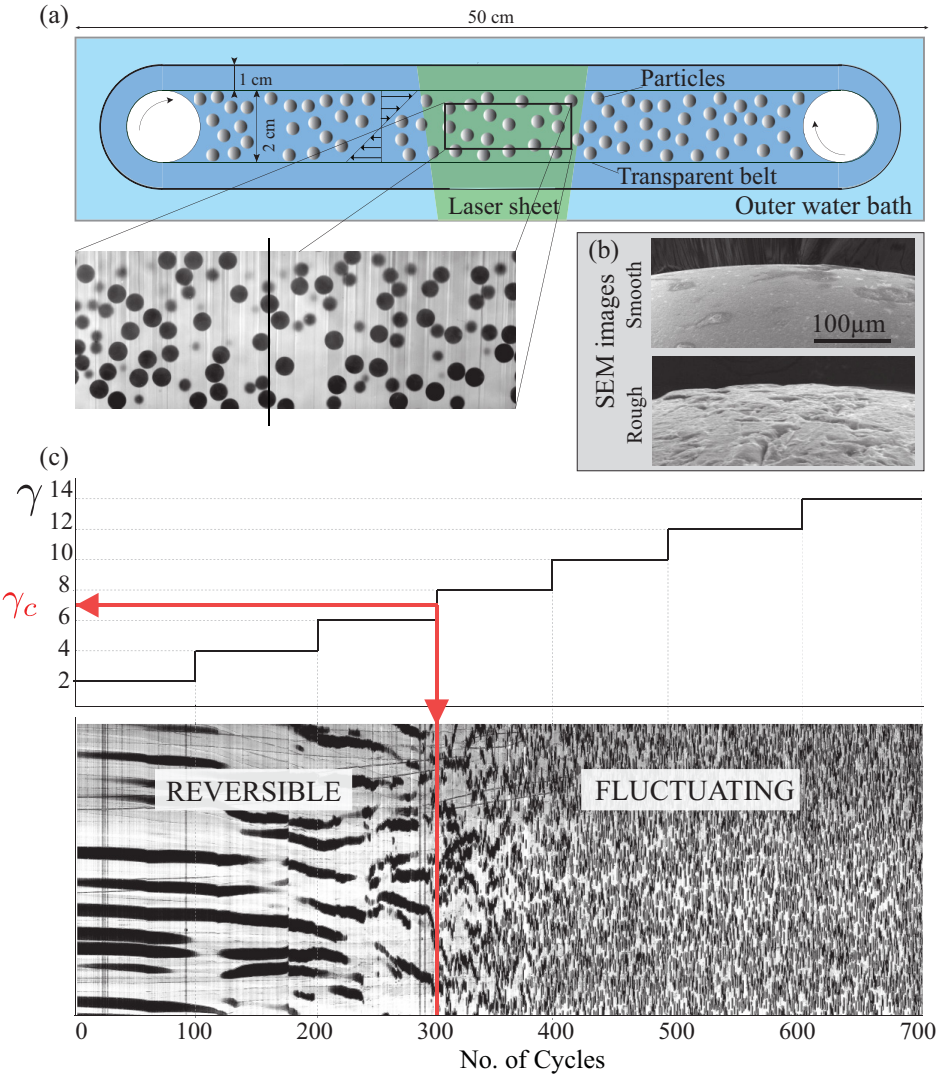


FIG. 3. (a) Top view of the experimental shear cell and a typical image of the suspension for a volume fraction $\phi = 25\%$. (b) Example images of the smooth and rough particles. (c) Determination of the critical strain amplitude. The stain amplitude is increased incrementally by steps of one strain unit. For each step, 100 cycles are performed and an image is recorded at the end of each cycle. The critical strain is directly determined from the spatiotemporal plot (red line).

The volume fraction was varied between $\phi = 25\%$ and 50% and two different batches of particles having different roughness were used. The smooth particles have a peak roughness of $\epsilon a = 1.9 \pm 1.4$ μm, as was determined from averaging over multiple scanning electron microscopy images [see Fig. 3(b) for examples]. The rough particles were produced by rotating the smooth particles for 10 min at 130 rpm between two circular plates that were covered with sandpaper sheets. The resulting particles are rougher, with $\epsilon a = 5.5 \pm 3.0$ μm.

Before beginning an experiment, first the suspension was spatially homogenized by preshearing it periodically at a large strain amplitude of $\gamma = 10$ for 200 cycles. Then 100 cycles were performed at each strain amplitude, as the strain amplitude was increased incrementally from 1 to 10 in steps of one strain unit as illustrated in Fig. 3(c). At the end of each cycle of oscillation, one image of the suspension was recorded and a vertical line from each image [as indicated in the example in Fig. 3(a)] was plotted in sequence. The resulting spatiotemporal plot, shown in Fig. 3(c) for $\phi = 25\%$, enables identification of the critical strain amplitude at which the particle positions become irreversible. At small strain amplitudes ($\gamma < \gamma_c$), the spatiotemporal plot shows only very small changes between each cycle, which are likely due to thermal convection and sedimentation. Conversely, at large strain

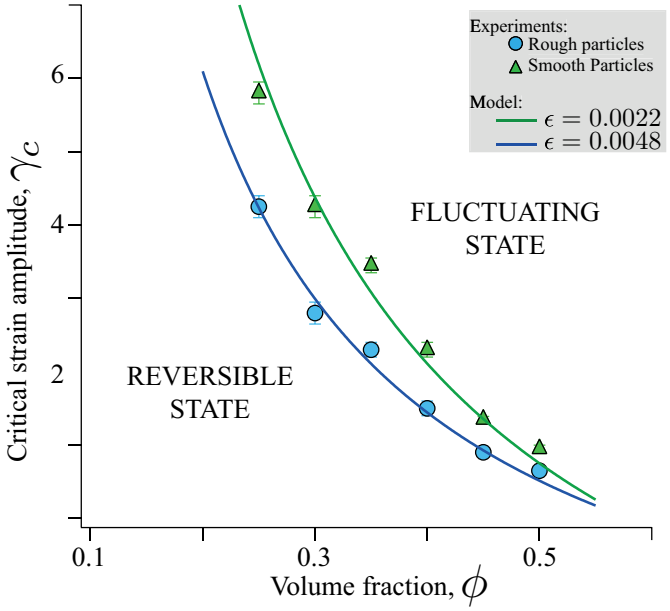


FIG. 4. Critical strain γ_c versus volume fraction ϕ, measured experimentally for the two batches of particles and comparison with the model (2): $\gamma_c = 0.22(0.58/\phi - 1)/\epsilon^{0.5}$.

amplitudes ($\gamma > \gamma_c$), the spatiotemporal plot shows that all time correlation is lost from one cycle to the next (from one vertical line of pixels to the next): The system reached its fluctuating state. The critical strain is directly determined from that spatiotemporal plot [red line in Fig. 3(c)]. After this initial coarse determination of the critical strain, the experiment was repeated with a smaller strain increment of 0.3 within the vicinity of the coarse estimate. The critical strain is thus determined within ± 0.15 strain units. Note that the critical strain amplitude characterizes the system at steady state, after oscillating a sufficient number of times to either organize the system into a reversible state if $\gamma < \gamma_c$ or into a fluctuating state if $\gamma > \gamma_c$. Therefore, the prediction of the critical strain amplitude does not depend on the initial configuration of the particles (random or presheared).

Figure 4 shows the critical strain γ_c versus volume fraction ϕ obtained for the smooth and rough particles. For rough particles, irreversibility is systematically reached at a smaller critical strain amplitude. The model (2) successfully predicts the experimental results when using values for ϵ that correspond closely to the measured values. The least-squares fit of the data, treating only ϵ as an adjustable parameter, returns $\epsilon = 0.0022$ for the smooth particles and $\epsilon = 0.0048$ for the rough particles, whereas the measurements indicate $\epsilon = 0.0019 \pm 0.0014$ and $\epsilon = 0.0055 \pm 0.003$. Note that although the model is based on the interaction of particle pairs, it predicts the critical strain surprisingly well for large volume fractions where multibody interactions might be expected to be of importance.

In conclusion, the role of solid-solid contacts on the transition occurring in periodically sheared suspensions was investigated experimentally by modifying the particle roughness. We find that changing the particle roughness has a significant impact on the amplitude of the critical strain: Smoother particles lead to a larger critical strain amplitude. We also derived a model to predict the critical strain amplitude as a function of both the volume fraction and roughness of the particles. This geometrical model is based on the assumption that irreversibility arises from solid-solid contacts between particles and considers a quasiparticle having a strain- and roughness-dependent effective volume. The interplay between the lubrication force (which diverges as the particle separation distance goes to zero) and the particle roughness (which sets the point of collision) leads to a nonlinear dependence of the critical strain amplitude on the particle roughness.

The good agreement between the model and the experimental results supports the paradigm that, in periodically sheared particulate suspensions, macroscopic reversibility is lost above a threshold strain amplitude when the particles can no longer self-organize into a configuration where time-irreversible

solid-solid contacts can be avoided. This transition occurs before (at a smaller strain) than that expected in the echo protocol. Indeed, as mentioned in the Introduction, in the pure hydrodynamic limit, when the system is fully governed by the Stokes (reversible) equations, one also expects the system to become macroscopically irreversible above a certain strain amplitude. That transition for now has been hidden by the loss of reversibility caused by solid contacts. However, according to our model, the critical strain amplitude arising from solid collisions can be increased by lowering the particle roughness. Whether it could be sufficiently increased, for instance, by using very smooth particles or a suspension of droplets, to observe macroscopic irreversibility from a loss of reversibility of the time-reversible laws constitutes an intriguing topic for further research.

We would like to thank D. Pine and E. Filippidi for discussions. P. Cervetti and S. Noel built the experimental setup. This work was supported by the National Science Foundation (Grants No. 0968313 and No. 1362060), ANR JCJC SIMI 9, and the Labex MEC Grants No. ANR-10-LABX-0092 and No. ANR-11-IDEX-0001-02.

[1] D. J. Pine, J. P. Gollub, J. F. Brady, and A. M. Leshansky, Chaos and threshold for irreversibility in sheared suspensions, Nature (London) **438**, 997 (2005).

[2] G. Düring, D. Bartolo, and J. Kurchan, Irreversibility and self-organization in hydrodynamic echo experiments, Phys. Rev. E **79**, 030101 (2009).

[3] G. I. Menon and S. Ramaswamy, Universality class of the reversible-irreversible transition in sheared suspensions, Phys. Rev. E **79**, 061108 (2009).

[4] N. Mangan, C. Reichhardt, and C. J. Olson Reichhardt, Reversible to irreversible flow transition in periodically driven vortices, Phys. Rev. Lett. **100**, 187002 (2008).

[5] R. Jeanneret and D. Bartolo, Geometrically protected reversibility in hydrodynamic Loschmidt-echo experiments, Nat. Commun. **5**, 3474 (2014).

[6] J. F. Morris, A review of microstructure in concentrated suspensions and its implications for rheology and bulk flow, Rheol. Acta **48**, 909 (2009).

[7] L. Corté, P. M. Chaikin, J. P. Gollub, and D. J. Pine, Random organization in periodically driven systems, Nat. Phys. **4**, 420 (2008).

[8] B. Metzger and J. E. Butler, Irreversibility and chaos: Role of long-range hydrodynamic interactions in sheared suspensions, Phys. Rev. E **82**, 051406 (2010).

[9] B. Metzger, P. Pham, and J. E. Butler, Irreversibility and chaos: Role of lubrication interactions in sheared suspensions, Phys. Rev. E **87**, 052304 (2013).

[10] P. A. Arp and S. G. Mason, The kinetics of flowing dispersions IX. Doublets of rigid spheres (experimental), J. Colloid Interface Sci. **61**, 44 (1977).

[11] B. Metzger and J. E. Butler, Clouds of particles in a periodic shear flow, Phys. Fluids **24**, 021703 (2012).

[12] P. Pham, B. Metzger, and J. E. Butler, Particle dispersion in sheared suspensions: Crucial role of solid-solid contacts, Phys. Fluids **27**, 051701 (2015).

[13] F. Blanc, F. Peters, and E. Lemaire, Experimental signature of the pair-trajectories of rough spheres in the shear-induced microstructure in non-colloidal suspensions, Phys. Rev. Lett. **107**, 208302 (2011).

[14] M. S. Ingber, A. A. Mammoli, P. Vorobieff, T. McCollam, and A. L. Graham, Experimental and numerical analysis of irreversibilities among particles suspended in a Couette device, J. Rheol. **50**, 99 (2006).

[15] L. Corté, S. J. Gerbode, W. Man, and D. J. Pine, Self-organized criticality in sheared suspensions, Phys. Rev. Lett. **103**, 248301 (2009).

[16] F. R. da Cunha and E. J. Hinch, Shear-induced dispersion in a dilute suspension of rough spheres, J. Fluid Mech. **309**, 211 (1996).

[17] F. Boyer, E. Guazzelli, and O. Pouliquen, Unifying suspension and granular rheology, Phys. Rev. Lett. **107**, 188301 (2011).

[18] See Supplemental Material at http://link.aps.org/supplemental/10.1103/PhysRevFluids.1.022201 for a video showing sequential images of the particles at the end of each cycle of shear along with the corresponding spatiotemporal plots.

Revealing the frictional transition in shear-thickening suspensions

Cécile Clavaud[a,1], Antoine Bérut[a], Bloen Metzger[a], and Yoël Forterre[a]

[a]Aix Marseille Univ, CNRS, Institut Universitaire des Systèmes Thermiques et Industriels, 13453 Marseille, France

Edited by Corey S. O'Hern, Yale University, New Haven, CT, and accepted by Editorial Board Member Pablo G. Debenedetti April 6, 2017 (received for review March 8, 2017)

Shear thickening in dense particulate suspensions was recently proposed to be driven by the activation of friction above an onset stress needed to overcome repulsive forces between particles. Testing this scenario represents a major challenge because classical rheological approaches do not provide access to the frictional properties of suspensions. Here we adopt a different strategy inspired by pressure-imposed configurations in granular flows that specifically gives access to this information. By investigating the quasi-static avalanche angle, compaction, and dilatancy effects in different nonbuoyant suspensions flowing under gravity, we demonstrate that particles in shear-thickening suspensions are frictionless under low confining pressure. Moreover, we show that tuning the range of the repulsive force below the particle roughness suppresses the frictionless state and also the shear-thickening behavior of the suspension. These results, which link microscopic contact physics to the suspension macroscopic rheology, provide direct evidence that the recent frictional transition scenario applies in real suspensions.

soft matter | shear thickening | dense suspensions | friction

Discontinuous shear thickening occurs in suspensions whose viscosity dramatically increases, sometimes by several orders of magnitude, when the imposed shear rate exceeds a critical value (1). The archetype of such suspensions is cornstarch immersed in water. When sheared vigorously or under impact, these fluids suddenly turn into solids (2). Such remarkable properties play a key role in the flowing behavior of modern concrete (3) and have motivated applications ranging from soft-body protections to sports equipment (4). They also offer promising perspectives for the design of smart fluids with tunable rheology (5). However, the potential realm of development and applications remains largely underexplored due to the lack of understanding of this transition (6).

This situation has improved very recently due to new theoretical and numerical works (7, 8). Because non-Brownian suspensions of hard frictional particles immersed in a viscous fluid are Newtonian, as imposed by dimensional analysis (8–10), the key idea of these studies is to add a short-range repulsive force between particles in addition to hydrodynamics and contact forces. This repulsive force can, for instance, stem from electrostatic charges or from a specific coating of polymers on the surface of the particle (11). At small shear rate (or small stress), the repulsive force prevents the grains from coming into contact; the suspension thus flows easily as if particles were frictionless. In the remainder of this paper, this state is referred to as frictionless. The viscosity of such a frictionless suspension would diverge at random close packing, whose volume fraction is $\phi_{\mathrm{rcp}} = 0.64$ for monodisperse spheres. Conversely, at large shear rate (or large stress), the repulsive force is overcome by the hydrodynamic forces and particles are therefore pressed into frictional contacts. The viscosity of such a suspension of frictional particles instead diverges at a lower critical volume fraction $\phi_c < \phi_{\mathrm{rcp}}$, with typically $\phi_c \simeq 0.58$ for monodisperse frictional spheres (9, 10, 12). In essence, the frictional transition described above brings the suspension closer to its jamming point: This critical volume fraction shift suddenly increases its apparent viscosity.

This scenario has been successfully tested and analyzed in discrete numerical simulations performed for non-Brownian (7, 10) and Brownian (13) suspensions. Supporting results are also provided by recent experimental investigations. For instance, standard rheological measurements were performed on suspensions of small poly(methyl methacrylate) (PMMA) particles sterically stabilized by a coating of poly-12-hydroxystearic acid (14). The suspension was indeed found to follow two separate viscosity curves with distinct critical volume fractions, depending on what shear rate was applied. A similar suspension was investigated under shear reversal (15), during which the viscosity first drops to a low value set by hydrodynamic interactions before increasing to a plateau dominated by contact interactions (16). As expected in such a framework, only the contact contribution to the viscosity increases with increasing shear rate, confirming the key role of contacts in shear-thickening suspensions. Another study reported that in shear-thickening suspensions, the first normal stress difference changes sign at the transition (17). This behavior was interpreted as indicating the formation of frictional contacts between particles, although this point is still a matter of debate (10, 18).

These experimental findings are encouraging; however, they also reflect a major difficulty in testing the frictional transition put forward in the recent theoretical scenario. The standard rheological techniques used, performed under fixed volume fraction, provide information about the suspension shear rate, shear stress, and viscosity. However, they do not give access to the suspension friction coefficient, which is here the key quantity one needs to access. In this article, we propose a different approach inspired by pressure-imposed experiments in granular flows (19), which specifically provides access to the friction coefficient of the

Significance

The sudden and severe increase in the viscosity of certain suspensions above an onset stress is one of the most spectacular phenomena observed in complex fluids. This shear thickening, which has major implications for industry, is a long-standing puzzle in soft-matter physics. Recently, a frictional transition was conjectured to cause this phenomenon. Using experimental concepts from granular physics, we provide direct evidence that such suspensions are frictionless under low confining pressure, which is key to understanding their shear-thickening behavior.

Author contributions: C.C., A.B., B.M., and Y.F. designed research, performed research, analyzed data, and wrote the paper.

The authors declare no conflict of interest.

This article is a PNAS Direct Submission. C.S.O. is a guest editor invited by the Editorial Board.

Freely available online through the PNAS open access option.

Data deposition: Data are now available on the open source database Zenodo at https://doi.org/10.5281/zenodo.556368.

[1]To whom correspondence should be addressed. Email: cecile.clavaud@univ-amu.fr.

suspension. We first compare the quasi-static avalanche angle, compaction, and dilatancy effects, in a standard Newtonian suspension (large glass beads) and a typical shear-thickening suspension (starch particles) flowing under gravity. This comparison reveals that particles in shear-thickening suspensions are frictionless under low confining pressure. Then, to bridge microscopic contact physics to the macroscopic rheology, we use a model suspension (silica beads) where the short-range repulsive force can be tuned. We find that this shear-thickening suspension, which has a frictionless state under low stress, no longer shear thickens when its frictionless state is suppressed.

Results

Steady Avalanches. A simple way to probe the frictional behavior of a suspension is to measure its quasi-static avalanche angle in a rotating drum using nonbuoyant particles (20, 21). For the sake of clarity, we compared the avalanche angle of a standard Newtonian suspension made of large frictional glass beads of diameter $d = 500$ μm (Fig. 1*A*, *Left*), to that of a typical shear-thickening suspension made of potato starch particles ($d = 25$ μm) immersed in water (Fig. 1*A*, *Right*). In both cases, the particle density ρ_p is larger than that of the suspending fluid ρ_f and the fluid viscosity η_f is chosen so that the Stokes number St is low and inertial effects can be neglected ($\mathrm{St} = \sqrt{\rho_p \Delta\rho g d^3}/18\eta_f \sim 10^{-2}$ where $\Delta\rho = \rho_p - \rho_f$ and g stands for gravity) (21). Both suspensions are placed within a rotating drum as shown in the experimental setup illustrated in Fig. 1*B*, *Center*. By imposing a slow and constant rotation speed ω, the nonbuoyant grains at the surface of the pile flow under their own weight, forming a steady avalanche of angle θ on top of a region experiencing a rigid rotation with the drum (20). In such a configuration, the confining pressure acting on the flowing layer of grains is $P = \phi\Delta\rho g h \cos\theta$, where h is the height of the flowing layer and ϕ its volume fraction; the corresponding tangential stress is $\tau = \phi\Delta\rho g h \sin\theta$. In the steady state, the macroscopic friction coefficient of the suspension μ is directly given by the avalanche angle because by definition $\mu = \tau/P = \tan\theta$. The avalanche angle θ thus provides access to the macroscopic friction coefficient of the suspension μ, which itself depends monotonically on the particle friction coefficient μ_p (22). For frictional grains, the macroscopic friction coefficient $\mu \simeq 0.4$ has only a weak dependence on μ_p and yields a typical avalanche angle $\theta \simeq 25^\circ$ (21). However, when the interparticle friction μ_p becomes very small (below 0.1), the macroscopic friction μ sharply drops. However, because of steric constraints, μ remains finite as $\mu_p \to 0$. For frictionless spherical particles ($\mu_p = 0$), discrete simulations predict a quasi-static macroscopic friction $\mu = 0.105$, corresponding to a nonzero avalanche angle $\theta = 5.76^\circ$ (23). Therefore, measuring the pile angle of steady avalanches constitutes a simple, yet decisive way to probe the interparticle friction coefficient in suspensions. Moreover, in this rotating drum configuration, the slope of the avalanche is set by the flowing layer of grains that is located near the free surface of the pile. For the low rotation speeds investigated here, the thickness of the layer h is of the order of a few particle diameters ($h \sim 10\, d$) (24). This means that the measure of the avalanche angle gives access to the frictional state of the grains under very low confining pressure. Typically, for the potato starch particles, the confining pressure within the flowing layer is $P \sim 10\phi\Delta\rho g d \simeq 1$ Pa.

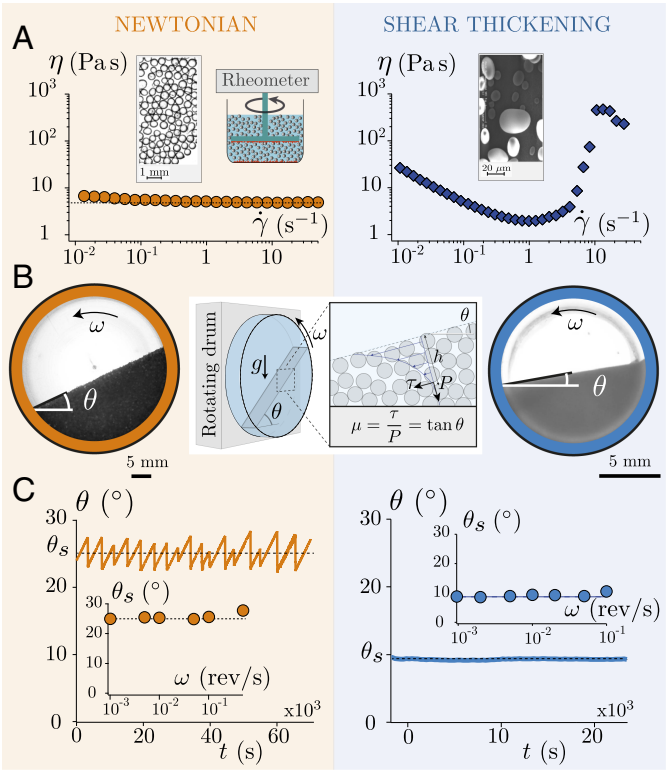


Fig. 1. Steady avalanches in (*Left*) Newtonian and (*Right*) shear thickening suspensions. (*A*) Picture and rheograms (viscosity η vs. shear-rate $\dot{\gamma}$) of (*Left*) a Newtonian suspension of large glass beads ($\phi = 50\%$) and (*Right*) a shear-thickening suspension of potato starch particles ($\phi = 40\%$). Rheograms were obtained in the configuration shown, using density-matched suspensions. (*B*, *Center*) Sketch of the rotating drum. Shown are pictures of a typical steady avalanche for (*B*, *Left*) the glass beads immersed in a mixture of Ucon oil and water and (*B*, *Right*) the potato starch immersed in water. (*C*) Angle of avalanche θ vs. time for (*Left*) the glass beads and (*Right*) the potato starch. (*C*, *Insets*) Steady-state avalanche angle θ_s vs. drum rotation speed ω (see *Materials and Methods* for the detailed description of particles, fluids, and experimental protocol).

Compaction and Dilatancy. Another robust way to probe the frictional behavior of a suspension is to investigate compaction and dilatancy effects (21). The protocol is the following: Particles are first suspended entirely within the drum before being allowed to sediment (Fig. 2*A*). The sediment is then compacted by gently hitting the drum with a rubber-head hammer N_{taps} times. The volume fraction ϕ of the sediment (the ratio of the particle volume to the total volume of the sediment) is measured throughout this compaction process. Finally, the drum is quickly rotated by a fixed angle $\theta_s + 10^\circ$ above the steady-state avalanche angle, to generate a transient avalanche whose angle θ_t is measured vs. time.

For the Newtonian suspension of large glass beads, the avalanche angle θ shows classical hysteretic fluctuations (20) around a time-averaged angle $\theta_s \simeq 25^\circ$ (picture in Fig. 1*B*, *Left* and data in Fig. 1*C*, *Left*). This angle corresponds to a suspension friction coefficient $\mu \simeq 0.47$, which is a usual value for frictional particles. The striking result is that, under the same flowing conditions, the shear-thickening suspension of potato starch particles yields a much lower avalanche angle (picture in Fig. 1*B*, *Right* and data in Fig. 1*C*, *Right*). The suspension can flow steadily with an angle of avalanche as small as $\theta_s \simeq 8.5^\circ$. This angle corresponds to a suspension friction coefficient $\mu \simeq 0.15$, showing that the friction coefficient between particles is nearly vanishing. The suspension friction coefficient ($\mu \simeq 0.15$) here is slightly larger than the expected value for frictionless spheres ($\mu = 0.105$) because potato starch particles are prolate, which geometrically increases the macroscopic friction coefficient (25, 26). Importantly, in the range of drum rotation speeds ω investigated, the avalanche angles reported here do not depend on ω (Fig. 1*C*, *Left* and *Right Insets*). They thus characterize the frictional properties of the suspension in its quasi-static regime, i.e., when the suspension reaches its critical jamming state (9).

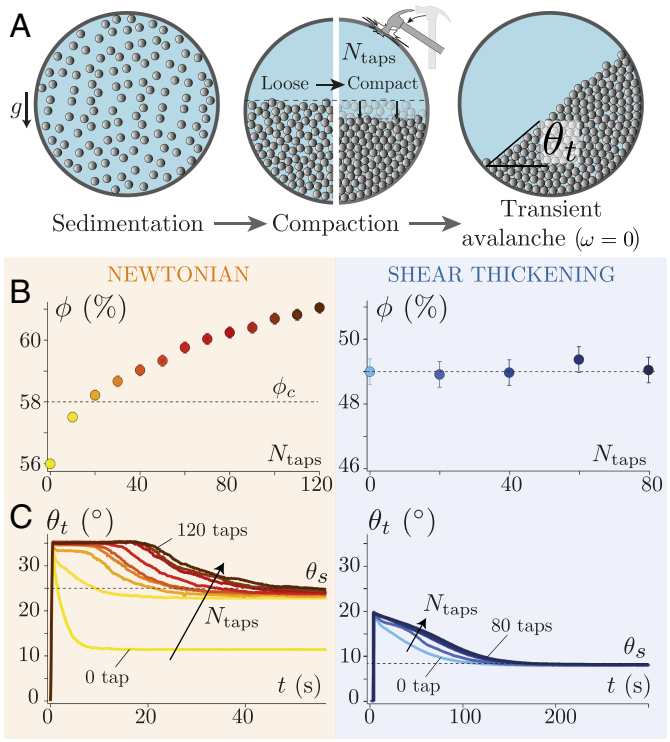


Fig. 2. Compaction and transient avalanches in (*Left*) Newtonian and (*Right*) shear-thickening suspensions. (*A*) Sketch of the experimental protocol to study compaction and dilatancy effects. (*B*) Volume fraction of the sediment ϕ vs. number of taps N_{taps} (*Left*) for the large glass beads and (*Right*) for the potato starch particles. (*C*) Angle of the transient avalanche θ_t vs. time obtained for different initial compactions of the sediment (*Left*) for the large glass beads and (*Right*) for the potato starch particles.

A conspicuous feature of frictional systems, such as a pile of large glass beads, is that it compacts under vibrations. As shown in Fig. 2*B*, *Left*, the packing fraction of the glass beads sediment, which right after sedimentation starts from a loose state ($\phi = 0.56 < \phi_c$), progressively increases with the number of taps to eventually reach a dense state ($\phi = 0.61 > \phi_c$). Remarkably, within this frictional system, very different transient avalanches are observed, depending on the initial preparation of the sediment (Fig. 2*C*, *Left*). For an initial loose packing (0 tap), the avalanche rapidly flows until its angle relaxes to an angle much lower than θ_s (the steady-state avalanche angle measured earlier). Conversely, for an initially compact sediment (120 taps), one observes a long delay during which the avalanche stays still. It then slowly flows, relaxing to θ_s. Such a drastic change in the avalanche dynamics with the packing of the initial sediment relies on a well-known pore pressure feedback mechanism (27–29), which applies only for dilatant (i.e., frictional) systems (23). As first described by Reynolds (30), deformation of a dense granular packing of frictional grains requires its dilation. Thus, as the drum is tilted for the avalanche to flow, the initially compact sediment must dilate. However, dilation in the presence of an incompressible interstitial fluid induces a fluid flow: Some fluid is sucked within the granular network. This fluid flow presses the grains against each other, thereby enhancing friction. As a result, for a compact pile of frictional grains, the avalanche is strongly delayed and then flows slowly, relaxing to θ_s (28, 31). Conversely, a loosely packed granular bed tends to compact when it deforms. This time, the interstitial fluid is expelled from the granular packing, thereby resulting in a fluidization of the grains: The avalanche flows rapidly and relaxes to an angle smaller than θ_s.

The compaction and dilatancy effects observed for the large glass beads are the phenomenological signature of frictional grains. For frictionless particles, the situation is markedly different because there is only one possible state of compaction ($\phi_c = \phi_{rcp}$) and no dilatancy effects are thus expected under shear (23). This is precisely what we observe with the shear-thickening suspension of potato starch particles: Tapping the settled bed of potato starch particles does not modify its packing fraction (Fig. 2*B*, *Right*) and hardly changes the dynamic of the transient avalanches that all relax to θ_s (Fig. 2*C*, *Right*). These experiments again show that, under low confining pressure, potato starch particles behave as if they were frictionless. Note that the maximum packing fraction of the potato starch particles, $\phi = 49\%$, may seem small. However, this low value can be explained by the anisotropic shape of the particles and also their tendency to swell when immersed in water (32).

Tuning Microscopic Friction Using a Model Suspension. We have shown that potato starch particles immersed in water produce a shear-thickening rheology and are frictionless under low confining pressure. These results are consistent with the frictional transition scenario for shear thickening presented in the Introduction (7, 8). They suggest the existence of a short-range repulsion force or a microscopic pressure-dependent friction between the starch particles. However, the origin of this force and more generally the surface physico-chemistry of starch remain unclear (6, 33, 34). To vary the interaction force between particles and investigate the frictional transition within a well-controlled system, we turn to a model suspension composed of silica beads immersed in water (Fig. 3*A*, *Top*). We use non-Brownian silica particles of diameter $d = 24\,\mu m$ comparable in size to the starch particles. When immersed in water, such silica particles spontaneously develop negative surface charges, which generates an electrostatic repulsive force between the grains (35–37). Moreover, this surface charge can easily be screened by dissolving electrolytes (salt) within the solvent. Increasing the salt concentration decreases the range of the repulsive force, i.e., the Debye length λ_D (Fig. 3*A*, *Bottom*), except at very high molarities not considered here (38). This model system is thus particularly appealing to test the recent frictional transition scenario and clarify the link between microscopic interactions between particles, friction, and the suspension macroscopic rheology.

We first use the rotating drum to systematically investigate steady avalanches, compaction, and dilatancy effects on two suspensions of silica beads: one with silica beads immersed in pure water and the second one with the beads immersed in a solution of water and NaCl with a large concentration of salt ($[NaCl] = 0.1$ mol·L^{-1}) to fully screen the Debye layer. Here again inertia is negligible ($St \sim 5 \times 10^{-3}$) and the flowing regime is quasi-static ($\omega \to 0$). As illustrated in Fig. 3 *B–D* (green data), in the presence of a large concentration of salt that screens the repulsive force, the suspension behaves as frictional. The steady-state avalanche angle is large, $\theta_s \simeq 27.5°$; the packing fraction of the sediment evolves from a loose packing right after sedimentation to a dense packing after 60 taps; and the dynamics of the transient avalanche strongly depend on the initial packing, showing features related to the dilatancy effects discussed earlier. [The absolute volume fraction is not reported in Fig. 3 because here it depends on the system size. This size effect can be explained by the large value of the Debye length in pure water ($\lambda_D \simeq 1\,\mu m$), which is not negligible relative to the silica particle diameter (39). Here, particles may be thought of as a hard core of diameter d surrounded by a soft crust of thickness equal to the Debye length. The maximum packing of such a system, when the confining pressure $P \to 0$, is $\phi_{max} \approx \phi_{rcp}(1 - 3\lambda_D/d) \approx 0.48$. However, due to the hydrostatic pressure within the granular bed that depends on the system size, grains deep in the bed must be closer to each other than those at the top. The absolute volume

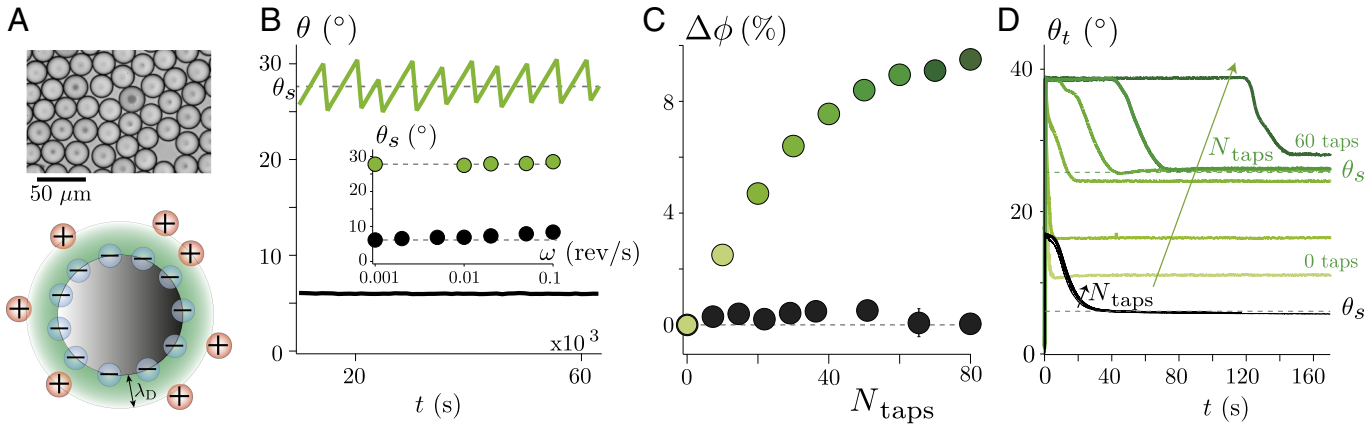


Fig. 3. Steady avalanches, compaction, and dilatancy effects in suspensions of silica beads in (black) pure water or (green) ionic solution. (*A*) Picture of the silica particles and sketch of a silica bead immersed in an ionic solution. Silica particles spontaneously carry negative charges on their surface when immersed in water. The range of the resulting repulsive force, i.e., the Debye length λ_D, can be tuned by changing the ionic concentration of the solvent. (*B–D*) Pile slope avalanche angle θ vs. time (*B*), relative packing fraction of the sediment $\Delta\phi = \phi(N_{\text{taps}}) - \phi(N_{\text{taps}} = 0)$ vs. number of taps (*C*), and transient avalanche angle θ_t vs. time (*D*) for the silica beads in (green) a sodium chloride solution with [NaCl] $= 0.1$ mol·L^{-1} and in (black) pure water.

fraction may thus lie anywhere between the latter value and 0.64 (random close packing), depending on the system size.] Conversely, the silica beads in pure water behave as frictionless particles (Fig. 3 *B–D*, black data). The steady-state avalanche angle is $\theta_s \simeq 6°$. This value is remarkably close to the quasi-static macroscopic friction angle obtained numerically for ideal frictionless spheres $\theta_s = 5.76° \pm 0.22$ (23). Additionally, no compaction of the granular bed and no discernable effect of the initial packing on the transient avalanches are observed. These results clearly demonstrate that the presence of a short-range repulsive force can lead under low stress to a frictionless behavior of the particles.

To further inquire about the microscopic origin of this frictionless behavior under low stress, we measured the steady avalanche angle θ_s as a function of the salt concentration [NaCl]. Fig. 4*A* shows that the suspension transits progressively from frictionless with $\theta_s \simeq 6°$ in pure water to frictional with $\theta_s \simeq 30°$ when the salt concentration [NaCl] is increased. In addition to this macroscopic measurement, we also characterized the particle roughness with an atomic force microscopy (AFM) and found that the peak roughness of the silica particles is $\ell_r = 3.73 \pm 0.80$ nm. Because the Debye length is entirely set by the salt concentration, $\lambda_D = 0.304/\sqrt{[\text{NaCl}]}$ nm (at $T = 25$ °C) (36), we can plot the steady avalanche angle θ_s as a function of ℓ_r/λ_D (Fig. 4*A*, *Top Inset*). Interestingly, the transition from frictionless to frictional occurs for $\ell_r/\lambda_D \sim 1$. This result strongly supports the idea that the frictionless state arises from the interparticle repulsive force caused by the electrostatic double layer. When its range is smaller than the particle roughness, this force becomes ineffective to prevent the grains from touching and the system is frictional. According to the scenario described in the Introduction (7, 8), the frictional transition should occur when the confining pressure P exerted by the weight of the granular layer equals the critical pressure P_c that the short-range repulsive forces can sustain. Assuming that the repulsive force follows an exponential decay as $F_{\text{rep}}(z) = F_0 \exp(-z/\lambda_D)$ (36), where z is the distance between the particles surfaces, the critical pressure at contact $z = 2\ell_r$ writes $P_c \sim F_{\text{rep}}(2\ell_r)/(\pi d^2/4) \sim (4F_0/\pi d^2)\exp(-2\ell_r/\lambda_D)$. Matching it to the confining pressure $P \sim 10\phi\Delta\rho g d$ predicts a transition when $\ell_r/\lambda_D \sim -(1/2)\log(10\pi\phi\Delta\rho g d^3/4F_0)$. Using $F_0/d \sim 1$ mN/m as reported for silica surfaces in NaCl electrolytes (35) yields $\ell_r/\lambda_D \simeq 1.9$, in fair agreement with the transition observed in Fig. 4*A*.

Finally, we investigate whether for this model suspension, the existence of a frictionless state under low confining pressure leads to a shear-thickening rheology and whether the elimination of this state (by screening repulsive forces) restores a Newtonian behavior. Rheograms of the silica suspensions were obtained using the configuration sketched in Fig. 4*B*, *Inset*. Because silica particles are denser than the aqueous suspending fluid, we used a double helix with tilted blades shearing the entire sample to avoid sedimentation and maintain the homogeneity of the suspension during the measurement. We then define an effective viscosity $\eta_{\text{eff}} = \alpha\Gamma/(2\pi\Omega L^3)$ given by the ratio of the effective stress Γ/L^3, where Γ is the torque and L the helix diameter, to the effective shear rate $2\pi\Omega$ given by the revolution speed Ω of the helix. The constant $\alpha \simeq 0.483$ is set to ensure that the effective viscosity matches the actual viscosity for a Newtonian fluid. We performed rheological measurements on two suspensions of silica particles immersed in water with a salt concentration [NaCl] $= 10^{-4}$mol·L^{-1} and

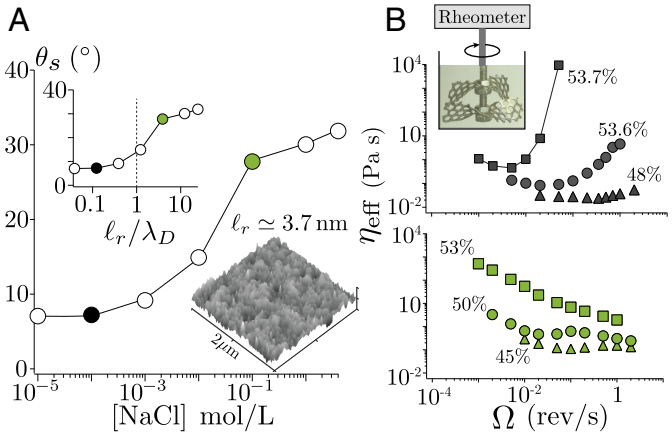


Fig. 4. Frictional transition in silica suspensions when varying the range of the repulsive force and link with macroscopic rheology. (*A*) Steady avalanche angle θ_s vs. salt concentration [NaCl]. (*A*, *Top Inset*) Steady avalanche angle θ_s vs. particle roughness normalized by the Debye length ℓ_r/λ_D. (*A*, *Bottom Inset*) AFM scan of a silica particle surface. The peak roughness is $\ell_r = 3.73 \pm 0.80$ nm. (*B*) Rheograms of silica bead suspensions obtained for different volume fractions in solutions of water and NaCl with salt concentration (*Top*) [NaCl] $= 10^{-4}$ mol·L^{-1} and (*Bottom*) [NaCl] $= 0.1$ mol·L^{-1}. The effective viscosity is $\eta_{\text{eff}} = \alpha\Gamma/(2\pi\Omega L^3)$, where Γ is the torque, Ω is the revolution speed, and $\alpha \simeq 0.483$ is a calibration constant. (*B*, *Inset*) Sketch of the experimental configuration used to obtain the rheograms.

$[\mathrm{NaCl}] = 10^{-1}\mathrm{mol}\cdot\mathrm{L}^{-1}$, respectively, i.e., just before and after the frictional transition observed in Fig. 4*A*. First, we find that the suspension that has a frictionless state under low confining pressure displays all of the features of a shear-thickening suspension (Fig. 4*B*, *Top*): Continuous shear thickening is observed at moderate volume fractions, whereas larger volume fractions lead to a dramatic increase of its effective viscosity (by about four orders of magnitude). Second, the striking result is that when the repulsive force is screened, so that no frictionless state exists under low confining pressure, the same suspension no longer shear thickens (Fig. 4*B*, *Bottom*). These measurements corroborate previous rheological characterizations using Brownian silica microspheres (17, 40, 41) and confirm the link between the existence of a repulsive force, friction, and shear-thickening rheology.

Discussion

In this article we propose a pressure-imposed approach, inspired from experiments in granular flows, to directly probe the microscopic frictional properties of non-Brownian shear-thickening suspensions. By systematically investigating steady avalanches, compaction, and dilatancy effects in rotating drum experiments, we provide direct proof that shear-thickening suspensions have a frictionless state under low confining pressure. Unlike Newtonian suspensions of frictional particles (9, 20, 28, 29), shear-thickening suspensions under low stress flow with a very small avalanche angle, do not compact, and show no dilatancy effect. This phenomenology clearly indicates the absence of friction between particles (23). Moreover, by using a model suspension of negatively charged silica beads, we find that lowering the range of the repulsive force below that of the particle roughness makes the suspension transit from a frictionless to a frictional state. The elimination of this frictionless state under low confining pressure also suppresses the shear-thickening behavior of the suspension. These experimental results, by linking microscopic contact physics to the suspension macroscopic rheology, provide strong evidence that the frictional transition scenario (7, 8) recently proposed to explain shear thickening applies in real suspensions. For discontinuous shear thickening to occur, the presence of short-range repulsive forces able to prevent interparticle friction at low stress thus seems essential. This picture contrasts with other models of shear thickening in which idealized lubrication hydrodynamics (42), confinement effects (43), particle migration phenomena (44), or inertia (45, 46) were put forward.

The rotating drum configuration used in our study provides a simple, yet robust way to characterize interparticle friction of dense nonbuoyant suspensions. Nevertheless, this configuration also has some limitations. When slowly rotating the drum filled with a nonbuoyant suspension, the thin flowing layer is on top of a pile experiencing solid rotation. Particles thus remain in static contact during long times. For microparticles coated with polymers, which are often involved in shear thickening, these enduring contacts may age and lead to cohesion between grains. In this case, the avalanche angle is no longer constant (47, 48). In our experiments performed with silica particles, small adhesive forces may have affected our results as they could for instance explain the slightly large avalanche angles measured at high salt concentrations (Figs. 3 and 4). However, the transition from low to high avalanche angles must be dominated by frictional effects as (*i*) the steady avalanche angle saturates as the salt concentration is increased, (*ii*) the avalanches have a constant slope from the top to the bottom of the avalanche unlike adhesive powders, and (*iii*) adhesion alone without friction would not lead to the dilatancy effects observed in Fig. 3*D*.

Finally, we emphasize that the rotating drum configuration gives access to the grains' frictional properties in the limit of low confining pressure ($P \to 0$) and in the quasi-static regime, i.e., when the viscous number of the suspension $J = \eta_f \dot{\gamma}/P \to 0$. Interestingly, we were still able to evidence the frictional transition predicted in the recent model by lowering the critical pressure P_c while the confining pressure P remained fixed (Fig. 4*A*). To fully explore the recent models, this transition should also be addressed by varying P while keeping P_c constant and also by varying the viscous number J. Recently, promising devices have been developed, opening the route to pressure-imposed rheometry of dense suspensions, but they are so far limited to the study of macroscopic particles (9). Extending such pressure-imposed approaches to suspensions of shear-thickening and colloidal particles represents a challenging, yet very exciting issue for future studies.

Materials and Methods

Particles. The grains used in Figs. 1 and 2 (*Left*) for the Newtonian suspension are large glass beads of diameter $d = 487 \pm 72$ μm and density $\rho_p = 2{,}500$ kg·m^{-3}. The grains used in Figs. 1 and 2 (*Right*) for the shear-thickening suspension are potato starch particles of major axis $d = 25 \pm 15$ μm and (dry) density $\rho_p = 1{,}500$ kg·m^{-3}. The silica beads used in Figs. 3 and 4 are commercial particles from Microparticles GmbH with diameter 23.46 ± 1.06 μm and density $\rho_p = 1{,}850$ kg·m^{-3}.

Rotating Drum Experiments. The drum used for the large glass beads (Fig. 1*B*, *Left*) has a diameter of 52 mm and a depth of 10 mm with a coarsened side wall. It is filled with a mixture of Ucon oil and pure (microfiltered) water of viscosity $\eta_f = 57$ mPa·s and density $\rho_f = 1{,}005$ kg·m^{-3}. The drum used for potato starch (Fig. 1*B*, *Right*) and silica particles (Figs. 3 and 4) has a diameter of 12 mm and a depth of 3 mm with a coarsened side wall. It is filled with pure water or sodium chloride solutions. Note that to avoid aging of the potato starch, the small drum was surrounded by a thermal bath maintaining its temperature at 7 °C. The drums were mounted on a precision rotating stage (M-061PD from PI piezo-nano positioning). To perform the experiment, the grains were first suspended by rotating the drum at $90° \cdot s^{-1}$. Then, the rotating speed ω was set to the desired value and pictures were taken using a Nikon D300S camera. Compaction experiments in Figs. 2 and 3 consisted of dropping a rubber-head hammer on the drum always from the same height in sequences of 10 taps. Between each sequence, a waiting time was respected to let the system relax. The relative variation of the packing fraction $\Delta\phi$ was inferred by image analysis from the variation of the area of the granular bed.

Rheological Measurements. The rheograms in Fig. 1 were obtained in the configuration sketched in Fig. 1*A*, *Inset*. To perform rheological measurements with a large gap (5 mm) in a plane–plane geometry, the top plate (diameter 50 mm) is fully immersed in the suspension, which itself is contained in a cylindrical vessel (diameter 60 mm). In both cases, the particles were density matched with the suspending fluid to avoid sedimentation. For the large glass beads, the suspending fluid was a mixture of water (30% wt), glycerol (13% wt), and sodium polytungstate (57% wt). For the potato starch, it was a mixture of water (45% wt) and cesium chloride (55% wt). The viscosity is obtained from increasing and decreasing ramps of shear rate after a preshear. No migration effects were noticeable. The rheograms in Fig. 4*B* were obtained in a different configuration because the need to control physico-chemistry (salt concentration) does not allow us to match the suspending fluid density. The configuration, sketched in Fig. 4*B*, *Inset*, uses a double helix with tilted blades of diameter $L = 3$ cm shearing the entire sample to maintain the homogeneity of the suspension during the measurement. The suspension volume fraction is controlled by first letting the particles settle down and adjusting the liquid level at the pile interface, which defined the packing fraction in the loose state, and then adding a given amount of liquid. For each measurement, the suspension is first thoroughly resuspended at a high rotation rate (1 rev/s) while vibrating the container to prevent shear thickening (5). The rotation rate is then set to a given value and the constant torque is measured before the effect of sedimentation is observed. In all cases, torques and rotation rates were measured using an Anton-Paar MCR 501 rheometer.

ACKNOWLEDGMENTS. We are thankful to Sarah Hormozy and Pauline Dame for helping us with preliminary experiments, Alain Rangis from Centre Interdisciplinaire de Nanosciences de Marseille (CINAM) for performing the AFM measurements, and our technical staff at Institut Universitaire des

Systèmes Thermiques et Industriels (IUSTI) for building the experiments. This work was supported by the European Research Council (ERC) under the European Union Horizon 2020 Research and Innovation program (ERC Grant 647384) and by the Labex MEC (ANR-10-LABX-0092) under the A*MIDEX project (ANR-11-IDEX-0001-02) funded by the French government program Investissements d'Avenir.

1. Barnes H (1989) Shear-thickening ("dilatancy") in suspensions of nonaggregating solid particles dispersed in Newtonian liquids. *J Rheol* 33:329–366.
2. Waitukaitis SR, Jaeger HM (2012) Impact-activated solidification of dense suspensions via dynamic jamming fronts. *Nature* 487:205–209.
3. Fernandez N (2014) From tribology to rheology: Impact of interparticle friction in the shear thickening of non-Brownian suspensions. PhD dissertation (ETH–Zürich, Zurich).
4. Wagner NJ, Brady JF (2009) Shear thickening in colloidal dispersions. *Phys Today* 62:27–32.
5. Lin NY, Ness C, Cates ME, Sun J, Cohen I (2016) Tunable shear thickening in suspensions. *Proc Natl Acad Sci USA* 113:10774–10778.
6. Brown E, Jaeger HM (2014) Shear thickening in concentrated suspensions: Phenomenology, mechanisms and relations to jamming. *Rep Prog Phys* 77:046602.
7. Seto R, Mari R, Morris JF, Denn MM (2013) Discontinuous shear thickening of frictional hard-sphere suspensions. *Phys Rev Lett* 111:218301.
8. Wyart M, Cates ME (2014) Discontinuous shear thickening without inertia in dense non-Brownian suspensions. *Phys Rev Lett* 112:098302.
9. Boyer F, Guazzelli É, Pouliquen O (2011) Unifying suspension and granular rheology. *Phys Rev Lett* 107:188301.
10. Mari R, Seto R, Morris JF, Denn MM (2014) Shear thickening, frictionless and frictional rheologies in non-Brownian suspensions. *J Rheol* 58:1693–1724.
11. Lee S, Spencer ND (2008) Sweet, hairy, soft, and slippery. *Science* 319:575–576.
12. Silbert LE (2010) Jamming of frictional spheres and random loose packing. *Soft Matter* 6:2918–2924.
13. Mari R, Seto R, Morris JF, Denn MM (2015) Discontinuous shear thickening in Brownian suspensions by dynamic simulation. *Proc Natl Acad Sci USA* 112:15326–15330.
14. Guy BM, Hermes M, Poon WCK (2015) Towards a unified description of the rheology of hard-particle suspensions. *Phys Rev Lett* 115:088304.
15. Lin NYC, et al. (2015) Hydrodynamic and contact contributions to continuous shear thickening in colloidal suspensions. *Phys Rev Lett* 115:228304.
16. Blanc F, Peters F, Lemaire E (2011) Local transient rheological behavior of concentrated suspensions. *J Rheol* 55:835–854.
17. Royer JR, Blair DL, Hudson SD (2016) Rheological signature of frictional interactions in shear thickening suspensions. *Phys Rev Lett* 116:188301.
18. Cwalina CD, Wagner NJ (2014) Material properties of the shear-thickened state in concentrated near hard-sphere colloidal dispersions. *J Rheol* 58:949–967.
19. Forterre Y, Pouliquen O (2008) Flows of dense granular media. *Annu Rev Fluid Mech* 40:1–24.
20. Courrech du Pont S, Gondret P, Perrin B, Rabaud M (2003) Granular avalanches in fluids. *Phys Rev Lett* 90:044301.
21. Andreotti B, Forterre Y, Pouliquen O (2013) *Granular Media: Between Fluid and Solid* (Cambridge Univ Press, Cambridge, UK).
22. Chialvo S, Sun J, Sundaresan S (2012) Bridging the rheology of granular flows in three regimes. *Phys Rev E* 85:021305.
23. Peyneau PE, Roux JN (2008) Frictionless bead packs have macroscopic friction, but no dilatancy. *Phys Rev E* 78:011307.
24. GDRMiDi (2004) On dense granular flows. *Eur Phys J E Soft Matter* 14:341–365.
25. Azéma E, Radjaï F (2010) Stress-strain behavior and geometrical properties of packings of elongated particles. *Phys Rev E* 81:051304.
26. Guo Y, Wassgren C, Hancock B, Ketterhagen W, Curtis J (2013) Granular shear flows of flat disks and elongated rods without and with friction. *Phys Fluids* 25:063304.
27. Iverson RM (1997) The physics of debris flows. *Rev Geophys* 35:245–296.
28. Pailha M, Nicolas M, Pouliquen O (2008) Initiation of underwater granular avalanches: Influence of the initial volume fraction. *Phys Fluids* 20:111701.
29. Jerome JJS, Vandenberghe N, Forterre Y (2016) Unifying impacts in granular matter from quicksand to cornstarch. *Phys Rev Lett* 117:098003.
30. Reynolds O (1885) LVII. On the dilatancy of media composed of rigid particles in contact. With experimental illustrations. *Philos Mag Ser* 20:469–481.
31. Rondon L, Pouliquen O, Aussillous P (2011) Granular collapse in a fluid: Role of the initial volume fraction. *Phys Fluids* 23:073301.
32. Hellman N, Boesch T, Melvin E (1952) Starch granule swelling in water vapor sorption. *J Am Chem Soc* 74:348–350.
33. Freundlich H, Röder H (1938) Dilatancy and its relation to thixotropy. *Trans Faraday Soc* 34:308–316.
34. Waduge RN, Xu S, Bertoft E, Seetharaman K (2013) Exploring the surface morphology of developing wheat starch granules by using atomic force microscopy. *Starch-Stärke* 65:398–409.
35. Vigil G, Xu Z, Steinberg S, Israelachvili J (1994) Interactions of silica surfaces. *J Colloid Interface Sci* 165:367–385.
36. Israelachvili JN (2011) *Intermolecular and Surface Forces* (Academic, London).
37. Valmacco V, et al. (2016) Dispersion forces acting between silica particles across water: Influence of nanoscale roughness. *Nanoscale Horiz* 1:325–330.
38. Smith AM, Lee AA, Perkin S (2016) The electrostatic screening length in concentrated electrolytes increases with concentration. *J Phys Chem Lett* 7:2157–2163.
39. Watanabe H, et al. (1999) Nonlinear rheology of concentrated spherical silica suspensions: 3. Concentration dependence. *Rheol Acta* 38:2–13.
40. Boersma WH, Laven J, Stein HN (1990) Shear thickening (dilatancy) in concentrated dispersions. *AIChE J* 36:321–332.
41. Lootens D, Van Damme H, Hémar Y, Hébraud P (2005) Dilatant flow of concentrated suspensions of rough particles. *Phys Rev Lett* 95:268302.
42. Phung TN, Brady JF, Bossis G (1996) Stokesian dynamics simulation of Brownian suspensions. *J Fluid Mech* 313:181–207.
43. Brown E, Jaeger HM (2012) The role of dilation and confining stresses in shear thickening of dense suspensions. *J Rheol* 56:875–923.
44. Fall A, et al. (2015) Macroscopic discontinuous shear thickening versus local shear jamming in cornstarch. *Phys Rev Lett* 114:098301.
45. Fall A, Lemaître A, Bertrand F, Bonn D, Ovarlez G (2010) Shear thickening and migration in granular suspensions. *Phys Rev Lett* 105:268303.
46. Fernandez N, et al. (2013) Microscopic mechanism for shear thickening of non-Brownian suspensions. *Phys Rev Lett* 111:108301.
47. Alexander AW, et al. (2006) Avalanching flow of cohesive powders. *Powder Technol* 164:13–21.
48. Liu P, Yang R, Yu A (2011) Dynamics of wet particles in rotating drums: Effect of liquid surface tension. *Phys Fluids* 23:013304.

Les fluides rhéo-épaississants : du principe aux applications

Shear thickening: from fundamentals to applications

Cécile Clavaud, Antoine Bérut, Bloen Metzger, Yoël Forterre

Résumé

Le rhéo-épaississement est un phénomène observé dans certaines suspensions denses de particules. Il consiste en une augmentation parfois brutale de leur viscosité lorsqu'elles sont soumises à une forte contrainte. Ce comportement, très utile pour certaines applications technologiques, peut aussi s'avérer hautement problématique dans certains processus industriels. Longtemps resté une énigme, le rhéo-épaississement possède désormais une description cohérente offerte par le modèle de transition frictionnelle. L'article présente ce modèle ainsi que les études numériques et expérimentales qui le valide. Sont ensuite abordées différentes perspectives d'applications offerte par la compréhension de ce phénomène.

Abstract

Shear-thickening is observed in dense particulate suspensions and consists in a severe increase of the suspension viscosity above an onset stress. This behavior, which is very useful to technological applications, can also be highly problematic in some industrial processes. For long considered as a puzzle, shear thickening can now be explained thanks to recent theoretical predictions. This paper presents this theoretical scenario and its numerical and experimental validations. Different perspectives of applications given by the understanding of this phenomenon are then discussed.

Mots-clés : rhéologie, suspensions de particules, fluides complexes, friction, béton, amortisseurs actifs.

Keywords: rheology, particulate suspensions, complex fluids, friction, concrete, active damper.

Table des matières

1 Contexte **2**

1.1 Qu'est ce que le rhéo-épaississement ? 2

1.2 Applications industrielles 4

1.3 Une origine physique discutée 5

1.4 Problématique 6

2 Le modèle de transition frictionnelle **7**

2.1 Rhéologie d'une suspension classique : analyse dimensionnelle 7

2.2 Les ingrédients clés du rhéo-épaississement : force répulsive et frottement 7

2.3 Simulations numériques du modèle 9

3 Mise en évidence expérimentale **11**

3.1 Expériences macroscopiques 11

3.2 Expériences microscopiques 13

4 Conclusion : vers les matériaux d'avenir **15**

Introduction

Liquide au repos, ou lorsqu'elles s'écoulent sous l'effet d'une faible contrainte, certaines suspensions denses de particules peuvent, au delà d'une contrainte critique, se rigidifier tel un solide. Cette propriété de *rhéo-épaississement'* a toujours fasciné les scientifiques et attiré l'attention de nombreux industriels. Ces derniers tentent pour la plupart d'éviter les dommages qu'une telle transition peut causer sur certaines installations (endommagement des mélangeurs, bouchage de conduites). D'autres en revanche utilisent cette propriété pour l'élaboration de matériaux innovants tels que des armures souples, des bétons auto-plaçants ou encore des protections médicales.

L'origine du rhéo-épaississement est longtemps resté obscure, cependant, des prédictions théoriques récentes fournissent enfin un scénario cohérent pour expliquer cette transition. L'objectif de cet article est de présenter ce modèle dit 'de transition frictionnelle' ainsi que les différentes études numériques et expérimentales qui le valide.

La compréhension du rhéo-épaississement devrait permettre de rationaliser certaines pratiques industrielles restées jusqu'alors empiriques. Nous illustrons en particulier dans l'encadré 'Le rhéo-épaississement et les bétons modernes' comment le modèle de transition frictionnel permet d'interpréter une innovation qui a révolutionné l'industrie du béton. Ce scénario offre aussi des perspectives prometteuses pour le design de fluides 'intelligents' dont la rhéologie peut être ajustée à la demande.

1 Contexte

1.1 Qu'est ce que le rhéo-épaississement ?

L'expérience quotidienne nous apprend que les fluides opposent une résistance à leur mise en mouvement, et que cette résistance est très variable selon la nature du fluide. Il est ainsi beaucoup plus difficile de déplacer une cuillère dans du miel que dans un verre d'eau. La grandeur physique qui caractérise cette résistance est la viscosité du fluide η, qui est le rapport entre la contrainte de

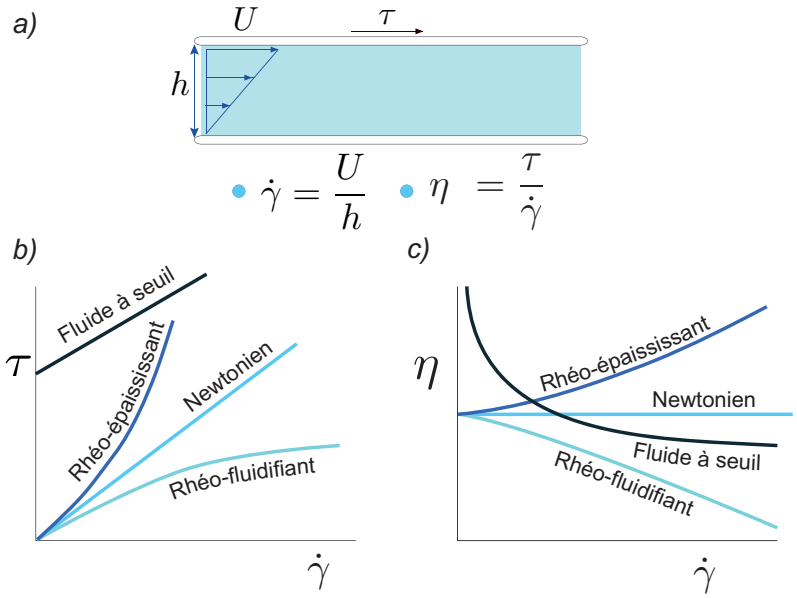


Figure 1 – Notion de base de rhéologie. a) Schéma d'un cisaillement simple dans lequel une couche de fluide d'épaisseur h est cisaillée entre une plaque fixe et une plaque mobile de vitesse U. Dans le régime stationnaire, le profil de vitesse est linéaire et permet de définir le taux de cisaillement $\dot{\gamma} = U/h$ (unité s^{-1}). La contrainte tangentielle τ (unité Pa) est la force tangentielle par unité de surface qu'il faut exercer sur la plaque supérieure assurer l'écoulement. La viscosité du fluide est définie par $\eta = \tau/\dot{\gamma}$ (unité Pa·s). b) Relations contrainte/taux de cisaillement des principaux comportements de fluides newtoniens et non-newtoniens. c) Viscosité en fonction du taux de cisaillement correspondant à b).

cisaillement appliqué au fluide τ et le taux de cisaillement $\dot{\gamma}$ du fluide, cf. figure 1a pour la définition des grandeurs élémentaires en rhéologie* [1]. Plus la viscosité est grande, plus la résistance du fluide à l'écoulement est importante. La viscosité du miel est ainsi de $\eta = 10$ Pa.s, tandis que celle de l'eau est parmi la plus faible des liquides, $\eta = 0,001$ Pa.s.

Pour la plupart des fluides comme les gaz ou les liquides simples, la viscosité est une grandeur qui ne dépend pas de la vitesse à laquelle le milieu s'écoule. La contrainte τ varie alors linéairement avec le taux de cisaillement $\dot{\gamma}$ (figure 1b,c). Ces fluides sont appelés fluides newtoniens*. Il existe cependant de nombreux fluides dans la nature ou l'industrie qui ont un comportement plus complexe, comme les solutions de polymères, les émulsions, les mousses ou les gels. Leur viscosité peut décroitre avec le taux de cisaillement (on parle de fluides rhéo-fluidifiants) ou augmenter avec le taux de cisaillement (on parle de fluides rhéo-épaississants) (figure 1b,c). Parfois même la viscosité de ces fluides varie au cours du temps (on parle de fluides thixotropes comme les yaourts). La viscosité peut également diverger quand le fluide est au repos ; ces fluides possèdent un seuil d'écoulement comme la boue ou le dentifrice, cf. figure 1b,c. Le point commun de tous ces fluides, dit non-newtoniens*, est qu'ils sont structurés à une échelle de taille intermédiaire entre l'échelle microscopique et macroscopique. Cette structure – macromolécules, particules solides, gouttes – est responsable des propriétés d'écoulement particulières des fluides complexes [1].

L'un des comportement les plus spectaculaire chez les fluides non-newtoniens est le rhéo-épaississement brutal que l'on observe dans certaines suspensions de particules à fortes fractions volumiques* en particules ϕ. C'est le cas de la fécule de maïs mélangé à l'eau, commercialisée en France sous la marque Maizena®, cf. figure 2a. À faibles fractions volumiques, la viscosité de ce mélange est constante tel un fluide newtonien. Quand la fractions volumique augmente, on observe un premier régime où la viscosité augmente de manière progressive avec le taux de cisaillement. On parle de rhéo-épaississement continu. Pour des fractions volumiques encore plus grandes, il apparaît une transition : la viscosité augmente brutalement, parfois de plusieurs ordres de grandeur, au-dessus d'un taux de cisaillement critique. On parle de rhéo-épaississement discontinu. Dans ce

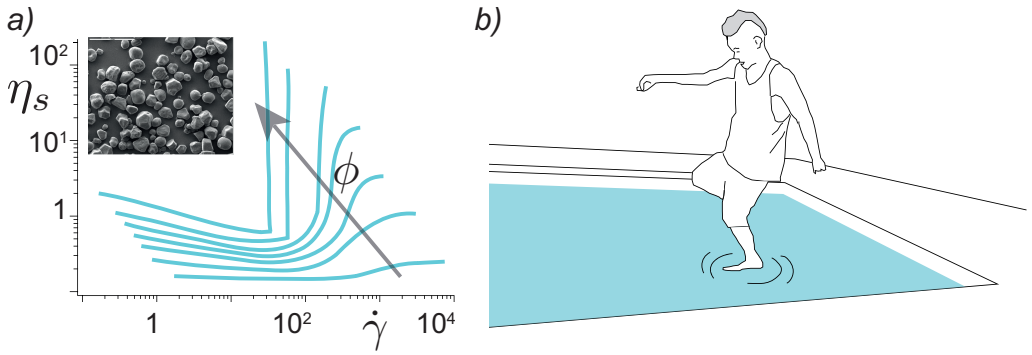


Figure 2 – Transition de rhéo-épaississement dans les suspensions concentrées. a) Viscosité d'une suspension d'amidon de maïs dans l'eau en fonction du taux de cisaillement pour différentes fractions volumiques ϕ. La taille des particules est de l'ordre de 5-20 μm (image obtenue en microscopie électronique à balayage). b) Une suspension rhéo-épaississante a un comportement transitoirement 'solide' sous impact : il est possible de courir à la surface d'une piscine remplie de ce matériau.

régime, le milieu peut aller jusqu'à se bloquer et se comporter comme un solide. Ce comportement 'solide' à grande vitesse de cisaillement explique qu'il soit possible de courir sur une piscine remplie de fluide rhéo-épaississant (figure 2b). De nombreuses vidéos existent sur internet illustrant le comportement remarquable de ces fluides.

Historiquement, le rhéo-épaississement a d'abord été observé sur des suspensions d'origine végétale comme l'amidon de maïs, de riz ou de pomme de terre [2]. Depuis, ce phénomène a été observé dans de nombreuses autres suspensions constituées de matériaux très variés (silice, carbonate de calcium, plastique, oxide de titane, alumine, etc). La plupart des données de la littérature concerne des suspensions browniennes* ou colloïdales* [3], c'est-à-dire composées de particules de taille sub-micronique soumises à l'agitation thermique. Cependant, le rhéo-épaississement est également observé dans des suspensions de particules de plus grande taille [2, 4, 5], démontrant que l'agitation thermique n'est pas indispensable pour observer ce phénomène. Il y a toutefois deux caractéristiques communes à l'ensemble des suspensions rhéo-épaississantes :

- La taille des particules doit être relativement petite (diamètre d typiquement inférieure à 50 microns) mais pas nécessairement browniennes.
- La physico-chimie du milieu joue un rôle déterminant comme la présence de traitement de surface sur les particules (charges, polymères greffés) ou le type de solvent (polaire ou apolaire, ionique, niveau de pH).

1.2 Applications industrielles

Le rhéo-épaississement n'est pas seulement une curiosité de la nature. L'encre, les peintures, le béton frais, le chocolat liquide ou les pâtes de céramiques sont autant de fluides rencontrés dans l'industrie qui présentent un caractère rhéo-épaississant. Comprendre et maitriser l'origine du rhéo-épaississement est essentiel à de nombreux secteurs industriels comme le verre, le génie civil, les cosmétiques, l'agroalimentaire ou l'industrie pharmaceutique.

Souvent, le rhéo-épaississement est une propriété que l'on cherche à éviter. L'augmentation brutale de la viscosité au-delà d'une vitesse critique peut en effet se traduire par un endommagement important des pompes et des mélangeurs, ou entraîner le bouchage de conduites. Les premières études sur le rhéo-épaississement ont ainsi été motivée par un problème touchant l'industrie papetière [6] lors de l'enduction de papier par des films de suspension. À grande vitesse, il arrivait que l'augmentation de la viscosité soit telle que le papier se déchirait, endommageant ainsi l'ensemble de l'installation.

À l'inverse, les fluides rhéo-épaississants sont également caractérisés par un régime de très faible viscosité à bas taux de cisaillement, qu'il peut être avantageux d'utiliser en particulier pour manipuler les suspensions très concentrées. C'est le cas lors des procédés de moulages utilisant des

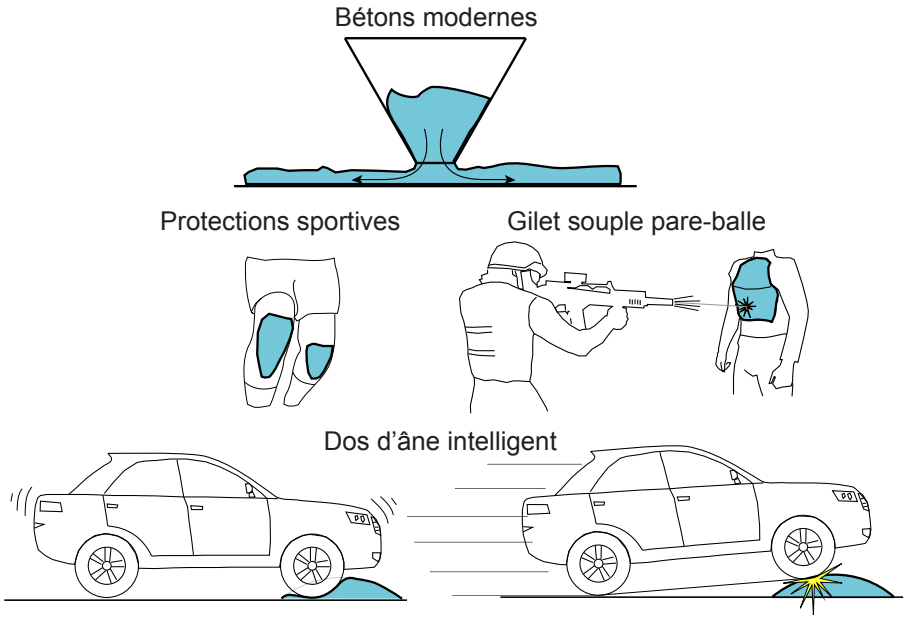


Figure 3 – Applications des suspensions rhéo-épaississantes.

poudres métalliques ou des poudres céramiques. Pour faciliter sa manipulation, la poudre est généralement dispersée dans un liquide. Un traitement des particules est effectué afin que la viscosité de la suspension soit faible même à la fraction volumique élevée. Un autre exemple est l'industrie chocolatière. Le chocolat est une suspension composée de grains de cacao et de sucre dans une phase continue grasse constitué principalement de beurre de cacao. L'ajout d'un adjuvant, la lecithine, permet d'obtenir une pâte très liquide tout en diminuant la teneur en graisse [7]. Mais l'application la plus importante est l'industrie du béton. Dans ce domaine, un enjeu majeur est de parvenir à augmenter au maximum la concentration en particules pour augmenter la résistance du matériau final, tout en maintenant la coulabilité du béton frais (figure 3). Nous discuterons en détail cet exemple dans l'encadré : *Le rhéo-épaississement et les bétons modernes.*

Récemment, le caractère rhéo-épaississant de certaines suspensions a inspiré aux industriels la formulation de nouveau matériaux pour la conception d'armures et de protections sportives ou de prothèses médicales souples, cf. figure 3. En effet, une suspension rhéo-épaississante est capable de dissiper une grande quantité d'énergie lors d'un choc tout en restant liquide en temps normal. Ainsi, ces vêtements autorisent le mouvement mais protègent le corps en cas d'impact de balle, de chute ou de mouvement brusque. La plupart des brevets récents portant sur la fabrication d'armure souple consiste en l'infiltration d'un milieu fibreux par un fluide rhéo-épaississant. Par exemple, on peut imprégner un textile de Kevlar avec une suspension de micro-particules de silice et de polyéthylène glycol. Ce matériau possède une capacité d'absorption en énergie jusqu'à 3 fois supérieures à celle d'une armure en Kevlar pur. Il existe aujourd'hui plusieurs marques (Armourgel, d3o, Artilage) qui vendent des vêtements ou des protections pour les articulations. La société STF Technologies, elle, propose des tissus médicaux protégeant des piqûres d'aiguilles. Une dernière application est la conception de ralentisseurs de type dos d'âne intelligent constitué d'une envelope souple remplie d'une suspension rhéo-épaississante, cf. figure 3. La transition de rhéo-épaississement est ajustée à la limitation de vitesse, de sorte que les automobilistes roulant sous la limitation n'endommage pas leur voiture. En revanche, à forte vitesse, l'effet est le même qu'un ralentisseur solide [8].

1.3 Une origine physique discutée

Plusieurs mécanismes ont été proposés pour expliquer le phénomène de rhéo-épaississement observé dans certaines suspensions concentrées.

Une première explication a émergé du développement, à la fin des années 1980, de la 'dynamique stokesienne'. Cette méthode numérique décrit la suspension comme un ensemble de sphères dures immergées dans un fluide newtonien et soumises aux forces hydrodynamiques (trainée visqueuse, lubrification) et à l'agitation thermique [9]. Dans ce cadre, le rhéo-épaississement est expliqué par la création, à fort taux de cisaillement, d'amas dense de particules localement dans le fluide (les 'hydro-clusters'), cf. figure 4a. Ces amas augmentent fortement la viscosité effective du milieu à cause des forces de lubrification visqueuses qui divergent lorsque les particules sont très proches les unes des autres. Ce mécanisme ne prédit cependant qu'un rhéo-épaississement faible et progressif, avec une augmentation de viscosité d'un facteur 2 à 3 bien inférieure aux expériences. De plus, la transition de rhéo-épaississement n'est observée dans ces simulations que lorsque les particules sont browniennes. La transition est alors contrôlée par le nombre de Péclet P_e, qui compare l'échelle de force visqueuse sur une particule, $\eta_f d^2\dot{\gamma}$, où η_f est la viscosité du fluide suspendant, avec la force d'agitation thermique, $k_B T/d$, où k_B est la constante de Boltzmann et T la température :

$$P_e = \frac{\eta_f d^3 \dot{\gamma}}{k_B T}. \tag{1}$$

Ce mécanisme ne permet donc pas d'expliquer le rhéo-épaississement qui s'observe dans les suspensions de particules non-browniennes.

Une deuxième explication associe le rhéo-épaississement à une transition entre un régime visqueux et un régime inertiel à l'échelle des particules [10, 11]. Selon ce mécanisme, lorsque le taux de cisaillement augmente, les particules subissent, en plus des forces visqueuses, des collisions comme dans un gaz. Ce transfert de quantité de mouvement par collision implique une contrainte sur les particules qui varie comme le carré du taux de cisaillement, $\tau \propto \dot{\gamma}^2$ (loi de Bagnold [12]) et donc une viscosité effective qui augmente linéairement avec le taux de cisaillement $\eta \propto \dot{\gamma}$, cf. figure 4b. Là encore, il s'agit d'un rhéo-épaississement modéré qui ne décrit pas l'augmentation brutale de viscosité observée dans certaines suspensions. De plus, ce mécanisme n'a lieu que lorsque les effets d'inertie deviennent importants. Plus précisément, la transition entre le régime visqueux et inertiel est contrôlée par le nombre de Stokes St, qui compare l'échelle de force collisionnelle sur une particule, $\rho d^3 \dot{\gamma}^2$, où ρ est la densité de la particule (unité $\mathrm{kg{\cdot}m^{-3}}$), à l'échelle de force visqueuse, $\eta_f d^2 \dot{\gamma}$:

$$St = \frac{\rho d \dot{\gamma}}{\eta_f}. \tag{2}$$

Toutefois, l'observation du rhéo-épaississement dans des suspensions pour lesquelles le nombre de Stokes est très petit (particules sub-microniques immergées dans un fluide très visqueux), semble indiquer que l'inertie n'est pas nécessaire pour observer ce phénomène.

En parallèle à ces mécanismes, plusieurs scientifiques ont questionné l'existence même du rhéo-épaississement [13, 14, 5]. De leur point de vue, le rhéo-épaississement n'est pas une propriété intrinsèque de la rhéologie mais provient d'artefacts spécifiques à la configuration expérimentale utilisée. Par exemple, la sédimentation dans le cas de particules plus denses que le fluide, la migration pour des configurations de cisaillement inhomogène ou encore la présence de confinement latéral (parois du rhéomètre) peuvent induire un rhéo-épaississement apparent sur la mesure de viscosité, cf. figure 4c. Ces hypothèses n'expliquent toutefois pas pourquoi le rhéo-épaississement n'est observée que dans des suspensions bien spécifiques.

1.4 Problématique

Cet état de l'art montre que, malgré l'importance des fluides rhéo-épaississants dans l'industrie, le mécanisme à l'origine de ce phénomène reste mal compris. Cette situation a toutefois changé suite à des travaux numériques et théoriques publiés en 2013-2014. Ces études proposent un scénario cohérent qui décrit le rhéo-épaississement comme une transition frictionnelle. Dans la suite de l'article, nous décrivons ce modèle et sa validation expérimentale.

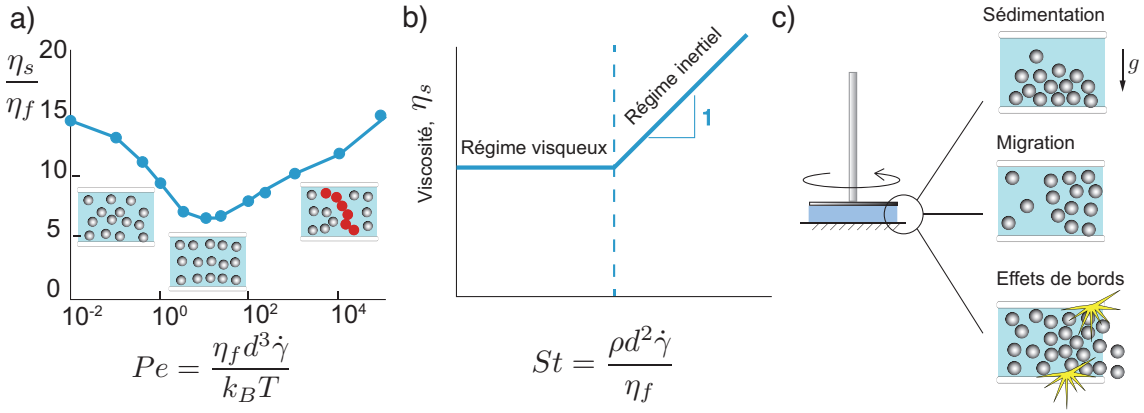


Figure 4 – Différentes hypothèses avancées pour expliquer le rhéo-épaississement : a) 'Hydrocluster', b) Transition inertielle, c) Rhéo-épaississement apparent due à des artefacts de mesures (sédimentation, migration latérale, effets de confinement due aux parois et à l'interface suspension/air).

2 Le modèle de transition frictionnelle

2.1 Rhéologie d'une suspension classique : analyse dimensionnelle

Pour comprendre le rhéo-épaississement, revenons d'abord au cas d'une suspension classique constituée de sphères dures non-browniennes immergées dans un fluide newtonien et visqueux telle qu'illustrée figure 5.a. Dans ce type de système, les particules interagissent via les forces hydrodynamiques (trainée, lubrification) et les forces de contact solide (non-interpénétration, frottement solide). On peut montrer par un argument d'analyse dimensionnelle que la rhéologie d'une telle suspension est, à l'instar du fluide suspendant, newtonienne. En effet, les variables dont dépend le comportement de cette suspension sont le diamètre des particules d, la viscosité du fluide suspendant η_f, le taux de cisaillement $\dot{\gamma}$ et la fraction volumique en particules ϕ qui décrit le rapport du volume occupé par les grains divisé par le volume de la suspension. Le problème est particulièrement simple car le seul paramètre sans dimension que l'on peut construire à partir de ces variables est la fraction volumique ϕ. L'analyse dimensionelle impose donc que la viscosité de la suspension η_s soit égale à la viscosité du fluide suspendant η_f multiplié par une fonction de ce seul nombre sans dimension ϕ :

$$\eta_s = \eta_f \times f(\phi), \tag{3}$$

où f est une fonction indéterminée. Ainsi, la viscosité d'une suspension classique ne dépend pas du taux de cisaillement imposé mais seulement de la fraction volumique en particules. Le comportement rhéologique d'une telle suspension est illustré sur la figure 5.b et c :

- Sa viscosité η_s augmente avec la fraction volumique en particules et diverge pour une fraction volumique critique ϕ_c à laquelle le système ne peut plus s'écouler car les grains occupent l'intégralité du volume disponible au sein du fluide, cf. figure 5.b. Les grains constituent alors un empilement compact et la suspension se comporte tel un solide. Cette divergence de la viscosité à forte fraction volumique vient de l'augmentation des fluctuations d'écoulement induite dans le fluide par la présence des particules qui augmente la dissipation d'énergie.
- Pour une fraction volumique donnée $\phi < \phi_c$, la viscosité de la suspension est indépendante du taux de cisaillement, cf. figure 5.c, comme stipulée par l'équation 3.

2.2 Les ingrédients clés du rhéo-épaississement : force répulsive et frottement

L'idée principale du modèle est que le rhéo-épaississement peut être induit dans les suspensions en introduisant une force répulsive entre les particules [15, 16]. Cette force peut avoir plusieurs

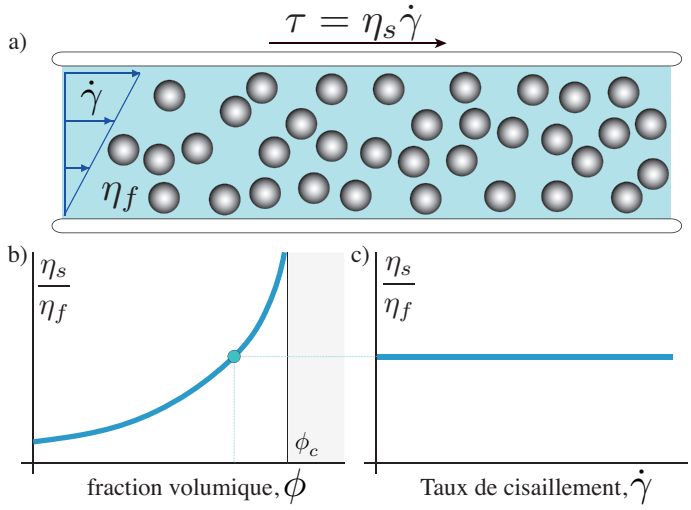


Figure 5 – a) Schéma d'une suspension classique de sphères dures non-browniennes immergées dans un fluide newtonien et visqueux. b) La viscosité augmente avec la fraction volumique en particules et diverge à une fraction volumique critique ϕ_c. c) Pour une fraction volumique donnée $\phi < \phi_c$, la viscosité de la suspension est constante quelque soit la valeur du taux de cisaillement, cf. equation 3.

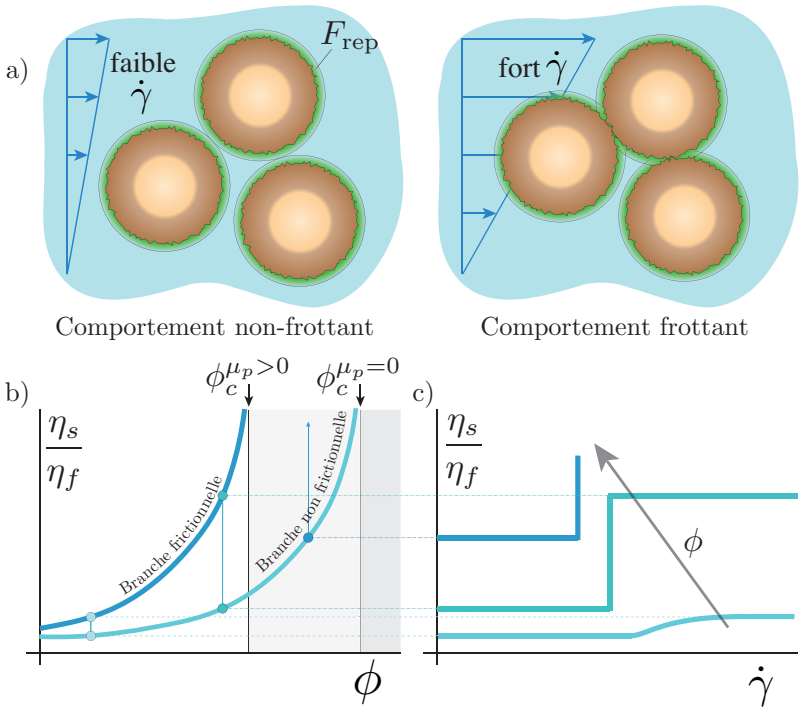


Figure 6 – Modèle de transition frictionnelle : a) Schéma illustrant la transition frictionnelle induite par la présence d'une force répulsive entre les particules. b) Une telle suspension présente deux rhéologies possibles : la branche non-frictionnelle à faible taux de cisaillement et la branche frictionnelle à fort taux de cisaillement. c) Viscosité en fonction du taux de cisaillement pour différentes fractions volumiques.

origines. Elle peut par exemple être induite en couvrant la surface des particules par des brosses de polymères ou bien en utilisant des particules qui, une fois immergées dans le fluide suspendant, développent spontanément une charge électrostatique de surface. La conséquence directe de cette force répulsive est illustrée sur la figure 6.a. À faibles taux de cisaillement, elle maintient les particules à distance ; les particules s'écoulent alors facilement sans frotter les unes contre les autres. À l'inverse, si on augmente le taux de cisaillement, les forces hydrodynamiques arrivent à vaincre les forces répulsives. Les particules sont alors poussées au contact solide et deviennent frottantes. Ainsi, la présence d'une force répulsive courte portée permet, en augmentant le taux de cisaillement imposé, de faire passer les particules d'un comportement non-frottant à frottant. Avant d'analyser les conséquences de cette transition frictionnelle sur la rhéologie, reprenons un instant l'analyse dimensionnelle.

Outre le diamètre des particules d, la viscosité du fluide suspendant η_f, le taux de cisaillement $\dot{\gamma}$ et la fraction volumique en particules ϕ, la suspension doit maintenant être décrite à l'aide d'une nouvelle variable F_{rep} qui décrit l'amplitude de la force répulsive entre les particules. L'introduction de cette nouvelle échelle de force permet de construire un nouveau nombre sans dimension :

$$\mathit{\Gamma} = \frac{\eta_f \dot{\gamma} d^2}{F_{\text{rep}}}, \tag{4}$$

qui représente le rapport entre les forces hydrodynamiques $\eta_f \dot{\gamma} d^2$ et la force la force répulsive F_{rep}. L'analyse dimensionelle impose alors que la viscosité de la suspension η_s soit une fonction de ϕ et de $\mathit{\Gamma}$:

$$\eta_s = \eta_f \times f\left(\phi, \mathit{\Gamma} = \frac{\eta_f \dot{\gamma} d^2}{F_{\text{rep}}}\right). \tag{5}$$

Contrairement à l'expression donnée par l'equation 3, la viscosité de la suspension peut désormais dépendre du taux de cisaillement imposé $\dot{\gamma}$.

Expliquons à présent comment cette transition entre un comportement non-frottant à frottant des particules modifie la viscosité de la suspension. Comme nous l'avons vu précédemment, la viscosité d'une suspension diverge à une fraction volumique critique ϕ_c. Le point important est que cette fraction volumique critique dépend du coefficient de friction* μ_p entre particules : pour des particules non-frottantes ($\mu_p = 0$), la fraction volumique critique $\phi_c^{\mu_p=0} = 0.64$, alors que pour des particules frottantes ($\mu_p > 0$), $\phi_c^{\mu_p>0} \approx 0.58$. Les courbes de viscosité correspondantes sont représenté sur la figure 6.b. L'interprétation du rhéo-épaississement est alors très simple : à faible taux de cisaillement, les particules sont non-frottantes ; la viscosité de la suspension est donnée par la branche non-frictionnelle de basse viscosité. En augmentant le taux de cisaillement, les particules deviennent frottantes ; la suspension transite sur la branche frictionnelle de viscosité plus élevée.

Dans ce cadre, on peut également comprendre comment, en augmentant la fraction volumique, on passe d'un rhéo-épaississement continu à discontinu voir au blocage de la suspension, cf. figure 6.c. À faible fraction volumique, le saut de viscosité est continu et relativement faible car les deux branches de viscosité sont proches l'une de l'autre. En augmentant la fraction volumique, le saut de viscosité devient discontinu et peut atteindre plusieurs ordres de grandeur car les branches s'éloignent rapidement l'une de l'autre en raison de la divergence plus précoce de la branche frictionnelle. Enfin, pour $\phi > \phi_c^{\mu_p>0}$, la transition conduit au blocage total de la suspension car il n'y a pas de branche frictionnelle sur laquelle la suspension puisse transiter.

2.3 Simulations numériques du modèle

Les idées du modèle de transition frictionnelles ont émergé grâce aux simulations numériques d'un groupe de chercheurs du Benjamin Levich Institute à New York [17, 16]. Leur approche diffère fondamentalement de la dynamique stokesienne discuté précédemment [18]. En effet, cette dernière suppose que le comportement des suspensions de particules est dominé par l'effet des interactions hydrodynamiques. Les chercheurs du Levich Institute, à l'inverse, ont introduit dans les suspensions l'idée de contact granulaire et mis en avant le rôle joué par la friction. La suspension consiste en un ensemble de sphères dures immergées dans un fluide soumis à un écoulement de cisaillement.

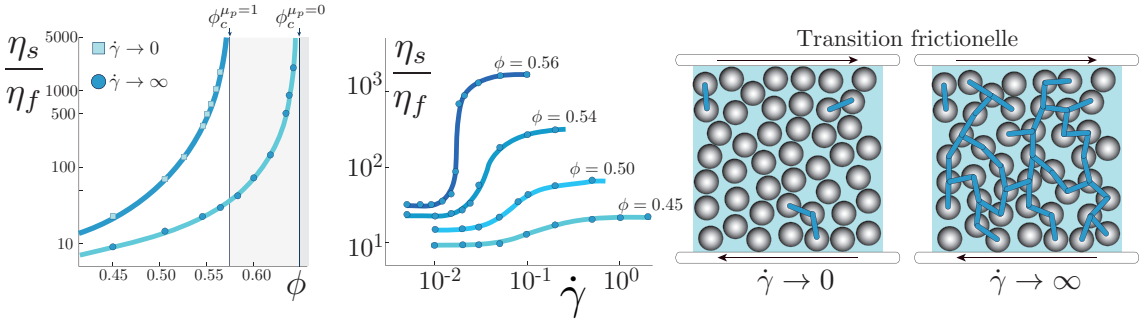


Figure 7 – Simulations numériques d'une suspension de sphères frottantes cisaillées dans un fluide Newtonien interagissant via une force répulsive (adapté de [16]). a) Viscosité versus fraction volumique obtenue à faible ($\dot\gamma \to 0$) et à fort ($\dot\gamma \to \infty$) taux de cisaillement. b) Viscosité versus taux de cisaillement pour différente fraction volumique. c) Représentation de la suspension et de la proportion de contacts frottants (bâtonnets bleus) à faible et à fort taux de cisaillement.

Chaque sphère est simulée individuellement et peut interagir avec les autres sphères. Les forces qui influent sur la dynamique de chaque sphère sont :

- la force de trainée qui est proportionnelle à la différence entre la vitesse de la particule et la vitesse locale de l'écoulement de cisaillement imposé.
- les forces de lubrifications qui sont pris en compte lorsque la distance de séparation entre les sphères devient petite. Leur amplitude est proportionnelle à la vitesse relative des sphères considérées et inversement proportionnel à leur distance de séparation.
- Surtout, le modèle inclut une description du contact de type granulaire. Celui-ci empêche les particules de s'interpénétrer et décrit la nature frictionnelle du contact avec un frottement de type Coulomb décrit par un coefficient de frottement inter-grains μ_p.
- Enfin, le modèle introduit une force répulsive de courte portée qui reproduit l'effet d'une couche de polymère adsorbée ou celui d'une double couche électronique à la surface de chaque sphère.

Les simulations ont été réalisées pour différentes fractions volumiques $\phi = [0.45 - 0.64]$ et une grande gamme de taux de cisaillement. Comme prédit par le modèle, deux courbes rhéologiques émergent de ces simulations, cf. figure 7.a. La première, à faible taux de cisaillement, diverge à la fraction volumique critique correspondant des sphères non-frottantes $\phi_c^{\mu_p=0}$. La présence d'une force répulsive courte portée empêche les grains de venir au contact solide frictionnel et les grains se comportent comme si leur coefficient de friction était nul. La seconde courbe, obtenue à fort taux de cisaillement, diverge pour $\phi = \phi_c^{\mu_p=1}$. Dans ce cas, les forces répulsives courtes portées ne jouent aucun rôle puisqu'elles sont dominée par les forces hydrodynamiques.

Les simulations reproduisent également les courbes rhéologiques classiques des suspensions rhéo-épaississantes, cf figure 7.b avec un rhéo-épaississement continu à faible fraction volumique et discontinu à plus forte fraction volumique. La transition de rhéo-épaississement discontinue a lieu au-delà d'une contrainte critique τ_c ou un taux de cisaillement critique $\dot\gamma_c$, qui sont liés à la force répulsive F_{rep} par la relation :

$$\tau_c = \beta \frac{F_{\text{rep}}}{d^2}, \qquad \dot\gamma_c = \beta \frac{F_{\text{rep}}}{\eta_s(\phi)^{\mu_p=0} d^2}, \tag{6}$$

avec $\beta \simeq 0.04$ et $\eta_s(\phi)^{\mu_p=0}$ la viscosité de la branche non-frottante. Toute chose égale par ailleurs, la contrainte critique de rhéo-épaississement est inversement proportionnelle à la taille des particules au carré. Cette relation explique que le rhéo-épaississement ne s'observe que pour des particules suffisamment petites. Pour des particules macroscopiques, la force de répulsion, si elle existe, est toujours vaincue par les forces extérieure et le système est toujours frottant. L'avantage des simulations est qu'elles permettent également de visualiser la prolifération du nombre de contacts frottant qui a lieu lors de la transition, 7.c.

Les chercheurs du Levich Institute ont aussi étendu leurs simulations numériques au cas des suspensions browniennes en décrivant l'effet de l'agitation thermique des particules [19]. Ils ont ainsi pu

montrer que cette agitation est équivalente à une force répulsive effective qui empêche les contacts frottants lorsque la suspension est soumise à un faible taux de cisaillement. Ainsi l'agitation thermique induit, à l'instar d'une force répulsive, un comportement rhéo-épaississant de la suspension. La contrainte critique de rhéo-épaississement généralisée aux particules browniennes s'écrit :

$$\tau_c \simeq \beta \frac{F_{\text{rep}}}{d^2} + 40 \frac{k_B T}{d^3}. \tag{7}$$

En général, la composante brownienne domine lorsque $d < 0.1$ μm.

3 Mise en évidence expérimentale

Le modèle de transition frictionnelle constitue un scénario cohérent pour expliquer le rhéo-épaississement des suspensions concentrées. Il est toutefois difficile à tester expérimentalement sur des suspensions réelles. En effet, les outils classiques de rhéologie donnent accès à la viscosité de la suspension mais pas au frottement entre les particules, qui est la grandeur clé du mécanisme. Dans ce chapitre, nous présentons deux approches expérimentales qui ont permis d'accéder à cette propriété. Ces études ont fourni une validation directe du modèle de transition frictionnelle pour les suspensions rhéo-épaississantes.

3.1 Expériences macroscopiques

Le premier type d'expérience, développé par des chercheurs de l'université d'Aix Marseille et du CNRS, s'est inspiré de la physique des écoulements granulaires, c'est-à-dire des milieux composés de grains macroscopiques comme le sable [20]. Leur idée a été de mesurer d'utiliser l'angle d'avalanche d'une suspension pour caractériser son comportement frictionnel.

Il est bien connu qu'un empilement de grains sous gravité forme un tas de forme conique ayant un angle θ bien défini. De même, si l'on place des grains dans un tambour que l'on tourne continûment, le système atteint un état stationnaire dans lequel une mince couche de grains (d'épaisseur de l'ordre d'une dizaine de tailles de grains) coule avec un angle θ, à la surface d'un empilement statique en rotation solide avec le tambour, cf. figure 8a.

Cet angle d'avalanche θ a deux origines très différentes. La première est purement liée à la géométrie des grains. Elle explique qu'un empilement de particules irrégulières comme le sable a un angle d'avalanche plus élevé qu'un empilement de billes sphériques. La deuxième provient de la friction solide entre particules. Plus les grains sont frottants, plus l'angle d'avalanche est élevé. Pour des coefficients de frottement usuels entre grains ($0.1 < \mu_p < 1$) et des particules de forme sphérique, l'angle d'avalanche est de l'ordre de $\theta = 20 - 25°$. Par contre, lorsque le frottement μ_p entre grains devient très faible ($\mu_p < 0.1$), l'angle d'avalanche chute brutalement. Pour des sphères non-frottantes ($\mu_p = 0$), les simulations numériques prédisent un angle d'avalanche très faible de $\theta = 5.76°$ [21]. Cet angle reste fini à cause de l'imbrication géométrique des particules.

La mesure de l'angle d'avalanche est donc un moyen simple mais direct pour accéder aux propriétés de frottement entre les particules. De plus, l'avalanche ayant lieu en surface, les grains sont soumis à des forces de confinement très faibles (leur propre poids). Cette configuration est donc appropriée pour tester l'existence d'un état non-frottant à faibles forces tel que prédit par le modèle de transition frictionnelle.

Cette équipe a dans un premier temps comparé l'angle d'avalanche d'une suspension rhéo-épaississante typique (amidon de pomme de terre dans l'eau) avec celui d'une suspension classique non rhéo-épaississante (un empilement de billes de verre macroscopique immergées dans un fluide visqueux) [22]. Les particules sont placées dans un tambour rempli de fluide et mis en rotation lentement à vitesse constante, jusqu'à la formation d'un tas stationnaire d'angle d'avalanche θ . Une image des expériences est présentée sur la figure 8b. On constate que la suspension classique non rhéo-épaississante coule avec un angle d'avalanche de l'ordre de 25°, caractéristique de particules frottantes. En revanche, la suspension rhéo-épaissante coule avec un angle très faible, de l'ordre de

8°. Cet angle est proche de l'angle d'avalanche théorique obtenu avec des sphères non-frottantes. Ce résultat montre qu'il existe bien pour les suspensions rhéo-épaississantes un état non-frottant entre particules, comme prédit par le modèle de transition frictionnelle.

Dans le cadre du modèle, l'état non-frottant provient d'une force répulsive courte portée entre les grains. Afin de tester cette hypothèse, les chercheurs ont étudié une suspension modèle de particules de silice non-browniennes (diamètre $d = 24\,\mu$m) immergées dans une solution aqueuses ionique (solution de chlorure de sodium NaCl et d'eau). La silice, de formule chimique SiO_2, réagit avec l'eau pour former des groupements SiO^- à la surface des billes, qui deviennent donc chargées négativement en surface. Il existe ainsi une force de répulsion, de nature électrostatique, entre les particules composant les suspensions étudiées. La portée de cette force répulsive, appelée longueur de Debye, peut être contrôlée en ajoutant des ions dans le milieu qui écrantent ces charges. L'expression de la longueur de Debye à température ambiante et pour des ions monovalents vaut :

$$\lambda_{\mathrm{D}} = \frac{0.304}{\sqrt{[\mathrm{NaCl}]}}\ \mathrm{nm}, \tag{8}$$

où [NaCl] est la concentration en ions sodium exprimée en mol/l. Ainsi, plus le milieu est concentré en ions, plus la portée de la force répulsive diminue.

La figure 8c présente l'angle d'avalanche d'une suspension de silice dans des solutions ioniques de concentration croissante. Lorsque l'eau est pure ou lorsque la concentration en ions très faible l'angle d'avalanche est $\theta \simeq 6°$. Cette valeur est précisément égale à l'angle d'avalanche prédit pour des sphères non-frottantes. Ces expériences montre que la présence d'une force de répulsion (ici d'origine électrostatique) induit un état non-frottant de la suspension. Lorsque la concentration en ions augmente, la portée des forces de répulsion diminue. Lorsque celle ci devient plus petite que la rugosité $\ell_r \approx 3$ nm des particules, les particules deviennent frottantes et par conséquent l'angle d'avalanche augmente rapidement, cf. figure 8c.

Ce résultat s'interprète dans le cadre du modèle de transition frictionnelle. Selon ce scénario, la transition entre l'état non-frottant et frottant doit apparaître quand la force extérieure appliquée sur les grains – ici la gravité déjaugée de la poussée d'Archimède F_g – atteint la force maximale F_{rep} que les forces répulsives peuvent subir. La force de Debye d'origine électrostatique entre deux sphères en suspension peut s'écrire sous la forme :

$$F_{\mathrm{rep}}(z) = F_0 \exp(-z/\lambda_{\mathrm{D}}), \tag{9}$$

où F_0 est une échelle de force dépendant de la taille des particule ($F_0/d \simeq 1$ mN/m) et z la distance entre la surface des particules. La force critique au contact ($z = 2\ell_r$) s'écrit donc $F_{\mathrm{rep}} = F_0 \exp(-2\ell_r/\lambda_{\mathrm{D}})$. En égalisant cette expression avec le poids des grains dans la couche en écoulement, $F_g = N(\pi/6)d^3\Delta\rho g$, où $\Delta\rho$ est la différence de densité entre la particule et le fluide et $N = 10$ le nombre de grains dans l'épaisseur de la couche, on trouve que la transition frictionnelle a lieu pour :

$$\frac{\ell_r}{\lambda_{\mathrm{D}}} = -\frac{1}{2}\ln\frac{N\pi\Delta\rho g d^3}{6F_0} \simeq 2. \tag{10}$$

Cette valeur est en accord avec la transition observée expérimentalement.

Les résultats précédent montrent que l'on peut passer continûment d'une suspension possédant un état non-frottant à une suspension frottante en diminuant la portée de la force de répulsion entre grains.

Les chercheurs ont aussi fait le lien entre le comportement frictionnel microscopique entre grains avec le comportement rhéologique macroscopique de la suspension, cf. figure 8c. Comme postulé dans le modèle de transition frictionnelle, la suspension possédant un état non-frottant est rhéo-épaississsante. Lorsque cet état non-frottant est supprimé par écrantage de la force répulsive, le comportement rhéo-épaississant disparaît.

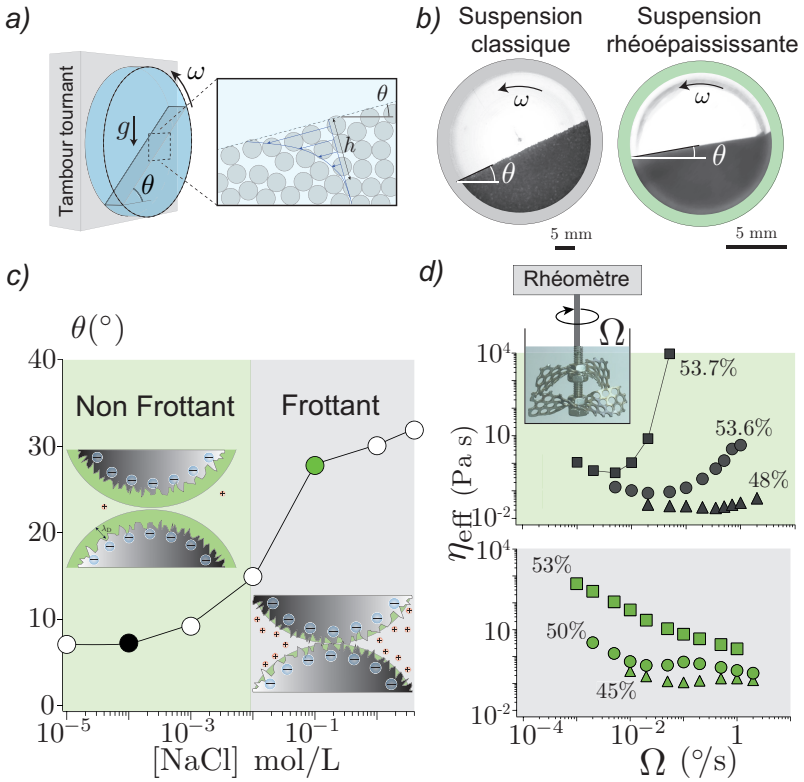


Figure 8 – Expériences macroscopiques pour la validation du modèle de transition frictionnelle (adaptées de [22]). a) Principe de mesure de l'angle d'avalanche θ de la suspension en tambour tournant. b) Comparaison entre l'angle d'avalanche stationnaire obtenu avec une suspension classique (billes de verre macroscopique de diamètre $d = 500$ μm dans une huile visqueuse) et rhéo-épaississante (amidon de pomme de terre dans l'eau). c) Angle d'avalanche d'une suspension de billes de silice immergées dans une solution ionique de chlorure de sodium montrant une transition entre un état non-frottant (faibles concentration ioniques, la portée de la répulsion électrostatique est grande devant la rugosité des billes) et un état frottant (fortes concentrations ioniques, la portée de la force de répulsion est faible devant la rugosité des billes). d) Caractérisation rhéologique de la suspension avant et après la transition frictionnelle. Le rhéo-épaississement est supprimé quand la force répulsive est écrantée.

3.2 Expériences microscopiques

Les expériences précédentes ont montré la validité du modèle de transition frictionnelle pour expliquer le rhéo-épaississement en utilisant une signature macroscopique du frottement entre particules : l'angle d'avalanche. Une deuxième validation de ce mécanisme est venue de mesures directes du coefficient de frottement microscopique μ_p entre deux particules, par des chercheurs de l'ESPCI, l'ENS et l'université Pierre et Marie Curie à Paris [23]. Pour cela, ces chercheurs ont développé une machine de force atomique originale constituée d'un résonateur mécanique (un mini-diapason). Une des particules est directement collé à la pointe du diapason, l'autre est fixée sur une plaque, cf. figure 9a. Le diapason est mis en résonance à l'aide d'un élément piezo-électrique dans ses deux modes normaux principaux, à la fois dans la direction normale et tangentielle. La présence d'interaction entre les deux particules a pour effet de décaler la fréquence propre du résonateur et l'amplitude de résonance. Ces mesures permettent de remonter aux force normales F_N et tangentielles F_T, et donc au coefficient de frottement $\mu_p = F_N/F_T$ entre les deux particules.

Les auteurs ont ainsi mesuré le coefficient de frottement μ_p de particules micrométriques de PVC (diamètre moyen $d = 2\mu$m) immergées dans une solution de plastifiant (Dinch) et d'huile minérale. Le Dinch est un liquide organique qui dissout légèrement la surface des particules de PVC, créant

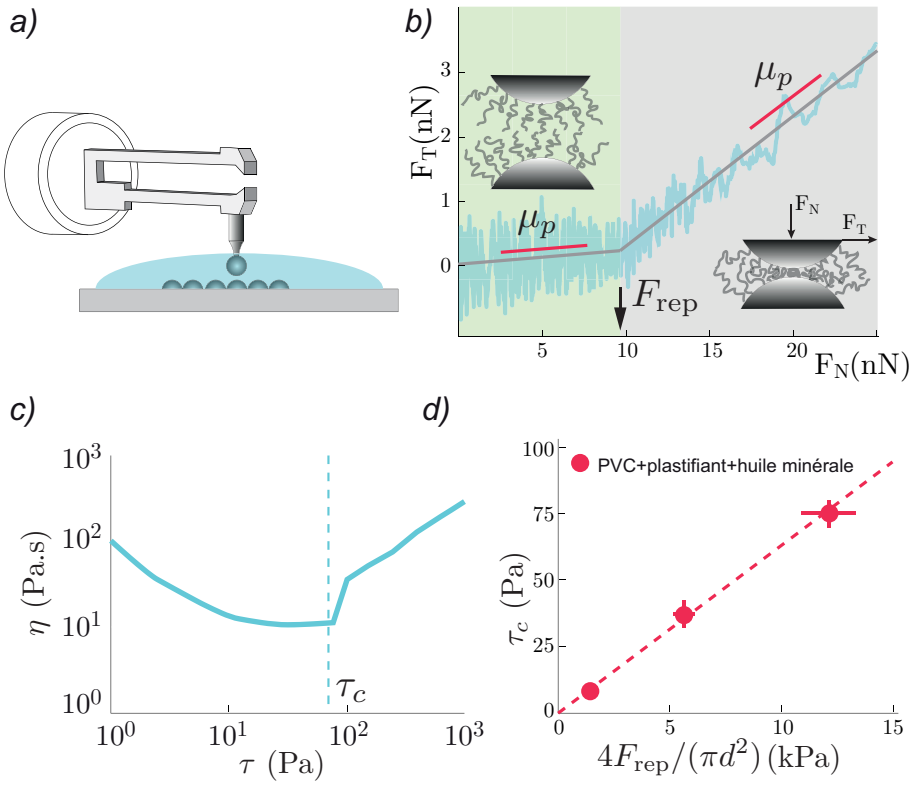


Figure 9 – Expériences microscopiques de validation du modèle de transition frictionelle (figures adaptées de [23]). a) Machine de force atomique basé sur la résonance d'un diapason utilisée pour mesurer le coefficient de frottement entre deux particules. b) Force tangentielle vs. force normale pour deux particules de PVC dans une solution de plastifiant (Dinch) montrant la transition entre un régime non-frottant et un régime frottant au delà d'une force normale critique Fc. c) Viscosité η d'une solution concentrée de particules de PVC dans du Dinch en fonction de la contrainte tangentielle τ. La transition de rhéo-épaississement a lieu pour une contrainte critique τ_c. d) Contrainte critique de rhéo-épaississement τ_c en fonction de la force inter-particule critique $F_{\rm rep}$ normalisée par la taille des particules pour différentes solutions de Dinch.

une brosse de polymère à la surface des particules, cf. figure 9). Lorsque les particules s'approchent à une distance de l'ordre de la longueur des brosses, les polymères se repoussent par entropie, ce qui induit une force de répulsion normale entre celles-ci du type $F_{\text{rep}} \propto \exp(-z/\lambda)$, avec $\lambda \approx$ qq nm.

La figure 9b montre comment la force tangentielle sur les particules varie en fonction de la force normale extérieure appliquée. À faibles forces normales, la force tangentielle est très faible, ce qui indique un coefficient de frottement solide quasi-nul ($\mu_p < 0.02$). Dans ce régime, la force de répulsion induite par les brosses de polymères est suffisante pour empêcher le contact solide. Au-dessus d'une force critique F_{rep}, la force de répulsion est vaincue. La force tangentielle augmente alors linéairement avec la force normale, ce qui indique un régime de frottement solide.

Les auteurs ont fait le lien entre cette force critique mesurée à l'échelle microscopique et la rhéologie macroscopique de la suspension. Ils ont tout d'abord montré que cette suspension est rhéo-épaississante au dessus d'une contrainte macroscopique critique τ_c, cf figure 9c. Ils ont ensuite montré que cette contrainte critique de rhéo-épaississement est proportionnelles à la force critique F_{rep} de la transition frictionnelle à l'échelle des grains, cf figure 9c.

4 Conclusion : vers les matériaux d'avenir

Le modèle de transition frictionnelle, validé par des simulations numériques, des expériences microscopiques (mesure à l'échelle des particules) et des expériences macroscopiques (mesure à l'échelle de la suspension) fournit un cadre cohérent pour décrire le rhéo-épaississement. L'ensemble des résultats présentés dans cet article montre que ce phénomène provient de la présence d'une force répulsive entre les particules qui induit un comportement non-frottant ou frottant des particules en fonction des contraintes présentes au sein du système. L'augmentation brutale de la viscosité observée lors de cette transition est lié au fait que la fraction volumique critique d'écoulement d'une suspension ϕ_c dépend de l'état frictionnel des particules.

Ces résultats montrent que la physique du contact à l'échelle nanométrique et micrométrique entre particules a un impact majeur sur le comportement macroscopique (la rhéologie) des suspensions. La vision longtemps acceptée dans le domaine, qui faisait jouer aux interactions hydrodynamique le rôle dominant, est ainsi remise en cause par ce nouveau paradigme qui ouvre des perspectives prometteuses vis à vis des applications. En effet la compréhension du rôle combiné du frottement et de la physico-chimie à l'échelle des particules sur la rhéologie des suspensions devrait permettre de comprendre et donc de mieux contrôler les innovations évoquées au chapitre 1 : protections sportives, armures souples ou bétons modernes, cf encadré 'Le rhéo-épaississement et les bétons modernes' . Elle ouvre également la voie au développement de suspensions dont la rhéologie peut être modifiée *in situ* par des sollicitations mécaniques externes, cf encadré 'Vers le contrôle actif de la rhéologie des suspensions'.

Vers le contrôle actif de la rhéologie des suspensions : Les propriétés d'écoulement des suspensions sont généralement déterminées au moment de leur formulation (fraction volumique, traitement de surface, choix du solvant). Une stratégie différente, basée sur la compréhension offerte par le modèle de transition frictionnelle, est le contrôle *in situ* de la viscosité des suspensions pendant leur utilisation [24]. Un groupe de l'université de Cornell à montré qu'il est possible d'éradiquer le comportement rhéo-épaississant d'une suspension en imposant une vibration externe de faible amplitude perpendiculaire à la direction principale de l'écoulement, cf. figure 10. La vibration, qui désolidarise les contacts frictionnels entres particules au sein de la suspension, donne un moyen de réguler sa viscosité sur plusieurs decades. Ce contrôle actif de la rhéologie pourrait être utilisé pour résoudre les problèmes de blocage dans les écoulement de conduites et offre aussi des perspectives pour l'impression 3D, la robotique et le stockage d'énergie.

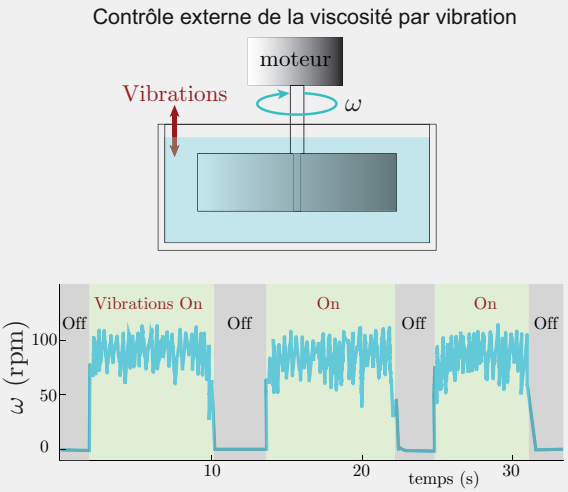


Figure 10 – *E*xemple de régulateur d'écoulement constitué d'une pale immergée dans une suspension rhéo-épaississante et entraînée par un moteur tournant (adaptée de [24]). Le réservoir peut être soumis à une vibration verticale. Le moteur qui fournit un couple constant, tourne lorsque les vibrations verticales sont activées et s'arrête à l'arrêt des vibrations.

Le rhéo-épaississement et les bétons modernes : Un domaine très actif de recherche s'est développé dans les années soixantes lorsque les constructeurs américains d'autoroutes ont découvert par accident que les performances des bétons sont bien plus grandes lorsqu'une faible quantité de polymère est ajouté à leur préparation. L'ajout de polymères s'est avéré être un moyen efficace de diminuer la viscosité des bétons à l'état frais mais aussi d'augmenter significativement leur résistance à long terme. Depuis, l'utilisation de polymères (superplastifiants) a largement contribué à la diversification et l'amélioration les propriétés du béton (ouvrabilité et résistance). Aujourd'hui, les industriels du secteur tentent de se distinguer en proposant des adjuvants qui offrent les plus grandes performances.

Les mécanismes à l'oeuvre dans les processus évoqués ci-dessus peuvent être compris dans le cadre du modèle de transition frictionnelle. Les particules entrant dans la composition des pâtes cimentaires, comme la poudre de carbonate de calcium, sont attractives et flocculent lorsqu'elles sont immergées dans l'eau. La suspension ainsi obtenue est frictionnelle et sa viscosité diverge à faible fraction volumique. En ajoutant un polymère choisi, celui-ci s'adsorbe à la surface des particules et les rend répulsives. L'effet bien connu est que les particules défloccculent et se dispersent de façon homogène dans le fluide rendant la suspension plus fluide. Le modèle de transition frictionnelle nous apprend de plus que la couche adsorbée de polymères empêche tout contact frictionnel entre particules. La suspension initialement très visqueuse transite alors sur la branche non-frictionnelle et voit sa viscosité diminuer drastiquement. L'adjonction de polymères permet ainsi d'augmenter l'ouvrabilité des bétons qui deviennent auto-nivelant, d'une grande fluidité à l'état frais et très facile à surfacer. Mais le gain obtenu par l'adjunction de polymères est double car une fois sur la branche non-frictionnelle, il est possible de préparer le béton à des fractions volumiques plus élevées car la fraction volumique critique est plus élevée en l'absence de frottement. On obtient ainsi un matériau final plus résistant. Ces comportement sont illustré sur la figure 11.a qui compare la rhéologie deux suspensions de poudre de carbonate de calcium préparée soit avec de l'eau pure soit avec de l'eau et 1% de superplastifiant. On constate que l'ajout de superplastifiant permet non seulement de diminuer la viscosité à fraction volumique donnée mais également, d'explorer une gamme de fractions volumiques plus élevée.

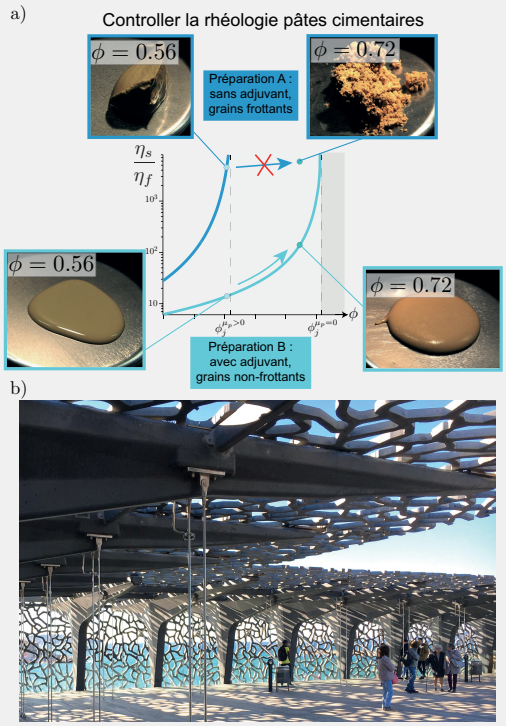


Figure 11 – *a) Suspensions de carbonate de calcium préparée avec de l'eau pure (A) ou avec de l'eau et un adjuvant (B) ; comparaison qualitative avec le scenario de transition frictionnelle. b) Exemple de bâtiment aux structures élancées (Mucem, Marseille) construit à l'aide de bétons modernes.*

Ces bétons modernes plus résistants, ont permis aux architectes d'envisager des constructions audacieuses, cf. figure 11.b. La recherche de formulations optimales pour les superplastifiants reste un enjeux majeur de recherche et développement. Des mesures rhéologiques récentes sur des suspensions de particules de carbonate de calcium montrent que le taux de cisaillement critique de rhéo-épaississement peut varier d'un ordre de grandeur en fonction du type de polymère utilisé.

Glossaire

- **Rhéologie :** Science qui étudie la réponse en écoulement des fluides à des sollicitations mécaniques.
- **Fluide newtonien :** Fluide dont la viscosité ne dépend pas de taux de cisaillement appliqué. Plus généralement, un fluide newtonien a une loi constitutive linéaire entre le tenseur des

contraintes et le tenseur des taux de déformation. Cette loi fait intervenir deux constantes physiques : une viscosité de cisaillement η (celle discutée dans cet article) et une viscosité de volume liée à la compressibilité du milieu.

- **Fluide non-newtonien :** Fluide dont la loi constitutive dévie de celle d'un fluide newtonien (exemple : viscosité dépendante du taux de cisaillement, viscosité évoluant dans le temps, présence d'élasticité, etc).
- **Fraction volumique :** Rapport entre le volume occupé par les particules et le volume total (fluides + particules) de la suspension.
- **Mouvement brownien :** Mouvement aléatoire d'une particule immergée dans un fluide causé par les collisions, d'origine thermique, entre la particule et les molécules du fluide.
- **Suspension brownienne :** Suspension composée de particules suffisamment petites pour être soumises au mouvement brownien ($d < 0.1 - 1$ μm).
- **Suspension colloïdale :** Suspension composée de particules suffisamment petites pour être soumises aux interactions colloïdales ($d < 10 - 100$ μm), c'est-à-dire aux interactions d'origine électromagnétique et entropique entre particules (force de Van der Waals, forces électrostatiques, répulsion stérique entre molécule, etc).
- **Coefficient de frottement :** Caractérise la résistance au mouvement relatif entre deux solides au contact. Le coefficient de frottement est le rapport entre la force tangentielle nécessaire pour mettre les solides en mouvement relatif de translation et la force normale qui s'applique sur les solides.

Sigles, notations et symboles

- U (m/s) vitesse
- h (m) hauteur
- τ (Pa) contrainte tangentielle
- $\dot{\gamma}$ (s^{-1}) taux de cisaillement
- η (Pa.s) viscosité
- η_f (Pa.s) viscosité du fluide suspendant
- η_s (Pa.s) viscosité de la suspension
- η_{eff} (Pa.s) viscosité effective
- μ_p (sans dimension) coefficient de frottement solide entre deux particules
- ϕ (sans dimension) fraction volumique de la suspension
- ϕ_c (sans dimension) fraction volumique critique de la suspension
- $\phi_c^{\mu_p=0}$ (sans dimension) fraction volumique critique d'une suspension de particules non frottantes
- $\phi_c^{\mu_p>0}$ (sans dimension) fraction volumique critique d'une suspension de particules frottantes
- Pe (sans dimension) nombre de Péclet
- k_B (J/K) constante de Boltzmann $k_B = 1,38 \times 10^{-23}$
- T (K) température
- d (m) diamètre des particules
- St (sans dimension) nombre de Stokes
- ρ (kg/m^3) densité des particules
- $f(\phi)$ (sans dimension) viscosité de la suspension normalisée par la viscosité du fluide suspendant
- F_{rep} (N) Amplitude de la force répulsive courte portée entre particules
- Γ (sans dimension) nombre sans dimension comparant les forces hydrodynamiques aux forces répulsive entre particules
- β (sans dimension) constante numérique
- τ_c (Pa) contrainte critique de rhéo-épaississement
- $\dot{\gamma}_c$ (s^{-1}) taux de cisaillement critique de rhéo-épaississement
- θ (degré) angle d'avalanche
- λ_D (m) longueur de Debye
- λ (m) portée de la force répulsive
- ℓ_r (m) rugosité des particules

- $\Delta\rho$ (kg/m^3) différence de densité entre les particules et le fluide suspendant
- g (m/s^2) accélération de la pesanteur (gravité)
- F_0 (N) force
- z (m) distance de séparation entre les surfaces des particules
- ω (deg/s) vitesse de rotation
- Ω (deg/s) vitesse de rotation
- F_N (N) force normale entre deux particules
- F_T (N) force tangentielle entre deux particules

Pour en savoir plus

Références

[1] Étienne Guyon, Jean-Pierre Hulin, and Luc Petit. *Hydrodynamique physique*. CNRS Édition, 3 edition, 2012.

[2] H Freundlich and HL Röder. Dilatancy and its relation to thixotropy. *Transactions of the Faraday Society*, 34 :308–316, 1938.

[3] Willem H Boersma, Jozua Laven, and Hans N Stein. Shear thickening (dilatancy) in concentrated dispersions. *AIChE journal*, 36(3) :321–332, 1990.

[4] Eric Brown and Heinrich M Jaeger. Shear thickening in concentrated suspensions : phenomenology, mechanisms and relations to jamming. *Reports on Progress in Physics*, 77(4) :046602, 2014.

[5] Eric Brown and Heinrich M Jaeger. The role of dilation and confining stresses in shear thickening of dense suspensions. *Journal of Rheology*, 56(4) :875–923, 2012.

[6] Arthur A Tracton. *Coatings technology handbook*. CRC press, 2005.

[7] Marlene B Stauffer. Chocolate behavior-what influences your selection ? *Manufacturing Confectioner*, 78 :75–80, 1998.

[8] Chttp ://www.badennova.es/badennova-en/.

[9] John F. Brady and Georges Bossis. The rheology of concentrated suspensions of spheres in simple shear flow by numerical simulation. *Journal of Fluid Mechanics*, 155 :105–129, 1985.

[10] Abdoulaye Fall, Anaël Lemaitre, François Bertrand, Daniel Bonn, and Guillaume Ovarlez. Shear thickening and migration in granular suspensions. *Physical review letters*, 105(26) :268303, 2010.

[11] Nicolas Fernandez, Roman Mani, David Rinaldi, Dirk Kadau, Martin Mosquet, Hélène Lombois-Burger, Juliette Cayer-Barrioz, Hans J Herrmann, Nicholas D Spencer, and Lucio Isa. Microscopic mechanism for shear thickening of non-brownian suspensions. *Physical Review Letters*, 111(10) :108301, 2013.

[12] Ralph A Bagnold. Experiments on a gravity-free dispersion of large solid spheres in a newtonian fluid under shear. *Proceedings of the Royal Society of London. Series A, Mathematical and Physical Sciences*, pages 49–63, 1954.

[13] Abdoulaye Fall, François Bertrand, David Hautemayou, Cédric Mezière, Pascal Moucheront, Anaël Lemaitre, and Guillaume Ovarlez. Macroscopic discontinuous shear thickening versus local shear jamming in cornstarch. *Physical review letters*, 114(9) :098301, 2015.

[14] Eric Brown and Heinrich M Jaeger. Shear thickening in concentrated suspensions : phenomenology, mechanisms and relations to jamming. *Reports on Progress in Physics*, 77(4) :046602, 2014.

[15] Matthieu Wyart and Michael E. Cates. Discontinuous shear thickening without inertia in dense non-brownian suspensions. *Phys. Rev. Lett.*, 112 :098302, Mar 2014.

[16] Romain Mari, Ryohei Seto, Jeffrey F. Morris, and Morton M. Denn. Shear thickening, frictionless and frictional rheologies in non-brownian suspensions. *Journal of Rheology*, 58(6) :1693–1724, 2014.

[17] Ryohei Seto, Romain Mari, Jeffrey F. Morris, and Morton M. Denn. Discontinuous shear thickening of frictional hard-sphere suspensions. *Phys. Rev. Lett.*, 111 :218301, Nov 2013.

[18] John F Brady and Georges Bossis. Stokesian dynamics. *Annual review of fluid mechanics*, 20(1) :111–157, 1988.

[19] Romain Mari, Ryohei Seto, Jeffrey F Morris, and Morton M Denn. Discontinuous shear thickening in brownian suspensions by dynamic simulation. *Proceedings of the National Academy of Sciences*, 112(50) :15326–15330, 2015.

[20] Bruno Andreotti, Yoël Forterre, and Olivier Pouliquen. *Granular media : between fluid and solid*. Cambridge University Press, 2013.

[21] Pierre-Emmanuel Peyneau and Jean-Noël Roux. Frictionless bead packs have macroscopic friction, but no dilatancy. *Phys. Rev. E*, 78 :011307, Jul 2008.

[22] Cécile Clavaud, Antoine Bérut, Bloen Metzger, and Yoël Forterre. Revealing the frictional transition in shear-thickening suspensions. *Proceedings of the National Academy of Sciences*, 114(20) :5147–5152, 2017.

[23] Jean Comtet, Guillaume Chatté, Antoine Niguès, Lydéric Bocquet, Alessandro Siria, and Annie Colin. Pairwise frictional profile between particles determines discontinuous shear thickening transition in non-colloidal suspensions. *Nature communications*, 8, 2017.

[24] Neil Y. C. Lin, Christopher Ness, Michael E Cates, Jin Sun, and Itai Cohen. Tunable shear thickening in suspensions. *Proceedings of the National Academy of Sciences*, 113(39) :10774–10778, 2016.

6.2 Dispersion et mélange

J. Fluid Mech. (2013), *vol.* 724, *pp.* 527–552. © Cambridge University Press 2013
doi:10.1017/jfm.2013.173

Heat transfer across sheared suspensions: role of the shear-induced diffusion

Bloen Metzger[1],†, Ouamar Rahli[1] and Xiaolong Yin[2]

[1]IUSTI – CNRS UMR 7343, Aix-Marseille University, 13453 Marseille, France

[2]Petroleum Engineering, Colorado School of Mines, Golden, CO 80401, USA

(Received 22 August 2012; revised 22 March 2013; accepted 27 March 2013)

Suspensions of non-Brownian spherical particles undergoing shear provide a unique system where mixing occurs spontaneously at low Reynolds numbers. Through a combination of experiments and simulations, we investigate the effect of shear-induced particle diffusion on the transfer of heat across suspensions. The influence of particle size, particle volume fraction and applied shear are examined. By applying a heat pulse to the inner copper wall of a Couette cell and analysing its transient temperature decay, the effective thermal diffusivity of the suspension, α, is obtained. Using index matching and laser-induced fluorescence imaging, we measured individual particle trajectories and calculated their diffusion coefficients. Simulations that combined a lattice Boltzmann technique to solve for the flow and a passive Brownian tracer algorithm to solve for the transfer of heat are in very good agreement with experiments. Fluctuations induced by the presence of particles within the fluid cause a significant enhancement ($>200\,\%$) of the suspension transport properties. The effective thermal diffusivity was found to be linear with respect to both the Péclet number ($Pe = \dot{\gamma} d^2/\alpha_0 \leqslant 100$) and the solid volume fraction ($\phi \leqslant 40\,\%$), leading to a simple correlation $\alpha/\alpha_0 = 1 + \beta\phi Pe$ where $\beta = 0.046$ and α_0 is the thermal diffusivity of the suspension at rest. In our Couette cell, the enhancement was found to be optimum for a volume fraction, $\phi \approx 40\,\%$, above which, due to steric effects, both the particle diffusion motion and of the effective thermal diffusion dramatically decrease. No such correlation was found between the average particle rotation and the thermal diffusivity of the suspension, suggesting that the driving mechanism for enhanced transport is the translational particle diffusivity. Movies are available with the online version of the paper.

Key words: flow control, mixing enhancement, suspensions

1. Introduction

Mixing at low Reynolds numbers is difficult (Hinch 2003). The difficulty mainly stems from the absence of small inertial length scales in the flow; mixing thus occurs through molecular diffusion which is extremely slow. Many attempts have been made to improve mixing under these conditions. One strategy is to force the path lines of

† Email address for correspondence: Bloen.Metzger@polytech.univ-mrs.fr

the fluid to be chaotic such that initially close fluid elements separate exponentially in time and thus rapidly visit different regions of the fluid (e.g. in the blinking vortices configuration (Daitche & Tél 2009) or in chaotic mixers for micro-channels (Stroock *et al.* 2002)). In micro-fluidic devices, some non-Newtonian fluids were found to produce efficient mixing due to an elastic flow instability that deviates the fluid streamlines from their laminar trajectories (Zilz *et al.* 2011). Other devices use solute density differences to promote natural convection which can boost the transport of colloids (Selva, Daubersies & Salmon 2012).

The aim of the present work is to study the effect of embedded neutrally buoyant particles on the transfer of heat across a sheared suspension. Mixing occurs spontaneously at low Reynolds numbers in such a system. A particle immersed in a viscous suspension of otherwise identical non-Brownian particles, is subject to random displacements normal to the fluid streamlines that scale diffusively with time. This phenomenon called 'sheared-induced diffusion' has been widely studied in recent years (Arp & Mason 1976; Eckstein, Bailey & Shapiro 1977; Da Cunha & Hinch 1996; Breedveld *et al.* 2002; Sierou & Brady 2004). It reminds one of the classical Brownian motion, except that here the diffusive motion of the particles does not arise from thermal energy, which is negligible, but from the collisions and the hydrodynamic interactions between the particles. We restrict our study to suspensions where the Péclet number associated with the particles is large (non-Brownian) which still embraces a wide range of important suspension flows, such as flow of red blood cells in arteries (Bishop *et al.* 2002), flow of sand or cement slurries in civil engineering as well as a large number of applications in the food (Lin *et al.* 2002), chemical and pharmaceutical industries.

In essence, particles in the fluid can be thought of as many 'stirrers'. The questions raised are how do they affect the transport of heat/mass across a sheared suspension and what will be the influence of the particle size, their volume fraction and the applied shear?

To investigate the above problems, we consider the transfer of heat across a suspension of neutrally buoyant, non-Brownian rigid and spherical particles sheared in a cylindrical Couette cell. Particles having similar thermal conductivity to the fluid are used in order to isolate the effect of shear-induced diffusion on the transfer of heat. The thermal diffusivity of the suspension at rest is α_0. When the suspension is sheared, the particles generate fluctuations which modify the effective thermal diffusivity. These fluctuations are generated by the particle diffusive motion for which the coefficient $D \propto \dot{\gamma} d^2$, where $\dot{\gamma}$ is the applied shear rate and d is the particle diameter (Leighton & Acrivos 1987). This scaling is expected since the only time scale in the system is the inverse of the shear rate and the relevant length scale, i.e. the characteristic length scale of the fluid velocity disturbances, is given by the particle size. The thermal diffusion coefficient of the sheared suspension normalized by the thermal diffusion of the suspension at rest, $\alpha^* = \alpha/\alpha_0$, should then depend upon the thermal Péclet number, $Pe = \dot{\gamma} d^2/\alpha_0$.

The rate of heat transfer could also depend upon the Reynolds number $Re = \rho \dot{\gamma} d^2/\eta$, where ρ and η are the density and the viscosity of the fluid, respectively, if the particle-induced velocity disturbances were modified by the virtue of inertial effects. However, in the present study as the Reynolds number is maintained very small ($Re \leqslant 10^{-2}$), we do not expect this number to affect the rate of heat transfer.

Despite its major importance for industry and its fascinating content, this problem transfer enhancement in sheared suspensions has not received much attention. Ahuja (1975*a*) experimentally demonstrated that heat transfer is significantly

augmented (>200 %) in sheared suspensions of polystyrene particles. His investigation was performed for finite Reynolds numbers ($Re > 1$) and the mechanism proposed to explain the enhancement is based on inertial effects where the fluid phase is centrifuged by the particle rotation. Sohn & Chen (1981) investigated the heat transfer across a sheared suspension for three different volume fractions. They found that suspensions of spherical particles exhibit a higher effective thermal conductivity that approach the power law $\propto Pe^{1/2}$ for $Pe \geqslant 300$. Zydney & Colton (1988) suggested that augmented solute transport arises from shear-induced particle migration and the concomitant dispersive fluid motion. Reviewing existing experimental results from a variety of experimental systems, they derived a model which predicts the augmented solute transport should vary linearly with the Péclet number. Shin & Lee (2000) measured the effective thermal conductivity of low volume fraction (<10 %) suspensions. They found the thermal conductivity to increase with shear rate and particle size. An unexplained saturation of the conductivity was also found at large shear rates.

Other studies, which bear close resemblance to our study, investigated the transfer of mass across a sheared suspension of particles. Wang & Keller (1985) used an electrochemical technique to measure the rate of augmented transport of solutes through erythrocyte suspensions in a Couette flow and found the correlation $\propto Pe^{0.89}$. More recently, Wang *et al.* (2009) used the same technique in suspensions of non-Brownian spherical particles. At moderate values of the Péclet number, they found an enhancement nearly linear with Pe and focused their investigation on the influence of the boundary layer near the solid wall which tends to limit the enhancement. They found the enhancement is damped at higher Péclet numbers. In that range the Reynolds number was finite $Re = O(1\text{–}7)$.

In summary, experimental results demonstrate that particles contribute to increasing the transfer properties of sheared suspensions. However, the phenomenon was studied in a wide range of experimental conditions: some experiments involve inertial effects, others are at low or finite Reynolds numbers; some use soft or anisotropic particles, others use non-Brownian hard spheres; some use quasi-linear shear flows, others use Poiseuille flows. There is thus a wide range of experimental correlations that are accurate only for specific systems and/or limited experimental conditions. In addition, many studies used steady-state measurements of heat/mass flux where the limiting effect of the bounding wall cannot be isolated from the bulk.

We chose to perform experiments (see § 2) and numerical simulations (see § 3) for the simplest possible physical system. The experiment was purposely designed to isolate the effect of shear-induced particle diffusion on the transport of heat. We investigated low-Reynolds-number flow regimes where inertial effects can be neglected. We also used non-Brownian hard spheres having the same density and similar thermal conductivity as the fluid to avoid thermal fluctuations, sedimentation and enhancement of the transfer due to a larger conductivity of the added particles. The simplicity of this configuration should help us to understand the underlying mechanism responsible for the heat transfer enhancement. These results should also constitute a solid basis to investigate more complex situations involving for instance inertia or deformable particles. The innovative aspect of our study is that it is the first to directly correlate microscopic measurements (at the particle scale) to the macroscopic transfer properties of the suspension. Transient-state measurements were designed to discount the effect of bounding walls. We also investigated systematically the influence of the particle volume fraction. In § 4, the shear rate and volume fraction dependencies of the effective thermal diffusivity of the suspension is depicted for two particle sizes. In

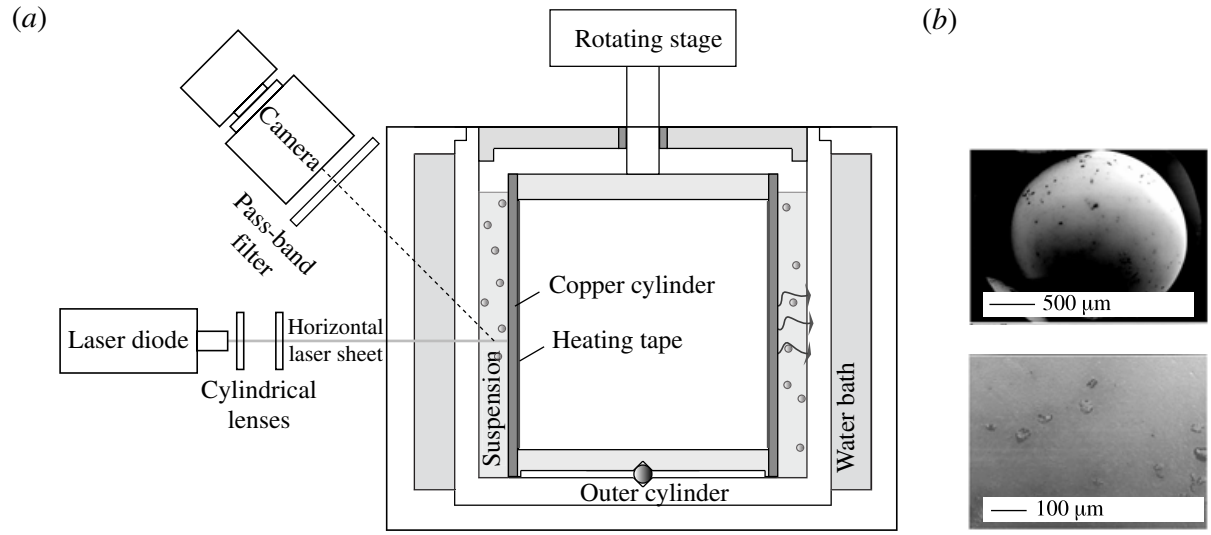


FIGURE 1. (*a*) Sketch of the experimental cylindrical Couette cell. (*b*) Scanning electron microscopy images of the PMMA particles.

the same section, the particle diffusion coefficient in the gradient direction of the flow is investigated and correlated with the effective thermal diffusivity. Finally, the results are discussed in § 5.

2. Experiment

The experimental set-up is sketched in figure 1. This Couette device with an inner cylinder of radius of 5 cm and height of 12 cm is driven by a precision rotating stage (M-061.PD from PI piezo-nano positioning) with high angular resolution (3×10^{-5} rad). The transparent and stationary outer cylinder was machined from a full block of PMMA. The gap between the two cylinders is $L_y = 12$ mm. The temperature of the whole set-up is controllable (± 0.05°C) as the Couette cell is embedded in a square water-bath jacket connected to a cryo-thermostat.

2.1. *Particles and fluid*

We employed spherical PMMA beads from Engineering Laboratories Inc. with density $\rho = 1.18$ g cm^{-3} and diameters $d = 1$ and 2 mm (see figure 1). These particles were specially chosen for their high surface quality and good transparency which significantly improved the index matching. Suspensions of different volume fractions ranging from 5 to 50 % were used for these experiments.

The fluid was a Newtonian mixture of Triton X-100 (77.4 wt %), zinc chloride (13.4 wt %) and water (9.2 wt %) having a viscosity of $\eta = 3$ Pa s and a density of $\rho = 1.18$ g cm^{-3} at room temperature. Its composition was carefully chosen to closely match both the refractive index and density of the particles. We achieved a density match such that the Stokes velocity of an individual particles was less than 10^{-8} m s^{-1}. A small amount of hydrochloric acid (≈ 0.05 wt %) was added to the solution to prevent the formation of zinc hypochlorite precipitate, thereby significantly improving the optical transparency of the solution. Once the suspension was poured into the cell, the index matching between the fluid and the particles was precisely tuned by adjusting the temperature of the bath control.

2.2. *Determination of the thermal diffusion coefficient of the suspension*

The inner cylinder was produced from a hollow copper pipe. The pipe wall was machined to a thickness of 2 mm. Then, we covered its inner surface entirely with flexible heating tape (see www.minco.com). We also placed four thermocouples in between the heating tape and the cylinder wall embedded in some high-conductivity thermal paste. The temperature of the inner cylinder could then be recorded through an acquisition A/N converter NI USB 9219 with an accuracy of ± 0.02 °C.

The experimental protocol was as follows. We first poured suspension with the desired volume fraction into the cell gap. The suspension was then thoroughly mixed by continuously shearing it at a large shear rate (10 s^{-1}) for 5 min. Then the shearing motion was stopped and we performed the reference experiment (suspension at rest): the inner cylinder was heated for 5 s (its typical temperature rise was 5 °C). We then let its temperature relax back to the room temperature. Throughout this process the temperature of the inner cylinder was measured. Experiments were then performed at the desired shear rates, waiting times of 30 min in between to reestablish the initial equilibrium condition. The combination of a moderate temperature increase and transient measurement within this geometry allowed us to neglect the effect of natural convection; no convection motion of the suspension could be observed when heating up the inner cylinder of the cell.

The temperature decay rate of the inner cylinder is directly related to the heat transfer properties of the suspension. As we estimate the relative increase of the thermal diffusivity of sheared suspensions with respect to that at rest, we can probe whether shear has an effect on the effective heat transfer properties of suspensions.

2.2.1. *First evidence of heat transfer enhancement*

We first performed an experiment with the fluid (Triton X-100, zinc chloride and water) without particles. As shown in figure 2, the decay rate of the wall temperature remains unchanged (within error bars) if the fluid is at rest or if it is sheared. This behaviour is expected since the laminar fluid flow around the cylinder is perpendicular to the temperature gradient; in the absence of particles, the flow does not contribute to the heat transfer which occurs purely by diffusion in the radial direction.

We then added a volume fraction $\phi = 30\,\%$ of particles to the fluid. When the suspension was at rest, the temperature response was the same. This is easily explained since PMMA particles have similar thermo-physical properties as the fluid used for these experiments. When the suspension was at rest, adding these particles to the fluid did not affect the effective heat transfer properties. However, when the suspension was sheared, we found that the inner cylinder temperature decayed significantly faster. This demonstrates the enhancement of the heat transfer due to shearing of this suspension.

To quantify this phenomenon, we now derive an analytical model to evaluate the effective thermal diffusion coefficient of the suspension from the decay of the inner cylinder temperature.

2.2.2. *Model to estimate the thermal diffusion coefficient*

The effective thermal diffusion coefficient is estimated from the decay rate of the inner cylinder temperature, T_w. We made the following assumptions (cf. figure 3): (i) the suspension behaves as an homogeneous fluid having an effective thermal diffusion coefficient α (discussion about this assumption can be found in Appendix); (ii) since the ratio of the Couette radius to the gap thickness is rather large, we considered the problem to be one-dimensional and neglect the curvature of the cell;

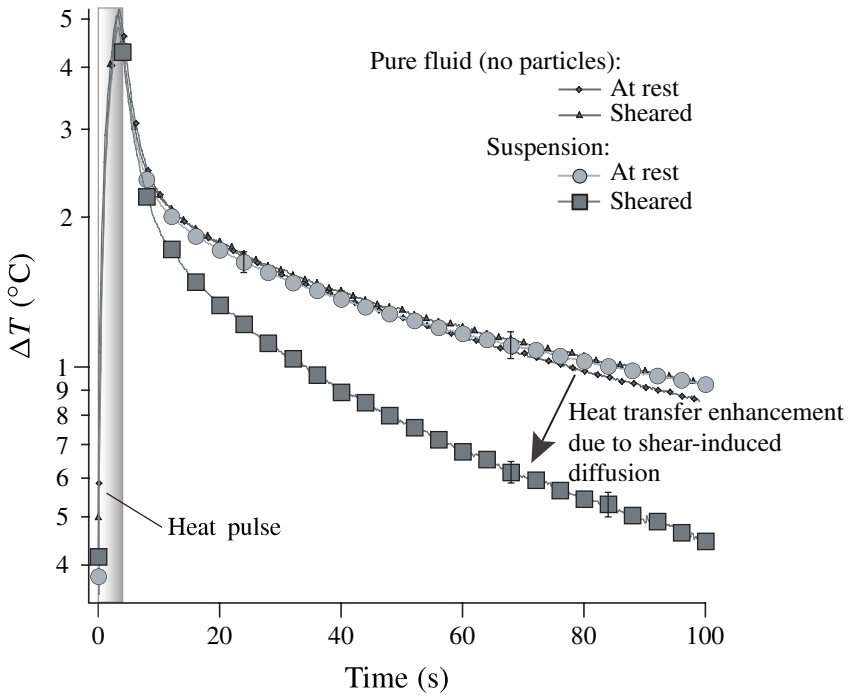


FIGURE 2. Inner cylinder temperature as a function of time for a pure fluid (without particles) at rest or sheared and for a suspension of volume fraction, $\phi = 30\,\%$, at rest or sheared at $\dot{\gamma} = 10\ \mathrm{s}^{-1}$. As in the reminder of the paper, a few error bars are plotted in each figure to give an indication of the typical statistical uncertainty between runs.

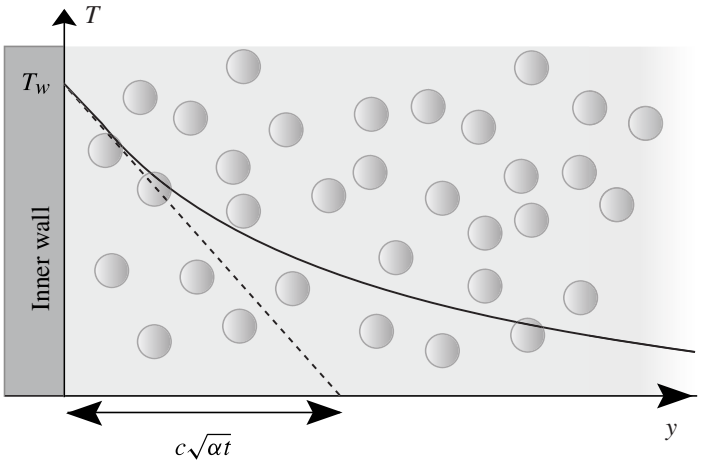


FIGURE 3. Schematic describing the model used to predict the evolution of the inner cylinder temperature, $T_w(t)$.

(iii) we neglected the heating time, $T_w(t = 0) = T_{max}$; and (iv) the suspension is semi-infinite. The decay rate of the inner cylinder temperature is then given by the heat flux into the suspension,

$$\rho_w e_w C_{p_w} \frac{\partial T_w}{\partial t} = -k_s \frac{\partial T}{\partial y}\bigg|_{y=0}, \tag{2.1}$$

where T_w, ρ_w, e_w and C_{p_w} are the temperature, the density, the thickness and the heat capacity of the inner cylinder, respectively. The temperature and the thermal

conductivity of the suspension are denoted by T and k_s. Assuming that the heat transfer across the suspension is diffusive, the temperature gradient at the wall (see figure 3) can be approximated as

$$\left.\frac{\partial T}{\partial y}\right|_{y=0} \approx \frac{T_w}{c\sqrt{\alpha t}}, \tag{2.2}$$

where c is an $O(1)$ constant. Integrating (2.1) using (2.2), the wall temperature is

$$T_w/T_{max} = \mathrm{e}^{-A\sqrt{t}} \tag{2.3}$$

where $A = (2/c)(\rho C_{p_s}/\rho_w e_w C_{p_w})\sqrt{\alpha}$ with ρ and C_{p_s} denoting the density and the heat capacity of the suspension, respectively. The latter expression (2.3) was used to fit the inner cylinder temperature measured experimentally. The fitting procedure was as follows. The temperature response of the suspension at rest was fitted using a least squares analysis by letting T_{max} and A vary. The temperature responses of the sheared suspensions were then fitted by letting A vary and fixing T_{max} to the value obtained for the stationary suspension. In the following, the results are presented in the normalized form $\alpha^* = \alpha/\alpha_0 = (A/A_0)^2$, where α_0 and A_0 are the thermal diffusivity and the fit parameter, respectively, of the stationary suspension. In order to estimate the effective thermal diffusivity, $\alpha^* = \alpha/\alpha_0$, it is thus not necessary to know the following parameters: ρ, C_{p_s}, ρ_w, e_w, C_{p_w} and the constant c. However, to estimate the Péclet number, we needed to estimate the absolute thermal diffusivity of the suspension at rest α_0. To do so, we first performed a calibration experiment using a pure silicon oil (47V1000) of known thermal diffusivity and found the constant c to be approximately equal to 1.7, close to $c = \sqrt{\pi}$, the expected value when (2.2) is exact with a time-invariant T_w. Equation (2.3) was then used directly to estimate the absolute thermal diffusion coefficient of the suspension at rest.

A strong assumption made within this model is the homogeneity of the suspension. It is well known that the particle diffusivity vanishes near the walls (Wang *et al.* 2009). To address this issue, other authors have considered the suspension as composed of a bulk and of boundary layers having different transfer properties than the bulk. This approach is indeed necessary to describe mass diffusion as the intrinsic molecular diffusivity of mass is very small. The diffusion of mass across a sheared suspension is thus dominated by the diffusion across the boundary layers. Diffusion of heat is much faster and the enhancement in the bulk is typically only of a factor of two. Diffusion of heat across a sheared suspension is thus dominated by the diffusion across the bulk. Consequently, the wall temperature transient is controlled by the thermal diffusivity of the bulk suspension. For a throughout discussion of the homogeneity assumption and the limits of validity of (2.3) see Appendix.

2.3. *Determination of the particle diffusion coefficients*

2.3.1. *Imaging*

Before pouring the suspension into the Couette cell, the fluid was dyed with rhodamine 6G. This dye fluoresces under illumination provided by a green laser diode (100 mW power and wavelength of 532 nm). Such a laser with a combination of plano-cylindrical lenses were used to generate a horizontal laser sheet of thickness $\approx$30 μm. While the index-matched suspension is transparent, the fluid within this light sheet fluoresces. The particles within this plane thus appeared in black (the particles do not contain any fluorescent dye), see figure 4. Imaging from the top was not possible as the free surface deforms when the suspension is sheared owing to the

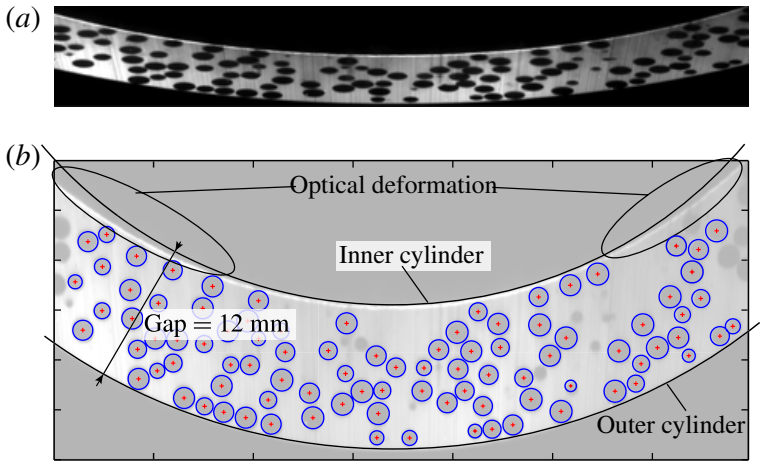


FIGURE 4. (Colour online) Steps to extract particle positions: (*a*) image of the suspension taken at an angle ≈45°; (*b*) image dilated to recover spherical shape of the particles and particle detection using the circular Hough transform algorithm. Some optical deformation can be observed on both sides of the image. (See movie 1 of the online supplementary material available at http://dx.doi.org/10.1017/jfm.2013.173.)

particle normal stress. When the light sheet is located mid-way into the suspension, imaging from the bottom of the cell produces blurry images. We found that the best contrast between the fluid and the particles was achieved by imaging at an angle $\approx 45°$ as shown on figure 1. We used a high-resolution digital camera (Bastler Scout) and a high-quality magnification lens (Sigma APO-Macro-180 mm-F3.5-DG). A 550 nm long-pass coloured glass filter was positioned before the lens to remove the light directly scattered from particle surfaces owing to a slight mismatch of the refractive index.

After delicately pouring the suspension into the Couette cell, the suspension was thoroughly mixed by continuously shearing it at a large shear rate ($10\ s^{-1}$) for 5 min. The shear rate was then lowered to $1\ s^{-1}$ to start the image acquisition. The experiment was performed 9 times for each volume fraction resulting in 9 movies of 400 images each (see movie 1 on the online supplementary material http://dx.doi.org/10.1017/jfm.2013.173).

2.3.2. *Image analysis*

The black ellipses on figure 4(*a*) represent the intersection between the laser sheet and the particles within that plane. Note that the particles all have the same size; the apparent size differences arise from their different vertical positions relative to the light plane. To obtain images as if taken from the top of the cell, we stretched the images in the y-direction to restore the sphericity of the particle images, see figure 4(*b*). The images were then thresholded (with the public domain image processing software ImageJ) and an algorithm of particle detection based on the circular Hough transform (Peng 2005) was applied to find the position of each particle, see figure 4(*c*). The particle trajectories were obtained by applying a tracking algorithm, see figure 5*a*).

The centre of the Couette cell was located by fitting a circle to the outer cylinder. Knowing the centre position of the cell and the gap size, we found, by plotting a circle that corresponds to the inner cylinder, that some optical aberration slightly distorted both sides of the images, see figure 4(*b*). We corrected this optical artifact using a conform mapping, see the corrected trajectories in figure 5(*b*). The final step

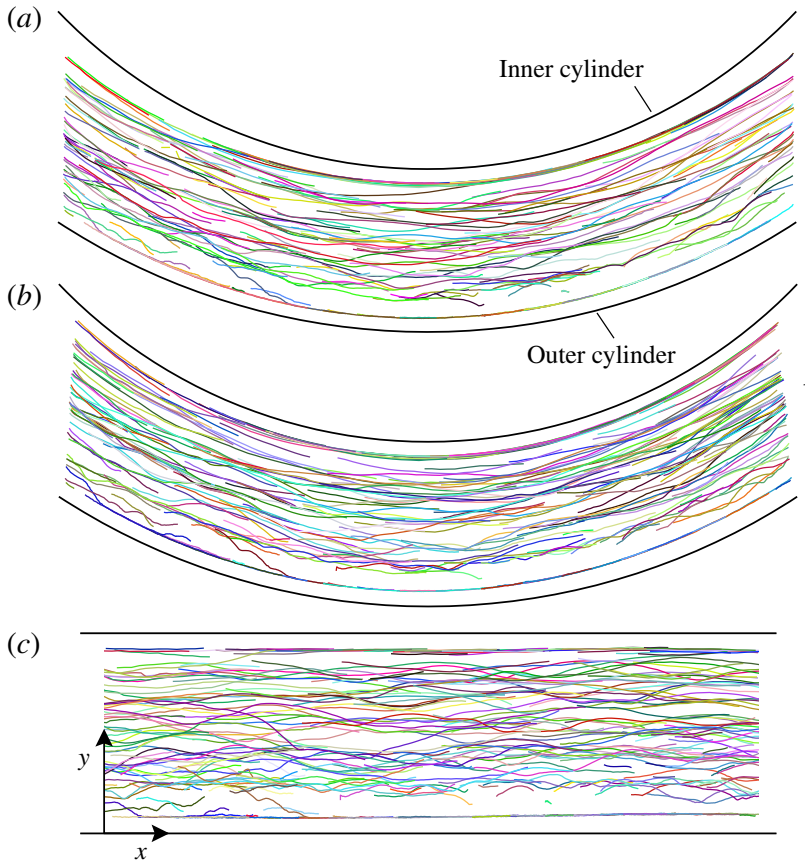


FIGURE 5. (Colour online) Steps to extract particle trajectories: (*a*) original particle trajectories; (*b*) trajectories where the optical aberration was corrected; (*c*) trajectories in curvilinear space. Here $\phi = 35\,\%$.

was to reconstruct the trajectories in a curvilinear reference frame where the x and y directions correspond to the flow and gradient directions, respectively, see figure 5(*c*).

2.3.3. *Measurement of the particle diffusion coefficients*

We now describe the calculation of the self-diffusion coefficients in the velocity-gradient direction. The self-diffusivity is defined as the time rate of change of half of the mean-square displacements. The diffusion coefficient in the gradient direction can be readily estimated using

$$\langle \Delta y \Delta y \rangle = 2D_{yy}t, \tag{2.4}$$

where $\Delta y = y(t) - y(t=0)$ and the angle brackets denote an average over all particles within the bulk of the flow. The particles within one particle diameter from the cell walls, which trajectories are highly influenced by the walls, were discarded from the average calculation. The self-diffusivity should scale as $\propto \dot{\gamma} d^2$ since the inverse of the shear rate and the particle diameter d are the only time and length scales in the bulk suspension. One can thus define the dimensionless diffusivity $D^*_{yy} = D_{yy}/\dot{\gamma} d^2$ and express the normalized mean square displacements using more natural units

$$\frac{\langle \Delta y \Delta y \rangle}{d^2} = 2D^*_{yy}\gamma, \tag{2.5}$$

where the total strain $\gamma = \dot{\gamma} t$. Sierou & Brady (2004) showed that strains of at least 10 need to be sampled for the long-time diffusive behaviour to be reached. Analyses

at smaller strains lead to an overestimation of the diffusivity as the short-term increase of the mean square displacements tends to be quadratic. Within our experimental configuration, particles could be followed for a strain up to 7. This represents an improvement relative to the set-up of Breedveld *et al.* (2002) where the maximum strain was 2.8. However, this limitation may still result in a slight overestimation of the diffusion coefficients.

Investigating the fluctuations of the particles in the flow direction is difficult as they are generally overwhelmed by the advection motion. To observe these fluctuations, the affine part of the motion needs to be subtracted from the trajectories. This is achieved by removing at each time step the instantaneous advection displacement of the particles. Starting from the origin, the non-affine particle positions, $X(t)$, are built as follows

$$X(t + \mathrm{d}t) = X(t) + \mathrm{d}x - \dot{\gamma} y(t)\,\mathrm{d}t, \tag{2.6}$$

where $\mathrm{d}x = x(t + \mathrm{d}t) - x(t)$ is the particle displacement in the flow direction between two successive images, $\mathrm{d}t$ denotes the time between two successive images and $\dot{\gamma}$ is the shear rate of the particle velocity field which we will define later. Note that this expression is simply a discrete version of the integral expression proposed by Sierou & Brady (2004):

$$X(t) = x(t) - \int_0^t \dot{\gamma}(\tau) y(\tau)\,\mathrm{d}\tau, \tag{2.7}$$

which provides a correct expression for the non-affine motion of the particles. The particle velocity field is obtained by binning the gap between the two walls into 24 equals segments and by averaging the velocities of the particles within those bins. The shear rate associated with the particle velocity field, $\dot{\gamma}$, is obtained by fitting the particle velocity profile by a straight line.

Figure 6(*a*) shows the mean square displacements and the particle displacement distributions obtained from the original trajectories. The mean square displacement, $\langle xx \rangle$, along the flow direction shows a large quadratic increase and the particle displacements in the flow direction are as expected all positive. Once the affine part of the motion is removed (see figure 6*b*), the mean square displacement both in the flow and the gradient directions, $\langle XX \rangle$ and $\langle yy \rangle$, increase linearly with strain. Both distributions of the particle displacements have a zero mean and a Gaussian shape. The diffusion coefficients are measured by fitting the mean square displacements for a strain comprised between 2 and 7. The lower limit of 2 was chosen as the linear regime establishes above that value, see the log–log inset of figure 6(*b*). The higher limit of 7 corresponds to the maximum strain for which individual particles could be tracked with the present set-up.

2.4. *Parameter range/limitations*

The adjustable parameters were the shear rate, $\dot{\gamma}$, the volume fraction, ϕ, and the particle diameter, d. The shear rate was varied in the range of [0–14] s^{-1}. The maximum value of the shear rate was chosen such that the largest Reynolds number associated with the flow was $Re = \rho \dot{\gamma} L^2/\eta \approx 0.3$, which confined our investigations to regimes where inertia is negligible. In addition, in this range of shear rates, the temperature increase of the suspension due to viscous dissipation was negligible (below temperature accuracy ≈ 0.02 °C). Indeed, this temperature increase can be estimated: $\Delta T \approx \eta \dot{\gamma}^2 \Delta t/(\rho C_p)$, where Δt denotes the duration of the experiment.

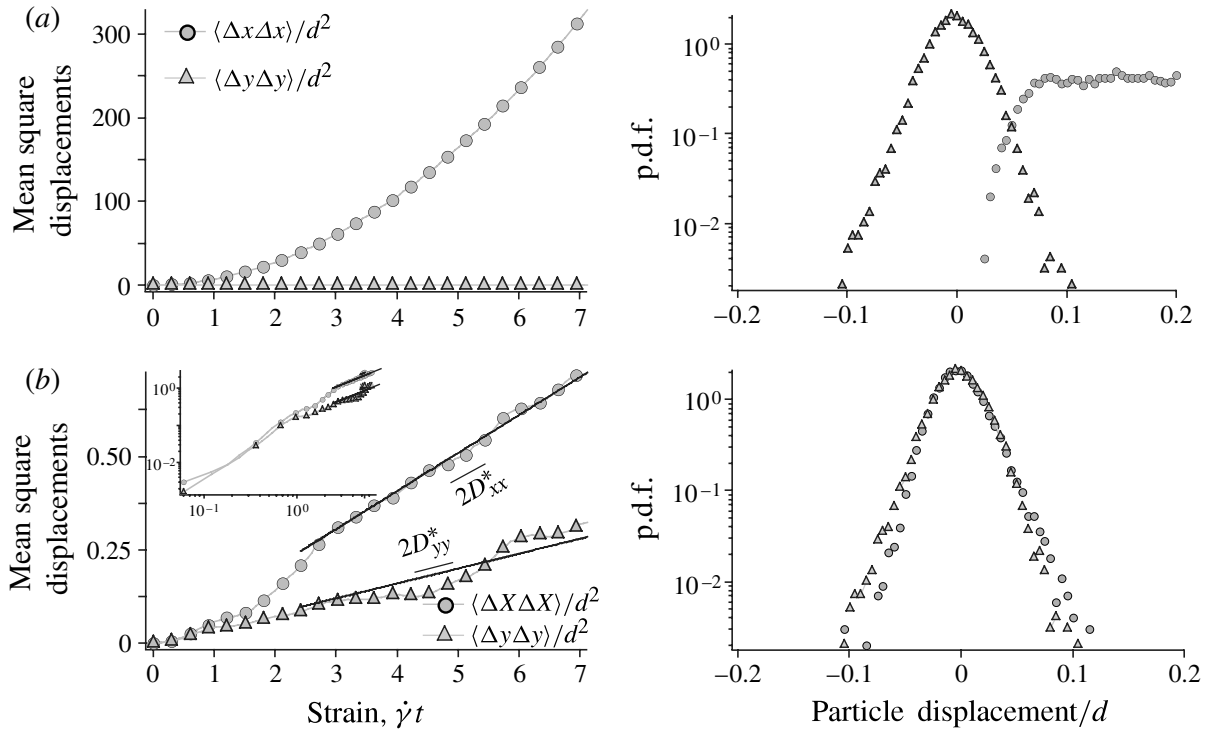


FIGURE 6. Mean square displacements versus strain and probability distribution functions of the particle displacements between two successive images (*a*) for the original trajectories and (*b*) for the non-affine trajectories. The data shown in this figure were obtained from a single run and for a volume fraction $\phi = 30\,\%$.

For $\dot{\gamma} = 20\ \mathrm{s}^{-1}$, one obtains an augmentation of the temperature, $\Delta T \approx 0.1\ ^\circ\mathrm{C}$ after straining the suspension for 100 s.

The volume fraction was varied from 5 to 50 % in steps of 5 %. It is worth noting that at $\phi = 50\,\%$, the particle stress is large enough that particles spontaneously migrate through the suspension free surface, slowly moving up the sidewalls, stacked up to 5 layers above the suspension free surface. As the fluid drains back into the suspension, this tends to lower the actual volume fraction of the suspension. This phenomenon was previously observed for dense suspensions (Deboeuf *et al.* 2009).

We have used two particle diameters, $d = 1$ and 2 mm. The measurement of the particle diffusion coefficients was performed with the 2 mm particles only. The 1 mm particles experiments did not provide sufficiently high-quality images to perform this analysis. However, the effective thermal diffusion coefficients were measured for both particles sizes. The Péclet number associated to the particles, $Pe_p = 3\pi\mu d^3\dot{\gamma}/4kT \gg 1$ so that we can neglect their Brownian motion. The thermal Péclet number, defined as $Pe = \dot{\gamma} d^2/\alpha_0$, was varied from 0 to 120.

3. Numerical simulation

3.1. *Method*

To capture particle-induced hydrodynamic disturbance and its effect on heat transfer numerically and to compare with experiments, the Navier–Stokes equation for the fluid is directly solved in sheared suspensions using a lattice Boltzmann method. Brownian passive tracers are used to simulate the diffusion of heat. In what follows, we will present a brief introduction to the method and its characteristics.

The lattice Boltzmann method for particulate flows used in this study was developed by Ladd and others (Ladd 1994*a*,*b*; Ladd & Verberg 2001), whereas a lattice Boltzmann solver is used to solve the fluid motion, and Newton's equations of motion is applied to the particles. The lattice Boltzmann method does not directly discretize and solve the Navier–Stokes equation. Instead, it simulates the evolution of a discretized fluid molecular velocity distribution on a space filling cubic lattice. Let $n_i(\boldsymbol{r}, t)$ be the fraction of molecules at location $\boldsymbol{r}$ and time t with molecular velocity $\boldsymbol{c}_i$, the evolution of n_i follows a collision step

$$n_i^*(\boldsymbol{r}, t) = n_i(\boldsymbol{r}, t) + \Omega_i[\boldsymbol{n}(\boldsymbol{r}, t) - \boldsymbol{n}^{neq}(\boldsymbol{r}, t)], \tag{3.1}$$

where Ω_i is a collision operator that relaxes the non-equilibrium part of $\boldsymbol{n}(\boldsymbol{r}, t)$ toward the Maxwellian equilibrium $\boldsymbol{n}^{eq}(\boldsymbol{r}, t)$, and a propagation step that redistributes the distributions for the next collision

$$n_i(\boldsymbol{r} + \boldsymbol{c}_i\Delta t, t + \Delta t) = n_i^*(\boldsymbol{r}, t). \tag{3.2}$$

The discretized molecular velocities $\boldsymbol{c}_i$ are specially designed such that if $\boldsymbol{r}$ is a location defined on a space filling cubic lattice, $\boldsymbol{r}+\boldsymbol{c}_i\Delta t$ is also a location on the lattice. Lattice Boltzmann models are typically denoted as D–X–Q–Y, where X stands for the dimensionality and Y for the number of discretized velocities included. In the lattice Boltzmann model used in this study, $X = 3$ and $Y = 19$. The 19 velocities correspond to distributions that stay at the current node ([000]) and those that propagate to the nearest ([100]) and the next-nearest ([110]) locations on the lattice. The collision operator can take many forms, and the lattice Boltzmann program used in this study uses the collision operator described in Ladd & Verberg (2001). The macroscopic density ρ, momentum $\boldsymbol{j}$ and stress $\boldsymbol{\Pi}$ of the fluid are computed as the zeroth-, first- and second-order moments of n_i

$$\rho = \sum_i n_i, \quad \boldsymbol{j} = \sum_i n_i\boldsymbol{c}_i, \quad \boldsymbol{\Pi} = \sum_i n_i\boldsymbol{c}_i\boldsymbol{c}_i, \tag{3.3}$$

and they obey the Navier–Stokes equation.

For multiphase flows such as studied here, distributions n_i propagated toward a fluid–solid boundary are reflected to where they came from, plus a small correction proportional to the solid velocity (Ladd & Verberg 2001). This link-bounce-back rule recovers the no-slip boundary condition halfway between the solid and the fluid nodes and is first-order accurate in the spatial discretization. Fluid–particle momentum exchanges are then integrated over particle surfaces, and Newton's equation of motion is applied to update particles' velocity and position. In this study, particles are monodisperse and their diameter is resolved by 5.84 lattice nodes. Earlier works (e.g. Verberg & Koch 2006) have shown that this resolution is sufficient to resolve the hydrodynamics for the range of solid volume fraction and Reynolds numbers considered in this study. Further, we showed through simulations conducted at different resolutions that this resolution is also sufficient for combined flow and heat transfer. When particles are less than one lattice spacing apart, analytical solutions are imposed to correctly capture the lubrication interaction between particles (Nguyen & Ladd 2002).

The heat transfer process was simulated following the tracer-based method developed by Wang *et al.* (2009) for the simulation of mass transfer in dynamically evolving suspensions. Tracers follow the discretized advection–diffusion equation

$$\boldsymbol{r}_j(t + \Delta t') - \boldsymbol{r}_j(t) = \boldsymbol{u}\Delta t' + \boldsymbol{\xi}\sqrt{6\alpha_0\Delta t'}, \tag{3.4}$$

where $\boldsymbol{r}_j$ is the position of tracer j, $\boldsymbol{u}$ is the local velocity linearly interpolated from the real-time lattice Boltzmann velocity field, $\boldsymbol{\xi}$ is a random unit vector and α_0 is the thermal diffusivity. Concentrations of tracers can be used to describe the evolution of a passive scalar field; diffusion of mass and diffusion of heat both obey the same advection–diffusion equation and can be simulated using this method. Wang *et al.* (2009) used a reflective boundary was used to prevent the tracers from penetrating the particles because mass transfer only takes place in the fluid phase. In this study, the program is modified to allow tracers to penetrate the particles. When tracers are inside the particles, their advective velocity $\boldsymbol{u}$ is calculated from particle's translational and angular velocities. The mean square displacement of tracers can be directly used to compute the effective thermal diffusion coefficients of the system. The time step $\Delta t'$ for the random walk can be set separately from the time step Δt for the hydrodynamics. In our simulations, we used $\Delta t' = 0.1\Delta t$, i.e. for every lattice Boltzmann time step every tracer particle conducts 10 random walks. Numerical tests showed that the results are independent of the time step size $\Delta t'$ relative to Δt.

3.2. *Simulation set-up and determination of the heat transfer coefficients*

Simulations were set up in cubic domains with $L_x = L_y = L_z = 6d$ which were designed to match experiments performed with 2 mm particles. The systems are bounded in the y direction by solid walls and are periodic in the x and z directions. Initially, particles are randomly distributed and both the particles and fluid are at rest. The velocities of the solid walls are equal and opposite, and are set to match the thermal Péclet number of the experiments. The ratio between the kinematic viscosity of the fluid and the thermal diffusivity of the tracers gives the Prandtl number, which was set to 2×10^4 also to simulate the experimental system. Unlike in the experiments where the heated copper wall provided a supply of heat to the fluid layer nearby, in our simulations both walls are considered to be insulating and adiabatic. This assumption reduces the interactive rule between the tracers and the walls to a simple reflective type.

We first simulated the dissipation of a thermal pulse applied to a thin layer of fluid next to a solid wall using the passive Brownian tracer method. The example shown in figure 7 was obtained in systems with 20 % solid fraction and a thermal Péclet number $Pe = 112$. The mean square displacement of tracers plotted as a function of time reflects interesting transient characteristics. As may be observed in figure 7, the mean square displacement (the short dashed line) first grows following the intrinsic Brownian diffusion of the tracers which was set to match α_0: the thermal diffusivity of the suspension at rest. This behaviour is reasonable because in the very vicinity of the wall the hydrodynamic disturbances are weak. As tracers diffuse into the bulk, they become more agitated, and the mean square displacement follows a larger slope which can be used to estimate the thermal diffusivity, α, of the sheared suspension.

Instead of releasing the tracers next to the solid wall, we chose, as illustrated on figure 8, to directly release the tracers in the middle of the suspension so that the tracers immediately feel the effect of hydrodynamic disturbances. As evidenced in figure 7, the initial slope of the mean square displacement (thick solid line) measured in $2 < \dot{\gamma} t < 10$ matches the previously measured slope of the short dashed line at longer times. The lower limit of 2 was selected because the mean square displacements of tracers start to grow linearly with t after $\dot{\gamma} t \approx 2$; the higher limit can be taken as any time before significant amount of tracers start to hit the bounding walls. As tracers typically start to reach the walls as $\dot{\gamma} t$ exceeds 20, a uniform strain range of $2 < \dot{\gamma} t < 10$ was selected to extract the effective tracer diffusion from

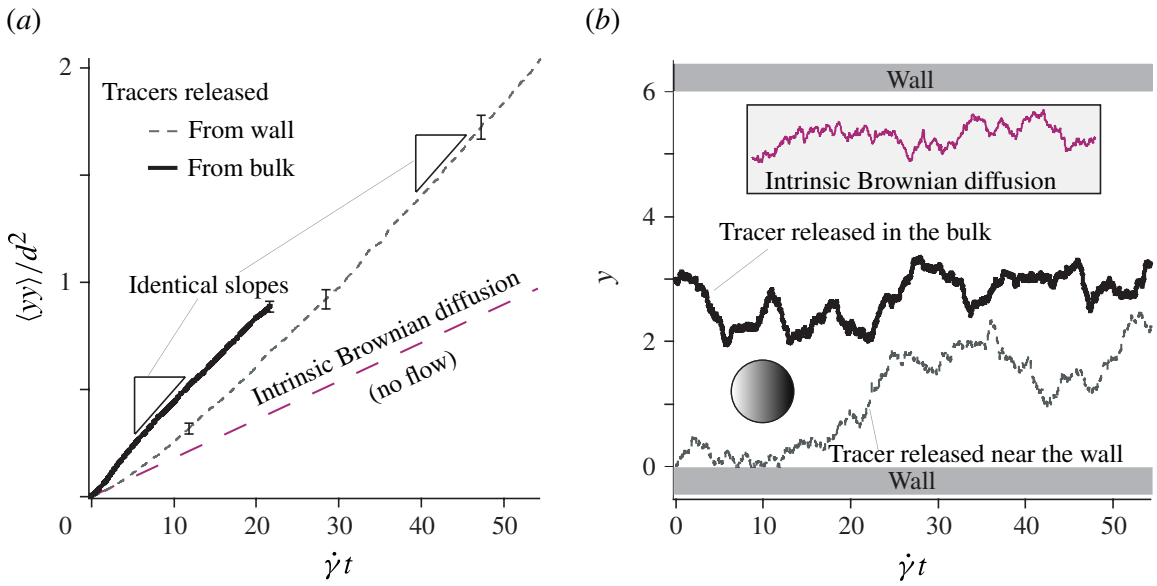


FIGURE 7. (Colour online) Simulations. (*a*) Mean square displacement $\langle yy\rangle/d^2$, plotted against the strain $\dot{\gamma}t$, of passive Brownian tracers that are initially released near the wall (short dashed line) and tracers that are initially released to the middle of a suspension (thick solid line). The slope of the long dashed line corresponds to the intrinsic Brownian diffusion of the tracers (without flow). The two thin solid lines next to the mean square displacements have identical slopes that are used to compute the effective thermal diffusivity. (*b*) The three curves presented are the typical fluctuations in the y positions of tracers as functions of time. From bottom to top: tracer released from the wall, tracer released to the centre of suspension, tracer that undergoes pure molecular diffusion.

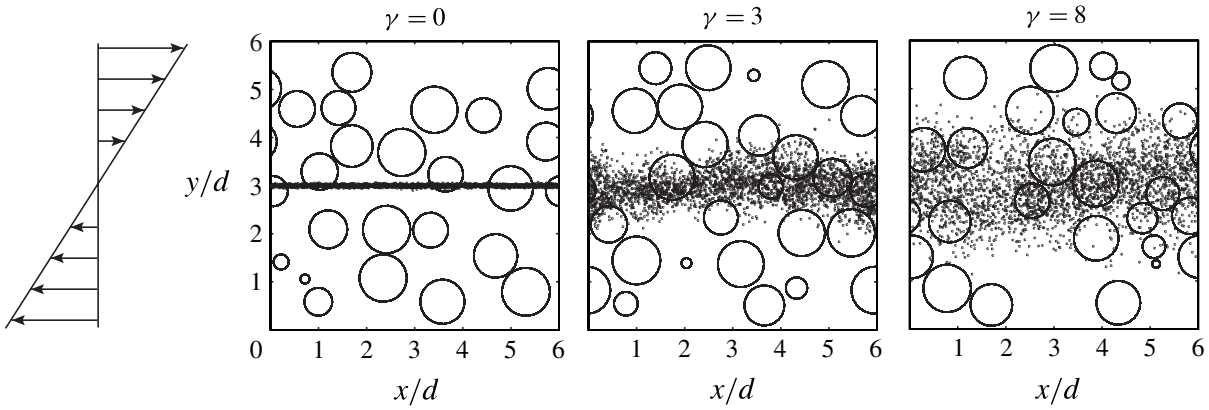


FIGURE 8. Simulations: successive snapshots of a simulation performed for $\phi = 30\,\%$. Only the cross-sections of particles intersecting with the mid-way plane are plotted (particles all have the same size). Passive Brownian tracers are initially released along the centre-line in the bulk of the suspension and their diffusive motion is used to calculate the effective thermal diffusivity of the suspension. (See movie 2 of the online supplementary material.)

all simulations. This approach leads to a significant reduction in the computational time. The efficacy of the method may also be observed in the figure 7(*b*), where some typical trajectories of tracers are presented. The trajectory for a tracer released near the wall (the bottom curve) shows initially weak fluctuations that only become stronger after the tracer diffuses into the bulk; the trajectory for a tracer released in the bulk (the centre curve), on the other hand, shows strong fluctuations from

the very beginning of the simulation. Compared with the trajectory based on the intrinsic Brownian diffusion (see the inset), the tracers within the suspension which are advected both by the fluid and by the particles, exhibit persistent large-scale fluctuations at the origin of the tracer diffusion enhancement.

Finally, it is worth noting that it has been verified that the size of the computational domain in the x direction as well as the specific way in which the tracers are released do not affect the results in any significant way. The effective thermal diffusivity obtained from test simulations conducted with $L_x = 12d$, $L_y = L_z = 6d$ agree with those obtained from cubic domains within 4 %; the cubic domain was thus chosen to reduce computation. The effective thermal diffusivity obtained in simulations where tracers were released uniformly in $-d < y - L_y/2 < d$ also agree with those obtained in suspensions with tracers released in the dead centre within 5 %. Both deviations were within the 90 % confidence intervals.

Based on the above discussion, we used the mean square displacement of tracers that are initially released at the centre of the suspension to compute the effective thermal diffusion coefficient. To examine the correlation between effective thermal diffusion and particle shear-induced diffusion, the particle diffusivity in the y direction is calculated using the approach that was discussed in § 2.2.1. We conducted 11 sets of simulations where ϕ was varied from 0.2 to 0.5 and the Péclet number from 28 to 128. For each set, five simulations with different initial particle configurations were used to provide a meaningful average. The numerical results will be presented and discussed in the next section together with the experimental data.

4. Results

4.1. *Thermal diffusion coefficients*

4.1.1. *Shear rate dependence*

Figure 9(*a*) shows the temperature evolution of the inner cylinder obtained at different shear rates for a suspension of volume fraction $\phi = 30\,\%$. The top curve corresponds to the zero shear rate experiment (suspension at rest). Then, when increasing the shear rate, the curves stack successively below each other; the larger the shear rate, the faster the temperature decay. The thermal diffusion coefficients, α, corresponding to the different shear rates, are directly estimated by fitting (2.3) to this set of data for times comprised between 15 and 90 s, see figure 9(*a*). The effective thermal diffusion coefficients, α^* (normalized by the thermal diffusion coefficient of the suspension at rest, $\alpha_0 = 1.6 \times 10^{-7}$ m^2 s^{-1}), are shown for the two particle sizes on figure 9(*b*). The trend indicates a linear dependence on the imposed shear rate. When α^* is plotted as a function of $\dot{\gamma} d^2$, the data collapse on the same master curve. The numerical results agree very well with the experimental data (see the inset to figure 9*b*).

Note that in the experiments for the 2 mm particles, the increase of the effective thermal diffusion coefficient is damped when $\alpha^* \geqslant 2.5$. We believe that this damping is an effect of the outer wall. When the effective thermal diffusion coefficient is large, heat diffuses quickly across the whole cell gap. With the outer wall being less conductive than the sheared suspension, the inner wall temperature decays slower than if the suspension were semi-infinite. As a result, fitting the temperature curve with (2.3) would lead to an underestimate of the thermal diffusion. Indeed, finite-element simulations describing the suspension first as semi infinite domain and then with an external wall validated this scenario.

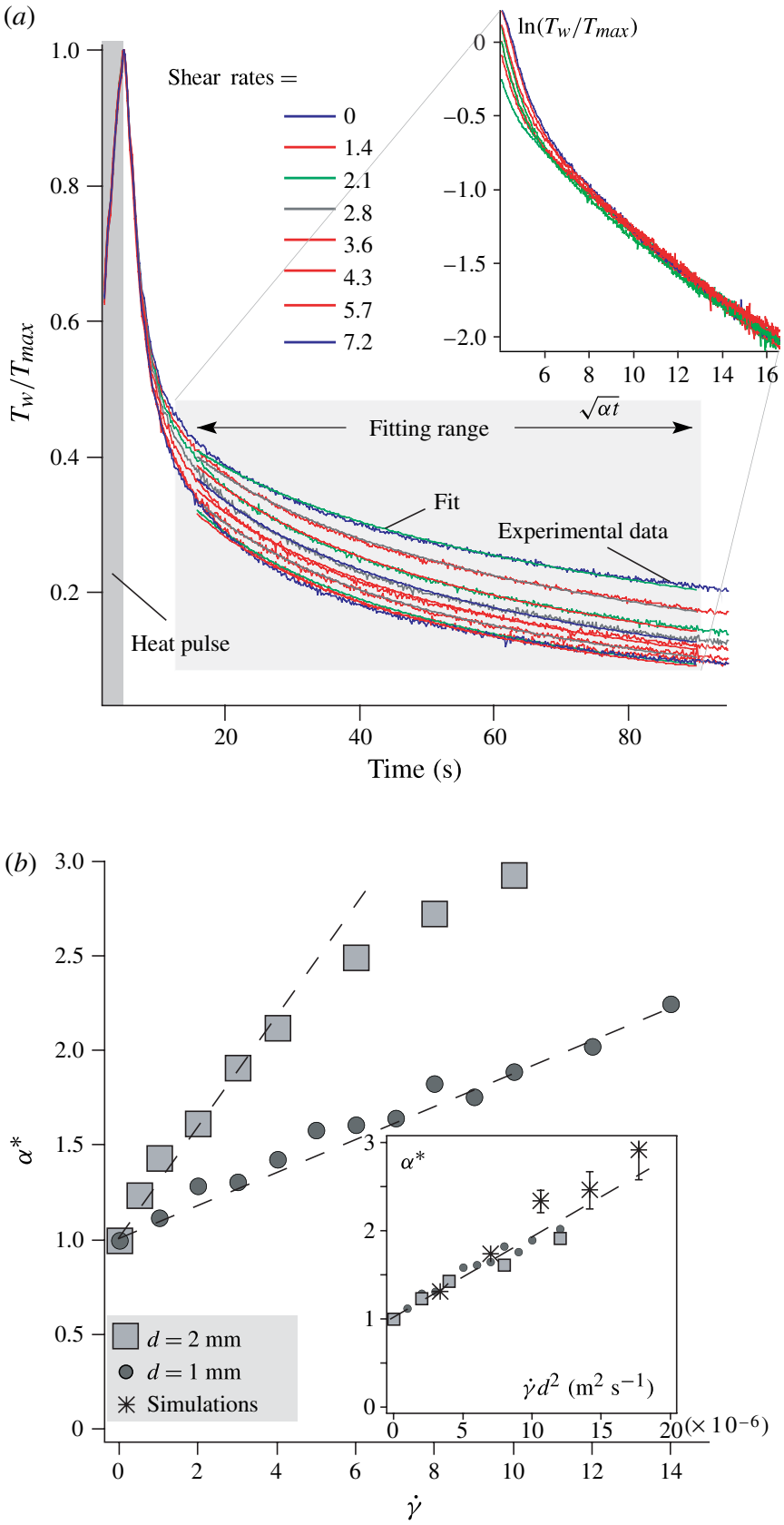


FIGURE 9. (Colour online) (*a*) Inner cylinder temperature versus time for different applied shear rates ($\phi = 35\,\%$). The continuous curves correspond to the fit using (2.3). Inset: $\ln(T_w/T_{max})$ versus $\sqrt{\alpha t}$. (*b*) Effective thermal diffusion coefficient, α^*, versus shear rate, $\dot{\gamma}$, for the two particle sizes. Inset: α^* versus $\dot{\gamma}d^2$.

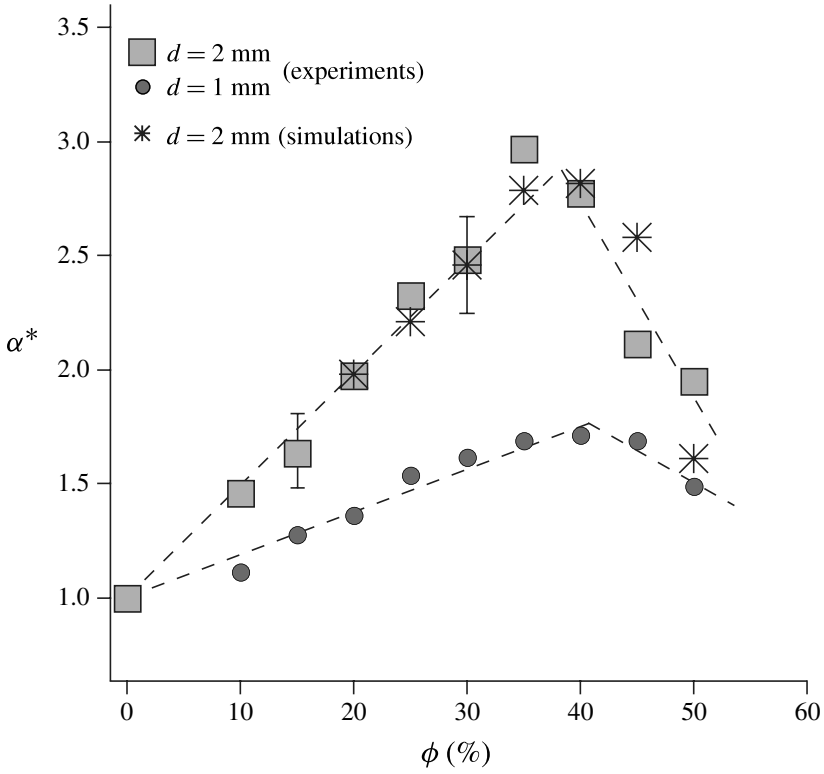


FIGURE 10. Effective thermal diffusion coefficient, α^*, versus volume fraction, ϕ.

The above results suggest that $\alpha = \alpha_0 + f(\phi)\dot{\gamma}d^2$. As expected (Wang *et al.* 2009), the effective thermal diffusivity $\alpha/\alpha_0 = f(Pe)$. In the next section, we will present the dependence of α on ϕ.

4.1.2. *Volume fraction dependence*

The evolution of the effective thermal diffusion coefficient as a function of the volume fraction is shown in figure 10. For the experiments, the shear rate was set to $\dot{\gamma} = 5$ s^{-1} and the volume fraction was increased from 5 to 50 % in steps of 5 %. To increase the volume fraction, the desired volume of fluid was removed from the suspension and the corresponding mass of particles was added to it. Prior to each experiment, the suspension was thoroughly mixed. For the simulations, the thermal Péclet number was set to 112, the same as that in the experiments, and the volume fraction was varied from 20 to 50 %.

For small volume fractions, $5 \leqslant \phi \lesssim 35$ %, the effective thermal diffusion coefficient is found to increase linearly with ϕ. However, it decreases dramatically for $\phi \gtrsim 35$ % when the 2 mm particles were used and for $\phi \gtrsim 40$ % when the 1 mm particles were used. We will discuss this transition later and focus presently on the linear regime ($\phi \lesssim 35$ %) where $f(\phi) = \beta\phi$. The effective thermal diffusion coefficient can be written as

$$\alpha^* = 1 + \beta\phi Pe, \tag{4.1}$$

where $\beta = 0.046$ and $Pe = \dot{\gamma}d^2/\alpha_0$. The data collected for the two particle sizes ($d = 1$ and 2 mm), for the different shear rates ($\dot{\gamma} = [0\text{–}12]$ s^{-1}), for the different volume fractions ($\phi = [0.05\text{–}0.40]$) and from the simulations, can all be very well described by this equation (see figure 11).

To discuss the transition of the effective heat diffusion coefficient at large ϕ, we need to examine the hydrodynamics of particles and their diffusive behaviour.

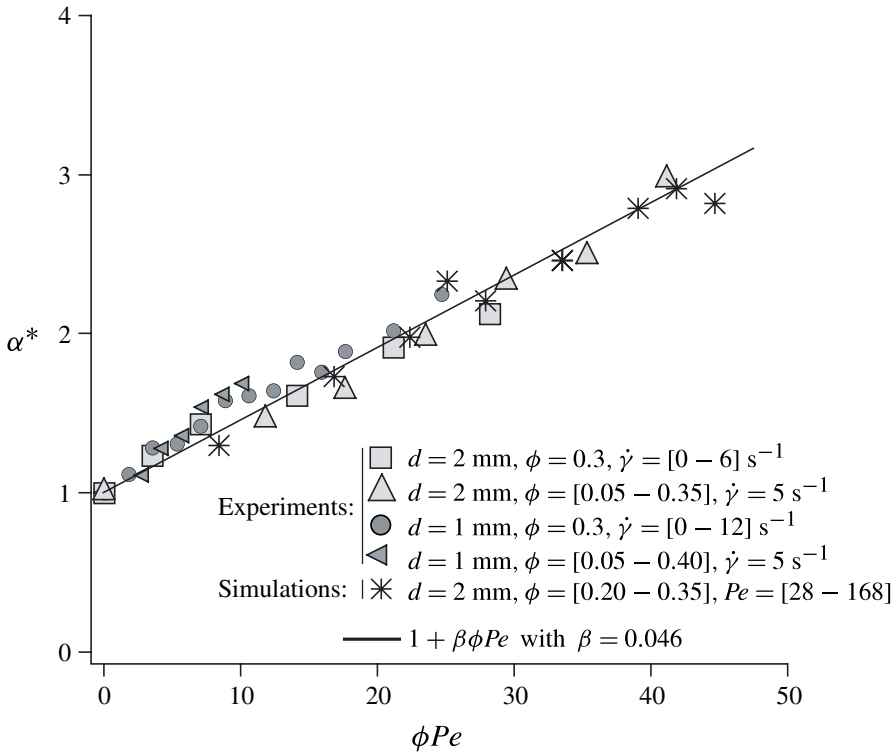


FIGURE 11. All data, experimental and numerical, collected for the two particle sizes ($d = 1$ and 2 mm), for the different shear rates ($\dot{\gamma} = [0–12]$ s^{-1}), and for the different volume fractions ($\phi = [0.05–0.40]$) as a function of ϕPe.

4.2. *Particle diffusion coefficients*

4.2.1. *Particle trajectories*

Examples of experimentally measured particle trajectories from which the affine motion was removed are shown in figure 12(*a*). For $\phi = 30\,\%$, trajectories are akin to an anisotropic random walk (with $D_{xx} > D_{yy}$). The corresponding probability distribution function (p.d.f.) of the particle displacement is close to Gaussian. Large particle displacements are better described by an exponential distribution. As in many complex physical systems (Kadanoff 2001; Drazer *et al.* 2002), p.d.f.s exhibit exponential tails; this behaviour is not clearly understood. For $\phi = 50\,\%$, particle trajectories are qualitatively different. It is highly confined in the y direction and particles are trapped for long times in cages. These events are highlighted by arrows on figure 12(*a*). This accumulation of very small displacements results in an exponential p.d.f. with a large probability of small displacements.

4.2.2. *Particle diffusion coefficients*

The particle diffusion coefficients in the gradient direction are plotted in figure 13 as functions of the volume fraction, ϕ. We also included two recently obtained data sets: one by Breedveld *et al.* (2002) who performed experiments using cone-and-plate rheometry, and another by Sierou & Brady (2004) who used Stokesian dynamics simulations. Our experimental data are in good agreement with Breedveld *et al.* (2002) at low volume fractions ($\phi < 0.4$), and our simulation results agree well with Sierou & Brady (2004) for $\phi < 0.35$. Still, there is a persisting difference between the experimentally measured diffusion coefficients and those from numerical simulations. Sierou & Brady (2004) proposed that the coefficients obtained by Breedveld *et al.* (2002) are larger because measurements were limited to small

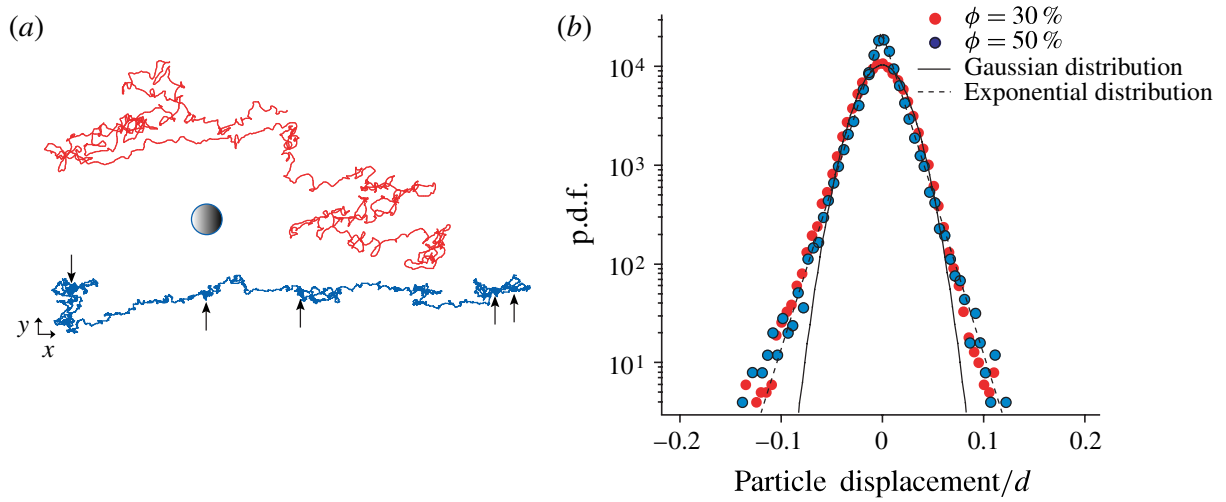


FIGURE 12. (Colour online) (*a*) Non-affine particle trajectories: (top) $\phi = 30\,\%$ and (bottom) $\phi = 50\,\%$. One particle is drawn to provide the length scale. Arrows indicate caging regions. (*b*) The p.d.f. of the particle displacements normalized by their radius.

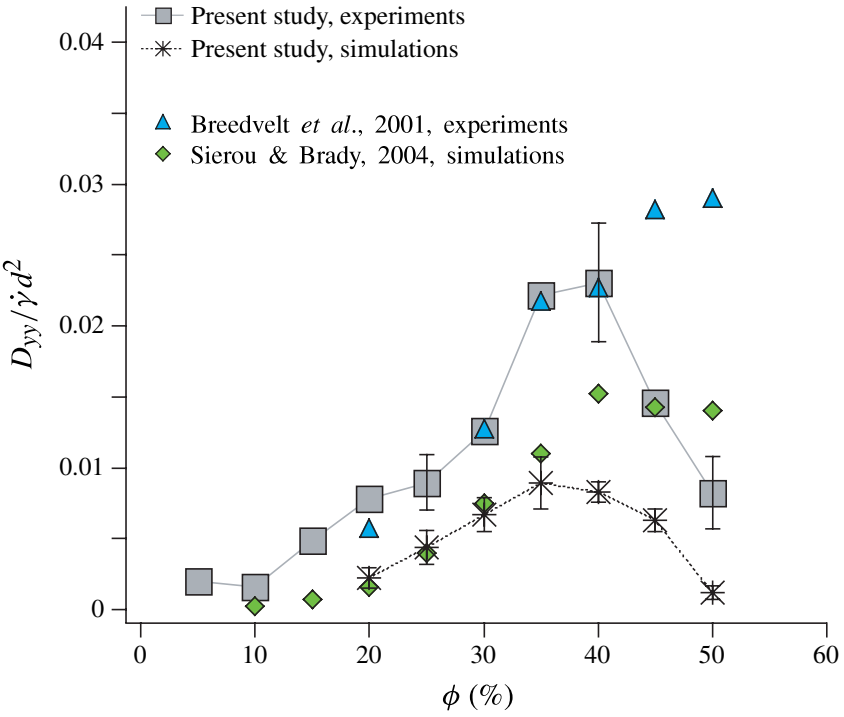


FIGURE 13. (Colour online) Normalized particle diffusion coefficient in the gradient direction, $D_{yy}/\dot{\gamma}d^2$, as a function of the volume fraction. Comparison is made to previous experiments and numerical simulations. The statistical uncertainty was evaluated as the standard deviation of the diffusivity coefficients obtained from nine independent runs.

strains where the diffusive motion was not yet fully established. In the present study, although the measurements were performed for larger strains, the diffusivities obtained experimentally are still about twice as large as the values obtained in simulations. We performed the fit on the simulations results using the same limited strain range as in the experiment ($2 < \dot{\gamma}t < 7$). However, reducing the strain range could not account for the quantitative difference between experiments and simulations. The persisting

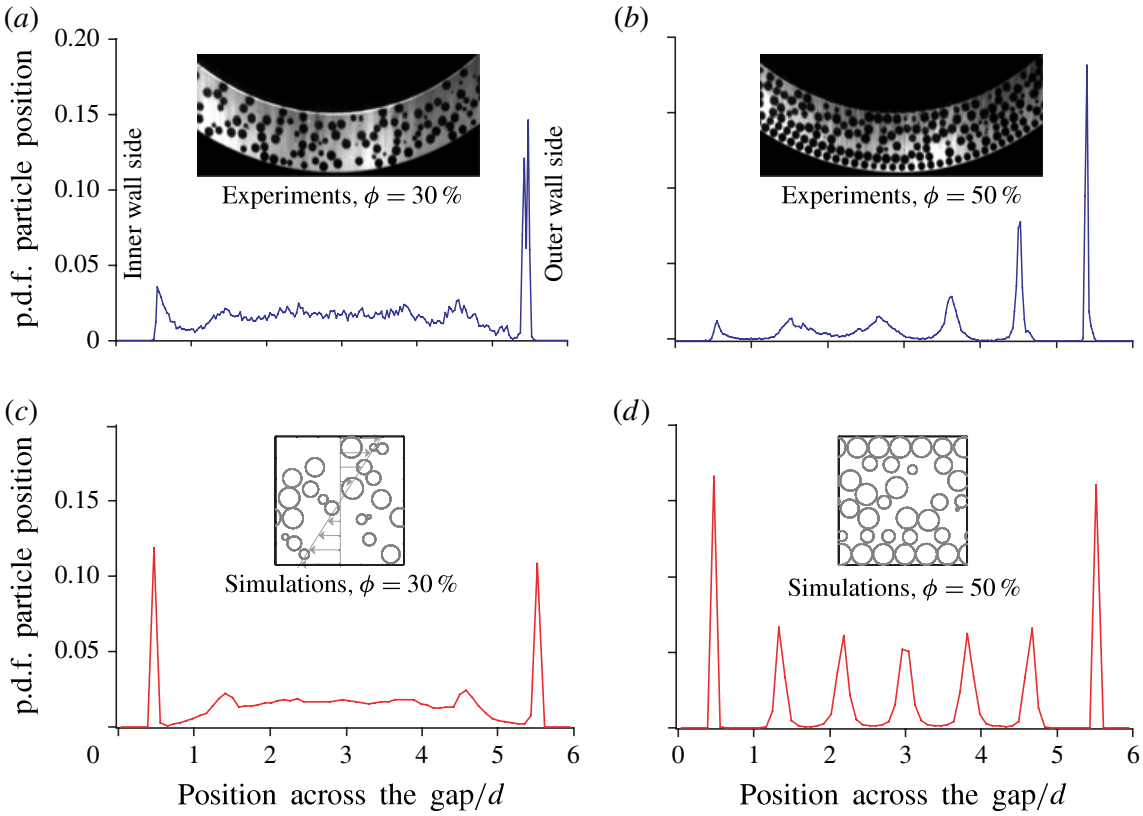


FIGURE 14. (Colour online) P.d.f.s of the particle position across the gap of the cell for (a,c) $\phi = 30\,\%$ and (b,d) $\phi = 50\,\%$. Images of the experiments and of the simulations show the corresponding state of the suspension.

difference may be due to the geometry of the flow set-up. In Couette cells, we have a stronger effect of curvature than in a cone-and-plate set-up that might have amplified the diffusion in the direction perpendicular to the mean flow, whereas in simulations there is no such effect.

The important feature is that at large ϕ, the particle diffusion coefficients dramatically decrease with increasing ϕ both in experiments and simulations (see figure 13). This behaviour results from a substantial change in the particle microstructure: particles organize into layers. This trend can be seen on figure 14: at moderate ϕ the p.d.f. of the particle positions within the bulk is homogeneous both in experiments and simulations. Conversely, at 50 %, particles within the bulk form layers that can be identified on the distributions by large regular peaks. In experiments, the curvature of the Couette cell causes an asymmetry in the particles' distribution.

The formation of layers at large ϕ is a common feature in monodisperse systems with strong confinement, see Yeo & Maxey (2010). This self-organization is the sign of important steric frustration within the system. The ability of particles to move around is damped and as a result the particle diffusion coefficients decrease. Breedveld *et al.* (2002) and Sierou & Brady (2004) did not observe as significant damping as observed in our studies at high volume fractions; this is presumably caused by the smaller gap-to-particle ratio used in our experiments and simulations.

4.3. *Correlation between thermal and particle diffusion coefficients*

In figure 15, particle and thermal diffusion coefficients are compared directly. The similarity in the shapes shows the correlation between the shear-induced diffusion

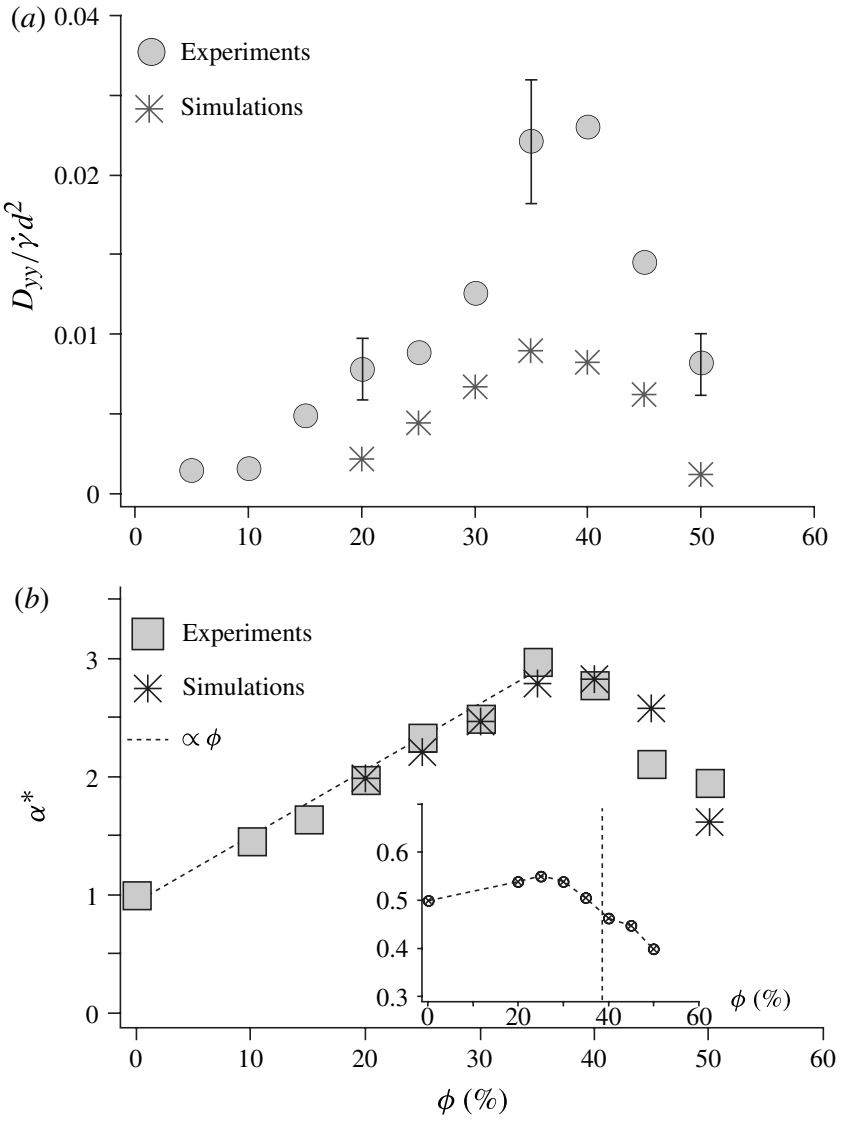


FIGURE 15. (*a*) Normalized particle diffusion coefficient, $D_{yy}/\dot{\gamma}d^2$ and (*b*) effective thermal diffusion coefficient, α^*, as a function of the volume fraction, ϕ. Inset: averaged dimensionless angular velocity of the particles, $\langle\omega/\dot{\gamma}\rangle$, versus ϕ.

motion of the particles and the effective thermal properties of the suspension. From low to moderate volume fractions, both particle and thermal diffusion coefficients increase with ϕ up to an optimum reached for $\phi = 40\,\%$. Above that critical volume fraction, where the system organizes into layers, the particle diffusion motion is significantly damped and as a consequence the effective thermal diffusion coefficient of the suspension decreases.

Previously, it has been speculated (Ahuja 1975*a*,*b*) that rotation of particles and the associated centrifuging action of the streamlines due to fluid inertia are the primary mechanism to enhance thermal diffusion in sheared suspensions. In the present study which concerns low Reynolds number flows, we found no correlation between the averaged dimensionless angular velocity of the particles, $\langle\omega/\dot{\gamma}\rangle$, (measured from simulations only) and the suspension thermal diffusion properties, see insert of figure 15. The particle average angular velocity slightly increases at low ϕ similar to the behaviour found in Drazer *et al.* (2004). However, it clearly starts to decrease (at $\phi = 25\,\%$) before the effective thermal diffusion coefficient decreases (at $\phi = 40\,\%$).

This result suggests that particle rotation does not have a significant influence on the suspension transfer properties.

Note that though the correlation between particle and thermal diffusion coefficients is striking, it is not possible, in the low to moderate ϕ range, to conclude whether both scale the same way with volume fraction. Even though the linear scaling of α^* is rather clear, we cannot say if $D_{yy}/\dot{\gamma}d^2$ scales linearly or quadratically with ϕ. Although some studies support a quadratic growth of the particle diffusion coefficient with the volume fraction (Drazer *et al.* 2002; Sierou & Brady 2004), the trend is not completely established since other studies suggest a linear dependence (Da Cunha & Hinch 1996; Beimfohrs, Biemfohrs & Leighton 2002) and in simulations the scaling is found to depend on the strength of the implemented repulsive force (Wang, Mauri & Acrivos 1998).

5. Summary and discussion

By using a combination of experiments and numerical simulations, we have investigated the effect of shear-induced diffusion on the transfer of heat across sheared suspension of non-Brownian particles. Experiments were conducted in a Couette cell where the effective thermal diffusion coefficients were extracted from the decay of a heat pulse applied to a bounding wall. Numerical simulations used a combination of the lattice Boltzmann method for the particle-laden flow and Brownian passive tracers for the advection–diffusion transport; the mean square displacements of tracers were used to directly compute the effective thermal diffusivity. The influence of particle size, particle volume fraction and applied shear were examined systematically.

The effective thermal diffusivity was found to be proportional to the Péclet number $Pe = \dot{\gamma}d^2/\alpha_0$ for moderate Pe ($\leqslant$100). We also found that in suspensions with low to moderate solid volume fractions ($\phi \leqslant 0.4$) the enhanced thermal transport increases linearly with increasing ϕ, leading to the following correlation

$$\frac{\alpha}{\alpha_0} = 1 + \beta\phi Pe, \tag{5.1}$$

where $\beta = 0.046$ based on experimental and numerical data.

The proposed scaling (5.1) is consistent with the empirical correlation of Wang & Keller (1985) ($\alpha^* \propto Pe^{0.89}$) and with the results of Shin & Lee (2000) who found a linear increase of the effective thermal diffusivity with shear rate for moderate Péclet numbers. Discrepancies with other proposed scaling presumably stem from the complicated nature of the phenomenon being studied and more precisely from the wide range of experimental conditions (soft or anisotropic particles versus hard spheres, inertial versus low-Reynolds-number flows and Poiseuille versus quasi-linear shear flows).

At large volume fraction ($\phi \geqslant 0.4$), we found the thermal diffusivity decreases as the volume fraction increases. By using an index-matched suspension and a laser-induced fluorescence technique, we were able to measure individual particle trajectories and show that the decrease of the thermal diffusion coefficient is caused by the decrease of the particle diffusion motion. At large volume fraction, steric effects reduce the ability of the particles to move around and force the particles to self-organize into layers: the particle diffusion coefficient decreases which in turn reduces the effective thermal diffusion coefficient of the suspension. There is thus an optimum volume fraction at which the transfer enhancement is maximized. For the experiments performed with

the 2 mm particles, the maximum was reached for $\phi \approx 40\,\%$ and the enhancement was $\sim 200\,\%$.

The passive Brownian tracer algorithm used in the simulations gave results in very good agreement with experiments. Simulations also allowed us to measure the average rotation velocity of the particles and showed that this quantity is not correlated with the thermal transport properties across the suspension. This suggests that the driving mechanism for enhancing the transport is the particle translational diffusion.

Nevertheless, many fundamental issues remain to be answered. (i) How to link the particle diffusivity, i.e. the microscopic quantity at the origin of the enhancement, to the macroscopic thermal diffusion coefficient is still an open question. One simple approach to estimate the thermal diffusivity enhancement is to write

$$\alpha^* - 1 \propto \phi D^*_{yy} + (1-\phi) D^*_{fluid}, \tag{5.2}$$

as both the particle diffusion D^*_{yy} and the fluid phase diffusion D^*_{fluid} contribute to enhancing the transfer of heat. Since the fluid phase diffusivity (arising from shear-induced diffusion) $D^*_{fluid} \approx D^*_{yy}$ (Zydney & Colton 1988), therefore $\alpha^* - 1 \propto D^*_{yy}$. If the particle diffusivity D_{yy} scales linearly with ϕ, then $\alpha^* - 1$ should also be linear in ϕ in agreement with (5.1). Now if D_{yy} scales quadratically with the volume fraction, this model fails to explain the observed linear scaling. At this point, the problem is that the dependence of D_{yy} with ϕ is not clearly established in the literature. We thus plan a thorough experimental study to determine the precise dependence of the particle diffusion coefficient with volume fraction. (ii) The linear dependence for the thermal diffusion coefficient with the Péclet number predicts well the thermal diffusion coefficient in the range of data we were able to investigate ($0 < Pe \lesssim 100$). However, one expects the effective diffusivity to always bear the memory of the molecular one, even at large Péclet number (Villermaux 2012); the scaling should thus follow the form $\alpha/\alpha_0 \propto Pe^n$ with $n < 1$. If we fit all of the data of figure 11 letting the exponent free to vary, one obtains $\alpha/\alpha_0 \propto Pe^{0.88}$ which is close to a linear dependence. We plan a better determination of this scaling by performing mass transfer experiments using the same configuration. Since the molecular diffusion of mass is much smaller than that of heat, we should be able to reach much larger values of the Péclet number and thus be able to determine with a higher accuracy the trend followed by the effective diffusivity.

Acknowledgements

We are grateful to P. Cervetti and S. Martinez for building the experimental set-up, J. Duplat for suggesting the wall temperature model, S. Barboza for the scanning electron microscopy images of the particles and J. E. Butler for discussions. The project was funded by ANR JCJC SIMI 9 and IC-Star.

Supplementary movies

Supplementary movies are available at http://dx.doi.org/10.1017/jfm.2013.173.

Appendix. Investigation of the homogeneity assumption using finite difference simulations

As mentioned previously, equation (2.3) assumes that the sheared suspension is homogeneous. It is well known, however, that particle hydrodynamic diffusion vanishes near the wall. In this appendix, we use a finite difference method to solve the

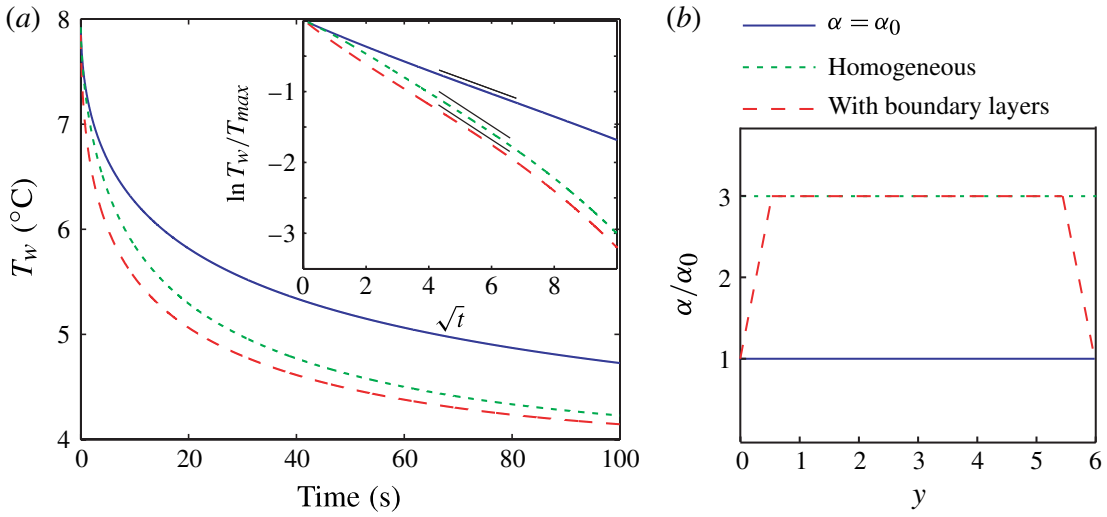


FIGURE 16. (Colour online) (*a*) Finite difference solutions of wall temperature versus time: solid line $\alpha = \alpha_0$; the dotted line $\alpha = 3\alpha_0$; the dashed line was calculated by assuming inhomogeneities in the effective thermal diffusion near the walls. Inset: same data using different scales. (*b*) Thermal diffusivity profiles used in the simulations, where y is the position across the gap.

coupled heat transfer problem in the experimental cell to illustrate the validity of (2.3). The finite difference scheme used is second-order accurate in space, and first-order accurate and fully implicit in time.

The heat transfer equation

$$\frac{\partial T}{\partial t} = \alpha \frac{\partial^2 T}{\partial x^2} \tag{A 1}$$

was solved in both the copper wall (-1.5 mm $< x < 0$) where $\alpha_w = 1.16 \times 10^{-3}$ m^2 s^{-1}, and in the suspension ($0 < x < 12$ mm) where $\alpha_0 = 1.6 \times 10^{-7}$ m^2 s^{-1}. The boundaries at $x = -1.5$ mm and $x = 12$ mm are insulated, i.e. $\partial T/\partial x = 0$.

The solution indicates that the temperature gradient inside the wall is negligible due to the high contrast in the thermal diffusivity. It is also observed in the inset of figure 16 that the decrease in the dimensionless wall temperature $\ln(T_w/T_{max})$ scales as $-A\sqrt{t}$ in the period of $t < 100$ s, with a coefficient of $A_0 = 0.164$. Note that this scaling is precisely that proposed in (2.3) and that it also matches the experimental collapse found in the inset of figure 9(*a*).

First, we assumed that the effective thermal conductivity of the suspension is uniformly increased to $\alpha = 3\alpha_0$. The factor of three is based on the maximum enhancement in the effective thermal diffusion observed in this study. The dimensional and dimensionless wall temperature are shown in figure 16. It is observed that $\ln(T_w/T_{max})$ follows the scaling of $-A\sqrt{t}$, with a coefficient of $A = 0.284$ when $t < 40$ s. We indeed obtain that $\alpha/\alpha_0 = (A/A_0)^2 = 3$, which indicates that (2.3) can be used to find the effective thermal diffusivity. We then added inhomogeneities into the suspension by letting α linearly vary from α_0 at the wall locations ($x = 0$ and $x = 12$ mm) to $\alpha = 3\alpha_0$ at $0.5d$ from the walls (see the thermal diffusivity profiles on figure 16*b*). It turns out that with this inhomogeneity, $\ln(T_w/T_{max})$ has the same slope, A, as the homogeneous suspension. Boundary heterogeneity effects are thus weak and (2.3) can be used to fit the experimental results obtained in the present study.

REFERENCES

AHUJA, A. S. 1975*a* Augmentation of heat transport in laminar flow of polystyrene suspensions. I. Experiments and results. *J. Appl. Phys.* **48**, 3408–3416.

AHUJA, A. S. 1975*b* Augmentation of heat transport in laminar flow of polystyrene suspensions. II. Analysis of the data. *J. Appl. Phys.* **48**, 3417–3425.

ARP, P. A. & MASON, S. G. 1976 The kinetics of flowing dispersions IX. Doublets of rigid spheres (experimental). *J. Colloid Interface Sci.* **61** (4095), 44–61.

BEIMFOHRS, LOOBY T., BIEMFOHRS, S. & LEIGHTON, D. T. 2002 Measurement of shear-induced coefficient of self-diffusion in dilute suspensions. In *Proc. DOEINSF Workshop on Flow of Particles and Fluids*, Ithaca, NY.

BISHOP, J. J., POPEL, A. S., INTAGLIETTA, M. & JOHNSON, P. C. 2002 Effect of aggregation and shear rate on the dispersion of red blood cells flowing in venules. *Am. J. Physiol. Heart Circ. Physiol.* **283**, 1985–1996.

BREEDVELD, V., VAN DEN ENDE, D., BOSSCHER, M., JONGSCHAAP, R. J. J. & MELLEMA, J. 2002 Measurement of the full shear-induced self-diffusion tensor of noncolloidal suspensions. *J. Chem. Phys.* **116**, 10529–10535.

DA CUNHA, F. R. & HINCH, E. J. 1996 Shear-induced dispersion in a dilute suspension of rough spheres. *J. Fluid Mech.* **309**, 211–223.

DAITCHE, A. & TÉL, T. 2009 Dynamics of blinking vortices. *Phys. Rev.* E **79**, 016210.

DEBOEUF, A., GAUTHIER, G., MARTIN, J., YURKOVETSKY, Y. & MORRIS, J. F. 2009 Particle pressure in a sheared suspension: a bridge from osmosis to granular dilatancy. *Phys. Rev. Lett.* **102**, 108301.

DRAZER, G., KOPLIK, J., KHUSID, B. & ACRIVOS, A. 2002 Deterministic and stochastic behaviour of non-Brownian spheres in sheared suspensions. *J. Fluid Mech.* **460**, 307–335.

DRAZER, G., KOPLIK, J., KHUSID, B. & ACRIVOS, A. 2004 Microstructure and velocity fluctuations in sheared suspensions. *J. Fluid Mech.* **511**, 273–363.

ECKSTEIN, E. C., BAILEY, D. G. & SHAPIRO, A. H. 1977 Self-diffusion of particles in shear flow of a suspension. *J. Fluid Mech.* **79**, 191–208.

ELRICK, D. E. 1962 Source functions for diffusion in uniform shear flow. *Austral. J. Phys.* **15**, 283–288.

HINCH, E. J. 2003 Mixing, turbulence and chaos – an introduction. In *Mixing: Chaos and Turbulence* (ed. H. Chaté, E. Villermaux & J.-M. Chomaz), NATO ASI Series, vol. 373. Kluwer Academic/Plenum Publishers.

KADANOFF, L. P. 2001 Turbulent heat flow: structures and scalings. *Phys. Today* **54**, 34–39.

LADD, A. J. C. 1994*a* Numerical simulations of particulate suspensions via a discretized Boltzmann equation. Part 1. Theoretical foundation. *J. Fluid Mech.* **271**, 285–309.

LADD, A. J. C. 1994*b* Numerical simulations of particulate suspensions via a discretized Boltzmann equation. Part 2. Numerical results. *J. Fluid Mech.* **271**, 311–339.

LADD, A. J. C. & VERBERG, R. 2001 Lattice-Boltzmann simulations of particle–fluid suspensions. *J. Stat. Phys.* **104**, 1191–1251.

LEIGHTON, D. & ACRIVOS, A. 1987 Measurement of shear-induced self-diffusion in concentrated suspensions of spheres. *J. Fluid Mech.* **177**, 109–131.

LIN, S. X. Q., CHEN, X. D., CHEN, Z. D. & BANDOPADHAYAY, P. 2002 Shear rate dependent thermal conductivity measurment of two fruit juice concentrates. *J. Food Sci.* **43**, 4275–4284.

NGUYEN, N.-Q. & LADD, A. J. C. 2002 Lubrication corrections for lattice-Boltzmann simulations of particle suspensions. *Phys. Rev.* E **66**, 046708.

PENG, T. 2005 Detect circles with various radii in grayscale image via Hough Transform (updated 17 November 2010) http://www.mathworks.com/matlabcentral/fileexchange/9168-detect-circles-with-various-radii-in-greyscale-image-via-hough-transform.

SELVA, B., DAUBERSIES, L. & SALMON, J.-B. 2012 Solutal convection in confined geometries: enhancement of colloidal transport. *Phys. Rev. Lett.* **108**, 198303.

SHIN, S. & LEE, S. 2000 Thermal conductivity of suspensions in shear flow fields. *Intl J. Heat Mass Transfer* **43**, 4275–4284.

SIEROU, A. & BRADY, J. F. 2004 Shear-induced self-diffusion in non-colloidal suspensions. *J. Fluid Mech.* **506**, 285–314.

SOHN, C. W. & CHEN, M. M. 1981 Microconvective thermal conductivity in disperse two-phase mixtures as observed in a low velocity Couette flow experiment. *Trans. ASME J. Heat Transfer* **103**, 47–51.

STROOCK, A. D., DERTINGER, S. K. W., AJDARI, A., MEZIC, I., STONE, H. A. & WHITESIDES, G. M. 2002 Chaotic mixer for microchannels. *Science* **295**, 647–651.

VERBERG, R. & KOCH, D. L. 2006 Rheology of particle suspensions with low to moderate fluid inertia at finite particle inertia. *Phys. Fluids* **18**, 083303.

VILLERMAUX, E. 2012 On dissipation in stirred mixtures. *Adv. Appl. Mech.* **45**, 91–107.

WANG, N. L. & KELLER, K. H. 1985 Augmented transport of extracellular solutes in concentrated erythrocyte suspensions in couette flow. *J. Colloid Interface Sci.* **103**, 210–225.

WANG, L., KOCH, D. L., YIN, X. & COHEN, C. 2009 Hydrodynamic diffusion and mass transfer across a sheared suspension of neutrally buoyant spheres. *Phys. Fluids* **21**, 033303.

WANG, Y., MAURI, R. & ACRIVOS, A. 1998 Transverse shear-induced gradient diffusion in a dilute suspension of spheres. *J. Fluid Mech.* **357**, 279–287.

YEO, K. & MAXEY, M. R. 2010 Ordering transition of non-Brownian suspensions in confined steady shear flow. *Phys. Rev.* E **81**, 051502.

YOUNG, W. R., RHINES, P. B. & GARRET, C. J. R. 1982 Shear flow dispersion, internal waves and horizontal mixing in the ocean. *J. Phys. Oceanogr.* **12**, 515–527.

ZILZ, J., POOLE, J., ALVES, M. A., BARTOLO, D., LEVACHÉ, B. & LINDNER, A. 2011 Geometric scaling of purely-elastic flow instabilities. *Cond. Mat.* 1109.5046v1.

ZYDNEY, A. L. & COLTON, C. K. 1988 Augmented solute transport in the shear flow of a concentrated suspension. *Physico Chem. Hydro.* **10**, 77–96.

PHYSICAL REVIEW FLUIDS **1**, 042001(R) (2016)

Taylor's experiment in a periodically sheared particulate suspension

Mathieu Souzy,[1] Phong Pham,[1,2] and Bloen Metzger[1]
[1]*Aix-Marseille Université, IUSTI-CNRS UMR 7343, 13453 Marseille Cedex 13, France*
[2]*Department of Chemical Engineering, University of Florida, Gainesville, Florida 32611, USA*
(Received 15 April 2016; published 5 August 2016)

We revisit Taylor's experiment investigating the evolution of a blob of dye in a periodically sheared suspension of non-Brownian particles. Above a critical strain amplitude, particulate suspensions are subject to phase transition where reversibility is lost and particles fail to return to their original positions. We investigate the effect of this transition on the dispersion of a blob of dye. Beyond the critical strain, the dispersion of the blob is found to increase significantly. The dispersion coefficient of the blob of dye is measured and compared to the self-diffusivity coefficient of the particles.

DOI: 10.1103/PhysRevFluids.1.042001

In 1966, Taylor illustrated in a now famous experiment the reversibility of Stokes flow [1]. A blob of dye is initially injected in a Couette cell filled with a very viscous and Newtonian fluid. When rotating one of the cylinder, the fluid is linearly sheared and the blob of dye stretches into a thin filament until almost disappearing. Then, upon reversing the rotation for the same number of turns, the drop astoundingly recovers its initial shape (except for slight blurring due to molecular diffusion).

Inspired by Taylor's work, we performed the exact same experiment but in a suspension of non-Brownian particles to investigate how the presence of particles within the fluid breaks the reversibility of the flow and influences the dispersion process of the blob of dye. Under periodic shear, Pine *et al.* [2] demonstrated that non-Brownian suspensions undergo a dynamical phase transition. For a given particulate volume fraction and a small enough strain amplitude, the suspension relaxes to an absorbing reversible state in which particles return to their original position after every cycle of shear. However, when the strain amplitude exceeds a critical value γ_c, which depends on the volume fraction and the particle roughness [3], the suspension transitions to a fluctuating state: the particles do not return to their original positions, and, when tracked stroboscopically at the end of each cycle of shear, the particles exhibit large fluctuations analogous to a random walk. In that fluctuating state, the loss of reversibility of the particles motion should also induce a loss of reversibility in the fluid motion. The goal in the present Rapid Communication is to perform Taylor's experiment in a particulate suspension to study the effect of this transition on the dispersion of the blob of dye.

Under continuous shear, the phenomenon called "shear-induced diffusion", which was widely investigated [3–10], was shown to significantly enhance the transfer of heat [9,11] or mass [12,13] across suspensions of non-Brownian particles. This enhancement occurs since under shear, particles within the fluid constantly collide with one another and change streamlines. The particles thus generate disturbances within the fluid which promote the dispersion of the scalar (temperature or concentration), prelude to its subsequent mixing. Particles also significantly affect transfers close to boundaries: the particle rotation was shown to disrupt the diffusive boundary layer by a "rolling-coating effect" (Souzy *et al.* [13]) which convects the scalar at a constant rate from the wall, where it is injected, to the bulk of the suspension.

The dispersion enhancement of a scalar field has already been exensively studied in suspensions undergoing a continuous shear flow, but it has not yet been studied under periodic shear. Our motivation is that this latter flow configuration is particularly appealing since, after each cycle of shear, the affine part of the flow (the reversible part) cancels out. Therefore, by measuring the evolution of the blob of ink stroboscopically, i.e., at the end of each cycle of shear, one can investigate the blob's dispersion solely focusing on the effect of the fluctuations induced by the particles, not having to account for the background linear stretching as in a continuous shear.

 ©2016 American Physical Society

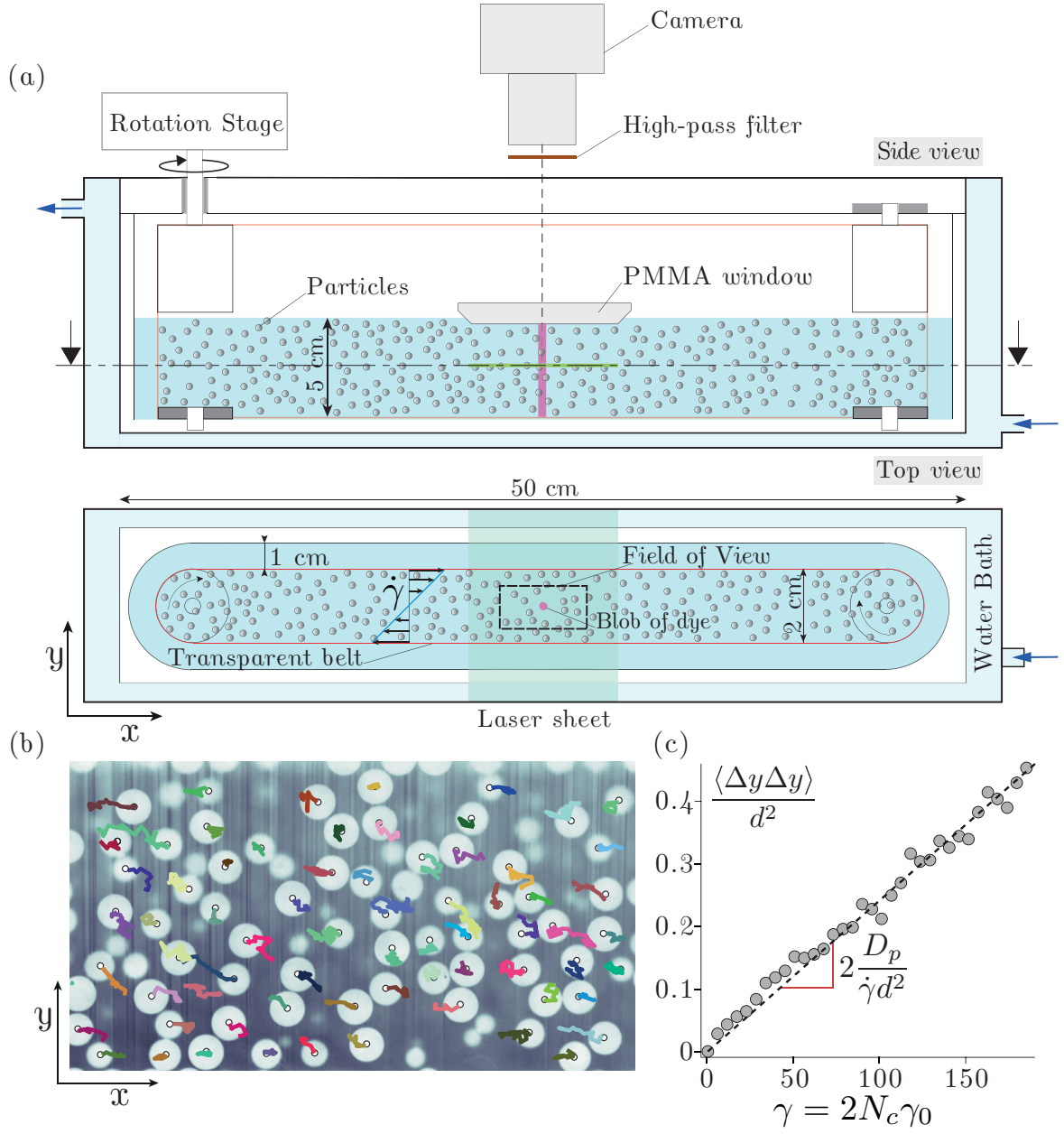


FIG. 1. (a) Schematic of the setup, top and side views. (b) Image of the suspension seen from the top (particles appear as white discs) and stroboscopic particle trajectories for cycles of shear of strain amplitude $\gamma_0 = 2.8$. (c) Corresponding particle mean square displacement versus total accumulated strain $\gamma = 2N_c\gamma_0$.

An original experimental setup was developed to perform direct visualizations of the dispersion of a blob of dye in a periodically sheared suspension of non-Brownian particles. By measuring the diffusion coefficients of both the particle and the fluid phases, we find that the blob's dispersion follows the same dynamical phase transition as the particles.

The experimental setup, shown in Fig. 1(a), consists of a transparent cell within which a transparent mylar belt, mounted tightly on two vertical rotating cylinders, generates a linear shear flow. A precision rotation stage drives the rotation of one of the vertical cylinders. The fluid is a Newtonian mixture of Triton X-100 (73.86 wt%), zinc chloride (14.24 wt%), and water (11.90 wt%), identical to that used in Souzy *et al.* [13]. Its viscosity $\eta = 3$ Pa s is large enough to ensure a viscous flow (Re $\approx 10^{-4}$), and its composition was chosen to match both the particle density ($\rho_f = \rho_p = 1.19\ \mathrm{g\,cm^{-3}}$) to avoid sedimentation and their optical index of refraction. A small amount of hydrochloric acid (≈0.05 wt%) is added to the solution to prevent the formation of zinc hypochlorite precipitate,

thereby significantly improving the optical transparency of the solution. The temperature of the setup is also adjusted ($\pm 0.05\,^{\circ}$C) with a water-bath jacket connected to a cryo-thermostat in order to finely tune index matching between the fluid and the particles. We use monodisperse spherical PMMA beads from Engineering Laboratories Inc. with a diameter $d = 2$ mm, which were chosen for their high surface quality and good transparency. Note that, above the region of interest, a small plexiglass window is placed on the free surface of the suspension to avoid its deflection during shear which would deteriorate the visualization. A small hole, through the window, is used to inject the blob of dye in the middle of the suspension with a thin needle. The molecular diffusion coefficient of the dye in the fluid at rest is $D_0 \approx 10^{-13}\,\mathrm{m^2\,s^{-1}}$ [14]. All experiments were done at a volume fraction of $\phi = 35\%$.

Two types of experiments were performed: (1) to follow the evolution of the blob of dye, the suspension is perfectly transparent and the blob consists in a small injection of fluid doped with a fluorescent tracer (rhodamine 6G), and (2) to track the particle motion, the whole fluid is homogeneously doped with the fluorescent dye. In both cases, visualization is performed from the top of the cell by imaging the rhodamine, which fluoresces under illumination provided by a thin horizontal laser sheet ($\approx 60\,\mu$m thick). Images are acquired using a high-resolution camera (Nikon D-300S). A high-pass filter ($\lambda > 590$ nm) is used to eliminate direct light reflections and collect the light solely emitted by the fluorescent rhodamine.

As presented in Fig. 1(b), when the whole fluid is doped with rhodamine, the particles within the light sheet appear as white discs, while the fluid is dark. Note that all the particles have the same size; the apparent size differences arises from their different vertical positions relative to the light plane. Images are first thresholded, then an algorithm of particle detection based on the circular Hough transform [9,15] is applied to find the center location of each particle within ± 1 pixel. Particles trajectories are then reconstructed by applying a tracking algorithm. A very important point is that for an experiment where periodic oscillations are performed at the strain amplitude γ_0, prior to injecting the blob or measuring the particle trajectories, the suspension is first presheared at that strain amplitude for 40 cycles in order to let the suspension self-organize into its steady-state configuration [16]. To track the particles, images are taken continuously every strain increment of 0.1, while for blob experiments, images are acquired only at the end of each cycle of shear. A cycle of shear consists in slowly shearing (at $0.1\ \mathrm{s^{-1}}$) the suspension forward for a strain γ_0, then shearing it backward to the initial position. For each experiment, N_c cycles of shear are performed, and the total accumulated strain is thus $\gamma = 2N_c\gamma_0$.

We first present results characterizing the dynamics of the particles. Trajectories of the particles are recorded continuously to be able to track particles from one cycle to the next. However, to quantify the amount of irreversibility, we compute the mean square displacement of the particles using only their positions at the end of each cycle. An example of such trajectories is represented in Fig. 1(b) for an experiment performed at large strain amplitude. The mean square displacement in the gradient (y) direction $\langle \Delta y \Delta y \rangle$, where $\Delta y = y(t) - y(t = 0)$ and the angle brackets denote an average over all particles, is close to zero for small applied strain amplitudes. This means that the particle motion is reversible. However, for experiments performed at larger strains, the mean square displacement increases linearly with time, indicating that the particles do not return to their original position and follow a diffusive behavior; see Fig. 1(c). Following Pine *et al.*, the slope of the particle mean square displacements is used to define a dimensionless particle diffusion coefficient $D_p^* = \langle \Delta y \Delta y \rangle / (2d^2\dot{\gamma}t)$, which quantifies the irreversible motion of the particles. We recover the results of Pine *et al.* that particles, beyond a critical strain amplitude of $\gamma_c \approx 2$ for the present volume fraction $\phi = 35\%$ (equivalent of $\gamma_c \approx 1$ with the definition of the strain amplitude used by Pine [2]), transit to a fluctuating state; see Fig. 4.

We now investigate the effect of this transition on the dispersion of a blob of dye. After pouring the suspension (without rhodamine) within the cell and preshearing it, a cylindrical blob of dyed fluid is injected at $t = 0$ and with the fluid at rest in the middle of the shear cell. The blob has an initial diameter $s_0 \simeq d$ and is aligned with the vorticity direction of the shear flow and centered on the neutral velocity plane. This results in a macroscopically two-dimensional initial configuration

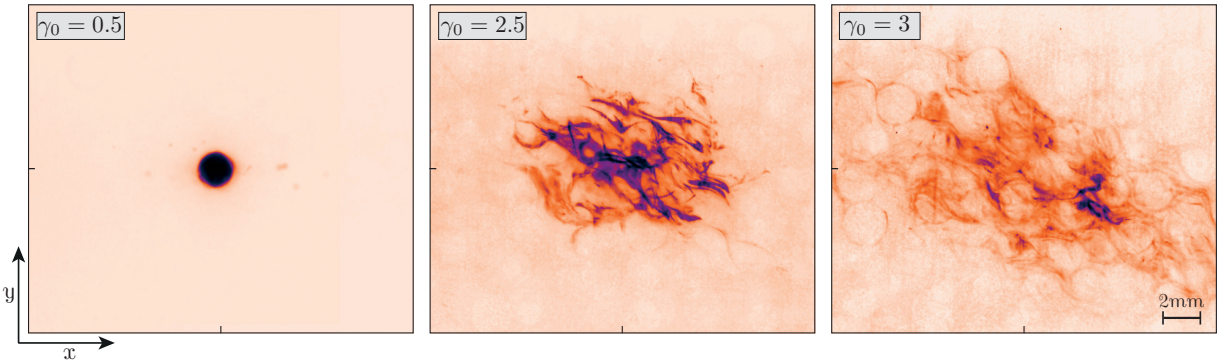


FIG. 2. Image of the blob after 40 cycles of shear performed at a strain amplitude: $\gamma_0 = 0.5$, $\gamma_0 = 2.5$, $\gamma_0 = 3$. Each image corresponds to the superposition of 10 pictures taken from 10 independent experiments performed at the same strain amplitude; see also Movie 1 and Movie 2 [18].

and ensures that the blob does not drift with the flow. The concentration of rhodamine within the blob was adjusted so that absorption of the light intensity can be neglected. The suspension is then slowly sheared back and forth over $N_c = 40$ cycles at the strain amplitude γ_0.

Figures 2(a)–2(c) show how the blob has evolved after 40 cycles of shear for experiments performed at different strain amplitudes. Note that each image is the superposition of pictures taken from 10 independent experiments performed with the same imposed strain amplitude. At small strain amplitude $\gamma_0 = 0.5$, as in Taylor's experiment, the blob after each cycle of shear recovers its initial shape; see Fig. 2(a). Conversely, for larger applied strain amplitudes, the blob rapidly spreads in the surrounding medium, evolving towards a topology constituted of filament-like structures [17] (to visualize the continuous evolution of the blob; see Movie 1 and Movie 2 [18]). Larger strain amplitudes result, after the same number of cycles, into a larger dispersion of the blob.

More quantitatively, we can characterize the blob effective dispersion by examining its spreading. Figure 3(a) shows successive concentration profiles obtained by averaging the light-intensity level along the x direction. The low concentration of rhodamine used for the experiments ensures a linear relation between light intensity and dye concentration. Two important observations can be made. First, the concentration distribution is normally distributed. The dashed curves are the best Gaussian fit where, once the amplitude of the initial distribution (for $N_c = 0$) is fixed, the sole remaining adjustable parameter is the standard deviation σ. Second, the relative variance of the concentration distribution $\Delta\sigma^2(t) = \sigma^2(t) - \sigma^2(t = 0)$ increases linearly with the total accumulated

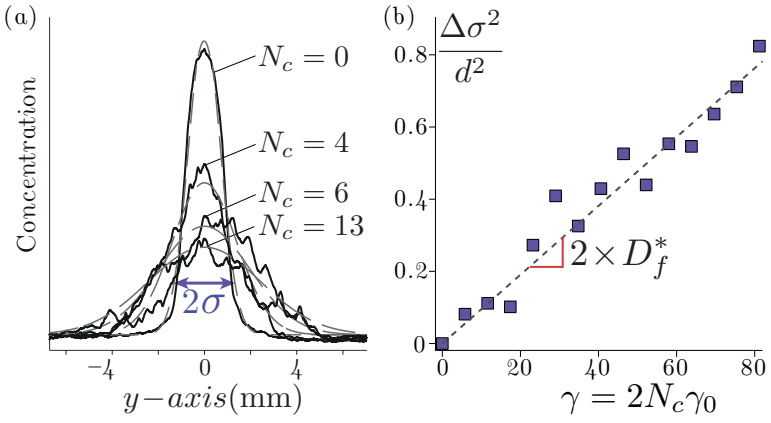


FIG. 3. (a) Successive concentration profiles for a blob submitted to a strain amplitude $\gamma_0 = 2.9$. The profiles are obtained by averaging over 10 independent runs. The dashed curves correspond to the best Gaussian fit. (b) Evolution of the corresponding dimensionless relative variance $\Delta\sigma^2/d^2$ as a function of the total accumulated strain $\gamma = 2N_c\gamma_0$.

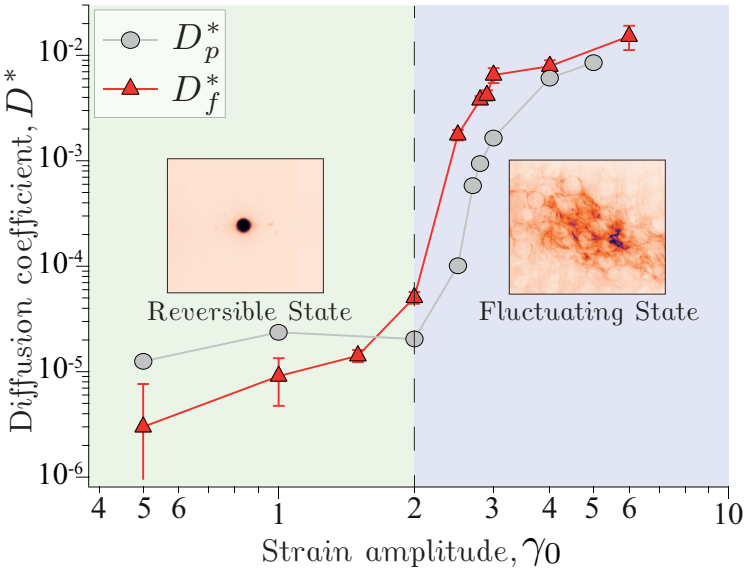


FIG. 4. Dimensionless self-diffusivity coefficient of the particle D_p^* and dimensionless dispersion coefficient of the fluid D_f^*, as a function of the applied strain amplitude γ_0. Reversibility is lost above a critical strain amplitude $\gamma_c \approx 2$.

strain $\gamma = 2N_c\gamma_0$ (equivalent to time); see Fig. 3(b). These two features evidence that the dispersion process of the blob, and thus of the interstitial fluid phase between the particles, is diffusive. The effective dispersion coefficient of the fluid phase is provided by the classical definition

$$\Delta\sigma^2 = 2D_f t. \tag{1}$$

The dimensionless effective dispersion coefficient of the fluid phase, D_f^*, can be defined by the dimensionless form of Eq. (1) ($\Delta\sigma^2/d^2 = 2\frac{D_f}{\dot{\gamma}d^2}\gamma$) as $D_f^* = D_f/\dot{\gamma}d^2$, which corresponds to one half the slope of the linear fits presented on Fig. 3(b). Error bars are also estimated from the typical standard deviation between runs; see Fig. 4.

Similarly to the behavior of the particles, for the volume fraction $\phi = 35\%$ investigated, above a critical strain $\gamma_c \approx 2$, the dispersion coefficient of the blob goes through an abrupt transition; see Fig. 4 where D_p^* and D_f^* are plotted versus the applied strain amplitude γ_0. The loss of reversibility induced by the presence of the particles significantly accelerates the dispersion process. Indeed, if one was only considering the effect of molecular diffusion, i.e., if the blob was sheared in a pure fluid without particle, the transverse dispersion coefficient of the dye would be $D_f = D_0$, leading to a dimensionless effective dispersion coefficient of the fluid phase, $D_f^* = D_0/\dot{\gamma}d^2 = 10^{-6}$. In the fluctuating state (beyond γ_c), the dimensionless dispersion coefficient of the fluid is $\approx 10^{-2}$, so about four orders of magnitude larger than that of molecular diffusion alone. Note that, as one can guess from Fig. 2, the dispersion coefficients in the flow direction (not shown here) follow very similar trends as those in the gradient direction.

For $\gamma_0 < \gamma_c$, in the so-called reversible state, we measure effective diffusion coefficients of $\approx 10^{-5}$ both for the particles and for the blob. For the particles, which are non-Brownian, D_p^* should vanish when $\gamma_0 \to 0$. This small discrepancy arises from experimental artifacts which are noise from the Hough detection algorithm (detection of the particle center locations within ± 1 pixel) and unavoidable slight sedimentation or natural convection currents within the fluid. In that limit, the latter two effects probably also bias the measurement of the blob dispersion coefficient. It is noteworthy that the measured self-diffusivity coefficient of the particles obtained at large strain amplitudes is in good agreement with previous measurements done in continuously sheared particulate suspensions [7,9]. Similarly, the enhancement of the dye diffusion coefficient at large applied strain amplitude is of the same order $\approx 10^4$ than in a continuously sheared suspension [13].

This result could be useful in certain mixing applications where oscillatory shear might be easier to implement than continuous shear [19].

The molecular diffusion coefficient of rhodamine 6G in the present suspending liquid is small ($D_0 \approx 10^{-13}$ m^2 s^{-1}). In such a condition of large Péclet number, Pe $= \dot{\gamma} d^2/D_0 = 10^6$, (with $s_0 \simeq d$) where the effect of molecular diffusion is negligible relative to the fluctuations induced by the presence of the particles [5,20], the measurement of the dye-effective dispersion coefficient provides a good estimate of the fluid dispersion coefficient. Conversely to what was reported by Breedveld *et al.* [21], we find that the fluid dispersion coefficient is always slightly larger than that of the particles; see Fig. 4. One can explain this trend by the fact that the self-diffusivity coefficient of the particles accounts only for their translational diffusivity, while the fluid dispersion coefficient arises from the perturbations induced by both the translational and the rotational motion of the particles.

We performed Taylor's experiment in a suspension of non-Brownian particles to investigate how the loss of reversibility induced by the presence of the particles affects the dispersion of the blob of dye. By measuring both the particles and the blob of dye transverse effective diffusion coefficients, we found that the dispersion of the blob undergoes the same transition as the one observed by the particles [2]. At small strain amplitude, as in Taylor's experiment, the system is reversible and the blob thus recovers its initial shape after each cycle of shear. For a volume fraction $\phi = 35\%$, beyond a critical strain amplitude $\gamma_c \approx 2$, the system transits to a fluctuating state where reversibility is lost. As a result, the blob spreads very rapidly. The blob dispersion is found to be diffusive with an effective diffusive coefficient of the same order as the self-diffusivity coefficient of the particles.

We would like to thank Paul Cervetti, Sady Noel, and Stephane Martinez for building the experimental setup. This work was supported by the National Science Foundation (Grants No. 0968313 and No. 1362060), ANR JCJC SIMI 9, the Labex MEC (ANR-10-LABX-0092) and the A*MIDEX project (ANR-11-IDEX-0001-02), funded by the "Investissements d'Avenir" French Government program managed by the French National Research Agency (ANR).

[1] G. I. Taylor, Kinematic Reversibility, in *Multi-Media Fluid Mechanics CD-ROM*, edited by G. M. Homsy (Cambridge University Press, Cambridge, 2000).

[2] D. J. Pine, J. P. Gollub, J. F. Brady, and A. M. Leshansky, Chaos and threshold for irreversibility in sheared suspensions, Nature (London) **438**, 997 (2005).

[3] P. Pham, J. E. Butler, and B. Metzger, Origin of critical strain amplitude in periodically sheared suspensions, Phys. Rev. Fluids **1**, 022201(R) (2016).

[4] P. A. Arp, and S. G. Mason, The kinetics of flowing dispersions IX. Doublets of rigid spheres (experimental), J. Colloid Interface Sci. **61**, 44 (1976).

[5] E. C. Eckstein, D. G. Bailey, and A. H. Shapiro, Self-diffusion of particles in shear flow of a suspension, J. Fluid Mech. **79**, 191 (1977).

[6] F. R. Da Cunha and E. J. Hinch, Shear-induced dispersion in a dilute suspension of rough spheres, J. Fluid Mech. **309**, 211 (1996).

[7] A. Sierou and J. F. Brady, Shear-induced self-diffusion in non-colloidal suspensions, J. Fluid Mech. **506**, 285 (2004).

[8] F. Blanc, F. Peters, and E. Lemaire, Experimental Signature of the Pair Trajectories of Rough Spheres in the Shear-Induced Microstructure in Noncolloidal Suspensions, Phys. Rev. Lett. **107**, 208302 (2011).

[9] B. Metzger, O. Rahli, and X. Yin, Heat transfer across sheared suspensions: role of the shear-induced diffusion, J. Fluid Mech. **724**, 527 (2013).

[10] P. Pham, B. Metzger, and J. E. Butler, Particle dispersion in sheared suspensions: Crucial role of solid-solid contacts, Phys. Fluids **27**, 051701 (2015).

[11] C. W. Sohn and M. M. Chen, Heat transfer enhancement in laminar slurry pipe flows with power law thermal conductivities, J. Heat Transfer **106**, 539 (1984).

[12] N. L. Wang and K. H. Keller, Augmented transport of extracellular solutes in concentrated erythrocyte suspensions in Couette flow, J. Colloid Interface Sci. **103**, 210 (1985).

[13] M. Souzy, X. Yin, E. Villermaux, C. Abid, and B. Metzger, Super-diffusion in sheared suspensions, Phys. Fluids **27**, 041705 (2015).

[14] C. T. Culbertson, S. C. Jacobson, and J. M. Ramsey, Diffusion coefficient measurements in microfluidic devices, Talanta **56**, 365 (2002).

[15] T. Peng, Detect circles with various radii in grayscale image via Hough Transform, http://www.mathworks.com/matlabcentral/fileexchange/9168-detect-circleswith-various-radii-in-greyscale-image-via-hough-transform.

[16] L. Corté, P. Chaikin, J. P. Gollub, and D. J. Pine, Random organization in periodically driven systems, Nature Phys. **4**, 420 (2008).

[17] J. M. Ottino, *The Kinematics of Mixing: Stretching, Chaos, and Transport* (Cambridge University Press, Cambridge, 1989).

[18] See Supplemental Material at http://link.aps.org/supplemental/10.1103/PhysRevFluids.1.042001 for two movies that show the evolution of a drop of dye in a particulate suspension (volume fraction $\phi = 35\%$) periodically sheared for a strain amplitude of 1.5 (Movie 1) and a strain amplitude of 4 (Movie 2).

[19] M. Workamp, V. Saggiomo, and J. A. Dijksman, A simple low pressure drop suspension-based microfluidic mixer, J. Micromech. Microeng. **25**, 094003 (2015).

[20] D. Leighton and A. Acrivos, Measurement of shear-induced self-diffusion in concentrated suspensions of spheres, J. Fluid Mech. **177**, 109 (1987).

[21] V. Breedveld, D. van den Ende, A. Tripathi, and A. Acrivos, The measurement of the shear-induced particle and fluid tracer diffusivities in concentrated suspensions by a novel method, J. Fluid Mech. **375**, 297 (1998).

CrossMark click for updates

PHYSICS OF FLUIDS **27**, 041705 (2015)

Super-diffusion in sheared suspensions

Mathieu Souzy,[1] Xiaolong Yin,[2] Emmanuel Villermaux,[3] Chérifa Abid,[1] and Bloen Metzger[1]
[1]*Aix-Marseille Université, IUSTI-CNRS UMR 7343, 13453 Marseille Cedex 13, France*
[2]*Petroleum Engineering, Colorado School of Mines, 80401 Colorado, USA*
[3]*Aix-Marseille Université, IRPHE-CNRS 7342, 13384 Marseille Cedex 13, France*

(Received 18 December 2014; accepted 3 April 2015; published online 15 April 2015)

We investigate the dispersion of a layer of dye initially applied at the outer wall of a cylindrical Couette-cell into a sheared suspension of non-Brownian spherical particles. The process is directly visualized and quantified at the particle scale. A "rolling-coating" mechanism is found to convectively transport the dye at a constant rate directly from the wall towards the bulk. The fluid velocity fluctuations, u', measured with particle image velocimetry, and the imposed shear-rate, $\dot{\gamma}$, are used to define a diffusion coefficient, $D \propto \langle u'u' \rangle / \dot{\gamma}$, which is found to increase linearly with the distance from the wall. A solution of the transport equation accounting for this inhomogeneous stirring field describes quantitatively the concentration profiles measured experimentally. It exhibits a super-diffusive character, a consequence of the increase of the stirring strength with distance from the wall. Movies are available with the online version of the paper. © *2015 AIP Publishing LLC.* [http://dx.doi.org/10.1063/1.4918613]

Advection-diffusion coupling and the wide range of length-scales present in turbulent flows lead to the rapid mixing of a scalar field. Conversely, at low Reynolds number, the flow is laminar and mixing, which is then driven solely by molecular diffusion, is extremely slow. This is problematic in numerous situations; practical examples include glass manufacturing, molten polymers, heavy crude oils, industrial processing of food and domestic cooking, pharmaceutical and food industries, and granular materials in civil engineering, to mention a few. How then, can one mix such fluids?

Given the molecular diffusion is extremely slow, mixing enhancement requires conferring to the flow as much complexity and disorder as possible. In the absence of spontaneous inertial instabilities within the fluid such as those occurring in turbulent flows, the only way to complexify the flow is through the boundaries. An archetypal example is having the fluid flow through a porous material: the fixed but tortuous boundaries disrupt the fluid flow which results in a mixing enhancement.[1,2] Oscillating the fluid flow is also known to enhance mixing.[3,4] This effect was found to be particularly important in porous materials such as bones. Biologists have shown that through physical activity, periodic load-induced fluid flow in bones is critical for nutrient transport and bone metabolism.[5,6]

Another approach consists in moving the boundaries in sequential ways or to carve them in order to force the path lines of the fluid to be chaotic, e.g., in the blinking vortices configuration[7] or in chaotic mixers for micro-channels.[8,9]

In the present study, we investigate how shearing suspensions of particles enhance the dispersion of a scalar field, prelude to its mixing. The latter is faster when the former is made efficient. Particles, i.e., solid inclusions, behave as moving boundaries. Their permanent re-organisation within the fluid spontaneously promotes mixing even under low Reynolds number conditions. Under flow, particles experience frequent collisions with one another and are thus deviated from their laminar streamlines. This phenomenon called "shear-induced dispersion" has been widely studied in recent years.[10–14] The particle diffusive motion $D_p \propto \dot{\gamma} d^2$ where $\dot{\gamma}$ and d denote the imposed shear rate and the particle diameter, respectively.[15] This scaling is expected since the only time scale in the system is the inverse of the shear rate and the relevant length scale, i.e., the characteristic length scale of the fluid velocity disturbances is given by the particle size. Particles in essence can be thought of as many

 ©2015 AIP Publishing LLC

This article is copyrighted as indicated in the article. Reuse of AIP content is subject to the terms at: http://scitation.aip.org/termsconditions. Downloaded to IP: 195.83.220.70 On: Wed, 15 Apr 2015 15:54:13

"stirrers": they confer to the flow a stochastic component of advection that produces an efficient mixing. Recent experimental results[16] demonstrated that the transfer of heat across a suspension of particles is substantially (>200%) increased when the suspension is sheared. Other studies[17,18] investigated the transfer of mass across a sheared suspension of particles using an electrochemical method to measure the macroscopic rate of augmented transport of solutes. These studies are very promising in terms of applications. However, from a fundamental point of view, many questions remain open. Specifically, there are to our knowledge, no measurements of the mixing process performed at the particle scale. Yet, this information is crucial to understand the mechanisms at the origin of the transfer intensification. This point constitutes the motivation of the present study. Following this aim, we developed an original experimental setup that allows direct visualization of the dispersion process of a layer of dye in a sheared suspension of non-Brownian particles.

The experimental setup is sketched in Figure 1. The inner cylinder that has a radius of 5 cm and a height of 12 cm is driven by a precision rotating stage (M-0.61.PD from PI piezo-nano positioning) with high angular resolution (3×10^{-5} rad). The transparent PMMA outer cylinder is stationary and the gap between the two cylinders is L_{gap} = 12 mm. The temperature of the whole setup is controllable (±0.05 °C) as the Couette cell is embedded in a square water-bath jacket connected to a cryo-thermostat. More details about the setup are provided in Metzger *et al.*[16]

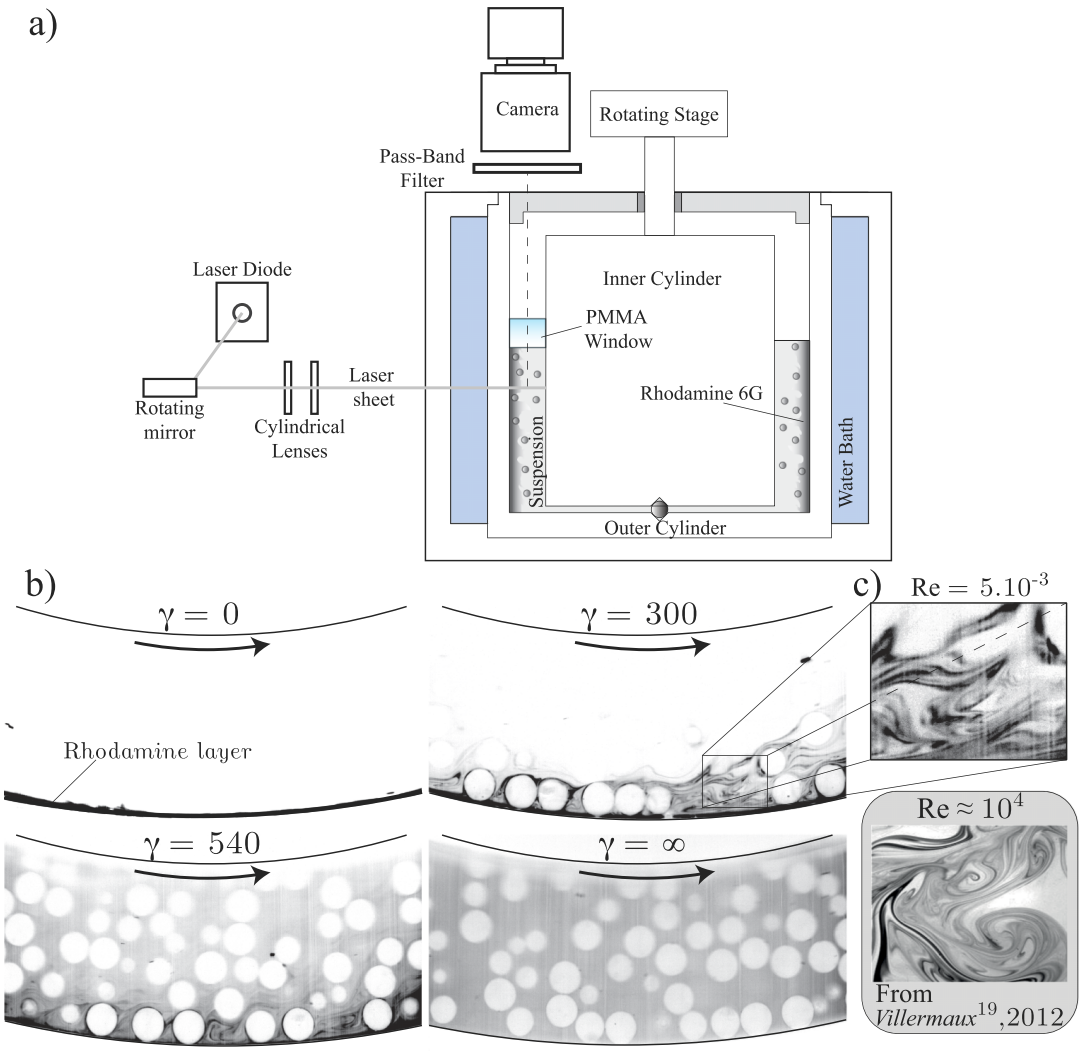


FIG. 1. (a) Sketch of the experimental setup. (b) Successive snapshots of the suspension. Initially, a thin layer of Rhodamine 6G (in black) is located on the outer cylinder. When the suspension is sheared, the dye progressively spreads across the cell-gap until homogeneity is reached. Particles appear as white discs. See Movie 1 in the supplementary material[24] for detailed evolution of the layer of dye. (c) Close-up view of the flow pattern. Note that this mixing pattern is reminiscent to those observed in turbulent flows,[20] see bottom picture.

This article is copyrighted as indicated in the article. Reuse of AIP content is subject to the terms at: http://scitation.aip.org/termsconditions. Downloaded to IP: 195.83.220.70 On: Wed, 15 Apr 2015 15:54:13

The fluid is a Newtonian mixture of Triton X-100, zinc chloride, and water. Its viscosity is $\eta = 3$ Pa s so that inertial effects can be neglected (the Reynolds number $Re = 5 \times 10^{-3}$). The composition of the fluid is also chosen to match both the density of the particles ($\rho_f = \rho_{part} = 1.19$ g cm^{-3}) to avoid sedimentation and their index of refraction to obtain an optically transparent suspension.[19] A small amount of hydrochloric acid (≈0.05 wt. %) is added to the solution to prevent the formation of zinc hypochlorite precipitate, significantly improving the transparency of the mixture. Finally, the temperature of the water-bath is adjusted in order to finely tune index-matching between the fluid and the particles (best index-matching was obtained for $T \approx 18.5$ °C). We use spherical PMMA beads from Engineering Laboratories, Inc., with a diameter $d = 2$ mm. These particles were specially chosen for their high surface quality and good transparency. All experiments are performed at a volume fraction $\phi = 35\%$.

As presented in Figure 1, the rhodamine fluoresces under illumination provided by a thin horizontal laser sheet. Images are acquired from the top using a high resolution camera (Basler Scout) and a high-pass filter ($\lambda > 550$ nm) is used to eliminate direct light reflexions due to the imperfect index-matching. The protocol is the following: a thin layer of fluid doped with Rhodamine 6G ($C_{rhod} = 9 \times 10^{-7}$ g ml^{-1}) is homogeneously applied on the outer cylinder using a brush. Then, the gap is carefully loaded with the suspension without disturbing the rhodamine layer applied on the outer cylinder. After waiting 30 min to reach thermal equilibrium (thus optimal index-matching), the suspension is sheared at a fixed shear-rate, $\dot{\gamma} = 0.5$ s^{-1}. The evolution of the mean dye concentration profiles across the gap is obtained by averaging the light intensity re-emitted by the Rhodamine 6G along the flow direction. In total, four experiments were performed for which the whole protocol was repeated entirely.

We performed Particle Image Velocimetry (PIV) to measure the velocity fluctuations of the fluid phase. The fluid was seeded with passive fluorescent tracers (MF-Rhodamine B-particles 3, 23 μm). Images were acquired into burst of five images separated by a strain interval $\gamma_0 = 0.02$. A total of 200 bursts, separated by a strain interval $\gamma \approx 10$, were acquired in order to obtain averages over a large ensemble of statistically uncorrelated configurations. Note that we do not report the velocity fluctuations near the inner (mobile) since it is very difficult to measure velocity fluctuations in regions of the flow where the mean velocity is large.

When shearing the suspension, the rhodamine layer initially applied on the outer cylinder progressively spreads into the gap until homogeneity is reached, as seen in Figure 1(b). Two qualitative yet important observations can be made. First, if no particles had been introduced into the fluid, thus having a dispersion process solely driven by molecular diffusion ($D_0 \approx 10^{-13}$ m^2 s^{-1}, see Culbertson *et al.*[21]), the time scale to reach homogeneity, $t = L_{gap}^2/D_0$, would have been of the order of 30 yr. Here, in the sheared suspension, homogeneity is reached after 30 min. The transfer enhancement is thus extremely large. We show in the sequel that the reason is that the dye dispersion process is super-diffusive but, if from a naive comparison of the timescales above one would define an effective coefficient, it would be such that $D_{eff}/D_0 \approx 10\,000$. Second, the patterns observed in the mixing layer, shown on Figure 1(c), strikingly remind those observed in turbulent mixing. For comparison, a picture from earlier work[20] of a blob of dye stirred in a turbulent flow at a Reynolds number $Re \approx 10^4$ is shown on Figure 1(c). In the suspension, even though the Reynolds number is small ($Re = 5 \times 10^{-3}$), the fluid velocity disturbances generated by the particles contribute to accelerate the dispersion process.

The dye concentration profiles as a function of the distance from the wall measured at successive strains, $\gamma = \dot{\gamma}t$, are shown on Figure 2(a). Their overall shape is interestingly analogous to the temperature profiles measured in turbulent Rayleigh-Benard convection.[22] In the latter configuration, the temperature is very homogeneous in the bulk thanks to the efficient mixing induced by the numerous thermal eddies. Conversely, strong temperature gradients are observed near the walls, in the thermal boundary layers, where heat transfer only occurs through thermal diffusion. Our system shows similar trends. Concentration profiles are flat in the bulk, suggesting that an efficient dispersion mechanism is at play in that region and a strong concentration gradient is observed close to the wall where the transfer of dye appears to be much slower. This is consistent with the scenario proposed by Wang *et al.*[18] that the particle shear-induced diffusivity drives the mixing process: in the bulk, after each collision, particles are free to translate in any direction. Conversely, particles located against the wall are sterically frustrated: when approaching the walls, their translational diffusivity must vanish. For comparison, the

This article is copyrighted as indicated in the article. Reuse of AIP content is subject to the terms at: http://scitation.aip.org/termsconditions. Downloaded to IP: 195.83.220.70 On: Wed, 15 Apr 2015 15:54:13

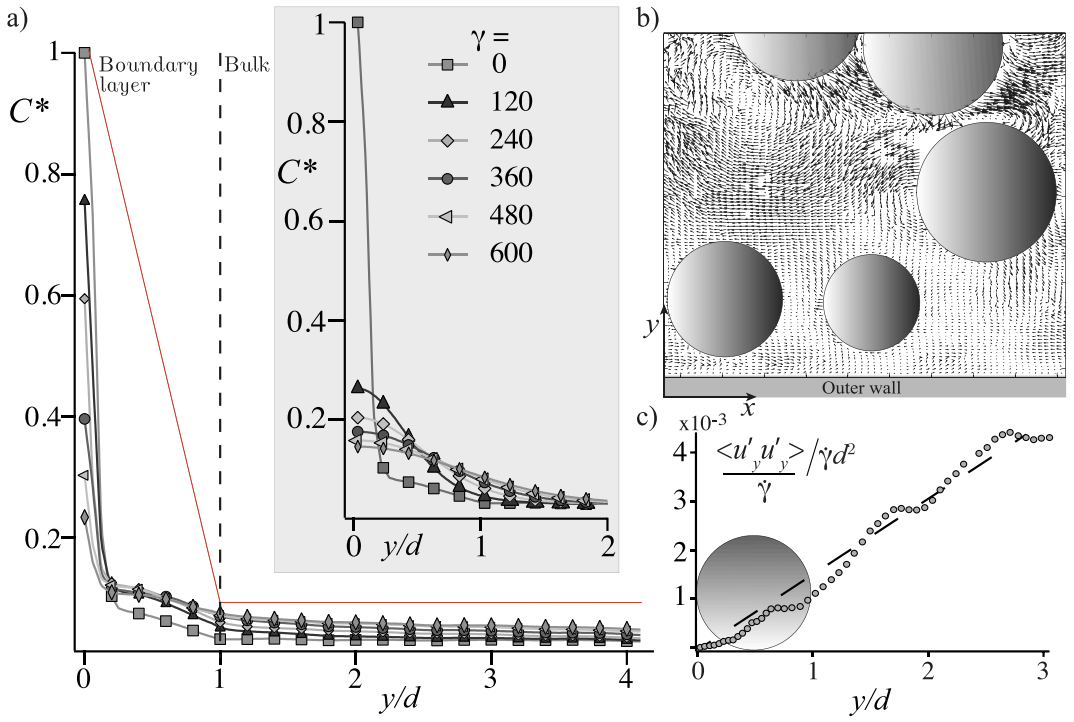


FIG. 2. (a) Concentration profiles versus distance from the wall, y/d at successive strains $\gamma = \dot{\gamma}t$. Inset: Concentration profiles one would obtain for a homogenous diffusion coefficient equal to D_{eff}. (b) Example of velocity-fluctuations field (the affine part of the flow was subtracted). See Movie 2 in the supplementary material[24] for raw images of the flowing suspension. (c) Dimensionless diffusion profile, $\frac{\langle u'_y u'_y \rangle}{\dot{\gamma}}/\dot{\gamma}d^2$, versus distance from the wall, y/d.

inset of Figure 2(a) shows the concentration profiles one would obtain for a homogeneous diffusion coefficient equal to D_{eff}. In that case, the concentration at the wall decays much faster.

To investigate how the dye is transported from the wall towards the bulk, we performed PIV measurement of the fluid velocity field. Owing to the extremely small value of the molecular diffusion coefficient D_0, this approach seems reasonable since the process we are investigating is likely to be a dispersion problem dominated by advection, i.e., the stirring motions caused by the particles themselves. A typical velocity fluctuation field is illustrated in Figure 2(b). Dimensionally, these velocity fluctuations can be used to build a diffusion coefficient, $D(y) \propto \langle u'_y u'_y \rangle/\dot{\gamma}$, quantifying the magnitude of the velocity disturbances induced by the particles. While existing models[23] proposed that the diffusion coefficient should increase as y^4, our experimental observations suggest a linear increase with the distance from the wall, namely, $D(y) = U\,y$, with U a constant velocity (Figure 2(c)). Note that for $y/d < 1$, a significant amount of fluctuations is present in the fluid, although in that region, as we mentioned before, the particle translational diffusivity must be zero. As can be seen in Movie 3 in the supplementary material,[24] particles located against the wall rotate within the shear flow; this rotation induces disturbances within the fluid.

This close examination of the boundary layer also reveals an unexpected transport-enhancing mechanism: as shown on Figure 3(a), by rolling against the wall, particles get coated with a thin layer of dye. The particle rotation thus contributes to a convective transport of the rhodamine located on the wall directly towards the bulk. This mechanism is crucial since it breaks the initially expected diffusive boundary layer.[18] Furthermore, when computing the total amount of rhodamine present in the bulk, $m = \int_d^{3d} C(y,t)\mathrm{d}y$, we find this quantity increases linearly with time or equivalently with strain, $m \propto t$, see Figure 3(b). This can easily be explained assuming the initial layer of rhodamine applied on the outer wall constitutes an infinite reservoir of dye. Since the particle rotation rate is fixed by the shear rate and calling δ the thickness of the rhodamine layer coating the particles, we expect this "rolling-coating" mechanism to produce a constant mass flux, $J = \delta\dot{\gamma}$, of rhodamine towards the bulk. This scenario indeed leads to a linear growth of the total amount of rhodamine present in the bulk, $m = \int_0^t J dt' = \delta\dot{\gamma}t$. Note that being driven by the rotation of the particles in the layer contacting the wall, the mass flux is *de facto* identical at $y = 0$ and $y = d$.

This article is copyrighted as indicated in the article. Reuse of AIP content is subject to the terms at: http://scitation.aip.org/termsconditions. Downloaded to IP: 195.83.220.70 On: Wed, 15 Apr 2015 15:54:13

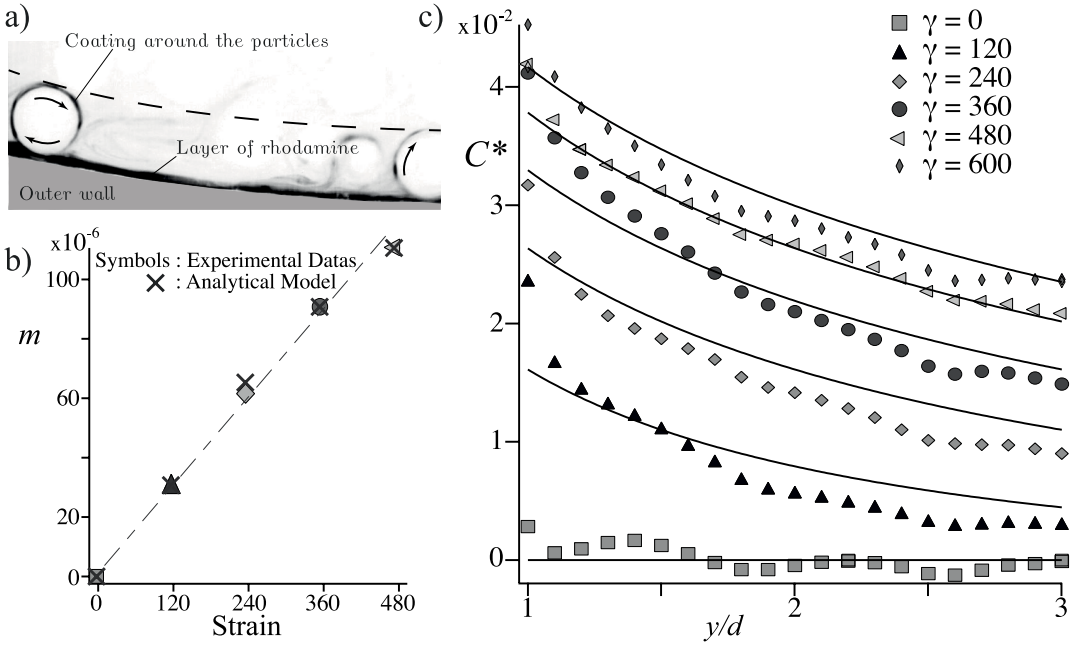


FIG. 3. (a) Close view of the "rolling-coating" mechanism. See also Movie 3 in the supplementary material.[24] (b) $m = \int_d^{3d} C(y,\gamma)dy$ for the experimental profile and the analytical solution, for successive strains. (c) Comparison between the experimentally measured concentration profiles (markers) and the analytical solution (full line, see Eq. (2)) versus distance from the wall, y/d.

Thus, considering the linear increase of the diffusion coefficient with the distance from the wall, the transport equation for the dye mean concentration field $C(y,t)$ becomes

$$\frac{\partial C}{\partial t} = \frac{\partial}{\partial y}\left(D(y)\frac{\partial C}{\partial y}\right), \qquad D(y) = Uy, \tag{1}$$

and can be solved assuming a constant mass flux as a boundary condition at $y = 0$. The solution is given by an incomplete gamma function

$$C(y,t) = \frac{J}{U}\,\Gamma\left(0, \frac{y}{Ut}\right) = \frac{J}{U}\int_{\frac{y}{Ut}}^{\infty} \frac{e^{-x}}{x}\mathrm{d}x. \tag{2}$$

This solution closely matches the experimental concentration profiles recorded in the bulk, when the parameter J is adjusted such that $\int_d^{3d} \frac{J}{U}\Gamma(0, \frac{y}{Ut})\mathrm{d}y = m$, ensuring that the amount of dye in the range $[d - 3d]$ coincides with the experimental concentration profiles, see Figure 3(b). Note that the integral of the model should not grow linearly over that restricted range (only the total mass should), yet a linear assumption is reasonable. This solution also demonstrates, not surprisingly considering the non-constancy of $D(y)$ with y, that the transport is enhanced, the dye being removed from the wall all the more rapidly that it is distant from it. Indeed, the penetration distance (typical width of the concentration profile) of the dye is $\int yC(y,t)\mathrm{d}y \sim mUt = JUt^2$, a clearly super-diffusive dispersion law. This shows the strong effect of the presence of the wall, and of the particles, on the overall transfer process. The parameter U is found to be equal to 2.12×10^{-6} m s^{-1} which leads to $D(y)/\dot{\gamma}d^2 = 2.12 \times 10^{-3} y/d$. At distances from the wall around 3 to 4 beads diameters, the diffusion coefficient $D(3d) \approx 10^{-2}\dot{\gamma}d^2$ which matches earlier bulk measurements[10,16] of the particle diffusion coefficient at this concentration. This also leads to $D(y) = 1.30\langle u'_y u'_y\rangle/\dot{\gamma}$ suggesting the dimensional approach based on the fluid velocity fluctuations provides a correct estimate of the particles diffusion coefficient.

Sheared suspensions happen to be a system where an efficient dispersion spontaneously occurs even under low Reynolds number conditions. Using planar laser-induced fluorescence, we directly visualized the spread of a layer of rhodamine initially applied on the outer wall of a cylindrical Couette-cell. For the flow conditions studied here ($Re = 5 \times 10^{-3}$ and $Pe = \dot{\gamma}d^2/D_0 = 10^7$), the dispersion of the dye has been shown to be super-diffusive close to the wall, leading to a transport four

This article is copyrighted as indicated in the article. Reuse of AIP content is subject to the terms at: http://scitation.aip.org/termsconditions. Downloaded to IP: 195.83.220.70 On: Wed, 15 Apr 2015 15:54:13

orders of magnitude more efficient than its molecular expectation in the fluid at rest. The dispersion coefficient in the bulk is of the same order of magnitude as the particle diffusion coefficient measured in earlier works.[10,16] The shape of the mean concentration profiles reflects an increase of the stirring intensity with distance to the wall, the sheared particles responsible for these motions being sterically damped at the wall. High-resolution PIV measurements of the fluid velocity disturbances generated by the particles have shown that their diffusion coefficient increases approximately linearly with the distance from the wall. The solution of the transport equation with a linear variation of the diffusion coefficient in space and a constant mass flux at the wall boundary condition provided concentration profiles in good agreement with the ones measured experimentally. However, mass transfer at the wall not only occurs through molecular diffusion. Direct visualization of the mixing process allowed us to identify a "rolling-coating" mechanism: particles rotate against the wall and get coated with a thin layer of dye. The particles convect, at a constant rate, the dye from the wall directly towards the bulk (see Movie 3 in the supplementary material[24]) breaking the diffusive boundary layer. In future experiments, we plan to vary the particle size and shear-rate to explore a large range of Péclet number and deeper range of distances from the wall.

We would like to thank Paul Cervetti, Sady Noel, and Stephane Martinez for building the experimental setup. This work was supported by ANR JCJC SIMI 9 and by the Labex MEC ANR-11-LABX-0092 and A*MIDEX ANR-11-IDEX-0001-02LABEX MEC.

[1] T. Le Borgne, M. Dentz, D. Bolster, J. Carrerra, J.-R. Dreuzy, and P. Davy, "Non-Fickian mixing: Temporal evolution of the scalar dissipation rate in heterogeneous porous media," Adv. Water Resour. **33**(12), 1468–1475 (2010).
[2] E. Villermaux, "Mixing by porous media," C. R. Mec. **340**(11), 933–943 (2012).
[3] G. Taylor, "Dispersion of soluble matter in solvent flowing slowly through a tube," Proc. R. Soc. A **219**(1137), 186–203 (1953).
[4] R. Aris, "On the dispersion of a solute in pulsating flow through a tube," Proc. R. Soc. A **259**(1298), 370–376 (1960).
[5] C. Price, X. Zhou, W. Li, and L. Wang, "Real-time measurement of solute transport within the lacunar–canalicular system of mechanically loaded bone: Direct evidence for load-induced fluid flow," J. Bone Miner. Res. **26**(2), 277–285 (2011).
[6] S. M. Schmidt, M. J. McCready, and A. E. Ostafin, "Effect of oscillating fluid shear on solute transport in cortical bone," J. Biomech. **38**(12), 2337–2343 (2005).
[7] A. Daitche and T. Tél, "Dynamics of blinking vortices," Phys. Rev. E **79**(1), 016210 (2009).
[8] A. D. Stroock, S. K. W. Dertinger, A. Ajdari, I. Mezic, H. A. Stone, and G. M. Whitesides, "Chaotic mixer for microchannels," Science **295**(5555), 647–651 (2002).
[9] E. Villermaux, A. D. Stroock, and H. A. Stone, "Bridging kinematics and concentration content in a chaotic micromixer," Phys. Rev. E **77**, 015301R (2008).
[10] A. Sierou and J. F. Brady, "Shear-induced self-diffusion in non-colloidal suspensions," J. Fluid Mech. **506**, 285–314 (2004).
[11] V. Breedveld, D. Van den Ende, M. Bosscher, R. J. J. Jongschaap, and J. Mellema, "Measurement of the full shear-induced self-diffusion tensor of noncolloidal suspensions," J. Chem. Phys. **116**, 23 (2002).
[12] F. R. Da Cunha and E. J. Hinch, "Shear-induced dispersion in a dilute suspension of rough spheres," J. Fluid Mech. **309**, 211–223 (1996).
[13] E. C. Eckstein, D. G. Bailey, and A. H. Shapiro, "Self-diffusion of particles in shear flow of a suspension," J. Fluid Mech. **79**, 191–208 (1977).
[14] P. A. Arp and S. G. Mason, "The kinetics of flowing dispersions IX. Doublets of rigid spheres (Experimental)," J. Colloid Interface Sci. **61**(4095), 44–61 (1976).
[15] D. Leighton and A. Acrivos, "Measurement of shear-induced self-diffusion in concentrated suspensions of spheres," J. Fluid Mech. **177**, 109–131 (1987).
[16] B. Metzger, O. Rahli, and X. Yin, "Heat transfer across sheared suspensions: Role of the shear-induced diffusion," J. Fluid Mech. **724**, 527–552 (2013).
[17] N. H. L. Wang and K. H. Keller, "Augmented transport of extracellular solutes in concentrated erythrocyte suspensions in Couette flow," J. Colloid Interface Sci. **103**(1), 210–225 (1985).
[18] L. Wang, D. L. Koch, X. Yin, and C. Cohen, "Hydrodynamic diffusion and mass transfer across a sheared suspension of neutrally buoyant spheres," Phys. Fluids **21**(3), 033303 (2009).
[19] J. A. Dijksman, F. Rietz, K. A. Lorincz, M. van Hecke, and W. Losert, "Invited article: Refractive index matched scanning of dense granular materials," Rev. Sci. Instrum. **83**(1), 011301 (2012).
[20] E. Villermaux, "On dissipation in stirred mixtures," Adv. Appl. Mech. **45**, 91–107 (2012).
[21] C. T. Culbertson, S. C. Jacobson, and J. M. Ramsey, "Diffusion coefficient measurements in microfluidic devices," Talanta **56**, 365–373 (2002).
[22] F. Chilla, S. Ciliberto, C. Innocenti, and E. Pampaloni, "Boundary layer and scaling properties in turbulent thermal convection," Il Nuovo Cimento **15 D**(09), 1229–1249 (1993).
[23] D. L. Koch, "Hydrodynamic diffusion near solid boundaries with applications to heat and mass transport into sheared suspensions and fixed-fibre beds," J. Fluid Mech. **318**, 31–47 (1996).
[24] See supplementary material at http://dx.doi.org/10.1063/1.4918613 for three movies: Movie 1) Dispersion of a rhodamine layer in a sheared suspension of particles, Movie 2) PIV in the flowing suspension, and Movie 3) Rolling-coating mechanism.

This article is copyrighted as indicated in the article. Reuse of AIP content is subject to the terms at: http://scitation.aip.org/termsconditions. Downloaded to IP: 195.83.220.70 On: Wed, 15 Apr 2015 15:54:13

J. Fluid Mech. (2017), *vol.* 812, *pp.* 611–635. © Cambridge University Press 2017
doi:10.1017/jfm.2016.828

Stretching and mixing in sheared particulate suspensions

M. Souzy[1], H. Lhuissier[1], E. Villermaux[2,3] and B. Metzger[1,†]

[1]Aix Marseille Université, CNRS, IUSTI UMR 7343, 13453 Marseille, France
[2]Aix Marseille Université, CNRS, Centrale Marseille, IRPHE UMR 7342, 13384 Marseille, France
[3]Institut Universitaire de France, Paris, France

(Received 15 April 2016; revised 23 November 2016; accepted 5 December 2016)

We experimentally investigate mixing in sheared particulate suspensions by measuring a crucial kinematic quantity of the flow: the stretching laws of material lines in the suspending liquid. High-resolution particle image velocimetry (PIV) measurements in the fluid phase are performed to reconstruct, following the Diffusive Strip Method (Meunier & Villermaux, *J. Fluid Mech.*, vol. 662, 2010, pp. 134–172), the stretching histories of the fluid material lines. In a broad range of volume fractions $20\,\% \leqslant \phi \leqslant 55\,\%$, the nature of the elongation law changes drastically from linear, in the absence of particles, to exponential in the presence of particles: the mean and the standard deviation of the material line elongations are found to grow exponentially in time and the distribution of elongations converges to a log-normal. A multiplicative stretching model, based on the distribution of local shear rates and on their persistence time, is derived. This model quantitatively captures the experimental stretching laws. The presence of particles is shown to accelerate mixing at large Péclet numbers ($\gtrsim 10^5$). However, the wide distribution of stretching rates results in heterogeneous mixing and, hence, broadly distributed mixing times, in qualitative agreement with experimental observations.

Key words: low-Reynolds-number flows, mixing enhancement, suspensions

1. Introduction

Sheared particulate suspensions represent a quasi-unique system where efficient dispersion spontaneously occurs even under low-Reynolds-number flow conditions. For instance, the transfer of heat (Sohn & Chen 1984; Metzger, Rahli & Yin 2013) or mass (Wang & Keller 1985; Wang *et al.* 2009; Souzy *et al.* 2015) across a suspension of non-Brownian particles is significantly enhanced when the suspension is submitted to a macroscopic shear. This would not happen in a pure Newtonian fluid, where the laminar streamlines remain perpendicular to the scalar (heat or concentration) gradients. In a sheared suspension, the macroscopic stationary imposed shear results at the particle scale in an unstationary flow: particles constantly collide with one another, change streamlines, and thus generate disturbances within the fluid which promote the dispersion of the scalar, prelude to its subsequent mixing. Two

† Email address for correspondence: bloen.metzger@univ-amu.fr

Downloaded from https://www.cambridge.org/core. Université d'Aix-Marseille, on 19 Jan 2017 at 18:25:05, subject to the Cambridge Core terms of use, available at https://www.cambridge.org/core/terms. https://doi.org/10.1017/jfm.2016.828

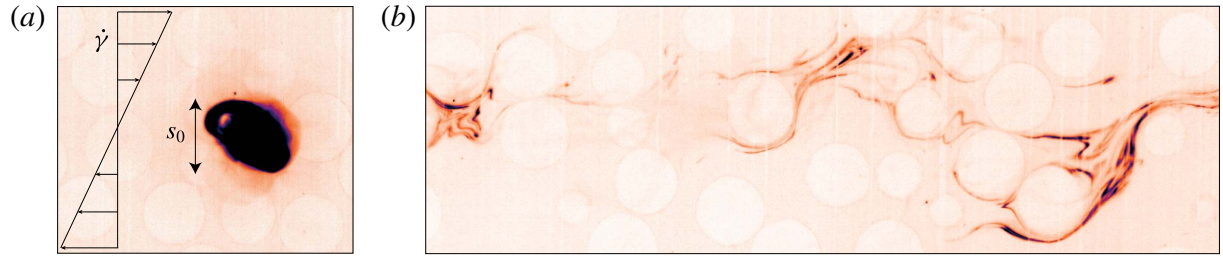


FIGURE 1. (Colour online) Some dye, initially confined to a small blob in a flowing particulate suspension (*a*), mixes with the rest of the suspension (*b*) by diffusing while the blob is stretched in the complex micro-flow generated by the particles.

mechanisms have been identified to explain the origin of the transfer enhancement. First, the particle translational shear-induced diffusivity, a phenomenon which has been widely investigated over the last decades (Arp & Mason 1976; Eckstein, Bailey & Shapiro 1977; Da Cunha & Hinch 1996; Breedveld *et al.* 2002; Sierou & Brady 2004; Metzger *et al.* 2013). Second, the particle rotation, whose impact is particularly important at the boundaries, where particles disrupt the diffusive boundary layer by a 'rolling-coating' effect (Souzy *et al.* 2015). These studies mainly focused on the rate of transfer across sheared suspensions, which is customarily characterized by an effective diffusion coefficient much larger than the scalar molecular diffusivity.

Another aspect of transport enhancement concerns the mixing properties of the system, namely its ability, starting from a given spatial scalar distribution, to reach homogeneity. Figure 1 shows how a blob of dye with initial size s_0, diffuses while it is deformed by the complex flow in the interstitial fluid of a suspension. The important question which naturally arises is to understand how this initially segregated system reaches homogeneity, and particularly how long this process takes. By essence, it involves both advection by the flow and molecular diffusion of the scalar. Such a problem has been studied in a wide range of situations involving a single fluid phase such as shear flows (Ranz 1979), vortex flows (Meunier & Villermaux 2003), turbulent jets (Duplat, Innocenti & Villermaux 2010), or flows in porous media (Le Borgne, Dentz & Villermaux 2015). These studies all underline the crucial importance of the rate at which fluid material lines are elongated by the flow (Villermaux 2012). The knowledge of these 'stretching laws' allows one to estimate the mixing time: the time when the scalar concentration fluctuations start to significantly decay (Batchelor 1959). For instance, in a simple shear flow with rate $\dot{\gamma}$, the material lines grow as $\dot{\gamma}t$. In the limit of large Péclet number $Pe = \dot{\gamma}s_0^2/D$, the mixing time for a scalar blob of initial size s_0 is $t_{mix} \sim \dot{\gamma}^{-1}Pe^{1/3}$, where D denotes the molecular diffusivity of the dye. In chaotic flows, where the stretching rate is maintained, the material lines stretch exponentially, as $e^{\dot{\gamma}t}$, and $t_{mix} \sim \dot{\gamma}^{-1} \ln Pe$.

In spite of their crucial importance for mixing issues, stretching laws in particulate suspensions have never been studied experimentally, nor has the general question about the mixing time in such a system. Stretching in particulate suspension has been addressed indirectly using numerical simulations through the measurement of the suspension largest Lyapunov exponent (Dasan *et al.* 2002; Drazer *et al.* 2002; Metzger & Butler 2012*b*; Metzger, Pham & Butler 2013). In such a chaotic system, the mean stretching rate of fluid elements can be assimilated to the largest Lyapunov exponent. The reported positive Lyapunov exponents indicate that the stretching laws must be exponential. Stretching has also been explored theoretically with the motivation of understanding the rheology of such systems when the suspending fluid

Downloaded from https://www.cambridge.org/core. Université d'Aix-Marseille, on 19 Jan 2017 at 18:25:05, subject to the Cambridge Core terms of use, available at https://www.cambridge.org/core/terms. https://doi.org/10.1017/jfm.2016.828

is viscoelastic. It was shown that the expected exponential stretching of the polymers should affect the pressure drop in fixed beds of spheres or fibres (Shaqfeh & Koch 1992) or the viscosity of freely suspended fibres in a simple shear flow (Harlen & Koch 1993).

In this paper, we specifically address the question of the stretching kinematics by performing experiments on non-Brownian and spherical particulates suspended in a viscous and Newtonian fluid that is steadily and uniformly sheared. In this limit, the flow kinematics is independent of both the shear rate $\dot{\gamma}$ and the molecular diffusivity. The sole parameter expected to affect the stretching process is the particulate volume fraction ϕ. We investigate the stretching laws in particulate suspensions varying the volume fraction over a wide range $20\,\% \leqslant \phi \leqslant 55\,\%$, for which collective effects between particles are present but the suspension still flows easily, since it is still far from jamming. After presenting the experimental set-up in § 2, we first compare the evolution of a blob of dye sheared in a pure fluid (without particles) to that of a blob sheared in a suspension (§ 3). This experiment illustrates the complexity of the advection field induced by the presence of the particles. Then, following the Diffusive Strip Method of Meunier & Villermaux (2010), accurate velocity field measurements of the fluid phase (§ 2.3) are used to determine the stretching laws. Material lines are found to stretch, on average, exponentially with time (§ 4), at a rate which agrees with the largest Lyapunov exponents reported in three-dimensional (3D) Stokesian dynamic simulations (Dasan *et al.* 2002; Drazer *et al.* 2002). Beyond the mean, we tackle the complete statistics of stretching, that is to say, the distributions of elongation as a function of strain and particle volume fraction, which are found to converge towards log-normal distributions. In § 5, we present a model, based on a multiplicative stretching process, which explains quantitatively the experimental distributions of the material line elongation and its dependence on $\dot{\gamma}t$ and ϕ. Finally, the crucial implication of these findings for scalar mixing are developed and discussed in § 6, before we conclude in § 7.

2. Experimental set-up

The experimental set-up is shown in figure 2. It aims at steadily and uniformly shearing a viscous particulate suspension, injecting a small blob of dyed fluid, and observing both the flow and the mixing of the dye. The set-up consists of a transparent cell in which a transparent mylar belt is tightly mounted at the top of the cell on two cylinders and at the bottom on two ball bearings. One cylinder is entrained by a rotating stage (M-061.PD from PI Piezo-Nano Positioning) with high angular resolution (3×10^{-5} rad). The motion of the belt generates in its central region a linear shear flow. The suspension is allowed to flow below the cylinders and a constant spacing between the belt and the inner wall of the cell is maintained all around the cell. This specific design, which is an evolution of that used in Metzger & Butler (2012*a*), minimizes secondary flows and ensures a velocity profile with constant shear rate within the belt.

2.1. *Particles and liquid*

The particles and the liquid are carefully chosen to allow the visualization of the dye and of the flow inside the suspension, as well as to ensure a purely viscous flow without buoyancy effects. This requires using a transparent media, matching both the density and the refraction index of the particles, and using a fairly viscous liquid.

Downloaded from https://www.cambridge.org/core. Université d'Aix-Marseille, on 19 Jan 2017 at 18:25:05, subject to the Cambridge Core terms of use, available at https://www.cambridge.org/core/terms. https://doi.org/10.1017/jfm.2016.828

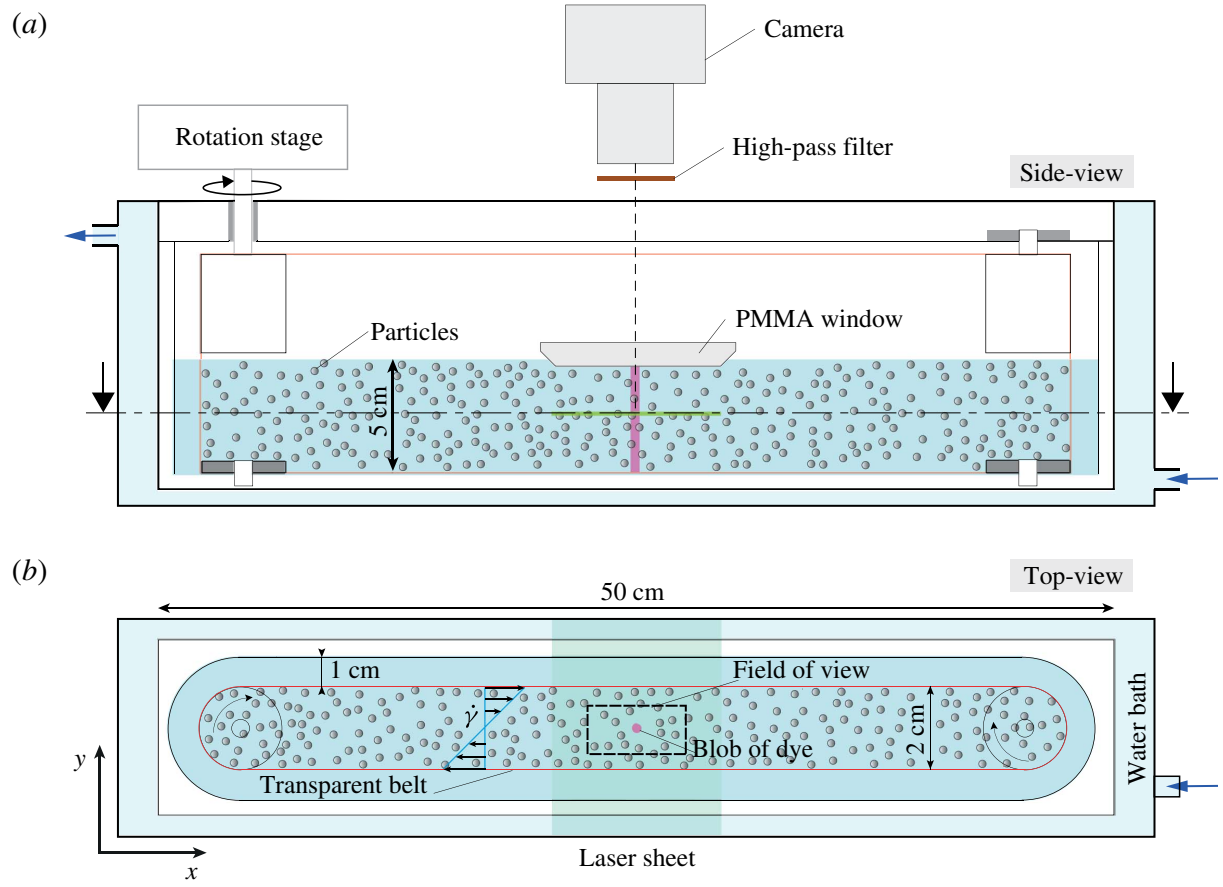


FIGURE 2. (Colour online) Schematics of the set-up.

To fulfil the above requirements, we use mono-disperse spherical particles (PMMA from Engineering Laboratories Inc.) with density $\rho = 1.18$ kg m^{-3} and diameter $d = 2$ mm, especially chosen for their smooth surface and good transparency. The liquid is a Newtonian mixture of Triton X-100 (77.4 wt.%), zinc chloride (13.4 wt.%) and water (9.2 wt.%) with viscosity $\eta = 3$ Pa s and having the same density as the particles at room temperature. Its composition is optimized to match both the refractive index and the density of the particles. A small amount of hydrochloric acid ($\approx$0.05 wt.%) is added to the solution to prevent the formation of zinc hypochlorite precipitate, thereby significantly improving the optical transparency of the solution. Last, to finely tune the index matching between the particles and the liquid, the temperature of the set-up is adjusted with a water bath surrounding the shear cell.

The solid volume fraction ϕ of the suspension is varied between 20 % and 55 %. To ensure that inertial effects are negligible, the shear rate $\dot{\gamma}$ is set to typically 0.15 s^{-1}, which corresponds to a particulate Reynolds number $\rho\dot{\gamma}d^2/\eta \sim 10^{-4}$.

2.2. *Imaging*

The suspension is observed in the flow-gradient plane (xy plane): a slice of suspension is illuminated by a laser sheet across the transparent belt and imaged from the top (see figure 2).

The laser sheet is formed by reflecting a laser beam (2 W, 532 nm) on a standard laser-printer mirror (rotating at $\sim$10 000 rpm). This technique was found to produce a light sheet with a better spatial homogeneity than that obtained with classical cylindrical or Powell lens techniques. The sheet is collimated and focused to a

Downloaded from https://www.cambridge.org/core. Université d'Aix-Marseille, on 19 Jan 2017 at 18:25:05, subject to the Cambridge Core terms of use, available at https://www.cambridge.org/core/terms. https://doi.org/10.1017/jfm.2016.828

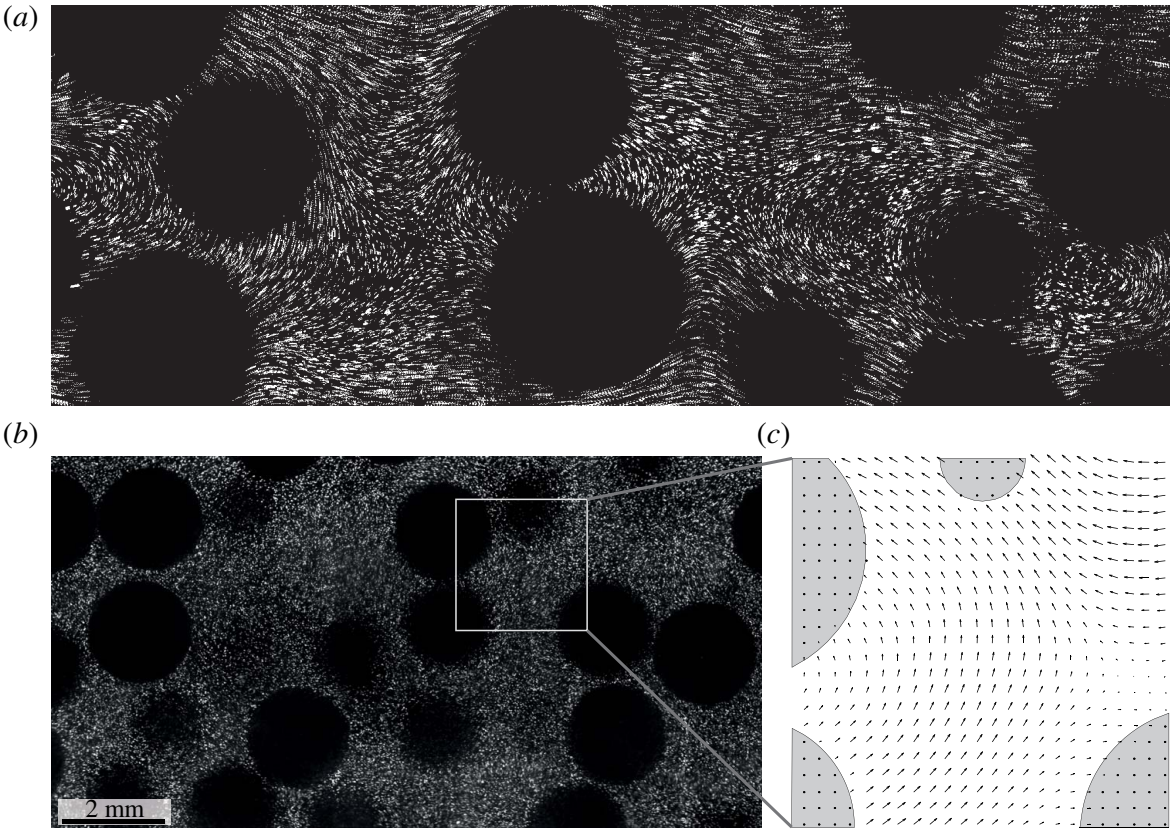


FIGURE 3. (*a*) Flow streamlines in the bulk of a suspension. (*b*) Slice of a sheared suspension illuminated by a laser sheet. The small fluorescent tracers seeding the suspending fluid appear as bright whereas the particle intersections with the laser sheet appear as dark, see also supplementary movie 1 available at https://doi.org/10.1017/jfm.2016.828. (*c*) Magnified view of the suspending liquid velocity field obtained from the PIV (the velocity is not computed in the particles).

thickness of $\sim 60\,\mu$m with the help of two perpendicular plano-convex lenses. Last, a high-pass filter (590 nm) eliminates direct light reflections. The suspension is imaged with a high-resolution camera (Basler Ace2000-50gm, 2048 $\times$ 1080 pixel^2, 12bit) coupled to a high-quality magnification lens (Sigma APO-Macro-180 mm-F3.5-DG). To avoid the particles distorting the free surface of the suspension through which the visualization is realized, a small Plexiglas window is positioned on the free surface, above the region of interest, which locally ensures a flat interface. The window has a small hole allowing the injection of a blob of dyed fluid with a syringe.

2.3. *Velocity field measurements*

The velocity field in the suspending liquid is measured in the plane of the laser sheet (xy), at half-distance between the bottom and the free surface (see figure 3), performing particle image velocimetry (PIV), which yields the two-dimensional (2D) velocity field $\{u, v\}$, which does not necessarily verify incompressibility. To perform PIV, the liquid is seeded with small passive fluorescent tracers (3.23 μm PMMA B-particles from MF-Rhodamine) at a very low volume fraction ($\sim 10^{-5} \ll \phi$). These small and diluted tracers do not affect the flow but allow its visualization and quantification, as shown in figure 3 and movie 1. The large (2 mm) particles of the suspension do not interact with the laser sheet, and appear as black discs. Note that

Downloaded from https://www.cambridge.org/core. Université d'Aix-Marseille, on 19 Jan 2017 at 18:25:05, subject to the Cambridge Core terms of use, available at https://www.cambridge.org/core/terms. https://doi.org/10.1017/jfm.2016.828

all the particles have the same size; the apparent size differences arise from their different vertical positions relative to the laser sheet plane. The PIV routine is adapted from a Matlab code developed by Meunier & Leweke (2003). Images are captured every 0.1 s, which corresponds to a strain increment of 0.015. To perform PIV, the images are divided into equally spaced and overlapping sub-images with a typical size of $d/20$ (32 pixels). The local velocity field is computed by cross-correlating successive sub-images. The presence of a particle in the sub-image is detected with the help of two filters (for the maximum of correlation and for the standard deviation of the sub-images), in which case the corresponding velocity vector is not used (see figure 3*b*). For each volume fraction, three independent runs over a strain of 20 are performed. The independence of the measured velocity field on the PIV sub-image size was verified by decreasing the latter to $\sim d/40$ (16 pixels). Besides increasing the data noise, no significant effect was found on the measured velocities.

2.4. *Molecular diffusivity measurements*

The molecular diffusion coefficient of the dye (rhodamine 6G) is measured by observing the spreading, in the absence of flow, of a slice of liquid depleted in dye. A small Hele-Shaw cell (100 μm thick) is filled with dye-doped suspending liquid without particles. A thin slice of liquid is initially depleted in dye by bleaching the dye with a high-power laser sheet across the cell (see figure 4). The depleted slice appears as a dark line having a Gaussian profile which diffuses with the diffusion coefficient of the dye. The spatial variance of the Gaussian profile χ^2 is measured over one day, and the diffusivity is determined from $D = [\chi^2(t) - \chi^2(0)]/2t \simeq 1.44 \times 10^{-13}$ m^2 s^{-1}. This value is consistent with that of 4.14×10^{-10} m^2 s^{-1} found by Culbertson, Jacobson & Ramsey (2002) for the diffusivity of the same dye in water, given that water is 3000 times less viscous than the suspending liquid and that, according to the Einstein–Sutherland law, $D \propto 1/\eta$.

3. General observations

To illustrate the influence of particles on mixing in a shear flow, we first compare the evolution of a blob of dye sheared in a pure fluid (without particles) to that of a blob sheared in the suspension of particles, see supplementary movie 2. A cylindrical blob of dyed fluid is injected, at rest and at $t = 0$, in the middle of the shear cell. Initially, the blob has a diameter $s_0 \simeq 2$ mm, is aligned with the vorticity direction and is centred on the neutral velocity plane. This results in a macroscopically 2D initial configuration, and ensures that the blob does not drift with the flow but only deforms. Figure 5 shows, for a Péclet number $Pe \approx 10^6$, how mixing proceeds in the two sheared media, from the initial segregated state up to a strain $\dot{\gamma}t = 20$. In the pure liquid, the blob of dye stretches homogeneously. Its length increases linearly with time and the blob transverse dimension thus decreases as $1/t$. In the suspension, the situation is markedly different: the fluctuations induced by the particles in the fluid phase strongly impact the evolution of the blob. Several conspicuous features deserve being highlighted: (i) the dispersion and the unfolded length of the blob are significantly enhanced by the particles, (ii) both translational diffusivity (transverse undulations of the blob, see figure 5*b*) and rotation (blob winding around particles, see figure 5*c*) of the particles contribute to these enhancements, (iii) the blob stretching is highly inhomogeneous: at some locations, its transverse dimension becomes much thinner and at others larger than in the pure fluid case, revealing regions of enhanced stretching and regions of compression, (iv) at large strains (figure 5*d*),

Downloaded from https://www.cambridge.org/core. Université d'Aix-Marseille, on 19 Jan 2017 at 18:25:05, subject to the Cambridge Core terms of use, available at https://www.cambridge.org/core/terms. https://doi.org/10.1017/jfm.2016.828

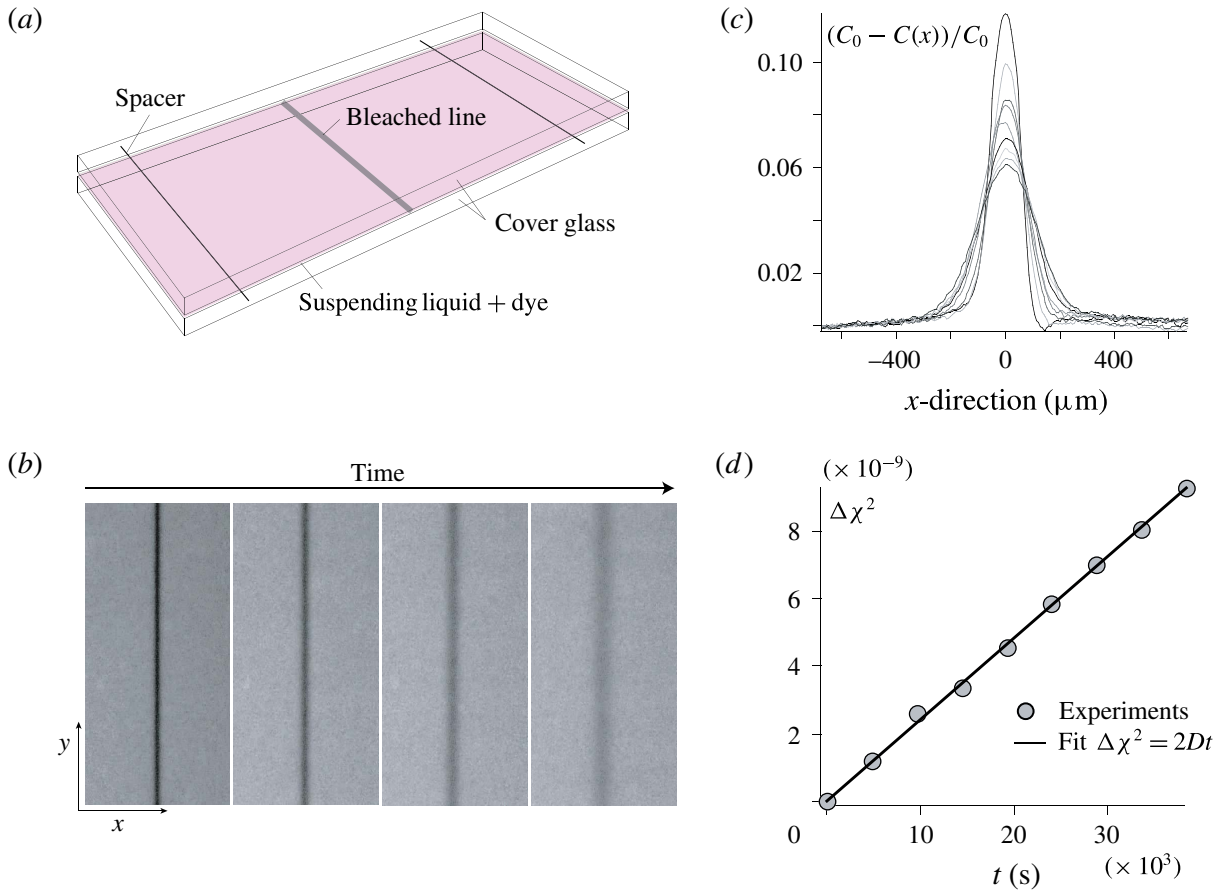


FIGURE 4. (Colour online) (*a*) Schematics of the set-up used to measure the molecular diffusivity D of the dye (rhodamine 6G), in the suspending liquid (TritonX + $ZnCl_2$ + H_2O). (*b*) Diffusive thickening of the bleached line at $t = 0$, 4800, 21 600 and 64 800 s (the image width is 5 mm). (*c*) Concentration profiles at successive times (0 s $< t <$ 64 800 s). (*d*) Increase of the spatial variance of the concentration $\chi^2(t) - \chi^2(0)$ versus time. Its fit to $2Dt$ yields $D = 1.44 \pm 0.2 \times 10^{-13}$ m^2 s^{-1}.

the blob has separated into several filaments, which means that some regions of the blob have already mixed, while in the pure liquid (without particles) mixing has not occurred yet, (v) in some regions, the blob evolves into bundles composed of several nearly overlapping filaments (Duplat & Villermaux 2008). This suggests an underlying stretching/folding mechanism similar to the well-known baker's transform (Ottino 1989).

The above features are generic to the flow of a viscous suspension at large Péclet number. Since inertial effects are negligible, these features are independent of the rate $\dot{\gamma}$ at which the suspension is sheared. Similarly, the value of the Péclet number does not influence the general stretching pattern of the blob, but only prescribes the strain $\dot{\gamma}t$ at which diffusion starts to becomes effective.

This direct comparison clearly illustrates how the liquid velocity fluctuations generated by the particles dramatically accelerate the blob deformation and dispersion. This acceleration is apparent here from the beginning of the shear, because the blob size s_0 is similar to the particle size d. It is, however, crucial to realize that the strain at which this acceleration establishes is expected to depend on the ratio s_0/d. If the initial size of the blob s_0 is larger than d, the blob is essentially not stretched by the particle fluctuation motions. It is thus essentially stretched by the linear macroscopic

Downloaded from https://www.cambridge.org/core. Université d'Aix-Marseille, on 19 Jan 2017 at 18:25:05, subject to the Cambridge Core terms of use, available at https://www.cambridge.org/core/terms. https://doi.org/10.1017/jfm.2016.828

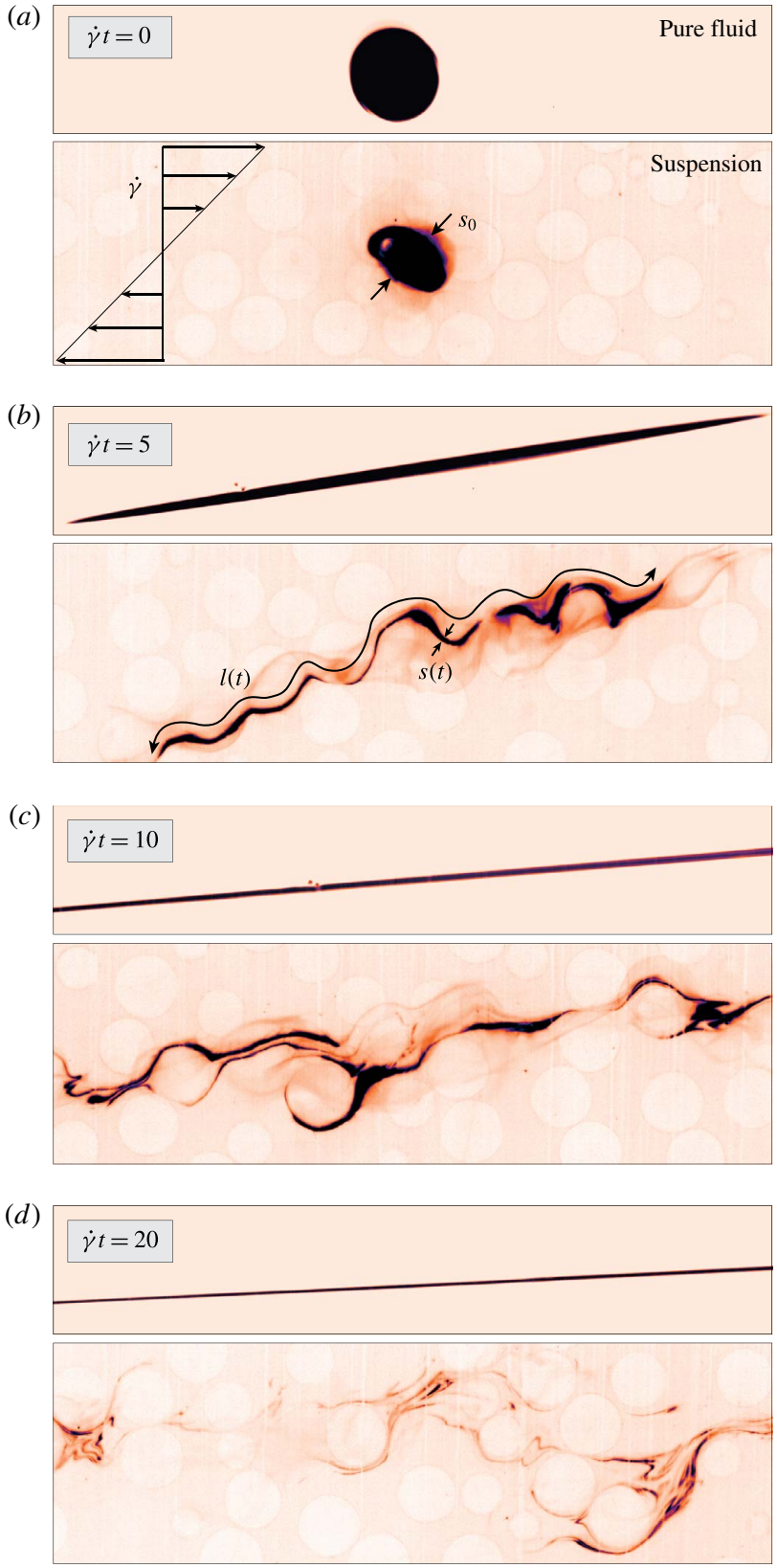


FIGURE 5. (Colour online) Comparison of the stretching processes of a blob of dye sheared at high Péclet ($\sim 10^6$) and low Reynolds numbers ($\sim 10^{-4}$), in a pure fluid (top), and in a particulate suspension with volume fraction $\phi = 35\,\%$ (bottom). The dye appears as dark, and the beads appear as bright, see also supplementary movie 2.

Downloaded from https://www.cambridge.org/core. Université d'Aix-Marseille, on 19 Jan 2017 at 18:25:05, subject to the Cambridge Core terms of use, available at https://www.cambridge.org/core/terms. https://doi.org/10.1017/jfm.2016.828

shear until the blob transverse size has thinned down to d, after a typical strain s_0/d. From that strain on, the particulate fluctuations are expected to contribute directly to the blob stretching.

In stirred flows, such as the case considered here, mixing results from the coupling between advection and molecular diffusion. In the experiment described above, the blob of dye is stretched by the local velocity field: the blob is stretched along its own longitudinal direction and conversely compressed along its transverse direction. The blob thus evolves towards a topology constituted of sheets, or filaments (Ottino 1989; Buch & Dahm 1996). Conversely to the effect of advection, molecular diffusion tends to broaden the filaments. This diffusive broadening will at some point counter-balance the rate of compression of the blob caused by the advection. As we already mentioned, this naturally sets a time scale called the mixing time, t_{mix}, beyond which the concentration levels drop significantly. The mixing time, a key element to understand the overall mixing process, can be estimated from the sole knowledge of the dye molecular diffusion coefficient and from the history of the transverse dimension of the blob. If one assumes that the flow is two-dimensional (this assumption is discussed in § 5.3), incompressibility and mass conservation relate at any time the transverse size of the blob to its length l, through $s_0 l_0 = s(t)l(t)$. The mixing time can therefore be estimated from the characterization of the evolution of $l(t)$. Our goal in the following is thus to determine the so-called 'stretching laws', i.e. the time dependence of l in sheared particulate suspensions.

4. Experimental stretching laws

Our first attempt to measure the unfolded length of the blob $l(t)$ was naturally to perform direct image analysis on images such as those shown in figure 5. However, the intrinsic dispersion process rapidly distorts the blob into bundles of very close (sometimes merging) filaments, which renders image analysis ineffective above strains of typically 5.

To overcome these limitations, we adopted a different approach inspired from the Diffusive Strip Method. This method happens to be a very powerful experimental tool allowing the determination of the stretching laws over unlimited strains. The key idea is to use the experimental fluid velocity field to numerically advect passive material lines representing portions of the blob. The lines are initially composed of three passive tracers, separated by a distance $d/20$, which discretize a fluid material line. The lines are randomly located in the 2D velocity field with a random orientation (see figure 6*a*). Each tracer with coordinate $\boldsymbol{x}$ is advected independently from each other according to the local fluid velocity $\boldsymbol{v}(\boldsymbol{x})$ (obtained by linear interpolation of the instantaneous PIV velocity field) as $\boldsymbol{x}(t + \Delta t) = \boldsymbol{x}(t) + \boldsymbol{v}(\boldsymbol{x})\Delta t$, where Δt is the time between consecutive measurements of the velocity field. As a material line is advected, it is refined by adding more tracers when its length increases or when its local curvature becomes too large (see Meunier & Villermaux (2010) for a detailed description of the refinement procedure).

Figure 6 shows the evolution of two material lines up to a strain of 15, see also movie 3. The red line successively stretches and folds very similarly to what is observed in the blob experiments (figure 5). Interestingly, the blue line behaves very differently. Although it sustains the same macroscopic strain as the red one, it experiences a much softer stretching only because it started from a different initial location. These different stretching histories reveal the stochastic nature of the stretching induced within particulate suspensions. The stretching laws therefore have

Downloaded from https://www.cambridge.org/core. Université d'Aix-Marseille, on 19 Jan 2017 at 18:25:05, subject to the Cambridge Core terms of use, available at https://www.cambridge.org/core/terms. https://doi.org/10.1017/jfm.2016.828

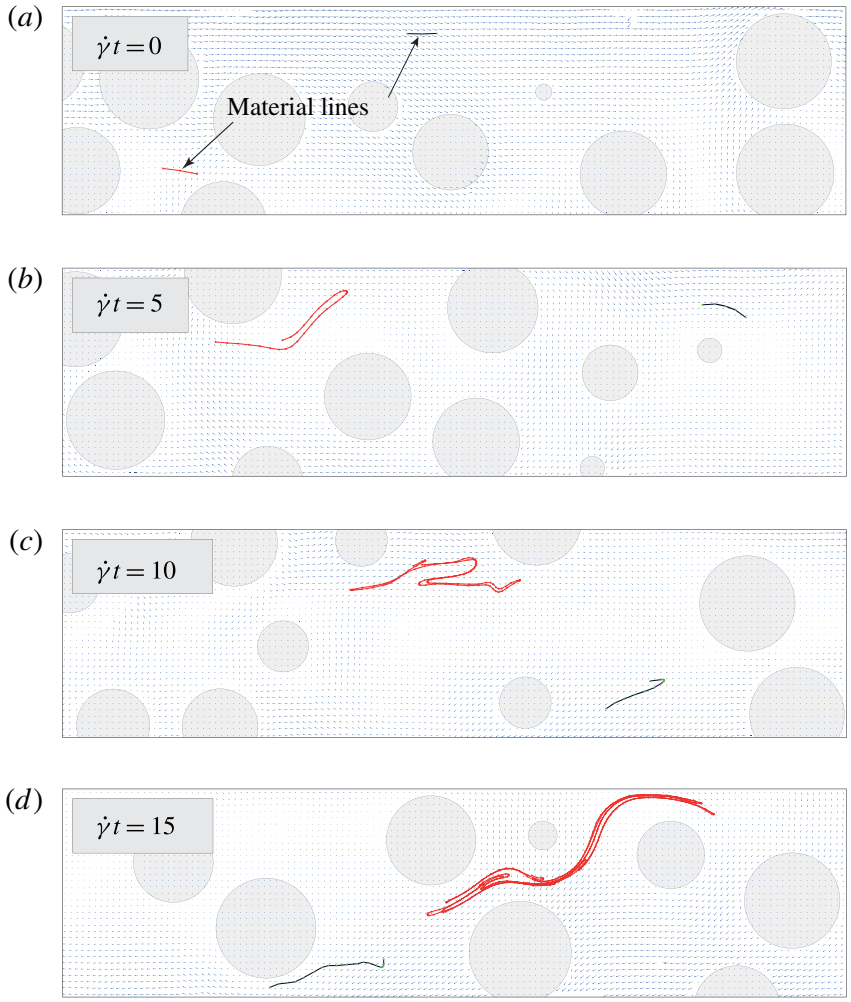


FIGURE 6. (Colour online) Example of stretching for two material lines numerically advected using the experimental fluid velocity field, see also supplementary movie 3.

to be sought in a statistical sense by repeating the advection procedure over a large number of independent material lines. However, as the material lines lengthen, they may reach the boundaries of the measured velocity field, which limits the maximum strain that can practically be investigated (typically $\dot{\gamma}t < 10$). This problem is easily circumvented by realizing that, as long as the stretching laws are concerned, the object of interest is not the material line as a whole but rather the small segments which compose this line and which all stretch differently from each other. We thus perform a new set of calculations focusing on segments: (i) initial segments (composed of two tracers) with length $d/20$ are positioned and oriented randomly in the flow, (ii) each time the length of a segment doubles, it is split in two individual segments that are subsequently advected independently, (iii) if a segment reaches the boundary of the velocity field, it is re-injected near the centre of the velocity field, (iv) when a segment overlaps with a particle, where the velocity field is undefined (as can happen due to the finite time Δt), it is frozen until the particle has moved away. Owing to these rules, virtually unlimited strains can be considered, and the stretching histories of each segment that have been created over this strain can be determined. We define the elongation of these segments as the ratio

$$\rho(t) \equiv \delta l(t)/\delta l_0 \tag{4.1}$$

Downloaded from https://www.cambridge.org/core. Université d'Aix-Marseille, on 19 Jan 2017 at 18:25:05, subject to the Cambridge Core terms of use, available at https://www.cambridge.org/core/terms. https://doi.org/10.1017/jfm.2016.828

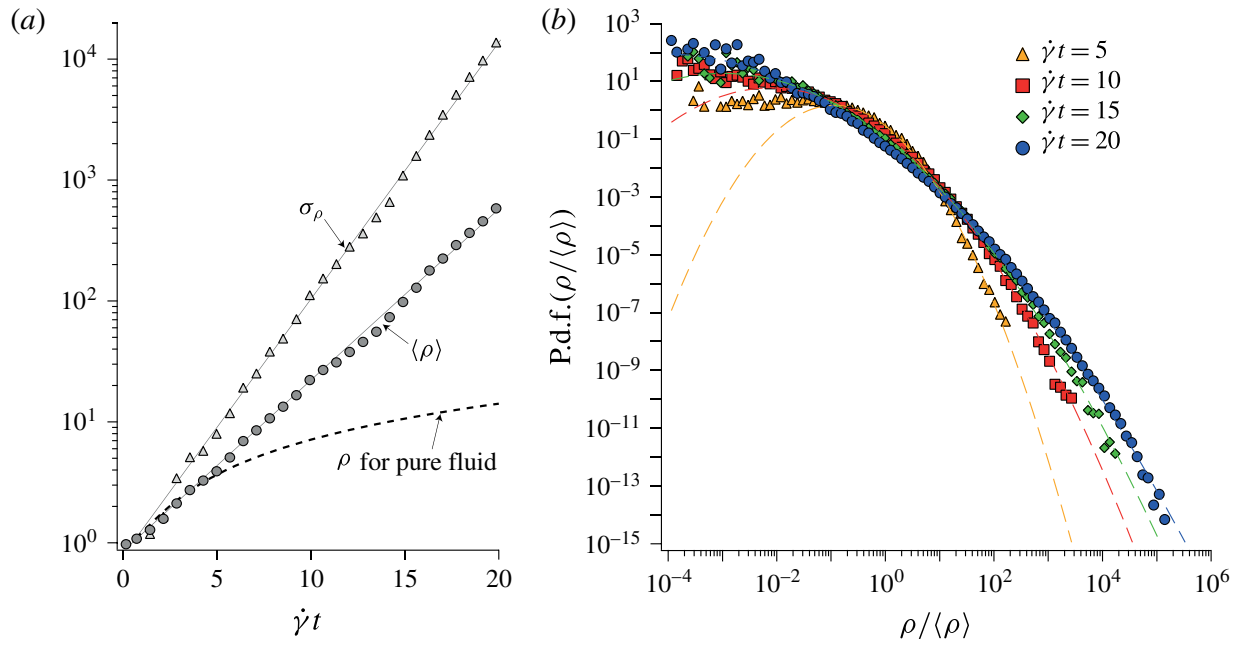


FIGURE 7. (Colour online) Stretching laws measured for a suspension with volume fraction $\phi = 35\,\%$. (*a*) Mean value $\langle\rho\rangle$ and standard deviation $\sigma_\rho = \sqrt{\langle\rho^2\rangle - \langle\rho\rangle^2}$ of the distribution of elongations versus macroscopic strain in a semilogarithmic representation. The dashed line corresponds to the mean elongation in a pure fluid $\rho_{lin}(t) = \sqrt{1 + \dot\gamma^2 t^2/2}$. (*b*) Distribution of the normalized elongations $\rho/\langle\rho\rangle$ at different strains. The dashed curves are log-normal distributions built from the mean value $\langle\rho\rangle$ and standard deviation σ_ρ of the experimental elongation distributions.

of their current length $\delta l(t)$ to their initial length δl_0, where $\delta l_0 = (d/20)/2^n$, with n the number of times the sub-segment was split in two. Note that to compute the distributions of elongations we present below, the contribution of each segment is weighted by its initial length. Note also that times for which a segment is frozen are not considered. The distribution of elongations at time t therefore represents the portion of the blob that has reached a given elongation after being advected for a duration t. It was built from the stretching histories of 25 000 segments advected over three independent experimental velocity fields, each of them recorded for a total strain of 20 (typically 4000 images).

Figure 7 shows the experimental stretching laws obtained for a suspension with $\phi = 35\,\%$, which is generic to the volume fraction range 20 %–55 % investigated. It presents the mean value $\langle\rho\rangle$ and the standard deviation $\sigma_\rho \equiv \sqrt{\langle\rho^2\rangle - \langle\rho\rangle^2}$ of the elongation for strains up to 20. At $\dot\gamma t = 20$, the segments have on average lengthened by typically 10^3, which is approximately one hundred times larger than in the case of a pure liquid. The striking result is that the presence of particles in a shear flow changes the very nature of the stretching laws from linear to exponential. Indeed, the elongation of material lines in a simple shear (without particles) follows

$$\rho_{lin}(\theta, t) = \sqrt{1 + 2\cos\theta\,\sin\theta\,\dot\gamma t + \sin^2\theta\,\dot\gamma^2 t^2}, \tag{4.2}$$

where θ denotes the angle between the line initial orientation and the flow direction. On averaging $\rho^2_{lin}(\theta, t)$ over all possible orientations, we obtain

$$\rho_{lin}(t) = \sqrt{1 + \dot\gamma^2 t^2/2}, \tag{4.3}$$

Downloaded from https://www.cambridge.org/core. Université d'Aix-Marseille, on 19 Jan 2017 at 18:25:05, subject to the Cambridge Core terms of use, available at https://www.cambridge.org/core/terms. https://doi.org/10.1017/jfm.2016.828

which is only of order 10 for a strain of 20, and increases linearly with time for large strains. Equation (4.3) is plotted in figure 7 to illustrate the contrast with the elongations actually measured in particulate suspensions: the mean elongation in suspensions is different both in magnitude and in law.

Moreover, by contrast with the pure fluid case, the stretching variability of individual material lines is very broad, as evidenced by the exponential growth of the standard deviation σ_p. These results corroborate the preliminary blob experimental visualizations where, in the suspension, many filaments having very different transverse thickness can be observed while the pure fluid case solely exhibits one uniform thickness (figure 5*d*). More precisely, figure 7(*b*) shows the distributions of the relative elongations $P(\rho/\langle\rho\rangle)$ at successive strains. The distribution of elongations broadens rapidly such that, at a strain $\dot{\gamma}t = 20$, it spans more than eight decades. At that strain, the right tail of the distribution contains segments elongated 10^4 times relative to the average $\langle\rho\rangle$, which corresponds to an absolute elongation of $\rho \sim 10^7$, in stark contrast with the uniform average elongation of 10 obtained in a simple shear. As figure 7(*b*) shows, these distributions are found to be well fitted by log-normal distributions (shown as dashed lines). Note that the apparent absence of data on the left-hand side of the distributions is fully consistent with log-normal distributions. Indeed, for broad distributions, the statistical weight of the left-hand side of the distribution vanishes. Our data thus fully resolve the meaningful part of the distribution.

The advective strip method presented above was repeated with velocity fields measured in suspensions with different volume fractions ϕ ranging from 20 % to 55 %. The same trends as those detailed for $\phi = 35\,\%$ are systematically observed. As shown in figure 8, it is moreover found that larger particulate volume fractions increase both the growth rate of the average elongation $\langle\rho\rangle$ and that of the standard deviation σ_ρ. This indicates that a larger volume fraction results in larger fluid disturbances which, in turn, induce a faster and more random elongation of the fluid material lines. Fitting these curves with exponential growths in strain $e^{\kappa\dot{\gamma}t}$ yields for $\langle\rho\rangle$, $\kappa_\rho = 0.09 + 0.74\,\phi$, and for σ_ρ, $\kappa_{\sigma_\rho} = 0.12 + 1.03\,\phi$. In the range of volume fraction investigated, the growth rates are found to increase linearly with ϕ. No measurements could be performed above 55 %, as the large normal stress built in the suspension starts to deform the belt.

To summarize, by kinematically advecting passive segments using the experimental velocity fields of the fluid phase, we measured the elongation of fluid material lines in sheared particulate suspensions. Two important features characterize these elongations: (i) the mean and the standard deviation grow exponentially, (ii) the distribution converges to a log-normal. In the following, using two measurable properties of the fluid velocity field, namely the local shear rate distribution and the Lagrangian correlation time, we present a mechanism accounting for these observations.

5. Origin of the stretching laws

5.1. *Principle*

We consider the elementary component of a fluid material line: the segment, see figure 9. At that scale, much smaller than the particle size, the local shear $\dot{\gamma}_{loc}$ is uniform. Considering the broad distribution of the segment orientations, we assume that the local shear rate has a random orientation with respect to the segment. Therefore, as long as the local shear rate $\dot{\gamma}_{loc}$ persists, the average elongation of the segment is (see (4.3))

$$\rho = \sqrt{1 + \dot{\gamma}_{loc}^2 t^2/2}. \tag{5.1}$$

Downloaded from https://www.cambridge.org/core. Université d'Aix-Marseille, on 19 Jan 2017 at 18:25:05, subject to the Cambridge Core terms of use, available at https://www.cambridge.org/core/terms. https://doi.org/10.1017/jfm.2016.828

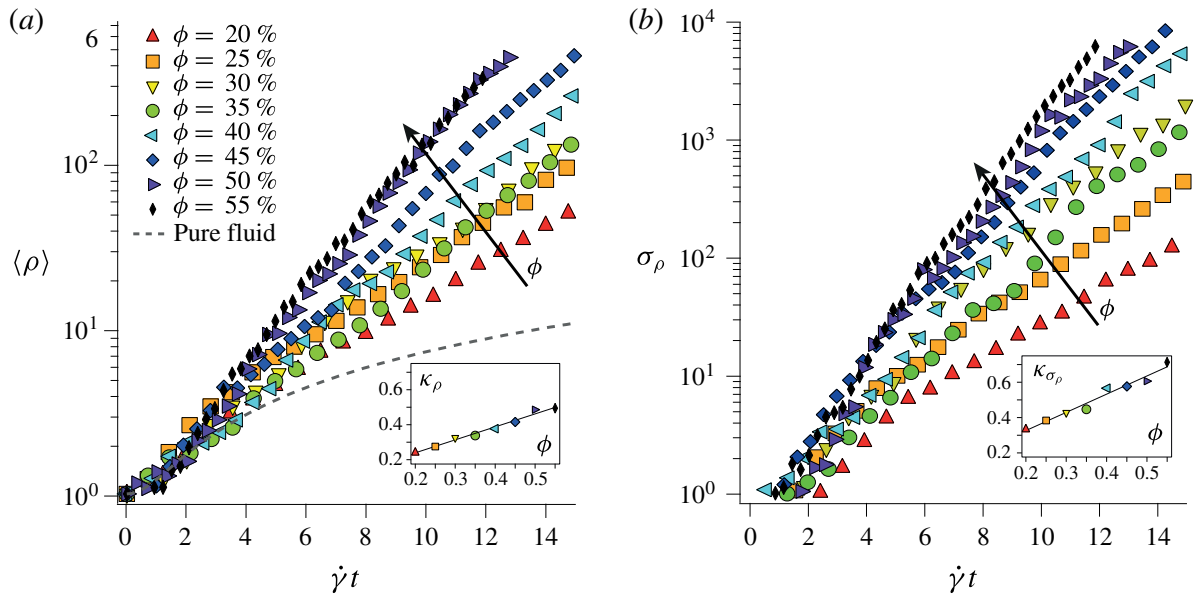


FIGURE 8. (Colour online) Mean elongation $\langle\rho\rangle$ (a) and standard deviation σ_ρ (b) versus strain for increasing volume fractions ranging from 20 % to 55 %. Insets: growth rate κ of the exponential fit $e^{\kappa\dot{\gamma}t}$ to the main curves, as a function of ϕ. The lines show $\kappa_\rho = 0.09 + 0.74\phi$ (a), and $\kappa_{\sigma_\rho} = 0.12 + 1.03\phi$ (b).

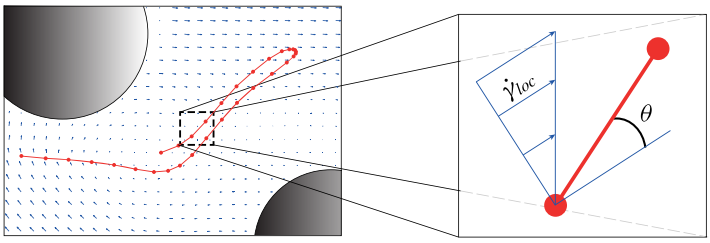


FIGURE 9. (Colour online) Each segment composing a fluid material line is locally stretched by a simple shear $\dot{\gamma}_{loc}$ which is oriented with a random angle θ with respect to the segment.

Note that an individual segment can be stretched or compressed depending on whether it is located in a diverging or compressive region of the flow, respectively. However, once averaged over all possible orientations, the segment net elongation is strictly larger than unity. Two questions then naturally emerge: what are the local shear rates? and how long do these shear rates persist? In the following two sections, we address these questions by providing information about the local shear rates and the Lagrangian correlation time of the velocity field.

5.1.1. *Local shear rate*

We measure the local shear rate from the experimental 2D velocity fields. To this end, we define the local shear rate by the norm of the symmetric part of the strain tensor:

$$\dot{\gamma}_{loc} = \sqrt{2\left(\frac{\partial u}{\partial x}\right)^2 + 2\left(\frac{\partial v}{\partial y}\right)^2 + \left(\frac{\partial u}{\partial y} + \frac{\partial v}{\partial x}\right)^2}, \tag{5.2}$$

Downloaded from https://www.cambridge.org/core. Université d'Aix-Marseille, on 19 Jan 2017 at 18:25:05, subject to the Cambridge Core terms of use, available at https://www.cambridge.org/core/terms. https://doi.org/10.1017/jfm.2016.828

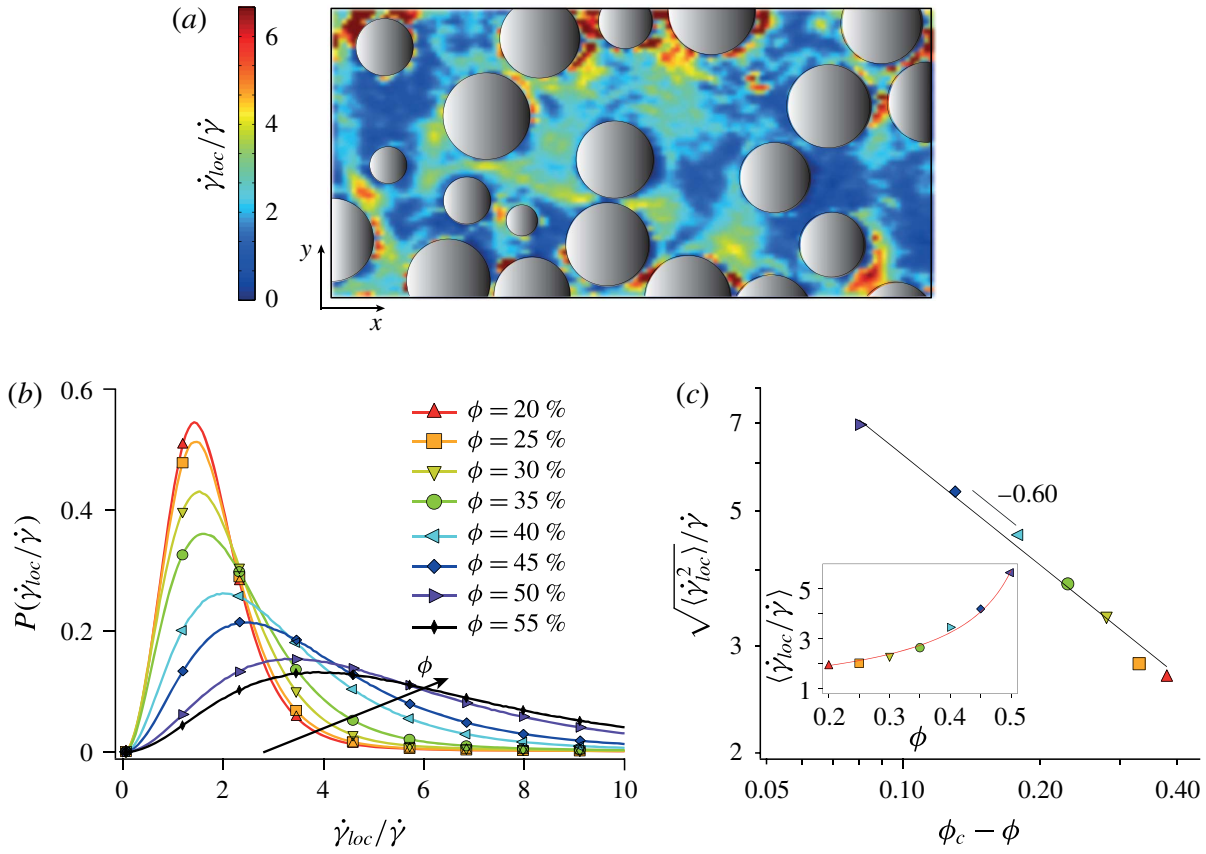


FIGURE 10. (Colour online) (*a*) Typical local shear rate map for a suspension with volume fraction $\phi = 35\,\%$. (*b*) Experimental distributions of normalized local shear rate $P(\dot{\gamma}_{loc}/\dot{\gamma})$ for different volume fractions (the solid line is not a fit but the experimental data, sparse markers are used for sake of clarity). (*c*) $\sqrt{\langle\dot{\gamma}_{loc}^2\rangle}/\dot{\gamma}$ versus $\phi_c - \phi$. The best fit $\sqrt{\langle\dot{\gamma}_{loc}^2\rangle}/\dot{\gamma} \sim (\phi_c - \phi)^{-\beta}$, with $\phi_c = 0.58$, yields $\beta = 0.601$ (see text). Inset: mean normalized local shear rate $\langle\dot{\gamma}_{loc}/\dot{\gamma}\rangle$ versus ϕ. The line is the best fit by $A/(\phi_c - \phi)^{\delta}$.

where $\{u, v\}$ are the $\{x, y\}$ components of the velocity field. This definition disregards the rotation part of the strain tensor. For a simple shear, one has $\dot{\gamma}_{loc} = \text{const.} = \dot{\gamma}$. Figure 10(*a*) shows a typical local shear rate map, obtained in a suspension with volume fraction $\phi = 35\,\%$. The colour scale represents the amplitude of $\dot{\gamma}_{loc}$ normalized by the applied macroscopic shear rate $\dot{\gamma}$, that is to say the amplification of the shear due to the presence of particles. The local shear rate is highly non-uniform and its value can greatly exceed the macroscopic shear rate. Interestingly, large local shear rates occur preferentially in the vicinity of the particles; however, there is no apparent correlation between large local shear rates and small inter-particle distances.

More quantitatively, we report in figure 10(*b*) the distribution of normalized local shear rates obtained for various volume fractions. Clearly, the local shear rate exceeds most of the time the imposed macroscopic shear rate, sometimes by one order of magnitude, and this trend accentuates with increasing volume fractions. The mean normalized value $\langle\dot{\gamma}_{loc}\rangle/\dot{\gamma}$ is plotted versus ϕ in the inset of figure 10(*c*). It is found to fit well $\langle\dot{\gamma}_{loc}\rangle/\dot{\gamma} = A/(\phi_c - \phi)^{\delta}$. Fixing $\phi_c = 0.58$ this yields $A \simeq 0.56$ and $\delta \simeq 0.7$. Note that the last point, corresponding to $\phi = 55\,\%$, was not included in the fitting procedure since we suspect that it is biased by the deflection of the belt mentioned above. Note also that PIV using smaller boxes resulted in very similar local shear rate distributions with less than 6 % difference on the average.

Downloaded from https://www.cambridge.org/core. Université d'Aix-Marseille, on 19 Jan 2017 at 18:25:05, subject to the Cambridge Core terms of use, available at https://www.cambridge.org/core/terms. https://doi.org/10.1017/jfm.2016.828

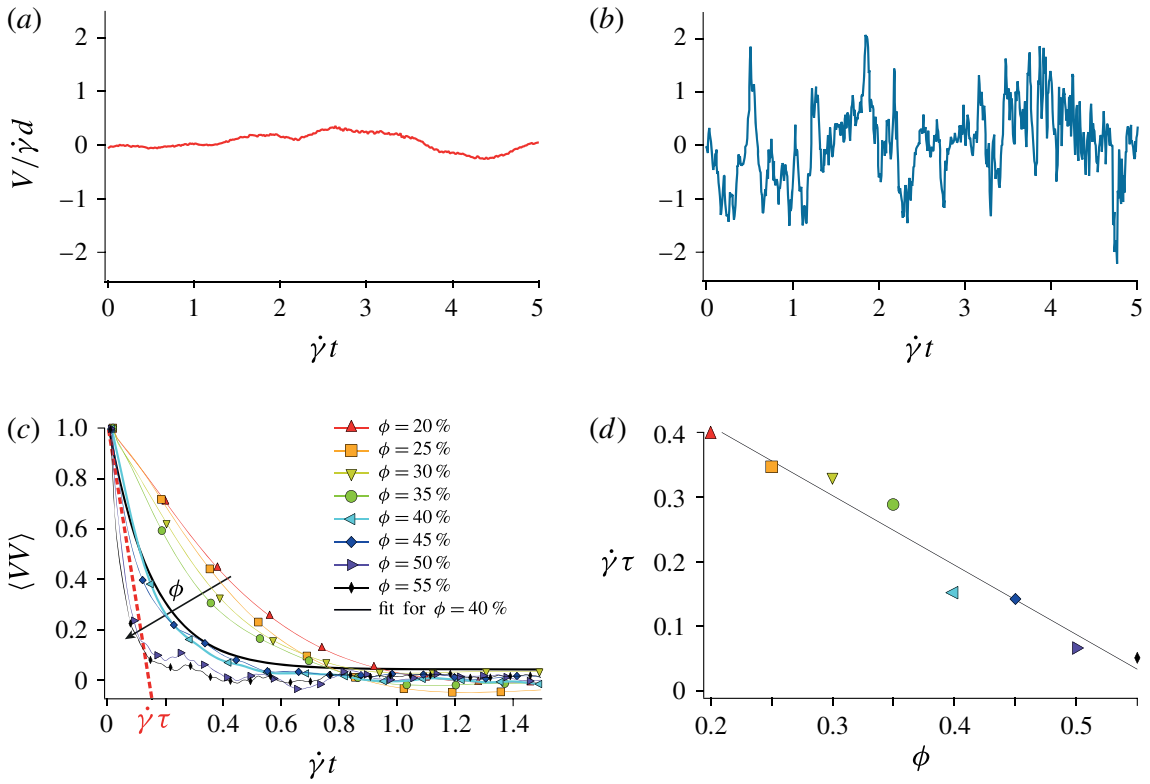


FIGURE 11. (Colour online) (*a*,*b*) Lagrangian velocity transverse to the flow of a tracer passively advected by the suspending liquid V, as a function of the strain $\dot{\gamma}t$. (*a*) $\phi = 20\,\%$ and (*b*) $\phi = 50\,\%$. (*c*) Average Lagrangian velocity auto-correlation function $\langle VV\rangle$ obtained for different volume fractions versus strain. The velocity auto-correlation functions fit well $\mathrm{e}^{-\dot{\gamma}t/\dot{\gamma}\tau}$, where τ denotes the correlation time. (*d*) Correlation strain $\dot{\gamma}\tau$ versus ϕ and corresponding linear fit $\dot{\gamma}\tau = 0.62 - 1.08\,\phi$.

The trends discussed above may also be interpreted in terms of a macroscopic viscosity. In such case, the relevant quantity to investigate is the second moment of the local shear rate distribution $\langle\dot{\gamma}_{loc}^2\rangle$ (Chateau, Ovarlez & Trung 2008; Lerner, Dring & Wyart 2012; Dagois-Bogy *et al.* 2015). Values of this quantity have recently been obtained by Trulson *et al.* from numerical simulations of dense frictional suspensions (Trulsson, DeGiuli & Wyart 2016). They report that $\sqrt{\langle\dot{\gamma}_{loc}^2\rangle}/\dot{\gamma} \sim (J/\mu)^{-1/3}$, where $J = \dot{\gamma}\eta_f/P$ is the viscous number, with P the confining pressure and μ the suspension macroscopic friction coefficient. Since $\eta_s/\eta_f = \sigma/\dot{\gamma}\eta_f = \mu/J$, this results in $\sqrt{\langle\dot{\gamma}_{loc}^2\rangle}/\dot{\gamma} \sim (\eta_s/\eta_f)^{1/3}$. Combining this with $\eta_s/\eta_f \sim (\phi_c - \phi)^{-2}$ and using $\phi_c = 0.58$ (Boyer, Guazzelli & Pouliquen 2011) leads to $\sqrt{\langle\dot{\gamma}_{loc}^2\rangle}/\dot{\gamma} \sim (\phi_c - \phi)^{-2/3}$, which is in fairly good agreement with the measured scaling, as figure 10(*c*) shows.

5.1.2. *Lagrangian correlation time*

The second important quantity of the suspending liquid flow is the persistence time of the velocity fluctuations induced by the particles. Figures 11(*a*) and 11(*b*) show the transverse Lagrangian velocity V (perpendicular to the flow) of a passive tracer advected by the fluid at a low and a large volume fraction, respectively. Consistently with the magnitude of the local shear, more concentrated particulate suspensions develop velocity fluctuations with larger amplitudes. However these fluctuations are found to persist on a much shorter time as ϕ increases. The duration t_c for which a

Downloaded from https://www.cambridge.org/core. Université d'Aix-Marseille, on 19 Jan 2017 at 18:25:05, subject to the Cambridge Core terms of use, available at https://www.cambridge.org/core/terms. https://doi.org/10.1017/jfm.2016.828

segment is coherently stretched by the flow is directly prescribed by this persistence time, which we define from the Lagrangian velocity auto-correlation functions. As shown in figure 11(*c*), these functions decorrelate exponentially with strain. In the range of volume fraction investigated, the dimensionless correlation time $\dot{\gamma}\tau$, inferred from this exponential decay, decreases linearly with ϕ as

$$\dot{\gamma}\tau \simeq 0.62 - 1.08\,\phi \tag{5.3}$$

(see figure 11*d*). We expect t_c to be of the order of τ, and thus write

$$t_c = \alpha\tau, \tag{5.4}$$

with α an order one constant. Note that, as shown in figure 7, this persistence time ($\lesssim\dot{\gamma}^{-1}$) is much shorter than the observation period ($\gtrsim 10\dot{\gamma}^{-1}$).

5.1.3. *Multiplicative stretching process*

With information about the local shear rates and their persistence time at hand, we now explain the elongations of fluid material lines as a sequence of uncorrelated cycles of stretching. During the first cycle of duration t_c, a given segment of a material line is elongated by the local shear rate $\dot{\gamma}_{loc,1}$ resulting in a stretching

$$\Delta\rho_1 = \sqrt{1 + (\dot{\gamma}_{loc,1}t_c)^2/2}, \tag{5.5}$$

where $\dot{\gamma}_{loc,1}$ is a local shear rate whose probability is prescribed by the distribution $P(\dot{\gamma}_{loc}/\dot{\gamma})$, cf. figure 10(*b*). After the duration t_c, the local velocity field decorrelates and the local shear rate map is entirely redistributed. The segment then experiences a new local shear rate $\dot{\gamma}_{loc,2}$, which at $t = 2t_c$ yields $\rho = \Delta\rho_1\sqrt{1 + (\dot{\gamma}_{loc,2}t_c)^2/2}$, and so on. The total elongation at time t, after $N = t/t_c$ cycles, is the product of all the elementary elongations occurring at each cycle $\rho(t) = \prod_{i=1}^{N=t/t_c}\Delta\rho_i$. The logarithm of this expression can be written as a sum

$$\ln\rho \equiv \sum_{i=1}^{t/t_c}\ln\Delta\rho_i = \frac{1}{2}\sum_{i=1}^{t/t_c}\ln[1 + (\dot{\gamma}_{loc,i}t_c)^2/2]. \tag{5.6}$$

Since the elementary stretchings are independent, the distribution of $\ln\rho$ is expected, by virtue of the central limit theorem, to be normal. This multiplicative stretching model thus predicts ρ to converge, after a few t/t_c cycles, to a log-normal distribution. This prediction is in agreement with the experimental results shown in figure 7(*b*). The distribution of $\ln\rho$, i.e. the normal distribution, is written as

$$P(x = \ln\rho) = \frac{1}{\sqrt{2\pi}\sigma}\,\mathrm{e}^{-(x-\mu)^2/2\sigma^2}, \tag{5.7}$$

with a non-zero mean

$$\mu \equiv \langle\ln\rho\rangle = \frac{\langle\ln\Delta\rho\rangle}{\dot{\gamma}t_c}\,\dot{\gamma}t, \tag{5.8}$$

and variance

$$\sigma^2 \equiv \langle\ln^2\rho\rangle - \mu^2 = \frac{\langle\ln^2\Delta\rho\rangle - \langle\ln\Delta\rho\rangle^2}{\dot{\gamma}t_c}\,\dot{\gamma}t. \tag{5.9}$$

Downloaded from https://www.cambridge.org/core. Université d'Aix-Marseille, on 19 Jan 2017 at 18:25:05, subject to the Cambridge Core terms of use, available at https://www.cambridge.org/core/terms. https://doi.org/10.1017/jfm.2016.828

Both the mean and the variance of the distribution of $\ln \rho$ increase linearly with time. They also vary with the particulate volume fraction due to the ϕ-dependence of $\dot{\gamma}_{loc}$ and t_c. This variation with ϕ is better appreciated by recasting equations (5.8) and (5.9) into

$$\mu = f(\phi)\, \dot{\gamma} t, \tag{5.10}$$

$$\sigma^2 = g(\phi)\, \dot{\gamma} t, \tag{5.11}$$

with $f(\phi) \equiv \langle \ln \Delta\rho \rangle / \dot{\gamma} t_c$ and $g(\phi) \equiv (\langle \ln^2 \Delta\rho \rangle - \langle \ln \Delta\rho \rangle^2)/\dot{\gamma} t_c$ depending only on ϕ. Note that $f(\phi)$ and $g(\phi)$ are crucial quantities. Since the time dependency is known, they contain all the information about the asymptotics of the stretching laws in suspensions.

The multiplicative stretching model not only explains the origin of the log-normal distributions of elongations measured experimentally, but also the exponential increase of the mean elongation ρ and variance σ_ρ^2 shown in figure 7. Indeed, the mean and variance of the (log-normal) distribution of ρ can be deduced from the mean and the variance of the (normal) distribution of $\ln \rho$ following

$$\langle \rho \rangle = \mathrm{e}^{(f+g/2)\dot{\gamma} t}, \tag{5.12}$$

and

$$\sigma_\rho^2 = (\mathrm{e}^{g\dot{\gamma} t} - 1)\mathrm{e}^{(2f+g)\dot{\gamma} t} \simeq \mathrm{e}^{2(f+g)\dot{\gamma} t}, \tag{5.13}$$

the last simplification in σ_ρ^2 becoming true after a few t_c.

Furthermore, the particulate volume fraction dependence of $f(\phi)$ and $g(\phi)$ can be computed from the persistence time t_c and the distribution of local shear rates, using (5.10) and (5.11) together with (5.8) and (5.9). In the experimental range $20\,\% < \phi < 55\,\%$, this yields

$$f(\phi) \simeq 0.104 + 0.298\,\phi, \tag{5.14}$$

and

$$g(\phi) \simeq -0.069 + 0.810\,\phi, \tag{5.15}$$

with the structure constant α, set once and for all ϕ, to 0.3 for computing μ, and to 3.9 for computing σ^2. These rates f and g both increase with ϕ, in agreement with the experimental trends. Note that this dependence on the volume fraction is non-trivial, since f and g result from the product of $\dot{\gamma}_{loc}$ and t_c, which have opposite trends with ϕ: the former increases whereas the latter decreases with increasing ϕ.

The predictions of the multiplicative stretching model are compared to the experimental stretching laws obtained by the Diffusive Strip Method in figure 12. The agreement is good for all volume fractions and all strains, which suggests that the multiplicative stretching model presented above captures the relevant mechanisms at the origin of the stretching laws.

5.2. *Comments on the stretching process*

Stretching of material elements in nature, may they be passive like in the present case, or with internal restoration forces like polymers (Shaqfeh & Koch 1992; Afonso & Vincenzi 2005), may have different origins. The stochastic models to describe them usually present a net drift, and a random noise terms. The relative amplitudes of these two contributions are in our analysis given by $f(\phi)$ and $g(\phi)$, respectively (see (5.10)

Downloaded from https://www.cambridge.org/core. Université d'Aix-Marseille, on 19 Jan 2017 at 18:25:05, subject to the Cambridge Core terms of use, available at https://www.cambridge.org/core/terms. https://doi.org/10.1017/jfm.2016.828

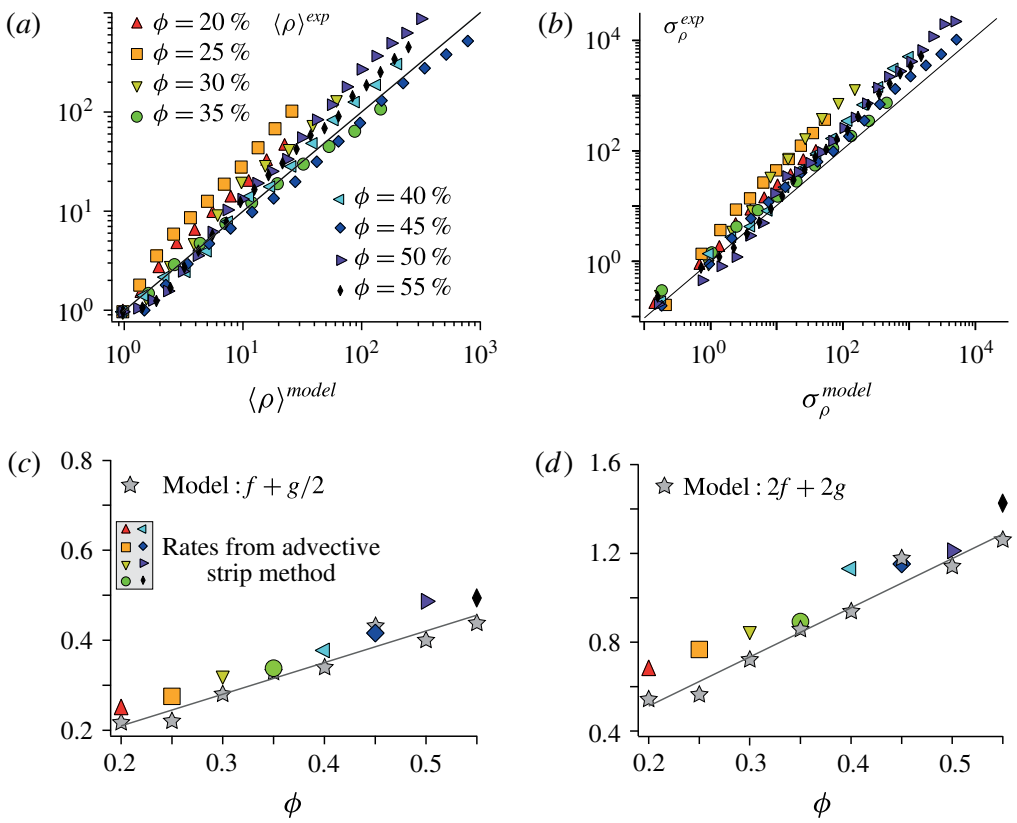


FIGURE 12. (Colour online) Comparison between the experimental stretching (extracted from figure 8) and the multiplicative stretching model. (*a*,*b*) Mean elongation $\langle\rho\rangle$ and standard deviation σ_ρ. The values from the advective strip method are plotted versus those predicted by the multiplicative stretching model. (*c*) Comparison between the exponential rates of the mean elongation κ_ρ obtained from the advective strip method (see figure 8*a*) and the model prediction $f + g/2$ (5.12). (*d*) Comparison between the exponential rates of the variance of the elongation $2\kappa_{\sigma_\rho}$ (see figure 8*b*) and the model prediction $2(f + g)$ (5.13).

and (5.11)). The first term sets the growth of $\langle \ln \rho\rangle$, while the second sets that of $\langle \ln^2 \rho\rangle - \langle \ln \rho\rangle^2$. At a microscopic level, the growth of a given material line depends on its orientation with that of the local velocity gradient. The line length $l(t)$ may increase or decrease depending on whether it is aligned with a diverging or compressive region of the flow. For instance, in a flow corresponding to the pure Brownian motion limit (Cocke 1971), for which $\dot{\rho}/\rho = B(t)$ with $B(t)$ a zero-mean, delta-correlated noise, i.e. $\langle B(t)\rangle = 0$ and $\langle B(t')B(t'')\rangle = (1/\tau_0)\delta(t' - t'')$, these two contributions are balanced and the net line growth $\mathrm{d}\ln \rho(t)/\mathrm{d}t = \dot{l}(t)/l(t)$ is, on averaging over all directions, identically zero. In that case, representative of $t_c \to 0$, the material lines only grow through the contribution of the fluctuations of $B(t)$, which results in $\mathrm{d}\langle \ln \rho\rangle/\mathrm{d}t = 0$, and $\langle (\ln \rho)^2\rangle \sim 2t/\tau_0$: the logarithm of the elongation diffuses.

In particulate suspensions, the situation is different since if the direction of the stretch indeed changes at random, it has a finite persistence time. In such case, it has been shown that material lines tend to preferentially align in the direction of elongations (see Cocke (1969), Orszag (1970), Girimaji & Pope (1990), Duplat & Villermaux (2000) and also (5.5)). Thus, over an observation period larger than the

Downloaded from https://www.cambridge.org/core. Université d'Aix-Marseille, on 19 Jan 2017 at 18:25:05, subject to the Cambridge Core terms of use, available at https://www.cambridge.org/core/terms. https://doi.org/10.1017/jfm.2016.828

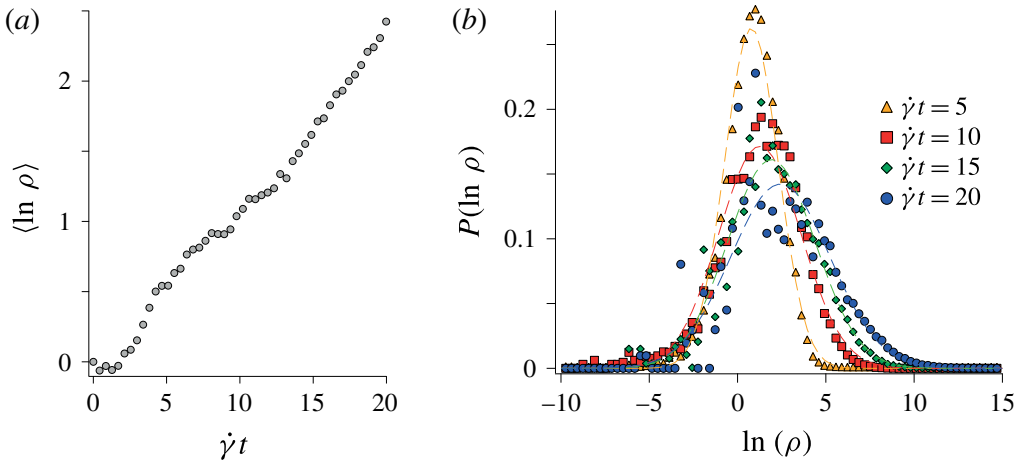


FIGURE 13. (Colour online) (*a*) Mean logarithm of the material line elongations, $\langle \ln \rho \rangle$ versus $\dot{\gamma} t$ for a suspension of volume fraction $\phi = 35\,\%$. (*b*) PDF of the logarithm of the material line elongations $P(\ln \rho)$ at successive times.

(non-zero) correlation time t_c, we expect

$$\frac{\mathrm{d}}{\mathrm{d}t}\langle \ln \rho \rangle > 0. \tag{5.16}$$

This agrees with our measurements shown in figure 13(*a*): the finite persistence time of the stretching field results in a positive drift term: $f(\phi) > 0$. Although some material lines are subject to compression (see the negative values on the distribution of $\ln \rho$ in figure 13*b*), on average, the logarithm of the elongations $\langle \ln \rho \rangle$ increases with time. Material lines in particulate suspensions thus grow from the contribution of both a drift and a noise. The stretching process thus corresponds to a noisy multiplicative sequence of correlated motions, like the random Sine Flow (Meunier & Villermaux 2010), or porous media flows (Le Borgne *et al.* 2015). Porous media and sheared particulate suspensions have similar exponential stretching laws. This is true in 3D systems, as in both cases the fluid trajectories are chaotic. Note, however, that for 2D systems the implications of steadiness change the picture qualitatively. In a 2D porous media, the flow is steady and there are only two degrees of freedom : the flow is thus not chaotic. The elongation of material lines in 2D synthetic porous media have been shown to grow algebraically rather than exponentially (Le Borgne *et al.* 2015). Conversely, in 2D sheared suspensions, the time dependence of the flow allows the system to be chaotic (Metzger *et al.* 2013). One therefore expect to observe exponential stretching laws in sheared particulate suspensions also in purely 2D configurations.

5.3. *Further remarks*

We would like to point out certain limitations of the present study. First, the present findings and their analysis are restricted to the particulate volume fraction $20\,\% \leqslant \phi \leqslant 55\,\%$, for which material lines in the suspending liquid stretch exponentially with strain. This is not necessarily the case outside this range. In particular, as $\phi \to 0$, this exponential trend must cross over to linear since the elongation of material lines in a simple shear is linear with strain. However, we anticipate that the exponential trend could hold down to fairly low volume fractions, but only emerge after increasingly large strains, since the velocity correlation time in

Downloaded from https://www.cambridge.org/core. Université d'Aix-Marseille, on 19 Jan 2017 at 18:25:05, subject to the Cambridge Core terms of use, available at https://www.cambridge.org/core/terms. https://doi.org/10.1017/jfm.2016.828

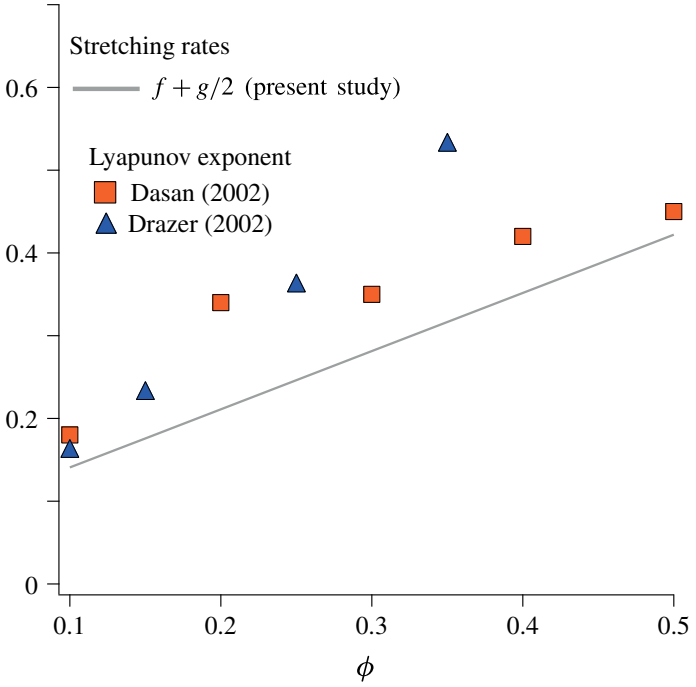


FIGURE 14. (Colour online) Comparison between the stretching rates obtained in the present study and the largest Lyapunov exponent obtained from 3D Stokesian dynamics simulations (Dasan *et al.* 2002; Drazer *et al.* 2002).

the dilute limit should follow $\tau \sim (\dot{\gamma}\phi)^{-1}$ and diverge at low ϕ. Further investigations are needed to characterize this dilute regime ($\phi < 20\,\%$).

Second, the PIV measurements performed here are two-dimensional and provide the fluid velocity projected in the (xy) plane only. They therefore neglect part of the stretching of the material lines, namely that involving deformations in the vorticity direction (z). However, we believe that they resolve the stretching mechanism and most of its magnitude for the following reasons. (i) These measurements resolve the fluid displacements in the gradient direction (y), which is the only direction for which displacements couple with the main shear flow to produce enhanced stretching. The fluctuations in the vorticity direction are thus expected to produce less stretching than those occurring in the gradient direction. (ii) Particles in a shear flow rotate mainly about the vorticity axis, thereby inducing fluid disturbances mostly in the velocity-gradient plane, which we consider. Here again, the effects of the velocity disturbances induced by the particle rotation should be smaller in the vorticity direction than those occurring in the velocity-gradient plane. (iii) More quantitatively, the stretching rates $f + g/2$ predicted by the present model based on 2D data are in good agreement with the largest Lyapunov exponents obtained from 3D Stokesian simulations, see figure 14. From the above considerations, it is likely that the mechanisms at the origin of the scalar dispersion, stretching and subsequent mixing are well characterized by the present measurements, even though those are limited to the information contained in the xy plane.

Third, as already mentioned in § 3, the stretching of material lines is exponential at every scale, but the stretching of a material blob with thickness s_0 is expected to follow that of material lines only if its thickness is smaller than the correlation scale of the fluid motion, which is of order d (in the other case, the blob is first essentially stretched by the macroscopic shear $\dot{\gamma}$ until $s \leqslant d$). In the following, we will therefore only consider the relevant case $s_0 \leqslant d$.

Downloaded from https://www.cambridge.org/core. Université d'Aix-Marseille, on 19 Jan 2017 at 18:25:05, subject to the Cambridge Core terms of use, available at https://www.cambridge.org/core/terms. https://doi.org/10.1017/jfm.2016.828

The latter considerations have important consequences on the estimation of the blob thickness s, hence on the mixing time that we will address in the next section. For an arbitrary elongation w/w_0 in the vorticity direction (z), mass conservation gives $s_0 l_0 w_0 = s(t)l(t)w(t)$. However, in light of the above discussion, the flow is assumed to be two-dimensional with $w/w_0 \ll l/l_0$. Mass conservation thus results in

$$s_0 l_0 = s(t)l(t). \tag{5.17}$$

Using direct image analysis, we have checked that this is experimentally verified. A blob with initial surface $s_0 l_0$ being converted into a strip with length $l(t)$ and thickness $s(t)$ indeed obeys, before it starts mixing, equation (5.17), suggesting that the flow is indeed area preserving.

6. Implications for mixing

In such area-preserving flow, the thickness $s(t)$ of a distorted blob decreases in inverse proportion of its length $l(t)$ according to (5.17). As recalled in the introduction, the mixing time for a given blob portion of thickness s is reached when its compression rate $-\dot{s}/s$ is balanced by its rate of diffusive broadening D/s^2. At that time, called the mixing time, the scalar concentration carried by that portion of the blob starts to significantly decay i.e., mix. Since in particulate suspensions $\rho = l(t)/l_0 = \mathrm{e}^{\kappa\dot{\gamma}t}$, the mixing time is written as $t_{mix} \simeq \dot{\gamma}^{-1} \ln(\kappa Pe)/(2\kappa)$.

We also found that the logarithm of the elongations of an ensemble of such material lines is normally distributed, with a mean and a variance growing linearly with time following $\mu = \langle \ln \rho \rangle = f(\phi)\dot{\gamma}t$ and $\sigma^2 = g(\phi)\dot{\gamma}t$ (see (5.10) and (5.11), respectively). These results are illustrated in figure 15(*a*). Since, similarly to the logarithm of the elongations, the stretching rates, $\kappa\dot{\gamma} = \ln \rho/t$ are normally distributed, the median mixing time, obtained for the mean stretching rate, i.e. for $\langle \kappa\dot{\gamma} \rangle = \langle \ln \rho \rangle / t = \mu/t = f(\phi)\dot{\gamma}$, is

$$t_{mix}^{med} \approx \frac{1}{2f(\phi)\dot{\gamma}} \ln(f(\phi)Pe). \tag{6.1}$$

Considering a blob distorted in such a way that it samples all the possible elongations in the global statistics, the above estimate provides the time at which half of the blob has reached its mixing time. The logarithmic dependence of the mixing time on the Péclet number is different from that obtained in a simple shear flow (without particles) for which $\rho \simeq \dot{\gamma}t$ yields $t_{mix} \simeq \dot{\gamma}^{-1} Pe^{1/3}$. Introducing particles in a viscous fluid therefore becomes more and more efficient at reducing the mixing time as the Péclet number increases. In the present study, the Péclet number is $Pe \sim 10^6$. The median mixing time for $\phi = 35\,\%$ is thus $t_{mix}^{med} \simeq 30/\dot{\gamma}$, which has to be compared with $t_{mix} \simeq 100/\dot{\gamma}$ in a pure shear flow. Note that varying the volume fraction from 20 % to 55 % increases $f(\phi)$ only by a typical factor of 2, which decreases the median mixing time by approximately the same moderate factor.

In practical situations, mixing half of the scalar may not be the relevant question, precisely because, in particulate suspensions, elongations are, as seen in figure 5, broadly distributed. So are mixing times. To address this point, we estimate, for the same conditions as previously, the mixing times for the portions of the blob that undergo the largest and the lowest stretching rates respectively, i.e. the mixing times corresponding to both tails of the distribution (highlighted in figure 15*a*). The 3 % most strongly stretched portions of the blob are bounded by $\ln \rho = \mu + 2\sigma$. The expression $-\dot{s}/s = D/s^2$ results in $2f(\phi)\dot{\gamma}t + 4\sqrt{g(\phi)\dot{\gamma}t} = \ln[(f(\phi) + \sqrt{g(\phi)/\dot{\gamma}t})Pe]$,

Downloaded from https://www.cambridge.org/core. Université d'Aix-Marseille, on 19 Jan 2017 at 18:25:05, subject to the Cambridge Core terms of use, available at https://www.cambridge.org/core/terms. https://doi.org/10.1017/jfm.2016.828

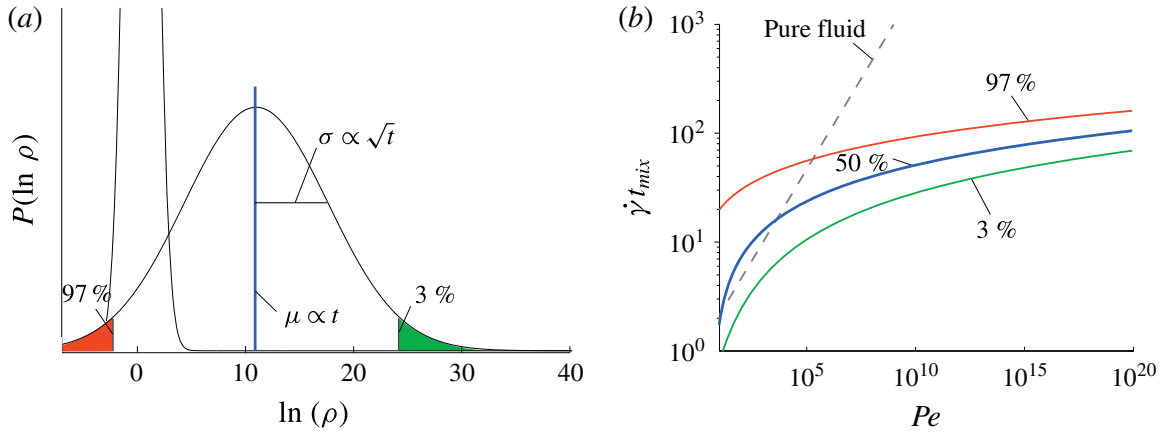


FIGURE 15. (Colour online) (*a*) Evolution of the distribution $P(\ln \rho)$ of the logarithm of the material line elongations in a particulate suspension. The mean of the distribution $\mu \sim t$ and its standard deviation $\sigma \sim \sqrt{t}$. (*b*) Dimensionless mixing times $\dot{\gamma} t_{mix}$ in a suspension ($\phi = 35\,\%$) as a function of Pe. The median (blue line), the most stretched $t_{mix}^{3\,\%}$ (green line), and the less stretched $t_{mix}^{97\,\%}$ (red line) dimensionless mixing times can be compared to the dimensionless mixing time $\sim Pe^{1/3}$ expected in a pure fluid (dashed line).

which yields the mean field mixing time $t_{mix}^{3\,\%} \simeq 14/\dot{\gamma}$. On the other end of the distribution, the less stretched portions of the blob, bounded by $\ln \rho = \mu - 2\sigma$, reach their mixing time at $t_{mix}^{97\,\%} \simeq 64/\dot{\gamma}$, later than if it were sheared in a pure fluid. In figure 15(*b*), the median (blue line), the most stretched $t_{mix}^{3\,\%}$ (green line), and the less stretched $t_{mix}^{97\,\%}$ (red line) dimensionless mixing times are plotted as a function of the Péclet number. This shows that if the concern is to mix essentially all the scalar, large Péclet numbers ($\gg 10^5$) are required before mixing in a suspension becomes more efficient than in a pure fluid. Persistent poorly stretched regions are deterring. The relative width σ/μ of the stretching rate distribution decreases in time like $t^{-1/2}$ but this only mildly decreases the spreading of the mixing times as Pe increases, since $t_{mix} \propto \ln Pe$. For instance, at $Pe = 10^{20}$, the mixing times remain fairly distributed with $t_{mix}^{97\,\%}/t_{mix}^{3\,\%} > 2$.

Finally, the results obtained on the stretching laws must be related to the overall dispersion of the blob. In a random flow, line stretching, and dispersion, are two different things: because the extent of the area occupied by the blob grows more slowly than the area where the scalar constitutive of the blob is dispersed, the blob will at some point unavoidably reconnect and merge by overlapping onto itself (Duplat & Villermaux 2008). Let us see how: after the mixing time, a scalar blob with length growing like $l(t) = l_0 e^{\dot{\gamma} t}$ has a transverse concentration profile whose width is confined to the Batchelor scale $\sqrt{Dt}$. The area $\mathcal{A}$ occupied by the scalar is thus $\mathcal{A} = \sqrt{Dt}\, l_0 e^{\dot{\gamma} t}$, growing exponentially in time. Now, the spatial support of the blob undergoes a dispersion induced by the particle effective dispersion coefficient $D_{eff} \sim \dot{\gamma} d^2$ (Eckstein *et al.* 1977). The total area explored by the blob of dye, within which the blob folds, is typically (see also Taylor (1953) in a related, but different context), $\Sigma \sim (l_0 + \sqrt{D_{eff} t}) \times (s_0 + \sqrt{D_{eff} t}) \dot{\gamma} t \sim d^2 (\dot{\gamma} t)^2$, growing algebraically in time. Because an exponential will always beat a power law, there will necessary be a time for which the area occupied by the scalar overcomes that visited by the blob (i.e. $\Sigma/\mathcal{A} < 1$) and, from that instant of time, overlaps of the folded scalar filaments will be unavoidable. Such an event is illustrated in figure 16. These overlaps will locally delay the mixing process and therefore affect the whole route of the mixture towards homogenization. This aspect, and more generally all aspects regarding the concentration content of the mixture and its evolution, are left for future research.

Downloaded from https://www.cambridge.org/core. Université d'Aix-Marseille, on 19 Jan 2017 at 18:25:05, subject to the Cambridge Core terms of use, available at https://www.cambridge.org/core/terms. https://doi.org/10.1017/jfm.2016.828

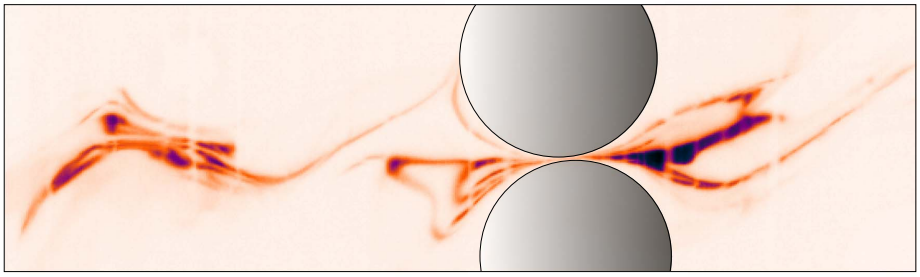


FIGURE 16. (Colour online) Picture illustrating the complexity of folding of the stretched blob of dye and the potential interaction (merging) of nearby filaments.

7. Conclusions

Motivated by the need to understand on a firm basis the mixing properties of particulate flows, we have provided a complete characterization of the kinematics of stretchings and consecutive elongations of material lines in non-Brownian particulate suspensions under a simple macroscopic shear. Our observations rely on high-resolution PIV measurements of the interstitial fluid velocity field, and our findings are as follows.

(i) Following the Diffusive Strip Method of Meunier & Villermaux (2010), we used the experimentally measured velocity fields to numerically advect passive segments in order to reconstruct the stretching histories of fluid material lines. In agreement with previous theoretical predictions and simulation results, we observe that adding particles in a shear flow changes the very nature of the stretching laws from linear to exponential in strain. The growth rate for the mean elongation are found to closely agree with the largest Lyapunov exponent obtained from 3D numerical simulations (Dasan *et al.* 2002; Drazer *et al.* 2002). Besides the mean, our analysis also provides the full statistics of the material line elongation: the variances of the elongations also grow exponentially in strain and the distributions of elongations converge towards log-normals. This statistics of elongation was characterized for a large range of volume fractions $20\,\% \leqslant \phi \leqslant 55\,\%$.

(ii) Using the same velocity fields, we determined the distribution of the local shear rate intensities and their persistence time. From these, we have shown how the fluid material lines undergo a multiplicative stretching process consisting in a noisy multiplicative sequence of correlated motions. We also discussed the important role of the finite correlation time of the velocity field. The model quantitatively predicts the evolution of the mean and the variance of the elongations of the fluid material lines as well as their evolution towards a log-normal distribution.

(iii) We have discussed the importance of this characterization of the flow kinematics to understand how mixing proceeds in sheared particulate suspensions. The exponential stretching results in a mixing time increasing logarithmically with the Péclet number. Moreover, the broad distribution of stretching rates implies a broad distribution of mixing times. The stochastic nature of the stretching process thus allows stretching rates that are smaller than in a pure shear flow. However,

Downloaded from https://www.cambridge.org/core. Université d'Aix-Marseille, on 19 Jan 2017 at 18:25:05, subject to the Cambridge Core terms of use, available at https://www.cambridge.org/core/terms. https://doi.org/10.1017/jfm.2016.828

our analysis shows that the occurrence of such events becomes negligible at large Péclet number ($\gg 10^5$), as mixing occurs at larger deformations.

The present study opens the way for a complete description of the mixing process occurring in sheared particulate suspension. In particular, it allows the prediction of the evolution of the concentration distribution $P(C, t)$ (Duplat *et al.* 2010). A quantitative verification of these predictions requires a specific experimental device that resolves the Batchelor scale $s(t_{mix})$ which corresponds to the transverse dimension of the filaments at the time when diffusion significantly modifies the concentration levels. Such challenging measurements will be addressed in future studies.

Acknowledgements

We would like to thank P. Meunier for letting us use his DSM code, S. Dagois Bohy, S. Gallier, E. DeGiuli, M. Wyart and O. Pouliquen for thoughtful discussions, and P. Cervetti, S. Noel and S. Martinez for helping us build the experimental set-up. This work was supported by ANR JCJC SIMI 9 and by the Labex MEC ANR-10-LABX-0092 et ANR-11-IDEX-0001-02.

Supplementary movies

Supplementary movies are available at https://doi.org/10.1017/jfm.2016.828.

REFERENCES

AFONSO, M. M. & VINCENZI, D. 2005 Nonlinear elastic polymers in random flow. *J. Fluid Mech.* **540**, 99–108.

ARP, P. A. & MASON, S. G. 1976 The kinetics of flowing dispersions IX. Doublets of rigid spheres (experimental). *J. Colloid Interface Sci.* **61** (4095), 44–61.

BATCHELOR, G. K. 1959 Small-scale variation of convected quantities like temperature in a turbulent fluid. Part 1. General discussion and the case of small conductivity. *J. Fluid Mech.* **5**, 113–133.

BOYER, F., GUAZZELLI, E. & POULIQUEN, O. 2011 Unifying suspension and granular rheology. *Phys. Rev. Lett.* **107**, 188301.

BREEDVELD, V., VAN DEN ENDE, D., BOSSCHER, M., JONGSCHAAP, R. J. J. & MELLEMA, J. 2002 Measurement of the full shear-induced self-diffusion tensor of noncolloidal suspensions. *J. Chem. Phys.* **116**, 23, 10529–10535.

BUCH, K. A. JR & DAHM, W. J. A. 1996 Experimental study of the fine-scale structure of conserved scalar mixing in turbulent shear flows. *J. Fluid Mech.* **317** (Part 1), 21–71.

CHATEAU, X., OVARLEZ, G. & TRUNG, K. L. 2008 Homogenization approach to the behavior of suspensions of noncolloidal particles in yield stress fluids. *J. Rheol.* **52**, 489–506.

COCKE, W. J. 1969 Turbulent hydrodynamic line stretching: consequences of isotropy. *Phys. Fluids* **12** (12), 2488–2492.

COCKE, W. J. 1971 Turbulent hydrodynamic line-stretching: the random walk limit. *Phys. Fluids* **14** (8), 1624–1628.

CULBERTSON, C. T., JACOBSON, S. C. & RAMSEY, J. M. 2002 Diffusion coefficient measurements in microfluidic devices. *Talanta* **56**, 365–373.

DA CUNHA, F. R. & HINCH, E. J. 1996 Shear-induced dispersion in a dilute suspension of rough spheres. *J. Fluid Mech.* **309**, 211–223.

DAGOIS-BOHY, S., HORMOZI, S., GUAZZELLI, E. & POULIQUEN, O. 2015 Rheology of dense suspensions of non-colloidal spheres in yield-stress fluids. *J. Fluid Mech.* **776**, R2.

DASAN, J., RAMAMOHAN, T. R., SINGH, A. & NOTT, P. 2002 Stress fluctuations in sheared Stokesian suspensions. *Phys. Rev.* E **66**, 021409.

DRAZER, G., KOPLIK, J., KHUSID, B. & ACRIVOS, A. 2002 Deterministic and stochastic behaviour of non-Brownian spheres in sheared suspensions. *J. Fluid Mech.* **460**, 307–335.

Downloaded from https://www.cambridge.org/core. Université d'Aix-Marseille, on 19 Jan 2017 at 18:25:05, subject to the Cambridge Core terms of use, available at https://www.cambridge.org/core/terms. https://doi.org/10.1017/jfm.2016.828

DUPLAT, J., INNOCENTI, C. & VILLERMAUX, E. 2010 A nonsequential turbulent mixing process. *Phys. Fluids* **22**, 035104.

DUPLAT, J. & VILLERMAUX, E. 2000 Persistence of material element deformation in isotropic flows and growth rate of lines and surfaces. *Eur. Phys. J.* B **18**, 353–361.

DUPLAT, J. & VILLERMAUX, E. 2008 Mixing by random stirring in confined mixtures. *J. Fluid Mech.* **617**, 51–86.

ECKSTEIN, E. C., BAILEY, D. G. & SHAPIRO, A. H. 1977 Self-diffusion of particles in shear flow of a suspension. *J. Fluid Mech.* **79**, 191–208.

GIRIMAJI, S. S. & POPE, S. B. 1990 Material-element deformation in isotropic turbulence. *J. Fluid Mech.* **220**, 427–458.

HARLEN, O. G. & KOCH, D. L. 1993 Simple shear flow of a suspension of fibres in a dilute polymer solution at high Deborah number. *J. Fluid Mech.* **252**, 187–207.

LE BORGNE, T., DENTZ, M. & VILLERMAUX, E. 2015 The lamellar description of mixing in porous media. *J. Fluid Mech.* **770**, 458–498.

LERNER, E., DRING, G. & WYART, M. 2015 A unified framework for non-Brownian suspension flows and soft amorphous solids. *Proc. Natl Acad. Sci. USA* **109**, 4798–4803.

METZGER, B. & BUTLER, J. E. 2012*a* Clouds of particles in a periodic shear flow. *Phys. Fluids* **24**, 021703.

METZGER, B. & BUTLER, J. E. 2012*b* Irreversibility and chaos: role of long-range hydrodynamic interactions in sheared suspensions. *Phys. Rev.* E **82**, 051406.

METZGER, B., PHAM, P. & BUTLER, J. E. 2013 Irreversibility and chaos: role of lubrication interactions in sheared suspensions. *Phys. Rev.* E **87**, 052304.

METZGER, B., RAHLI, O. & YIN, X. 2013 Heat transfer across sheared suspensions: role of the shear-induced diffusion. *J. Fluid Mech.* **724**, 527–552.

MEUNIER, P. & LEWEKE, T. 2003 Analysis and minimization of errors due to high gradients in particle image velocimetry. *Exp. Fluids* **35**, 408–421.

MEUNIER, P. & VILLERMAUX, E. 2003 How vortices mix. *J. Fluid Mech.* **476**, 213–222.

MEUNIER, P. & VILLERMAUX, E. 2010 The diffusive strip method for scalar mixing in two dimensions. *J. Fluid Mech.* **662**, 134–172.

ORSZAG, S. A. 1970 Comments on 'Turbulent hydrodynamic line stretching: consequences of isotropy'. *Phys. Fluids* **13**, 2203–2204.

OTTINO, J. M. 1989 *The Kinematics of Mixing: Stretching, Chaos, and Transport*. Cambridge University Press.

RANZ, W. E. 1979 Applications of a stretch model diffusion, and reaction in laminar and turbulent flows. *AIChE J.* **25**, 1.

SHAQFEH, E. S. G. & KOCH, D. L. 1992 Polymer stretch in dilute fixed beds of fibres or spheres. *J. FLuid Mech.* **244**, 17–54.

SIEROU, A. & BRADY, J. F. 2004 Shear-induced self-diffusion in non-colloidal suspensions. *J. Fluid Mech.* **506**, 285–314.

SOHN, C. W. & CHEN, M. M. 1984 Heat Transfer enhancement in laminar slurry pipe flows with power law thermal conductivities. *Trans. ASME J. Heat Transfer* **106**, 539–542.

SOUZY, M., YIN, X., VILLERMAUX, E., ABID, C. & METZGER, B. 2015 Super-diffusion in sheared suspensions. *Phys. Fluids* **27**, 041705.

TAYLOR, G. 1953 Dispersion of soluble matter in solvent flowing slowly through a tube. *Proc. R. Soc. Lond.* A **219**, 1137.

TRULSSON, M., DEGIULI, E. & WYART, M. 2016 Effect of friction on dense suspension flows of hard particles. Preprint, 2016 (https://arxiv.org/abs/1606.07650).

VILLERMAUX, E. 2012 On dissipation in stirred mixtures. *Adv. Appl. Mech.* **45**, 91–107.

WANG, N. L. & KELLER, K. H. 1985 Augmented transport of extracellular solutes in concentrated erythrocyte suspensions in couette flow. *J. Colloid Interface Sci.* **103**, 210–225.

WANG, L., KOCH, D. L., YIN, X. & COHEN, C. 2009 Hydrodynamic diffusion and mass transfer across a sheared suspension of neutrally buoyant spheres. *Phys. Fluids* **21**, 033303.

Downloaded from https://www.cambridge.org/core. Université d'Aix-Marseille, on 19 Jan 2017 at 18:25:05, subject to the Cambridge Core terms of use, available at https://www.cambridge.org/core/terms. https://doi.org/10.1017/jfm.2016.828

Mixing of lamellae in a shear flow

Mathieu Souzy[2], Imen Zaier[1], Henri Lhuissier[1], Tanguy Le Borgne[2] & Bloen Metzger[1]

[1] Aix-Marseille Université, IUSTI-CNRS UMR 7343, 13453 Marseille Cedex 13, France.
[2] Geosciences Rennes, UMR 6118 Université Rennes 1 CNRS 35042 Rennes France

(Received 8 December 2017)

Mixing dynamics in flows are governed by the coupled action of diffusion and stretching by velocity gradients. This leads to the development of elongated lamellar structures in scalar fields where concentration fluctuations exist at scales set by the Batchelor scale. Because the latter is generally too small to be resolved experimentally, observation of these mechanisms remains an outstanding challenge. Here we present high resolution experiments allowing for the precise quantification of the evolution of concentration distributions at the scale of a single lamella experiencing diffusion, stretching and aggregation with other lamellae. Quantitative agreement is found with analytical predictions for the lamella's concentration profile, Batchelor time, Batchelor length-scale, and concentration distribution for a large range of Péclet numbers and without adjustable parameter. This benchmark configuration is used to set the experimental spatial-resolution required to quantify the concentration Probability Density Functions (PDF) of scalar mixtures in fluids. The diffusive coalescence of two nearby lamellae, the mechanism by which scalar mixtures ultimately reach uniformity, is shown to induce a complex transient evolution of the concentration PDFs.

1. Introduction

Mixing is a key process in many industrial applications and natural phenomena (Ottino 1989). Practical examples include glass manufacture, processing of food, micro-fluidic manipulations, and contaminant transport in the atmosphere, oceans and hydrological systems. During the last decades, substantial progresses have been made in the description of mixing in systems as complex as turbulent flows (Warhaft 2000, Shraiman & Siggia 2000, Falkovich *et al.* 2001, Duplat & Villermaux 2008, Kalda 2000), oceanic and atmospheric flows (Rhines & Young 1983), the earth mantle (Allègre & Turcotte 1986), porous media (Dentz *et al.* 2011, Villermaux 2012, Le Borgne *et al.* 2015) and sheared particulate suspensions (Souzy *et al.* 2017). In particular, the conceptualization of scalar mixtures as ensembles of 'lamellae' evolving through stretching, diffusion and aggregation (Ranz 1979, Villermaux & Duplat 2003) has allowed deriving quantitative accurate theoretical predictions for the evolution of the full concentration Probability Density Functions (PDF) for a broad range of flows. Within this framework (valid for lamellae thinner than the smallest scale within the flow), mixing is driven by three processes occurring simultaneously: i) stretching a scalar field by a given flow creating elongated lamellar structures, ii) diffusion and compression that compete to define concentration gradients and iii) lamella coalescence leading ultimately to the final homogeneity of the system (Duplat & Villermaux 2008).

In complex configurations such as those listed above, the evolution of the concentration distribution is sensitive to a number of characteristics of the system: the distribution of

stretching rates, the macroscopic dispersion rate, the scalar molecular diffusion coefficient and the rate at which lamellae aggregate. While their influence on the dynamics of mixing is clear from a theoretical point of view, they can rarely be observed independently. Moreover, in spite of the numerous experimental studies on mixing, the question of the spatial resolution required to quantify the evolution of a concentration field has received little attention. This latter point is obviously crucial since under-resolved images, by artificially broadening the concentration distribution of isolated lamellae or conversely, by sharpening the concentration distribution of bundles of adjacents lamellae, lead to an erroneous appreciation of the mixing rate.

Here, we present highly resolved experiments where the basic mechanisms governing mixing are quantified individually: the formation of elongated lamellae by stretching, the establishment of a Batchelor scale by competition between compression and diffusion, the enhancement of diffusive mixing by stretching and the diffusive aggregation of lamellae. We consider for this a lamella formed by photo-bleaching of a fluorescent dye in a laminar shear flow where the concentration distribution can be quantified using a well controlled experimental set-up, built specifically to resolve small length scales. This benchmark experiment was chosen precisely because it is well established theoretically. Unambiguous conclusions can therefore be drawn regarding the spatial resolution required to capture the evolution of the concentration distribution of an isolated lamella, and more generally within any mixing protocols. Moreover, it illustrates with an unprecedented resolution and level of details the basic lamellar theories for mixing at the scale of a single lamella. Last, we investigate the coalescence of two nearby lamellae specifically focusing on its impact on the evolution of the concentration distribution. The theoretical prerequisites are recalled in § 2. After presenting the experimental set-up in § 3, the measurements are reported in § 4. Conclusions are drawn in § 5.

2. Mixing in a laminar shear flow

2.1. *General picture*

We consider a lamella of dye of length l_0 and half width s_0 initially positioned perpendicular to the flow as illustrated in Figure 1.a. As the lamella is advected by a laminar shear flow with a shear-rate $\dot{\gamma}$, its length increases as $l(t) = l_0\sqrt{1+(\dot{\gamma}t)^2}$. Thus, considering the sole effect of the advection field (for now neglecting that of molecular diffusion), the half width of the lamella $s_A(t)$ decreases following $s_A(t) = s_0/\sqrt{1+(\dot{\gamma}t)^2}$ (see Figure 1.b) since in this two dimensional flow, mass conservation prescribes $s_0 l_0 = s_A(t)l(t)$. The effect of the shear flow can thus be quantified by a compression rate $-1/s_A ds_A/dt$ which describes how fast the lamella transverse dimension thins down owing to its stretching by the advection field. Conversely, molecular diffusion tends to broaden the lamella with a diffusive broadening rate D_0/s_A^2, where D_0 is the molecular diffusion coefficient of the scalar. Balancing these two rates, $-1/s_A ds_A/dt \sim D_0/s_A^2$ and assuming $\dot{\gamma}t \gg 1$, naturally defines a time-scale, also called the Batchelor time, $t_B \sim Pe^{1/3}/\dot{\gamma}$ where $Pe = \dot{\gamma}s_0^2/D_0$ denotes the Péclet number. This time corresponds to the onset of the homogenization of the concentration levels within the system, beyond which the concentration levels within the lamella start to significantly decay.

2.2. *Exact solution*

The complete description of the evolution of the lamella of dye can be found by directly solving the full advection-diffusion equation

$$\frac{\partial C}{\partial t} + \mathbf{u}.\nabla C = D_0\nabla^2 C, \tag{2.1}$$

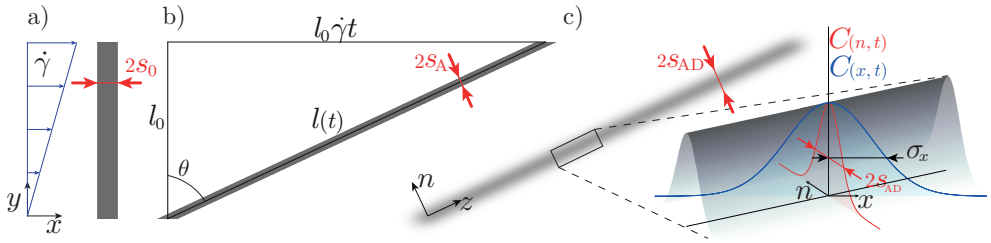


FIGURE 1. a) Schematic of a lamella of dye of initial length l_0 and half width s_0 advected in a laminar shear flow. b) Effect of the advection field alone: the strain $\dot{\gamma}t$ has stretched the lamella and thinned down its transverse dimension to $2s_A(t)$. c) Effect of both advection and molecular diffusion: at the same strain, the half width of the lamella is denoted $s_{AD}(t)$. Inset: schematic of the gaussian concentration field of the lamella with its concentration profiles along the flow $C(x,t)$ and transverse to the lamella $C(n,t)$.

where $\mathbf{u} = (\dot{\gamma}y, 0, 0)$ denotes the advection field, and C the concentration field.

This equation can be simplified (Ranz 1979, Rhines & Young 1983, Ottino 1989, Meunier & Villermaux 2003) if written in a moving frame (n, z) aligned with the directions of maximal compression and stretching of the lamellae (see Figure 1.c), and by using Ranz's transform (Ranz 1979) which uses warped time units, $\tau = \int_0^t D_0/s_A^2(t')dt'$, and distances normalized by the lamella transverse dimension, $\xi = n/s_A(t)$. Equation (2.1) then reduces to a simple diffusion equation

$$\frac{\partial C}{\partial \tau} = \frac{\partial^2 C}{\partial \xi^2}, \tag{2.2}$$

whose solution for an initial gaussian concentration profile with maximum C_0 is

$$C(\xi, \tau) = \frac{C_0}{\sqrt{1+4\tau}} e^{-\frac{\xi^2}{1+4\tau}}. \tag{2.3}$$

The maximum concentration of the lamella thus decays with time according to

$$C_{\max}(t) = \frac{C_0}{\sqrt{1+4\tau}}. \tag{2.4}$$

Since the half width of the lamella in Ranz's units is $\sigma_\xi = (1+4\tau)^{1/2}$ (see equation 2.3), the transverse dimension of the lamella $s_{AD}(t)$, accounting both for the effect of advection and diffusion, and expressed in standard unit of length is

$$s_{AD}(t) = \sigma_\xi s_A(t) = \frac{s_0(1+4\tau)^{1/2}}{\sqrt{1+(\dot{\gamma}t)^2}}. \tag{2.5}$$

The latter expression gives access to the half width of the lamella along the flow ($x-$direction)

$$\sigma_x(t) = \frac{s_{AD}(t)}{\cos\theta} = \sigma_0(1+4\tau)^{1/2}, \tag{2.6}$$

with $\sigma_0 = s_0$ and $\cos\theta = 1/\sqrt{1+(\dot{\gamma}t)^2}$ (see Figure 1).

We now have access to a more accurate estimation of the Batchelor time which by definition is reached when $\tau = 1$ (Ranz 1979). Since $\tau = D_0(t+\dot{\gamma}^2t^3/3)/s_0^2$, the Batchelor time, for $Pe \gg 1$, is

$$t_B \approx \frac{(3Pe)^{\frac{1}{3}}}{\dot{\gamma}}. \tag{2.7}$$

At this time, the transverse dimension of the lamella, from now on referred to as the

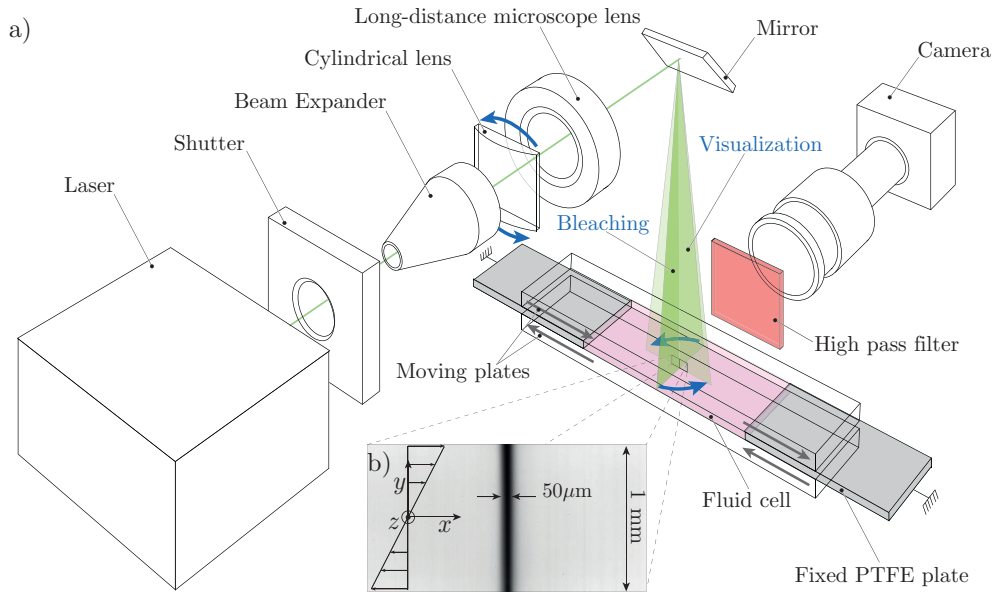


FIGURE 2. (color version online) a) Schematic of the set-up. b) Typical image of a lamella obtained by photo-bleaching.

Batchelor scale (Batchelor 1959), is found to be

$$s_{\mathrm{AD}}(t_{\mathrm{B}}) = s_0\sqrt{5}(3Pe)^{-\frac{1}{3}}. \tag{2.8}$$

Last, the evolution of the concentration distribution $P(C,t)$ of the lamella can be derived. Using the following change of variables $P(C)dC = P(x)dx$ yields $P(C) = P(x)|dC/dx|^{-1}$ which can easily be expressed from

$$C(x,t) = C_{\max}(t)e^{-\frac{x^2}{\sigma_0^2(1+4\tau)}}, \tag{2.9}$$

and the uniformity of $P(x)$. Considering the range of concentration $C_{\mathrm{th}} \leqslant C \leqslant C_{\max}(t)$, above any arbitrary threshold concentration C_{th} (larger than the experimental background noise), one obtains

$$P(C,t) = \frac{1}{\beta C\sqrt{\ln(C_{\max}/C)}}, \tag{2.10}$$

where β is a normalizing prefactor insuring that $\int_{C_{\mathrm{th}}}^{C_{\max}(t)} P(C,t)dC = 1$.

The above set of equations fully describes the evolution of a lamella of dye advected in a laminar shear flow.

3. Experimental set-up

The experimental set-up is shown in Figure 2. It consists of a shear-cell made of two parallel plexiglass plates sandwiching a fluid cell 85 mm long, 25 mm wide and of height $h = 3$ mm. The fluid is sheared by setting the two plates into opposite motion with two high-resolution translation stages (not shown on the schematic). The travel-range of the plate enables a maximum strain of 30. The cell is sealed on both ends by two PTFE plates (grey in Figure 2), and on the sides by two transparent side walls (not shown on the schematic) mounted on the bottom moving plate.

The fluid is a Newtonian mixture of triton X-100 (77.4 wt%), zinc chloride (13.4 wt%) and water (9.2 wt%) having a density $\rho = 1.19\,\mathrm{g.cm^{-3}}$ and viscosity $\eta = 4.2\,\mathrm{Pa.s}$ which ensures laminar flow conditions (over the full range of shear rates investigated $\mathrm{Re} = \rho\dot{\gamma}\mathrm{h}^2/\eta \leqslant 10^{-3}$). Prior to filling the cell, some fluorescent dye (Rhodamine 6G)

is thoroughly mixed to the fluid at a concentration of $2\ 10^{-6}$g.mL^{-1}. The molecular diffusion coefficient of this dye was measured in the cell with the fluid at rest using a technic similar to that reported in Souzy *et al.* 2017. We find $D_0 \approx 2.66\ 10^{-13}$m^2 s^{-1} at a temperature of $22°C$.

The initial lamella is generated using fluorescent recovery after photo-bleaching, (Axelrod *et al.* 1976). A high-power-laser-diode beam (Laser Quantum Gem512-2.5W) is shaped into a thin laser sheet using the combination of lenses set in their 'bleaching' configuration as shown in Figure 2.a. This sheet, oriented in the $y-z$ plane (perpendicular to the flow) and used with full intensity, locally changes the conformation of the rhodamine molecules which irreversibly become unable to fluoresce.

Then, the set-up is set into its 'visualization' configuration by rotating the cylindrical lens 90°: this orients the laser sheet along the $x-y$ plane (along the flow). The lamella then appears as a thin dark vertical line, see Figure 2.b. Note that the initial lamella is in fact a transverse sheet, rather than just a line. This avoids diffusion in the $z-$direction and enables us to study a purely 2D process. This photo-bleaching technic, relative to a direct injection of fluorescent dye, also insures well-controlled initial conditions: the lamella is uniform and its initial concentration profile is gaussian owing to the gaussian nature of the impacting laser beam.

Immediately after bleaching, the fluid is sheared at the desired shear rate and images of the evolution of the lamella are acquired using a camera (Basler Ace2000-50gm, 2048×1080 pixel^2, 12 bit) coupled to a high-resolution macroscope (Leica Z16 APO×1). The set-up was designed to provide an image resolution (0.8 μm/pixel) small enough to resolve the Batchelor scale (equation 2.8). For instance, with $\dot\gamma = 0.01$ s^{-1} and $s_0 = 25\mu$m, we have $s_{\rm AD}(t_B) = s_0\sqrt{5}(3\dot\gamma s_0^2/D_0)^{-\frac{1}{3}} \approx 10\mu$m. A high-pass filter (590 nm) is positioned between the sample and the camera to eliminate direct light reflexions. To avoid photo-bleaching during the image acquisition, the intensity of the laser is lowered to 100 mW and the image acquisition is synchronized with a shutter opening only during acquisition times. Note that all experiments are performed at $T = 22 \pm 0.05$ °C by setting the temperature of the water running through the bottom moving plate with a cryo-thermostat.

4. Experimental results

4.1. *A single lamella*

Figure 3.a shows successive pictures of a lamella undergoing a laminar shear (see also supplementary movie 1). Initially vertical and highly contrasted, the lamella progressively tilts under the effect of the shear flow while blurring under the effect of molecular diffusion. Accurate measurement of the lamella's concentration profile along the flow ($x-$direction) are obtained by averaging over all horizontal lines of pixels after translating these lines to make their maximum concentration coincide. The resulting average concentration profile of the lamella is shown in Figure 3.b for successive strains: the maximum concentration decays while the width increases. These trends are well captured by fitting each concentration profile with a gaussian of the form $C(x,t) = C_{\max}(t)e^{-x^2/\sigma_x^2(t)}$ (see Figure 3.b).

The resulting maximum concentration $C_{\max}(t)$ and width $\sigma_x(t)$ are plotted in Figure 3.c and 3.d versus time for experiments performed at different Péclet number ($4.5 \leqslant Pe \leqslant 1190$). The Péclet number was varied by repeating the experiment at various shear-rates $\dot\gamma = [6 \times 10^{-4} - 0.3]$ s^{-1}. The agreement with equations 2.4 and 2.6 is very good for both $C_{\max}(t)$ and $\sigma_x(t)$. Note that in both cases, $\dot\gamma$, s_0 and D_0 are fixed by the experimental conditions; there is thus no adjustable parameter. When plotted as a

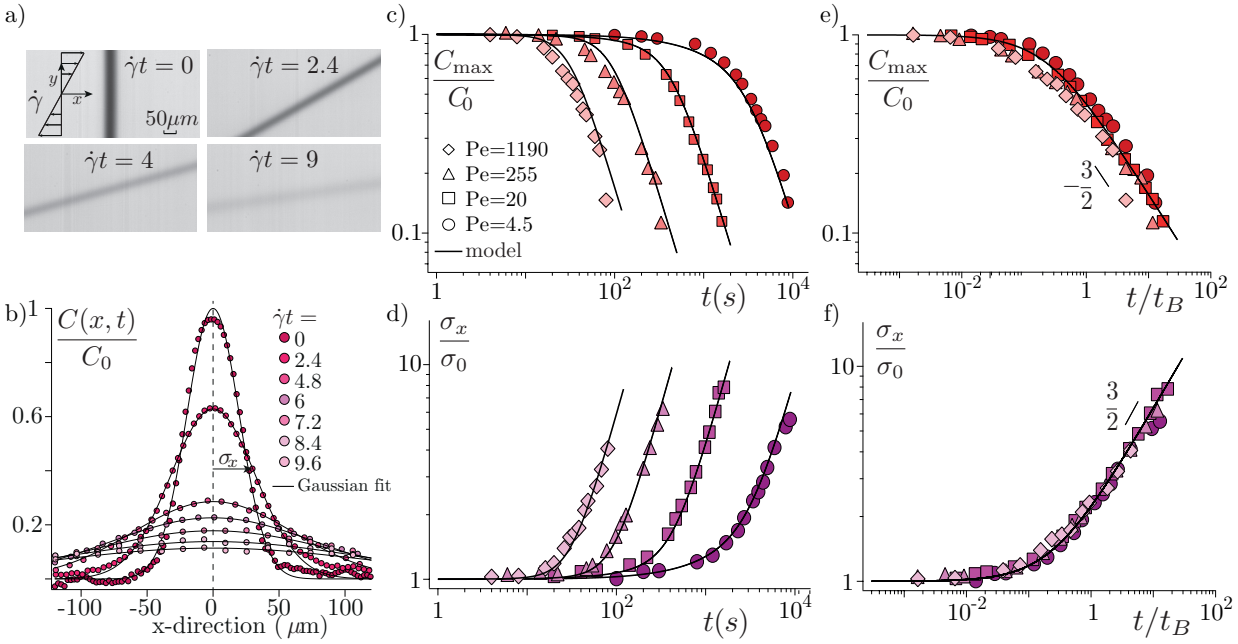


FIGURE 3. (color version online) a) Successive images of a lamella undergoing shear (see also supplementary movie 1). b) Corresponding averaged concentration profiles along the flow ($x-$direction). The black lines are fitting gaussian profiles. c) Normalized maximum concentration $C_{\max}/C_0$ and d) normalized half width of the concentration profiles σ_x/σ_0 versus time for experiments performed at different Péclet numbers. The black lines correspond to equation 2.4 in c) and equation 2.6 in d). In both cases, $\dot{\gamma}$, s_0 and D_0 are set and fixed by the experimental conditions. e) and f) Same data plotted versus t/t_B.

function of the dimensionless time t/t_B, where $t_B = (3\mathrm{Pe})^{1/3}/\dot{\gamma}$ is the Batchelor time, these data are found to collapse, for all Pe, on the same master curve, see Figure 3.e and f. For $t < t_B$, $C_{\max}$ and σ_x remain constant. Then when the effect of molecular diffusion becomes significant, *i.e* for $t > t_B$, $C_{\max}$ (respectively σ_x) starts to decrease (respectively increase) following the power law $t^{-3/2}$ (respectively $t^{3/2}$), consistently with the long time trends of equations 2.4 and 2.6. These measurements clearly illustrate how mixing is accelerated by imposing an external macroscopic shear: larger applied shear rates (larger Péclet numbers) result in earlier mixing times.

We have so far probed the lamella along the direction of the flow. However, further insight into the mixing process, specifically on the advection-diffusion coupling presented above, are provided by probing the lamella width along its transverse direction (along n, see Figure 1). Figure 4.a shows the evolution of $s_{\mathrm{AD}}(t)$ measured experimentally. At an intermediate time, the thickness of the lamella is found to decrease like t^{-1}. After reaching a minimum, it increases like $t^{1/2}$. These trends precisely illustrate the expected interplay between advection and diffusion. The lamella width initially decreases as imposed by the kinematics of the flow following the intermediate time trend (for $t < t_B$) of equation 2.5, $s_{\mathrm{AD}}(t) \sim s_0(\dot{\gamma}t)^{-1}$. However, this compression of the lamella progressively steepens its concentration gradients which beyond the Batchelor time, eventually makes the broadening effect due to molecular diffusion become dominant. The transverse dimension of the lamella then re-increases diffusively like $t^{1/2}$. At the Batchelor time t_B, the lamella typically reaches its minimum thickness which is equal to the Batchelor scale $s_{\mathrm{AD}}(t_B)$ (within 3%). As shown in Figure 4.b, reporting this direct measurement of the Batchelor scale obtained for various Péclet numbers matches the expected prediction $s_{\mathrm{AD}}(t_{\mathrm{B}}) = s_0\sqrt{5}(3Pe)^{-\frac{1}{3}}$, see equation 2.8.

To fully describe the mixing process, we also measure the evolution of the lamella's

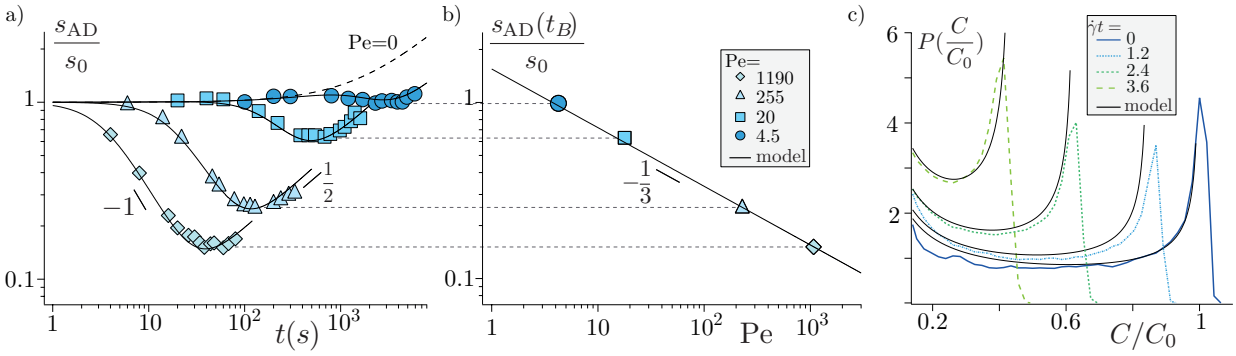


FIGURE 4. (color version online) a) Evolution of transverse dimension of the lamella $s_{AD}(t)/s_0$ versus time for experiments performed at different Péclet numbers. The black lines correspond to equation 2.5. The dotted line corresponds to the solution in the absence of shear, *i.e.* in the pure diffusion limit (Pe = 0). b) Corresponding Batchelor scale $s_{AD}(t_B)/s_0$ versus Péclet number; the black line corresponds to equation 2.8. c) Concentration distribution $P(C/C_0)$ measured at successive strains, $\dot{\gamma}t$, for a lamella sheared at $Pe = 4.5$. The black lines correspond to equation 2.10 with $\dot{\gamma}$. In all cases, $\dot{\gamma}$, s_0 and D_0 are fixed by the experimental conditions.

concentration distribution $P(C, t)$. The distribution $P(C)$ is obtained from the histogram of intensities collected from all the pixels constituting the lamella which are above a threshold $C_{th} = 0.1C_0$. This discards the background image noise enabling us to focus on the peak of interest, that of high concentration. Changing the value of the threshold above the background noise, changes the extend of the spatial domain over which $P(C)$ is computed, but it does not affect its shape. We obtain concentration distributions which have a characteristic U-shape (Ottino 1989), see Figure 4.c. The distribution's maximum probability, initially located at $C = C_0$, progressively drifts to lower values as the lamella is stretched and diffuses. The prediction provided by equation 2.10 is in good agreement with the measured concentration distributions obtained for all Péclet number and again, without adjustable parameter.

The distributions shown above are well resolved since the Batchelor scale is always larger than 10 pixels. However, in most studies on mixing, such a large resolution is not achieved. Moreover, when mixing is investigated in complex systems such as turbulent flows (Duplat & Villermaux 2006), porous media (Le Borgne *et al.* 2015) or recently in sheared particulate suspensions (Souzy *et al.* 2017), the initial lamella of dye does not evolve towards a single lamella with uniform thickness but instead, towards a large number of lamellae having widely distributed thicknesses. In such situations, it is important to know which part of the distribution of lamellae can be resolved experimentally.

To address this point, we systematically investigate how the set-up spatial resolution can bias the measured concentration distribution of a single lamella. This can be achieved by a simple coarsening protocol: the reference concentration distribution (blue dotted line in Figure 5) is obtained from a highly resolved image where the lamella half width spans 8 pixels. When coarsening the pixels of this reference image, (merging 2×2 pixels into one, 4×4 pixels into one and so on) we find that the concentration distribution remains unchanged for images having 4 and 2 pixels across the lamella half width (green dotted lines in Figure 5). Conversely, larger coarsening, *i.e.* images having 1 pixels or less across the lamella half width, yield erroneous results: the concentration distribution departs from the reference one (red dotted lines in Figure 5). The limit of 1 pixels per lamella half width is surprisingly small and comes as encouraging news for experimentalists. This limit holds as long as the concentration profile is smooth (*e.g* gaussian) and there is a finite tilt between the lamella and the lines of pixels. In such case, the progressive drift

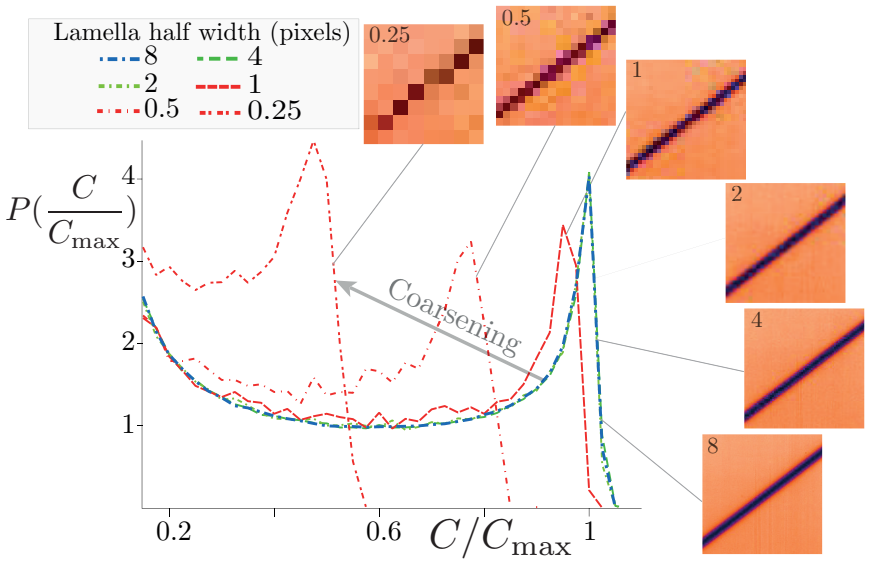


FIGURE 5. (color version online) Distributions of concentration $P(C/C_{\max})$ obtained from the progressive digital coarsening of an experimental image.

of the lamella position relative to that of the pixels scans all the possible concentration levels, thereby providing results consistent with the fully resolved PDF.

4.2. *Two Lamellae*

As mentioned in the introduction, mixing in complex systems generally involves coalescence between dispersed lamellae. This latter step is crucial for the system to reach its final homogeneity. Here, the photo-bleaching technic is used to produce two adjacent lamellae and investigate a single coalescence event.

Figure 6.a shows images of two parallel lamellae captured at successive strains (see also supplementary movie 2). The two lamellae are initially distinct from each other and, as they are stretched by the flow and diffuse, they progressively merge to eventually form one single entity. The evolution of their concentration profiles measured along the flow $x-$direction are shown in Figure 6.b. The two maxima of concentration, corresponding to each lamella, decay (blue arrows) while the minimum located in between increases (green arrow). This goes on until the two lamellae merge into one single lamella whose maximum subsequently decreases (yellow arrow). This evolution can easily be predicted owing to the linearity of the diffusion equation: the concentration profile of a set of two lamellae, with individual profiles $C_1(x,t)$ and $C_2(x,t)$, is simply obtained from the summation $C(x,t) = C_1(x,t) + C_2(x,t)$ (Fourier 1822). Using, for each lamella, equation 2.9 with the initial experimental maximum intensity and width, we thereby obtain the concentration profiles shown in Figure 6.d.

To anticipate the impact of this coalescence on the evolution of the concentration distribution, lets recall that $P(C) \sim |dC/dx|^{-1}$. Thus, each value of $C(x,t)$ where the concentration profile presents an horizontal slope gives rise to a peak in the concentration distribution. This can be clearly observed on the experimental concentration distributions shown in Figure 6.c. As long as the two lamellae are distinct, one not only observes two peaks at large concentrations (corresponding to the maximum of concentration of each lamellae), but also one peak at small concentration (corresponding to the minimum concentration located in between the two lamellae). Then, as the lamellae are stretched and diffuse, the two peaks corresponding to the two concentration maxima, move to the left (blue arrow in Figure 6.c). Conversely, as the concentration in between the two lamellae increases, the small concentration peak moves to the right (green arrow in

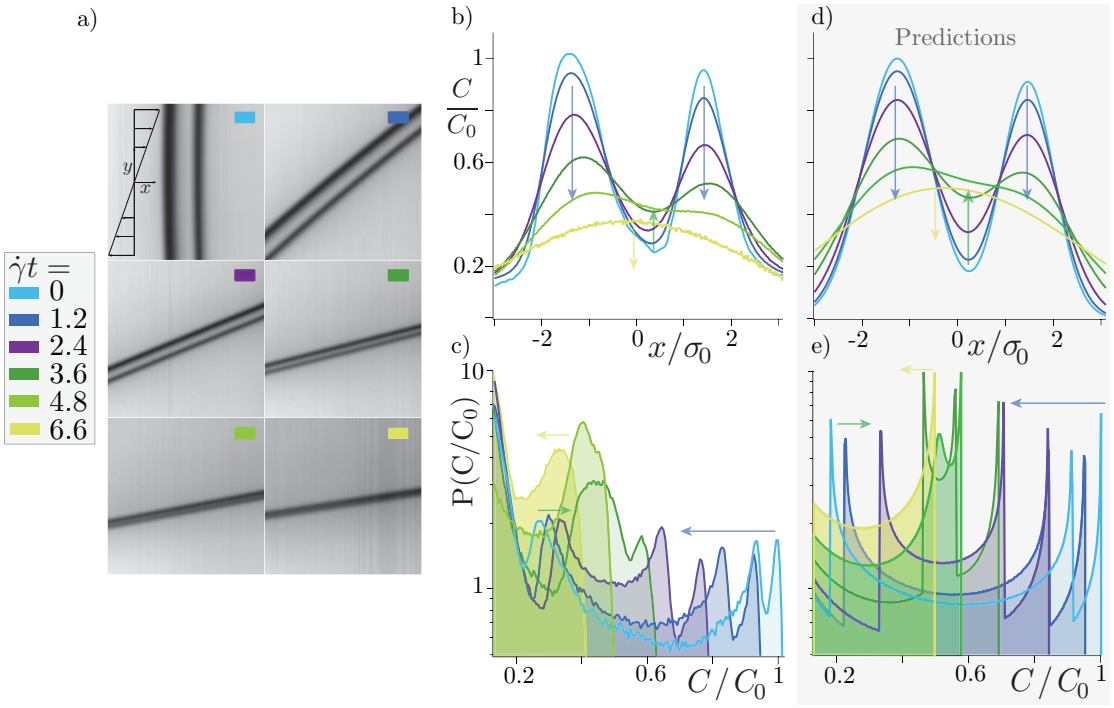


FIGURE 6. (color version online) a) Coalescence of two nearby lamellae advected in a laminar shear flow (see also supplementary movie 2). Evolution of the corresponding experimental b) concentration profiles and c) concentration distributions obtained at successive strains $\dot{\gamma}t$. Predictions for the evolution of d) the concentration profiles and e) the concentration distributions at the same strains. Again, $\dot{\gamma}$, s_0 and D_0 are fixed by the experimental conditions.

Figure 6.c. Coalescence occurs when the three peaks collide; the distribution eventually recovers its characteristic U-shape as the lamellae have coalesced into a single entity. The same phenomenology can be observed on the concentration distributions obtained from numerically computing the slope of the predicted concentration profiles, see Figure 6.e.

5. Discussion and conclusions

We have explored experimentally the basic mechanisms of mixing in stirred flows by thoroughly investigating the evolution of an initially segregated scalar (a lamella of fluorescent dye) stretched within a laminar shear flow. A high resolution set-up, using a photo-bleaching technic to generate and control the shape of the initial lamella, was built in order to resolve length scales at which diffusion plays a significant role. Our measurements of the evolution of the lamella concentration profiles and concentration distributions are, without adjustable parameter, in excellent quantitative agreement, for $Pe = [4.5 - 1190]$, with the theoretical predictions.

We also investigated the evolution of the lamella's transverse dimension which conspicuously illustrates the advection-diffusion coupling yielding at intermediate time to a t^{-1} compression of the lamella dominated by the kinematics of the flow, followed, after the Batchelor time, by a $t^{1/2}$ broadening dominated by molecular diffusion. The Batchelor scale, which to our knowledge was experimentally observed only once (Meunier *et al.* 2015), was here measured systematically for various Péclet number and found to follow the expected behavior, $s_{\mathrm{AD}}(t_B)/s_0 = \sqrt{5}(3Pe)^{-\frac{1}{3}}$.

Most importantly, through a coarsening protocol, we determined the minimal experimental spatial resolution required to resolve the concentration distribution of a single lamella: its half width must be larger than 1 pixel. This requirement is general and

constrains the measurement of any mixing protocol. Indeed, for all stretching protocol, lamellae reach their minimum thickness at the Batchelor time while they are still isolated individual entities. Resolving $P(C)$ at this time, which requires to resolve each individual lamella, therefore is the most demanding in term of spatial resolution: the half width of the lamella at the Batchelor time, $s_{\mathrm{AD}}(t_B)$, shall at least span 1 pixel. Note that measuring P(C) at longer times can be less stringent. Indeed, beyond the Batchelor time, lamellae diffuse sufficiently that, when their spacing becomes sufficiently small, nearby lamellae start merging together. The concentration gradients then no longer vary over the lamellae transverse dimension but instead, over a larger length-scale which reflects the size of the bundles of merging lamellae. In the context of turbulent mixtures for instance, this 'coarse-grained scale' was proposed to follow $\eta = LSc^{-2/5}$ where L denotes the stirring length and Sc the Schmidt number (Duplat & Villermaux 2006). However, the latter length-scale is only relevant after lamellae have merged which occurs after the Batchelor time. Therefore, resolving P(C) at all times requires an experimental spatial resolution satisfying $s_{\mathrm{AD}}(t_B) > 1$ pixel.

Finally, we have investigated the coalescence between two lamellae and its impact on the evolution of the concentration distribution. Lamellae's overlap gives rise to a non-trivial peak at low concentration. This observation is important as it may be relevant to interpret more complex situations.

To conclude, the high resolution experimental technics developed for the present study and the determination of its limitations, open promising perspectives for future studies on mixing.

We thank E. Villermaux and P. meunier for their inspiring comments and suggestions. We would also like to thank Sady Noel for machining the experimental set-up. This work was supported by ANR JCJC SIMI 9, by the Labex MEC ANR-10-LABX-0092, by ANR-11-IDEX-0001-02 and by ERC consolidator grant ReactiveFronts 648377.

REFERENCES

Allègre C. J., & Turcotte D. L. 1986 Implications of a two-component marble-cake mantle *Nature* **323**, 123-127.

Axelrod D., Koppel D. E., Schlessinger J., Elson E., & Webb W. W. 1976 Mobility measurement by analysis of fluorescence photobleaching recovery kinetics *Biophysical journal* **16**, 1055-1069.

Batchelor G. K. 1959 Small-scale variation of convected quantities like temperature in a turbulent fluid. part 1. general discussion and the case of small conductivity, *J. Fluid Mech.*, **5**, 113-133.

Dentz, M., LeBorgne, T., Englert, A. & Bijeljic, B. 2011 Mixing, spreading and reaction in heterogeneous media: A brief review. *J. Cont. Hydrol.* **120-121**, 1–17.

Villermaux E., & Duplat, J. 2006 Coarse grained scale of turbulent mixtures *Physical review letters*, **97** 144506.

Duplat, J. & Villermaux, E. 2003 Mixing by random stirring in confined mixtures *J. Fluid Mech.*, **617** pp 51-86.

Falkovich, G., Gawedzki, K. & Vergassola, M. 2001 Particles and fields in fluid turbulence. *Rev. Mod. Phys.* **73** (4), 913–975.

Fourier, J. 1822 Théorie Analytique de la Chaleur, *Firmin Didot.*

Kalda, J. 2000 Simple model of intermittent passive scalar turbulence. *Phys. Rev. Lett.* **84** (3), 471–474.

Le Borgne T., Dentz M. & Villermaux E. 2015 The lamellar description of mixing in porous media, *J. Fluid Mech.* **770**, 458-498.

Meunier P. & Villermaux E. 2003 How vortices mix, *J. Fluid Mech.* **476**, 213-222.

Meunier P. & Villermaux E. 2010 The diffusive strip method for scalar mixing in two dimensions. *J. Fluid Mech.* **662**, 134-172.

Meunier P., Huck P., Nobili C.,& Villermaux E. 2015 Transport and diffusion around a homoclinic Point, *In Chaos, Complexity and Transport: Proceedings of the CCT 15* pp. 152-162.

Ottino J.M. 1989 "The Kinematics of Mixing: Stretching, Chaos, and Transport", *Cambridge University Press.*

Ranz W. E. 1979 Applications of a stretch model diffusion, and reaction in laminar and turbulent flows, *AlChE Journal* **25**, 1.

Rhines, P. B., & Young, W. R. 1983 How rapidly is a passive scalar mixed within closed streamlines?, *Journal of Fluid Mechanics* **133**, 133-145.

Shraiman, B. I. & Siggia, E. D. 2000 Scalar turbulence. *Nature* **405**, 639–646.

Souzy M., Lhuissier H. , Villermaux E., & Metzger B. 2017 Stretching and mixing in sheared particulate suspensions *J. Fluid Mech.* **812**, 611–635.

Villermaux, E. & Duplat, J. 2003 Mixing as an aggregation process. *Phys. Rev. Lett.* **91** (18), 184501–1–4.

Villermaux, E. 2012 Mixing by porous media *Comptes Rendus Mcanique* **340**, 933-943.

Warhaft, Z. 2000 Passive scalars in turbulent flows *Annu. Rev. Fluid Mech.* **32**, 203-240.

6.3 Autres articles

PHYSICS OF FLUIDS **25**, 093301 (2013)

How rotational vortices enhance transfers

D. Griffani,[1] P. Rognon,[2] B. Metzger,[2] and I. Einav[1]
[1]*Particles and Grains Laboratory, School of Civil Engineering, The University of Sydney, Sydney, NSW 2006, Australia*
[2]*IUSTI-CNRS UMR 7343, Aix-Marseille University, 13453 Marseille, France*

(Received 29 April 2013; accepted 18 July 2013; published online 5 September 2013)

Inspired by recent observations of granular flow, we examine how rotational vortices contribute to heat or mass transfer enhancement in a fluid. We use a *tracer method* to simulate both diffusion and advection in systems of differing intrinsic diffusivities D_0, vortex sizes R, vortex rotation frequencies f, and vortex lifetimes ℓ. The results reveal that these systems exhibit an effective diffusive behavior, characterized by an effective diffusivity D^{eff}. A striking finding is the existence of two regimes, dichotomised by the Péclet number $Pe = R^2 f/D_0$. When the Péclet number is less than one, there is no transfer enhancement, $D^{eff} = D_0$. For higher values, vortices produce some transfer enhancement with a corresponding power law $D^{eff}/D_0 \approx Pe^n$. The power n ranges from a lower bound of 0.5 for stationary vortices of lifetime infinity, to an upper bound of 1 for vortices of lifetimes shorter than half a rotation. This difference is attributed to two different internal mechanisms involving the coupling of diffusion and advection. These results could provide new insights on the transfer properties of fluid systems comprising rotational vortices, such as granular materials, suspensions, foams, and emulsions, as well as low Reynolds number stirred flows. © *2013 AIP Publishing LLC*. [http://dx.doi.org/10.1063/1.4817671]

I. INTRODUCTION

In a number of fluid systems, heat and mass transfers are intimately related to the nature of the flow field. In turbulent flows, stirred flows, and even dense granular flows, vortices appear to play a central role in enhancing transfers. Quantifying this advection-diffusion coupling is often a challenge.

In a recent study, we investigated the transfer of heat in dense granular flows.[1] This phenomenon is of considerable importance to both industrial and geophysical applications.[2] It was found that the heat transfer across a layer of grains is strongly enhanced when a shear deformation is applied. This enhancement was shown to arise from the development of granular vortices within the sheared layers.

The development of granular vortices is a fascinating property of dense granular flows. By analogy with turbulence, this phenomenon was coined *granulence*.[3–5] There are, however, fundamental differences between turbulence and granulence. Turbulence results from a visco-inertial instability, and thus develops at high Reynolds numbers. By contrast, granulence results from a *steric* instability; grains must move across the laminar streamlines to avoid each other. This phenomena is related to the Reynolds dilatancy.[6] Unlike visco-inertial instability, steric instability develops even at low strain rates, which is a significant practical advantage. Furthermore, granulence becomes more pronounced in the vicinity of the jamming transition where the granular flows exhibit transient islands of jammed grains with a typical size that increases and diverges as the flow decelerates and stops.[7,8] The systematic characterization of granular vortices is still an emerging field of research. Nevertheless, two significant features have consistently been reported. First, granular vortices are ephemeral, with a typical lifetime much shorter than a shear deformation of 1.[3–5] Second, their velocity field is approximately rotational, given that a jammed island of grains moves as a rigid

 © 2013 AIP Publishing LLC

Downloaded 06 Sep 2013 to 195.83.220.70. This article is copyrighted as indicated in the abstract. Reuse of AIP content is subject to the terms at: http://pof.aip.org/about/rights_and_permissions

body. By contrast, the vortices that arise in turbulence are typically irrotational and the vortices can last for several revolutions.[9,10]

Greater similarities may exist between granular vortices and the vortices that develop in viscous liquids that are mechanically stirred. Whilst their lifetimes tend to be controlled by the stirring protocol, these vortices are also rotational. Mixing viscous liquids such as melted polymers is an important industrial issue, and a number of studies have quantified the efficiency of various stirring protocols by focusing on the rate of homogenization of the mixture. Efficient mixing has been shown to occur with protocols producing chaotic pathlines and so-called *chaotic advection*.[11–14] Stretching and folding of fluid elements were shown to play a crucial role, increasing the interface area between the two fluids and the concentration gradients, thereby intensifying the mixing process.[15–20]

In the field of dense granular flows where grains tend to transiently rotate in rotational islands, the advection-diffusion coupling leads to a significant transfer enhancement.[1] However, the link between typical rotational vortex characteristics and the degree of transfer enhancement has not yet been clearly quantified. How do vortex characteristics such as their size, their rotation frequency, and lifetime influence heat and/or mass transfers? This question seems to be a fundamental step toward a comprehensive and unified understanding of transfer mechanisms underlying stirring protocols and fluid systems exhibiting granulence. These include dry granular materials,[1] suspensions,[21] and other particulate fluids such as foams and emulsions.[22,23]

In this paper, we tackle this question numerically by considering a model fluid system comprising a periodic array of rotational vortices, and we analyze the transfer properties obtained when varying the vortex size, rotation frequency, and lifetime. The study is based on a *passive Brownian tracer method*, which is used to solve for the advection-diffusion coupling and extract the effective transfer properties of the system. The tracer method and the characteristics of the simulated system will be presented in Sec. II. The results for stationary vortices and transient vortices will be successively introduced in Secs. III and IV, respectively. The mechanisms at the origin of the resulting transfer enhancement will be discussed in Sec. V.

II. SIMULATING ADVECTION-DIFFUSION WITH THE TRACER METHOD

We consider an idealised two-dimensional fluid system having an intrinsic diffusivity D_0 (m^2/s) and comprising a rotational vortex. This rotational vortex is circular, centred at $\vec{x}_c$, of radius R (m) and rotation frequency f (s^{-1}). Inside the vortex, the velocity field is given by $v_\theta(r) = 2\pi f r/R$ where r is the distance to the vortex centre, and $v_\theta(r)$ the angular velocity. Outside the vortex, for $r > R$, $v_\theta = 0$ (see Figure 1(a)). The radial velocity v_r is null both inside and outside the vortex.

In systems where both diffusion and advection occur simultaneously, the local evolution of the temperature or concentration field, here called c, satisfies the advection-diffusion equation. The idealized fluid we consider is incompressible and has a homogeneous and isotropic diffusivity D_0. As is the case in dense granular flows, neither the diffusivity D_0 or the flow velocity field depend on the local value of c. Accordingly, the advection-diffusion equation reads

$$\dot{c} = D_0 \nabla^2 c - \vec{v} \cdot \nabla c. \tag{1}$$

$\vec{v}(t, \vec{x})$ is the local, possibly time dependent velocity field. Given a set of boundary and initial conditions for c, it is possible to simulate the local evolution of $c(t, \vec{x})$ according to the advection-diffusion equation (1). Methods based on a discretization of the gradient operator are available for this purpose.[24–28]

We chose an alternative simulation method, coined the *tracer method* to investigate the effective transfer properties of these systems.[21,29–32] Its principle is to inject a large number of passive Brownian tracers into the flow. Each tracer is advected by the local flow field but it is also assigned a random velocity characterised by a vector of constant designated norm v_0 and an orientation that changes randomly after each time step dt. The norm of the random velocity is set to achieve the desired intrinsic diffusivity, D_0 according to (in two-dimensions): $v_0 = 2\sqrt{D_0/dt}$. To produce an isotropic diffusivity, the orientation is randomly selected within the range 0–2π with a uniform likelihood.

Downloaded 06 Sep 2013 to 195.83.220.70. This article is copyrighted as indicated in the abstract. Reuse of AIP content is subject to the terms at: http://pof.aip.org/about/rights_and_permissions

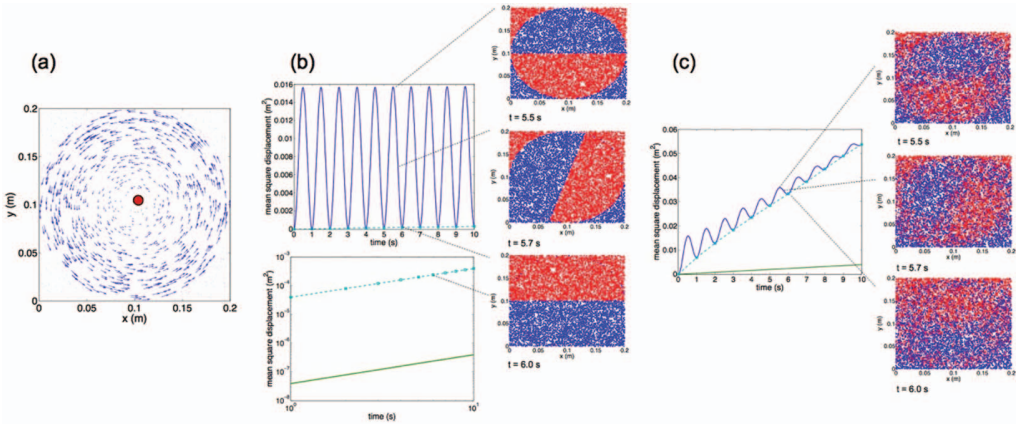


FIG. 1. (a) Flow system for a stationary vortex. Blue arrows indicate the velocity of the tracers which are initially randomly distributed. (b) and (c) Mean square displacements versus time obtained for two systems with the same vortex ($R = 0.1$ m, $f = 1\,\mathrm{s}^{-1}$) but with different intrinsic diffusivity $D_0 = 10^{-8}$ m^2/s (b) and $D_0 = 10^{-4}$ m^2/s (c). The bottom (green) curve corresponds to the mean square displacements obtained in the absence of a vortex. Pictures represent the location of tracers tagged initially in blue and red in the bottom and top halves of the system.

The effective transfer properties of the system can simply be measured by tracking the tracers' trajectories and measuring their mean square displacement λ (m^2) which is defined at any time t as: $\lambda(t) = \frac{1}{N}\sum_{i=1}^{N} \|\vec{x}_i(t) - \vec{x}_i(0)\|^2$. The sum runs over all the tracers in the system, and $\vec{x}_i(t)$ refers to the position of tracer i. In a diffusive system, the mean square displacements increase linearly with time and the effective diffusivity D^{eff} (m^2/s) is defined as $\lambda(t) = 4D^{eff}t$. In the absence of a vortex, $D^{eff} = D_0$. For such systems, the results from the method were validated against closed form analytic solutions. In the following, we investigate how the presence of a vortex changes the effective diffusivity of the system.

All simulations comprise 10 000 tracers initially randomly displaced in a square, two-dimensional domain of size $2R$, R being the radius of the vortex. The domain is periodic in both directions; tracers that leave the domain through one boundary, re-enter it through the opposite boundary. The tracer displacements are simulated over short time steps $dt = 10^{-5}$ s. We systematically checked that smaller time steps and/or more tracers produce the same results. The integration scheme comprises a first order Eulerian integration of the random motion, followed by a rigid body rotation of the tracers inside the vortex. This scheme is applied to each tracer at each time step.

III. TRANSFER ENHANCEMENT WITH A STATIONARY VORTEX

We first consider a rotational vortex with a fixed location, coined the *stationary vortex* (see Figure 1(a)). In this configuration, the adjustable parameters are the intrinsic diffusivity D_0, the vortex rotation frequency f, and the vortex radius R which were varied in the ranges specified in Table I. For each run, the tracer motions were simulated over a period of time corresponding to 100 vortex rotations.

Figures 1(b) and 1(c) show the evolution over time of the mean square displacement for two systems with the same vortex ($R = 0.1$ m, $f = 1\,\mathrm{s}^{-1}$) and two different intrinsic diffusivities ($D_0 = 10^{-4}$ m^2/s, $D_0 = 10^{-8}$ m^2/s). The mean square displacements increase on average linearly

TABLE I. Range of parameters investigated for a stationary vortex (lifetime infinity).

D_0 (m^2/s)	f (s^{-1})	R (m)
$10^{-8} \rightarrow 10^{-4}$	$0.1 \rightarrow 10$	$10^{-3} \rightarrow 1$

Downloaded 06 Sep 2013 to 195.83.220.70. This article is copyrighted as indicated in the abstract. Reuse of AIP content is subject to the terms at: http://pof.aip.org/about/rights_and_permissions

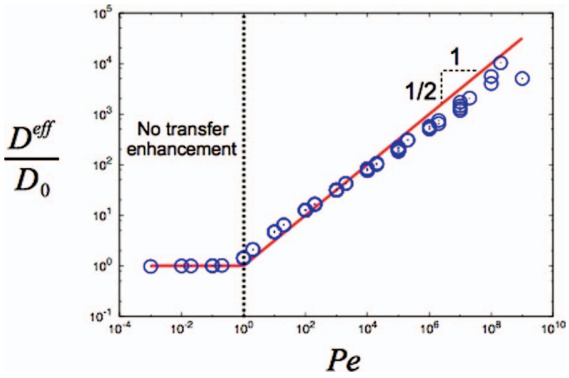


FIG. 2. Effective diffusivity D^{eff} for a stationary vortex as a function of the Péclet number $Pe = R^2 f/D_0$. The data were obtained for different intrinsic diffusivities D_0, vortex rotation frequencies f, and radii R (ranges reported in Table I).

in time with oscillations which correspond to the vortex rotation. The values of the mean square displacements taken after each rotation were used to determine the effective diffusivity.

The effective diffusivity measured using this method was obtained for different vortex sizes, rotation frequencies, and intrinsic diffusivities. The ratio D^{eff}/D_0 was used to quantify the transfer enhancement attributable to the presence of a vortex. This ratio corresponds to either the Nusselt number for heat transfers, or to the Sherwood number for mass transfers. The values obtained for this ratio range from 1 (no enhancement) to several orders of magnitude. When plotted as a function of the Péclet number $Pe = R^2 f/D_0$ (see Figure 2), the data collapse onto the same curve.

This scaling is observed for a wide range of intrinsic diffusivities, vortex sizes, and rotation frequencies. Figure 2 also reveals an interesting trend, exhibiting two main features. Namely, the Péclet number dichotomizes two regimes: there is no transfer enhancement for $Pe < 1$ ($D^{eff} = D_0$), and there is some (potentially considerable) transfer enhancement for $Pe > 1$. For $Pe > 1$, the effective diffusivity scales like: $\frac{D^{eff}}{D_0} \approx Pe^{\frac{1}{2}}$.

IV. TRANSFER ENHANCEMENT WITH A TRANSIENT VORTEX

Let us now consider the transfer properties of a system comprising a transient rotational vortex. After a designated lifetime ℓ, the vortex centre moves instantaneously to a new, random location akin to the transient vortices observed in granular flows.

A lifetime $\ell = 1/4$ means that a vortex completes a quarter of a rotation before its centre changes position. We ran simulations covering a large range of intrinsic diffusivities D_0, vortex sizes R, rotation frequencies f, and different lifetimes between 1/8 and 1 (see Table II).

Again the mean square displacement is found to increase linearly in time (see Figure 3). The effective diffusion coefficient can thus be measured directly from its slope. Figure 4(a) presents the effective diffusivity obtained for differing lifetimes. The effective diffusivity is almost constant for lifetimes shorter than 1/2 a rotation, and tends to decrease for longer lifetimes. This decrease becomes steeper for high Péclet numbers. Figure 4(b) shows that the behavior of the ratio D^{eff}/D_0 is also governed by the Péclet number. For a given lifetime, the effective diffusivities of systems of differing intrinsic diffusivity, different vortex size and rotation frequency, collapse onto the same

TABLE II. Range of parameters investigated for a transient vortex.

D_0 (m^2/s)	f (s^{-1})	R (m)	ℓ
$10^{-8} \rightarrow 10^{-4}$	$1 \rightarrow 10$	$10^{-3} \rightarrow 1$	$1/8 \rightarrow 1$

Downloaded 06 Sep 2013 to 195.83.220.70. This article is copyrighted as indicated in the abstract. Reuse of AIP content is subject to the terms at: http://pof.aip.org/about/rights_and_permissions

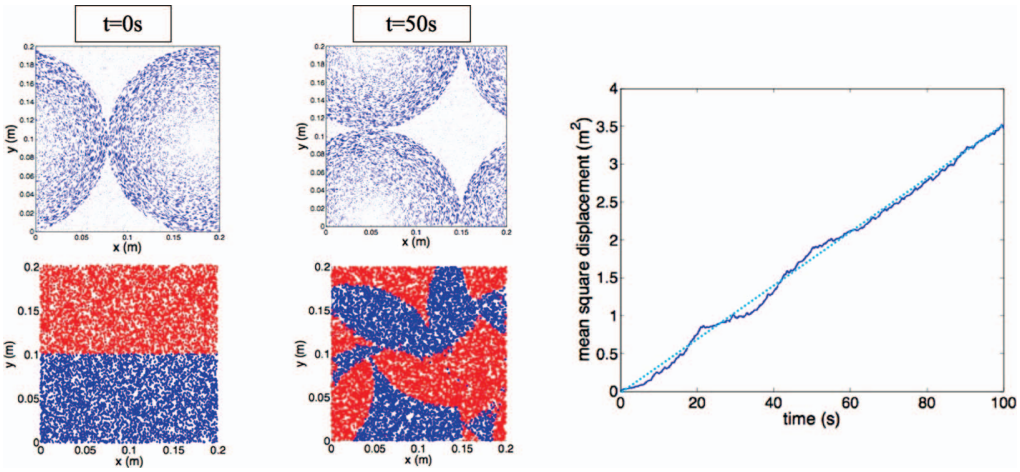


FIG. 3. (Top) Velocity fields and (bottom) tracer positions for transient vortices at $t = 0$ s and $t = 50$ s. Mean square displacement of the tracers versus time.

curve

$$\frac{D^{eff}}{D_0} \approx Pe^n. \tag{2}$$

However, different lifetimes result in a different exponent n. This exponent is close to 1 for lifetimes shorter than half a rotation, and decreases toward 0.5 for lifetimes between half a rotation and a complete rotation, see Figure 4(c).

V. DISCUSSION

The above results show that the effective diffusivity of a system equals the intrinsic diffusivity D_0 for low Péclet numbers, and, for higher values, scales like $D^{eff}/D_0 \approx Pe^n$ with $n = 0.5$ for stationary vortices and $0.5 < n < 1$ for transient vortices. In this section, we seek to understand the origin of such dependencies.

Let us first consider the regime of low Péclet numbers, approximately $Pe < 1$, for which neither stationary or transient vortices have a significant effect on transfers. This result can be understood by comparing the time scale associated with vortex advection, f^{-1}, and the time scale associated with tracers diffusion across a vortex, R^2/D_0. For $Pe = R^2 f/D_0 < 1$, the diffusion time is much shorter than the advection time. As a consequence, in this regime, tracers diffuse across a vortex before it

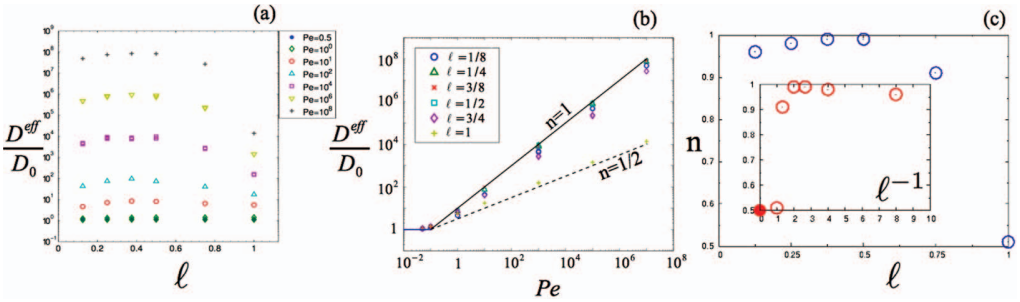


FIG. 4. (a) Effective diffusivity versus vortex lifetime obtained with transient rotational vortex systems of different intrinsic diffusivity D_0, vortex size R, and rotation frequency f (ranges specified in Table II). (b) Same data versus Péclet number. The data scale like $D^{eff}/D_0 \approx Pe^n$. (c) Exponent n versus lifetime ℓ.

Downloaded 06 Sep 2013 to 195.83.220.70. This article is copyrighted as indicated in the abstract. Reuse of AIP content is subject to the terms at: http://pof.aip.org/about/rights_and_permissions

can significantly advect them, and the contribution of the vortex to the transfer is negligible. For $Pe > 1$, however, advection does significantly contribute to the transfer, as we will now discuss.

For a stationary vortex, let us consider the positions of the tracers at the end of each cycle of rotation of the vortex. The tracers that always remain outside or inside the vortex are not affected by the flow. Only the tracers that cross the vortex boundary during the rotation, coined *the crossers*, contribute toward enhancing the transfer since their displacement at the end of a cycle is much larger than if they only moved due to their intrinsic diffusion. The typical displacement of such a tracer during one cycle is R and its displacement occurs at a frequency f. Thus, the diffusion coefficient averaged over all tracers is

$$D^{eff} \propto R^2 f \mathcal{P}, \tag{3}$$

where $\mathcal{P}$ is the proportion of *crossers*. These crosser tracers are located within a distance $\delta \propto \sqrt{D_0/f}$ from the vortex boundary. Other tracers do not have enough time or do not diffuse fast enough to reach the vortex boundary within one rotation. Consequently, crossers are located within a ring of inner radius $R - \delta$ and outer radius $R + \delta$. The proportion of crossers thus scales like the ratio of the ring area to the total area of the system, $\mathcal{P} \propto R\delta/R^2 = \sqrt{D_0/fR^2} = Pe^{-\frac{1}{2}}$. Introducing this proportion in (3) leads to the measured scaling for stationary vortices, $D^{eff}/D_0 \approx Pe^{\frac{1}{2}}$.

Note that a similar scaling with a power exponent of a half has been reported for non-rotational vortices.[33,34] This suggests that the mechanism just described could also apply to these non-rotational vortices.

For transient vortices, the lifetime plays a central role in the power law $D^{eff}/D_0 \approx Pe^n$ (see Figures 4(b) and 4(c)). The exponent n is close to 1 for lifetimes shorter than half a rotation and drops to 0.5 for a lifetime of one rotation. The tracers advected by a vortex of lifetime ℓ typically move a distance $2R\sin(\pi\ell)$ during one lifetime. During each subsequent vortex lifetime, tracers experience the same kind of displacement, but with a new and random centre of rotation. The tracer motions during a series of lifetimes can thus be seen as a macroscopic random walk with a typical lengthscale $2R\sin(\pi\ell)$, and a frequency of step f/ℓ. This produces an effective diffusivity scaling like: $D^{eff} \propto R^2 f \sin^2(\pi\ell)/\ell$ which is consistent with the scaling $D^{eff}/D_0 \propto Pe$ obtained for short lifetimes.

For lifetimes longer than half a rotation, the typical step of the macroscopic random walk, $2R\sin(\pi\ell)$, decreases. It vanishes for a lifetime of $\ell = 1$ rotation, and this macroscopic random walk then has no effect on the effective diffusivity. In this case, the tracer motions during one rotation involve the same mechanism described for stationary vortices. These two systems thus have the same exponent $n \approx 0.5$.

Transient vortices with a short lifetime lead to a power law $n \approx 1$. The corresponding effective diffusivity can thus be expressed as $D^{eff} \approx R^2 f$. As a result, these vortices produce an effective diffusive behavior even if the intrinsic diffusivity is null, $D_0 = 0$. This is a consequence of the macroscopic random walk described above. This property is not shared with stationary vortices and transient vortices of lifetime one. With a power $n \approx 1/2$, their effective diffusivity can be expressed as $D^{eff} \approx R\sqrt{D_0 f}$. It is therefore null when D_0 is null. This is consistent with the fact that, with no intrinsic diffusivity, tracers advected by these vortices follow closed loop pathlines. After each rotation, they return to their initial positions, and the vortex alone does not lead to any transfer enhancement.

VI. CONCLUSION

By using a *Brownian tracer method*, we quantified how the transfer properties of a 2D fluid system are affected by the presence of a rotational vortex. Systematic simulations with differing intrinsic diffusivities D_0, vortex sizes R, rotation frequencies f, and lifetimes ℓ revealed the following features: (i) These systems which involve both advection and diffusion exhibit a macroscopic diffusive behavior that can be characterized by an effective diffusion coefficient. (ii) The effective diffusivity is governed by the Péclet number $Pe = R^2 f/D_0$. (iii) The Péclet number dichotomizes two regimes. For $Pe < 1$, the vortex produces no significant transfer enhancement: $D^{eff} \approx D_0$. For $Pe > 1$,

Downloaded 06 Sep 2013 to 195.83.220.70. This article is copyrighted as indicated in the abstract. Reuse of AIP content is subject to the terms at: http://pof.aip.org/about/rights_and_permissions

the vortex does produce a significant transfer enhancement, and the ratio D^{eff}/D_0 increases as a power law of the Péclet number: $D^{eff}/D_0 \approx Pe^n$. The value of the power n ranges from a lower bound of 1/2 to an upper bound of 1 depending on the lifetime of the vortex.

The two extreme values of the power law exponent, i.e., $n = 1$ and $n = 0.5$, correspond to two distinct mechanisms that enhance transfers. The value $n \approx 1$ obtained for transient vortices with lifetimes shorter than half a rotation, results from a large scale random walk of the tracers induced by the transient vortices. By contrast, the value $n \approx 1/2$ obtained for stationary vortices and vortices with a lifetime of 1 rotation, involves a mechanism coupling the intrinsic diffusion and the vortex advection. In this case, only tracers located within a ring around the vortex boundary contribute to the transfer enhancement. The thickness of this ring is determined by the vortex rotation frequency, and the intrinsic diffusivity of the tracers.

This study, performed using a 2D model system, constitutes a first step toward a better understanding of the mechanisms underlying the transfer properties of fluid systems comprising rotational vortices, such as stirred flows and dense granular flows. Further investigations will be undertaken for more complex velocity fields such as irrotational vortices present in turbulent flows and actual velocity fields directly measured in granular systems. It is thought that the specific properties of the involved vortices, including their three-dimensional shape, their internal velocity field, and their spatial distribution may lead to a different advection diffusion coupling and different power law exponents n.

[1] P. Rognon and I. Einav, "Thermal transients and convection in dense granular materials," Phys. Rev. Lett. **105**, 218301 (2010).
[2] Y. Gan, P. Rognon, and I. Einav, "Phase transitions and cyclic pseudotachylyte formation in simulated faults," Philos. Mag. **92**, 3405–3417 (2012).
[3] F. Radjaï and S. Roux, "Turbulentlike fluctuations in quasistatic flow of granular media," Phys. Rev. Lett. **89**, 064302 (2002).
[4] F. Radjaï and S. Roux, "Scaling behaviour of velocity fluctuations in slow granular flows," *Nonsmooth Mechanics and Analysis* (Springer U.S., 2006), pp. 233–245.
[5] C. Campbell, "Clusters in dense-inertial granular flows," J. Fluid Mech. **687**, 341–359 (2011).
[6] O. Reynolds, "On the dilatancy of media composed of rigid particles in contact," Philos. Mag. Ser. **20**, 469–481 (1885).
[7] O. Pouliquen, "Velocity correlation in dense granular flows," Phys. Rev. Lett. **93**, 248001 (2004).
[8] P. Mills, P. Rognon, and F. Chevoir, "Rheology and structure of granular materials near the jamming transition," Europhys. Lett. **81**, 64005 (2008).
[9] F. Incropera, D. Dewitt *et al.*, *Fundamentals of Heat and Mass Transfer* (Wiley, 2010), pp. 490–515.
[10] Y. Gasteuil, W. Shew, M. Gibert, F. Chillá, B. Castaing, and J. Pinton, "Lagrangian temperature, velocity, and local heat flux measurement in Rayleigh-Bénard convection," Phys. Rev. Lett. **99**, 234302 (2007).
[11] H. Aref, "Stirring by chaotic advection," J. Fluid Mech. **143**, 1–21 (1984).
[12] J. Ottino, "Mixing, chaotic advection, and turbulence," Annu. Rev. Fluid Mech. **22**, 207–254 (1990).
[13] S. Wiggins, "Coherent structures and chaotic advection in three dimensions," J. Fluid Mech. **654**, 1–4 (2010).
[14] E. Gouillart, O. Dauchot, and J.-L. Thiffeault, "Measures of mixing quality in open flows with chaotic advection," Phys. Fluids **23**, 013604 (2011).
[15] E. Villermaux and J. Duplat, "Mixing as an aggregation process," Phys. Rev. Lett. **91**, 184501 (2003).
[16] E. Villermaux, A. Stroock, and H. Stone, "Bridging kinematics and concentration content in a chaotic micromixer," Phys. Rev. E **77**, 015301 (2008).
[17] H. Stone, A. Stroock, and A. Ajdari, "Engineering flows in small devices," Annu. Rev. Fluid Mech. **36**, 381–411 (2004).
[18] V. Hessel, H. Löwe, and F. Schönfeld, "Micromixers – A review on passive and active mixing principles," Chem. Eng. Sci. **60**, 2479–2501 (2005).
[19] M. Robinson and P. Cleary, "The influence of cam geometry and operating conditions on chaotic mixing of viscous fluids in a twin cam mixer," AIChE J. **57**, 581–598 (2010).
[20] K. El Omari and Y. Le Guer, "Alternate rotating walls for thermal chaotic mixing," Int. J. Heat Mass Transfer **53**, 123–134 (2010).
[21] B. Metzger, O. Rahli, and L. Yin, "Heat transfer across sheared suspensions: Role of the shear-induced diffusion," J. Fluid Mech. **724**, 527–552 (2013).
[22] O. Dauchot, D. J. Durian, and M. van Hecke, "Dynamical heterogeneities in grains and foams," *Dynamical Heterogeneities in Glasses, Colloids, and Granular Media* (Oxford University Press, 2011), Vol. 150, p. 203.
[23] P. Jop, V. Mansard, P. Chaudhuri, L. Bocquet, and A. Colin, "Microscale rheology of a soft glassy material close to yielding," Phys. Rev. Lett. **108**, 148301 (2012).
[24] D. Spivakovskaya, A. Heemink, and E. Deleersnijder, "Lagrangian modelling of multi-dimensional advection-diffusion with space-varying diffusivities: Theory and idealized test cases," Ocean Dyn. **57**, 189–203 (2007).
[25] P. Shankar and R. Kidambi, "Mixing in internally stirred flows," Proc. R. Soc. London **465**, 1271–1290 (2009).
[26] P. Meunier, E. Villermaux *et al.*, "The diffusive strip method for scalar mixing in two dimensions," J. Fluid Mech. **662**, 134 (2010).

Downloaded 06 Sep 2013 to 195.83.220.70. This article is copyrighted as indicated in the abstract. Reuse of AIP content is subject to the terms at: http://pof.aip.org/about/rights_and_permissions

[27] S. Chevalier and O. Banton, "Modelling of heat transfer with the random walk method. Part 1. Application to thermal energy storage in porous aquifers," J. Hydrol. **222**, 129–139 (1999).
[28] D. Fereday and P. Haynes, "Scalar decay in two-dimensional chaotic advection and Batchelor-regime turbulence," Phys. Fluids **16**, 4359 (2004).
[29] S. Jones, "Interaction of chaotic advection and diffusion," Chaos, Solitons Fractals **4**, 929–940 (1994).
[30] J. Phelps and C. Tucker, "Lagrangian particle calculations of distributive mixing: Limitations and applications," Chem. Eng. Sci. **61**, 6826–6836 (2006).
[31] P. Salamon, D. Fernàndez-Garcia, J. Gómez-Hernández *et al*., "A review and numerical assessment of the random walk particle tracking method," J. Contam. Hydrol. **87**, 277–305 (2006).
[32] Z. Pouransari, M. Speetjens, and H. Clercx, "Formation of coherent structures by fluid inertia in three-dimensional laminar flows," J. Fluid Mech. **654**, 5 (2010).
[33] M. Rosenbluth, H. Berk, I. Doxas, and W. Horton, "Effective diffusion in laminar convective flows," Phys. Fluids **30**, 2636 (1987).
[34] O. Cardoso and P. Tabeling, "Anomalous diffusion in a linear array of vortices," Europhys. Lett. **7**, 225 (1988).

Downloaded 06 Sep 2013 to 195.83.220.70. This article is copyrighted as indicated in the abstract. Reuse of AIP content is subject to the terms at: http://pof.aip.org/about/rights_and_permissions

Eddy Viscosity in Dense Granular Flows

T. Miller,[1] P. Rognon,[1,2] B. Metzger,[2] and I. Einav[1,3,*]

[1]*Particles and Grains Laboratory, School of Civil Engineering, The University of Sydney, Sydney, New South Wales 2006, Australia*
[2]*IUSTI-CNRS UMR 7343, Aix-Marseille University, 13453 Marseille, France*
[3]*Department of Civil, Environmental and Geomatic Engineering, Faculty of Engineering Science, University College London, London WC1E 6BT, United Kingdom*

(Received 9 November 2012; published 2 August 2013)

We present a seminal set of experiments on dense granular flows in the stadium shear geometry. The advantage of this geometry is that it produces steady shear flow over large deformations, in which the shear stress is constant. The striking result is that the velocity profiles exhibit an *S* shape, and are not linear as local constitutive laws would predict. We propose a model that suggests this is a result of wall perturbations which span through the system due to the nonlocal behavior of the material. The model is analogous to that of eddy viscosity in turbulent boundary layers, in which the distance to the wall is introduced to predict velocity profiles. Our findings appear pivotal in a number of experimental and practical situations involving dense granular flows next to a boundary. They could further be adapted to other similar materials such as dense suspensions, foams, or emulsions.

DOI: 10.1103/PhysRevLett.111.058002 PACS numbers: 45.70.Mg, 81.05.Rm, 83.10.Bb, 83.50.Ax

Dense granular flows exhibit complex properties that challenge unified description. For the last decade, major advances have been made towards the expression of a local constitutive law. Within flows in various geometries the local shear strain rate $\dot{\gamma}$ and the local shear stress τ were found to satisfy the Bagnold scaling $\tau = \rho d^2 f_1(\phi)\dot{\gamma}^2$ [1], involving the grain size d, density ρ, and a function f_1 that diverges as the solid fraction ϕ approaches a maximum value. However, the constitutive law that describes the bulk flow does not usually apply close to walls. In fact, there can be significant deviation from the Bagnold scaling over large distances—possibly spanning through the entire flow. Therefore, predicting flows not only requires the knowledge of the constitutive law but also that of a law describing the wall perturbation. No consensus has yet emerged on the general form of such a law of the wall for dense granular flows.

A fascinating property of dense granular flows is the spontaneous development of transient collective grain motions [2–10]. By making analogies with turbulent eddies these phenomena were termed granulence [3]. As opposed to turbulent eddies, the typical size ℓ of these structures tends to increase and diverge as the flow slows down and jams. Local constitutive laws were reformulated introducing this mesoscopic length scale ℓ in place of the grain size d. This gave a consistent prediction for the viscosity divergence when approaching the jamming [2,5,7,11].

These correlated structures lead to an even deeper reformulation of the flow description, using nonlocal models. The underlying idea is that the behavior at a given point in the flow depends on the nature of the flow in the surrounding region, which is given by some typical cooperativity length. Two main models were introduced, considering either nonlocal self-activated processes [12], or nonlocal fluidity [13]. These models significantly improved the prediction of local rheology in flows involving stress gradients such as cylindrical Couette flows and flows down a slope. Despite these advances, these models are not conclusive on the role of walls and the flow perturbations they may induce.

In this Letter, we present a seminal set of experiments revealing long-range wall perturbation in dense granular flows. Results suggest a simple model that consists of introducing the distance to the wall as a typical length scale for the diffusion of momentum. This model is similar to the eddy viscosity model and its application to derive the law of the wall in turbulent boundary layers.

S-shaped velocity profile in plane shear flows.—For this study we designed an original experimental device named stadium shear that can produce plane shear of a 2D granular material (see Fig. 1). The grains are 10 mm high nylon cylinders of three different diameters (12, 15, and 20 mm) to prevent crystallization. They stand on a glass plate, and the flow is driven by a belt system. The nylon-faced rubber belt has asperities that are semicircular in cross section with a 6 mm radius and a center-to-center spacing of 14 mm. Grains are sheared between two parallel sections of the belt in the central region and recirculate underneath the sprockets at both ends. The advantage of this setup is the ability to have plane shear in the central region while the recirculation of the particles allows continuous shear for deformations as large as desired. The 2D nature of the granular system allows individual particles in the plane shear region (see Fig. 1) to be tracked by a high-speed camera which sits above the apparatus. From consecutive images—and using a circular Hough transformation algorithm—the displacement of the grains over time can be obtained. The normal stress acting on the central region of the belt is measured

 © 2013 American Physical Society

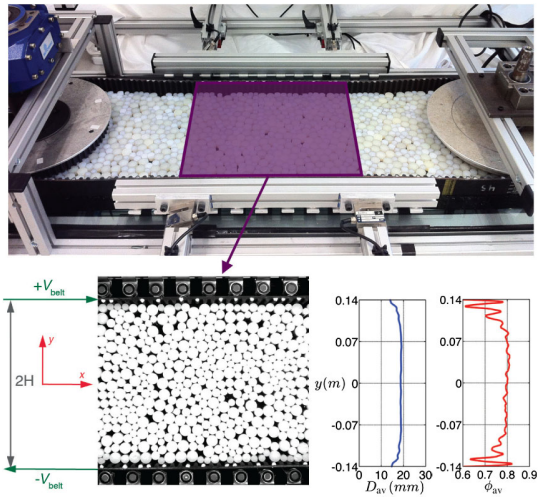


FIG. 1 (color online). Stadium shear device: 2000 plastic cylinders set on a glass plate are sheared by a belt system. Time averaged profiles ($V^{\text{belt}} = 0.1$ m/s) of average particle diameter (blue or dark gray) and solid fraction (red or light gray). In the center of the flow, $D_{\text{av}} \approx 18$ mm and $\phi_{\text{av}} \approx 0.80$.

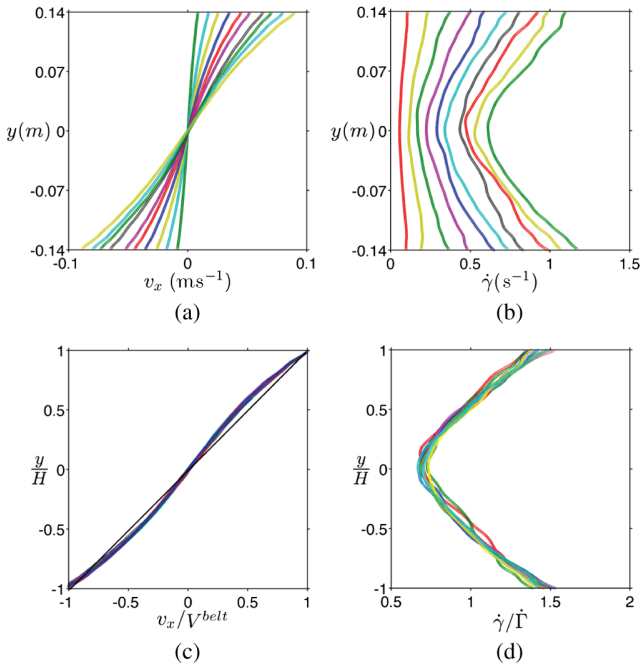


FIG. 2 (color online). (a) Velocity profiles and (b) shear rate profiles for all the runs. The profiles are temperospatial averages of data from the captured central region, which is approximately 368 mm wide, over the entire duration of the test. (c) The normalized velocity profiles and (d) the normalized shear rate profiles (where $\dot{\Gamma} = V^{\text{belt}}/H$). In (c) the linear profile (solid black line) has been included for comparison.

through a series of four load cells, one on each arm of the roller assembly (see Fig. 1).

We performed a set of experiments by varying the belt velocity V^{belt} from 1.18 to 11.8 cm s^{-1}, which correspond to a nominal shear rate $\dot{\Gamma} = (V^{\text{belt}}/H)$ between 0.08 and 0.8 s^{-1}. The material was presheared over a deformation of 100, which was large enough to ensure the system reached a steady state independent of the initial configuration at rest. Images were then recorded over a period of time $100/\dot{\Gamma}$ corresponding to a total shear deformation of 100. To ensure that particles could be tracked in an effective and efficient manner, the frame rate f of the camera was set so that the maximum displacement between images was less than $0.17d_{\text{min}}$, which corresponds to a shear deformation of 0.012, and to $f = 0.17V^{\text{belt}}/d_{\text{min}}$. Grain velocities are computed by tracking the individual grain position over subsequent frames. The resolution of the images is $r = 2.7$ pixels/mm and the particle tracking algorithm gives subpixel resolution for the grain centers. Considering a typical error of 1 pixel on grain displacement, the typical error on the grain velocity is then $\Delta v = (f/2.7) = (0.17V^{\text{belt}}/2.7d_{\text{min}})$, and the typical error on v_x/V^{belt} is $(0.17/(2.7 \times 12)) \approx 0.5\%$.

For all the runs, we observed that the solid fraction and the average grain size are constant along the flow direction x. They are mostly constant along the shear direction y (see Fig. 1). However smaller grains are slightly segregated toward the layer close to the belt as their size is equal to the size of the belt asperities; they are thus more likely to be trapped by the belt. The average normal stress acting on the central region of the belt increased from 8.81 kPa for $\dot{\Gamma} = 0.08$ s^{-1} to 12.47 kPa for $\dot{\Gamma} = 0.8$ s^{-1}. Thus the inertial number [1] $I = (\dot{\gamma}D_{\text{av}}/\sqrt{P/\rho})$ is in the range 5.2×10^{-4}–4.4×10^{-3}.

The striking result is the shape of the velocity profile $v_x(y)$, shown in Fig. 2(a). The velocity profiles are not linear; instead they exhibit some curvature. Profiles from all the experiments collapse on to a single S-shaped curve when the velocity $v_x(y)$ is normalized by the belt velocity V^{belt} [see Fig. 2(c)]. The shear rate $\dot{\gamma}(y) = (\partial v_x(y)/\partial y)$ is thus not constant through the flow [see Fig. 2(b)]. It happens to be a minimum at the center of the flow, increasing with proximity to the belt. The magnitude of the variation between the shear rate at the center and at the belt is significant, with a factor of approximately 2 between these values. Like the velocity profiles, the shear rate profiles when rescaled by the nominal shear rate $\dot{\Gamma}$ collapse on to a single curve for all the experiments [see Fig. 2(d)]. As we shall discuss further on, these results appear to be a consequence of the nonlocal behavior of the dense granular flow combined with the presence of walls.

Observation of correlated motions.—The velocity fields for the flows reveal the existence of correlated motions for all shear rates (see Fig. 3), providing further evidence of nonlocal behavior within our system. Individual correlated motions were transient in nature and we observed the ongoing formation and dissipation of such structures throughout each test.

Eddy viscosity and law of the wall.—The stadium shear geometry produces plane shear flows in the central region, which has the advantage of avoiding a stress gradient due

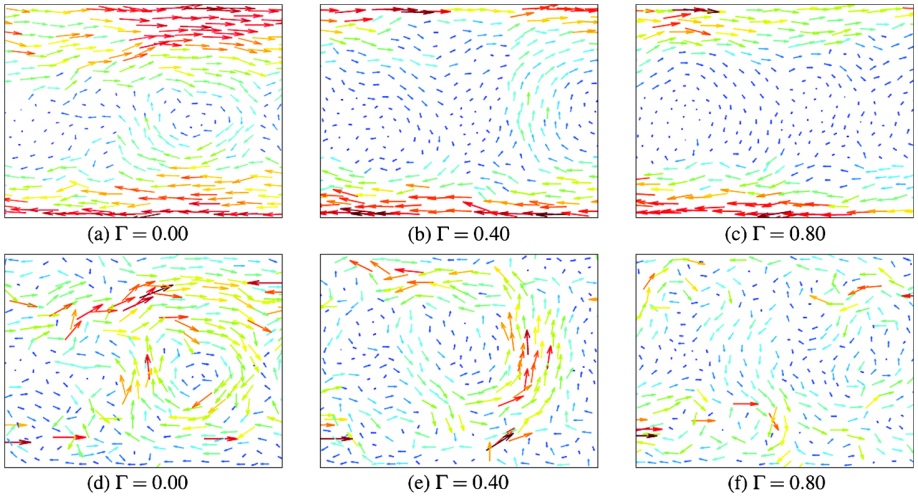


FIG. 3 (color online). (a)–(c) Velocity fields in the steady flow regime during one run ($\dot{\Gamma} = V^{\text{belt}}/H = 0.4\ \text{s}^{-1}$). (d)–(e) Fluctuation velocity fields, where the corresponding velocity from the profile in Fig. 2(a) has been subtracted from each vector in (a)–(c). Snapshots are at equal intervals of shear deformation. The arrow color is graded by magnitudes of velocity (with a maximum of $1.03^{*}V^{\text{belt}}$) and fluctuation velocity (with a maximum of $0.57^{*}V^{\text{belt}}$), respectively.

to gravity or to a curved geometry. Therefore, unlike flows down a slope or flows in a cylindrical Couette cell, one would expect homogeneity of both the shear stress τ and the normal stress σ. That is, they should not vary along the y direction.

Given that the solid fraction and the grain size are almost constant in the flow (see Fig. 1), any local constitutive law would then predict a constant shear rate $\dot{\gamma}(y)$ along the y direction. For example, the Bagnold scaling [1] $\tau(y) = \rho d^2 f_1(\phi)\dot{\gamma}^2(y)$ predicts $\dot{\gamma}(y) = \sqrt{\tau/\rho d^2 f_1(\phi)}$, which requires a nonconstant stress $\tau(y)$ to obtain a nonconstant shear rate $\dot{\gamma}^2(y)$. Friction between the cylinders and the glass plate could be responsible for such a shear stress gradient. The momentum balance would then read $(\partial\tau/\partial y) = \mu\rho g$, where ρg is the weight per unit volume of the grains, and μ is the coefficient of friction between the grains and the glass. This leads to the prediction that the shear stress linearly increases when moving from the center toward the belt: $\tau(y) = \tau(0) + \mu\rho g|y|$ (the absolute value accounts for the fact that friction forces act against the motion). Using the Bagnold local constitutive law leads to the shear rate profile $\dot{\gamma}^2(y) = \dot{\gamma}^2(0) + (\mu g/d^2 f_1(\phi))|y|$. In this, the predicted increase of shear rate with $|y|$ is qualitatively consistent with the experimental data. However, this expression does not account for the reported scaling of $\dot{\gamma}(y)$ with the belt velocity. This suggests that friction is not responsible for the shape of the shear rate in these experiments. This conclusion finds strong support in Refs. [1,14], which show numerical results from two-dimensional shear flows of grains between two parallel walls. S-shaped velocity profiles were obtained, even in the absence of base friction.

Let us now introduce a model that can explain the curved shape of the shear rate profiles, considering that the shear stress is constant through the flow. The Bagnold scaling, while being unable to predict such results, relies on an essential idea: the kinematic viscosity scales with $d^2|\dot{\gamma}|$. It suggests that the momentum diffuses at a rate $|\dot{\gamma}|$ over a typical length of one grain size. Given that dense granular flows develop large structures of typical size $\ell \gg d$, one can expect the momentum to transfer over such a distance. This is the core of several models in which the kinematic viscosity scales with $\ell^2|\dot{\gamma}|$ [1,14]. The question is then to establish how this length scale ℓ depends on the flow condition. It happens that ℓ tends to increase as the flow slows down, and can reach very large values. Let us assume that, with our flow conditions, ℓ would tend to be much larger than the flow width H if there were no walls. The presence of the belt thus truncates the maximum distance of momentum diffusion, limiting it to the distance to the wall $H - |y|$. Using this framework, the relationship between shear rate and shear stress at a given location y can be given by

$$\tau = \rho f_1(\phi)(d^2 + a^2(H - |y|)^2)\dot{\gamma}^2(y) \tag{1}$$

with a being a numerical constant. This model then predicts the following shear rate profile:

$$\dot{\gamma}(y) = \dot{\gamma}_H\left(1 + a^2\left(\frac{H - |y|}{d}\right)^2\right)^{-(1/2)} \tag{2}$$

with $\dot{\gamma}_H = \dot{\gamma}(H)$ denoting the shear rate at the belt, which according to Eq. (1) is

$$\dot{\gamma}_H = \sqrt{\frac{\tau}{\rho f_1(\phi) d^2}}. \tag{3}$$

By definition, the belt velocity is given by $V^{\text{belt}} = \int_0^H \dot{\gamma}(y)dy$. Using Eq. (2) leads to $\dot{\gamma}_H = V^{\text{belt}}/\mathcal{C}$, with $\mathcal{C}$ a constant that is explicitly defined by the integral

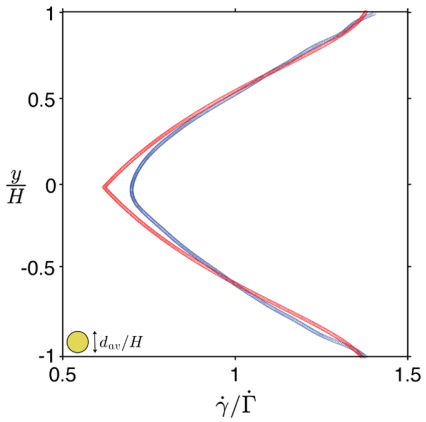


FIG. 4 (color online). The prediction of the model of Eq. (5) with $a = 0.21$ (red or light gray). The normalized average shear rate profile, i.e., the average of the profiles shown in Fig. 2(d) (blue or dark gray).

$$\mathcal{C} = \int_0^H \frac{1}{\sqrt{1 + a^2(\frac{H-|y|}{d})^2}} dy = \frac{d}{a}\sinh^{-1}\left(\frac{aH}{d}\right). \quad (4)$$

We can thus write the shear rate profile as

$$\dot{\gamma}(y) = \frac{aV^{\text{belt}}}{d\sinh^{-1}(aH/d)}\left(1 + a^2\left(\frac{H-|y|}{d}\right)^2\right)^{-(1/2)}. \quad (5)$$

At this point, the only unknown parameter is a. It can be determined from experimental values of the shear rate at the belt $\dot{\gamma}_H$ and in the center of the flow $\dot{\gamma}_0 = \dot{\gamma}(0)$, as from Eq. (5) $a = \frac{d}{H}\sqrt{(\dot{\gamma}_H^2/\dot{\gamma}_0^2) - 1}$. We know that $d/H \approx 0.12$, and Fig. 2(b) indicates that $(\dot{\gamma}_H/\dot{\gamma}_0) \approx 2$, leading to a value for a: $a \approx 0.21$. Figure 4 shows the model prediction against the normalized average shear rate from the experiments. The model captures the scaling of $\dot{\gamma}(y)$ with the belt velocity V^{belt} (i.e., $\dot{\gamma}(y) \propto V^{\text{belt}}$).

Conclusions.—The stadium shear experiments we presented in this Letter revealed an important feature of dense granular flows: even in the absence of a stress gradient, the shear rate significantly increases when approaching the walls. This property is central to many applications involving granular flows near a solid boundary. This includes tribology and the prediction of basal sheared layers of landslides or snow avalanches. It also seems that such long-range wall effects should be considered to refine the interpretation of experimental granular flows in Couette cells, and thin granular layers flowing down a slope.

The model we suggested to describe the long-range wall effect of the shear rate is analogous to the eddy viscosity model used to predict the velocity profiles in boundary layers of turbulent flows. Our model is also based on the idea that the transfer of momentum could occur over large length scales if it was not truncated by the presence of a wall. This is therefore a nonlocal model. It could complement existing nonlocal models which have mainly focused on the effect of a stress gradient in the bulk flow.

Our experimental study covered a range of shear rates in a fixed geometry condition for a particular system width H, and a particular solid fraction. Velocity profiles always exhibited S shapes. It may be expected that different flow conditions could lead to more or less linear profiles. They could for instance lead to different values of the parameter a, thereby tuning the relative effect of the eddy viscosity to the local viscosity.

This work may be useful in understanding the existence of vortices within shear bands, such as those observed recently in sands [15]. Also, long-range wall effects are thought to exist in other particulate systems, such as dense suspensions, foams, and emulsions. Given that the proposed model only involves the system size, it is hoped that it could be adapted to them by considering their specific local constitutive law.

*Corresponding author.
itai.einav@sydney.edu.au

[1] GDR MiDi, Eur. Phys. J. E **14**, 341 (2004); Y. Forterre and O. Pouliquen, Annu. Rev. Fluid Mech. **40**, 1 (2008).
[2] D. Ertas and T. C. Halsey, Europhys. Lett. **60**, 931 (2002).
[3] F. Radjaï and S. Roux, Phys. Rev. Lett. **89**, 064302 (2002).
[4] F. Radjaï and S. Roux, in *Nonsmooth Mechanics and Analysis*, edited by P. Alart, O. Maisonneuve, and R. T. Rockafellar, Advances in Mechanics and Mathematics Vol. 12 (Springer, New York, 2006), pp. 233–245.
[5] O. Pouliquen, Phys. Rev. Lett. **93**, 248001 (2004).
[6] A. V. Orpe and A. Kudrolli, Phys. Rev. Lett. **98**, 238001 (2007).
[7] P. Mills, P. Rognon, and F. Chevoir, Europhys. Lett. **81**, 64 005 (2008).
[8] P. Rognon and I. Einav, Phys. Rev. Lett. **105**, 218301 (2010).
[9] P. Chaudhuri, V. Mansard, A. Colin, and L. Bocquet, Phys. Rev. Lett. **109**, 036001 (2012).
[10] V. Richefeu, G. Combe, and G. Viggiani, arXiv:1208.0485.
[11] C. Bonnoit, T. Darnige, E. Clement, and A. Lindner, J. Rheol. **54**, 65 (2010); C. Bonnoit, J. Lanuza, A. Lindner, and E. Clement, Phys. Rev. Lett. **105**, 108302 (2010).
[12] O. Pouliquen and Y. Forterre, Adv. Compl. Syst. **04**, 441 (2001); Phil. Trans. R. Soc. A **367**, 5091 (2009).
[13] J. Goyon, A. Colin, G. Ovarlez, A. Ajdari, and L. Bocquet, Nature (London) **454**, 84 (2008); K. Kamrin and G. Koval, Phys. Rev. Lett. **108**, 178301 (2012).
[14] F. da Cruz, F. Chevoir, J. N. Roux, and I. Iordanoff, in *Transient Processes in Tribology*, edited by G. Dalmaz, A. A. Lubrecht, D. Dowson, and M. Priest (Elsevier, New York, 2004), pp. 53–61.
[15] S. Abedi, A. L. Rechenmacher, and A. D. Orlando, Granular Matter **14**, 695 (2012).

CrossMark

J. Fluid Mech. (2015), *vol.* 764, *pp.* 171–192. © Cambridge University Press 2014
doi:10.1017/jfm.2014.707

Long-range wall perturbations in dense granular flows

Pierre G. Rognon[1,2,†], Thomas Miller[1,3], Bloen Metzger[2] and Itai Einav[1]

[1]Particles and Grains Laboratory, School of Civil Engineering, The University of Sydney, Sydney, NSW 2006, Australia

[2]IUSTI-CNRS UMR 7343, Aix-Marseille University, 13453 Marseille, France

[3]Department of Civil, Environmental and Geomatic Engineering, Faculty of Engineering Science, University College London, Gower Street, London WC1E 6BT, UK

(Received 8 February 2014; revised 12 September 2014; accepted 2 December 2014)

We explore how the rheology of dense granular flows is affected by the presence of sidewalls. The study is based on discrete element method simulations of plane-shear flows between two rough walls, prescribing both the normal stress and the shear rate. Results confirm previous observations for different systems: large layers near the walls develop where the local viscosity is not constant, but decreases when approaching the walls. The size of these layers can reach several dozen grain diameters, and is found to increase when the flow decelerates, as a power law of the inertial number. Two non-local models are found to adequately explain such features, namely the kinetic elasto-plastic fluidity (KEP) model and the eddy viscosity model (EV). The analysis of the internal kinematics further shows that the vorticity and its associated length scale may be a key component of these non-local behaviours.

Key words: granular mixing, particle/fluid flow, rheology

1. Introduction

When subjected to sufficient stresses, dense granular materials flow. This property is at the core of various industrial processes involving manufacturing and transport of various kinds of powders and grains. It is also at the core of the dynamics of geophysical flows such as landslides and snow avalanches. A robust and accurate modelling of the flowing behaviour of dense granular materials is needed for these applications.

Dense granular flows exhibit a non-Newtonian behaviour. They are characterised by a visco-plastic constitutive law, that relates the local stresses to the local strain rates (GDR MiDi 2004; da Cruz *et al.* 2005; Jop, Forterre & Pouliquen 2006; Andreotti 2007; Forterre & Pouliquen 2008; Andreotti, Forterre & Pouliquen 2013). This constitutive law is sufficient to describe dense granular flows far from walls in various geometries. However, it generally fails to predict the flow close to walls.

The presence of walls in granular flows may induce two important effects. First, with smooth walls some slip velocity may develop. This slip velocity vanishes for

† Email address for correspondence: pierre.rognon@sydney.edu.au

rough walls featuring asperities larger than the grain size (Goujon, Thomas & Dalloz-Dubrujeaud 2003; Shojaaee *et al.* 2012*a*,*b*). Second, even without slip velocity, the behaviour of the flowing granular materials appears to be strongly modified near walls. Such effects were interpreted as resulting from the non-local behaviour of granular materials: the ability to flow at a given location depends on the nature of the flow in the surrounding region.

Various models have been developed and have successfully captured such non-local effects. They are based on Cosserat-plasticity (Mohan, Rao & Nott 2002), visco-plasticity combined with non-local self-activated processes (NL model) (Pouliquen & Forterre 2001, 2009) or non-local kinetic elasto-plastic fluidity (KEP model) (Goyon *et al.* 2008; Kamrin & Koval 2012; Bouzid *et al.* 2013; Mansard *et al.* 2013). These models involve some typical length characterising the extent of the non-locality. This length was found to increase as the flows decelerate and stop. These models successfully capture and rationalise non-trivial variations in local viscosities and jamming conditions within flows featuring stresses and shear rate gradients, such as cylindrical-Couette flows, plane-shear flows with or without gravity, flows down a slope and flows in pipes. However, the predictions of these models critically rely on the assumptions made regarding the role of bounding walls. With the NL model, walls may be assumed either to absorb stress fluctuations coming from the flowing materials or to reflect them back into the flow. Depending on which of these two assumptions is considered, the model predicts an increase or a decrease in local viscosity near walls. Similarly, the variation in viscosity near walls predicted by the KEP model strongly depends on the value of the material's fluidity at the wall, which needs to be assumed or empirically determined for each flow configuration.

Another type of non-local model, inspired by the eddy viscosity (EV model) concept developed in turbulence, was introduced to predict the variation in viscosity near walls without relying on such assumptions. This model successfully captured the variation in granular viscosity near walls measured numerically in flow down a slope (Staron 2008; Staron *et al.* 2010), and experimentally in plane-shear flows (Miller *et al.* 2013; Miller 2014). Nonetheless, the validity of the model was only demonstrated for narrow systems in quasi-static flow regimes, and whether or not it could capture similar non-local features in larger systems and faster flows is still an open question. Further, this model is based on the existence of large granular vortices, whose typical size would decrease near walls. However, the existence of such a vorticity length scale has not been demonstrated, and there is no consensus on how it should evolve near walls.

In this paper, we investigate the range and the nature of wall perturbations in dense granular flows. To this end, we use a discrete element method to simulate the flow of a two-dimensional granular material between two parallel walls, prescribing both the shear rate and the normal stress. We analyse the stresses and strain rate near the walls to demonstrate possible deviations from the constitutive law predictions. The goal is to establish an empirical model describing these deviations, and discuss how they can be rationalised by non-local models.

The simulated system will be presented in § 2. In § 3 we present the measurements of the macroscopic friction and dilatancy laws as a function of the system size. In § 4, we analyse the stresses and strain rates within the flows to demonstrate long-range wall perturbations, and propose an empirical model capturing their observed features. In § 5, we discuss how such wall effects can be captured by the KEP and EV non-local models, and we analyse the internal flow kinematics to support the relevance of these models, focusing on the local vorticity and its associated length scale.

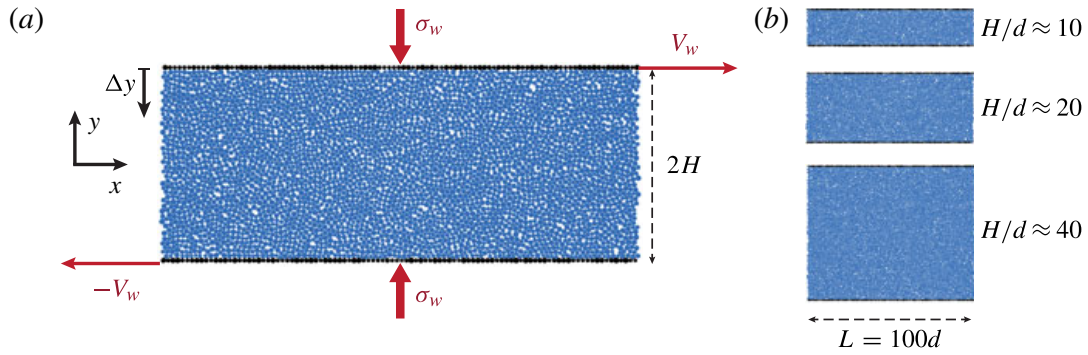


FIGURE 1. (Colour online) Plane-shear flow geometry. (*a*) Thousands of grains are subjected to shear between two rough walls (black grains) imposing both shear rate $\dot{\Gamma}_w = V_w/H$ and normal stress σ_M. Periodic boundaries are applied in the x-direction. (*b*) Three systems with different half-widths H are analysed.

2. Dense granular flows in the plane-shear geometry

In this section, we present the simulated system and define the measured quantities.

2.1. *Plane-shear geometry*

We consider flows in a plane-shear geometry as illustrated in figure 1(*a*). It comprises two parallel walls shearing a two-dimensional assembly of grains, prescribing both shear rate and normal stress. The wall separation distance is $2H$. They are made out of aligned grains having the same mechanical and physical properties as the flowing grains. The wall velocity in the shear direction x, V_w, is controlled such that the macroscopic shear rate,

$$\dot{\Gamma}_M = \frac{V_w}{H}, \tag{2.1}$$

is constant in time. The wall separation distance, $2H(t)$, is free to vary in time in order to ensure that the external stress, σ_w, is balanced by the total force of the grains contacting the wall, F^{int}. $H(t)$ satisfies inertial dynamics, $M\ddot{H} = F^{int} - \sigma_w Ld$, with M being the total mass of the walls.

2.2. *Grain properties*

The grains are disks of density ρ, mass m and diameter d. A polydispersity of $\pm 20\,\%$ is introduced in the grain diameter to avoid crystallisation. Grains interact with their neighbours through inelastic and frictional contacts. These interaction laws are detailed in appendix A. They only depend on the elastic coefficient of the grains, E (Pa), Newton's coefficient of restitution, e, and the coefficient of friction between two grains, μ_g. Unless otherwise specified, the grain-to-grain friction and restitution coefficient are set to $\mu_g = 0.5$ and $e = 0.5$, respectively. The value of the deformation number, $\kappa = \sigma_w/E = 10^{-3}$, is fixed to be in the rigid-grain limit, characterised by small elastic deformations (see appendix A).

2.3. *Numerical experiments*

The numerical experiments comprise two steps: the preparation of a steady flow, and the steady flow during which measurements are performed. The preparation of the

steady flow consists of applying both normal stress, σ_w, and shear rate, $\dot{\Gamma}_M$, on a loose configuration of grains, initially set randomly with no contact. The system width, $H(t)$, decreases and the solid fraction ϕ_M, the ratio of the grain surface area to the total system area, increases. They both eventually reach steady-state values with small time fluctuations.

In the following, the analysis will focus on steady flows in systems of varying width, $H/d = 10$, 20, and 40 (see figure 1*b*), with different values of the macroscopic inertial number I_M,

$$I_M = \dot{\Gamma}_M d\sqrt{\frac{\rho}{\sigma_w}}, \tag{2.2}$$

ranging from 10^{-3} to 10^{-1}, which corresponds to flows in the dense regime (GDR MiDi 2004; da Cruz *et al.* 2005).

2.4. *Macroscopic quantities and profiles*

In the following, the analysis will be based on quantities such as stresses, velocities, velocity gradient and solid fraction in the steady regime. These quantities will be averaged in time by considering a set of 100 snapshots, the system undergoing a shear deformation of one between two consecutive snapshots. We will distinguish the macroscopic quantities corresponding to a spatial average over the entire system, denoted by a subscript M, from their profile along the transverse direction y, obtained by averaging in the direction of shear, x, and in time, using the procedure described in appendix B.

We denote as ϕ_M, τ_M, σ_M and $\dot{\Gamma}_M$ the macroscopic solid fraction, shear and normal stresses and shear rate; $\phi(y)$, $\tau(y)$, $\sigma(y)$ and $\dot{\gamma}(y)$ refers to their profiles. The relationship between macroscopic quantities and their profile is, taking the example of the solid fraction, $\phi_M = (1/2H)\int_{-H}^{H}\phi(y)\mathrm{d}y$.

3. Effect of system size on macroscopic friction and dilatancy laws

As a way to demonstrate possible wall effects in our systems, let us first analyse the stresses and strain rate at a macroscopic level in our systems by comparing them with the prediction of the visco-plastic constitutive law of dense granular flows.

3.1. *Local friction and dilatancy laws*

The local visco-plastic constitutive law describing dense granular flow can be expressed by a friction law combined with a dilatancy law (GDR MiDi 2004; da Cruz *et al.* 2005; Jop *et al.* 2006; Forterre & Pouliquen 2008; Andreotti *et al.* 2013). These two laws specify how the effective friction coefficient, μ, the ratio of the shear and normal stresses, and the solid fraction, ϕ, depend on the shear rate $\dot{\gamma}$. In the dense regime, both laws are approximately linear functions of the local shear rate:

$$\mu(y) = \frac{\tau(y)}{\sigma(y)} \approx \mu_s + aI(y), \tag{3.1}$$

$$\phi(y) \approx \phi_0 - bI(y), \tag{3.2}$$

$$I(y) = \dot{\gamma}(y)d\sqrt{\frac{\rho}{\sigma(y)}}. \tag{3.3}$$

The coefficients μ_s, a, ϕ_0 and b are positive numerical constants which depend on the nature of the grains and of their interactions, such as friction, shape and adhesion (da Cruz *et al.* 2005; Rognon *et al.* 2006, 2007, 2008).

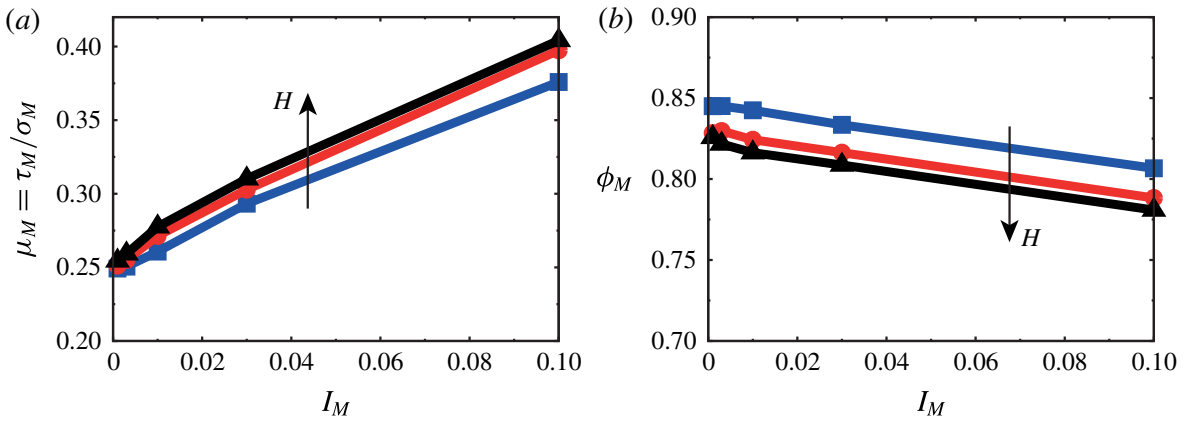


FIGURE 2. (Colour online) Macroscopic constitutive behaviour measured in systems of differing sizes $H/d = 10$ (■), 20 (●) and 40 (▲): (*a*) friction law and (*b*) dilatancy law.

3.2. *Macroscopic friction and dilatancy laws*

In steady sheared flows between two parallel plates, the momentum balance predicts that there should be no stress gradient in the transverse direction y, $\sigma(y) = \sigma_w = \sigma_M$ and $\tau(y) = \tau_M$. According to (3.1) and (3.2), the local shear rate and solid fraction should thus be constant: $\dot{\gamma}(y) = \dot{\Gamma}_M$ and $\phi(y) = \phi_M$. Integrating the local friction and dilatancy laws would thus lead to a macroscopic expression for the constitutive behaviour of the form

$$\mu_M = \frac{\tau_M}{\sigma_M} \approx \mu_s + aI_M, \tag{3.4}$$

$$\phi_M \approx \phi_0 - bI_M. \tag{3.5}$$

We measured such macroscopic laws in our systems (see figure 2). For a given system width H, the macroscopic friction and dilatancy laws approximately exhibit a linear dependence on the macroscopic inertial number I_M (2.2), consistent with (3.4) and (3.5). However, with the same inertial number I_M different values of the macroscopic coefficient of friction and solid fraction are obtained in systems of differing width H. Larger systems leads to higher coefficient of friction μ_M and lower solid fraction ϕ_M.

The local visco-plastic constitutive law as expressed in (3.4) and (3.5) does not predict this system size effect. It suggests that walls may affect the material rheology, and the next sections will focus on characterising and understanding such an effect.

4. Characterisation of long-range wall perturbations

In this section we analyse the profiles of stresses, solid fraction and shear rate to characterise the effect of walls in the flowing behaviour of the materials.

4.1. *Demonstrating wall effects*

Let us first describe a particular flow obtained with $I_M = 10^{-2}$ and $H/d = 20$. We observe that the local friction coefficient, $\mu(y) = \tau(y)/\sigma(y)$, is constant (see figure 3*a*). This is consistent with the momentum balance applied to this geometry, which predicts no stress gradient in the y-direction. The solid fraction $\phi(y)$ is also mostly constant, but slightly decreases in the wall vicinity. The important result is that, although

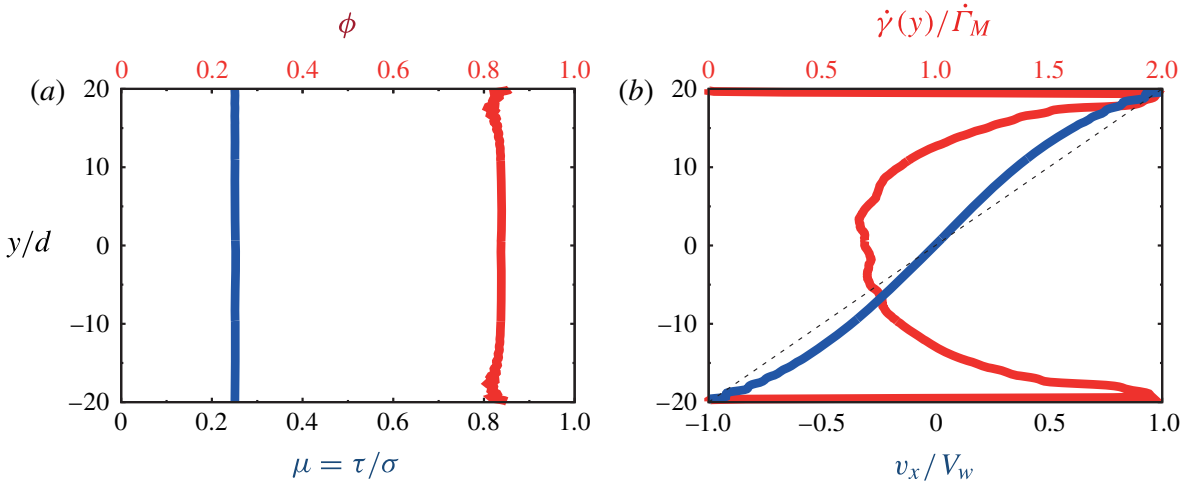


FIGURE 3. (Colour online) Time-averaged profiles along the y-direction within a steady flow ($H = 20d$, $I_M = 0.01$). (a) Friction coefficient, ratio of shear to normal stresses $\mu(y) = \tau(y)/\sigma(y)$ (bottom axis, dark grey curve, blue online) and solid fraction $\phi(y)$ (top axis, light grey curve, red online). (b) Velocity profile $v_x(y)$ normalised by the wall velocity V_w (bottom axis, dark grey curve, blue online) and the linear velocity profile $V_w y/H$ is shown for comparison (dashed line); and shear rate $\dot{\gamma}(y)$ normalised by the nominal shear rate $\dot{\Gamma}_M = V_w/H$ (top axis, light grey curve, red online).

stresses are constant throughout the layer, the velocity profile $v_x(y)$ is not linear (see figure 3b) but exhibits an S-shape. The corresponding shear rate profile,

$$\dot{\gamma}(y) = \frac{\partial v_x(y)}{\partial y}, \tag{4.1}$$

is thus not constant. It increases significantly when approaching the walls while staying approximately constant in the central region of the flow. Similar S-shape profiles in plane-shear flows were reported in da Cruz *et al.* (2004), GDR MiDi (2004), Miller *et al.* (2013) and Miller (2014).

The fact that the shear rate $\dot{\gamma}(y)$ varies near the wall while the stresses are constant shows that the local friction and dilatancy laws in (3.1) and (3.2) fail to describe the flow in these regions. An additional effect of the walls leads to an increase of the local shear rate in the wall vicinity.

Flows were computed varying two grain contact parameters: their coefficient of friction μ_g and the coefficient of restitution e. Figure 4 shows that similar non-constant shear rate profiles are obtained when varying these parameters, even with frictionless grains ($\mu_g = 0$). This suggests that neither the friction nor restitution coefficient is responsible for the curvature of the velocity profile.

4.2. *Shear rate variation near walls*

Figure 5(a) shows the variation in shear rate as a function of the distance to the wall Δy:

$$\Delta y = H - |y|, \tag{4.2}$$

for $H = 40d$ and $I_M = 10^{-2}$. The shear rate is maximum near the wall and approximately constant in a first layer of size $\delta \approx 2d$. For $\Delta y > \delta$, the shear rate

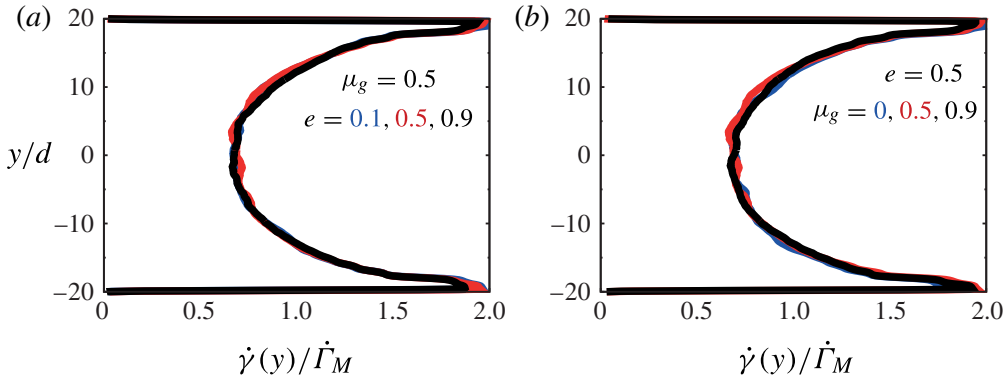


FIGURE 4. (Colour online) Shear rate profiles along the y-direction within steady flows ($H = 20d$, $I_w = 0.01$) for (a) differing contact restitution coefficient e (0.1, dark grey, blue online; 0.5, light grey, red online; 0.9, black) and (b) differing contact friction coefficient μ_g (0, dark grey, blue online; 0.5, light grey, red online; 0.9, black).

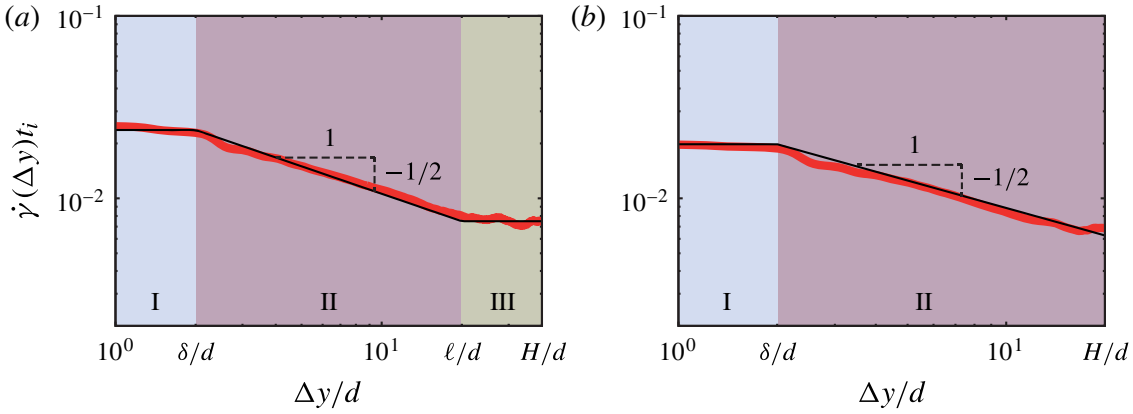


FIGURE 5. (Colour online) Shear rate $\dot{\gamma}$ versus distance to the wall Δy for two simulations with similar inertial number, $I_M = 10^{-2}$, but different widths: (a) $H/d = 40$ and (b) $H/d = 20$. The wall is at $\Delta y = 0$ while the centre of the sheared layer is at $\Delta y = H$. The shear rate, $\dot{\gamma}$, is expressed in inverse unit of inertial time, $t_i = d\sqrt{\rho_g/\sigma_M}$. Thick grey lines (red online) represent simulation results and thin black lines the empirical model defined in (4.4).

decreases when the distance to the wall Δy increases. In this zone, the shear rate decay can be represented by a power law:

$$\dot{\gamma}(y) \propto (\Delta y)^{-1/2}. \tag{4.3}$$

For large distance to the wall, $\Delta y > \ell$, the shear rate seems again constant.

Figure 5(b) shows the shear rate profile $\dot{\gamma}(\Delta y)$ for a flow with the same inertial number as in figure 5(a), but in a narrower system, $H = 20d$. The first layer of constant shear rate for $\Delta y < \delta \approx 2d$ and the second layer of decaying shear rate for $\Delta y > \delta \approx 2d$ are still present. However, in this case the shear rate decays until the middle of the flow and there is thus no central zone with a constant shear rate.

4.3. *Empirical model capturing shear rate profiles*

The profiles shown on figure 5 suggest how the shear rate can be modelled in each of the three zones, I, II and III. Accounting for the fact that the shear rate is continuous,

these profiles can be captured by the following empirical model:

$$\dot{\gamma}(\Delta y) = \begin{cases} \dot{\gamma}_b \sqrt{\dfrac{\ell}{\delta}} : \Delta y \leqslant \delta & \text{(I)} \\ \dot{\gamma}_b \sqrt{\dfrac{\ell}{\Delta y}} : \delta \leqslant \Delta y \leqslant \ell & \text{(II)} \\ \dot{\gamma}_b : \ell \leqslant \Delta y \leqslant H & \text{(III)}. \end{cases} \tag{4.4}$$

The numerical results shown in figures 5(*a*) and 5(*b*) are both captured by this empirical model using $\delta = 2d$, $\ell = 20d$ and $\dot{\gamma}_b = 0.75\,\dot{\Gamma}_M$, where $\dot{\gamma}_b$ is the bulk shear rate.

4.4. *Range of wall perturbations*

We denote as ℓ the range of the wall perturbations, the region comprising zones I and II ($0 < \Delta y < \ell$) where the shear rate differs from the constant bulk value found in zone III.

For the flow conditions of figure 5(*a*), the wall perturbation range is remarkably large, $\ell \approx 20d$. Within the same conditions, $I_M = 10^{-2}$, but in a narrower system, $H = 20d$, zone III no longer exists (see figure 5*b*) which can be interpreted as an overlap of the perturbations from each wall.

Figure 6 shows the velocity and shear rate profiles for flows with various inertial numbers I_M and various widths H. For large systems, the wall perturbation range seems to increase as the inertial number decreases, and never exceeds the system width. For narrow systems, the wall perturbation spans the entire system width.

In the largest system, $H = 40d$, the size ℓ of the wall perturbation is estimated for flows of different internal number I_M by adjusting the empirical model (4.4) to the measured shear rate profiles. Figure 7(*a*) shows the best fit of the empirical model to the measured shear rate profiles. All the shear rate profiles were captured by the model using similar values of δ ranging between 1.5 and 2. Conversely, the range of the wall perturbation, ℓ, was found to vary from $6.5d$ to $25d$.

Figure 7(*b*) shows the values of wall perturbation range ℓ thus estimated as a function of the macroscopic inertial number I_M. For macroscopic inertial number ranging from 6×10^{-3} to 10^{-1}, the size of the wall perturbation exhibits a power law:

$$\frac{\ell}{d} \approx 2 I_M^{-1/2}. \tag{4.5}$$

For the lowest inertial numbers, ℓ could not be estimated since zone III did not exist even in the largest systems.

5. Modelling wall perturbations

In the previous section, we have identified two empirical laws: one capturing the increase in shear rate observed near walls (4.4) and the other capturing the range of this perturbation (4.5). Let us now discuss the mechanisms and analytical models that may explain these perturbations.

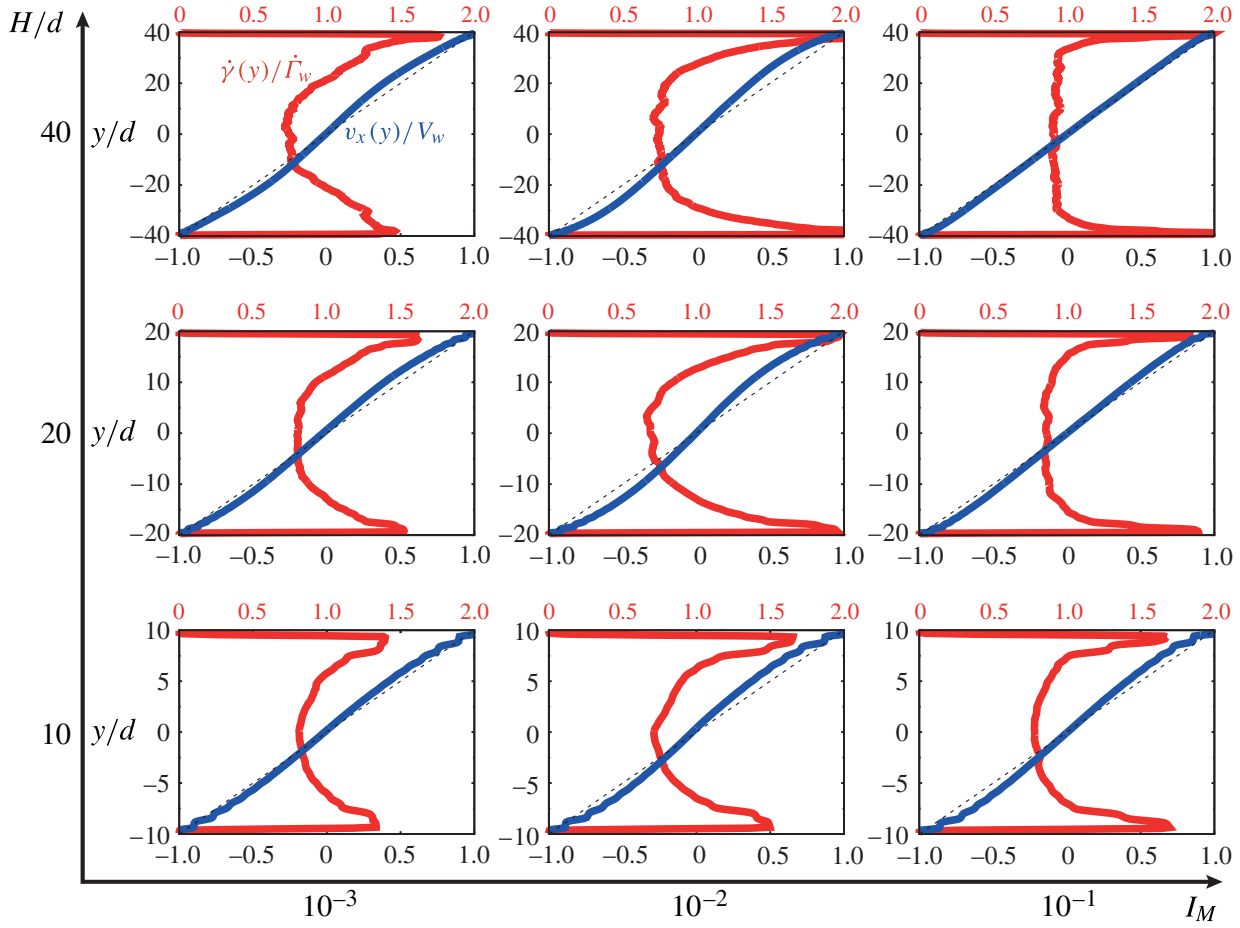


FIGURE 6. (Colour online) Time-averaged velocity and shear rate profiles for flows with various inertial numbers I_M and widths H as indicated by arrows. Same colour code as figure 3(*b*).

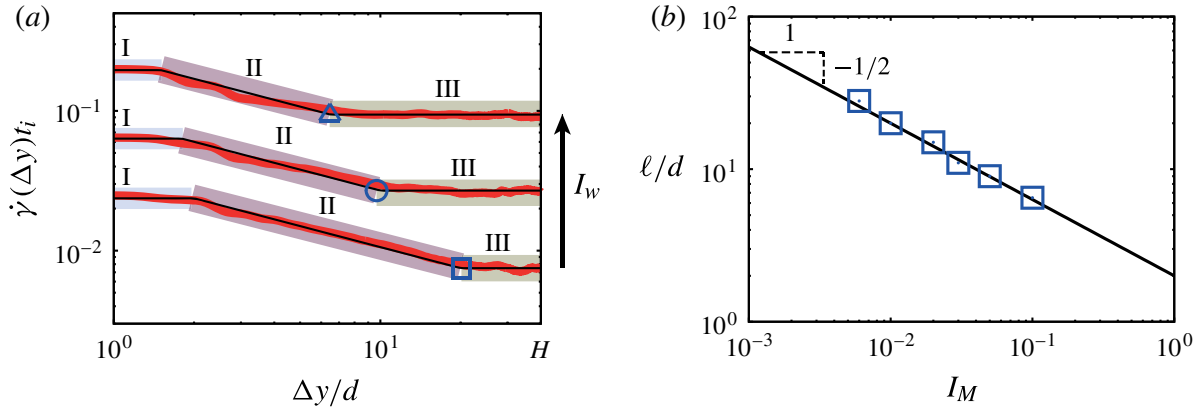


FIGURE 7. (Colour online) (*a*) Shear rate profiles versus distance to the wall, Δy, for three different inertial numbers, $I_M = 10^{-2}$, 3×10^{-2}, 10^{-1}. Grey curves (red online) represent simulation results and thin black lines the empirical model defined in (4.4). Symbols mark the width, ℓ, of the boundary layer for each system. (*b*) Width of the boundary layer, ℓ, versus inertial number, I_M; the line represents the function $\ell/d \approx 2I_M^{-1/2}$.

5.1. *Local constitutive law and viscosity length scale*

The local constitutive laws, as expressed by the friction and dilatancy laws (3.1) and (3.2), fail to capture the wall perturbations as they predict a constant shear rate throughout the layer when the stresses are constant: $\dot{\gamma} = (\mu - \mu_s)/ad\sqrt{\rho/\sigma}$. They nonetheless contain important information regarding the characteristic length scale involved into the diffusion of momentum. This length scale appears when one formulates these laws using the kinetic viscosity ν ($\mathrm{m^2\ s^{-1}}$), which is also referred to as momentum diffusivity, defined as

$$\nu = \frac{1}{\rho}\frac{\partial \dot{\gamma}}{\partial \tau}. \tag{5.1}$$

Using the kinetic viscosity, the friction law becomes

$$\tau = \mu_s \sigma + \rho \nu \dot{\gamma}, \tag{5.2}$$

which is equivalent to a Bingham constitutive law, with a yield stress $\mu_s\sigma$ increasing with the normal stress, and a kinetic viscosity $\nu \propto d\sqrt{P/\rho} = d^2\dot{\gamma}/I$. This kinetic viscosity can be expressed as a function of a typical time scale, $\dot{\gamma}^{-1}$, and a length scale ℓ_ν as

$$\nu \propto \ell_\nu^2 \dot{\gamma}, \tag{5.3}$$

$$\ell_\nu \propto \frac{d}{\sqrt{I}}. \tag{5.4}$$

Note that, considering the friction law (3.1), the typical length scale (5.4) can also be expressed as function of the quantity $\mu - \mu_s$: $\ell_\nu \propto d/\sqrt{\mu - \mu_s}$.

Equation (5.4) highlights an important feature of dense granular flows: at low inertial number, the momentum diffuses on a typical length scale much larger than the grain size d. Remarkably, the scaling of this length with I is identical to the scaling of 'cooperativity' length with I, measured and predicted in different configurations within the KEP non-local model framework (Kamrin & Koval 2012; Bouzid *et al.* 2013; Mansard *et al.* 2013).

Quantitative predictions of the viscosity in the zone affected by walls requires identifying the long-range mechanisms underpinning the momentum diffusion. Different analyses have been developed to address this question. Two non-local models, namely the NL process and KEP models, were derived from an analysis of the internal dynamics and the mode of stress propagation within the materials. By contrast, the EV model was developed from the analysis of the internal kinematics and the momentum transport within a non-affine displacement field. Let us now discuss these models and their ability to capture the observed long-range wall perturbations.

5.2. *Non-local self-activated process (NL model)*

This model, introduced in Pouliquen & Forterre (2001, 2009), is based on the following ideas: (i) the shear between two layers of grains leads to topologic rearrangements, also called plastic events, that locally release the stresses; (ii) the associated stress relaxation induces some stress fluctuations that propagate through the network of contact with a typical length scale; (iii) the propagating stress fluctuations contribute to triggering plastic rearrangements far from their origin. In this model, the viscosity at a given point is derived from the sum of the stress fluctuations which have

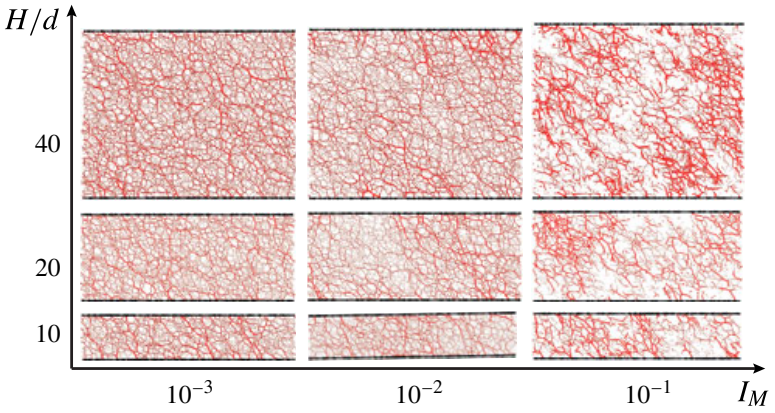


FIGURE 8. (Colour online) Snapshots of the contact network for various inertial numbers, I_w, and system widths H, as indicated by the arrows. The lines connect the centre of each pair of contacting grains. Their thickness is proportional to the normal contact force.

propagated to this point, originating from remote plastic events. As a consequence, the local viscosity depends on the rate of plastic events in the surroundings, and is lower when the shear rate in the surroundings is higher.

Consistent with Hartley & Behringer (2003), Majmudar & Behringer (2005), da Cruz *et al.* (2005), Tordesillas, Zhang & Behringer (2009), Tordesillas *et al.* (2011), Azéma & Radjaï (2014), figure 8 shows that contact force networks within the flows exhibit long length scales, which mechanically connect remote grains to the walls. Further, the contact network seems to be less connected for high values of the inertial number. This supports the relevance of relating non-local behaviour to the force network.

The NL model successfully predicts three observations that the local constitutive law alone is unable to capture: the shear rate profiles within flow in pipes; the dependence of the angle of arrest on the thickness of the granular layer in the inclined plane geometry; more generally, the existence of some flow in zones where the stresses are below the yield stress when there is some flow in the surroundings.

However, the role of the wall is not directly accounted for in the NL model formulation. An additional hypothesis needs to be made regarding the ability of the wall to reflect or absorb stress fluctuations. Considering that the wall absorbs the stress fluctuations, the model predicts that a layer near the wall is subjected to less fluctuation than a layer far from the wall, and its viscosity is higher. Accordingly, the predicted shear rate is lower near the wall, which is not consistent with our results. Assuming that the wall reflects stress fluctuations back into the flow, an opposite trend is predicted that is consistent with our results. Unfortunately, there is no clear rationale to determine whether or not and to what extent walls may reflect stress fluctuations. While the NL model may be able to capture our results, further understanding of the effect of the wall on stress propagation is needed to draw robust conclusions.

5.3. *Non-local KEP model*

This model was introduced in Goyon *et al.* (2008) and Bocquet, Colin & Ajdari (2009) to rationalise the flow of dense emulsions flowing in micro-channels, and was then adapted to dense granular flows in Kamrin & Koval (2012) and Bouzid *et al.* (2013). It is based on the same conceptual ideas as the NL model, considering that

(i) the local viscosity is inversely proportional to the local rate of plastic events; (ii) a plastic event at one location may trigger other plastic events at remote locations through the propagation of stress fluctuations through the contact network.

This model successfully predicts shear rate profiles of soft glassy materials such as emulsions and dry granular matter in geometries where the stresses are not spatially constant, such as pipes, inclined plane and plane shear with gravity, including in zones where the stresses are lower than the yield conditions predicted by their respective local constitutive laws.

In Mansard *et al.* (2013), the non-local KEP model is able to capture wall effects in plane-shear flows of a model dense emulsion. This system has some similarities with the one discussed here: it comprises disks sheared between two rough walls in the absence of gravity, a configuration where stresses are spatially constant. However, it differs from our system in some important points: the disks are soft and interact by strongly dissipative contacts, and the shear was performed at fixed volume and the solid fraction investigated is large, ranging from 90 % to 110 %, which is made possible by large overlaps of soft disks. As a result of these differences, the model emulsion did not satisfy a visco-plastic constitutive law such as (3.1) and (3.2), but instead a Herschel–Bulkley constitutive law typical of soft glassy materials such as foams and emulsions. Nonetheless, in spite of these differences, the reported velocity profiles exhibit an S-shape qualitatively similar to that obtained in our systems. The KEP model, in the plane-shear configuration, can be expressed as

$$\dot{\gamma}(y) - \dot{\gamma}_b = \xi^2 \frac{\partial^2 \dot{\gamma}(y)}{\partial y^2}, \tag{5.5}$$

where ξ is referred to as the 'cooperativity' length, and represents the spatial extent of the non-locality; $\dot{\gamma}(y)$ is the local shear rate, $\dot{\gamma}_b$ the bulk shear rate, which corresponds to the value of the shear rate in a flow with no heterogeneities, e.g. far from the wall in plane-shear flows. To predict the shear rate profile $\dot{\gamma}(y)$, (5.5) can be solved by introducing a boundary condition, the value of the shear rate at the wall, $\dot{\gamma}_w$. The predicted shear rate profile $\dot{\gamma}(y)$ is then

$$\dot{\gamma}(y) = (\dot{\gamma}_w - \dot{\gamma}_b) \frac{\cosh(y/\xi)}{\cosh(H/\xi)} + \dot{\gamma}_b. \tag{5.6}$$

This prediction involves the bulk shear rate, $\dot{\gamma}_b$, the shear rate at the wall, $\dot{\gamma}_w$, and the cooperativity length, ξ. In Mansard *et al.* (2013), this equation was shown to predict S-shape velocity profiles matching the numerical results for a given value of the imposed shear stress and different values of system width H, using a values of $\xi = 2.5d$ and $\dot{\gamma}_w = 1.7\dot{\gamma}_b$.

Figure 9 (*a*i–*a*iii) shows a comparison of the KEP model prediction with our numerical results for three different flows. Equation (5.6) was plotted after measuring $\dot{\gamma}_b$ as the shear rate in the middle of the flow in the largest system, and $\dot{\gamma}_w$ as the maximum value of the shear rate near the walls. Numerical data are well represented using $\xi/d = 5.4$ and $\dot{\gamma}_w/\dot{\gamma}_b = 2.2$ for flow (*a*i), $\xi/d = 5.4$ and $\dot{\gamma}_w/\dot{\gamma}_b = 2.45$ for flow (*a*ii), and $\xi/d = 2.2$ and $\dot{\gamma}_w/\dot{\gamma}_b = 2$ for flow (*a*iii).

A fundamental component of the non-local KEP model is identifying the inverse relation between the viscosity and the rate of plastic rearrangement. This was verified experimentally in Jop *et al.* (2012) and numerically in Mansard *et al.* (2013), by showing that zones of low viscosity exhibit a higher rate of particle rearrangement.

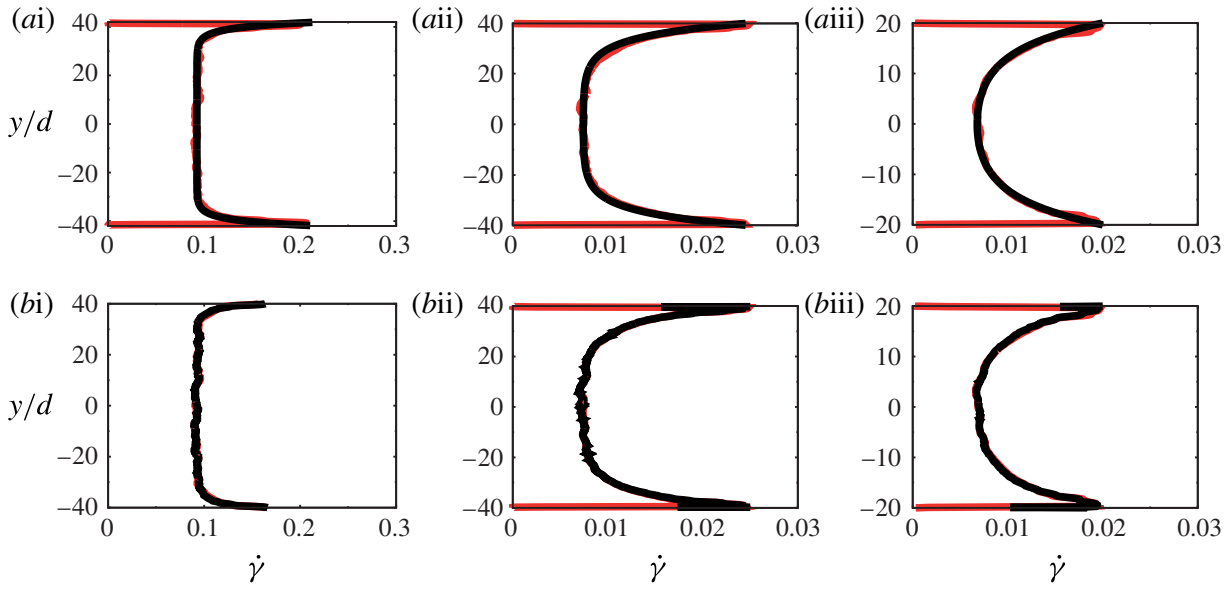


FIGURE 9. (Colour online) Comparison of shear rate profiles between numerical results (grey lines, red online) and and model prediction (black lines). (*a*) The KEP model prediction obtained from (5.6) is shown for three systems: (*a*i) $H/d = 40$, $I_M = 0.1$; (*a*ii) $H/d = 40$, $I_M = 0.01$; and (*a*iii) $H/d = 20$ $I_M = 0.01$. (*b*) The EV model prediction obtained from (5.14) is shown for the same three systems, and with values of β of (*b*i) 3.3, (*b*ii) 2, and (*b*iii) 1.85. Shear rates are expressed in units of inverse of inertial time.

Consistently, it was shown that zones of low viscosity exhibit higher level of velocity fluctuations, thought to be due to the higher rate of rearrangement (Mansard *et al.* 2013).

Figure 10, column (ii), shows the profile of velocity fluctuations δv measured in our systems, defined as the standard deviation of the grain velocity fluctuations $\boldsymbol{v}_i' = \boldsymbol{v}_i - \boldsymbol{v}(y_i)$. Results indicate that the velocity fluctuations are constant in the central region of the flow where the shear rate is constant. Near the walls, where the shear rate is higher and the apparent viscosity lower, the velocity fluctuations do not increase but decrease. This result differs from the measurements reported in Mansard *et al.* (2013), which may be due to the differences in the systems considered. While it does not affect the validity of the KEP model, which relies on the relationship between viscosity and rate of plastic rearrangement, this result suggests that there should exist a mode of grain rearrangement that allows for a higher rate of rearrangement together with lower velocity fluctuations when approaching the walls.

5.4. *Vorticity and vorticity length scale*

Let us now analyse the internal kinematics at the scale of the grains to seek a mechanism consistent with these observations. We focus on the local velocity gradient tensor defined as:

$$\boldsymbol{F}_{\alpha\beta} = \frac{\partial v_\alpha}{\partial x_\beta}, \tag{5.7}$$

which can be measured locally around each grain following a method introduced by Marmottant, Raufaste & Graner (2008) and detailed in appendix B. By definition, the component F_{yx} is equal to the shear rate $\dot{\gamma}$, and the anti-symmetric component of $\boldsymbol{F}_{\alpha\beta}$ is the vorticity w:

$$w = \tfrac{1}{2}(F_{yx} - F_{xy}). \tag{5.8}$$

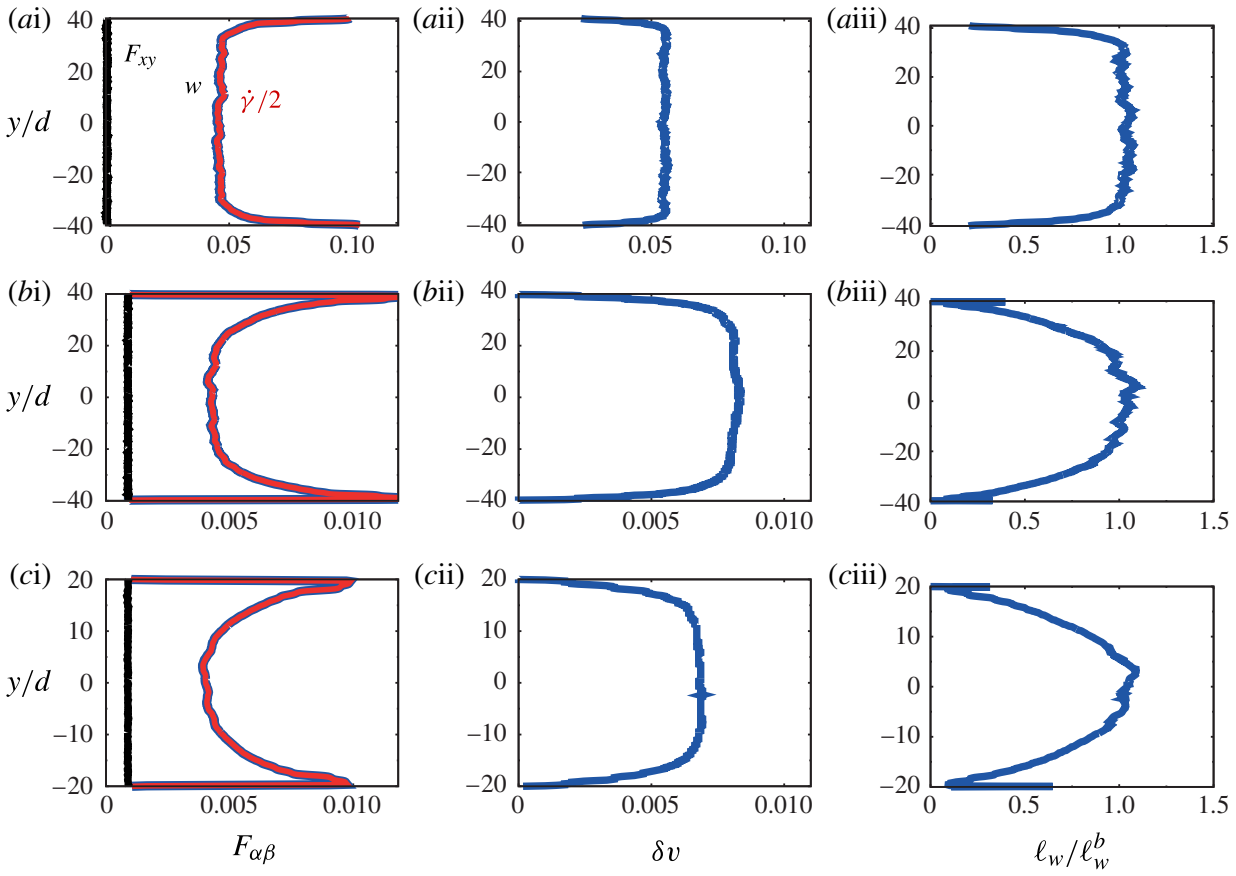


FIGURE 10. (Colour online) Vorticity and vorticity length scale in three flows: (*a*) $H/d = 40$, $I_M = 0.1$; (*b*) $H/d = 40$, $I_M = 0.01$; (*c*) $H/d = 20$, $I_M = 0.01$. Profiles of shear rate $\dot{\gamma}$, vorticity w and F_{xy} are shown in column (i). Profiles of velocity fluctuations δv are shown in column (ii). Profiles of the deduced vorticity length scale ℓ_w are shown in column (iii), measured according to (5.9) and normalised by the value at the centre of the flow, ℓ_w^b.

Figure 10, column (i), shows the profiles of $F_{xy}(y)$, $\dot{\gamma}(y)$ and $w(y)$ for three different flows ($H/d = 20$ and 40, $I_M = 0.1$ and 0.01). The component F_{xy} appears to always be much smaller than the shear rate $\dot{\gamma}$. As a consequence, there is a direct link between the local shear rate and the vorticity: $w(y) \approx \dot{\gamma}(y)/2$. Accordingly, the vorticity $w(y)$ is higher near the wall and constant in the centre of the flow. This property was consistently observed with all the flows investigated with different width H/d and inertial number I_M.

Figure 11 illustrates snapshots of the local vorticity fluctuation field $w_i' = w_i - \dot{\Gamma}_M/2$. It shows layers of high vorticity near the wall (light grey, red online) and a lower vorticity in the centre of the flow (dark grey, blue online). Further, figure 11 shows that the local vorticity exhibits some spatially correlated patterns comprising large zones with higher or lower vorticity than their surroundings. Note that previous analyses focusing on velocity fluctuations instead of vorticity revealed similar patterns (Blair & Kudrolli 2001; Radjaï & Roux 2002; Mueth 2003; Pouliquen 2004; Brito & Wyart 2007; Behringer *et al.* 2008; Lechenault *et al.* 2008; Liu & Nagel 2010; Abedi & Rechenmacher 2011; Rechenmacher & Abedi 2011; Abedi, Rechenmacher & Orlando 2012; Richefeu, Combe & Viggiani 2012; Miller *et al.* 2013; Miller 2014). Measuring the typical size of these correlated structures is challenging given their seemingly complex shape and large size distribution. As a consequence, statistical

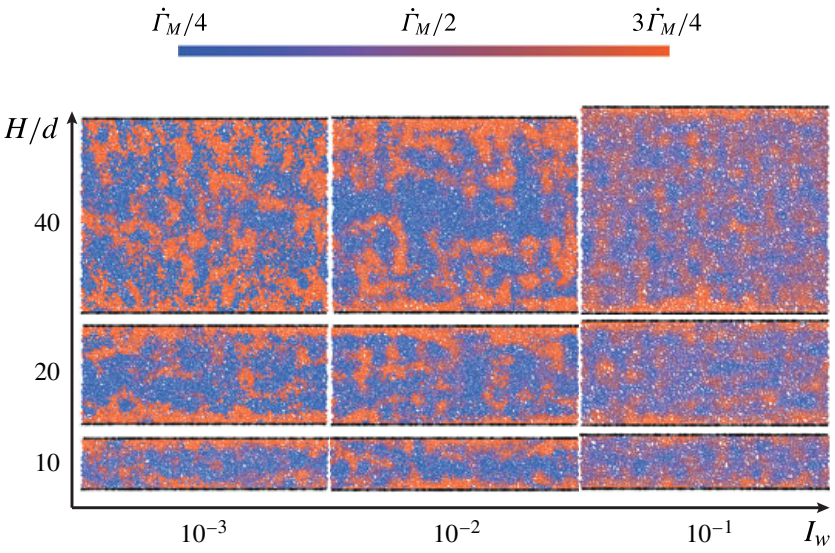


FIGURE 11. (Colour online) Vorticity field snapshots for different system widths, H, and different inertial numbers, I_w, as indicated by the arrows. The local vorticity around each grain is measured according to the method detailed in appendix B.

indicators such as spatial correlations of the vorticity field were found not to be conclusive to measure such a length scale.

Nonetheless, a typical vorticity length scale can be indirectly estimated from the combined measurements of the velocity fluctuation profile and the vorticity profile. The underlying idea is that a vortex of size ℓ_w rotating at a frequency w induces a level of velocity fluctuations of the order of $\delta v \propto w\ell_w$. Thus, the typical length scale associated with the vorticity can be estimated at any location y as

$$\ell_w(y) = \frac{\delta v(y)}{w(y)}. \tag{5.9}$$

Figure 10, column (iii), shows the corresponding profiles of vorticity length scale $\ell_w(y)$. In the bulk of the flow, where the shear rate is constant, the vorticity length is approximately constant: $\ell_w(y) \approx \ell_w^b$. By contrast, close to the walls, the vorticity length scale decreases. Figure 12 shows the values of the bulk vorticity length ℓ_w^b measured in the largest system ($H/d = 40$) as a function of the macroscopic inertial number I_M. It follows a power law:

$$\ell_w^b \propto \frac{d}{I_M^{1/2}}, \tag{5.10}$$

which is remarkably similar to the wall perturbation range empirically determined in (4.5), to the length scale of granular momentum diffusivity deduced from the local friction law in (5.3), and to the cooperativity length scale measured and predicted in the KEP framework (Kamrin & Koval 2012; Bouzid *et al.* 2013; Mansard *et al.* 2013).

To summarise, we extracted a vorticity length scale from the measurements of the velocity fluctuations. When approaching the walls, where the shear rate of the material increases, this length scale is found to decrease. This trend can be understood since, close to the walls, the lack of space mean that the correlated structures cannot freely develop: the presence of the wall tends to truncate the largest possible vortex in the flow. Let us now present a non-local model based on vorticity that could quantitatively capture the wall perturbations.

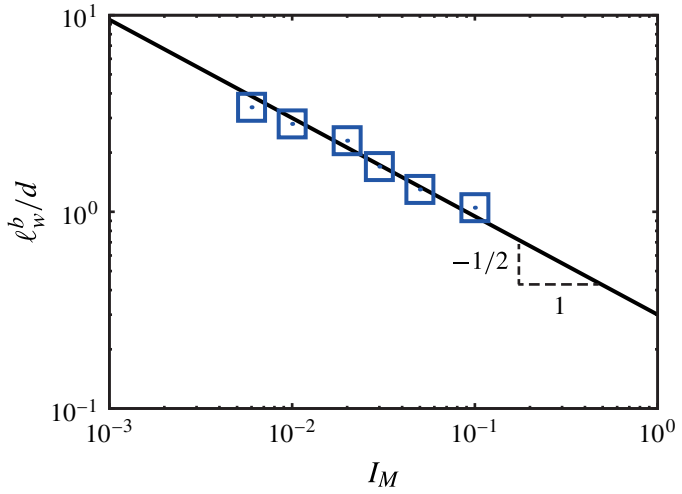


FIGURE 12. (Colour online) Vorticity length scale in the bulk of the flow, ℓ_w^b, as a function of the macroscopic inertial number, I_M, measured in the largest systems, $H/d = 40$. The line represents the power law in (5.10).

5.5. *EV model*

The EV model was first developed in the context of turbulent flows of Newtonian fluids to explain the increase in apparent viscosity observed between turbulent and laminar flow regimes. The underlying ideas are (i) there is an intrinsic viscosity ν_0 due to the transfer of momentum by molecular collisions in both regimes and (ii) in turbulent regimes, vortices develop and lead to an additional mode of momentum transfer and an associated viscosity ν^{eddy}. The effective viscosity ν^{eff} is thus expressed as the sum of the two contributions:

$$\nu^{eff} = \nu_0 + \nu^{eddy}. \tag{5.11}$$

Prandtl's mixing length model provides an estimation of the typical momentum diffusivity associated with a vortex of size ℓ_w rotating at a frequency w, as

$$\nu^{eddy} \propto w\ell_w^2. \tag{5.12}$$

In Staron *et al.* (2010) and Miller *et al.* (2013), the EV model was adapted to dense granular flows in the inclined-plane and plane-shear geometries. Both approaches consist of considering two mechanisms of momentum transfer in granular materials: pairwise grain collisions and large-scale vortex rotations. Accordingly, the apparent granular viscosity (5.3) can be expressed by

$$\nu = d^2\dot{\gamma} + \beta\ell_w^2\dot{\gamma}, \tag{5.13}$$

where β denotes a numerical constant reflecting the actual contribution to momentum transfer of vortices. The first term represents the diffusion of momentum by grain collision and the second term that by rotation of vortices of size ℓ_w. Note that the corresponding effective length scale of momentum diffusion would then be $\ell_\nu = d\sqrt{1+\beta(\ell_w/d)^2}$. Introducing this expression for viscosity into the friction law (3.1) leads to the following prediction of the shear rate profile:

$$\dot{\gamma}(y) = \frac{A}{\sqrt{1+\beta\,(\ell_w(y)/d)^2}}, \tag{5.14}$$

with $A = (\mu - \mu_s/a)(1/d\sqrt{\rho/\sigma})$.

In Staron *et al.* (2010) and Miller *et al.* (2013), no vorticity length scale was measured or estimated. This length scale was assumed to be given by some function of the distance to the walls. Various functions of the distance to the wall were introduced, so that the model (5.13) would predict the correct viscosity variation near walls. However, there is no established rationale for the choice of this function, and different choices may equally well represent the results.

In our systems, a typical vorticity length scale ℓ_w was estimated from the analysis of the grain velocity fluctuations, and can thus directly be introduced in (5.14). Figure 9 (*b*i–*b*iii) shows that the prediction of this model can successfully match the numerical results. The parameter A was directly measured as the shear rate at the wall, $\dot{\gamma}(y=H)$, using the fact that the vortex size $\ell_w(H)$ tends to zero, as shown on figure 10; β is thus the only fitting parameter, with values of the order of 2.

The empirical model (4.4) for wall perturbations can be interpreted within the EV framework. Zone III corresponds to the region in the middle of the flow where the vorticity length scale can fully develop: it is not affected by the walls. Zone II corresponds to the region where the vorticity length scale is truncated by the proximity of the walls, yet it still contributes significantly to the effective viscosity. Zone I corresponds to the first layers of grains near the wall where the vorticity length scale is so small that the grain collisions become the dominant mode of momentum transfer. Given that the EV model, (5.14), correctly captures the shear rate profiles, i.e. $\dot{\gamma} \propto \Delta y^{-1/2}$ in zone II, the vorticity length must scale as $\ell_w(y)/d \propto (\Delta y/d)^{1/2}$ when approaching the walls and not as $\ell_w(y) \propto \Delta y$ as is usually assumed in EV models.

6. Conclusion

The discrete element method simulations of plane-shear flow between walls presented in this paper show that walls significantly affect the viscosity of dense granular flows over large distances. Near walls, the viscosity is much lower than in the bulk flow. The range of this perturbation can reach several dozens of grains and increases for slower flows.

The practical implication of these results is to question a common way to measure the constitutive law of granular materials. Often, both experimentally and numerically, these laws are measured by averaging stresses or strain rate over the entire system width. We observed on figure 2 that both the friction law and the dilatancy laws measured by this method exhibit strong and non-trivial system size dependences, which results from a combination of the material constitutive behaviour and wall effects. We compare two different non-local models, namely the KEP and the EV models, which are able to rationalise these wall effects.

Interestingly, the KEP and EV models arise from radically different analyses of the mechanisms underpinning non-local effects. On one hand, the KEP model is developed by considering the non-local dynamic of the system, namely the stress propagation through the contact network. On the other hand, the EV model is developed by considering the non-local kinematics of the system, namely the existence of structures of grains rotating in a correlated fashion and their contribution to the momentum transfer. The fact that both models are able to capture the long-range wall perturbations suggests that force networks and vorticity may be intimately related in granular flows. Establishing such a connection constitutes a promising research avenue to further understand non-local behaviours.

The strength of the KEP model is its ability to capture many non-trivial behaviours of dense granular flows in geometries with a stress gradient. However, it is

comparatively weaker in predicting wall perturbations, given that it then critically relies on a parameter, the fluidity at the wall. To date, there is no prediction of this parameter, which must be determined empirically. Then, the KEP correctly captures the shear increase measured close to the walls. This increase is associated with a decrease of the viscosity which, in the KEP framework, arises from an increase of the number of rearrangements. One could expect that a local increase of the shear rate and of the number of rearrangements should lead to an increase of the velocity fluctuations. However, we observe the opposite trend in our simulation results.

The EV model involves the length scale associated with the vorticity. When approaching the walls, due to the lack of space, the largest possible vortex becomes smaller and smaller. This trend was shown by measuring the vorticity length scale from the local velocity fluctuations and the local vorticity, see (5.9). Using the EV model, we can introduce this length scale in the local constitutive friction law. This predicts the correct shear rate profiles and is also consistent with the decrease of the velocity fluctuations observed near the walls.

This study suggests that the vorticity length scale can be a key parameter to further understand the non-local behaviour of grains within dense granular flows. This length scale was found to exhibits a striking correlation with the material viscosity, and to significantly vary in the large zone affected by the walls. The EV model provides the rationale between the material viscosity and its vorticity length scale. Finding a link between the cooperativity length scale of the KEP and this vorticity length scale is a promising question.

Similarly, the vorticity analysis developed here for dry granular flows could help further understand non-local effects in other particulate fluids such as such as suspensions (Bonnoit *et al.* 2010*a*,*b*; Nordstrom, Gollub & Durian 2011), flowing blood cells (Freund 2014), foams (Sexton, Möbius & Hutzler 2011; Hagans & Feitosa 2013) and emulsions (Goyon *et al.* 2008).

Acknowledgements

This work was supported by ANR JCJC SIMI 9 and by the Labex MEC ANR-11-LABX-0092 and A*MIDEX ANR-11-IDEX-0001-02.

Appendix A. Discrete element simulation

Dense granular flows are simulated using discrete element method, such as introduced by Cundall & Strack (1979). The motion of each grain, both translation and rotation, is integrated over small time steps dt using a second-order predictor–corrector scheme. The acceleration and angular acceleration of each grain is evaluated at each time step as a function of the force and momentum balance, including contact forces between pairs of grains. The contact forces involve a normal elastic repulsion F^{ela}. A small overlap between two grains i and j is possible, $\delta_{ij}^n = \|\boldsymbol{X}_j - \boldsymbol{X}_i\| - (R_i + R_j)$, with $\boldsymbol{X}$ denoting the position of the grain centre and R its radius.

The elastic force that grain i experiences is then proportional to that overlap, $\boldsymbol{F}_{ij}^{ela} = ER_{ij}\delta_{ij}^n \boldsymbol{n}_{ij}$, where $\boldsymbol{n}_{ij} = (\boldsymbol{X}_j - \boldsymbol{X}_i)/(\|\boldsymbol{X}_j - \boldsymbol{X}_i\|)$ is the unit vector normal to the surface of grain i at the contact point, $R_{ij} = (R_i R_j)/(R_i + R_j)$ is the effective radius of the contact and E is an elastic constant of the order of Young's modulus of the grains. Note that the linear Hookean elastic model chosen here is consistent with the elastic contact between two two-dimensional disks (or two cylinders). Hertzian nonlinear elasticity would represent the elastic force between two spheres. The force would then

be $\boldsymbol{F}_{ij}^{ela} = ER_{ij}^2(\delta_{ij}^n/R_ij)^{3/2}\boldsymbol{n}_{ij}$. We consider here rather stiff grains, with small elastic deformations. The typical overlap δ^n is of the order of $\kappa = \sigma_w/E = 10^{-3}$. Then, both the Hertzian and Hookean models are equivalent at the first order.

Normal collisions between two grains dissipate energy. This is represented by a viscous-like normal force $\boldsymbol{F}_{ij}^{vis}$, proportional to the grains relative normal velocity, $\boldsymbol{F}_{ij}^{vis} = -\zeta\|\boldsymbol{V}_j - \boldsymbol{V}_i\|\boldsymbol{n}_{ij}$. The coefficient ζ is related to Newton's coefficient of restitution e, the ratio of post- to pre-impact relative velocities in a binary collision: $\zeta = \sqrt{m_{ij}ER_{ij}}(-2\log(e)/\sqrt{\pi^2 + \log(e)^2})$, with $m_{ij} = (m_i * m_j)/(m_i + m_j)$ the effective mass of the two colliding grains.

Grains are frictional, and a friction force $\boldsymbol{F}^{fri}$ is introduced, tangential to the contact. Grains may deform elastically in the tangent direction. The tangential force evolution, $\dot{F}^{fri}$ is driven by the tangential deformation evolution, $\dot{F}^{fri} = \Delta V_{ij}^t \mathrm{d}t\, ER_{ij}$, with ΔV_{ij}^t denoting the relative velocity at the contact point, including grain translation and rotation. This tangential elastic force is limited by a Coulomb criterion involving the grain-to-grain coefficient of friction μ_g. If $\|F^{fri}\| = \mu_g\|F^{ela}\|$, the grains slide and $\|\dot{F}^{fri}\|$ can only decrease. Rolling resistance and twist torque, which could be introduced as in Rognon, Einav & Gay (2010), are not included here. The friction forces are then the only component of the contact interaction that induces torque and grain rotation.

Appendix B. Averaging method

In this paper, various quantities are presented in the form of a profile in the y direction, averaged in time. The method of averaging consists of considering a series of snapshots, typically 100. For each snapshot, the system is divided into slices of size $d/10$. The properties of each grain, such as its velocity, are collected in each slice and weighted by the surface of the grains that belong to the slice, w_i^s. The average velocity in a slice at the position y_s is thus $\boldsymbol{v}(y_s) = \sum_i \boldsymbol{V}_i w_i^s / \sum_i w_i^s$, where the sum runs over all the grains. The solid fraction in that slice is $\langle\phi(y_s)\rangle = \sum_i w_i^s/(0.1dL)$. The final time-averaged profile is obtained by averaging all these instantaneous profiles.

The time-averaged velocity gradient profile, $\dot{\gamma}(y_s)$, can be deduced by differentiating the velocity profile obtained with the method just described. However, this differentiation induces a large level of noise. We preferred to evaluate, for each grain at each time step, the local velocity gradient tensor $\boldsymbol{F}_{\alpha\beta}$ following the method introduced in Marmottant *et al.* (2008):

$$\boldsymbol{F}_{\alpha\beta} = \langle \boldsymbol{l}_{ij} \otimes \boldsymbol{l}_{ij}\rangle^{-1} \cdot \langle \boldsymbol{l}_{ij} \otimes \boldsymbol{V}_{ij}\rangle. \tag{B 1}$$

The symbols $\cdot$ and $\otimes$ denote the tensor product and the outer product, respectively. The symbol $\langle\cdot\rangle$ represents the average of pairs of neighbouring grains i and j, with a centre-to-centre vector $\boldsymbol{l}_{ij}$ and a relative translation velocity $\boldsymbol{V}_{ij} = \boldsymbol{V}_j - \boldsymbol{V}_i$ (see figure 13). Note that these neighbouring grains may or may not be contacting. A cutoff distance of $1.5d$ was chosen to ensure that the averaging is performed on a zone as small as possible, with enough neighbours to evaluate the velocity gradient. Different values of cutoff were tested with no significant change in the results. The velocity gradient profile $\dot{\gamma}(y_s)$ is then obtained by averaging the relevant component of the tensor $\boldsymbol{F}$ with the slice method described above.

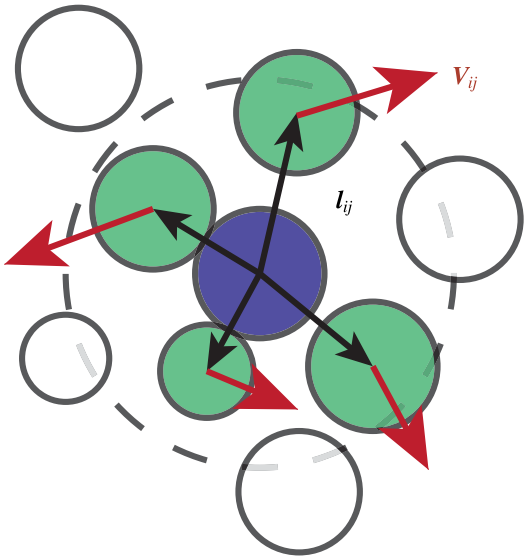


FIGURE 13. (Colour online) Local velocity gradient measurement. The local velocity gradient tensor can be estimated for each grain by considering the neighbouring grains, their relative position and relative velocity according to (B 1). Here, the velocity gradient associated with the dark central grain (purple online) involves the lighter grains (green online), but excludes the white grains, which are further away than the cutoff distance represented by the dashed circle.

REFERENCES

ABEDI, S. & RECHENMACHER, A. 2011 Vortex structures inside shear bands in sands. In *Multiscale and Multiphysics Processes in Geomechanics*, pp. 21–24. Springer.

ABEDI, S., RECHENMACHER, A. L. & ORLANDO, A. D. 2012 Vortex formation and dissolution in sheared sands. *Granul. Matt.* **14** (6), 695–705.

ANDREOTTI, B. 2007 A mean-field model for the rheology and the dynamical phase transitions in the flow of granular matter. *Europhys. Lett.* **79** (3), 34001.

ANDREOTTI, B., FORTERRE, Y. & POULIQUEN, O. 2013 *Granular Media: Between Fluid and Solid*. Cambridge University Press.

AZÉMA, E. & RADJAÏ, F. 2014 Internal structure of inertial granular flows. *Phys. Rev. Lett.* **112** (7), 078001.

BEHRINGER, R. P., DANIELS, K. E., MAJMUDAR, T. S. & SPERL, M. 2008 Fluctuations, correlations and transitions in granular materials: statistical mechanics for a non-conventional system. *Phil. Trans. R. Soc. Lond.* A **366** (1865), 493–504.

BLAIR, D. L. & KUDROLLI, A. 2001 Velocity correlations in dense granular gases. *Phys. Rev.* E **64** (5), 050301.

BOCQUET, L., COLIN, A. & AJDARI, A. 2009 Kinetic theory of plastic flow in soft glassy materials. *Phys. Rev. Lett.* **103** (3), 36001.

BONNOIT, C., DARNIGE, T., CLEMENT, E. & LINDNER, A. 2010*a* Inclined plane rheometry of a dense granular suspension. *J. Rheol.* **54**, 65–79.

BONNOIT, C., LANUZA, J., LINDNER, A. & CLEMENT, E. 2010*b* Mesoscopic length scale controls the rheology of dense suspensions. *Phys. Rev. Lett.* **105** (10), 108302.

BOUZID, M., TRULSSON, M., CLAUDIN, P., CLÉMENT, E. & ANDREOTTI, B. 2013 Nonlocal rheology of granular flows across yield conditions. *Phys. Rev. Lett.* **111** (23), 238301.

BRITO, C. & WYART, M. 2007 Heterogeneous dynamics, marginal stability and soft modes in hard sphere glasses. *J. Stat. Mech.* **2007** (8), L08003.

DA CRUZ, F., CHEVOIR, F., ROUX, J. N. & IORDANOFF, I. 2004 Macroscopic friction of dry granular materials. In *Transient Processes in Tribology* (ed. G. Dalmaz, A. A. Lubrecht, D. Dowson & M. Priest), pp. 53–61. Elsevier.

DA CRUZ, F., EMAM, S., PROCHNOW, M., ROUX, J.-N. & CHEVOIR, F. 2005 Rheophysics of dense granular materials: discrete simulation of plane shear flows. *Phys. Rev.* E **72**, 021309.

CUNDALL, P. A. & STRACK, O. D. L. 1979 A discrete numerical model for granular assemblies. *Géotech.* **29**, 47–65.

FORTERRE, Y. & POULIQUEN, O. 2008 Flows of dense granular media. *Annu. Rev. Fluid Mech.* **40**, 1–24.

FREUND, J. B. 2014 Numerical simulation of flowing blood cells. *Annu. Rev. Fluid Mech.* **46**, 67–95.

GDR MIDI 2004 On dense granular flows. *Eur. Phys. J.* E **14**, 341–365.

GOUJON, C., THOMAS, N. & DALLOZ-DUBRUJEAUD, B. 2003 Monodisperse dry grain flows on inclined planes: role of roughness. *Eur. Phys. J.* E **11**, 147–157.

GOYON, J., COLIN, A., OVARLEZ, G., AJDARI, A. & BOCQUET, L. 2008 Spatial cooperativity in soft glassy flows. *Nature* **454** (7200), 84–87.

HAGANS, N. & FEITOSA, K. 2013 Extensional rheology of a two dimensional foam. *Bull. Am. Phys. Soc.* **58**, 1198.

HARTLEY, R. R. & BEHRINGER, R. P. 2003 Logarithmic rate dependence of force networks in sheared granular materials. *Nature* **421** (6926), 928–931.

JOP, P., FORTERRE, Y. & POULIQUEN, O. 2006 A constitutive law for dense granular flows. *Nature* **441**, 727–730.

JOP, P., MANSARD, V., CHAUDHURI, P., BOCQUET, L. & COLIN, A. 2012 Microscale rheology of a soft glassy material close to yielding. *Phys. Rev. Lett.* **108**, 148301.

KAMRIN, K. & KOVAL, G. 2012 Nonlocal constitutive relation for steady granular flow. *Phys. Rev. Lett.* **108** (17), 178301.

LECHENAULT, F., DAUCHOT, O., BIROLI, G. & BOUCHAUD, J.-P. 2008 Critical scaling and heterogeneous superdiffusion across the jamming/rigidity transition of a granular glass. *Europhys. Lett.* **83** (4), 46003.

LIU, A. J. & NAGEL, S. R. 2010 The jamming transition and the marginally jammed solid. *Annu. Rev. Condens. Matter Phys.* **1** (1), 347–369.

MAJMUDAR, T. S. & BEHRINGER, R. P. 2005 Contact force measurements and stress-induced anisotropy in granular materials. *Nature* **435** (7045), 1079–1082.

MANSARD, V., COLIN, A., CHAUDHURI, P. & BOCQUET, L. 2013 A molecular dynamics study of non-local effects in the flow of soft jammed particles. *Soft Matt.* **9** (31), 7489–7500.

MARMOTTANT, P., RAUFASTE, C. & GRANER, F. 2008 Discrete rearranging disordered patterns, part II: 2D plasticity, elasticity and flow of a foam. *Phys. Rev.* E **25** (4), 371–384.

MILLER, T. 2014, The kinematics of dense granular materials under indefinite plane-shear. PhD thesis, School of Civil Engineering, The University of Sydney.

MILLER, T., ROGNON, P., METZGER, B. & EINAV, I. 2013 Eddy viscosity in dense granular flows. *Phys. Rev. Lett.* **111** (5), 058002.

MOHAN, L. S., RAO, K. K. & NOTT, P. R. 2002 Frictional Cosserat model for slow shearing of granular materials. *J. Fluid Mech.* **457**, 377–409.

MUETH, D. M. 2003 Measurements of particle dynamics in slow, dense granular couette flow. *Phys. Rev.* E **67** (1), 011304.

NORDSTROM, K. N., GOLLUB, J. P. & DURIAN, D. J. 2011 Dynamical heterogeneity in soft-particle suspensions under shear. *Phys. Rev.* E **84** (2), 021403.

POULIQUEN, O. 2004 Velocity correlation in dense granular flows. *Phys. Rev. Lett.* **93**, 248001.

POULIQUEN, O. & FORTERRE, Y. 2001 Slow dense granular flows as a self-induced process. *Adv. Complex Syst.* **4**, 441–450.

POULIQUEN, O. & FORTERRE, Y. 2009 A non-local rheology for dense granular flows. *Phil. Trans. R. Soc. Lond.* A **367** (1909), 5091–5107.

RADJAÏ, F. & ROUX, S. 2002 Turbulentlike fluctuations in quasistatic flow of granular media. *Phys. Rev. Lett.* **89** (6), 064302.

RECHENMACHER, A. L. & ABEDI, S. 2011 Length scales for nonaffine deformation in localized, granular shear. In *Advances in Bifurcation and Degradation in Geomaterials*, pp. 59–65. Springer.

RICHEFEU, V., COMBE, G. & VIGGIANI, G. 2012 An experimental assessment of displacement fluctuations in a 2d granular material subjected to shear. *Géotech. Lett.* **2** (July–September), 113–118.

ROGNON, P., EINAV, I. & GAY, C. 2010 Internal relaxation time in immersed particulate materials. *Phys. Rev.* E **81**, 061304.

ROGNON, P. G., ROUX, J. N., NAAÏM, M. & CHEVOIR, F. 2007 Dense flows of bidisperse assemblies of disks down an inclined plane. *Phys. Fluids* **19**, 058101.

ROGNON, P. G., ROUX, J. N., NAAIM, M. & CHEVOIR, F. 2008 Dense flows of cohesive granular materials. *J. Fluid Mech.* **596**, 21–47.

ROGNON, P. G., ROUX, J.-N., WOLF, D., NAAIM, M. & CHEVOIR, F. 2006 Rheophysics of cohesive granular materials. *Europhys. Lett.* **74**, 644–650.

SEXTON, M. B., MÖBIUS, M. E. & HUTZLER, S. 2011 Bubble dynamics and rheology in sheared two-dimensional foams. *Soft Matt.* **7** (23), 11252–11258.

SHOJAAEE, Z., BRENDEL, L., TÖRÖK, J. & WOLF, D. E. 2012*a* Shear flow of dense granular materials near smooth walls. II. Block formation and suppression of slip by rolling friction. *Phys. Rev.* E **86** (1), 011302.

SHOJAAEE, Z., ROUX, J. N., CHEVOIR, F. & WOLF, D. E. 2012*b* Shear flow of dense granular materials near smooth walls. I. Shear localization and constitutive laws in the boundary region. *Phys. Rev.* E **86** (1), 011301.

STARON, L. 2008 Correlated motion in the bulk of dense granular flows. *Phys. Rev.* E **77** (5), 051304.

STARON, L., LAGRÉE, P.-Y., JOSSERAND, C. & LHUILLIER, D. 2010 Flow and jamming of a two-dimensional granular bed: toward a nonlocal rheology? *Phys. Fluids* **22**, 113303.

TORDESILLAS, A., LIN, Q., ZHANG, J., BEHRINGER, R. P. & SHI, J. 2011 Structural stability and jamming of self-organized cluster conformations in dense granular materials. *J. Mech. Phys. Solids* **59** (2), 265–296.

TORDESILLAS, A., ZHANG, J. & BEHRINGER, R. 2009 Buckling force chains in dense granular assemblies: physical and numerical experiments. *Geomech. Geoengin.* **4** (1), 3–16.

Des particules qui se la coulent douce...

Bloen Metzger (bloen.metzger@polytech.univ-mrs.fr) et Élisabeth Guazzelli
IUSTI, UMR CNRS 6595, Technopôle de Château-Gombert, 13453 Marseille Cedex 13

Formation d'un tore, déstabilisation en gouttelettes, puis cascade auto-similaire : la sédimentation d'un nuage de particules dans un fluide visqueux est spectaculaire. Comment un système conceptuellement aussi simple peut-il développer une telle richesse de comportements ? La longue portée des interactions hydrodynamiques entre particules et le comportement collectif qu'elles entraînent (du type problème à N-corps) sont les composantes essentielles pour comprendre cette dynamique.

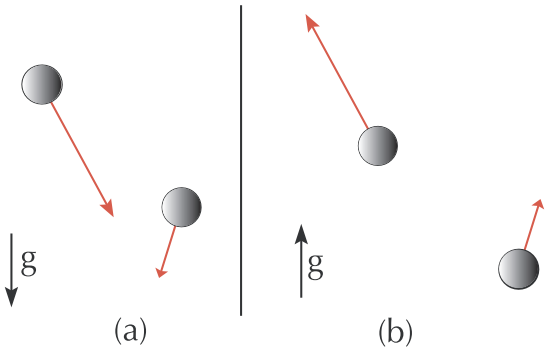
Lorsque de petites particules sédimentent (tombent sous l'effet de la gravité) à faible vitesse dans un fluide initialement au repos, elles génèrent des perturbations d'écoulement dont la décroissance spatiale est très lente. Les particules s'influencent mutuellement *via* le fluide. Chaque particule voit ainsi sa trajectoire modifiée par rapport à celle qu'elle aurait si elle tombait de façon isolée.

Ces interactions hydrodynamiques, propres aux écoulements de Stokes (encadré, p. 9), sont à l'origine de phénomènes complexes d'un grand intérêt. Cette situation préfigure de nombreux phénomènes naturels comme le comportement de globules rouges, la sédimentation d'alluvions ou, pour citer une expérience quotidienne, la chute des grains de marc dans votre tasse de café. Ce système donne surtout une occasion quasiment unique en physique classique d'étudier expérimentalement le problème à N-corps(1). En effet, à l'instar de l'interaction gravitationnelle qui régit le mouvement des planètes, les interactions hydrodynamiques entre particules sont de type longue portée.

Nous commencerons par décrire la dynamique de sédimentation d'une, de deux, puis de trois particules. Au passage de deux à trois particules, on aborde le problème à N-corps ; apparaissent alors certains comportements chaotiques. La deuxième partie de l'article est consacrée à la sédimentation d'un « nuage de particules ». Des films sont disponibles sur le lien de la référence [1].

1, 2, 3 particules

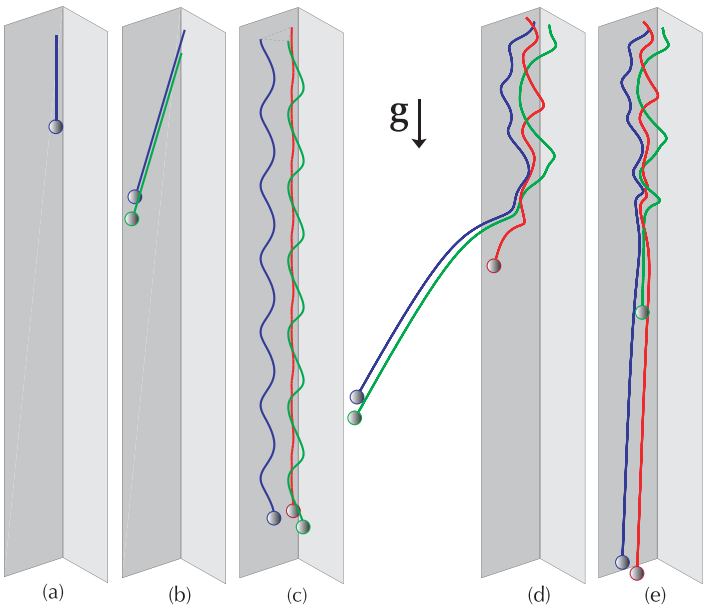
Le problème de la chute d'une particule sphérique dans un fluide visqueux sous l'effet de la gravité a été complètement résolu par Stokes en 1851 [2]. La perturbation d'écoulement induite au sein du fluide par la chute de la sphère possède une propriété remarquable : son amplitude décroît très lentement, comme l'inverse de la distance au centre de la sphère (encadré, p. 9). On verra que cette propriété est essentielle pour comprendre la dynamique d'évolution d'un ensemble de particules.



1. Deux sphères identiques tombent lentement dans un fluide visqueux sous l'effet de leur propre poids : la linéarité des équations de Stokes permet de montrer que les vitesses des deux sphères sont nécessairement les mêmes.
a) Supposons que les deux sphères ont des vitesses différentes : la sphère située à l'arrière (par rapport au sens du mouvement) rattrape la première sphère et les deux sphères se rapprochent. b) Inversons le sens de la pesanteur **g**. En utilisant la propriété de linéarité, l'inversion du sens des forces entraîne l'inversion du sens des vitesses. Cette fois, la sphère située à l'avant se déplace plus rapidement et les deux sphères s'éloignent l'une de l'autre.
Les deux situations sont pourtant formellement identiques, la dynamique doit donc nécessairement être la même. Les vitesses des deux sphères sont donc identiques.

Imaginons maintenant la sédimentation d'un doublet de particules identiques. Le mouvement du fluide induit par le déplacement de chacune des sphères influence la trajectoire de l'autre. La vitesse de chaque sphère peut ainsi être évaluée en ajoutant la vitesse propre de sédimentation d'une sphère isolée à celle induite dans le fluide par le mouvement de l'autre. La vitesse du doublet de particules a donc un module supérieur à la vitesse de sédimentation d'une particule isolée (fig. 2 – a et b). La linéarité des équations de Stokes permet de montrer que les vitesses résultantes des deux sphères sont nécessairement identiques (fig. 1). Les deux particules sédimentent donc sans mouvement relatif l'une par rapport à l'autre.

La situation est très différente pour trois particules [3]. Certaines configurations initiales très particulières produisent un mouvement périodique (fig. 2c) : lorsque, par exemple, les trois particules sont initialement positionnées aux sommets d'un triangle isocèle horizontal. Dans



2. Simulations numériques : sédimentation d'une (a), de deux (b) ou de trois (c, d, e) particules dans un fluide visqueux.
c) Initialement positionnées aux sommets d'un triangle isocèle horizontal, les particules suivent un mouvement périodique.
d) Initialement distribuées aléatoirement, les particules passent par une phase d'interaction à trois, puis un doublet (particules bleue et verte) « s'échappe » et laisse la particule rouge isolée.
e) Même configuration initiale que pour d, sauf pour la particule bleue dont la position initiale a été légèrement modifiée. Si l'évolution aux temps courts est similaire, l'évolution aux temps longs, par contre, est très différente d'une configuration à l'autre. Cette fois, le doublet rouge et bleu s'échappe et laisse la particule verte isolée. Cette extrême sensibilité aux conditions initiales est caractéristique des systèmes chaotiques.

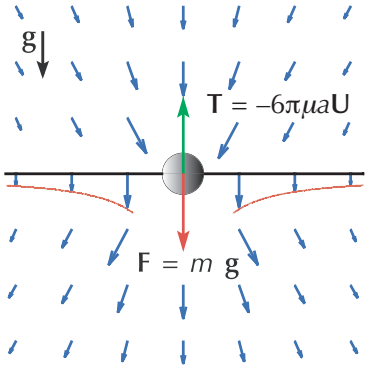
les autres cas, la dynamique d'évolution est chaotique (fig. 2 – d et e). On distingue une phase d'interaction à trois particules, pendant laquelle la position relative des particules change totalement. Ensuite, un doublet « s'échappe » et laisse en arrière la troisième particule. Le doublet sédimente plus rapidement que la particule isolée, car chacune des particules du doublet est entraînée par la perturbation d'écoulement générée par l'autre particule du doublet. La nature chaotique de la configuration à trois particules est bien illustrée dans la figure 2 (d et e) par la sensibilité du système aux conditions initiales.

Les équations de Stokes qui déterminent le mouvement de ces particules sont linéaires et instantanées. Elles sont par conséquent réversibles en temps. Comment se fait-il alors que les particules présentent une dynamique d'évolution si complexe ? Pourquoi une telle sensibilité aux conditions initiales ? Cette dynamique chaotique apparaît dès que le nombre de particules est supérieur à deux. Elle a pour origine le couplage entre l'écoulement du fluide et la distribution spatiale des particules. À un instant donné, la distribution spatiale des particules détermine complètement l'écoulement, mais l'écoulement produit entraîne les particules et donc modifie aussitôt cette distribution. Cette perpétuelle rétroaction entre écoulement et microstructure donne lieu à une dynamique temporelle fortement non linéaire, qui est à l'origine du comportement chaotique observé.

>>>

Chute d'une petite particule sphérique dans un fluide visqueux sous l'effet de la gravité.

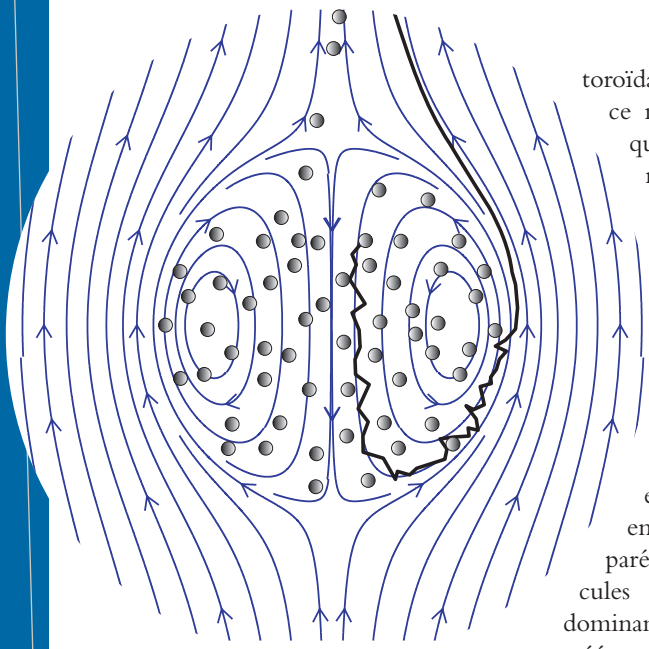
Lorsqu'une petite particule de rayon a tombe dans un fluide visqueux de viscosité μ, la force de traînée $\mathbf{T} = -6\pi\mu a\mathbf{U}$ exercée par le fluide sur la particule compense exactement la force de gravité $\mathbf{F}$, de sorte que la vitesse de sédimentation de la particule $\mathbf{U} = \mathbf{F}/6\pi\mu a$ est constante. L'écoulement $\mathbf{u}$ induit dans le fluide est solution des équations de Stokes (1), où p est le champ de pression et δ la fonction de Dirac qui décrit la distribution du champ de forces au sein du fluide, si on assimile la particule à une masse ponctuelle. Ces équations, valables si l'écoulement est suffisamment lent et/ou la viscosité du fluide suffisamment grande et/ou la taille de la particule suffisamment petite, sont linéaires ; elles sont donc aussi réversibles (pour plus de détails, consultez la référence [1]). La solution analytique de cet écoulement est connue (2) ; elle correspond à la solution de Green des équations de Stokes.



$$\nabla.\mathbf{u} = 0 \qquad (1)$$
$$\nabla p - \mu\,\Delta\mathbf{u} = \rho\,\delta(r)$$

$$\mathbf{u}(r) = \frac{\mathbf{F}}{8\pi\mu}\left(\frac{\mathbf{I}}{r} + \frac{\mathbf{r}\otimes\mathbf{r}}{r^3}\right) \qquad (2)$$

Sur la figure, les flèches bleues représentent le champ de vitesse induit dans le fluide par la chute de la particule, et la courbe rouge indique sa propriété la plus remarquable, qui est la lente décroissance (en 1/r) de son amplitude.



3. Simulation numérique de l'écoulement produit (dans le référentiel du nuage) **par un nuage de particules.** Le mouvement général est celui d'une recirculation toroïdale d'axe vertical. Les fluctuations dues au caractère discret et aléatoire de la distribution des particules à l'intérieur du nuage conduisent certaines particules à traverser l'interface entre le nuage et le fluide externe. Ces particules, entraînées par le fluide externe, forment un fin filet à l'arrière du nuage.

>>>

Nuage de particules

Nous allons maintenant examiner le mouvement d'un grand nombre de particules soumises à la gravité. Les particules sont initialement distribuées aléatoirement à l'intérieur d'un volume prescrit du fluide, de sorte qu'elles forment ce que l'on appellera dans la suite un « nuage de particules ».

Le phénomène le plus surprenant, et certainement le plus spectaculaire, est la dynamique collective des particules pendant leur chute (fig. 3). Le mouvement général apparent est celui d'une recirculation toroïdale d'axe vertical. Remarquez que ce mouvement collectif résulte uniquement des interactions hydrodynamiques entre particules.

Un modèle simple pour décrire ces interactions est de considérer que chaque particule produit dans le fluide ambiant une perturbation d'écoulement équivalente à celle que produirait à sa place une particule ponctuelle[2] (encadré, p. 9). Cette approximation est naturelle en milieu dilué, puisque la distance entre les particules est grande comparée à leur taille typique ; les particules ne ressentent alors que l'ordre dominant des perturbations d'écoulement créées par leurs voisines (en $1/r$).

La linéarité des équations de Stokes peut nous aider à comprendre la dynamique collective des particules. Chacune des particules à l'intérieur du nuage est *advectée* par la somme des perturbations d'écoulement induites par la chute de toutes les autres particules du nuage. Comme deux particules voisines voient quasiment la même distribution de particules autour d'elles, elles ont des vitesses presque identiques et donc des trajectoires fortement similaires ; au lieu de se disperser rapidement dans le fluide ambiant, les particules du nuage forment une entité « cohésive » qui perdure pendant un temps très long.

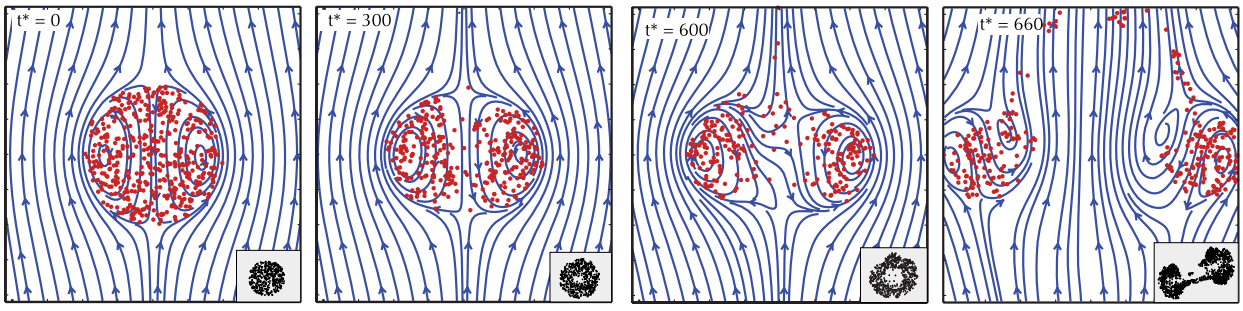
Ce mouvement de recirculation toroïdal est aussi observé lorsqu'une goutte de fluide pur sédimente dans un fluide plus léger [4]. La suspension peut être assimilée à un fluide effectif plus dense que le fluide ambiant, mais cette analogie a des limites ; les suspensions possèdent des caractéristiques intrinsèques qui ne peuvent être traduites dans un modèle de type milieu effectif.

Le mécanisme de perte de particules illustre bien ces différences. Certaines particules s'échappent spontanément du nuage (fig. 3). Le caractère multiple des interactions et le réarrangement permanent des particules au sein du nuage génèrent d'importantes fluctuations (comme l'illustre schématiquement la ligne brisée de la figure 3). Certaines particules traversent spontanément l'interface entre le nuage et le fluide externe, et sont alors entraînées par ce dernier. Malgré la nature réversible des équations de Stokes, on observe un mécanisme qui génère un transport diffusif irréversible des particules vers l'extérieur du nuage.

Les particules qui « s'échappent » viennent de la couche externe du mouvement toroïdal de recirculation du nuage ; leur départ crée un déficit de particules au niveau de son axe vertical de symétrie (fig. 4). Le nuage initialement sphérique évolue donc lentement vers un tore.

Le tore continue de perdre des particules et son rapport d'aspect (rapport de sa dimension horizontale sur sa dimension verticale) augmente. Au-delà d'un rapport d'aspect critique, la topologie de l'écoulement change brutalement : le fluide externe passe alors au centre de l'anneau formé par le nuage au lieu de le contourner (fig. 4). À cet instant précis, le tore se fragmente en plusieurs gouttelettes. Chaque gouttelette forme un tore plus petit qui se déstabilise à son tour, formant ainsi une cascade de gouttelettes de particules (fig. 5).

Cette déstabilisation nous donne l'occasion de revenir sur la notion de rétroaction entre microstructure et écoulement. Juste avant la déstabilisation, la distribution spatiale des particules est telle que l'écoulement du fluide externe contourne le nuage de particules : le tore est stable (fig. 4). Au-delà du rapport d'aspect critique, *i.e.* pour une



4. Simulation numérique de l'écoulement (dans le référentiel du nuage) **généré par un nuage comportant initialement 3000 particules.** Le nuage, initialement sphérique (t* = 0), évolue progressivement vers un tore (t* = 300). Lorsque le fluide externe passe au centre du nuage (t* › 600), il y a déstabilisation en deux gouttelettes similaires au nuage initial. Les inserts représentent les vues de dessous correspondantes. Le temps est adimensionné par le temps mis par le nuage pour parcourir son rayon : $t^* = t(R/V_n)$, où R et V_n sont respectivement le rayon et la vitesse de sédimentation du nuage à t*=0.

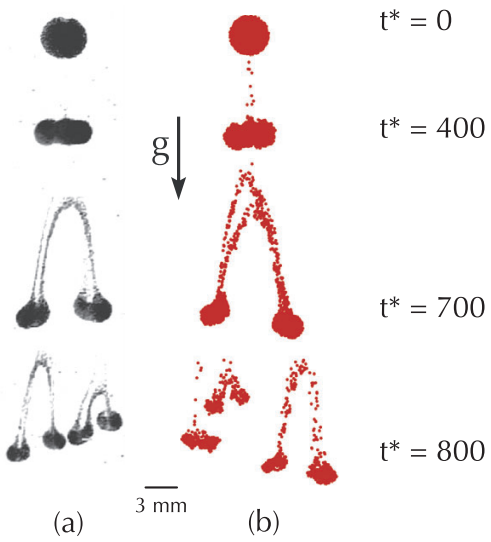
microstructure légèrement différente, le fluide externe passe au centre de l'anneau formé par les particules et le sens de recirculation est alors nécessairement inversé. Ce changement topologique de l'écoulement rend le tore instable : il se brise en gouttelettes, et la distribution spatiale des particules est ainsi totalement modifiée.

Conclusion

Malgré sa simplicité conceptuelle, la sédimentation d'un nuage de particules dans un fluide visqueux présente une grande richesse de comportements. Dès que le nombre de particules est supérieur à deux, le système devient chaotique. Les trajectoires des particules sont tortueuses et extrêmement sensibles aux conditions initiales. On se retrouve dans la situation du problème à trois corps. La sédimentation donne une occasion quasiment unique d'étudier expérimentalement ce problème, considéré comme l'un des plus difficiles des mathématiques. Pour approfondir ce point, le lecteur peut se reporter à la référence [3].

Pour un nombre plus élevé de particules, l'évolution est plus complexe. Le « nuage de particules » évolue d'abord vers un tore, qui se déstabilise ensuite en gouttelettes plus petites. Les équations qui gouvernent le mouvement des particules sont linéaires et donc réversibles en temps. On observe pourtant un certain nombre de phénomènes irréversibles comme la perte de particules, qui sont déterminants dans l'évolution subséquente du nuage. Un modèle numérique très simple, basé sur une approximation de particules ponctuelles est suffisant pour capturer l'évolution du nuage jusque dans ses détails (fig. 5). Cette étude montre à quel point les interactions hydrodynamiques dominent la dynamique de ces systèmes.

Un autre phénomène saisissant est le mouvement général de recirculation toroïdale observé par les particules. Cette dynamique collective, qui naît de la lente décroissance des interactions hydrodynamiques, peut paraître assez singulière. Elle est en fait d'une importance majeure dans un très grand nombre de systèmes moins académiques. On observe, par exemple, des « tourbillons » dans les suspensions de particules sphériques [6] ; des « amas », qui s'organisent ensuite en colonnes, caractérisent la sédimentation des suspensions de fibres [7]. Ces structures, qui naissent des effets collectifs et qui se développent en général sur des échelles bien supérieures à la taille typique des particules, ont une influence profonde sur la dynamique de ces systèmes. Il est donc particulièrement important de les étudier. ■



5. Images successives de la chute d'un nuage de particules tombant dans un liquide visqueux.
a) Expérience de laboratoire réalisée à l'aide de particules de verre de diamètre 100 µm dans une cuve remplie d'huile silicone 1000 fois plus visqueuse que l'eau. b) Simulation numérique [5]. Des films sont en visualisation et téléchargement libre sur le lien de la référence [1].

(1) Le problème à N-corps consiste à prédire la dynamique d'un grand nombre de corps ou particules (atomes, électrons…), qui interagissent *via* des interactions souvent fortes et à longue portée. En physique classique, on le rencontre en astronomie (étude des trajectoires de N corps célestes en interaction gravitationnelle). On le rencontre aussi en physique des solides et dans d'autres systèmes quantiques.

(2) Cette approximation est équivalente à celle effectuée en astronomie : remplacer deux solides à répartition sphérique de masse par deux masses ponctuelles coïncidant avec leurs centres respectifs.

Références

1 • http://iusti.polytech.univ-mrs.fr/~metzger/CloudSedimentation.html

2 • É. Guyon, J.P. Hulin et L. Petit, *Hydrodynamique physique*, Savoirs Actuels, EDP Sciences/CNRS Éditions (1982).

3 • I.M. Jánosi, T. Tél, D.E. Wolf, J.A.C. Gallas, "Chaotic particle dynamics in viscous flows: The three-particle Stokeslet problem", *Phys. Rev. E* **56** (1997) 2858–2868.

4 • J.S. Hadamard, « Mouvement permanent lent d'une sphère liquide et visqueuse dans un liquide visqueux », *C. R. Acad. Sci. (Paris)* **152** (1911) 1735–1738.

5 • B. Metzger, M.L. Nicolas et É. Guazzelli, "Falling clouds of particles in viscous fluids", *J. Fluid Mech.*, **580** (2007) 283–301.

6 • É. Guazzelli, "Evolution of particle-velocity correlations in sedimentation", *Phys. Fluids*, **13** (2001) 1537–1540.

7 • B. Metzger, J. E. Butler et É. Guazzelli, "Experimental investigation of the instability of a sedimenting suspension of fibres", *J. Fluid Mech.*, **575** (2007) 307-332.

J. Fluid Mech. (2010), *vol.* 648, *pp.* 351–362. © Cambridge University Press 2010
doi:10.1017/S0022112009993909

A cloud of rigid fibres sedimenting in a viscous fluid

JOONTAEK PARK[1], BLOEN METZGER[2]†, ÉLISABETH GUAZZELLI[2] AND JASON E. BUTLER[1]

[1]Department of Chemical Engineering, University of Florida, Gainesville, FL 32611, USA

[2]IUSTI-CNRS UMR 6596, Polytech-Marseille, Aix-Marseille Université (U1), Technopôle de Château-Gombert, 13453 Marseille cedex 13, France

(Received 2 October 2009; revised 7 December 2009; accepted 8 December 2009)

Experiments and numerical simulations have been performed to investigate the deformation and break-up of a cloud of rigid fibres falling under gravity through a viscous fluid in the absence of inertia and interfacial tension. The cloud of fibres is observed to evolve into a torus that subsequently becomes unstable and breaks up into secondary droplets which themselves deform into tori in a repeating cascade. This behaviour is similar to that of clouds of spherical particles, though the evolution of the cloud of fibres occurs more rapidly. The simulations, which use two different levels of approximation of the far-field hydrodynamic interactions, capture the evolution of the cloud and demonstrate that the coupling between the self-motion and hydrodynamically induced fluctuations are responsible for the faster break-up time of the cloud. The dynamics of the cloud are controlled by a single parameter which is related to the self-motion of the anisotropic particles. The experiments confirm these findings.

1. Introduction

The dispersion of swarms of particles occurs in natural processes of sedimentation of silt in rivers and on the continental shelf. The process has importance for the delivery of injected particles, such as catalysts, drugs and inoculated cells, into a bulk medium. Most of these natural phenomena or industrial applications involve anisotropic particles, but rod-like particles have received little attention as compared to spherical particles. In this paper, we consider the motion of a cloud of rigid fibres settling due to gravity in an otherwise pure liquid at low Reynolds number and in the absence of interfacial tension.

The deformation of clouds of spherical particles has been studied since Adachi, Kiriyama & Koshioka (1978) reported a complex evolution of the shape. A cloud having an initially spherical shape generally evolves into a torus that subsequently becomes unstable and breaks up into secondary droplets which deform themselves into tori in a repeating cascade. An extensive review has been presented by Machu *et al.* (2001). The cloud break-up was attributed to either inertia or to a perturbation on the shape of the initial cloud (Nitsche & Batchelor 1997; Schaflinger & Machu 1999; Machu *et al.* 2001; Bosse *et al.* 2005). Recent numerical simulations and experiments by Metzger, Nicolas & Guazzelli (2007) demonstrated that the break-up occurs even

† Email address for correspondence: bloen.metzger@polytech.univ-mrs.fr

in the complete absence of inertia and also without needing to perturb the initial shape.

Understanding the instability requires consideration of the discrete nature of the cloud of particles. Fluctuations arising from the multi-body character of the hydrodynamic interactions cause particles to depart from the closed toroidal circulation predicted by the continuum approach where the cloud is modelled as an effective medium of excess mass. Some of the particles may thus cross the cloud boundary and be carried into a downstream tail. Because the lost particles are those located in the toroidal circulation rim, this depletes the central region of the cloud and leads to the formation of a torus. The mechanism responsible for the further expansion of the torus remains unclear, but Metzger *et al.* (2007) described the break-up and showed a relationship with a change in the flow topology that occurs when the torus reaches a critical aspect ratio.

The present work investigates the deformation and break-up of a cloud of rigid fibres, focusing on the role of the particle anisotropy. Similar to clouds of spherical particles, we find that an initially spherical cloud of rigid fibres slowly evolves into a torus, which subsequently shatters into secondary droplets. However, the fluctuations in the velocities of the fibres originating from the particle anisotropy accelerates the break-up process as compared to clouds of spherical particles. We numerically identify the parameter that controls the break-up time and confirm it experimentally.

The simulations involved in this study are described in § 2. They have two different degrees of approximation for the far-field hydrodynamic interactions: the point-fibre, or 'fiblet' as we will designate it in the following, and slender-body dynamics. The former approximates the hydrodynamic interactions between fibres as those of point-particles and ignores short-range interactions (Mackaplow & Shaqfeh 1998; Saintillan, Shaqfeh & Darve 2006). The latter evaluates the long-range interaction at a higher level of approximation but, for simplicity, still does not consider the short-range interactions such as lubrication and excluded volume effects (Harlen, Sundararajakumar & Koch 1999; Butler & Shaqfeh 2002). The experiments are described in § 3 and compared with simulation results in § 4.

2. Simulation method

The initial clouds consist of N_0 rigid fibres, with length l and diameter d, distributed randomly in space and orientation inside a prescribed spherical volume of an unbounded fluid. The cloud settles under gravity through fluid that is Newtonian with viscosity μ. The fluid flow generated by the sedimenting particles satisfies the Stokes equations.

2.1. *Minimal description: the 'fiblet'*

This minimal model approximates the disturbance generated by fibres sedimenting in the fluid as that of point-particles. This approximation is sound for dilute suspensions where the distance between particles is large as compared to the length of the fibre, and the first-order term of the perturbation (Stokeslet) to the fluid velocity dominates. However, each particle rotates due to the velocity induced by the other sedimenting particles, and accordingly sediments through the fluid with a velocity that depends on its orientation.

Within this approximation, the translational velocity of particle α with position $\boldsymbol{r}_\alpha$ and orientation $\boldsymbol{p}_\alpha$ is the sum of its settling velocity $\boldsymbol{U}_s(\boldsymbol{p}_\alpha)$ when in isolation and

of the disturbance velocity $\boldsymbol{u}(\boldsymbol{r}_\alpha)$ generated by the other fibres and evaluated at the centre of mass:

$$\dot{\boldsymbol{r}}_\alpha = \boldsymbol{U}_s(\boldsymbol{p}_\alpha) + \boldsymbol{u}_\alpha(\boldsymbol{r}_\alpha). \tag{2.1}$$

The settling velocity in a pure fluid is the product of the particle mobility, which is taken from the leading order of slender-body theory (Batchelor 1970; Cox 1970), and the buoyancy force acting upon the particle

$$\boldsymbol{U}_s(\boldsymbol{p}_\alpha) = \frac{\ln(2A)F}{4\pi\mu l}\left(\boldsymbol{I} + \boldsymbol{p}_\alpha\boldsymbol{p}_\alpha\right)\cdot\boldsymbol{e}_z, \tag{2.2}$$

where $A = l/d$ is the fibre aspect ratio, $\boldsymbol{I}$ is the identity tensor and F is the magnitude of the buoyancy force that acts along the z direction as designated by the unit vector $\boldsymbol{e}_z$. The disturbance velocity is the sum of point-forces as derived in the Appendix:

$$\boldsymbol{u}_\alpha(\boldsymbol{r}_\alpha) = \frac{F}{8\pi\mu}\sum_{\beta\neq\alpha}^{N_0}\left(\frac{\boldsymbol{I}}{|\boldsymbol{r}|} + \frac{\boldsymbol{r}\boldsymbol{r}}{|\boldsymbol{r}|^3}\right)\cdot\boldsymbol{e}_z, \tag{2.3}$$

where $\boldsymbol{r} = \boldsymbol{r}_\beta - \boldsymbol{r}_\alpha$ and $|\boldsymbol{r}|$ is the scalar length between the centres of particles α and β.

The rotational velocity of the fibres, also derived in the Appendix, is influenced only by the disturbances caused by the sedimentation of other fibres in the suspension,

$$\dot{\boldsymbol{p}}_\alpha = \frac{F}{8\pi\mu l}\left(\boldsymbol{I} - \boldsymbol{p}_\alpha\boldsymbol{p}_\alpha\right)\cdot\sum_{\beta\neq\alpha}^{N_0}\left[\frac{\left(\boldsymbol{r}\cdot\boldsymbol{p}_\alpha\right)\boldsymbol{I} - \boldsymbol{p}_\alpha\boldsymbol{r} - \boldsymbol{r}\boldsymbol{p}_\alpha}{|\boldsymbol{r}|^3} + \frac{3\left(\boldsymbol{r}\cdot\boldsymbol{p}_\alpha\right)\boldsymbol{r}\boldsymbol{r}}{|\boldsymbol{r}|^5}\right]\cdot\boldsymbol{e}_z. \tag{2.4}$$

Equations (2.1)–(2.4) represent the minimal model, which is referred to as the fiblet model because it is based upon point-particle interactions and includes the important aspect of particle rotation.

The only difference between (2.1) and the equation given for the motion of a cloud of point-particles by Metzger *et al.* (2007) is in the self-term $\boldsymbol{U}_s(\boldsymbol{p}_\alpha)$. Metzger *et al.* (2007) ignored the self-term when calculating the dynamics of a cloud of point-particles since it does not affect the relative motion of identical point-forces within a cloud and thus does not alter the overall dynamics of the cloud. For clouds of fiblets, the self-term depends on the particle orientation and generates a relative motion between the particles; therefore, this term must be retained to give even a qualitatively accurate solution.

Because the correct scaling of the length and time scales is not known *a priori*, we choose to scale the length and velocities by the initial radius of the cloud R_0 and the velocity $N_0F/5\pi\mu R_0$ of a spherical cloud of Stokeslets, respectively (Ekiel-Jeżewska, Metzger & Guazzelli 2006). The set of (2.2)–(2.4) becomes

$$\dot{\boldsymbol{r}}^*_\alpha = \frac{5c}{8N_0}\left(\boldsymbol{I} + \boldsymbol{p}_\alpha\boldsymbol{p}_\alpha\right)\cdot\boldsymbol{e}_z + \frac{5}{8N_0}\sum_{\beta\neq\alpha}^{N_0}\left(\frac{\boldsymbol{I}}{|\boldsymbol{r}^*|} + \frac{\boldsymbol{r}^*\boldsymbol{r}^*}{|\boldsymbol{r}^*|^3}\right)\cdot\boldsymbol{e}_z, \tag{2.5}$$

where $c = 2R_0\ln(2A)/l$ and * denotes dimensionless variables. Renormalizing (2.4) in the same manner gives

$$\dot{\boldsymbol{p}}^*_\alpha = \frac{5}{8N_0}\left(\boldsymbol{I} - \boldsymbol{p}_\alpha\boldsymbol{p}_\alpha\right)\cdot\sum_{\beta\neq\alpha}^{N_0}\left[\frac{\left(\boldsymbol{r}^*\cdot\boldsymbol{p}_\alpha\right)\boldsymbol{I} - \boldsymbol{p}_\alpha\boldsymbol{r}^* - \boldsymbol{r}^*\boldsymbol{p}_\alpha}{|\boldsymbol{r}^*|^3} + \frac{3\left(\boldsymbol{r}^*\cdot\boldsymbol{p}_\alpha\right)\boldsymbol{r}^*\boldsymbol{r}^*}{|\boldsymbol{r}^*|^5}\right]\cdot\boldsymbol{e}_z. \tag{2.6}$$

For a sufficiently large number of particles, the governing equations for the sedimentation velocity of fiblets reduces to the case of a cloud of Stokeslets as studied by Metzger *et al.* (2007). However, the self-term prevails over the hydrodynamic interactions between the particles as c becomes large relative to N_0. Consequently, different behaviours are expected for the cloud of fiblets, as compared to the cloud of Stokeslets.

Integration of positions and orientations was performed using a Bulirsch–Stoer method (Press *et al.* 1994). The method enforces a precision of 1×10^{-4} for the centre-of-mass positions over each time step. For each simulation, the time step was chosen such that an average particle sediments a distance of $l/20$ when in the initial spherical geometry with randomized positions and orientations.

2.2. *Higher level of description: slender-body dynamics*

Simulations are also performed with a higher level of description for the far-field hydrodynamic interactions. The code is similar to that presented by Butler & Shaqfeh (2002). The velocities of the N_0 fibres are related to the forces and torques acting on them through a mobility matrix $\mathscr{M}$,

$$\begin{vmatrix} \dot{\boldsymbol{r}} \\ \dot{\boldsymbol{p}} \end{vmatrix} = \mathscr{M} \cdot \begin{vmatrix} \boldsymbol{F} \\ \boldsymbol{T} \end{vmatrix}, \tag{2.7}$$

where $\dot{\boldsymbol{r}}$ and $\dot{\boldsymbol{p}}$ contain all components of the centre-of-mass and rotational velocities for all fibres, and $\boldsymbol{F}$ and $\boldsymbol{T}$ contain the components of force and torque acting on the fibres.

As constructed here, the mobility matrix contains the effects of far-field hydrodynamic interactions as distributed over the full length of both fibres, as opposed to the localization of the interactions at the centre of mass of the fibres as done for the fiblet calculation. The simulation scheme is the same as that described by Butler & Shaqfeh (2002), except the Oseen–Burgers tensor is used instead of the periodic Greens function of Hasimoto (1959) to enable simulations of swarms of concentrated particles in an infinite space. A fourth-order Runge–Kutta method advances the particle positions and orientations in time, with the time step determined by using an adaptive algorithm as described in Butler & Shaqfeh (2002).

This more accurate slender-body simulation requires more computational resources than the fiblet simulation; the maximum N_0 for the full simulation was limited to 1000 particles, whereas 4000 particles could be calculated using the fiblet algorithm. An aspect ratio of $A = 10$ is used for all simulations to match the experiments as well as to satisfy the slender-body limit.

Both codes were tested for convergence with regard to time step, and the limits (single particle, dilute and two-particle interactions) were tested with success. Note that for both simulations methods, interactions were not calculated between pairs of fibres when their separation distance was smaller than one fibre diameter. We found that including the cut-off distance for the hydrodynamic interaction is necessary, unlike in the case of Stokeslets used by Metzger *et al.* (2007). Other methods for controlling the singularities returned results similar to those when using this method, and the results were insensitive to the exact cut-off distance.

2.3. *Parameters describing the deformation*

Numerical simulations were performed with initially spherical clouds comprised of $500 \leqslant N_0 \leqslant 4000$ particles that were tracked over a typical time interval of $0 \leqslant t^* \leqslant 800$. To identify the time evolution of the deformation of a sedimenting cloud, we define

some parameters such as the number of particles N that remain in the cloud, the sedimentation rate V of the cloud and the horizontal radius R and its rate of growth $\mathrm{d}R/\mathrm{d}t$. Because large variation exists from one run to the next for the same N_0, ten runs for different realizations of the initial particle positions were performed. This generates an ensemble of data over which to average the macroscopic quantities of the cloud as a function of time t^*. The mean values of parameters $\langle N \rangle$ and $\langle R \rangle$ are normalized by their initial values N_0 and R_0, respectively; the mean values of velocity parameters $\langle V \rangle$ and $\langle \mathrm{d}R/\mathrm{d}t \rangle$ are normalized by $N_0 F/5\pi\mu R_0$. The dispersion of the data among runs is quantified by the standard deviation.

Particles are lost from the initially spherical cloud as it sediments through the fluid. The particles considered to belong to the cloud are those for which the vertical position from the centre of mass of the cloud is $\leqslant R_0$. This yields a definition for the particles inside the cloud $N^*(t^*)$ and, by averaging the individual velocities of these particles, the cloud velocity $V^*(t^*)$. The horizontal radius of the cloud $R^*(t^*)$ is calculated by dividing the cloud into four quadrants, measuring the maximum distance in the direction perpendicular to gravity of a particle from the centre of mass of the cloud, and averaging over the four values. Though alternatives can be proposed for quantifying the cloud radii, this option provides a method that is similar to that used for the experiments.

3. Experimental techniques

The experimental set-up and techniques are similar to those used by Metzger *et al.* (2007) where further detail can be found. The vessel has a width of 9.8 cm, a depth of 4cm, and a filled height of 100 cm. The rigid fibres are made of copper with a dimension of $l = 0.127 \pm 0.013$ cm and $d = 0.0149 \pm 0.0020$ cm, and density $\rho_p = 8.97 \pm 0.03$ g cm^{-3}. For these fibres, the aspect ratio is $A \approx 8.5$. The fluid is a mixture of 50 % by volume Ucon oil supplied by Chempoint and 50 % distilled water, and has a density $\rho = 1.079 \pm 0.19$ g cm^{-3} and a dynamic viscosity $\mu = 2170 \pm 60$ cP. With this combination of fluid and fibres, the typical Reynolds number, as based upon the radius and sedimentation velocity of the cloud, is less than 10^{-2}.

The suspension of rigid fibres is prepared with a desired volume fraction ϕ in a small beaker. Clouds are produced by injecting a given volume of suspension at the top of the filled container using a syringe. The shape of evolution of the clouds is recorded with a digital video camera CANON XM2 mounted on a vertical sliding rail. Homogeneous lighting is ensured by backlighting the vessel using a neon tube while placing a double layer of tracing paper to the back wall of the container.

The supplementary movies (available at journals.cambridge.org/FLM) are analysed with ImageJ (digital imaging software available at http://rsb.info.nih.gov/ij/). Each image is thresholded and the cloud contour is fitted with an ellipse. This provides the position of the centre of mass and the horizontal R dimension of the cloud. The instantaneous cloud velocity V is measured from two successive frames. The initial dimension R_0 and velocity V_0 of the experimental cloud are used to normalize the data in the same way as in the simulations. Statistics were obtained as in the numerical simulations by doing several runs (typically five).

4. Results and comparisons

As evident from the fiblet model (see § 2.1), the settling behaviour of a spherical cloud depends strongly on the value of c/N_0. For large c/N_0, the self-term overwhelms

the hydrodynamic interactions between particles and the fibres behave as when in isolation. In the other limit of $c/N_0 = 0$, the governing equations become identical to the case of a cloud of Stokeslets and the cloud behaves accordingly. We are interested in the regime where $c/N_0 < 1$ so that the hydrodynamic interactions prevail, yet the values of c are large enough for the self-term, and thus the anisotropy of the particles, to have a substantial influence on the evolution of the cloud.

Figure 1 illustrates the typical evolution of a cloud of fibres versus time in the experiments and the fiblet simulations which have been undertaken in the range $0.01 \leqslant c/N_0 \leqslant 0.1$ (see supplementary movies). This evolution closely resembles that of a falling cloud of spheres which has been successfully modelled by Stokeslets (Metzger *et al.* 2007). The initially spherical cloud begins to lose particles at a slow, steady rate while falling through the viscous fluid. The cloud continuously expands in the direction perpendicular to gravity and transitions into a toroidal shape. This torus eventually fractures into multiple droplets of particles (usually into more than two droplets in contrast with a cloud of spheres which mostly breaks up into two). Each of these droplets can destabilize again in a repeating cascade if the cloud contains a large enough number of particles.

In figure 2, the mean value of the break-up time, $\langle t_b^* \rangle$, estimated as the normalized time for which the torus starts to bend before breaking, is plotted versus c and c/N_0. The major trend seen in figure 2(a) is that $\langle t_b^* \rangle$ declines with increasing c, i.e. with increasing prominence of the self-term. The two simulation methods give similar results. As found for the falling cloud of spheres (or Stokeslets, i.e. $c = 0$), $\langle t_b^* \rangle$ increases with N_0. By plotting $\langle t_b^* \rangle$ versus c/N_0 in figure 2(b), the numerical data corresponding to both simulation methods collapse onto the same curve. Excellent quantitative agreement is found between simulations and experiments.

In this latter figure, in addition to the present experimental data obtained for $A \approx 8.5$, we have also included experimental data from figure 3(b) of Metzger *et al.* (2007). These data, obtained for $A = 1$ and for $c/N_0 \approx 0.01$, also collapse onto the master curve. These results from two different values of A strengthen the finding from the simulations that the break-up time depends solely on c/N_0. Additional tests with moderately higher aspect ratios, such as $A \approx 30$, are feasible, but would reveal little as the fundamental parameter c has a weak logarithmic dependence on A; problems caused by the bending of our fibres at very large aspect ratios unfortunately prevent experiments on a wider range of parameters. Note that for the c/N_0 examined in the experiments, the volume fraction of the cloud ranges from 1 to 10 %.

The decrease of the break-up time with increasing c is linked to the faster growth of the horizontal radius of the cloud, R^*, with increasing c, i.e. with increasing importance of the self-term. This is evidenced in figure 3(a) by comparing the simulation results for $c = 40$ and 80. Good agreement is found between experiments and simulation results having similar c/N_0 despite large variations among runs.

Another distinct feature of falling clouds of rigid fibres, as compared to clouds of spheres, is seen in the evolution at the start of sedimentation; see figure 3(b). The initial sedimentation rate $\langle V_0^* \rangle$ is slightly faster than that of a cloud of Stokeslets with the same R_0 and a sufficiently large number of N_0 owing to the contribution of the self-term. At short times after the start of sedimentation, $\langle V^* \rangle$ rapidly increases to a maximum value (which is more pronounced for larger c) then decreases continuously, while $\langle V^* \rangle$ of the Stokeslet cloud only declines (Metzger *et al.* 2007). This initial increase in $\langle V^* \rangle$ is caused by a combination of the change in orientation distribution and a compaction of the cloud at short times as reflected by the small initial decrease in $\langle R^* \rangle$. This initial feature does not seem to be observed in the experiments. While there

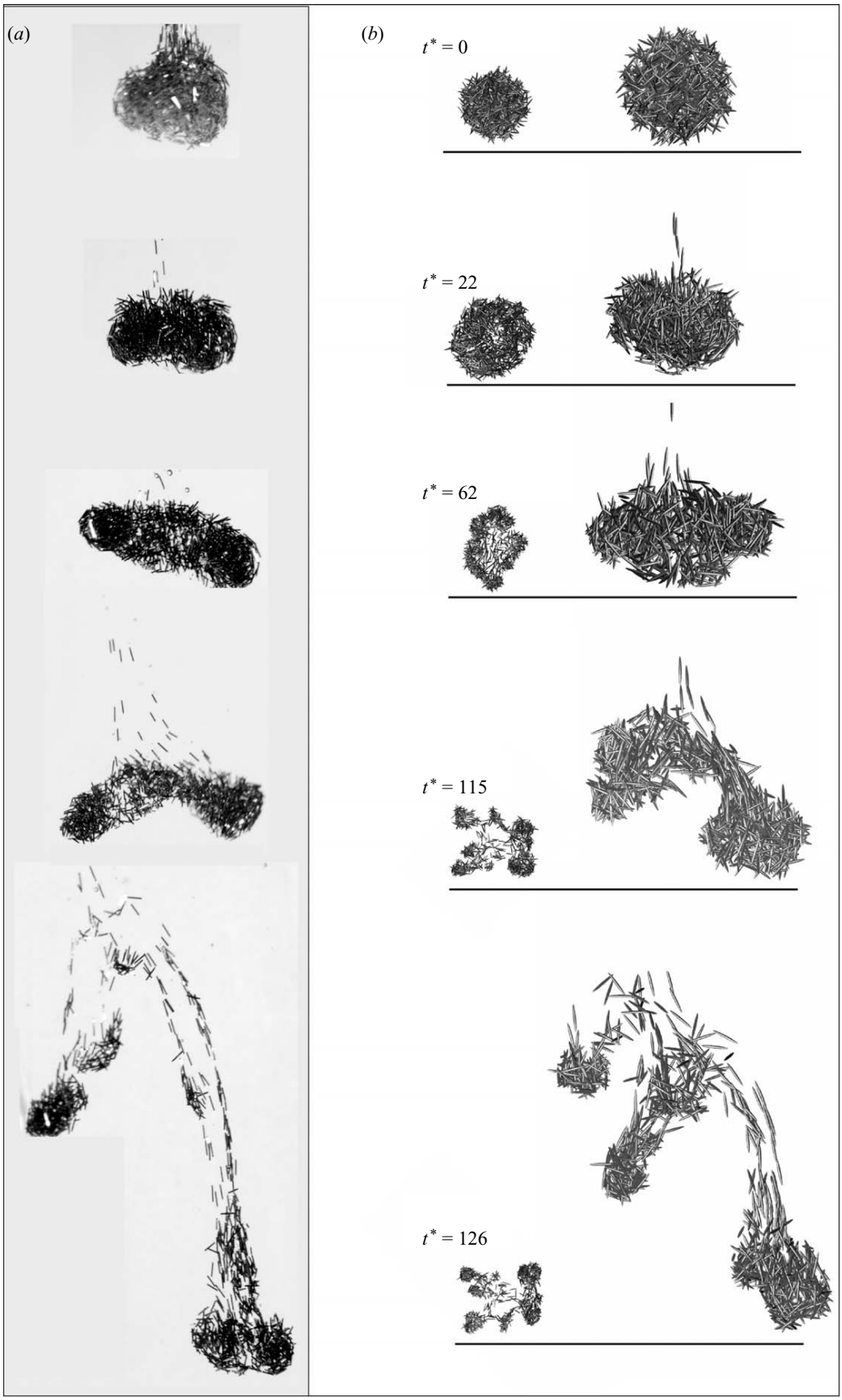


FIGURE 1. Typical evolution of a cloud of rigid fibres. (*a*) Experiment with $N_0 \approx 1000$ and $c \approx 30$, which corresponds to a cloud volume fraction of 5 %. (*b*) The fiblet algorithm for $c = 40$ and $N_0 = 1000$. The side views are accompanied by bottom views on the small side pictures. The complete dynamics coming from different runs are shown in the supplementary movies.

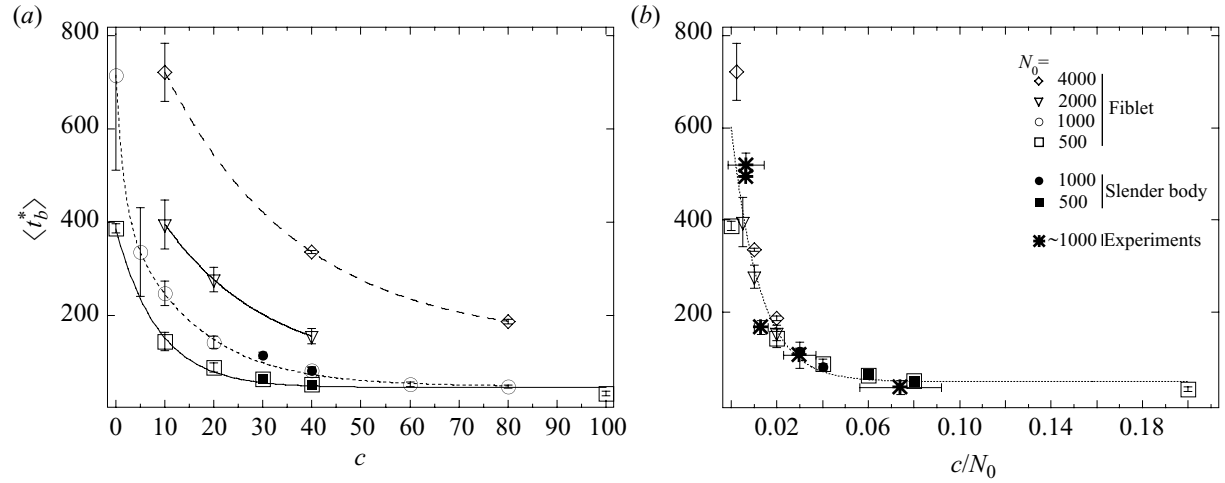


FIGURE 2. Mean value of the break-up time, $\langle t_b^* \rangle$, vs. (*a*) c and (*b*) c/N_0. The error bars correspond to the variance between runs.

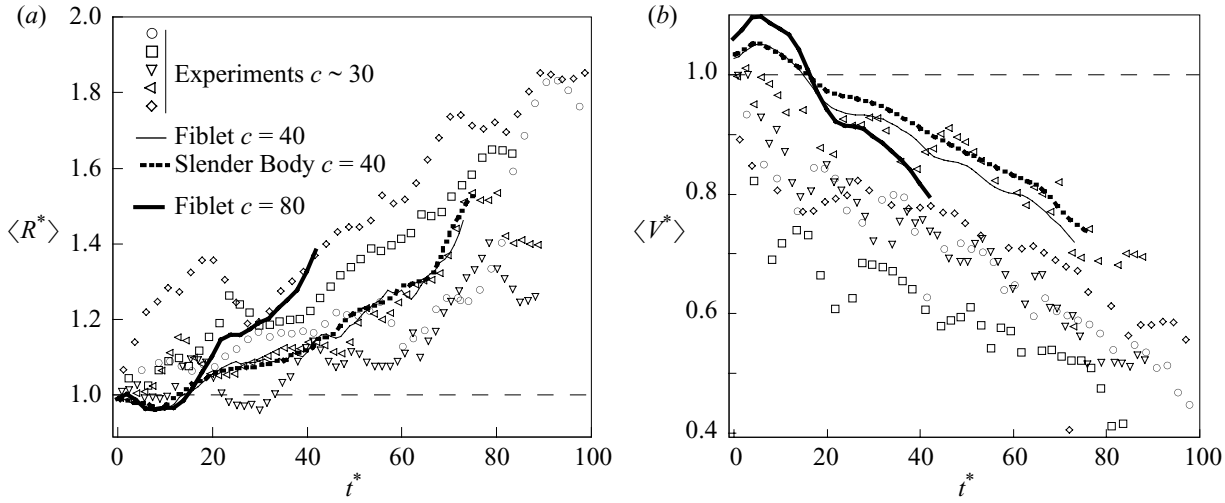


FIGURE 3. Simulation results for the time evolution of (*a*) the mean horizontal radius of the cloud, $\langle R^* \rangle$, and (*b*) the cloud settling velocity, $\langle V^* \rangle$ for clouds having $N_0 = 1000$. The two figures also show the values of R^* and V^* for five individual experimental runs. The dashed lines are guidelines for comparison with the initial radius and velocity of the cloud.

is a considerable variation among runs, the further decrease of $\langle V^* \rangle$ is comparable in experiments and simulations having the same c/N_0.

The influence of the self-term on the rate of growth of the cloud, $\langle \mathrm{d}R^*/\mathrm{d}t^* \rangle$, is examined with more detail in figure 4 for the fiblet simulations. Figure 4(*a*) shows the evolution of $\langle \mathrm{d}R^*/\mathrm{d}t^* \rangle$ for $c = 10$ according to each contribution: the self-term and the hydrodynamic term in (2.5). Comparing each contribution, the hydrodynamic term controls $\langle \mathrm{d}R^*/\mathrm{d}t^* \rangle$ and the self-term seems to contribute only relatively small fluctuations. However, even being small, the self-term contribution is fundamental to the accelerated break-up of clouds of fibres as compared to clouds of spheres. The value of $\langle \mathrm{d}R^*/\mathrm{d}t^* \rangle$ fluctuates between negative and positive values as the fibres tumble within the cloud, but the overall value becomes positive (indicating an expansion of the horizontal radius) and increases rapidly just prior to break-up of the unstable torus in stark contrast with the situation shown in figure 4(*b*) in which the self-term has been removed as in a Stokeslet cloud ($c = 0$).

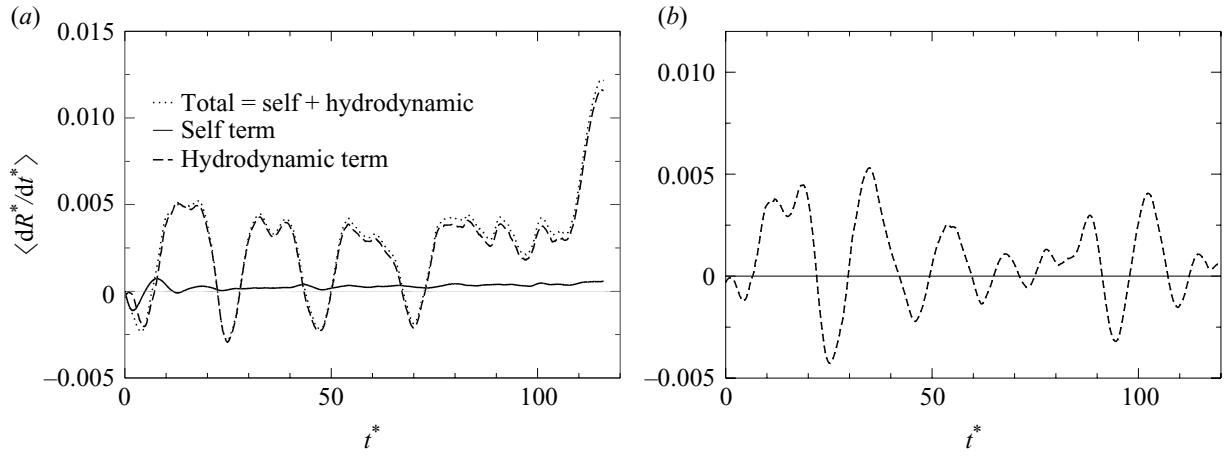


FIGURE 4. Time evolution of $\langle dR^*/dt^* \rangle$ resulted from fiblet simulations with $N_0 = 500$ and (*a*) $c = 10$ and (*b*) $c = 0$. Results are shown according to contributions from (2.5).

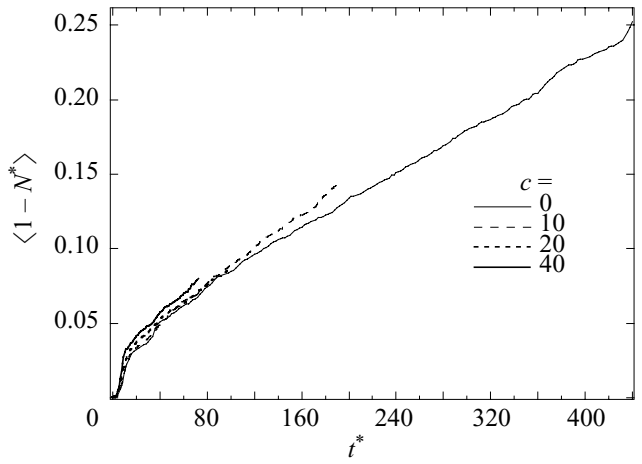


FIGURE 5. Fraction, $1 - N^*$, of particles that have leaked away from the cloud vs. time t^* for fiblet simulations having $N_0 = 1000$.

Finally, we have examined the fraction, $1 - N^*$, of particles that have leaked away from the cloud versus time t^* in figure 5 for the fiblet simulations. Clearly, the rate of leakage does not vary with c. This shows that the time evolution of the fraction of particles escaping from a cloud of fibres follows the same behaviour as that found from a cloud of spheres which has been examined in detail by Nitsche & Batchelor (1997) and Metzger *et al.* (2007).

5. Conclusions

We have studied the sedimentation of a cloud of rigid fibres through numerical simulations and experiments. The general evolution of the cloud deformation is found to be qualitatively similar to that of a cloud of spheres. However, quantitative differences in the time evolution are observed. For example, the particle anisotropy accelerates the expansion of the cloud and leads to a faster break-up.

Two simulations having different levels of approximation for the far-field hydrodynamic interactions, the fiblet and the slender-body, are performed and found to give similar results. These simulations demonstrate that the dynamics of the cloud are controlled by a single parameter, c/N_0, which is related to the self-term

contribution to the motion of the anisotropic particles. The experiments confirm these findings.

Note also that the fiblet simulation, which contains the minimal physics, captures the cloud dynamics extremely well. The success of this minimal description indicates that (i) the first-order term of the far-field hydrodynamic interactions between the particles is sufficient and (ii) including the short-range interactions is not necessary for the range of volume fractions used in the experiments. It is indeed interesting to note that this later range extends from the dilute to the semi-dilute regime as $0.16 \lesssim n(l/2)^3 \lesssim 1.6$ where n is the number of particles per unit volume.

This work was supported by the National Science Foundation through a CAREER Award (CTS-0348205). Visits were supported by the Partner University Fund on 'particulate flows' and by Aix-Marseille Université (U1) visiting professorships.

Supplementary movies are available at journals.cambridge.org/FLM.

Appendix. Formulation of the fiblet approximation

Slender-body theory (Moran 1963; Batchelor 1970; Cox 1970) is assumed to describe the motions of the high aspect fibres sedimenting in the Newtonian fluid under Stokes conditions, or vanishing Reynolds number. At the leading order of approximation within the slender-body equations, the centre-of-mass velocity of a fibre α is

$$\dot{\boldsymbol{r}}_\alpha = \frac{\ln(2A)F}{4\pi\mu l}\left(\boldsymbol{I}+\boldsymbol{p}_\alpha\boldsymbol{p}_\alpha\right)\cdot\boldsymbol{e}_z + \frac{1}{l}\int_{-l/2}^{l/2}\boldsymbol{u}_\alpha\left(\boldsymbol{r}_\alpha+s_\alpha\boldsymbol{p}_\alpha\right)\mathrm{d}s_\alpha, \tag{A 1}$$

where $\boldsymbol{u}_\alpha(\boldsymbol{r}_\alpha + s_\alpha\boldsymbol{p}_\alpha)$ is the fluid velocity evaluated at position $\boldsymbol{r}_\alpha + s_\alpha\boldsymbol{p}_\alpha$ along the centreline of fibre α. The coordinate s_α is set such that $-l/2 \leqslant s_\alpha \leqslant l/2$ and $s_\alpha = 0$ at the centre of mass. The rotational velocity of the fibre α is

$$\dot{\boldsymbol{p}}_\alpha = \frac{12}{l^3}\left(\boldsymbol{I}-\boldsymbol{p}_\alpha\boldsymbol{p}_\alpha\right)\cdot\int_{-l/2}^{l/2}\boldsymbol{u}_\alpha\left(\boldsymbol{r}_\alpha+s_\alpha\boldsymbol{p}_\alpha\right)s_\alpha\,\mathrm{d}s_\alpha, \tag{A 2}$$

where the external torque on the fibre is zero.

In an otherwise quiescent fluid, the fluid velocity at a position on fibre α is generated by the sedimentation of the other fibres, labelled β, in the suspension. This velocity is calculated by summing the disturbance created by distributing Stokeslets along the centreline of each fibre β (Harlen *et al.* 1999; Butler & Shaqfeh 2002) as

$$\boldsymbol{u}_\alpha\left(\boldsymbol{r}_\alpha+s_\alpha\boldsymbol{p}_\alpha\right) = \sum_{\beta\neq\alpha}^{N_0}\int_{-l/2}^{l/2}\boldsymbol{J}\left(\boldsymbol{r}_\beta+s_\beta\boldsymbol{p}_\beta-\boldsymbol{r}_\alpha-s_\alpha\boldsymbol{p}_\alpha\right)\cdot\boldsymbol{f}\left(s_\beta\right)\mathrm{d}s_\beta, \tag{A 3}$$

where $\boldsymbol{J}$ is the Oseen–Burger tensor and $\boldsymbol{f}(s_\beta)$ is the line force density of Stokeslets on fibre β. The description of the dynamics is completed by specifying that the fibres are torque-free, $\int s_\beta\boldsymbol{f}_\beta(s_\beta)\,\mathrm{d}s_\beta = 0$, and acted on by a net buoyancy force, $\int \boldsymbol{f}_\beta(s_\beta)\,\mathrm{d}s_\beta = F\boldsymbol{e}_z$.

Equations (2.1)–(2.4) are developed by linearizing both the velocity on fibre α and the velocity generated by fibre β about their respective centres. For particles that are widely separated, the velocity variation along the length of the fibre varies little and can be approximated by two terms of the Taylor series about the centre of mass, $s_\alpha = 0$,

$$\boldsymbol{u}\left(\boldsymbol{r}_\alpha+s_\alpha\boldsymbol{p}_\alpha\right) \approx \boldsymbol{u}\left(\boldsymbol{r}_\alpha\right) + s_\alpha\left.\frac{\partial\boldsymbol{u}}{\partial s_\alpha}\right|_{\boldsymbol{r}_\alpha}. \tag{A 4}$$

Using this approximation gives

$$\dot{\boldsymbol{r}}_\alpha = \frac{\ln(2A)F}{4\pi\mu l}\left(\boldsymbol{I} + \boldsymbol{p}_\alpha\boldsymbol{p}_\alpha\right)\cdot\boldsymbol{e}_z + \boldsymbol{u}_\alpha\left(\boldsymbol{r}_\alpha\right) \tag{A 5}$$

and

$$\dot{\boldsymbol{p}}_\alpha = \left(\boldsymbol{I} - \boldsymbol{p}_\alpha\boldsymbol{p}_\alpha\right)\cdot\left.\frac{\partial\boldsymbol{u}}{\partial s_\alpha}\right|_{\boldsymbol{r}_\alpha}. \tag{A 6}$$

Likewise, the velocity disturbance at $\boldsymbol{r}_\alpha$ due to the force applied at point s_β on a fibre β is linearized about the centre. Integrating along the length of fibre β and summing over all fibres β as designated in (A 3) gives

$$\boldsymbol{u}_\alpha\left(\boldsymbol{r}_\alpha + s_\alpha\boldsymbol{p}_\alpha\right) = \sum_{\beta\neq\alpha}^{N_0}\int_{-l/2}^{l/2}\left[\boldsymbol{J}\left(\boldsymbol{r}_\alpha + s_\alpha\boldsymbol{p}_\alpha - \boldsymbol{r}_\beta\right) + s_\beta\left.\frac{\partial\boldsymbol{J}}{\partial s_\beta}\right|_{\boldsymbol{r}_\alpha+s_\alpha\boldsymbol{p}_\alpha-\boldsymbol{r}_\beta} + \cdots\right]\cdot\boldsymbol{f}\left(s_\beta\right)\mathrm{d}s_\beta. \tag{A 7}$$

The second term in the expansion makes no contribution to $\boldsymbol{u}_\alpha(\boldsymbol{r}_\alpha + s_\alpha\boldsymbol{p}_\alpha)$ and higher-order terms are ignored. Consequently, (A 7) becomes

$$\boldsymbol{u}_\alpha\left(\boldsymbol{r}_\alpha + s_\alpha\boldsymbol{p}_\alpha\right) \approx \sum_{\beta\neq\alpha}^{N_0}\boldsymbol{J}\left(\boldsymbol{r}_\alpha + s_\alpha\boldsymbol{p}_\alpha - \boldsymbol{r}_\beta\right)\cdot F\boldsymbol{e}_z, \tag{A 8}$$

where the approximation removes the dependence of the velocity on fibre α upon the orientation of fibre β. Substituting this approximation into (A 5) with $s_\alpha = 0$ results in (2.1)–(2.3). Substituting (A 8) into (A 6) to calculate the rotational velocity within the approximation gives

$$\dot{\boldsymbol{p}}_\alpha = \left(\boldsymbol{I} - \boldsymbol{p}_\alpha\boldsymbol{p}_\alpha\right)\cdot\left.\frac{\partial\boldsymbol{J}}{\partial s_\alpha}\right|_{\boldsymbol{r}_\alpha-\boldsymbol{r}_\beta}\cdot F\boldsymbol{e}_z. \tag{A 9}$$

Calculating the gradient of the Oseen–Burger tensor and evaluating at $\boldsymbol{r} = \boldsymbol{r}_\alpha - \boldsymbol{r}_\beta$ gives

$$\left.\frac{\partial\boldsymbol{J}}{\partial s_\alpha}\right|_{\boldsymbol{r}} = \frac{1}{8\pi\mu}\left[\frac{\left(\boldsymbol{r}\cdot\boldsymbol{p}_\alpha\right)\boldsymbol{I} - \boldsymbol{p}_\alpha\boldsymbol{r} - \boldsymbol{r}\boldsymbol{p}_\alpha}{|\boldsymbol{r}|^3} + \frac{3\left(\boldsymbol{r}\cdot\boldsymbol{p}_\alpha\right)\boldsymbol{r}\boldsymbol{r}}{|\boldsymbol{r}|^5}\right], \tag{A 10}$$

where $|\boldsymbol{r}|$ is the distance between centres. Placing this relation in (A 9) gives (2.4), the rotational velocities for the fibres as used for the 'fiblet' simulations.

REFERENCES

Adachi, K., Kiriyama, S. & Koshioka, N. 1978 The behaviour of a swarm of particles moving in a viscous fluid. *Chem. Engng Sci.* **33**, 115–121.

Batchelor, G. K. 1970 Slender-body theory for particles of arbitrary cross-section in Stokes flow. *J. Fluid Mech.* **44**, 419–440.

Bosse, T., Kleiser, L., Härtel, C. & Meiburg, E. 2005 Numerical simulation of finite Reynolds number suspension drops settling under gravity. *Phys. Fluids* **17**, 037101.

Butler, J. E. & Shaqfeh, E. S. G. 2002 Dynamic simulations of the inhomogeneous sedimentation of rigid fibres. *J. Fluid Mech.* **468**, 205–237.

Cox, R. G. 1970 The motion of long slender bodies in a viscous fluid. Part 1. General theory. *J. Fluid Mech.* **44**, 791–810.

Ekiel-Jeżewska, M. L., Metzger, B. & Guazzelli, É. 2006 Spherical cloud of point particles falling in a viscous fluid. *Phys. Fluids* **18**, 038104.

Harlen, O. G., Sundararajakumar, R. R. & Koch, D. L. 1999 Numerical simulation of a sphere settling through a suspension of neutrally buoyant fibres. *J. Fluid Mech.* **388**, 355–388.

Hasimoto, H. 1959 On the periodic fundamental solutions of the Stokes equations and their application to viscous flow past a cubic array of spheres. *J. Fluid Mech.* **5**, 317–328.

Jeffery, G. B. 1922 The motion of ellipsoidal particles immersed in a viscous fluid. *Proc. R. Soc. Lond.* A **102**, 161–179.

Machu, G., Meile, W., Nitsche, L. C. & Schaflinger, U. 2001 Coalescence, torus formation and breakup of sedimenting drops: Experiments and computer simulations. *J. Fluid Mech.* **447**, 299–336.

Mackaplow, M. B. & Shaqfeh, E. S. G. 1998 A numerical study of the sedimentation of fibre suspensions. *J. Fluid Mech.* **376**, 149–182.

Metzger, B., Nicolas, M. & Guazzelli, É. 2007 Falling clouds of particles in viscous fluids. *J. Fluid Mech.* **580**, 283–301.

Moran, J. P. 1963 Line source distributions and slender-body theory. *J. Fluid Mech.* **17**, 285–304.

Nitsche, J. M. & Batchelor, G. K. 1997 Breakup of a falling drop containing dispersed particles. *J. Fluid Mech.* **340**, 161–175.

Press, W. H., Teukolsky, S. A., Vetterling, W. T., & Flannery, B. P. 1994 *Numerical Recipes in Fortran, The Art of Scientific Computing*. 2nd edn., pp. 719–725. Cambridge University Press.

Saintillan, D., Shaqfeh, E. S. G. & Darve, E. 2006 The growth of concentration fluctuations in dilute dispersions of orientable and deformable particles under sedimentation. *J. Fluid Mech.* **553**, 347–388.

Schaflinger, U. & Machu, G. 1999 Interfacial phenomena in suspensions. *Chem. Engng Technol.* **22**, 617–619.

Forward Problem Study of an Effective Medium Model for Ultrasound Blood Characterization

Emilie Franceschini, *Member, IEEE*, Bloen Metzger, and Guy Cloutier, *Senior Member, IEEE*

***Abstract*—The structure factor model (SFM) is a scattering model developed to simulate the backscattering coefficient (BSC) of aggregated red blood cells (RBCs). However, the SFM can hardly be implemented to estimate the structural aggregate parameters in the framework of an inverse problem formulation. A scattering model called the effective medium theory combined with the SFM (EMTSFM) is thus proposed to approximate the SFM. The EMTSFM assumes that aggregates of RBCs can be treated as individual homogeneous scatterers, which have effective properties determined by the acoustical characteristics and concentration of RBCs within aggregates. The EMTSFM parameterizes the BSC by three indices: the aggregate radius, the concentration of RBCs within aggregates (the aggregate compactness), and the systemic hematocrit. The goodness of fit of the EMTSFM approximation in comparison with the SFM was then examined. Based on a 2-D study, the EMTSFM was found to approximate the SFM with relative errors less than 30% for a product of the wavenumber times the mean aggregate radius $kr_{ag} \leq 1.32$. The main contribution of this work is the parameterization of the BSC with the RBC aggregate compactness, which is of relevance in clinical hemorheology because it reflects the binding energy between RBCs.**

I. Introduction

Ultrasonic tissue characterization techniques using the RF backscattered signals have received broad interest for the past 25 years. One approach is to use the magnitude and frequency dependence of backscatter echoes to quantify the tissue structures such as the size, acoustic impedance, and concentration of the scatterers. This approach has been successfully used for the characterization of the eye [1], the prostate [2], apoptotic cells [3], and the breast [4]. Blood has also been studied by employing this technique [5], [6]. In the field of ultrasonic blood characterization, the objective is to assess the level of red blood cell (RBC) aggregation, which is a surrogate marker of inflammation [7]. It is well known that when RBCs are under low shear rates ($<10\ s^{-1}$), they interact strongly with each other and form complex rouleaux, or 3-D structures. When the shear rate increases, these rouleaux or structures disaggregate. The aggregation phenomenon in human blood is normal, however hyperaggregation, an abnormal increase of RBC aggregation, is a pathological state associated with several circulatory diseases such as deep venous thrombosis, atherosclerosis, and diabetes mellitus. Ultrasonic blood characterization using the ultrasound backscatter technique has the potential to provide a method for the noninvasive estimation of the RBC aggregate size. This quantification would help to elucidate the role of RBC aggregation in the etiology of such diseases.

Ultrasound backscattering by blood is mainly due to RBCs that constitute the vast majority (97%) of the blood cellular content. Blood can thus be described as a biphasic fluid composed of RBCs immersed in plasma. Because RBCs are acoustically considered to be weak scatterers (impedance contrast between RBCs and plasma being around 13%), multiple scattering can be neglected. However, for such tissue, it is not straightforward to develop a theoretical scattering model because of the high density of RBCs (their volume fraction or hematocrit varies between 30 and 50%) and their ability to form aggregates. Theoretical efforts have been made to take into account the high density of RBCs [5], [8]–[10]. In the Rayleigh scattering regime (i.e., for a product of the wavenumber times the scatterer radius $ka \ll 1$), Twersky [9] proposed an expression of the backscattered intensity in terms of the single-particle backscattering cross section, number density of particles and packing factor. The packing factor is dependent on the hematocrit but independent of the frequency. This model succeeded in explaining the nonlinear relationship between the backscatter amplitude and hematocrit for non-aggregating RBCs [11] but failed to predict the magnitude and frequency dependence of backscatter echoes observed in *in vitro* experiments when considering aggregating RBCs. That is why Savery and Cloutier [12] proposed generalization of the packing factor theory for aggregating RBCs at a low hematocrit by introducing the frequency-dependent structure factor, named the structure factor model (SFM). This model was later generalized to a normal hematocrit of 40% [13]. The SFM sums the contributions from individual RBCs and models the RBC interaction by a statistical mechanics structure

Manuscript received August 17, 2011; accepted September 19, 2011. This work was supported by the Fonds Incitatifs Recherche 2010 of the Université de Provence and by a grant from the Canadian Institutes of Health Research (#MOP-84358).

E. Franceschini is with the Laboratoire de Mécanique et d'Acoustique (LMA), Centre National de la Recherche Scientifique (CNRS) UPR 7051, Marseille, France (e-mail: franceschini@lma.cnrs-mrs.fr).

B. Metzger is with the Institut Universitaire des Systèmes Thermiques Industriels (IUSTI), Centre National de la Recherche Scientifique (CNRS), Marseille, France.

G. Cloutier is with the Laboratory of Biorheology and Medical Ultrasonics, University of Montreal Hospital Research Centre (CRCHUM), Montreal, Quebec, Canada, and with the Department of Radiology, Radio-Oncology, and Nuclear Medicine, and the Institute of Biomedical Engineering, University of Montreal, Montreal, Quebec, Canada.

Digital Object Identifier 10.1109/TUFFC.2011.2129

0885–3010/$25.00 © 2011 IEEE

TABLE I. ACOUSTICAL PROPERTIES OF BLOOD FOUND IN [11] AND [21].

	Density ρ (kg·m^{-3})	Compressibility κ (Pa^{-1})	Impedance Z (MRayl)
RBC*	1092	3.41×10^{-10}	1.766
Plasma	1021	4.09×10^{-10}	1.580

*RBC = red blood cells.

factor, which is, by definition, the Fourier transform of the spatial distribution of RBCs [12]–[14]. Note that the low-frequency limit of the structure factor is, by definition, the packing factor used under Rayleigh conditions, and that the structure factor cannot analytically be calculated contrary to the packing factor [9]. The SFM was largely used to perform simulation studies on RBC aggregation [12], [13], [15]–[17]. Simulations enabled prediction of the frequency dependence of the backscattering coefficient (BSC) from various RBC spatial distributions and thus helped the interpretation of experimental observations. However, the SFM cannot directly be used to estimate the RBC aggregate size in the framework of an inverse problem approach because of the intensive computational time required to assess the structure factor by realizing distributions of aggregating RBCs with simulations. Note that the SFM should not be confused with the structure factor size estimator (SFSE) recently proposed by Yu *et al.* [18], [19]. The SFSE approximates the SFM for practical assessments of RBC structural features (i.e., in an inverse problem formulation).

Yu *et al.* [18], [19] developed the SFSE scattering theory that approximates the SFM by using a second-order Taylor expansion of the structure factor. The SFSE is thus not as accurate as the SFM. The SFSE parameterizes the BSC by two structure indices: the packing factor and the mean aggregate diameter, assumed to be isotropic. However, experiments with pig blood in controlled flow devices [18], [19] and 3-D numerical simulations of isotropic aggregates [16] showed that the two indices are correlated and follow a quadratic relationship under the assumption of isotropic monodisperse aggregates, thus reducing the BSC parameterization to one structural index. Moreover, the SFSE model did not produce good fits to the simulated BSCs computed with the SFM [16, Fig. 4]. Thus, the SFSE model is not sufficient to approximate the SFM accurately; even if the relation between the simulated aggregate sizes and its SFSE parameterization followed a proportional relationship [16]. The goal of this paper is to propose a new scattering model that better approximates the SFM for structural RBC aggregate characterization.

The scattering theory we propose is based on an effective medium theory (EMT) combined with the SFM, labeled EMTSFM. The EMT was initially developed by Kuster and Toksoz [20] in the field of geophysics. Here, the EMT assumes that aggregates of RBCs can be treated as individual homogeneous scatterers, which have effective properties determined by the concentration of RBCs within aggregates and acoustical properties of blood constituents. The approximation of RBC aggregates as homogeneous effective particles is combined with the SFM to consider the concentrated blood medium. The effective particle interactions were thus modeled by a structure factor, as in [12] and [13]. The EMTSFM parameterizes the BSC by three indices: the aggregate radius, the internal hematocrit (i.e., the concentration of RBCs within aggregates, also called the aggregate compactness) and the systemic hematocrit. Note that the new EMTSFM model would allow characterizing, for the first time in the quantitative ultrasound field, the compactness of RBC aggregates (or of any other cellular structures). In the field of clinical hemorheology, assessing the compactness of RBC aggregates is of high clinical importance because it is related to the binding energy between cells. Normal RBC aggregates form rouleaux-type structures, whereas pathologies associated with stronger binding energies result in clumps of RBCs (close to a spherical isotropic packing).

The purpose of this study was to compare the EMTSFM and SFM in the framework of a forward problem study, i.e., determining the BSC from known distributions of RBCs with known acoustical parameters using both EMTSFM and SFM. The goodness of fit of the EMTSFM approximation in comparison with the SFM was examined as a function of the frequency and of the structural aggregate parameters (i.e., the aggregate size and the internal hematocrit). Because of the computational load required to generate 3-D RBC distributions with various internal hematocrits with the SFM, 2-D models were used for the BSC computation. Although limiting, this choice allowed us to simulate randomly various internal hematocrits for a given range of systemic hematocrits, and to isolate the effects of aggregate size and internal hematocrit on the BSC.

II. ULTRASOUND BACKSCATTERING THEORY

In the following, it is assumed that the incident wavelength λ is large compared with the RBC size. Consequently, the RBC shape could be approximated by a simple geometry having an equivalent volume of an RBC in 3-D or having an equivalent surface in 2-D [21]. In the present 2-D study, RBCs were modeled as parallel infinite cylinders of radius a, that have small contrast in acoustical properties relative to the plasma (see Table I). Two scattering models of RBC aggregation are presented in this section: the SFM and the new EMTSFM.

A. The Structure Factor Model (SFM)

The SFM of ultrasound backscattering by blood consists of summing contributions from individual RBCs and

modeling the RBC interaction by a statistical mechanics structure factor [12], [13], [15]. By considering a collection of N identical and weakly scattering RBCs, the BSC expression can be written as

$$\mathrm{BSC}_{\mathrm{SFM}}(-2\mathbf{k}) = m\sigma_b(-2\mathbf{k})S(-2\mathbf{k}), \tag{1}$$

where $\mathbf{k}$ is the incident wave vector and m is the number density of RBCs that is related to the systemic hematocrit ϕ as $m = \phi/A_p$ (where A_p is the RBC area). The backscattering cross section σ_b of a single weak RBC can be written as the product of the backscattering cross section of a single RBC in the Rayleigh limit [9, Eq. (16)] and the backscatter form factor F as

$$\sigma_b(-2\mathbf{k}) = \frac{k^3 A_p^2 \gamma_z^2}{2\pi} F(-2k, a) = \frac{k^3 A_p^2 \gamma_z^2}{2\pi}\left(\frac{J_1(2ka)}{ka}\right)^2, \tag{2}$$

where J_1 is the first-order Bessel function of the first kind and $\gamma_z = (Z_{\mathrm{RBC}} - Z_{\mathrm{plasma}})/Z_{\mathrm{plasma}}$ is the fractional variation of impedance between the RBC and its suspending medium (i.e., the plasma). The form factor F serves as a useful descriptor of a scatterer with a simple shape [21], [22] and characterizes here the cylindrical shape and size of the 2-D RBC scatterer. The demonstration of the cylindrical form factor expression in 2-D is given in the Appendix. The function S in (1) is the structure factor representing the spatial positioning of RBCs; it is defined by

$$S(-2\mathbf{k}) = E\left[\frac{1}{N}\left|\sum_{i=1}^{N} e^{-i2\mathbf{k}\mathbf{r}_i}\right|^2\right], \tag{3}$$

where E is the expected value of a random variable and $\mathbf{r}_i$ is the position vector defining the center of the ith RBC in space. Note that the aggregation phenomenon only affects the structure factor because RBC properties (i.e., σ_b) and the systemic hematocrit are expected to remain constant in the modeled region of interest.

In the case of disaggregated RBCs, the low-frequency limit of the structure factor is a constant with this model [$S(k) \to S(0) = W$], which is the packing factor. The BSC expression can thus be simplified as

$$\mathrm{BSC}_{\mathrm{LF}}(-2\mathbf{k}) = mW\sigma_b(-2\mathbf{k}). \tag{4}$$

The most often used packing factor expression is based on the Percus-Yevick pair-correlation function for identical, hard, and radially symmetrical particles. The Percus-Yevick packing factor W_{PY} was first applied to blood by Shung *et al.*, and it is related to the systemic hematocrit in the 2-D space as [11]

$$W_{\mathrm{PY}} = \frac{(1-\phi)^3}{1+\phi}. \tag{5}$$

The packing factor reflects the positional correlation among particles: $W = 1$ for completely random distributions and W tends toward zero as the particle number and the spatial correlation between particles increase.

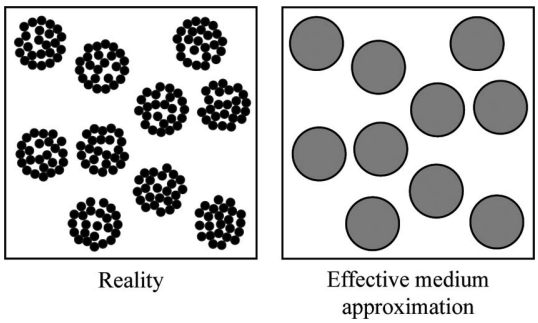


Fig. 1. Schematic representation of aggregates treated as individual scatterers. The aggregates of red blood cells in blood (left side) are assumed to be homogeneous particles (right side) with effective properties that depend on the internal hematocrit and on the density and compressibility of the red blood cells within them.

B. The Proposed Model: An Effective Medium Theory Combined With the SFM (EMTSFM)

As a first approximation, we assume that all the RBCs are aggregated in blood, that the aggregates are identical and isotropic and that the RBCs within the aggregates are evenly distributed. The EMTSFM assumes that aggregates of RBCs can be treated as individual homogeneous scatterers as shown in Fig. 1. Each aggregate is thus approximated by an effective single particle (i.e., in this 2-D study, an effective single cylinder) having a radius r_{ag}. The density ρ_{ag} and compressibility κ_{ag} of the new effective particle are determined by considering the EMT [20]. This means that ρ_{ag} and κ_{ag} are derived from the acoustical properties of the two fluids that constitute the aggregates (i.e., ρ_1, ρ_2, κ_1, and κ_2, where 1 indicates properties of RBCs and 2 those of plasma) and from the internal concentration of RBCs within the aggregates, defined as the internal hematocrit ϕ_i, as follows:

$$\begin{aligned} \rho_{\mathrm{ag}} &= \phi_i\rho_1 + (1-\phi_i)\rho_2 \\ \frac{1}{\kappa_{\mathrm{ag}}} &= \frac{\phi_i}{\kappa_1} + \frac{1-\phi_i}{\kappa_2}. \end{aligned} \tag{6}$$

The acoustic interaction of RBCs within aggregates is therefore taken into account with the EMT, similarly to the SFM, where it is considered by the structure factor that models the individual position of RBCs and their acoustical interaction, whether they are within an aggregate or not. The main advantage of the EMTSFM is the consideration of the compactness of aggregates with the parameter ϕ_i.

The BSC from blood is then obtained by summing contributions from individual effective particles of radius r_{ag} and modeling the effective particle interaction by a statistical mechanics structure factor, S_{ag}. The equivalent BSC expression is thus

$$\mathrm{BSC}_{\mathrm{eq}}(-2\mathbf{k}) = m_{\mathrm{ag}}\sigma_{\mathrm{ag}}(-2\mathbf{k})S_{\mathrm{ag}}(-2\mathbf{k}), \tag{7}$$

where m_{ag} is the number density of aggregates, which is related to the effective area fraction of aggregates, ϕ_{ag}. The effective area fraction of aggregates is equal to the area fraction of RBCs in blood, ϕ, divided by the internal hematocrit ϕ_i: $\phi_{\mathrm{ag}} = \phi/\phi_i$. The backscattering cross section, σ_{ag}, of an effective single cylinder was calculated using the fluid-filled cylinder model developed by Doolittle and Uberall [23]. That model provides an exact solution for the backscattering of sound by a single fluid cylinder, not necessarily small compared with the wavelength, in a surrounding fluid medium (i.e., the plasma). In the proposed forward problem study, the radius r_{ag}, density ρ_{ag}, and compressibility κ_{ag} of the aggregates, and the density, ρ_2, and compressibility, κ_2, of the plasma are known *a priori* (see Table I) such that the backscattered pressure of the effective fluid cylinder could be computed as a function of frequency. The structure factor S_{ag} was calculated for a collection of N_{ag} identical and disaggregated particles (mimicking RBC aggregates) of radius r_{ag}, randomly distributed as follows:

$$S_{\mathrm{ag}}(-2\mathbf{k}) = E\left[\frac{1}{N_{\mathrm{ag}}}\left|\sum_{i=1}^{N_{\mathrm{ag}}} e^{-i2\mathbf{k}\mathbf{r}_i'}\right|^2\right], \tag{8}$$

where $\mathbf{r}_i'$ are the position vectors defining the center of the ith effective particle (or aggregate) in space. Note that in the research field of optics [24], the applicability of the modeling approach based on the structure factor (called the interference approximation) is limited to a product $kR \leq 3.5$ (or $kR \leq 1.5$, respectively) for a relative refractive index of the particles equal to 1.19 (or 1.8), where R is the radius of isotropic identical particles. Because the relative acoustic impedance of RBCs, z_1/z_2, is around 1.12 (see Table I), we are thus expecting the same limitation for the EMTSFM (i.e., a validity of this modeling approach restricted to $kr_{\mathrm{ag}} \leq 3.5$).

In the low-frequency limit, for aggregate sizes which are small compared with the wavelength, the structure factor S_{ag} can be well approximated by the Percus-Yevick packing factor of (5) for effective particles. The equivalent BSC expression is thus simplified as

$$\mathrm{BSC}_{\mathrm{eq_{LF}}}(-2\mathbf{k}) = m_{\mathrm{ag}}\frac{(1-\phi_{\mathrm{ag}})^3}{1+\phi_{\mathrm{ag}}}\sigma_{\mathrm{ag}}(-2\mathbf{k}), \tag{9}$$

where σ_{ag} is calculated using the exact model of fluid-filled cylinders [23], such that, in comparison with (7), the only approximation is the structure factor S_{ag}.

III. Simulation Methods

The computation of the $\mathrm{BSC_{SFM}}$ and $\mathrm{BSC_{eq}}$ requires the knowledge of the structure factors S and S_{ag}, as described in (1) and (7). Because the structure factor S (or equivalently S_{ag}) is, by definition, a statistical quantity, an average of all structure factors obtained from several particle distributions can give an estimated value of S (or equivalently S_{a}). Note that 2-D models were used because of the computational time required to generate 3-D RBC distributions with the SFM. Although limiting, this choice allowed us to simulate randomly varied internal hematocrits for a given range of systemic hematocrits.

A. Computation of Particle Distributions

1) Distribution of RBCs for the Computation of S With the SFM: We describe here how random distributions for non-aggregating and aggregating RBCs were computed within the simulated surface area L^2 of 600^2 $\mu\mathrm{m}^2$. The RBC particle radius a was set to 2.75 μm for all simulations. In the case of disaggregated RBCs, particles were randomly distributed (using a random number generator) with non-overlapping positions to give the desired area fraction of RBCs in blood (i.e., the systemic hematocrit ϕ). In the case of aggregated RBCs, we first specified the aggregate radius and then aggregates were randomly distributed with non-overlapping positions to give the desired area fraction of aggregates ϕ_{ag}. RBC distributions within aggregates were then generated by considering the number of RBCs within aggregates n_i and the area fraction of RBCs within aggregates ϕ_i. It is important to emphasize that random particle distributions could be easily generated using a random number generator up to an area fraction of approximately 0.5. In our study, the area fraction of RBCs within aggregates ϕ_i could be enlarged, up to a maximum value $\phi_{i_{\max}}$ fixed at 0.6. The procedure we chose to reach such a high number of RBCs within aggregates is described in the following.

We first randomly distributed n_i RBCs in a total area that was larger than the aggregate area, such that the initial area fraction of RBCs within aggregates was lower than 0.5. Then, to increase this area fraction, the RBCs were submitted to an external force oriented toward the center of mass of the RBC spatial distribution. RBCs moved toward each other while a repulsive force prevented them from overlapping. These forces were maintained until the area fraction of RBCs inside the considered aggregate reached the desired area fraction ϕ_i. This distribution procedure was repeated for each aggregate, such that the distribution of RBCs within each aggregate was different. Note that this procedure is not time consuming if a small number of RBCs is used: herein the maximum number of RBCs within aggregates was 38 for the maximum aggregate radius of $7.95a = 21.86$ μm. The maximum value of aggregate area fraction $\phi_{\mathrm{ag}_{\max}}$ was thus fixed to 0.5 and as a consequence, the maximum value of the systemic hematocrit $\phi_{\max}$ was limited to: $\phi_{\max} = \phi_{\mathrm{ag}_{\max}}\phi_{i_{\max}} = 0.3$.

Fig. 2 illustrates spatial arrangements of RBCs for three internal hematocrits of 40%, 50%, and 60%. In these simulations, the aggregate radius had a constant value of $r_{\mathrm{ag}}/a = 6.32$ (i.e., $r_{\mathrm{ag}} = 17.39$ μm) and a constant systemic hematocrit of 20%.

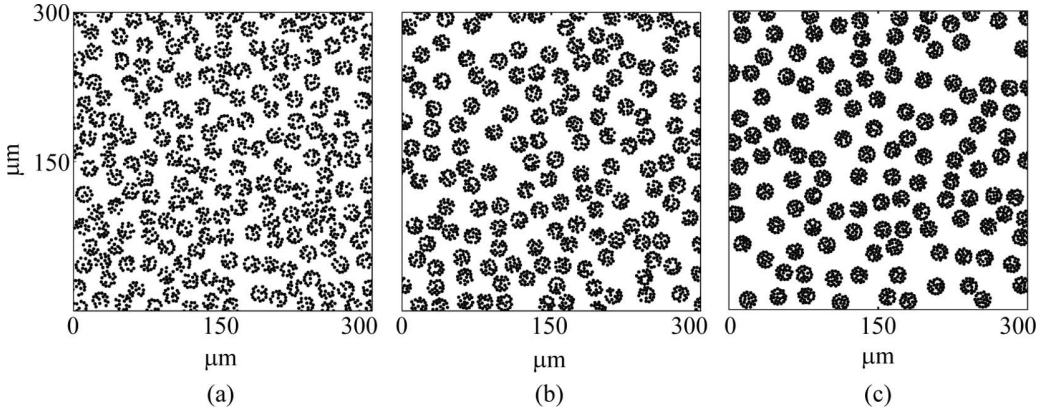


Fig. 2. Distributions of aggregated red blood cells for a constant aggregated radius $r_{ag} = 6.32a = 17.32$ μm and a constant systemic hematocrit $\phi = 20\%$ at three internal hematocrits: (a) $\phi_i = 40\%$, (b) $\phi_i = 50\%$, and (c) $\phi_i = 60\%$. The displayed areas are 300 × 300 μm to enhance the red blood cell visualization.

2) Distribution of Effective Particles for the Computation of S_{ag} With the EMTSFM: Once the effective particle radius was specified, particles were randomly distributed using a random number generator with non-overlapping positions to give the desired area fraction ϕ_{ag}. Several distributions were performed with different effective particle radii varying from $3.16a$ (= 8.69 μm) to $7.95a$ (= 21.86 μm) corresponding to different studied aggregate sizes.

B. BSC Computation

For each distribution of RBCs (or effective particles, respectively), density matrices D (or D_{ag}) were computed by dividing the square simulation plane L^2 in N_p^2 pixels (here, $N_p = 512$) and by counting the number of RBCs (or the number of effective particles) falling into each pixel. These matrices represented samplings of microscopic density functions defined by $D(r)$ for the BSC computation with the SFM or by $D_{ag}(r')$ for the BSC_{eq} computation with the proposed EMTSFM:

$$D(\mathbf{r}) = \sum_{i=1}^{N} \delta(\mathbf{r} - \mathbf{r}_i),$$
$$D_{ag}(\mathbf{r}') = \sum_{i=1}^{N_{ag}} \delta(\mathbf{r}' - \mathbf{r}_i'), \tag{10}$$

where N is the number of RBCs in blood, N_{ag} is the number of aggregates, and δ is the Dirac distribution. According to (3) and (8), and as explicitly described in [14, Appendix], the structure factors can thus be described by

$$S(-2\mathbf{k}) = E\left[\frac{1}{N}\left|\int D(\mathbf{r}) e^{-i2\mathbf{kr}} d\mathbf{r}\right|^2\right] \text{ and}$$
$$S_{ag}(-2\mathbf{k}) = E\left[\frac{1}{N_{ag}}\left|\int D_{ag}(\mathbf{r}') e^{-i2\mathbf{kr}'} d\mathbf{r}'\right|^2\right]. \tag{11}$$

Each structure factor was thus computed by averaging 2-D fast Fourier transforms (2-D FFT) of 400 density matrices for averaging purposes. The FFTs gave the structure factor values $S(-2\mathbf{k})$ and $S_{ag}(-2\mathbf{k})$ on a centered grid of wavevectors between $\pm\pi N_p/2L$ with a step of $\Delta k = \pi/L$. For the SFM, the BSC_{SFM} was thus obtained using (1). For the EMTSFM, the BSC_{eq} was computed using (7).

IV. Results

In the following, the relative errors for BSC_{eq} computed with the new EMTSFM were evaluated as $(BSC_{eq} - BSC_{SFM})/BSC_{eq}$, where the BSC_{SFM} of the SFM is assumed to be the exact solution.

A. Influence of the Internal Hematocrit

A key feature of the new simulation method was the possibility to simulate randomly various internal hematocrits corresponding to different degrees of compactness of aggregates. Frequency-dependent backscattering coefficients with different internal hematocrits from 30% to 60% are given in Figs. 3(a) and 3(b) at systemic hematocrits of 10% and 20% over a large frequency range (4 to 100 MHz). Corresponding relative errors for the BSC_{eq} are given in Figs. 3(c) and 3(d). It was assumed that the aggregates had a constant radius of $r_{ag}/a = 6.32$ (i.e., $r_{ag} = 17.39$ μm). Note that for the 20% systemic hematocrit, internal hematocrits smaller than 40% could not be computed because the corresponding area fractions of aggregates were too high: $\phi_{ag} > 0.5$. As seen in Figs. 3(a) and 3(b), as the internal hematocrit ϕ_i increases, the BSC_{SFM} amplitude increases at low frequencies (<23 MHz) and decreases at high frequencies (>28 MHz). The first peaks of the BSC_{SFM} are between 18.0 and 20.6 MHz for all simulated conditions. The relative error for BSC_{eq} was less than 30% for frequencies below 18 MHz [see Figs. 3(c) and 3(d)]. This 18 MHz frequency corresponds to a product $kr_{ag} = 1.27$. More generally, at frequencies less than 23 MHz, backscattering coefficients obtained with the SFM and the EMTSFM have the same behaviors: the first peaks of BSC_{SFM} and BSC_{eq} occur at the same frequencies

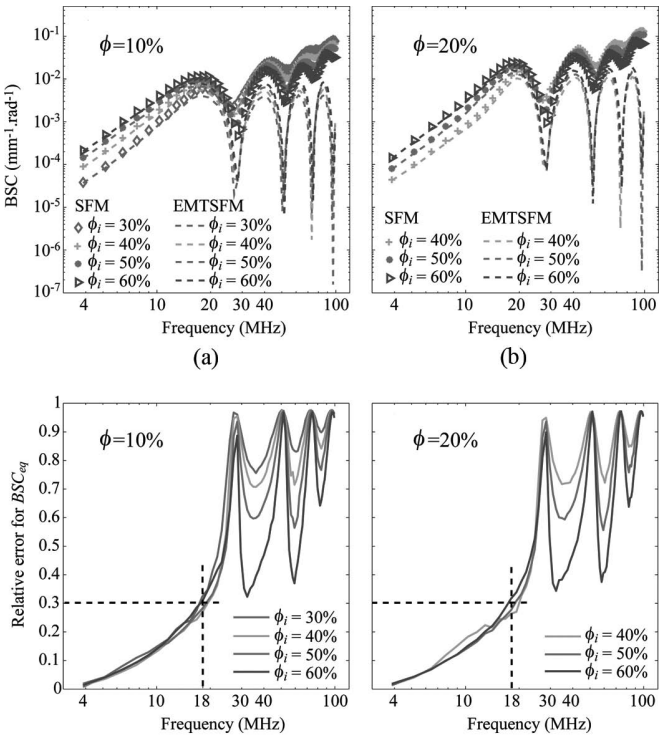


Fig. 3. (a) and (b) Dependence of the backscattering coefficients (BSCs) on the internal hematocrit: (a) $r_{ag}/a = 6.32$ and $\phi = 10\%$, and (b) $r_{ag}/a = 6.32$ and $\phi = 20\%$. The symbols are the BSC_{SFM} computed with the structure factor model (SFM) and the dashed lines are the BSC_{eq} computed with the effective medium theory combined with the SFM (EMTSFM). (c) and (d) Corresponding relative errors for the BSC_{eq} versus frequency.

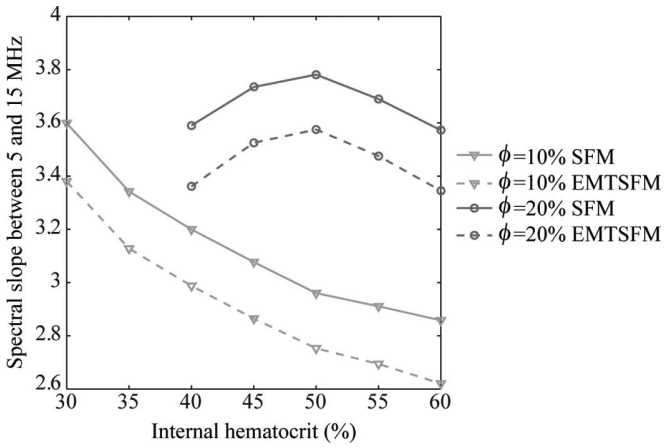


Fig. 4. Spectral slope in the frequency bandwidth 5 to 15 MHz as a function of the internal hematocrit at different systemic hematocrits, the aggregate size being fixed ($r_{ag}/a = 6.32$). The solid lines are the spectral slopes (SSs) for the BSC_{SFM} computed with the structure factor model (SFM) and the dashed lines are the SSs for the BSC_{eq} computed with the effective medium theory combined with the SFM (EMTSFM).

and the magnitude of both BSC_{SFM} and BSC_{eq} increase as the internal hematocrit increases.

A quantitative ultrasonic parameter that has often been used for tissue characterization is the spectral slope (SS). The SS is the linear slope of the BSC as a function of frequency on a log-log scale. The variation of SS with the internal hematocrit is given in Fig. 4 for systemic hematocrits of 10% and 20%. The solid lines represent the SSs for the BSC_{SFM} computed with the SFM and the dashed lines represent the SSs for the BSC_{eq} computed with the EMTSFM. For both SFM and EMTSFM, the SS behavior versus the internal hematocrit is the same: the SS decreases with increasing internal hematocrit, except for the configuration $\phi = 20\%$, $\phi_i = 40\%$. Note also that the SS of the EMTSFM slightly underestimated the SS of the SFM with a maximum difference of 0.23.

B. Influence of the Aggregate Size

Fig. 5 shows backscattering coefficients as a function of frequency for different aggregate sizes and for systemic hematocrits of 10%, 20%, and 30%. In these simulations, the internal hematocrit was the highest: $\phi_i = 60\%$. The symbols represent the BSC_{SFM} computation for the disaggregated case ($r_{ag}/a = 1$) and for aggregated cases with radii of $r_{ag}/a = 3.16$, 5.0, and 7.07. The corresponding BSC_{eq} computed with the EMTSFM [see (7)] are given in dashed lines. For frequencies less than 20 MHz, the amplitudes of both BSC_{SFM} and BSC_{eq} increase with the size of aggregates. Moreover, the peaks of both BSC_{SFM} and BSC_{eq} occur at lower frequencies as the aggregate radius increases.

The low-frequency approximation of the EMTSFM (i.e., using the Percus-Yevick packing factor) was also studied for the same configurations. The BSC_{eq} values computed by (9) are given in Fig. 6, along with plots of the BSC_{SFM} computed with the SFM. As expected, the error for $BSC_{eq_{LF}}$ is larger than the error for BSC_{eq} at high frequencies. The error between $BSC_{eq_{LF}}$ and BSC_{SFM} increases as the systemic hematocrit ϕ increases. Nevertheless, it is interesting to observe that at low frequencies less than 5 MHz, the amplitude of the $BSC_{eq_{LF}}$ matches the exact BSC_{SFM} very well, as expected.

For systemic hematocrits of 10%, 20%, and 30%, the relative errors for BSC_{eq} and $BSC_{eq_{LF}}$ were studied for a constant value of the internal hematocrit $\phi_i = 60\%$ and for eleven sizes of r_{ag}/a varying from 3.16 to 7.95 with a step of around 0.5. For each case, the frequency limit f_l and the corresponding product $k_l r_{ag}$ for which the relative error was less than 30% were determined. Results are summarized in Fig. 7. The solid lines are for the EMTSFM and the dashed lines for the low-frequency approximation of the EMTSFM using the Percus-Yevick packing factor. Fig. 7 reveals that the EMTSFM gives accurate estimates of BSC_{SFM} until $kr_{ag} \leq 1.32$ on average (i.e., for all the tested values of r_{ag}/a), whereas the EMTSFM at low frequency is only accurate until approximately $kr_{ag} \leq 0.73$.

Fig. 8 shows the influence of the aggregate size on the SS for different systemic hematocrits. The solid lines represent the SSs for the BSC_{SFM} computed with the SFM and the dashed lines represent the SSs for the BSC_{eq} computed with the EMTSFM. The results of SS presented in

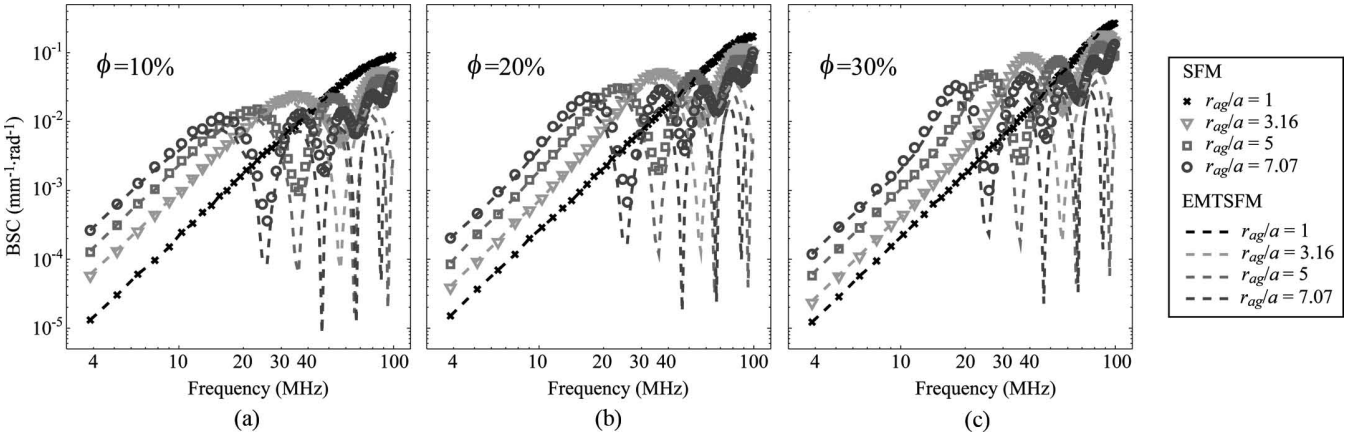


Fig. 5. Dependence of the backscattering coefficients (BSCs) for different aggregate sizes and a constant internal hematocrit $\phi_i = 60\%$ at systemic hematocrits of 10%, 20%, and 30%. The symbols are the $\mathrm{BSC_{SFM}}$ computed with the structure factor model (SFM) and the dashed lines are the $\mathrm{BSC_{eq}}$ computed with the effective medium theory combined with the SFM (EMTSFM).

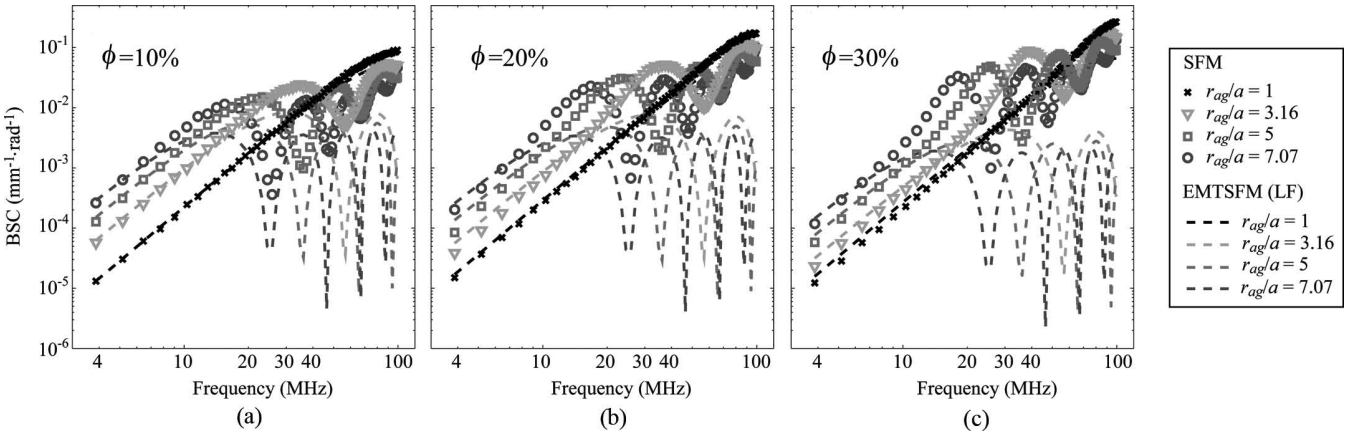


Fig. 6. Dependence of the backscattering coefficients (BSCs) for different aggregate sizes and a constant internal hematocrit $\phi_i = 60\%$ at systemic hematocrits of 10%, 20%, and 30%. The symbols are the $\mathrm{BSC_{SFM}}$ computed with the structure factor model (SFM) and the dashed lines are the $\mathrm{BSC_{eq_{LF}}}$ computed with the effective medium theory combined with the SFM (EMTSFM) using the Percus-Yevick approximation.

Fig. 8 showed that the backscattered power by disaggregated RBCs ($r_{\mathrm{ag}}/a = 1$) increased with the third power of wave frequency (SS = 3), as was expected using the Rayleigh theory in 2-D. The SS behavior with the aggregate size is the same for both SFM and EMTSFM: as the aggregate size increases, the SS decreases at $\phi = 10\%$, whereas the SS increases at $\phi = 20\%$ and 30%. The maximum difference between slopes of the EMTSFM and slopes of the SFM is around 0.35 for all studied hematocrits (i.e., relative error for the SS of $\mathrm{BSC_{eq}}$ around 9%) and it corresponds to the largest aggregate size.

V. Discussion

A. Limitation of the EMTSFM With Respect to kr_{ag}

Based on the new EMTSFM theory, the BSC from aggregated RBCs was parameterized by three indices: the aggregate size, internal hematocrit, and systemic hematocrit. The aim of our study was to estimate the goodness of fit of the EMTSFM approximation in comparison with the SFM. We found that the EMTSFM had a relative error of less than 30% for a mean product $kr_{\mathrm{ag}} \leq 1.32$ at all internal hematocrits and systemic hematocrits studied. Although the EMTSFM gave estimates with large errors for $kr_{\mathrm{ag}} > 1.32$, the EMTSFM fitted very well the $\mathrm{BSC_{SFM}}$ curve computed with the SFM for all tested factors (i.e., r_{ag}, ϕ_i, and ϕ) in the frequency bandwidth between 4 MHz and the frequency position of the first peak. This result is qualitatively consistent with works in optics [24], in which the limits of applicability of the interference approximation based on the structure factor were found for a volume fraction of particles smaller than 10% and for a product $kR \leq 3.5$ (or $kR \leq 1.5$, respectively) when the relative refractive index of the particles is 1.19 (or 1.8). These limits were determined by comparing theoretical predictions of the interference approximation with theoretical predictions of a much more exact quasi-crystalline approximation and with experimental data of a polystyrene latex suspension in water. In comparison with our results in acoustics in which the relative acoustic impedance of

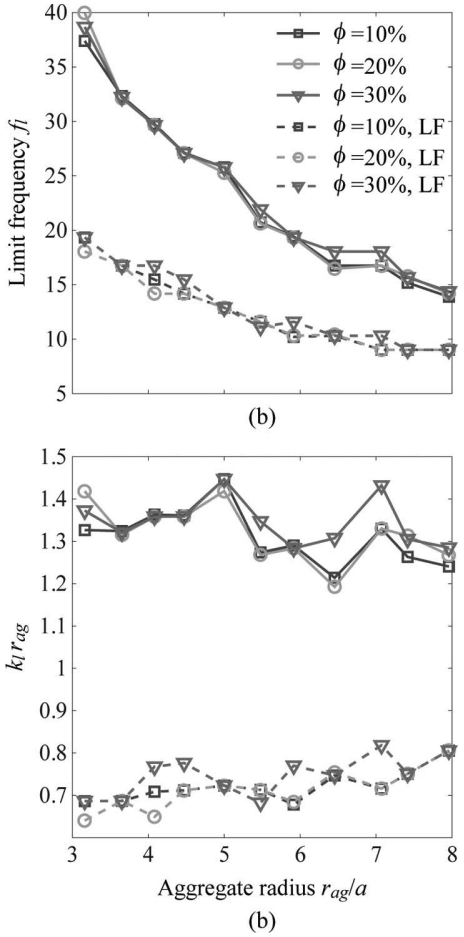


Fig. 7. (a) Frequency limit f_l for which the relative error of BSC_{eq} was less than 30% as a function of the aggregate size studied. The solid lines are the effective medium theory combined with the structure factor model (EMTSFM) and the dashed lines are the low-frequency approximation of the EMTSFM. (b) Corresponding product $k_l r_{ag}$.

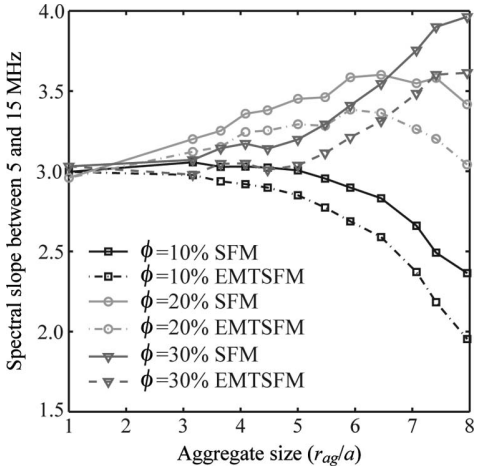


Fig. 8. Spectral slope in the frequency bandwidth 5 to 15 MHz as a function of the aggregate size at different systemic hematocrits, the internal hematocrit being fixed ($\phi_i = 60\%$ for aggregated red blood cells). The solid lines are the spectral slopes (SSs) for the BSC_{SFM} computed with the structure factor model (SFM) and the dashed lines are the SSs for the BSC_{eq} computed with the effective medium theory combined with the SFM (EMTSFM).

the RBCs is around 1.12, the limit of applicability of the proposed EMTSFM in terms of particle size is surprisingly close to the optic limit $kR \leq 1.5$, when one considers a large relative refractive index of 1.8. In terms of particle concentration, the EMTSFM showed no limitation with respect to the studied hematocrit (up to 30%), contrary to the interference approximation, valid up to a volume fraction of 10%.

B. Variation of the Spectral Slope With ϕ_i and With r_{ag}

On the goodness of the EMTSFM modeling the SS, notice that the variations of SS with ϕ_i and r_{ag} followed similar trends for both SFM and EMTSFM (Figs. 4 and 8). The SS of the EMTSFM slightly underestimated the SS of the SFM with a maximum relative error of 9%. As can be observed in Fig. 8, as the aggregate size increased, the difference between slopes of the EMTSFM and SFM increased. This is due to the constant frequency bandwidth chosen between 5 and 15 MHz for all studied aggregate sizes. Indeed, in the frequency bandwidth between 4 MHz and the frequency position of the first peak, the relative error for the BSC_{eq} increased with the frequency as was shown in Figs. 3(c) and 3(d). Because the relative error was less than 30% for a mean product $kr_{ag} \leq 1.32$, the mean relative error in the frequency bandwidth 5 to 15 MHz for the smallest aggregates was smaller than the relative error for the largest aggregates in the same frequency bandwidth.

Contrary to blood modeling, the ultrasound characterization of tissues such as the breast [4] or the liver [25] assumes scatterers to be randomly distributed at a low number density. Tissue models are generally based on 3-D spatial autocorrelation functions describing the shape and isotropic random distribution of scatterers in the medium, and modeling of the spatial autocorrelation function could be Gaussian, spherical, or exponential [22], [25]. Based on these models, the SS is an indicator of the scatterer size, and a decrease in slope usually corresponds to an increase in scatterer size [25]. That is why it is interesting to discuss the variation of the SS with the aggregate size in the framework of the SFM or EMTSFM which consider the structure factor (see Fig. 8). For the lowest systemic hematocrit of 10%, the SS decreased with the increase in aggregate size. Because the hematocrit is low, the known behavior of the SS was observed. However, the SS increased with the aggregate size for systemic hematocrits of 20 and 30%. The structure factor, which models the spectral behavior of the scatterer spatial distributions, caused this behavior of the SS. Indeed, according to (1) [or (7), respectively], the BSC_{SFM} frequency dependence (or the BSC_{eq} frequency dependence) is determined by the frequency dependences of σ_b and S (or σ_{ag} and S_{ag}). To illustrate this, the structure factors S and S_{ag} corresponding, respectively, to the SFM and the EMTSFM are displayed in Fig. 9 for a fixed systemic hematocrit $\phi = 30\%$, a fixed internal hematocrit $\phi_i = 60\%$, and three aggregate radii $r_{ag}/a = 3.16$, 5.0, and 7.07. The plot of S is represented in

a larger frequency bandwidth up to 320 MHz to show the high-frequency oscillations of the structure factor around 1. In the frequency bandwidth 5 to 15 MHz, the frequency dependence of the structure factors S and S_{ag} do not follow a simple power law, because the structure factors S and S_{ag} versus frequency on a log-log scale are non-linear curves. One could observe that, in the frequency bandwidth 5 to 15 MHz, both the structure factors S and S_{ag} increase with the frequency, and the larger the aggregate size is, the larger is the increase. That is why the SS for both BSC_{SFM} and BSC_{eq} increased above 3 with the aggregate size for this studied systemic hematocrit of 30%. The increase of SS with the aggregate size we observed in the current study is consistent with an earlier 2-D numerical simulation study performed by Fontaine and Cloutier [17]. In this 2-D study, the SS between 5 and 25 MHz could increase from 3.1 to 3.3 when the level of aggregation increased for a hematocrit of 40%. Moreover, *in vitro* Couette flow experiments performed in [18] showed the SS greater than 4 between 9 and 15 MHz for shear rates of 2 and 10 s^{-1} at a systemic hematocrit of 40% [18, Fig. 4(b)].

It is important to note that we found that the SS decreased as ϕ_i increased for all studied systemic hematocrits. On the other hand, the behavior of the SS as a function of the aggregate size depended on the systemic hematocrit. As a consequence, the parameter SS seems well adapted to observe a change in the internal hematocrit. However, in experimental conditions where effects of aggregate size and internal hematocrit are mixed, the SS cannot be a useful index for blood characterization.

C. Computation of RBC Distributions

The method we proposed here to obtain the RBC spatial distribution did not take into consideration realistic interactions between RBCs. It was a simple and fast method to generate samples containing non-overlapping, identical, and isotropic aggregates. The main advantage of this method was the possibility to have various internal hematocrits with the same size of aggregates. The simulation results showed that the frequency position of the BSC first peak was very little affected by changes in the internal hematocrit, whereas it was greatly affected by changes in the aggregate size. Indeed, the change in frequency position was only 1.5 MHz (and, respectively, 2.1 MHz) for the hematocrit of 10% (and 20%) when the internal hematocrit increased from 30 to 60%. Moreover, theoretical predictions of the BSC with the SFM showed that its amplitude increases as r_{ag} and ϕ_i increase (see Figs. 3 and 5). To our knowledge, the influence of the internal hematocrit on the BSC has not been studied previously, mainly because of the simulation methods used to realize distributions of aggregating RBCs. These methods were based on particle dynamics or statistical mechanics [12], [13], [15]–[17] and had the objective of mimicking the rheological behavior of blood. The RBC distributions obtained showed aggregates with anisotropic shape [12], [13], [15], [17], [26] and a polydispersity in terms of aggregate sizes, aggregate shapes, and internal hematocrits [12], [13], [15]–[17]. As mentioned previously, contrary to those earlier studies, the 2-D simulation method we proposed for distributing RBCs allowed isolation of the effects of the aggregate size and internal hematocrit to better understand the role of each parameter. In that sense, our study has provided some insights into the influence of the aggregate size and internal hematocrit on the BSC frequency dependency. The internal hematocrit and the aggregate size can greatly influence the BSC amplitude. The frequency position of the BSC first peak was found not to be significantly affected by changes in the internal hematocrit, whereas it was greatly affected by changes in the aggregate size.

D. On the Use of the EMTSFM In Vivo

Although the present work allowed a fundamental study on the influences of the internal hematocrit and aggregate

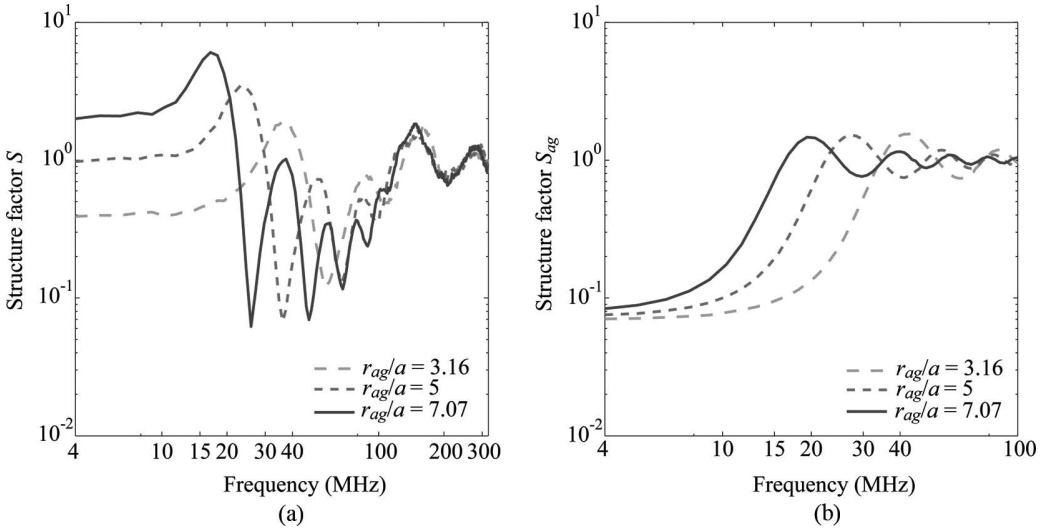


Fig. 9. (a) Structure factors S versus frequency used in the computation of the structure factor model (SFM) for a fixed systemic hematocrit $\phi = 30\%$, a fixed internal hematocrit $\phi_i = 60\%$, and three aggregate radii $r_{ag}/a = 3.16$, 5.0, and 7.07. (b) Structure factors S_{ag} versus frequency used in the computation of the effective medium theory combined with the SFM (EMTSFM) for the same aggregating conditions.

size on the BSC, the method we chose to distribute particles was limited to area fractions of aggregates $\phi_{ag} \leq 0.5$, area fraction of RBCs within aggregates $\phi_i \leq 0.6$, and systemic hematocrits $\phi \leq 0.3$. One might thus question the use of the EMTSFM for *in vivo* experiments with a physiological hematocrit ϕ typically varying between 0.3 and 0.5. It is important to recall that the only intensive computation with the proposed EMTSFM is the structure factor S_{ag}, which needs the computation of effective particle distributions. If one considers the application of the EMTSFM *in vivo*, 3-D effective particle distributions must be considered as well as the range of typical volume fractions. For example, the volume fraction of RBCs within aggregates ϕ_i may physiologically be larger than 60% because RBCs are deformable. By considering a systemic hematocrit of 40% (and 20%, respectively) and extrema values of ϕ_i between 60 and 90%, the volume fraction of aggregates ϕ_{ag} would then vary between 44 and 66% (between 22 and 33%). For future simulations, particle distributions in 3-D could be easily generated using a random number generator up to a volume fraction of approximatively 0.3, meaning that the method used to compute the BSC_{eq} in this paper may easily be applied in 3-D up to a volume fraction ϕ of 20%. For such low volume fractions of cells, one could envisage the use the EMTSFM for other biomedical applications such as cancer [4], [27], where the cells can be locally densely packed (see, for example, [4, Fig. 5]). In the case of blood applications, to deal with a physiological hematocrit of 40% and a maximum volume fraction of aggregates of 66%, one may envisage distributing particles in a random close packing configuration in which the attainable volume fraction could be up to 64% [28].

On the use of the EMTSFM *in vivo*, one can also question the practical value of that model assuming isotropic aggregates. In human blood, low shear rates can promote the formation of RBC aggregates having anisotropic (i.e., rouleaux) or isotropic (i.e., clump) structures. The rouleaux-like pattern is typically associated with normal blood. However, as the binding energy between RBCs increases with inflammation [29], aggregates form clump structures such as in diabetes mellitus [30], [31]. The assumption of isotropic aggregates in the EMTSFM is thus valid as far as we are concerned with the study of pathological states. In the case of normal human rouleaux of RBCs, if the EMTSFM is applied to estimate structural parameters such as the internal hematocrit and the aggregate size, this assumption would obviously create a bias against the parameter estimation.

Another important aspect to consider is the assumption of identical aggregates in the current EMTSFM implementation. Under *in vivo* conditions with ultrasound measurements on a blood vessel, the shear rate distribution varies with the radial position, and consequently, the aggregate size distribution does too. That is why the backscattered echoes from blood are generally analyzed over a rectangular or a Hamming window which is moved along the RF signal to examine the whole vessel at different depths [19], [32]. For example, at a central frequency of 25 MHz, the window length was typically around 400 μm [19], [32], [33]. RBC aggregates may thus be assumed to be locally identical. However, one may also expect that the aggregate size varies around a mean value for a given radial position within a blood vessel. An interesting simulation study was recently performed in 2-D by Vlad *et al.* [34]. According to this paper, the increase in particle size variance (or equivalently, in aggregate size variance) is expected to increase the BSC amplitude and not to significantly affect the frequency position of the BSC first peak [34, Fig. 2]. One could thus predict the bias against the parameter estimation with the EMTSFM if there is a variance in aggregate sizes. The discussion next considers small and large aggregates with respect to the observation of Vlad *et al.* [34].

In the case of small aggregates, the BSC first peak occurs at high frequencies and is thus generally not captured in the measured frequency bandwidth of the transducer (typically from 12 to 38 MHz for a 100% bandwidth at 25 MHz). Readers may refer to [18, Fig. 4(b)] and to [19, Fig. 3] to see measured BSCs from aggregating porcine RBCs in a controlled Couette flow. Because of the predicted increase in BSC amplitude with the increase in particle size variance [34], the assumption of identical aggregates in the current study may result in overestimations of the aggregate size and of the internal hematocrit. On the other hand, in the case of large aggregates, the BSC first peak occurs at low frequencies and would likely be within the measured frequency bandwidth of the transducer. In this case, the assumption of identical aggregates may not greatly affect the aggregate size estimation but may result in an overestimation of the internal hematocrit. The EMTSFM is thus expected to better estimate the size of large aggregates and the estimation of the internal hematocrit may be overestimated in the case of polydisperse aggregates, whatever their dimensions.

VI. Conclusion

The SFM is recognized to be a good model to simulate the BSC from aggregated RBCs. However, it cannot directly be applied to estimate the structural aggregate parameters in the framework of an inverse problem formulation. The EMTSFM was thus proposed to approximate the SFM and the goodness of fit of the EMTSFM in comparison with the SFM was examined. Contrary to the SFM, the EMTSFM can be implemented to estimate structural aggregate parameters.

The EMTSFM parameterizes the BSC by three indices: the aggregate size, the internal hematocrit (or aggregate compactness), and the systemic hematocrit. In comparison with the SFM, the EMTSFM provided accurate quantitative estimates of the BSC for $kr_{ag} \leq 1.32$ for the studied conditions. Moreover, even if $kr_{ag} > 1.32$, the EMTSFM provided a good approximation of the BSC: indeed, the BSC amplitude was well approximated in the frequency bandwidth between 4 MHz and the frequency position of the first peak, and the high-frequency positions of peaks were well identified.

Another important finding was the variation of the SS with ϕ_i and r_{ag}. The SSs for both BSC_{SFM} and BSC_{eq} computed with the SFM and EMTSFM followed the same trends of variations with ϕ_i and r_{ag}. We found that the SS decreased as the internal hematocrit increased for all studied systemic hematocrits. On the other hand, the behavior of the SS as a function of the aggregate size depended on the systemic hematocrit. For the largest hematocrits (20 and 30%), the SS increased as the aggregate size increased. Consequently, the SS cannot be a useful index for blood characterization of RBC aggregation.

To conclude, the EMTSFM approximates the SFM satisfactorily for a product $kr_{ag} \leq 1.32$. This suggests that the EMTSFM is an adequate model for blood characterization. An important contribution of this new model is the parameterization of the BSC with the aggregate compactness, which is a structural parameter not available in any other modeling strategies proposed in quantitative ultrasound imaging. In the future, it would be interesting to study two other important factors: the polydispersity in terms of aggregate sizes and internal hematocrits, and the non-sphericity of the aggregates. Another important study would be the estimation of structural aggregate parameters with the EMTSFM that could be compared with existing methods such as the SFSE [16], [18], [19] and the traditional Gaussian model developed by Lizzi [6], [25].

Appendix

The form factor is generally given in 3-D [21], [22]. That is why the demonstration to obtain the 2-D form factor of a fluid infinite cylinder of radius a is given here. In the Born approximation (i.e., for weak scattering conditions), the form factor has a simple expression that is related to the spatial Fourier spectrum of the impedance contrast (see [21, Eq. (5)] for the form factor expression in 3-D):

$$F(-2k,a) = \frac{1}{A_p^2\gamma_z^2}\left|\int_{A_p}\gamma_z(\mathbf{r})e^{2i\mathbf{kr}}\mathrm{d}^2\mathbf{r}\right|^2. \tag{12}$$

We can introduce cylindrical coordinates to obtain

$$\begin{aligned} F(-2k,a) &= \frac{1}{A_p^2\gamma_z^2}\left|\int_0^a\int_{-\pi}^{\pi}\gamma_z e^{2ikr\cos(\theta)}r\mathrm{d}r\mathrm{d}\theta\right|^2 \\ &= \frac{1}{A_p^2}\left|\int_0^a 2\pi r J_0(2kr)\mathrm{d}r\right|^2 \\ &= \frac{(2\pi)^2}{(\pi a^2)^2}\left(\frac{2kaJ_1(2ka)}{(2k)^2}\right)^2 \\ &= \left(\frac{J_1(2ka)}{ka}\right)^2, \end{aligned} \tag{13}$$

where J_0 is the Bessel function of the first kind of order 0.

Acknowledgments

The authors thank Prof. R. E. Challis for his helpful discussion on the effective medium approach.

References

[1] E. J. Feleppa, F. L. Lizzi, D. J. Coleman, and M. M. Yaremko, "Diagnostic spectrum analysis in ophthalmology: A physical perspective," *Ultrasound Med. Biol.*, vol. 12, no. 8, pp. 623–631, 1986.

[2] E. J. Feleppa, T. Liu, A. Kalisz, M. C. Shao, N. Fleshner, and V. Reuter, "Ultrasonic spectral-parameter imaging of the prostate," *Int. J. Imaging Syst. Technol.*, vol. 8, no. 1, pp. 11–25, 1997.

[3] M. C. Kolios, G. J. Czarnota, M. Lee, J. W. Hunt, and M. D. Sherar, "Ultrasonic spectral parameter characterization of apoptosis," *Ultrasound Med. Biol.*, vol. 28, no. 5, pp. 589–597, 2002.

[4] M. L. Oelze and J. F. Zachary, "Examination of cancer in mouse models using high frequency quantitative ultrasound," *Ultrasound Med. Biol.*, vol. 32, no. 11, pp. 1639–1648, 2006.

[5] L. Y. L. Mo and R. S. C. Cobbold, "Theoretical models of ultrasonic scattering in blood," in *Ultrasonic Scattering in Biological Tissues*, K. K. Shung and G. A. Thieme, Eds., Boca Raton, FL: CRC, 1993, ch. 5, pp. 125–170.

[6] H. Kitamura, B. Sigel, J. Machi, E. J. Feleppa, J. Sokil-Melgar, and J. Justin, "Roles of hematocrit and fibrinogen in red cell aggregation determined by ultrasonic scattering properties," *Ultrasound Med. Biol.*, vol. 21, no. 6, pp. 827–832, 1995.

[7] R. B. Ami, G. Barshtein, D. Zeltser, Y. Goldberg, I. Shapira, A. Roth, G. Keren, H. Miller, V. Prochorov, A. Eldor, S. Berliner, and S. Yedgar, "Parameters of red blood cell aggregation as correlates of the inflammatory state," *Am. J. Physiol. Heart Circ. Physiol.*, vol. 280, no. 5, pp. H1982–H1988, 2001.

[8] L. Y. L. Mo and R. S. C. Cobbold, "A stochastic model of the backscattered Doppler ultrasound from blood," *IEEE Trans. Biomed. Eng.*, vol. 33, no. 1, pp. 20–27, 1986.

[9] V. Twersky, "Low-frequency scattering by correlated distributions of randomly oriented particles," *J. Acoust. Soc. Am.*, vol. 81, no. 5, pp. 1609–1618, 1987.

[10] L. Y. L. Mo and R. S. C. Cobbold, "A unified approach to modeling the backscattered Doppler ultrasound from blood," *IEEE Trans. Biomed. Eng.*, vol. 39, no. 5, pp. 450–461, 1992.

[11] K. K. Shung, "On the ultrasound scattering from blood as a function of hematocrit," *IEEE Trans. Sonics Ultrason.*, vol. SU-29, no. 6, pp. 327–331, 1982.

[12] D. Savéry and G. Cloutier, "A point process approach to assess the frequency dependence of ultrasound backscattering by aggregating red blood cells," *J. Acoust. Soc. Am.*, vol. 110, no. 6, pp. 3252–3262, 2001.

[13] I. Fontaine, D. Savery, and G. Cloutier, "Simulation of ultrasound backscattering by red blood cell aggregates: Effect of shear rate and anisotropy," *Biophys. J.*, vol. 82, no. 4, pp. 1696–1710, 2002.

[14] I. Fontaine, M. Bertrand, and G. Cloutier, "A system-based approach to modeling the ultrasound signal backscattered by red blood cells," *Biophys. J.*, vol. 77, no. 5, pp. 2387–2399, 1999.

[15] D. Savéry and G. Cloutier, "Effect of red cell clustering and anisotropy on ultrasound blood backscatter: A Monte Carlo study," *IEEE Trans. Ultrason. Ferroelectr. Freq. Control*, vol. 52, no. 1, pp. 94–103, 2005.

[16] R. K. Saha, E. Franceschini, and G. Cloutier, "Assessment of accuracy of the structure-factor-size-estimator method in determining red blood cell aggregate size from ultrasound spectrum backscattering coefficient," *J. Acoust. Soc. Am.*, vol. 129, no. 4, pp. 2269–2277, 2011.

[17] I. Fontaine and G. Cloutier, "Modeling the frequency dependence (5–120 MHz) of ultrasound backscattering by red cell aggregates in shear flow at a normal hematocrit," *J. Acoust. Soc. Am.*, vol. 113, no. 5, pp. 2893–2900, 2003.

[18] F. T. H. Yu and G. Cloutier, "Experimental ultrasound characterization of red blood cell aggregation using the structure factor size estimator," *J. Acoust. Soc. Am.*, vol. 122, no. 1, pp. 645–656, 2007.

[19] F. T. H. Yu, E. Franceschini, B. Chayer, J. K. Armstrong, H. J. Meiselman, and G. Cloutier, "Ultrasonic parametric imaging of erythrocyte aggregation using the structure factor size estimator," *Biorheology*, vol. 46, no. 4, pp. 343–363, 2009.

[20] G. T. Kuster and M. N. Toksoz, "Velocity and attenuation of seismic waves in two-phase media: Part I. Theoretical formulations," *Geophysics*, vol. 39, no. 5, pp. 587–606, 1974.

[21] D. Savery and G. Cloutier, "High-frequency ultrasound backscattering by blood: Analytical and semi-analytical models of the erythrocyte cross section," *J. Acoust. Soc. Am.*, vol. 23, no. 4, pp. 3963–3971, 2007.

[22] M. F. Insana and D. G. Brown, "Acoustic scattering theory applied to soft biological tissues," in *Ultrasonic Scattering in Biological Tissues*, K. K. Shung and G. A. Thieme, Eds., Boca Raton, FL: CRC, 1993, ch. 4, pp. 76–124.
[23] R. D. Doolittle and H. Uberall, "Sound scattering by elastic cylindrical shells," *J. Acoust. Soc. Am.*, vol. 39, no. 2, pp. 272–275, 1965.
[24] V. P. Dick and A. P. Ivanov, "Extinction of light in dispersive media with high particle concentrations: Applicability limits of the interference approximation," *J. Opt. Soc. Am.*, vol. 16, no. 5, pp. 1034–1039, 1999.
[25] F. L. Lizzi, M. Ostromogilsky, E. J. Feleppa, M. C. Rorke, and M. M. Yaremko, "Relationship of ultrasonic spectral parameters to features of tissue microstructure," *IEEE Trans. Ultrason. Ferroelectr. Freq. Control*, vol. 34, no. 3, pp. 319–329, 1987.
[26] B. Lim and R. S. C. Cobbold, "On the relation between aggregation, packing and the backscattered ultrasound signal for whole blood," *Ultrasound Med. Biol.*, vol. 25, no. 9, pp. 1395–1405, 1999.
[27] T. E. Doyle, A. T. Tew, K. H. Warnick, and B. L. Carruth, "Simulation of elastic wave scattering in cells and tissues at the microscopic level," *J. Acoust. Soc. Am.*, vol. 125, no. 3, pp. 1751–1767, 2009.
[28] W. S. Jodrey and E. M. Tory, "Computer simulation of close random packing of equal spheres," *Phys. Rev. A*, vol. 32, no. 4, pp. 2347–2351, 1985.
[29] X. Weng, G. Cloutier, R. Beaulieu, and G. O. Roederer, "Influence of acute-phase proteins on erythrocyte aggregation," *Am. J. Physiol.*, vol. 271, no. 6, pp. H2346–H2352, 1996.
[30] H. Schmid-Schönbein, H. Malotta, and F. Striesow, "Erythrocyte aggregation: Causes, consequences and methods of assessment," *Ned. Tijdschr. Klin. Chem.*, vol. 15, pp. 88–97, 1990.
[31] H. Schmid-Schönbein, G. Gallasch, J. V. Gosen, E. Volger, and H. J. Klose, "Red cell aggregation in blood flow. I. New methods of quantification," *Klin. Wochenschr.*, vol. 54, no. 4, pp. 149–157, 1976.
[32] F. T. H. Yu, J. K. Armstrong, J. Tripette, H. J. Meiselman, and G. Cloutier, "A local increase in red blood cell aggregation can trigger deep vein thrombosis: Evidence based on quantitative cellular ultrasound imaging," *J. Thromb. Haemost.*, vol. 9, no. 3, pp. 481–488, 2011.
[33] E. Franceschini, F. T. H. Yu, F. Destrempes, and G. Cloutier, "Ultrasound characterization of red blood cell aggregation with intervening attenuating tissue-mimicking phantoms using the structure factor size and attenuation estimator," *J. Acoust. Soc. Am.*, vol. 127, pp. 1104–1115, 2010.
[34] R. M. Vlad, R. K. Saha, N. M. Alajez, S. Ranieari, G. J. Czarnota, and M. C. Kolios, "An increase in cellular size variance contributes to the increase in ultrasound backscatter during cell death," *Ultrasound Med. Biol.*, vol. 36, no. 9, pp. 1546–1558, 2010.



Emilie Franceschini received her M.S. degree in mechanical engineering from the Ecole Supérieure d'Ingénieurs de Marseille in 2003, and her Ph.D. degree in acoustics from the University of Provence, Marseille, 2006. In 2007, she was a Postdoctoral Fellow at the Laboratory of Biorheology and Medical Ultrasonics, Research Center of the University of Montreal Hospital, Montreal, QC. Since October 2008, she has been a Researcher at the French National Centre for Scientific Research (CNRS) in the Laboratory of Mechanics and Acoustics CNRS–UPR 7051, Marseille. Her current research interests include ultrasound imaging for biomedical applications, inverse problems, and ultrasound characterization of biological tissues at the microscopic level. She is a member of the French Acoustical Society (SFA) and IEEE.



Bloen Metzger received his M. S. degree from the Ecole Normale Supérieure de Lyon in 2003, and his Ph.D. degree in physics from the University of Provence, Marseille in 2006. In 2007, he was a Postdoctoral Fellow at the Benjamin Levich Institute, New York, NY. Since October 2007, he has been a Researcher at the French National Centre for Scientific Research (CNRS) in the laboratory IUSTI CNRS–UMR 6595, Marseille. His current research interests include microhydrodynamics, suspension flows at low Reynolds numbers, hydrodynamic diffusion, and heat and mass transfers in sheared suspensions.



Guy Cloutier (S'89–M'90–SM'07) obtained his B.Eng. degree in electrical engineering in 1984, and his M.Sc. and Ph.D. degrees in biomedical engineering in 1986 and 1990, respectively. Between 1990 and 1992, he was a post-doctoral fellow at The Pennsylvania State University with Prof. K. Kirk Shung. Prof. Cloutier is Director of the Laboratory of Biorheology and Medical Ultrasonics at the University of Montreal Hospital Research Center (http://www.lbum-crchum.com), and Professor of Radiology and Biomedical Engineering at the University of Montreal. His research interests are in quantitative ultrasound imaging of red blood cell aggregation; quasi-static and dynamic ultrasound elastography of atherosclerotic plaques, vascular aneurysms, deep vein thrombi, and breast cancers; 3-D morphologic and hemodynamic assessment of lower limb arterial stenoses; and mathematical and biomechanical modeling. He has published more than 120 peer-reviewed articles in these fields, holds 8 patents, and was recipient of the National Scientist award of the Fonds de Recherche en Santé du Québec (2004–2009).

PHYSICAL REVIEW E **82**, 010402(R) (2010)

Particle-pressure-induced self-filtration in concentrated suspensions

Sandeep D. Kulkarni,[1] Bloen Metzger,[2] and Jeffrey F. Morris[1]
[1]*Levich Institute and Chemical Engineering, City College of New York, New York, New York 10031, USA*
[2]*CNRS Laboratoire IUSTI, Marseille, France*
(Received 9 November 2009; published 21 July 2010)

Gravity-driven flow of concentrated suspensions (solid volume fraction $\phi > 0.50$) of non-Brownian spherical particles through a channel contraction at low Reynolds number is studied experimentally. The abrupt change in the flow area at the contraction forms distinct shear-rate regions having different fluid pressures, which are related to the concept of particle pressure. A model involving particle pressure variation coupled to a Darcy-like behavior for the fluid captures the phenomenon of "self-filtration," in which the effluent material has lower solid fraction than the input suspension. For $\phi \doteq \phi_{crit} \approx 0.58$, under added load from a weighted piston, the flow periodically alternates between fast and slow motions.

DOI: 10.1103/PhysRevE.82.010402 PACS number(s): 83.80.Hj, 82.70.Kj

I. INTRODUCTION

Flows of concentrated suspensions, from mud to ceramic precursor slurries, are commonly encountered in nature and industry. Suspensions range from colloidal dispersions to wet granular flows and thus have rich and varied dynamics. Concentrated colloidal suspension flows, with solid fraction ϕ approaching the maximum packing limit, exhibit phenomena including erratic speed fluctuations [1], confinement-induced flow oscillations [2], and "giant" stress fluctuations when the imposed shear rate approaches a transition value [3]. In liquid-immersed granular flows, dilatancy effects are seen for underwater granular avalanches [4], while flow instabilities are observed for inclined-plane flows beyond a critical inclination angle [5]. In this work, we address self-filtration, in which the effluent from a pressure-driven contraction flow has lower solid loading than the upstream material [1]; this phenomenon is similar to behavior previously studied in the context of suspension and paste extrusion [6,7]. The present study of flow of dense noncolloidal suspensions through a contraction elucidates the development of a flow-induced liquid pressure field and its relation to self-filtration in steady and oscillatory flows.

Particle migration is observed in a number of low-Reynolds-number suspension flows, including curvilinear [8] and pressure-driven rectilinear flows [9]. The migration has been modeled based on "particle pressure" as driving potential [10–12]. The particle pressure Π is the mean normal stress exerted by the particle phase $\Pi = -\frac{1}{3}[\Sigma^p_{11} + \Sigma^p_{22} + \Sigma^p_{33}]$ in a sheared suspension [13]. A compressive particle pressure Π quantifies the tendency of the dispersed phase to spread under shear. For this spreading to take place, liquid must replace the particles, and there must be an equal but opposite (and hence, suction) pressure in the suspending liquid $\Pi_{liq} = -\Pi(\dot{\gamma}, \phi)$; this is deduced as a result of the constraint of material incompressibility [12,14]. The relation of diffusion with liquid pressure in solid-liquid systems is a broadly relevant topic, e.g., for the ultrafiltration process, where theory of the suspending liquid pressure has established equivalency of Fick's and Darcy's laws [15]. Measurements at a porous boundary show evidence of opposing normal stresses in the two phases of sheared suspensions [16]. A clear demonstration is provided by measurement of the solvent pressure in a sheared suspension by a method analogous to measurement of osmotic pressure in quiescent solutions across a semipermeable membrane [14].

In this work, we study a contraction geometry, in which distinct shear-rate regions form and are found to have significantly different solvent phase suction pressures Π_{liq}. In addition, at large ϕ, we observe a reduction in suspension concentration downstream of the contraction relative to the upstream. This dilation or self-filtration and its relation to the flow-induced liquid pressures are studied for steady and oscillatory flow conditions.

II. EXPERIMENTS

The suspensions are composed of spherical polystyrene particles (380–500 μm in diameter; Maxi-Blast Inc.) and UCON 50-HB-660 (Dow Chemical), a Newtonian liquid with viscosity $\eta_f = 0.3$ Pa s and density 1.05 g cm^{-3} at 23°, very close to that of polystyrene. Inertia is negligible as $Re_p = \rho U a / \eta_f \ll 1$, where U is the average flow speed, a is the sphere radius, and ρ and η_f are the fluid density and viscosity, respectively. Flows of two more viscous liquids without particles, mixtures of UCON 75-H-90000 and 75-H-1400 (both of density 1.09 g cm^{-3}) having viscosities 36.5 Pa s (liquid X) and 7 Pa s (liquid Y) at 23°, are also studied.

The flow passes through a contraction in a vertical channel constructed of acrylic, with geometry shown in Fig. 1. The length, width (W) and depth of the channel are 20, 2.5, and 2 cm, respectively. The contraction is formed by symmetrically inserting two rectangular blocks of length 4 cm, depth 2 cm (equaling the channel depth), and of width yielding the ratio of the contraction channel width to that of original channel $w/W = 1/6$ (Fig. 1). A charge coupled device (CCD) camera (Basler $A1021$) images the flow along an axis orthogonal to the channel wall.

The suspension is poured into the channel to a level 15 cm above the contraction, and then a bottom plate restricting outflow is removed. The effluent material collected at the exit as the suspension column height drops about 7 cm is weighed; the particles are recovered by thorough washing and drying, then weighed separately to obtain the outlet concentration. Unless mentioned, the upper surface of the suspension is open to the atmosphere. Experiments with addi-

 ©2010 The American Physical Society

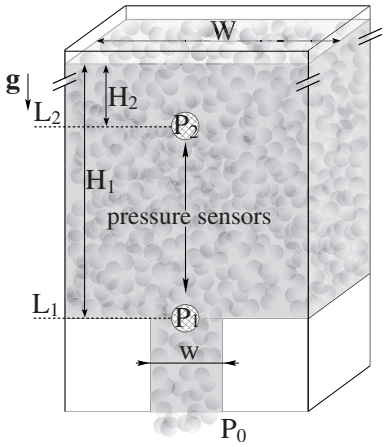


FIG. 1. Sketch of the experiment.

tional driving force use a closely fitted weighted piston placed on the upper surface of the mixture.

The liquid pressures P_1 and P_2 in flowing systems are measured by differential transducers (Omega; ± 1 psi) attached across holes in the channel wall at the contraction (level L_1) and 5 cm above (level L_2); reported pressures are thus relative to atmospheric. We confirm experimentally that the extent of significant nonaxial flow above the contraction level is $\approx 3w$: L_2, well above this zone, is in a unidirectional flow region. For suspension flows, liquid pressure alone rather than that exerted by both particles and fluid is measured by placing a mesh across each hole to retain the particles, as previously shown [14].

Figure 2 shows P_1 vs H_1 and P_2 vs H_2 for flow of different materials through the contraction, where H_1 and H_2 are heights of liquid (or suspension) column at respective measurement levels as shown in Fig. 1. For the pure liquid ($\phi=0$) flow, the pressures P_1 and P_2 are slightly below the corresponding static heads $\rho g H_1$ and $\rho g H_2$ (indicated by solid lines), as a result of viscous pressure losses accounted as $\Delta P_1 = \rho g H_1 - P_1$, as labeled in Fig. 2(a), and $\Delta P_2 = \rho g H_2 - P_2$. Figure 2 shows that, for pure liquids X and Y differing in viscosity by a factor of over five, the pressure (and hence ΔP) dependence on fluid-column height is identical. In contrast, suspension flows are characterized by reduction in liquid pressures, differing with volume fraction; this reduction for a suspension of $\phi=0.5$ is labeled as Π_1 in Fig. 2(a) to indicate the relationship to particle pressure which we develop later.

We note that the equivalence of pressure dependence for different viscosity pure liquids is a consequence of hydrodynamic linearity under the Stokes-flow conditions. The viscous loss ΔP_1 (or ΔP_2) is proportional to the shear stress $\eta_s \dot{\gamma}$. The shear rate may be written as $\dot{\gamma} = K(\mathbf{x})(\rho g H_1 / \eta_s)$, where $K(\mathbf{x})$ accounts for spatial variation in shear rate due to the contraction; the liquid column head $\rho g H_1$ above the contraction is the driving force for flow, and the resistance to flow scales with η_s. Thus $\Delta P_1 \sim \eta_s \dot{\gamma} \sim \rho g H_1$, confirming independence of viscous losses on material viscosity. The experimental data for both liquids yield $\Delta P_1 = 0.16 \rho g H_1$ and $\Delta P_2 = 0.03 \rho g H_1$. We have confirmed that in the absence of flow, the liquid pressure is equivalent to the static fluid head.

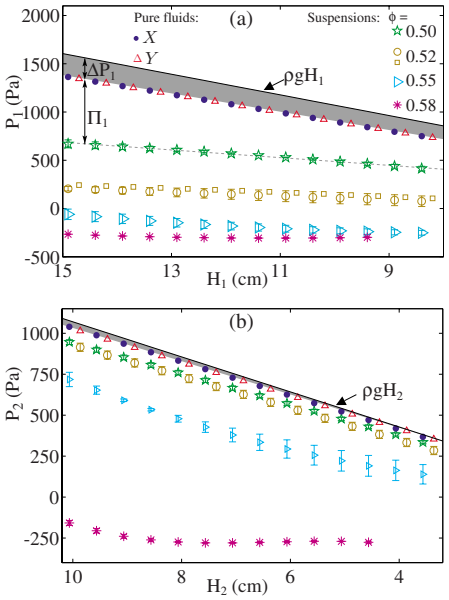


FIG. 2. (Color online) Liquid pressure of flowing systems measured (a) at L_1 in the beginning of the contraction; (b) at L_2, 5 cm vertically above L_1, plotted against fluid-column height at each measurement level. The legend in (b) applies also to (a). Viscosities are for liquid X 36.5 Pa s and for liquid Y 7 Pa s; For suspensions, the suspending fluid has $\eta_f=0.3$ Pa s, except for one set of data at P_1 for $\phi=0.52$, where $\eta_f=0.9$ Pa s (open squares).

Also, when the particle flow is restricted by a mesh at the bottom yielding Darcy flow through a column of particles, we find $dP/dz \approx 50$ Pa/cm for $\phi \geq 0.55$.

We now assess the liquid pressure for flow of suspensions at solid fraction $\phi=0.50$, 0.52, 0.55, and 0.58, with $\eta_f=0.30$ Pa s (in one case $\eta_f=0.9$ Pa s). The suspension effective viscosity satisfies $\eta_s = \eta_s^*(\phi)\eta_f$, where $\eta_s^* \sim (1-\phi/\phi_{max})^{-2}$, with $\phi_{max} \approx 0.6$ the maximum packing fraction. Recall that the liquid pressure *alone* is obtained by placing screens across holes at L_1 and L_2 [14] and that the pressure drop due to viscous losses is independent of the viscosity η_s and depends (for fixed density) only on fluid-column height H_1. Yet Fig. 2 shows that the measured liquid pressure values for a suspension decrease relative to those found for the pure liquid flows, and the decrease becomes more pronounced with increasing ϕ. The striking conclusion is that the additional decrease in liquid-phase pressures P_1 and P_2 observed for suspensions must be due to another physical process unique to a two-phase flow. As noted above, experiments [14] and simulations [12] have shown that uniform shearing in suspensions generates suction pressure in the suspending liquid $\Pi_{liq} = -\Pi(\dot{\gamma}, \phi)$, which is accounted here as

$$P_1 = \rho g H_1 - \Delta P_1 - \Pi_1, \quad P_2 = \rho g H_2 - \Delta P_2 - \Pi_2. \quad (1)$$

Because ΔP_1 and ΔP_2 were previously evaluated and independent of viscosity, we are able to determine Π_1 and Π_2 separately as a function of fluid-column height.

The measurement of self-filtration, where effluent concentration ϕ_{out}^m is below the input ϕ_{in}, is shown in Fig. 3. For

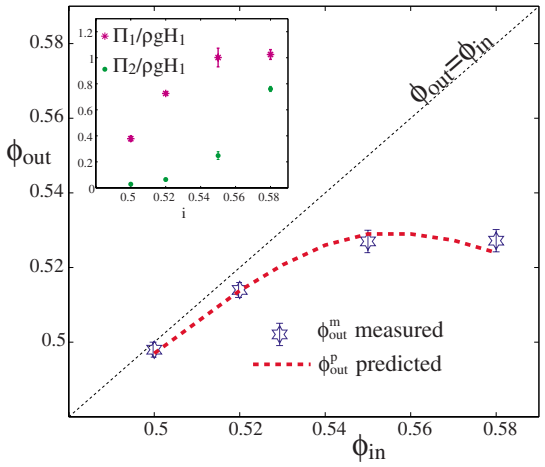


FIG. 3. (Color online) Comparison of the measured and predicted outlet particle volume fractions, ϕ_{out}^m and ϕ_{out}^p for contraction geometry $w/W=1/6$; the inset shows $\Pi_1/\rho g H_1$ and $\Pi_2/\rho g H_1$ plotted against input particle concentration ϕ_{in}.

$\phi_{in} \geq 0.55$, we find $\phi_{out}^m \approx 0.528 \pm 0.003$. Also, ϕ_{out}^m remains unchanged as the suspension column drops from $H_1=15$ to 8 cm. As a result of mass conservation and dilution of the effluent, the top of the column would become dry (as we observed in early experiments), unless a layer of a few mm depth of pure liquid is added on top of the suspension, and we follow this practice. Similar filtration behavior for colloidal systems was observed by [1], where it was suggested that colloidal jamming or flow instabilities are necessary to induce self-filtration. On the contrary, we observe this phenomena under steady flow.

III. MODEL

We now propose a mechanistic model for self-filtration invoking particle pressure and check its consistency with our experimental results. Constitutive modeling [10] and simulation at uniform shear and ϕ [11,12] have shown that particle pressure may be expressed as $\Pi=\eta_n\dot{\gamma}$ for non-Brownian suspensions, where $\eta_n=\eta_n^*(\phi)\eta_f$ is the suspension "normal stress viscosity" modeled as $\eta_n^* \sim 0.75(\phi/\phi_{max})^2(1-\phi/\phi_{max})^{-2}$. Combining the local rheology $\Pi \sim \eta_n\dot{\gamma}$ with dependence of the shear rate on driving head, $\dot{\gamma}=K(\mathbf{x})(\rho g H_1/\eta_s)$,

$$\frac{\Pi}{\rho g H_1} \approx K(\mathbf{x})q(\phi), \tag{2}$$

where $q(\phi)=\eta_n/\eta_s$ is the ratio of normal to shear stress (or inverse of friction coefficient in granular rheology) which increases with ϕ and is independent of η_f [10,17]. This formulation leads to the remarkable implication that for a fixed configuration and ϕ in gravity-driven flow, particle pressure is independent of the suspending liquid viscosity. We confirm this experimentally, as illustrated by the two identical curves for P_1 (within error bar) in Fig. 2(a) at $\phi=0.52$, for $\eta_f=0.3$ or 0.9 Pa s. A second implication is that at a given point in the channel the ratio $\Pi/\rho g H_1$ is independent of H_1 and increases sharply with ϕ. At the positions of the pressure sensors, we plot $\Pi_1/\rho g H_1$ and $\Pi_2/\rho g H_1$ averaged over $8<H_1<15$ cm for experiments with different ϕ_{in} (Fig. 3 inset). The small error bars confirm independence of H_1 and no considerable change in local ϕ over any experiment. The sharp rise in $\Pi_2/\rho g H_1$ with ϕ_{in} is expected, but given the constitutive modeling, the flattening of $\Pi_1/\rho g H_1$ suggests that ϕ at the contraction is reduced relative to ϕ_{in} and is essentially unchanged for $\phi_{in} \geq 0.55$. This interpretation of dilation at the contraction agrees with flattening of measured outlet concentration ϕ_{out}^m for $\phi_{in} \geq 0.55$.

To address the basis of the observed dilation, we now assume that the fluid pressure variation between contraction and bulk regions induces flow of liquid relative to particles, similar to Darcy flow, sucking liquid toward the contraction. This suction force can be estimated as $[\Pi_1-\Pi_2]_{\phi=\phi_{in}}$. A direct measure is difficult, as Π_1 is affected by dilation at the contraction. We reformulate the suction force in terms of Π_2 using Eq. (2),

$$[\Pi_1-\Pi_2]_{\phi=\phi_{in}} = (K_1/K_2-1)\Pi_2, \tag{3}$$

where we recall that K represents the spatial dependence of the shear rate. The flow of liquid relative to particles $\Delta V=V_l-V_p$ is stated as

$$\frac{\Delta V}{V_p} \sim \frac{\Pi_2/\eta_s}{\rho g H_1/\eta_s} \sim \frac{\Pi_2}{\rho g H_1}. \tag{4}$$

As $\Pi_2/\rho g H_1$ is independent of H_1, Eq. (4) implies steady dilution, consistent with the experimental observation. Writing a conservation equation for the particles and incorporating Eq. (4) yield

$$\phi_{out} = \frac{\phi_{in}V_p}{\phi_{in}V_p+(1-\phi_{in})V_l} = \frac{\phi_{in}}{1+A\dfrac{\Pi_2}{\rho g H_1}(1-\phi_{in})}. \tag{5}$$

Using the experimental measurement of $\Pi_2/\rho g H_1$ and ϕ_{out} from Fig. 3, we obtain the dimensionless $A=0.34\pm0.04$. With this value of A and a quadratic interpolation of $\Pi_2/\rho g H_1$ data in Fig. 3 inset, the prediction of the effluent concentration is in satisfactory agreement with the experimental data (Fig. 3); the downward curvature is an artifact of the quadratic fit.

Considering the spatial dependence of the shear rate $\dot{\gamma}=K(\mathbf{x})(\rho g H_1/\eta_s)$, one would expect $K_1/K_2=6$ in the present geometry where the ratio of the contraction channel $w/W=1/6$. However, for $\phi=0.50$ and 0.52, where the observed dilation is small, Eq. (2) suggests $K_1/K_2 \approx \Pi_1/\Pi_2 \approx 13$. This larger value shows that K_1/K_2 is influenced both by the variation in shear rate and change in flow type from pure shear flow to extensional flow at the contraction. We also conducted experiments with smaller particles (150–250 μm in diameter) at $\phi=0.58$. The pressure responses P_1 and P_2 as well as the effluent concentration ($\phi_{out}^m \approx 0.53$) remains unaffected by the particle size for the studied range.

IV. OSCILLATORY FLOW UNDER ADDED LOAD

We now consider flow under additional load supplied by a 100 g piston added to the top of the mixture. The weight is

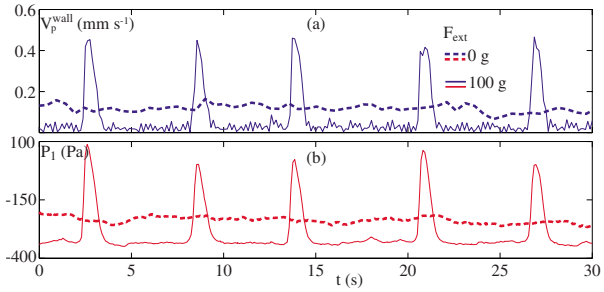


FIG. 4. (Color online) (a) Velocity, V, and (b) liquid pressure, P_1, at the contraction for $\phi=0.58$ and $w/W=1/6$: dashed lines correspond to no external force; solid lines correspond to a weighted piston of 100 g load.

equivalent to 2 kPa additional pressure. Images are captured using a high magnification lens (Sigma DG HSM) with wide field of view (1.5 cm$\times$2 cm) focused on the contraction, illuminated by white light. Particle tracking velocimetry (PTV) is used to obtain the average particle speed along the wall. The bulk flow determined from the decline of the suspension column is 4–5 times the observed near wall motion for both steady and oscillatory flows. In the contraction of $w/W=1/6$, at $\phi=\phi_{crit}\approx 0.58$ with the weighted piston, PTV shows that the flow alternates between fast and slow motions with a surprising periodicity as shown in Fig. 4 (see also the movie available with the online version of the paper [18]). The oscillations are absent below a particular threshold load as seen in earlier work [2], but the oscillation frequency here decreases with added load, contrary to that study. Robustness of periodic flow to changes in geometry, suspending liquid viscosity and piston weight has been established but to be brief we focus on $\phi=0.58$, $w/W=1/6$ and added piston load of 100 g. Under this condition, the measured effluent concentration is $\phi_{out}^{m}=0.527\pm 0.003$ with the stated variance based on multiple experimental trials. Figure 4 shows that the particle speed in slow motion of the alternating flow is lower than with no external force. This suggests the weighted piston makes contact with particles at the upper surface, activating a granular network which supports most of the piston weight. Slow creep of the deforming granular network causes a decrease in liquid pressure P_1. When the network abruptly breaks, as indicated by the faster motion, the internal stress in the particle phase is released and the liquid pressure goes up simultaneously (Fig. 4). Thus, dilational motion near the contraction in the slow regime ultimately leads to breakage of the granular network. As the diluted batch passes through the contraction, the granular network is reestablished and begins again to creep, thus leading to periodic flow variation. Similar correlation between flow speed and pore pressure is observed in avalanching flows [4]. As a final point, note that the threshold load needed to induce oscillations is approximately 50 g for typical particles (380–500 μm in diameter) and 500 g for smaller particles (150–250 μm in diameter), suggesting the influence of channel size/particle ratio.

We conclude that in concentrated suspension flow in a contraction geometry, the change in shear rate at the contraction induces a spatially varying pressure field in the liquid phase, with the pressure reduced well below the value expected due to viscous losses. In the same flow, we observe self-filtration with a reduced outlet solid concentration relative to the imposed inlet concentration. We have related the reduction in the liquid pressure field to particle pressure and proposed a model which rationalizes the self-filtration phenomenon. When driving the system with a weighted piston at $\phi_{crit}\approx 0.58$, the flow shows consistent periodic oscillations where fast and slow motion of the suspension correspond, respectively, to low and high internal stress states of the particle phase. The same type of coupling involving dilation and failure of the solid network seems responsible for this striking phenomenon. Note that the liquid pressure in the porous medium state of the mixture is equivalent to a pore pressure in granular and soil mechanics [19]. We conclude that the concept of pore pressure is directly related to shear-induced particle pressure, Π, in suspensions, which has been established both as a nonequilibrium continuation of osmotic pressure [12] and a general drive toward particle phase dilation [14].

[1] M. D. Haw, Phys. Rev. Lett. **92**, 185506 (2004).
[2] L. Isa, R. Besseling, A. N. Morozov, and W. C. K. Poon, Phys. Rev. Lett. **102**, 058302 (2009).
[3] D. Lootens, H. Van Damme, and P. Hebraud, Phys. Rev. Lett. **90**, 178301 (2003).
[4] M. Pailha and O. Pouliquen, J. Fluid Mech. **633**, 115 (2009).
[5] C. Cassar, M. Nicolas, and O. Pouliquen, Phys. Fluids **17**, 103301 (2005).
[6] P. Yaras, D. M. Kalyon, and U. Yilmazer, Rheol Acta. **33**, 48 (1994).
[7] S. L. Rough, J. Bridgwater, and D. I. Wilson, Int. J. Pharm. **204**, 117 (2000).
[8] D. Leighton and A. Acrivos, J. Fluid Mech. **181**, 415 (1987).
[9] C. J. Koh, P. Hookham, and L. G. Leal, J. Fluid Mech. **266**, 1 (1994).
[10] J. F. Morris and F. Boulay, J. Rheol. **43**, 1213 (1999).
[11] A. Sierou and J. F. Brady, J. Rheol. **46**, 1031 (2002).
[12] Y. Yurkovetsky and J. F. Morris, J. Rheol. **52**, 141 (2008).
[13] D. J. Jeffrey, J. F. Morris, and J. F. Brady, Phys. Fluids A **5**, 2317 (1993).
[14] A. Deboeuf, G. Gauthier, J. Martin, Y. Yurkovetsky, and J. F. Morris, Phys. Rev. Lett. **102**, 108301 (2009).
[15] S. S. L. Peppin, J. A. W. Elliott, and M. G. Worster, Phys. Fluids **17**, 053301 (2005).
[16] D. Prasad and H. K. Kytomaa, Int. J. Multiphase Flow **21**, 775 (1995).
[17] I. E. Zarraga, D. A. Hill, and D. T. Leighton, J. Rheol. **44**, 185 (2000).
[18] See supplementary material at http://link.aps.org/supplemental/10.1103/PhysRevE.82.010402 for a movie showing the periodic flow, $\phi=0.58$, $w/W=1/6$, $F_{ext}=100$ g.
[19] R. M. Iverson, M. E. Reid, and R. G. LaHusen, Annu. Rev. Earth Planet. Sci. **25**, 85 (1997).

Bibliographie

[1] Arp, P., and Mason, S. The kinetics of flowing dispersions : Doublets of rigid spheres (theoretical). *Journal of colloid and interface science 61*, 1 (1977), 21–43.

[2] Batchelor, G. The effect of brownian motion on the bulk stress in a suspension of spherical particles. *Journal of fluid mechanics 83*, 01 (1977), 97–117.

[3] Blanc, F., Peters, F., and Lemaire, E. Experimental signature of the pair trajectories of rough spheres in the shear-induced microstructure in noncolloidal suspensions. *Physical review letters 107*, 20 (2011), 208302.

[4] Boyer, F., Guazzelli, É., and Pouliquen, O. Unifying suspension and granular rheology. *Physical Review Letters 107*, 18 (2011), 188301.

[5] Brady, J. F., and Bossis, G. Stokesian dynamics. *Annual review of fluid mechanics 20*, 1 (1988), 111–157.

[6] Bricker, J. M., and Butler, J. E. Correlation between stresses and microstructure in concentrated suspensions of non-brownian spheres subject to unsteady shear flows. *Journal of rheology 51*, 4 (2007), 735–759.

[7] Cecile, C., Berut, A., Metzger, B., and Forterre, Y. Revealing the frictional transition in the shear thickening transition. *soumis à PNAS*.

[8] Cichocki, B., and Felderhof, B. Short-time diffusion coefficients and high frequency viscosity of dilute suspensions of spherical brownian particles. *The Journal of chemical physics 89*, 2 (1988), 1049–1054.

[9] Corte, L., Chaikin, P., Gollub, J. P., and Pine, D. Random organization in periodically driven systems. *Nature Physics 4*, 5 (2008), 420–424.

[10] Corté, L., Gerbode, S. J., Man, W., and Pine, D. Self-organized criticality in sheared suspensions. *Physical review letters 103*, 24 (2009), 248301.

[11] Da Cunha, F., and Hinch, E. Shear-induced dispersion in a dilute suspension of rough spheres. *Journal of Fluid Mechanics 309* (1996), 211–223.

[12] Drazer, G., Koplik, J., Khusid, B., and Acrivos, A. Deterministic and stochastic behaviour of non-brownian spheres in sheared suspensions. *Journal of Fluid Mechanics 460* (2002), 307–335.

[13] Duplat, J., Innocenti, C., and Villermaux, E. A nonsequential turbulent mixing process. *Physics of Fluids 22*, 3 (2010), 035104.

[14] Düring, G., Bartolo, D., and Kurchan, J. Irreversibility and self-organization in hydrodynamic echo experiments. *Physical Review E 79*, 3 (2009), 030101.

[15] Durlofsky, L. J., and Brady, J. F. Dynamic simulation of bounded suspensions of hydrodynamically interacting particles. *Journal of Fluid Mechanics 200* (1989), 39–67.

[16] Eckstein, E. C., Bailey, D. G., and Shapiro, A. H. Self-diffusion of particles in shear flow of a suspension. *Journal of Fluid Mechanics 79*, 01 (1977), 191–208.

[17] Einstein, A. Eine neue bestimmung der moleküldimensionen. *Annalen der Physik 324*, 2 (1906), 289–306.

[18] Ferrini, F., Ercolani, D., De Cindio, B., Nicodemo, L., Nicolais, L., and Ranaudo, S. Shear viscosity of settling suspensions. *Rheologica Acta 18*, 2 (1979), 289–296.

[19] Gallier, S., Lemaire, E., Peters, F., and Lobry, L. Rheology of sheared suspensions of rough frictional particles. *Journal of Fluid Mechanics 757* (2014), 514–549.

[20] Goldstein, R. E., and van de Meent, J.-W. A physical perspective on cytoplasmic streaming. *Interface focus 5*, 4 (2015), 20150030.

[21] Jánosi, I. M., Tél, T., Wolf, D. E., and Gallas, J. A. Chaotic particle dynamics in viscous flows : The three-particle stokeslet problem. *Physical Review E 56*, 3 (1997), 2858.

[22] Jeanneret, R., and Bartolo, D. Geometrically protected reversibility in hydrodynamic loschmidt-echo experiments. *Nature communications 5* (2014).

[23] Karnis, A., Goldsmith, H., and Mason, S. The kinetics of flowing dispersions : I. concentrated suspensions of rigid particles. *Journal of Colloid and Interface Science 22*, 6 (1966), 531–553.

[24] Krieger, I. M., and Dougherty, T. J. A mechanism for non-newtonian flow in suspensions of rigid spheres. *Transactions of the Society of Rheology 3*, 1 (1959), 137–152.

[25] Ladd, A. J. Hydrodynamic transport coefficients of random dispersions of hard spheres. *The Journal of chemical physics 93*, 5 (1990), 3484–3494.

[26] Lerner, E., Düring, G., and Wyart, M. A unified framework for non-brownian suspension flows and soft amorphous solids. *Proceedings of the National Academy of Sciences 109*, 13 (2012), 4798–4803.

[27] Luying, W., Donald, L. K., Xiaolong, Y., and Cohen, C. Hydrodynamic diffusion and mass transfer across a sheared suspension of neutrally buoyant spheres. *PHYSICS OF FLUIDS 21*, 5 (2009), 033303.

[28] Mangan, N., Reichhardt, C., and Reichhardt, C. O. Reversible to irreversible flow transition in periodically driven vortices. *Physical review letters 100*, 18 (2008), 187002.

[29] Marchioro, M., and Acrivos, A. Shear-induced particle diffusivities from numerical simulations. *Journal of fluid mechanics 443* (2001), 101–128.

[30] Menon, G. I., and Ramaswamy, S. Universality class of the reversible-irreversible transition in sheared suspensions. *Physical Review E 79*, 6 (2009), 061108.

[31] Metzger, B., and Butler, J. E. Irreversibility and chaos : Role of long-range hydrodynamic interactions in sheared suspensions. *Physical Review E 82*, 5 (2010), 051406.

[32] Metzger, B., and Butler, J. E. Clouds of particles in a periodic shear flow. *Physics of Fluids 24*, 2 (2012), 021703.

[33] Metzger, B., Nicolas, M., and Guazzelli, É. Falling clouds of particles in viscous fluids. *Journal of Fluid Mechanics 580* (2007), 283–301.

[34] Metzger, B., Pham, P., and Butler, J. E. Irreversibility and chaos : Role of lubrication interactions in sheared suspensions. *Physical Review E 87*, 5 (2013), 052304.

[35] Meunier, P., and Villermaux, E. The diffusive strip method for scalar mixing in two dimensions. *Journal of fluid mechanics 662* (2010), 134–172.

[36] Morris, J. F. A review of microstructure in concentrated suspensions and its implications for rheology and bulk flow. *Rheologica acta 48*, 8 (2009), 909–923.

[37] Morris, J. F., and Boulay, F. Curvilinear flows of noncolloidal suspensions : The role of normal stresses. *Journal of rheology 43*, 5 (1999), 1213–1237.

[38] Nguyen, N.-Q., and Ladd, A. J. Sedimentation of hard-sphere suspensions at low reynolds number. *Journal of Fluid Mechanics 525* (2005), 73–104.

[39] Nicolai, H., Herzhaft, B., Hinch, E., Oger, L., and Guazzelli, E. Particle velocity fluctuations and hydrodynamic self-diffusion of sedimenting non-brownian spheres. *Physics of Fluids 7*, 1 (1995), 12–23.

[40] Pailha, M., and Pouliquen, O. A two-phase flow description of the initiation of underwater granular avalanches. *Journal of Fluid Mechanics 633* (2009), 115–135.

[41] Pham, P., Metzger, B., and Butler, J. E. Particle dispersion in sheared suspensions : Crucial role of solid-solid contacts. *Physics of Fluids 27*, 5 (2015), 051701.

[42] Pine, D., Gollub, J. P., Brady, J., and Leshansky, A. Chaos and threshold for irreversibility in sheared suspensions. *Nature 438*, 7070 (2005), 997–1000.

[43] Pozrikidis, C. A spectral-element method for particulate stokes flow. *Journal of Computational Physics 156*, 2 (1999), 360–381.

[44] Ranz, W. E. Applications of a stretch model to mixing, diffusion, and reaction in laminar and turbulent flows. *AIChE Journal 25*, 1 (1979), 41–47.

[45] Ryohei, S., Romain, M., F, M. J., and Denn, M. M. Discontinuous shear thickening of frictional hard-sphere suspensions. *Physical review letters 111*, 21 (2013), 218301.

[46] Snook, B., Butler, J. E., and Guazzelli, É. Dynamics of shear-induced migration of spherical particles in oscillatory pipe flow. *Journal of Fluid Mechanics 786* (2015), 128–153.

[47] Snook, B., Guazzelli, E., and Butler, J. E. Vorticity alignment of rigid fibers in an oscillatory shear flow : Role of confinement. *Physics of Fluids 24*, 12 (2012), 121702.

[48] Souzy, M., Lhuissier, H., Villermaux, E., and Metzger, B. Stretching and mixing in sheared particulate suspensions. *Journal of Fluid Mechanics 812* (2017), 611–635.

[49] Souzy, M., Pham, P., and Metzger, B. Taylor's experiment in a periodically sheared particulate suspension. *Physical Review Fluids 1*, 4 (2016), 042001.

[50] Souzy, M., Yin, X., Villermaux, E., Abid, C., and Metzger, B. Super-diffusion in sheared suspensions. *Physics of Fluids 27*, 4 (2015), 041705.

[51] Stokes, G. G. *On the effect of the internal friction of fluids on the motion of pendulums*, vol. 9. Pitt Press, 1851.

[52] Workamp, M., Saggiomo, V., and Dijksman, J. A. A simple low pressure drop suspension-based microfluidic mixer. *Journal of Micromechanics and Microengineering 25*, 9 (2015), 094003.

[53] Wyart, M., and Cates, M. Discontinuous shear thickening without inertia in dense non-brownian suspensions. *Physical review letters 112*, 9 (2014), 098302.

[54] Yeo, K., and Maxey, M. R. Simulation of concentrated suspensions using the force-coupling method. *Journal of computational physics 229*, 6 (2010), 2401–2421.